Rational Design of Afterglow and Storage Phosphors

Lyu, T.

DOI
10.4233/uuid:11fc3020-2e13-4825-92ca-d4c9f7fd6815

Publication date
2020

Document Version
Final published version

Citation (APA)
Lyu, T. (2020). *Rational Design of Afterglow and Storage Phosphors*. https://doi.org/10.4233/uuid:11fc3020-2e13-4825-92ca-d4c9f7fd6815

Rational Design of Afterglow and Storage Phosphors

Rational Design of Afterglow and Storage Phosphors

Dissertation

for the purpose of obtaining the degree of doctor
at Delft University of Technology
by the authority of the Rector Magnificus, prof. dr. ir. T. H. J. J. van der Hagen,
chair of the Board for Doctorates
to be defended publicly on
Wednesday, 9 September 2020 at 10:00 o'clock

by

Tianshuai Lyu

Master of Science in Materials Science,
Kunming University of Science and Technology, Kunming, China,
born in Anshun, Guizhou, China.

This dissertation has been approved by the promotor:

Prof. dr. P. Dorenbos

Composition of the doctoral committee:

Rector Magnificus,	chairman
Prof. dr. P. Dorenbos,	Delft University of Technology
Independent members:	
Prof. dr. P. Smet,	Ghent University, Belgium
Prof. dr. R.J.M. Konings,	Joint Research Center EC, Karlsruhe (Germany) / Delft University of Technology
Prof. dr. C. Pappas,	Delft University of Technology
Prof. dr. E.H. Brück,	Delft University of Technology
Dr. H.T. Hintzen,	Delft University of Technology
Prof. dr. L.D.A. Siebbeles,	Delft University of Technology

The research resulting in this thesis was partly funded by the China Scholarship Council (CSC).

The research presented in this thesis has been carried out in the Delft University of Technology, Faculty of Applied Sciences, Department of Radiation Science and Technology, Section Luminescence Materials, Mekelweg 15, 2629JB Delft, The Netherlands.

Keywords: afterglow, storage phosphor, energy storage, Bi^{2+}, Bi^{3+}, lanthanides, charge carrier trapping processes, trap depth engineering
Printed by: ProefschriftMaken || www.proefschriftmaken.nl
Cover design: Tianshuai Lyu

ISBN 978-94-6380-906-1

I wish to dedicate this thesis to my country,
to my parents, and to my wife

Table of Contents

1

General introduction

1.1 Introduction to afterglow

The objective of this thesis is to understand and to tailor the capturing and detrapping processes of electrons and holes in afterglow and storage phosphors. With that we aim to arrive at rational design concepts for the development of new afterglow and storage phosphors with high charge carrier storage capacity.

Afterglow, also named persistent luminescence, is known as a self-sustained light emission phenomenon[1] where a material first stores charge carriers liberated by excitation with ultraviolet light, visible light, α-, β-, γ-, or X-rays, and then continuously emits photons from seconds to hours after the excitation source is removed[2-6].

An afterglow phosphor is an inorganic compound in which anions and cations are periodically arranged in a crystalline lattice that contains the luminescence centre(s) and the charge carrier capturing centres[7-9]. The luminescence centre, also known as the recombination centre, is where holes and electrons are recombined to generate photon emission. The charge carrier capturing centres are often host intrinsic defects or dopants where electrons and holes can be captured for a period of time and then upon heating or optical stimulation can be released[10-13].

Thermoluminescence (TL), also called thermally stimulated luminescence, is a photon emission phenomenon when a phosphor is thermally stimulated[14]. Fig. 1.1a) shows an illustration of the thermoluminescence (TL) technique. A sample is first heated from a starting to the ending temperature to empty all randomly filled traps and next cooled to the starting temperature usually 300 K or 100 K. The sample is charged at that starting temperature for a certain amount of time in the dark by using ionizing radiation or monochromatic photons and next gradually heated to the end temperature in a controlled way by using a constant heating rate like 1 K/s[15]. A bandpass filter is usually placed between the photomultiplier (PMT) and the sample to select the characteristic emission from the sample[16]. A so-called thermoluminescence (TL) glow curve is obtained by plotting the thermally stimulated luminescence as a function of temperature. Fig. 1.1b) shows such a TL glow curve for the commercial afterglow phosphor $SrAl_2O_4:Eu^{2+},Dy^{3+}$ after β irradiation charging. A TL glow peak near 328 K with Eu^{2+} green emission is observed when using a heating rate of 1 K/s. For afterglow phosphor applications at room temperature, the TL glow peak should appear near 300 K. The trap depth of a charge carrier capturing centre is approximately proportional to the temperature where a TL glow curve emerges. Equations to describe a TL glow have been reviewed by Bos in Ref. [14]. Assuming first-order TL-recombination kinetics, the trap depth of a charge carrier capturing centre in a compound can be estimated by using the peak maximum (T_m) of the TL glow curve and solving[14, 17-20]

$$\frac{\beta E}{kT_m^{\ 2}} = s \times \exp\left(-\frac{E}{kT_m}\right) \tag{1.1}$$

in which s (s^{-1}) is the frequency factor, β stands for the heating rate (K/s), E (eV) denotes the trap depth, and k is the Boltzmann constant.

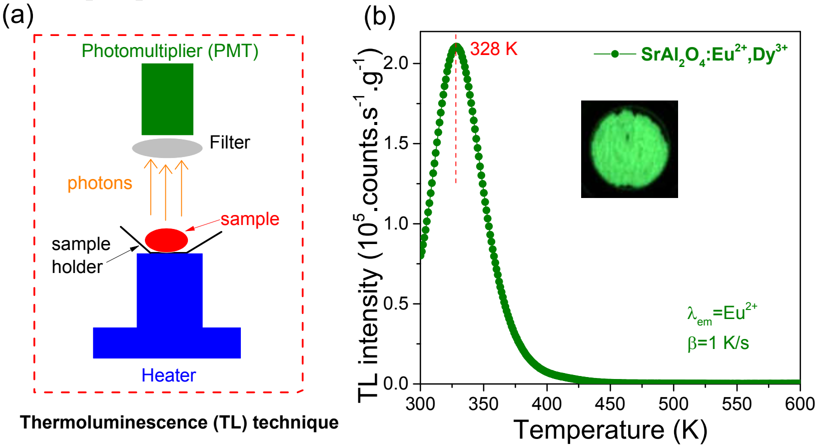

Fig. 1.1. (a) Demonstration of the thermoluminescence (TL) technique. (b) TL glow curve of the commercial afterglow phosphor $SrAl_2O_4:Eu^{2+},Dy^{3+}$ (G-300M, LumiNova) recorded at a heating rate of 1 K/s after 300s β irradiation while monitoring the Eu^{2+} emission. The inset in b) shows a photograph of the afterglow from $SrAl_2O_4:Eu^{2+},Dy^{3+}$ after 365 nm UV lamp charging for 30s in the dark at room temperature.

The afterglow phenomenon is known from the ancient Song dynasty of China (960-1279 A.D.)[4, 21-23]. Y.Wen recorded a story describing an afterglow painting in a Chinese miscellaneous book named "*Xiang-Shan Ye-Lu*". In that painting, when viewed in daylight, a cow emerged as eating grass outside of a barn, but it emerged as resting inside of the barn when viewed in the dark[24]. The glow-in-the-dark ink used for this painting could be the first man-made afterglow phosphor that may be imported from Japan because at that time there were frequent product trades between Japan and China[4].

The beginning of modern afterglow materials dates back to 1602. An Italian alchemist called Vincenzo Cascariolo synthesized an orange afterglow stone by sintering a barite ($BaSO_4$) mineral obtained from Bologna at high temperature under a reducing atmosphere[23]. About 400 years later, the afterglow stone was reproduced and studied further by M. Lastusaari *et al.* [25] using modern experimental facilities like X-ray powder diffraction, photoluminescence spectroscopy, and thermoluminescence technique. Results showed that an afterglow emission band peaking near ~610 nm and ranging from 475 to 800 nm was observed, which was attributed to the $3d^94s^1 \rightarrow 3d^{10}$ transition of Cu^+ in BaS. The charge carrier capturing and detrapping processes in Cu^+-codoped BaS still remain unclear.

During the 20th century, limited work has been done to discover new afterglow phosphors or to unravel charge carrier trapping processes. It turns out that Cu^+, Co^{2+}-codoped ZnS with a green emission band peaking near 530 nm is the dominant afterglow phosphor. To enhance its afterglow brightness for practical applications, radioactive elements like radium (Ra), tritium (^3H), or promethium (Pm) are codoped into $ZnS:Cu^+,Co^{2+}$ to induce ionizing radiation that continuously charges or excites the afterglow phosphor[4, 26]. The use of radioactive elements in afterglow phosphors has led to both environmental contamination and health problems. The most tragic story is about the "radium girls" who died because of the over exposure to ionization radiation during working with the radioactive afterglow phosphor in the United States Radium Company around 1917[27]. The sulphide-based $ZnS:Cu^+,Co^{2+}$ afterglow phosphor is hygroscopic, which limits its long-term durability.

A new generation afterglow phosphor $SrAl_2O_4:Eu^{2+},Dy^{3+}$ was developed by the Japanese company (Nemoto & Co., Ltd.) after two years of trial-and-error research in 1996[28]. Fig. 1.2a) shows a photograph of the commercial product of $SrAl_2O_4:Eu^{2+},Dy^{3+}$ (LumiNova). Upon full charging by UV-light, about 30h afterglow intensity above 0.32 mcd/m^2 can be observed by the dark adapted eye in $SrAl_2O_4:Eu^{2+},Dy^{3+}$[4]. The ZnS-based afterglow phosphor has been replaced by $SrAl_2O_4:Eu^{2+},Dy^{3+}$ in the business market because of its better properties like radioactive element free, ten times higher brightness and longer afterglow duration time[4]. Since 1996, the research topic on afterglow phosphors has attracted great interest. During the past 20 years, a lot of research work has been carried out and several good afterglow phosphors with different afterglow colours have been developed like $CaAl_2O_4:Eu^{2+},Nd^{3+}$ (blue)[29, 30], $Sr_2MgSi_2O_7:Eu^{2+},Dy^{3+}$ (blue)[31], $Sr_4Al_{14}O_{25}:Eu^{2+},Dy^{3+}$ (cyan)[32], $Y_2O_2S:Eu^{3+},Mg^{2+},Ti^{4+}$ (red)[24, 33], $(Ca_{1-x}Sr_x)S:Eu^{2+}$ (red)[34], $Zn_3Ga_2Ge_2O_{10}:Cr^{3+}$ (infrared)[35], and $Y_3Al_2Ga_3O_{12}:Er^{3+},Ce^{3+},Cr^{3+}$ (infrared)[36].

Fig. 1.2b)-d) show the characteristic display applications of safety signage, watch dials, and afterglow indicators using the commercial $SrAl_2O_4:Eu^{2+},Dy^{3+}$ (LumiNova) afterglow phosphor in the dark. In 2011, the commercial $SrAl_2O_4:Eu^{2+},Dy^{3+}$ afterglow phosphor paint was coated on the edges of the highway (N329) near Amsterdam in the Netherlands. The afterglow phosphor paint can be charged by sunlight during daytime and gives more than 8h green persistent luminescence that illuminates the edges of highway in the dark. Drivers can be guided since our eyes are very sensitive to the green afterglow light. Another new application recently appeared in the long-term in vivo optical imaging by using infrared afterglow nanoparticle phosphors[37]. High contrast image can be obtained because the infrared afterglow phosphor can continuously emit infrared photons without real-time external excitation resulting in high signal-to-noise ratio[38].

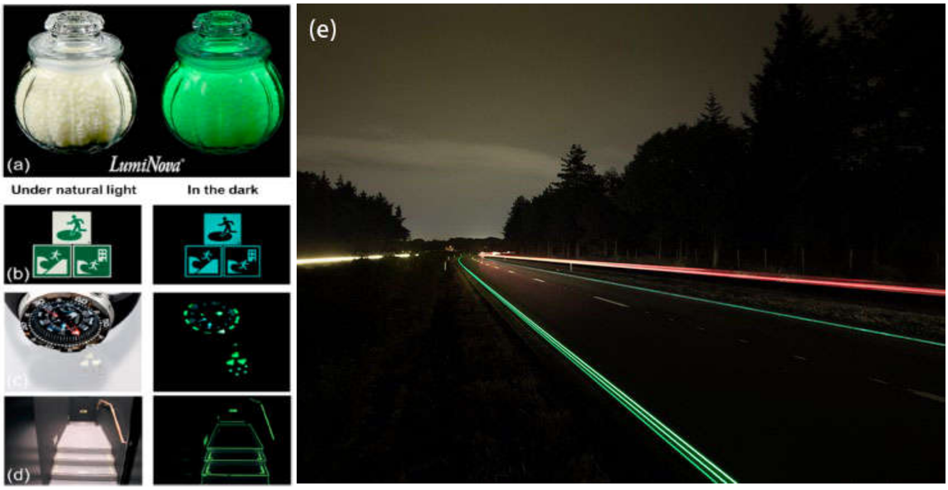

Fig. 1.2. (a) The commercial $SrAl_2O_4$:Eu^{2+},Dy^{3+} (LumiNova) afterglow phosphor and its application for (b) safety signage, (c) display of watch dials, and afterglow indicators in the dark for (d) indoor and (e) highway (N329) in the Netherlands. The pictures in a)-d) and e) are obtained from Refs. [4, 39] and Refs. [40, 41], respectively. Reproduction permission (copyright 2019, Elsevier) from Ref. [4] is obtained for pictures in a)-d).

1.2 Introduction to storage phosphor

X-rays were rapidly applied in medical radiography after its discovery by Wilhelm Conrad Röntgen on November 8, 1895[42]. X-ray medical radiography is based on the properties that X-rays are penetrative to many solid materials like human tissues, and that the X-ray absorption coefficient is different in various materials. Bone contains a lot of calcium, resulting in much more X-ray absorption compared with soft tissues. For medical imaging application, the normally used X-ray energy is between ~10 and 150 keV. The main interaction between such X-ray and solid materials, like an inorganic compound $LiLuSiO_4$, is photoelectric absorption.

Storage phosphors are known as information storage compounds which store free electrons and holes in charge carrier capturing centres upon charging by ionizing radiation like X-rays[43-47]. Like an afterglow phosphor, a storage phosphor is composed of the host lattice, the recombination centres, and the electron and hole trapping centres. The duration time that the charge carriers are captured in a storage phosphor is determined by the trap depths of the electrons and holes capturing centres and their spatial distribution in the host lattice[44]. To avoid the release of the trapped charge carriers at room temperature (RT), deep traps (>~1 eV) are needed for storage phosphor applications[7].

The beginning of digital radiographic technologies dates back to 1970s. At January of 1975, Luckey *et al.* [48] reported a principle of computed radiography (CR) technique in which a storage phosphor was used. Fig. 1.3 shows such a CR technique to demonstrate the information storage and read-out. An imaging plate (IP) is made by using a storage phosphor. A patient is placed between an X-ray source and an imaging plate. The image information of a patient is stored in the imaging plate in a cassette during X-ray exposure. The imaging plate is stimulated point by point using a red laser to generate the recombination or stimulated photon emission from the storage phosphor, which is then detected by a photomultiplier tube (PMT). The imaging plate can be reused after erasure of stored information by intense photon stimulation or heating.

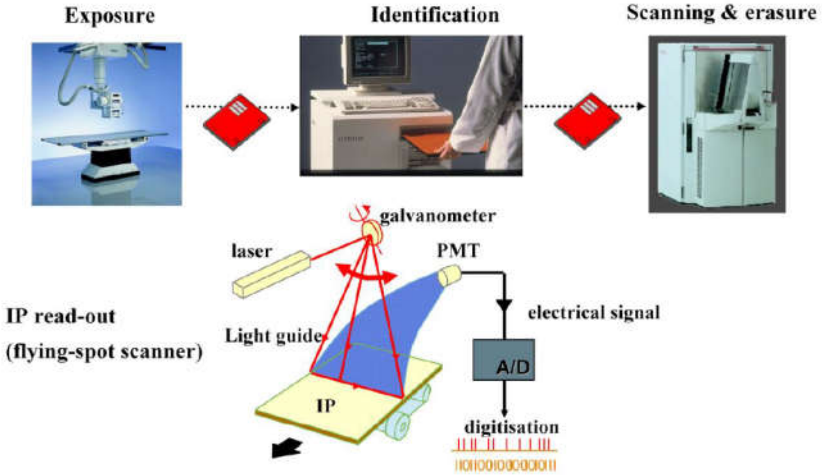

Fig. 1.3. Demonstration of information storage and read-out by using an X-ray storage phosphor based imaging plate (IP). This figure is reproduced with permission from Ref. [49].

The requirements for a good storage phosphor for computed radiography application have been summarized in Refs. [47, 49-51]. They comprise 1) high absorption of X-rays and high conversion coefficient of stored X-ray energy to free charge carriers captured in a storage phosphor for the medical X-rays with energies between ~10 and ~150 keV; 2) slow fading of stored information at room temperature in dark; 3) the stored charge carriers in defect traps can be stimulated to recombine using an inexpensive laser excitation source; 4) the emission from a storage phosphor after photon stimulation should fall between ~300 and ~450 nm in order to be efficiently detected by a traditional photomultiplier tube; 5) the decay time of the recombination centre should be short (<~2 μs), and 6) the residual stored information in a storage phosphor after readout by laser stimulation should be erasable for re-use by an intense light source.

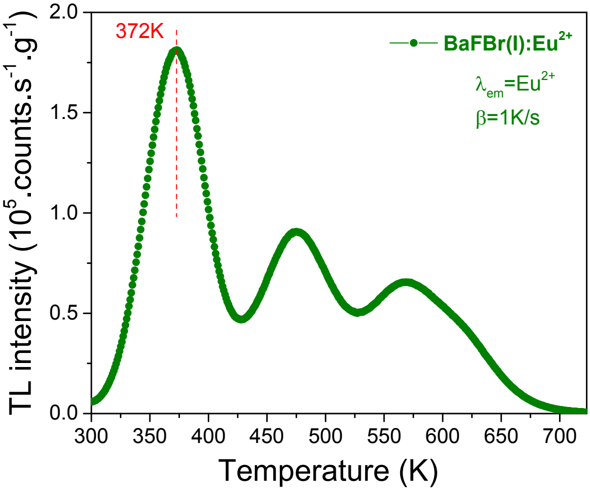

Fig. 1.4. Thermoluminescence (TL) glow curve for the commercial BaFBr(I):Eu^{2+} storage phosphor after 300s β irradiation. The used heating rate was 1 K/s and the Eu^{2+} emission was monitored during TL recording.

BaFCl:Eu^{2+} and BaFBr:Eu^{2+} were first developed as X-ray storage phosphors for computed radiography in 1975[52]. Their family of compounds were further studied and a related patent appeared in Ref. [53] on December 16 of 1980. Today BaFBr(I):Eu^{2+} is still the commercial X-ray storage phosphor for computed radiography[49]. Fig. 1.4 shows the thermoluminescence (TL) glow curve for the commercial BaFBr(I):Eu^{2+} storage phosphor after β irradiation. BaFBr(I):Eu^{2+} suffers from fading of the stored information because the TL glow peak near 372 K is close to room temperature. BaFBr(I):Eu^{2+} absorbs water in humid air leading to decrease of its storage capacity. Researchers have tried to develop new storage phosphors like $BaBr_2$ nanocrystal based glass ceramic[54], SrS:Eu^{2+},Sm^{3+}[55], CsBr:Eu^{2+}[56], $Li_2BaP_2O_7$:Ln (Ln=Ce, Eu, Tb, or Yb)[45], and lanthanide doped $LiLnSiO_4$ (Ln=Y or Lu)[43, 44, 57] in order to replace the BaFBr(I):Eu^{2+}. A good $LiLuSiO_4$:Ce^{3+},Tm^{3+} storage phosphor recently appeared in Ref. [44]. The integrated TL intensity of optimized $LiLuSiO_4$:Ce^{3+},Tm^{3+} is about 4 times higher than that of the commercial BaFBr(I):Eu^{2+} after an equal amount of β irradiation.

1.3 Fundamentals of afterglow and storage phosphors

There are defects in afterglow and storage phosphors that can trap electrons and holes. The energy level locations of the defects in the forbidden gap are useful information and their predictability can guide us to select electron and hole capturing centres with different trap depths for afterglow and storage phosphor applications. In this thesis, we will show how vacuum referred binding energy (VRBE) level diagrams[58-60] can be constructed for different inorganic compounds. The VRBE diagrams are helpful to study these metastable defects and to guide us to the rational design of new afterglow and storage phosphors.

1.3.1 The vacuum referred binding energy levels (VRBE) diagram

In 2012, the chemical shift model[58] was developed to construct a vacuum referred binding energy (VRBE) diagram based on lanthanide spectroscopy[59]. In a VRBE diagram, the reference energy, also called zero point energy, is defined as the energy of an electron at rest in vacuum. The VRBE of an electron is referred to as the energy required to extract that electron from a system and to move it to the vacuum. The electron may be originated from a compound host band or from the ground or excited states of a dopant[59]. The VRBE diagram allows us to compare the binding energy of an electron in the conduction band (CB), valence band (VB), or impurity states like that of bismuth and lanthanides[8, 9].

To demonstrate how to construct a VRBE diagram, Fig. 1.5 shows as example that of the lanthanides in Sr_3SiO_5. Details to construct this VRBE diagram can be found in Ref. [61]. The binding energies in the ground state $4f^n$ levels of the divalent and trivalent lanthanides are indicated by the red and the blue zigzag curves named $Ln^{2+/3+}$ and $Ln^{3+/4+}$, respectively. The binding energies in the excited first $5d_1$ levels reached by spin allowed 4f-5d transitions of trivalent lanthanides are linked by the blue curve named ES (3+).

The host exciton creation energy (E^{ex}) in Sr_3SiO_5 is indicated by arrow a. This energy was derived to be ~6.0 eV by a low-temperature (10 K) photoluminescence excitation (PLE) spectrum of undoped Sr_3SiO_5 in Ref. [61]. To reach the mobility conduction band bottom, the electron-hole binding energy of the exciton needs to be added[60], which is estimated by $0.008*(E_{ex})^2$. It is near 8% of the exciton creation energy for a wide band gap (E_{gap}>7 eV) compound[62].

The electron transitions from 4f to $5d_1$, $5d_2$, and $5d_3$ of Ce^{3+} in Sr_3SiO_5 are indicated by arrows b1, b2, and b3, respectively. These transitions were determined by a low-temperature photoluminescence excitation spectrum of Ce^{3+} single doped Sr_3SiO_5 in Ref. [61].

Arrow c shows the charge transfer (CT) from the valence band (VB) to Eu^{3+}. It is 3.96 eV (313 nm) determined from the low-temperature (10 K) excitation spectrum of Eu^{3+} single doped Sr_3SiO_5. During this Eu^{3+}-CT excitation, electrons at the valence band top are excited to Eu^{3+} and the $4f^7$ ($^8S_{7/2}$) ground state of Eu^{2+} is generated which is then located 3.96 eV above the valence band top. The vacuum referred binding energy of an electron in the $4f^7$ ($^8S_{7/2}$) ground state of Eu^{2+} can be obtained by the chemical shift model with the formula[58]:

$$E_{4f}(7,2+,A) = -24.92 + \frac{18.05 - U(6,A)}{0.777 - 0.0353U(6,A)} \qquad (1.2)$$

in which E_{4f} (7, 2+, A) denotes the VRBE in the $4f^7$ ($^8S_{7/2}$) ground state of Eu^{2+} in a compound (A) and U(6, A) represents the Coulomb repulsion energy for europium. U(6, A) is defined as the binding energy difference between the ground state levels of divalent and trivalent europium:

$$U(6,A) \equiv E_{4f}(7,2+,A) - E_{4f}(6,3+,A) \qquad (1.3)$$

U(6, A) can be estimated using an empirical formula[63]:

$$U(6,A) = 5.44 + 2.834 \times e^{-\varepsilon_{cs}(1,3+,A)/2.2} \qquad (1.4)$$

in which the ε_{cs} (1, 3+, A), also called 5d centroid shift, is defined as the lowering of the average energy of the five 4f→$5d_i$ (i=1, 2, 3, 4, and 5) transitions of Ce^{3+} ion in a compound (A) compared with that of Ce^{3+} as a free ion (6.35 eV)[63]. The five Ce^{3+} 4f→$5d_i$ (i=1-5) transitions are known in many compounds[63], and one can use Eq. (1.4) to estimate the U(6, A) value. Because the 4f→$5d_4$ and 4f→$5d_5$ transitions of Ce^{3+} were not derived from the photoluminescence excitation spectrum of $Sr_3SiO_5:Ce^{3+}$, the U(6, A) value for Sr_3SiO_5 cannot be obtained with Eq. (1.4). It is estimated to be ~6.7 eV by comparing the known U values for other related silicate compounds[63]. The E_{4f} (7, 2+, A) is then estimated to be about -3.9 eV by Eq. (1.2). Based on the obtained E_{4f} (7, 2+, A), the VRBE at the valence band top and the conduction band bottom can be determined by using the charge transfer energy of O^{2-}→Eu^{3+} and the host exciton energy, respectively.

The electron trap depth of Ln^{3+} is defined as the distance between the conduction band bottom and the $4f^n$ ground state levels of Ln^{2+} in a VRBE scheme as shown in Fig. 1.5. The hole trapping depth is defined as the distance between the valence band top and the 4f ground state levels of trivalent lanthanides. The shapes of the divalent Ln^{2+}/Ln^{3+} and the trivalent $Ln^{3+/4+}$ zigzag curves as shown in Fig. 1.5 are in first approximation independent on type of compound[60, 64, 65]. In this thesis we have used shapes as defined in Ref. [60].

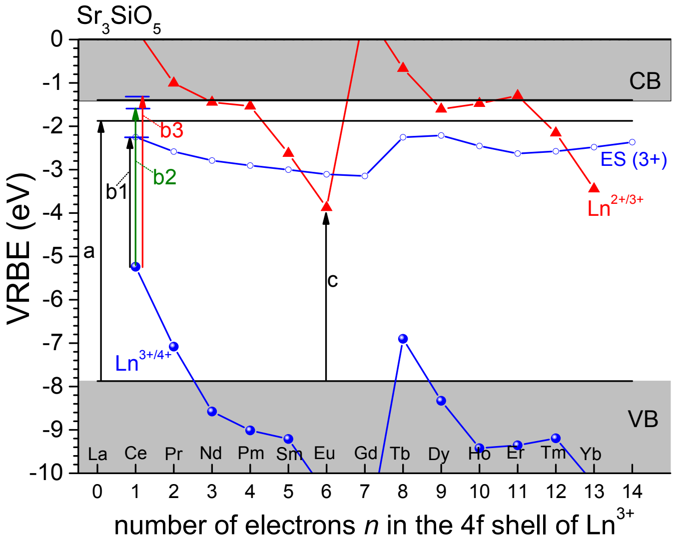

Fig. 1.5. The VRBE scheme for Sr_3SiO_5. The host exciton creation energy (E_{ex}) is indicated by arrow a. The electron transition from 4f to $5d_1$, $5d_2$, or $5d_3$ of Ce^{3+} is indicated by arrows b1, b2, and b3, respectively. The charge transfer from O^{2-} to Eu^{3+} is indicated by arrow c. This figure is adapted from Ref. [61] with permission from the PCCP Owner Societies.

1.3.2 Electron capturing and electron liberation

With the constructed VRBE diagram, we will demonstrate how it can be used to guide us to develop afterglow phosphor.

Fig. 1.6a) shows the VRBE scheme for Sr_3SiO_5 containing the energy level locations of lanthanides. The $5d_3$ excited state of Ce^{3+} is located in the conduction band. It means that upon Ce^{3+} 4f→$5d_3$ excitation (arrow 1a) the electrons at the $5d_3$ excited state can directly transfer to the conduction band. The $5d_2$ excited state of Ce^{3+} is close to but below the conduction band. It means that upon Ce^{3+} 4f→$5d_2$ excitation (arrow 1b) the electrons at the $5d_2$ excited state can only transfer to the conduction band at room temperature (RT) via thermal activation (arrow 2)[66-68]. The liberated electrons freely transport in the conduction band (arrow 3) and are trapped by the shallow electron capturing centre of Dy^{3+} (arrow 4). Ce^{3+} is converted to Ce^{4+} and one may consider this as a hole trapped on Ce^{3+}. The electron trap depth of Dy^{3+} is less deep than the hole trap depth of Ce^{3+} (E1<E2). The electrons trapped at Dy^{2+} are liberated slowly at RT to recombine with holes at Ce^{4+} producing characteristic afterglow emission of Ce^{3+} (arrows 5-7). That Dy^{3+} has captured an electron was evidenced in Ref. [61] by a TL glow peak near 320 K in Fig. 1.6b).

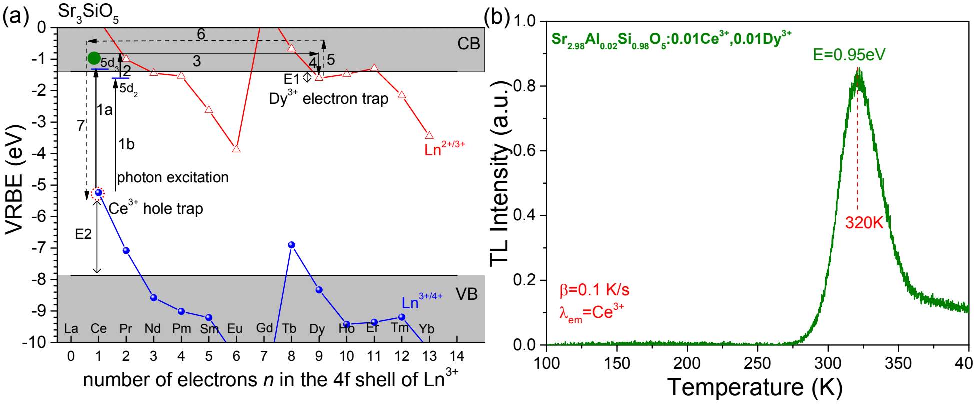

Fig. 1.6. (a) Illustration of the electron capturing (solid arrows 1-4) and detrapping (dash arrows 5-7) processes in Sr_3SiO_5:Ce^{3+},Dy^{3+}. The electron is indicated by the green filled circle and the hole is shown by the red dashed circle. (b) TL glow curve of $Sr_{2.98}Al_{0.02}Si_{0.98}O_5$:0.01$Ce^{3+}$,0.01$Dy^{3+}$ after β irradiation. The sample was preheated at 300 K to clean the TL peaks from host intrinsic traps. The figures are adapted from Ref. [61] with permission from the PCCP Owner Societies.

Another example is the orange afterglow phosphor $Ca_3Si_2O_7$:0.1%Eu^{2+},0.5% Tm^{3+} in which Tm^{3+} acts as an electron capturing centre as studied in Ref. [69]. A so-called thermoluminescence excitation[16] (TLE) spectrum was recorded by studying what photon energy can charge the electron trap of Tm^{3+}. The TLE spectrum of $Ca_3Si_2O_7$:0.1%Eu^{2+},0.5%Tm^{3+} overlaps with the Eu^{2+} photoluminescence excitation spectrum of $Ca_3Si_2O_7$:Eu^{2+}. It evidences that the excitation of the Eu^{2+} 5d states results in the electron liberation from Eu^{2+} which is then followed by electron capture by Tm^{3+}.

The depth of an electron capturing centre can be designed by the choice of lanthanide co-dopant. The trivalent lanthanide co-dopants may act as electron capturing centres when the $4f^n$ ground state level locations of the corresponding divalent lanthanides are located below the conduction band. The red zigzag curve $Ln^{2+/3+}$ in Fig. 1.6a) shows that a predictable variation appears in the trap depth as a function of the type of lanthanide ions.

In 2005, Dorenbos first proposed this assumption in Ref. [70], which later was experimentally verified using a thermoluminescence (TL) study on YPO_4:Ce^{3+},Ln^{3+} by Bos *et al.* [71, 72] in 2008. Here, Ce^{3+} is the deep hole capturing centre and Ln^{3+} co-dopants are the less deep electron capturing centres. During exposure to β irradiation, holes are captured by Ce^{3+} to form Ce^{4+} while electrons are trapped by Ln^{3+} generating Ln^{2+}. Different Ln^{3+} co-dopants create electron traps with different trap depth. It means that different TL glow peak maxima appear due to electron liberation from Ln^{2+} and recombination with holes at Ce^{4+} in YPO_4. Fig. 1.7 compares the trap depths of lanthanides derived from the VRBE scheme and the experimental TL glow curves of $YPO_4:Ce^{3+},Ln^{3+}$ (Ln=Pr, Nd, Tm, Er, Ho, Dy, Sm, or Yb). The VRBE scheme predicts that Yb^{3+} has the deepest trap depth and Pr^{3+} has the shallowest trap depth. The experimental TL glow peak maxima induced by Ln^{3+} co-dopants are consistent with the prediction from the VRBE scheme.

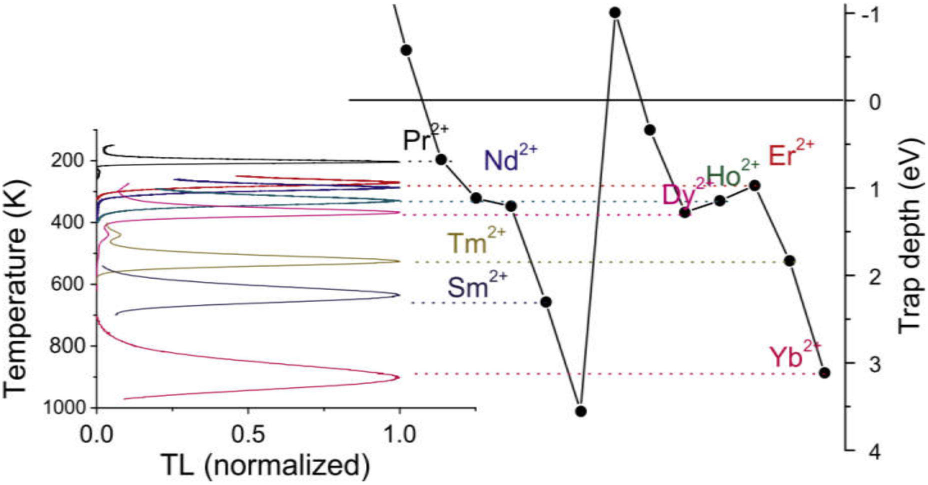

Fig. 1.7. A comparison of the trap depths of lanthanides determined from the VRBE scheme and the experimental TL glow curves of $YPO_4:Ce^{3+},Ln^{3+}$. The figure is reproduced from Ref. [71] with permission (copyright 2011, Elsevier).

The design of the electron trap depth by the choice of lanthanide has been applied to $Y_3Al_5O_{12}:Ln^{3+},RE^{3+}$ (Ln=Ce, Tb, or Pr; RE=Eu or Yb)[73], $Sr_3SiO_5:Ce^{3+},Ln^{3+}$[61], and $GdAlO_3:Ce^{3+},Ln^{3+}$[74]. In this thesis, we will apply the same methods for $LaPO_4:Ce^{3+},Ln^{3+}$[8], $NaYGeO_4:Bi^{3+},Eu^{3+}$[75], and $LiLuSiO_4:Ce^{3+},Ln^{3+}$ (Ln=Tm or Sm). We will discuss the three cases in detail in Chapters 2, 5, and 6.

Quantum tunnelling recombination is another type of electron-hole recombination process. In this case, the captured electrons are recombined with holes via a localized tunnelling process between the electron traps and the neighbouring excited states of the recombination centre rather than by a traditional thermal excitation to the conduction band. It was deeply studied by Dobrowolska *et al*. [76] in $YPO_4:Ce^{3+},Ln^{3+}$ (Ln=Er, Ho, Nd, or Dy) in 2014. The tunnelling recombination model has been utilized to discuss the afterglow mechanisms in different compounds like $Ba_5Si_8O_{21}:Eu^{2+},Dy^{3+}$ in Ref. [77] and $Zn_3Ga_2Ge_2O_{10}:Cr^{3+}$ in Ref. [35].

1.3.3 Hole capturing and hole liberation

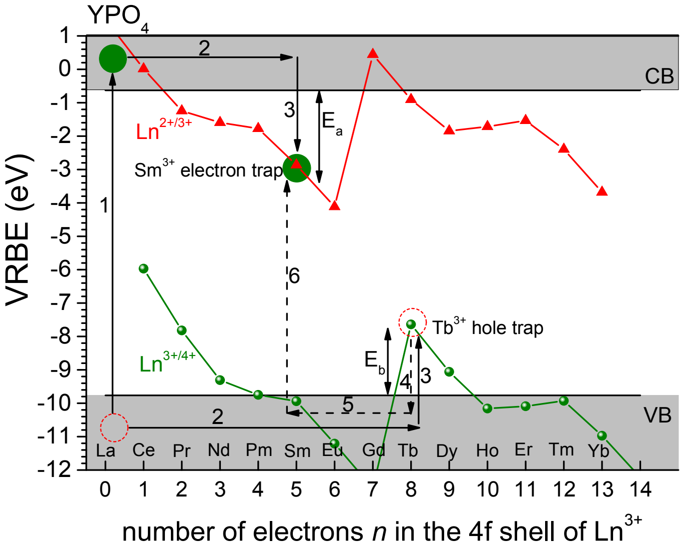

Fig. 1.8. Demonstration of the hole capturing and decapturing processes in YPO_4:Sm^{3+},Tb^{3+}: (1) production, (2) transport, and (3) capturing of charge carriers; (4) hole liberation; (5) hole transport; and (6) recombination of electron and hole. The electrons and holes are indicated by the green filled circles and the red open circles, respectively.

In Fig. 1.8 the hole capturing and decapturing processes are demonstrated in YPO_4:Sm^{3+},Tb^{3+}. Upon external excitation like the exposure to β or γ irradiation, free charge carriers are formed. The holes can be captured by the Tb^{3+} hole capturing centre to form Tb^{4+} while the electrons can be trapped by Sm^{3+} electron capturing centre to form Sm^{2+}[8, 71]. The thermal energy to liberate a hole from Tb^{4+} is less than that to liberate an electron from Sm^{2+} (E_b<Ea). The holes captured at Tb^{4+} will be liberated at a lower temperature than electrons at Sm^{2+} and migrate through valence band or migrate as a V_k centre (a hole bonded with two neighbouring oxygen anions) to recombine with Sm^{2+} to generate characteristic red 4f-4f emission of Sm^{3+}.

The type of hole capturing centre can be controlled by a choice of lanthanide co-dopant. Fig. 1.8 shows that trivalent lanthanides may act as hole capturing centres when their 4f ground state levels are above the valence band top and that as a function of the type of lanthanide ion there is a predictable variation of the hole trapping depth as indicated by the green Ln$^{3+/4+}$ zigzag curve.

The hole capturing and detrapping processes are rarely studied and only a few reports have appeared. In 1988, Chakrabarti *et al.* [78] reported that Sm^{3+} acts as a deep electron capturing centre while Ce^{3+} acts as a less deep hole capturing centre in MgS:Ce^{3+},Sm^{3+}. During TL-readout, the holes are released from Ce^{4+} to recombine with electrons captured at Sm^{3+} to generate characteristic 4f-4f emission of Sm^{3+}. The other recent examples of hole capturing and liberation are reported by Luo *et al.* on lanthanides co-doped $GdAlO_3$[74] and RE_2O_2S[79]. A hole liberation from Tb^{4+} or Pr^{4+} was observed in $GdAlO_3$. A hole detrapping process from unidentified host-related defect(s) resulting in an orange Ti^{4+} charge transfer emission and typical Eu^{3+} 4f-4f emission was found in Y_2O_2S:Ti^{4+},Eu^{3+}.

In Chapter 2, it will be further demonstrated that holes can be captured by a lanthanide hole capturing centre M (M=Tb or Pr) in YPO_4:Ln^{3+},M^{3+} (Ln=Sm, Eu, or Yb) and then be liberated during TL-readout. Here, Sm^{3+}, Eu^{3+}, and Yb^{3+} act as deep electron capturing and recombination centres, while Tb^{3+} and Pr^{3+} act as less deep hole capturing centres. The captured holes are liberated from Tb^{4+} or Pr^{4+} to recombine with the electrons captured at Sm^{2+}, Eu^{2+}, or Yb^{2+} to give characteristic 4f-4f emission of Sm^{3+}, Eu^{3+}, or Yb^{3+}.

In Chapter 3, we will evidence that Bi^{3+} can also act as a hole capturing centre in YPO_4:Ln^{3+},Bi^{3+} (Ln=Tm, Sm, Eu, or Yb). In this case, Ln^{3+} co-dopants act as deep electron capturing centres while Bi^{3+} appears as a less deep hole capturing centre. During TL-readout, the holes at Bi^{4+} are released at a lower temperature to recombine with electrons captured at Ln^{2+} to produce typical 4f-4f emission of Ln^{3+}.

The hole detrapping model is further verified in Chapter 6, where hole liberation processes from Tb^{4+}, Pr^{4+}, and Bi^{4+} were identified in $LiLuSiO_4$:Eu^{3+}, Ln^{3+} (Ln=Tb or Pr), $LiLuSiO_4$:Eu^{3+},Bi^{3+}, and $LiLuSiO_4$:Bi^{3+}. We will show that the storage mechanism in $LiLuSiO_4$:Bi^{3+} is due to the hole liberation from Bi^{4+} and recombination with electrons trapped at Bi^{2+}.

1.3.4 Trap depth engineering

For afterglow and storage phosphor applications, different depths are required. Trap depths can be controlled by the choice of lanthanide ion but also by using a band structure engineering approach.

One may tailor the electron trap depth through changing the vacuum referred binding energy (VRBE) at the conduction band bottom. One reported example is $Y_3Al_{5-x}Ga_xO_{12}$:Ce^{3+},Cr^{3+} in Ref. [20], where Cr^{3+} acts as the electron capturing centre and Ce^{3+} acts as the hole capturing and recombination centre. With increasing x, the conduction band bottom moves downwards. Since the VRBE of the electron captured at Cr^{2+} remains almost constant, the trap depth of Cr^{3+} is then decreased, resulting in a shifting of the TL glow curve towards lower temperature.

In this thesis we will apply the same methods for the solid solutions of $Gd_{1-x}La_xPO_4$:Ce^{3+},Ho^{3+}, $NaLu_{1-x}Y_xGeO_4$:Bi^{3+},Eu^{3+}, and $LiLu_{1-x}Y_xSiO_4$:Ce^{3+},Ln^{3+} (Ln=Tm or Sm), which will be presented in detail in Chapters 2, 5, and 6.

One may tailor the hole trap depth by changing the VRBE at the valence band top. One example is reported by Luo *et al.* [7] for $Gd_{1-x}La_xAlO_3$:Eu^{3+},Ln^{3+} (Ln=Tb or Pr). With increasing x, the valence band top moves upwards whereas the VRBE in the 4f ground state level of Tb^{3+} or Pr^{3+} remains almost constant. The hole trap depth of Tb^{3+} or Pr^{3+} decreases leading to a shifting of the TL glow curve towards a lower temperature. In this thesis, we will systematically explore the hole trap depth tailoring in five other solid solutions of $Y_{1-x}Lu_xPO_4$:Eu^{3+},Ln^{3+} (Ln=Tb or Pr), $Y_{1-x}Lu_xPO_4$:Eu^{3+},Bi^{3+}, $La_{1-x}Gd_xPO_4$:Eu^{3+},Pr^{3+}, $LiLu_{1-x}Y_xSiO_4$:Eu^{3+},Ln^{3+} (Ln=Tb or Pr), and $LiLu_{0.25}Y_{0.75}Si_{1-y}Ge_yO_4$:$Bi^{3+}$ solid solutions. The detailed results will be presented in Chapters 2, 3, 4, and 6.

1.4 Bismuth and its luminescence

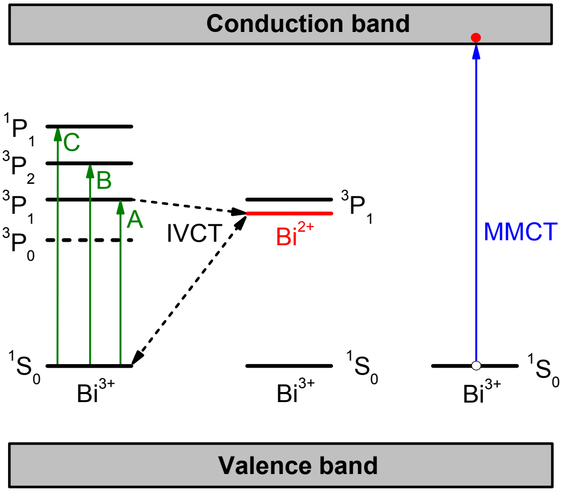

Fig. 1.9. Illustration of the optically excited electronic transitions, the intervalence charge transfer (IVCT), and the metal-to-metal charge transfer (MMCT) transition for the trivalent bismuth in a compound. This figure is adapted from Ref. [84] with permission (copyright 2017, Elsevier).

The earliest record of bismuth as an element dates back to 1739 by Potts and Bergmann[80]. Bismuth often exists in minerals in the form of sulfide (Bi_2S_3), carbonate ($(BiO)_2CO_3$), or oxide (Bi_2O_3)[81]. The bismuth element has the electronic configuration of $[Xe]4f^{14}5d^{10}6s^26p^3$. Bi can show various valence states like Bi^0 (outermost electrons are $6p^3$), Bi^+ ($6p^2$), Bi^{2+} ($6p^1$), Bi^{3+} ($6s^2$), Bi^{4+} ($6s^1$), or Bi^{5+}

$(5d^{10})$[81, 82]. Bi^{3+} is the most common and stable form configuration. The free Bi^{3+} ion has a $6s^2$ electron configuration with $^1S_0$ ground state. Optical transitions to the 6s6p configuration lead to the excited $^1P_1$ singlet state and the triplet levels of $^3P_0$, $^3P_1$, and $^3P_2$[83]. The transition of $^1S_0 \rightarrow ^1P_1$ is a spin-allowed transition. The transitions of $^1S_0 \rightarrow ^3P_0$, $^1S_0 \rightarrow ^3P_1$, and $^1S_0 \rightarrow ^3P_2$ are spin-forbidden[84]. Because of spin-orbit coupling and mixing with the $^1P_1$ state, the $^1S_0 \rightarrow ^3P_1$ transition becomes allowed. The $^1S_0 \rightarrow ^3P_2$ transition can be induced via coupling with unsymmetrical lattice vibrational modes[82]. In Fig. 1.9 the optical transitions from the $^1S_0$ ground state of Bi^{3+} to its excited states of $^3P_1$, $^3P_2$, and $^1P_1$ are shown, which are referred to as A-, B-, and C-band transitions, respectively[84, 85]. In addition to these Bi^{3+} transitions one may also observe a metal-to-metal charge transfer (MMCT) transition of an electron from Bi^{3+} to a compound host cation (M^{n+}) as illustrated at the right side of Fig. 1.9. This can be expressed as $Bi^{3+}/M^{n+} \rightarrow Bi^{4+}/M^{(n-1)+}$.

On the basis of the MMCT band, one can locate the $^1S_0$ ground state of Bi^{3+} in a VRBE diagram for a compound. Then with the A-, B-, and C- excitation bands of Bi^{3+} from photoluminescence excitation spectra, the excited states of Bi^{3+} can also be located. Awater *et al.* [84] compiled the spectroscopic data of Bi^{3+} electronic transitions in 117 compounds to determine Bi^{3+} VRBE energies. A part of the results is shown in Fig. 1.10. With increasing of the U value of the compound, the VRBE in the Bi^{3+} $^1S_0$ ground state decreases from about -5 to -10 eV, while the VRBE in the $^3P_1$ excited state of Bi^{3+} decreases less strongly from about -2 eV to -4 eV. We have used low-temperature Bi^{3+} photoluminescence excitation spectra to locate the ground and excited states of Bi^{3+} in the VRBE diagrams of $REPO_4$ (RE=Lu, Y, or La) and $ARE(Si,Ge)O_4$ (A=Li, Na; RE=Y or Lu). This will be presented in Chapter 3 and Chapter 5.

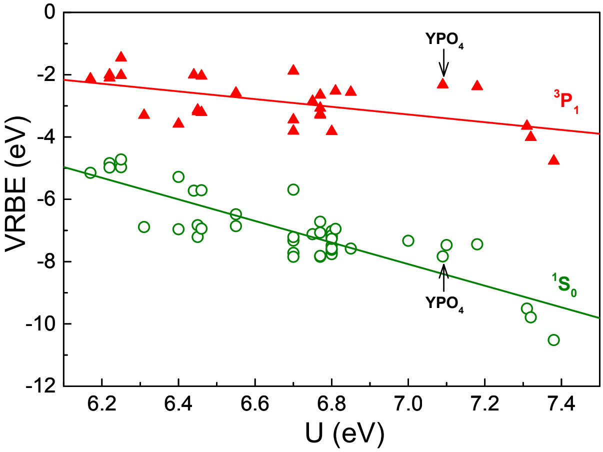

Fig. 1.10. The vacuum referred electron binding energies (VRBEs) at the level locations of the $^1S_0$ ground and the $^3P_1$ excited states of the trivalent bismuth as a function of the U

parameter in 44 different compounds. This figure is adapted from Ref. [84] with permission (copyright 2017, Elsevier).

Bi^{2+} as a luminescence centre has been reported in few reports. In 1994, Blasse *et al.* [86] reported an orange emission in bismuth doped SrB_4O_7, which was assigned to Bi^{2+} luminescence. Later, Bi^{2+} emission was studied for light-emitting diode (LED) based lighting applications in different compounds like phosphates, borates, and sulphates[87-89]. The free Bi^{2+} ion has the $[Xe]4f^{14}5d^{10}6s^{2}6p^{1}$ electron configuration with a ^2P ground state. The ^2P ground state is split into the $^2P_{1/2}$ ground state and the excited $^2P_{3/2}$ state due to spin-orbit splitting. The excited $^2P_{3/2}$ state in a compound is further split into $^2P_{3/2}$ (1) and $^2P_{3/2}$ (2) due to crystal field splitting[89]. The orange or red luminescence of Bi^{2+} is assigned to arise from the $^2P_{3/2}$ (1)→ $^2P_{1/2}$ transition[82].

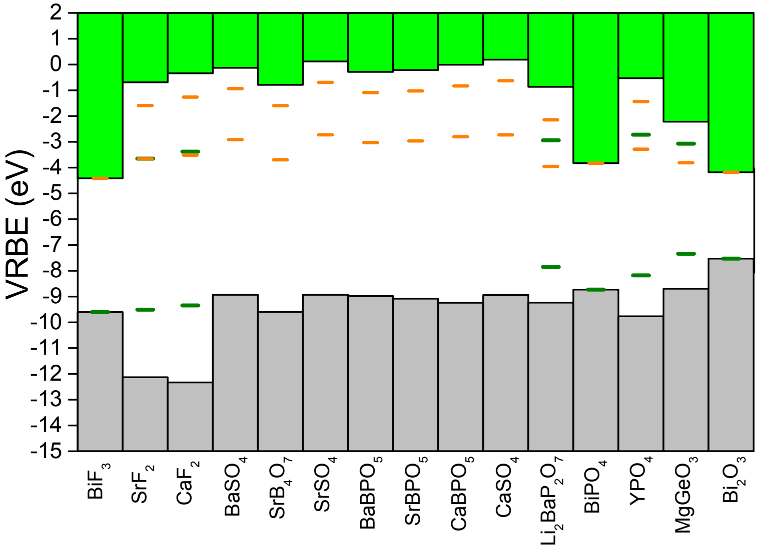

Fig. 1.11. Stacked VRBE schemes of 15 compounds containing the VRBEs in the ground and excited states of the Bi^{2+} (orange horizontal bars) and Bi^{3+} (green horizontal bars). This figure is adapted from Ref. [90] with permission (copyright 2017, Elsevier).

Based on the thermal quenching curves of Bi^{2+} $^2P_{3/2}$ (1)→ $^2P_{1/2}$ emission and the excitation spectra of Bi^{2+}, Awater *et al.* [90] estimated the VRBEs in the excited and ground states of Bi^{2+} in several compounds. The excited and ground state level locations of Bi^{2+} are indicated by the horizontal orange bars in Fig. 1.11. The excited and ground states of Bi^{3+} are also indicated by the horizontal green bars. The VRBE in the Bi^{2+} ground state emerges between -3.5 and -4 eV. It is about 0.7±0.3 eV lower than that of the Bi^{3+} excited state near -3 eV in the five compounds of SrF_2, CaF_2, $Li_2BaP_2O_7$, YPO_4, and $MgGeO_3$ in Fig. 1.11. Awater *et* *al.* [84, 90] then proposed that an intervalence charge transfer (IVCT) of an electron from the Bi^{3+} excited state to its neighbouring Bi^{3+} can occur to form a Bi^{4+} and Bi^{2+} pair. This process is illustrated in Fig. 1.9. After Bi^{3+} A-band excitation, an electron is excited from the Bi^{3+} $^1S_0$ ground state to the excited $^3P_1$ state. Energy is released by the electron transfer from the $^3P_1$ state to a neighbouring Bi^{3+} producing a Bi^{4+}-Bi^{2+} pair. A radiative transfer of the electron from the Bi^{2+} ground state to the hole at Bi^{4+} is possible to generate a broad Bi^{3+} pair emission in the visible range. When the transition is non-radiative this route acts as a mechanism to quench Bi^{3+} A-band luminescence[90].

1.5 Thesis outline

In Chapter 2, the capturing and release processes of charge carriers are studied in double lanthanide doped rare earth ortho-phosphates. We found that in $LaPO_4:Ce^{3+},Ln^{3+}$ (Ln=Er, Nd, Ho, Dy, Tm, or Sm) the lanthanide codopants are the electron capturing centres while Ce^{3+} acts as the hole capturing and recombination centre. The electron trap depth induced by lanthanide codopants can be controlled by the choice of lanthanide, and for a fixed set of lanthanide codopants like in $Gd_{1-x}La_xPO_4:Ce^{3+},Ho^{3+}$ solid solutions, by adjusting x, resulting in conduction band engineering. We also found that Ln^{3+} ions (Ln=Eu, Yb, or Sm) act as deep electron capturing and recombination centres, while Tb^{3+} and Pr^{3+} are less deep hole capturing centres in double lanthanide doped YPO_4. The holes are liberated from Tb^{4+} or Pr^{4+} to recombine with the electrons captured at Ln^{2+} to produce typical 4f-4f emission of Ln^{3+}. Finally, we used Lu^{3+} to replace Y^{3+} to engineer the VB energy and to tailor the hole trap depths of Tb^{3+} and Pr^{3+} in $Y_{1-x}Lu_xPO_4:Eu^{3+},Ln^{3+}$ (Ln=Tb or Pr) solid solutions. The VB appears to move downwards and the hole trap depths of Tb^{3+} and Pr^{3+} increase. The hole liberation from Tb^{4+} or Pr^{4+} was explored in $LaPO_4:Eu^{3+},Ln^{3+}$ (Ln=Tb, Pr, or Ce).

In Chapter 3, we studied the dual role of Bi^{3+} in capturing electrons and holes in lanthanide co-activated rare earth ortho phosphates. By combining Bi^{3+} with the less deep hole capturing centre of Tb^{3+} or Pr^{3+}, Bi^{3+} emerges to act as deep electron capturing and recombination centre in YPO_4. By combining Bi^{3+} with the deep electron capturing centre of Ln^{3+} (Ln=Tm, Sm, Yb, or Eu), Bi^{3+} emerges to act as less deep hole capturing centre in YPO_4. The captured hole is liberated from Bi^{4+} to recombine with the electrons at Ln^{2+} to generate characteristic 4f-4f emission of Ln^{3+}. The hole trap depth of Bi^{3+} can be controlled in $Y_{1-x}Lu_xPO_4:Eu^{3+},Bi^{3+}$, by changing x, leading to valence band engineering. The hole liberation from Bi^{4+} was also explored in $LaPO_4:Eu^{3+},Bi^{3+}$.

In Chapter 4, based on the results of Chapters 2 and 3, we explored a general methodology to the rational design of thermally stimulated short-wave infrared

(SWIR) luminescence between ~900 and 1700 nm for the second bio-imaging window. This methodology is based on using Bi^{3+} as recombination centre and combining that with efficient energy transfer from Bi^{3+} to Nd^{3+}. Nd^{3+} SWIR afterglow emerges in $La_{1-x}Gd_xPO_4$:Bi^{3+},Tb^{3+},Nd^{3+} via adjusting hole liberation from Tb^{4+} by changing x leading to valence band engineering.

Based on the results of Chapters 2, 3, and 4, we suspected that one may develop good afterglow and storage phosphors if the charge carrier storage capacity can be tailored in a compound. Therefore, in Chapter 5, we explored the methodology for designing afterglow and storage phosphors by VRBE diagram guided band structure engineering and crystal synthesis optimization.

Low-temperature (10 K) photoluminescence excitation and emission spectra of the bismuth and lanthanide doped ARE(Si,Ge)O_4 (A=Li or Na; RE=Y or Lu) system were studied and the corresponding VRBE diagrams were constructed to guide the study of charge carrier trapping processes. By combining Bi^{3+} with Eu^{3+} or Bi^{3+} itself, Bi^{3+} emerges to act as a deep hole capturing and recombination centre, while Bi^{3+} and Eu^{3+} are less deep electron capturing centres. Trap depth tailorable afterglow and storage were obtained in Bi^{3+} single and Bi^{3+},Eu^{3+} co-doped $NaLu_{1-x}Y_xGeO_4$ by changing x resulting in conduction band engineering. Finally, good Bi^{3+} afterglow and storage phosphors appear in $NaYGeO_4$:0.001Bi^{3+} and $NaYGeO_4$: 0.01Bi^{3+},0.001Eu^{3+} by optimizing synthesis condition at 1200 ^{o}C during 24h.

In Chapter 6, based on the VRBE diagrams established in Chapter 5, we studied the charge carrier trapping processes in lanthanide and/or bismuth doped LiRE(Si,Ge)O_4 (RE=Y or Lu) system. We demonstrated that one can develop a good storage phosphor through fully engineering the colour of recombination emission, the trap depths of both electrons and holes, and the crystal synthesis optimization.

1.6 Reference

1. Y. Li, M. Gecevicius and J. Qiu, *Chemical Society Reviews*, 2016, **45**, 2090-2136.
2. Y. Wang, Y. Gong, X. Xu and Y. Li, *Journal of Luminescence*, 2013, **133**, 25-29.
3. K. Van den Eeckhout, D. Poelman and P. F. Smet, *Materials*, 2013, **6**, 2789-2818.
4. J. Xu and S. Tanabe, *Journal of Luminescence*, 2019, **205**, 581-620.
5. S. Wang, X. Liu, B. Qu, Z. Song, Z. Wang, S. Zhang, F. Wang, W.-T. Geng and Q. Liu, *Journal of Materials Chemistry C*, 2019, **7**, 12544-12551.
6. Y. Zhuang, Y. Lv, Y. Li, T. Zhou, J. Xu, J. Ueda, S. Tanabe and R.-J. Xie, *Inorganic Chemistry*, 2016, **55**, 11890-11897.
7. H. Luo, A. J. J. Bos and P. Dorenbos, *The Journal of Physical Chemistry C*, 2016,

120, 5916-5925.
8. T. Lyu and P. Dorenbos, *Journal of Materials Chemistry C*, 2018, **6**, 369-379.
9. T. Lyu and P. Dorenbos, *Journal of Materials Chemistry C*, 2018, **6**, 6240-6249.
10. Y. Katayama, A. Hashimoto, J. Xu, J. Ueda and S. Tanabe, *Journal of Luminescence*, 2017, **183**, 355-359.
11. J. Xu, D. Murata, J. Ueda, B. Viana and S. Tanabe, *Inorganic Chemistry*, 2018, **57**, 5194-5203.
12. J. Ueda, J. L. Leaño, C. Richard, K. Asami, S. Tanabe and R.-S. Liu, *Journal of Materials Chemistry C*, 2019, **7**, 1705-1712.
13. Y. Lv, L. Wang, Y. Zhuang, T.-L. Zhou and R.-J. Xie, *Journal of Materials Chemistry C*, 2017, **5**, 7095-7101.
14. A. J. J. Bos, *Radiation Measurements*, 2006, **41**, S45-S56.
15. A. J. J. Bos, *Materials*, 2017, **10**, 1357.
16. A. J. J. Bos, R. M. van Duijvenvoorde, E. van der Kolk, W. Drozdowski and P. Dorenbos, *Journal of Luminescence*, 2011, **131**, 1465-1471.
17. S. W. S. McKeever, *Thermoluminescence of Solids*, Cambridge University Press, Cambridge, 1985.
18. R. Chen and S. A. A. Winer, *Journal of Applied Physics*, 1970, **41**, 5227-5232.
19. W. Hoogenstraaten, *Philips Res. Rep*, 1958, **13**, 515–693.
20. J. Ueda, P. Dorenbos, A. J. J. Bos, K. Kuroishi and S. Tanabe, *Journal of Materials Chemistry C*, 2015, **3**, 5642-5651.
21. E. N. Harvey, *A history of luminescence from the earliest times until 1900*, American Philosophical Society, 1957.
22. W. M. Yen and M. J. Weber, *Inorganic phosphors: compositions, preparation and optical properties*, CRC press, 2004.
23. P. F. Smet, I. Moreels, Z. Hens and D. Poelman, *Materials*, 2010, **3**, 2834-2883.
24. C.-C. Kang, R.-S. Liu, J.-C. Chang and B.-J. Lee, *Chemistry of Materials*, 2003, **15**, 3966-3968.
25. M. Lastusaari, T. Laamanen, M. Malkamäki, K. O. Eskola, A. Kotlov, S. Carlson, E. Welter, H. F. Brito, M. Bettinelli, H. Jungner and J. Hölsä, *European Journal of Mineralogy*, 2012, **24**, 885-890.
26. L. Nemoto & Co., Japanese Pat., 751505, 1974.
27. https://en.wikipedia.org/w/index.php?title=Radium_Girls&oldid=766100626.
28. T. Matsuzawa, Y. Aoki, N. Takeuchi and Y. Murayama, *Journal of the Electrochemical Society*, 1996, **143**, 2670-2673.
29. B. Qu, B. Zhang, L. Wang, R. Zhou and X. C. Zeng, *Chemistry of Materials*, 2015, **27**, 2195-2202.
30. J. Hölsä, H. Jungner, M. Lastusaari and J. Niittykoski, *Journal of Alloys and Compounds*, 2001, **323-324**, 326-330.

31. C. Shi, Y. Fu, B. Liu, G. Zhang, Y. Chen, Z. Qi and X. Luo, *Journal of Luminescence*, 2007, **122-123**, 11-13.
32. N. Suriyamurthy and B. S. Panigrahi, *Journal of Luminescence*, 2008, **128**, 1809-1814.
33. W. Li, Y. Liu and P. Ai, *Materials Chemistry and Physics*, 2010, **119**, 52-56.
34. D. Jia, W. Jia, D. R. Evans, W. M. Dennis, H. Liu, J. Zhu and W. M. Yen, *Journal of Applied Physics*, 2000, **88**, 3402-3407.
35. Z. Pan, Y.-Y. Lu and F. Liu, *Nat Mater*, 2012, **11**, 58-63.
36. J. Xu, D. Murata, J. Ueda and S. Tanabe, *Journal of Materials Chemistry C*, 2016, **4**, 11096-11103.
37. Q. le Masne de Chermont, C. Chanéac, J. Seguin, F. Pellé, S. Maîtrejean, J.-P. Jolivet, D. Gourier, M. Bessodes and D. Scherman, *Proceedings of the National Academy of Sciences*, 2007, **104**, 9266-9271.
38. J. Wang, J. Li, J. Yu, H. Zhang and B. Zhang, *ACS Nano*, 2018, **12**, 4246-4258.
39. https://www.nemoto.co.jp/nlm/?lang=en.
40. L. Stinson, https://www.wired.com/2014/2011/awesome-glowing-roads highways-future/.
41. https://www.studioroosegaarde.net/cn/project/glowing-lines.
42. *Wikipedia. X-ray. https://en.wikipedia.org/wiki/X-ray*.
43. A. Dobrowolska, A. J. J. Bos and P. Dorenbos, *Radiation Measurements*, 2019, **127**, 106147.
44. A. Dobrowolska, A. J. J. Bos and P. Dorenbos, *physica status solidi (RRL) – Rapid Research Letters*, 2019, **13**, 1800502.
45. A. Dobrowolska, A. J. J. Bos and P. Dorenbos, *Journal of Luminescence*, 2016, **170, Part 2**, 497-504.
46. H. Riesen and W. A. Kaczmarek, *Inorganic Chemistry*, 2007, **46**, 7235-7237.
47. H. v. Seggern, *Brazilian Journal of Physics*, 1999, **29**, 254-268.
48. G. W. Luckey, Rochester N.Y. , *US Patent No. 3,859,527*, 1975.
49. P. Leblans, D. Vandenbroucke and P. Willems, *Materials*, 2011, **4**, 1034.
50. S. Schweizer, *physica status solidi (a)*, 2001, **187**, 335-393.
51. J. M. Spaeth, *Radiation Measurements*, 2001, **33**, 527-532.
52. A. L. N. Stevels and F. Pingault, *Philips Research Reports*, 1975, **30**, 277-290.
53. N. Kotera, S. Eguchi, J. Miyahara, S. Matsumoto and H. Kato, *U.S. Patent No. 4,239,968*, 1980.
54. M. Secu, S. Schweizer, J. M. Spaeth, A. Edgar, G. V. M. Williams and U. Rieser, *J. Phys.-Condes. Matter*, 2003, **15**, 1097-1108.
55. H. Nanto, Y. Hirai, M. Ikeda, M. Kadota, J.-i. Nishishita, S. Nasu and Y. Douguchi, *Sensors and Actuators A: Physical*, 1996, **53**, 223-226.
56. G. A. Appleby, J. Zimmermann, S. Hesse, O. Karg and H. v. Seggern, *Journal of*

Applied Physics, 2009, **105**, 073511.
57. A. V. Sidorenko, P. Dorenbos, A. J. J. Bos, C. W. E. van Eijk and P. A. Rodnyi, *J. Phys.-Condes. Matter*, 2006, **18**, 4503-4514.
58. P. Dorenbos, *Physical Review B*, 2012, **85**, 165107.
59. P. Dorenbos, *ECS Journal of Solid State Science and Technology*, 2013, **2**, R3001-R3011.
60. P. Dorenbos, *Optical Materials*, 2017, **69**, 8-22.
61. H. Luo, A. J. J. Bos, A. Dobrowolska and P. Dorenbos, *Physical Chemistry Chemical Physics*, 2015, **17**, 15419-15427.
62. P. Dorenbos, *Journal of Luminescence*, 2005, **111**, 89-104.
63. P. Dorenbos, *Journal of Luminescence*, 2013, **135**, 93-104.
64. P. Dorenbos and E. G. Rogers, *ECS Journal of Solid State Science and Technology*, 2014, **3**, R150-R158.
65. P. Dorenbos, *Journal of Luminescence*, 2013, **136**, 122-129.
66. P. Dorenbos, *J. Phys.-Condes. Matter*, 2005, **17**, 8103-8111.
67. E. van der Kolk, P. Dorenbos, J. T. M. de Haas and C. W. E. van Eijk, *Physical Review B*, 2005, **71**, 045121.
68. J. Ueda, P. Dorenbos, A. J. J. Bos, A. Meijerink and S. Tanabe, *The Journal of Physical Chemistry C*, 2015, **119**, 25003-25008.
69. J. Ueda, R. Maki and S. Tanabe, *Inorganic Chemistry*, 2017, **56**, 10353-10360.
70. P. Dorenbos, *Chemistry of Materials*, 2005, **17**, 6452-6456.
71. A. J. J. Bos, P. Dorenbos, A. Bessière, A. Lecointre, M. Bedu, M. Bettinelli and F. Piccinelli, *Radiation Measurements*, 2011, **46**, 1410-1416.
72. A. J. J. Bos, P. Dorenbos, A. Bessière and B. Viana, *Radiation Measurements*, 2008, **43**, 222-226.
73. F. You, A. J. J. Bos, Q. Shi, S. Huang and P. Dorenbos, *Physical Review B*, 2012, **85**, 115101.
74. H. D. Luo, A. J. J. Bos and P. Dorenbos, *Journal of Physical Chemistry C*, 2016, **120**, 5916-5925.
75. T. Lyu and P. Dorenbos, *Chemistry of Materials*, 2020, **32**, 1192-1209.
76. A. Dobrowolska, A. J. J. Bos and P. Dorenbos, *Journal of Physics D: Applied Physics*, 2014, **47**, 335301.
77. P. Wang, X. Xu, D. Zhou, X. Yu and J. Qiu, *Inorganic Chemistry*, 2015, **54**, 1690-1697.
78. K. Chakrabarti, V. K. Mathur, J. F. Rhodes and R. J. Abbundi, *Journal of Applied Physics*, 1988, **64**, 1363-1366.
79. H. Luo, A. J. J. Bos and P. Dorenbos, *The Journal of Physical Chemistry C*, 2017, **121**, 8760-8769.
80. J. R. Partington, *History of chemistry*, Macmillan International Higher

Education, 1964.
81. P. J. Sadler, H. Li and H. Sun, *Coordination Chemistry Reviews*, 1999, **185-186**, 689-709.
82. H.-T. Sun, J. Zhou and J. Qiu, *Progress in Materials Science*, 2014, **64**, 1-72.
83. A. M. Srivastava and S. J. Camardello, *Optical Materials*, 2015, **39**, 130-133.
84. R. H. P. Awater and P. Dorenbos, *Journal of Luminescence*, 2017, **184**, 221-231.
85. P. W. M. Jacobs, *Journal of Physics and Chemistry of Solids*, 1991, **52**, 35-67.
86. G. Blasse, A. Meijerink, M. Nomes and J. Zuidema, *Journal of Physics and Chemistry of Solids*, 1994, **55**, 171-174.
87. M. Peng and L. Wondraczek, *Opt. Lett.*, 2009, **34**, 2885-2887.
88. P. Boutinaud and E. Cavalli, *Chemical Physics Letters*, 2011, **503**, 239-243.
89. R. H. P. Awater and P. Dorenbos, *The Journal of Physical Chemistry C*, 2016, **120**, 15114-15118.
90. R. H. P. Awater and P. Dorenbos, *Journal of Luminescence*, 2017, **188**, 487-489.

2

Charge carrier trapping processes in lanthanide doped La-, Gd-, Y-, and LuPO$_4$

Graphical abstract

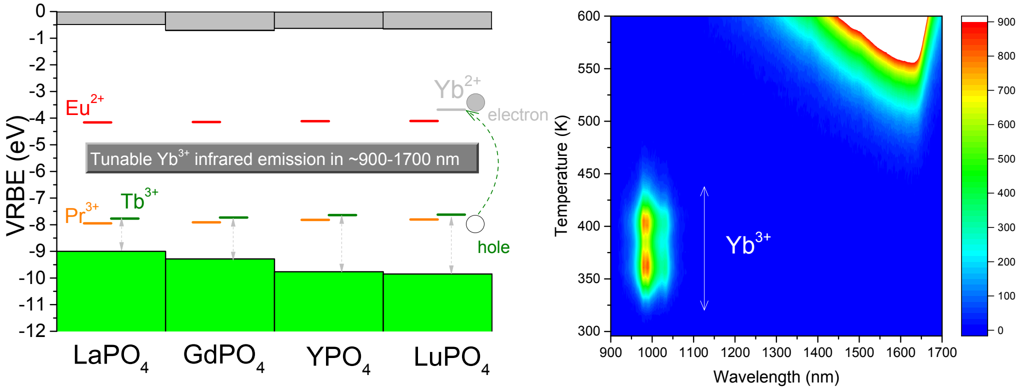

This chapter is based on the publication: **T. Lyu*** and P. Dorenbos, ***Journal of Materials Chemistry C***, 2018, 6, 369-379.

2.1. Abstract

Various methods for deliberate design electron and hole trapping materials are explored with a study on double lanthanide doped rare earth ortho phosphates. Cerium acts as recombination center while lanthanide codopants as electron trapping centers in $LaPO_4:0.005Ce^{3+},0.005Ln^{3+}$. The electron trap depth generated by lanthanide codopants can be tailored by the choice of lanthanide, and for fixed set of lanthanide dopants like in $Gd_{1-x}La_xPO_4:0.005Ce^{3+},0.005Ho^{3+}$ solid solutions by changing x leading to conduction band (CB) engineering. Here, the electrons liberated from Ho^{2+} recombine through the conduction band at Ce^{4+} to yield Ce^{3+} 5d-4f emission. In contrast, samarium, europium and ytterbium are recombination centers, while Tb^{3+} and Pr^{3+} act as hole trapping centers in double lanthanide doped YPO_4. For Tb^{3+} and Pr^{3+} codopants recombination is realized via hole release rather than the more common reported electron release. The holes recombine via the valence band with the electrons trapped at Yb^{2+}, Sm^{2+}, or Eu^{2+} to generate 4f-4f luminescence from Yb^{3+}, Sm^{3+}, or Eu^{3+}. Lu^{3+} was introduced in YPO_4 to tailor the valence band (VB) energy and to tune the hole trap depths of Tb^{3+} and Pr^{3+} in $Y_{1-x}Lu_xPO_4:0.005Ln^{3+}$ solid solutions. Our results promote the deliberate design electron and hole trapping materials from deep understanding of trap level locations and on the transport and trapping processes of charge carriers.

2.2. Introduction

The trapping and release processes of charge carriers are of interest for practical applications and from a theoretical point of view[1, 2]. When electron and hole trapping materials are exposed to high energy radiation, for instance, beta radiation or ultraviolet (UV) light, free electron and hole charge carriers will be generated and then trapped in trapping centers, which are usually lattice defects or impurities[3]. The trapped holes or electrons can be released by optical, thermal, or mechanical excitation, ultimately yielding photon emission at wavelengths that can range from ultraviolet to infrared, depending on the recombination centers and type of compound[1, 4]. For storage phosphors applied in X-ray imaging, deep traps (~2 eV) are needed to avoid thermal fading at room temperature (RT)[5]. Relatively shallow traps (<~0.7 eV) are required to generate RT afterglow[6, 7]. So, if we can control the trap depth of holes or electrons, then in principle one may engineer or deliberate design storage and afterglow properties.

The electron trapping and release process has been widely investigated[1, 8-11]. Ueda *et al.* reported the valence change of Ce^{3+} and Cr^{3+} in $Y_3Al_2Ga_3O_{12}$ persistent phosphors using X-ray absorption near edge structure (XANES) spectroscopy[12]. Concentration of both Ce^{4+} and Cr^{2+} rises after exposing the sample to UV light. This shows that Ce^{3+} is the electron donor and the electrons produced via photoionization can be trapped by Cr^{3+} electron trapping centers. By thermal excitation at room temperature, the electrons trapped at Cr^{2+} will be liberated slowly to the conduction band and then recombine with Ce^{4+} to finally generate Ce^{3+} emission peaked at ~510 nm[13]. A similar partial oxidation of Eu^{2+} to Eu^{3+} after UV light excitation is observed in the well-known persistent phosphor $SrAl_2O_4$:Eu^{2+},Dy^{3+} using XANES[14].

Holes can also be liberated to recombine with a luminescence center. The hole transport can be as a migrating V_k center or through the valence band[2]. Such hole trapping and release processes are scarcely reported. One of the few cases is by Chakrabarti *et al.* in the 1980s who observed that cerium acts as a hole trapping center and samarium as a recombination center in MgS:Ce^{3+},Sm^{3+} after UV light excitation[15]. The holes liberate from Ce^{4+} earlier than electrons from Sm^{2+} and recombine with Sm^{2+} generating Sm^{3+} 4f-4f emission. The other two examples are from studies by Luo *et al.* on $Gd_{1-x}La_xAlO_3$[7] and RE_2O_2S[2]. The trap depth of the Tb^{3+} hole trapping center in $Gd_{1-x}La_xAlO_3$ can be adjusted by changing x leading to valence band energy changes. In RE_2O_2S:Ti^{4+} a hole release process leading to Ti^{4+} charge transfer emission was identified.

The rare reporting on hole trapping and release processes is associated with a lack in our knowledge on how to distinguish such a hole trapping process from an electron trapping process. For that we need information on where the hole or electron traps are located within the bandgap. It is not until 2012 that the chemical shift model was published that enables one to create a vacuum referred binding energy (VRBE) diagram. One may now compare the binding energy at the valence band top or conduction band bottom in various compounds with respect to a same reference energy[16-19]. This model shows that the VRBE in the $4f^n$ ground state of trivalent and divalent lanthanides is almost independent on the type of compound[20-23]. Consequently, lanthanide related hole trap depth can be tuned by altering the VRBE at the top of the valence band and electron trap depth through tailoring the VRBE at the bottom of the conduction band[7].

In this paper, based on the constructed VRBE diagrams and band gap engineering, we will show how to deliberate design storage phosphors through precisely controlling both the releases of electrons and of holes. La-, Gd-, Y-, and $LuPO_4$ phosphates were selected as hosts due to their simple structures with only one site to substitute for a trivalent lanthanide. To demonstrate the design concept, the constructed VRBE diagram of YPO_4 is already shown in Fig. 2.1. The zigzag curves I and II link the VRBE of an electron in the ground states of the divalent and trivalent lanthanides, respectively. Such diagram is very useful to decide what shallow and deep electron hole trap combinations can be used to arrive at specific properties. For example, Eu^{3+} 4f-4f emission will be observed for the Eu^{3+}-Tb^{3+}

pair in YPO_4 after hole release from Tb^{4+} since it is predicted that Eu^{3+} will act as a much deeper electron trap than Tb^{3+} as a hole trap.

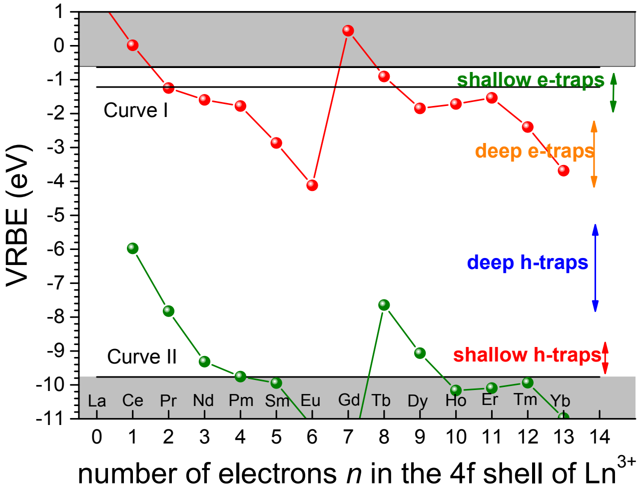

Fig. 2.1. Vacuum referred binding energy (VRBE) diagram of YPO_4 with various Ln traps.

Fig. 2.2 shows the stacked VRBE diagram for the four $REPO_4$ compounds studied in this work. It shows that the lanthanide trap depth can be engineered by changing the VRBE at the conduction band bottom or valence band top. For instance, the hole trap depth of Pr^{3+} or Tb^{3+} can be decreased by replacing Lu^{3+} by Y^{3+}, Gd^{3+}, or La^{3+}.

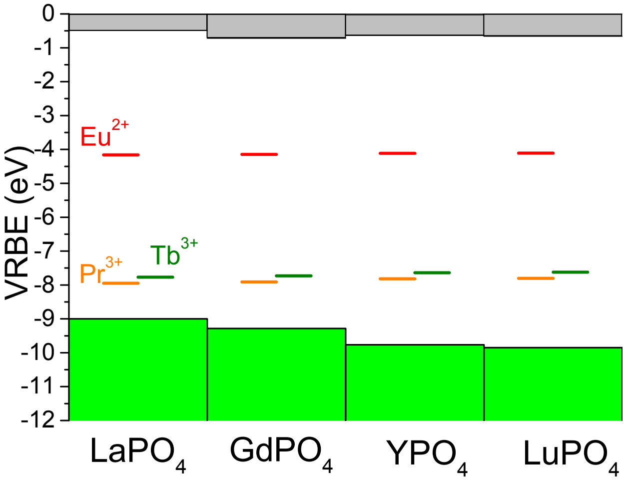

Fig. 2.2. Stacked VRBE diagram of $REPO_4$ with the binding energy in the ground states of Eu^{2+}, Pr^{3+}, and Tb^{3+}.

2.3. Experimental

All starting chemicals were purchased from Sigma-Aldrich and used without further treatment. Polycrystals were fabricated by a high temperature solid state reaction. The appropriate stoichiometric mixture of $NH_4H_2PO_4$ (99.99%), La_2O_3 (99.99%), Gd_2O_3 (99.99%), Y_2O_3 (99.99%), Lu_2O_3 (99.999%) and other rare earth oxides (99.999%) were accurately weighted and mixed well in an agate mortar with the help of acetone. The concentrations of the other rare earth oxides were fixed at 0.5 mol %. Afterwards, it was fired in an alumina crucible for 10 h at 1400 ^{o}C under a reducing atmosphere of H_2/N_2 (H_2:N_2 7%:93%). After cooling, the as-synthesized polycrystals were ground again and fired at 1400 ^{o}C for another 10 h under the same reducing atmosphere. Finally, the polycrystals were naturally cooled to room temperature, and the obtained compounds were ground into powder before subjecting them to further measurements.

The crystal structures were characterized by a PANalytical XPert PRO X-ray diffraction system with cobalt Kα (λ=0.1788901 nm) X-ray tube at 40 mA and 45 kV. The collected X-ray diffraction (XRD) patterns were compared with reference data derived from the Pearson's Crystal Database. The photoluminescence emission (PL) and PL excitation (PLE) spectra were recorded with equipment that has a UV/VIS branch with a 500 W Hamamatsu CW xenon lamp and Horiba Gemini 180 monochromator, and a VUV/UV branch that is constituted of an ARC VM502 vacuum monochromator and a deuterium lamp (D_2 lamp). Princeton Instruments Acton SP 2300 monochromator and PerkinElmer Photon Counting Module MP1993 were used to disperse and record the emission from the samples. The sample temperature was controlled with a closed-cycle helium (He) cryostat (Model HC-4, APD Cryogenics Inc.) and a temperature controller of Lake Shore 331. All presented excitation curves were corrected for the incident photon flux.

Thermoluminescence (TL) measurements were recorded utilizing a RISØ TL/OSL reader (model DA-15) with DA-20 controller. All samples were irradiated with a ^{90}Sr/^{90}Y β source with a dose rate of 0.7 mGy s^{-1} in the TL setup in complete darkness. All TL measurements were performed under a flow of nitrogen gas. Samples with masses <20 mg and area ~0.6 cm^2 were used. For the TL measurements on samples where Ce^{3+} is the recombination center a 3 mm Hoya C5-58 filter in the wavelength range of 350-470 nm was placed between the EMI 9635QA photomultiplier tube (PMT) and the sample to record Ce^{3+} emission only. In order to select the red emission when for example Eu^{3+} is the recombination center, a 600 nm bandpass filter of 600FS40-50 (S250-07) was placed between the PMT and the samples.

For the low temperature TL (LTTL) measurements (90-450 K), the samples were first heated to 450 K for 2 min to empty all relevant traps and then cooled to 90 K followed by 600 s β irradiation with a ^{90}Sr/^{90}Y β source at a dose rate of 0.4 mGy s^{-1}. LTTL recordings were measured at the heating rate of 1 K/s in a sample chamber operating under vacuum (10^{-7} mbar) monitoring Eu^{3+} red emission with a PerkinElmer channel photomultiplier tube (MP-1393). Liquid nitrogen was utilized as a cooling medium.

Prior to the recording the TL emission (TLEM) spectra, the samples were heated to 900 K 3 times to empty all relevant traps and then exposed to γ-ray irradiation from a ^{60}Co source to charge the traps. Emission was recorded with a UV/vis spectrometer (Ocean Optics, model QE65000) in the 200-900 nm range, and a near-infrared (NIR) spectrometer (Ocean Optics, model NIRQ512) in the 900-1700 nm range. Both spectrometers have a high-resolution composite grating of 300 lines/mm and an 100 mm entrance aperture, leading to wavelength resolution of full width at half maximum (FWHM) of 3.3 nm.

TL excitation (TLE) spectra were recorded by means of first illuminating samples during 2400 s using a monochromatic photon beam from a 150 W xenon lamp (Hamamatsu L2273) filtered by a monochromator (Oriel Cornerstone 130). The system was operated under Labview^{TM} allowing the collection of multiple TL glow curves from room temperature to 720 K at heating rate of 5 K/s with changing illumination wavelength. The wavelength step is 10 nm, and the slit width was set at 0.1 cm resulting in a spectrum resolution of 8 nm. The plot of the integrated TL glow curve versus the excitation wavelength is called the TL excitation spectrum[24]. To collect Eu^{3+} emission a 600 nm bandpass filter of 600FS40-50 was placed between the PMT and the samples.

2.4. Results

2.4.1. X-ray diffraction and photoluminescence spectroscopy

Fig. 2.3 shows part of the XRD patterns of $Gd_{1-x}La_xPO_4$:0.005Ce^{3+},0.005Ho^{3+} (x=0-1) solid solutions. $GdPO_4$ and $LaPO_4$ have the same crystal structure with space group $P12_1/c1$. Compared to pure $GdPO_4$ the diffraction peaks show a slight shift towards smaller 2θ angles because the lanthanum ions enter into the smaller gadolinium sites and increase the cell volume. Similar solid solutions were prepared for $Y_{1-x}Lu_xPO_4$:0.005Eu^{3+},0.005Tb^{3+} and the XRD patterns shown in Fig. S2.1 agree with that in Levushkina *et al.*[25]

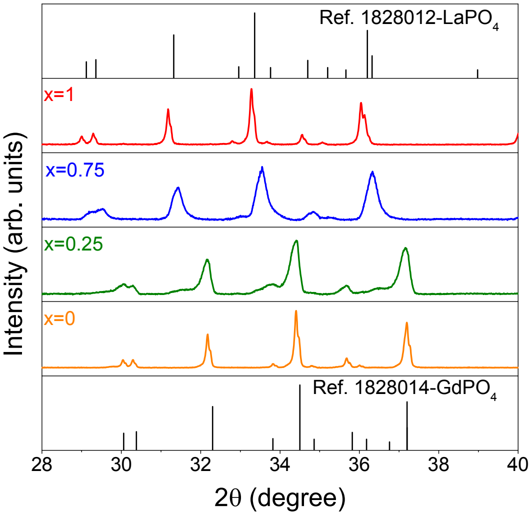

Fig. 2.3. XRD patterns in the range from 28 to 40° for $Gd_{1-x}La_xPO_4$:$0.005Ce^{3+}$,$0.005Ho^{3+}$ solid solutions.

Fig. 2.4 shows the VUV excitation spectra of 590 nm Eu^{3+} emission in $REPO_4$: $0.005Eu^{3+}$,$0.005Tb^{3+}$ at 10 K. The shortest wavelength peak is due to host exciton creation. Its energy E^{ex} increases from 8.05 eV for $LaPO_4$ to 8.67 eV for $LuPO_4$ which agrees with previous reports, i.e., 8.00 eV for $LaPO_4$[22] and 8.60 eV for $LuPO_4$[26].

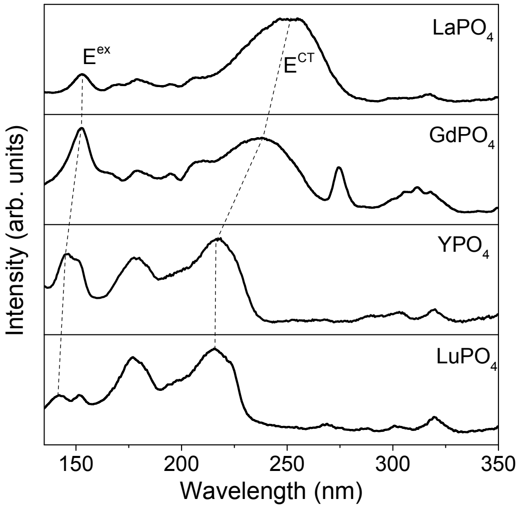

Fig. 2.4. Photoluminescence excitation (PLE) spectra (λ_{em}=590 nm) of $REPO_4$:$0.005Eu^{3+}$, $0.005Tb^{3+}$ (RE=La, Gd, Y, and Lu) samples at 10 K.

The broad excitation bands near 200-260 nm are due to electron transfer from the valence band to Eu^{3+} which are known as the charge transfer (CT) bands. The energy E^{CT} at the maximum of the CT-band increases from 4.88 eV for $LaPO_4$ to 5.76 eV for $LuPO_4$. These CT-energies are similar to those in literature: e.g., 4.84 eV for $LaPO_4$ and 5.74 eV for $LuPO_4$[22, 27].

2.4.2. Engineering the electron trap depth

A series of $LaPO_4$:$0.005Ce^{3+}$,$0.005Ln^{3+}$ samples was prepared to demonstrate electron trap depth engineering. All samples are of single phase as demonstrated in the XRD spectra of Fig. S2.1. Fig. 2.5 shows the normalized TL glow curves. Each of the Ln^{3+} codopants induces a TL glow at different temperature T_m as listed in column 2 of Table 2.1.

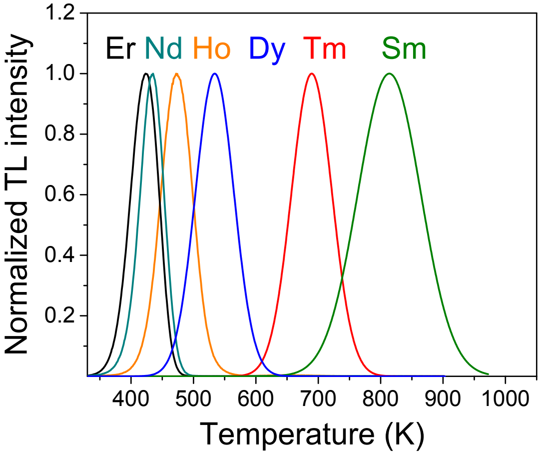

Fig. 2.5. Normalized TL glow curves of $LaPO_4$:$0.005Ce^{3+}$,$0.005Ln^{3+}$ at heating rate β=5 K/s while monitoring the Ce^{3+} 5d-4f emission.

Table 2.1. TL results on $LaPO_4$:$0.005Ce^{3+}$,$0.005Ln^{3+}$ showing T_m (K), and the trap depths E (eV) derived from the variable heating rate plot.

Ln	T_m	E
Nd	434	1.08
Sm	817	2.07
Dy	535	1.34
Ho	474	1.18
Er	424	1.05
Tm	690	1.74

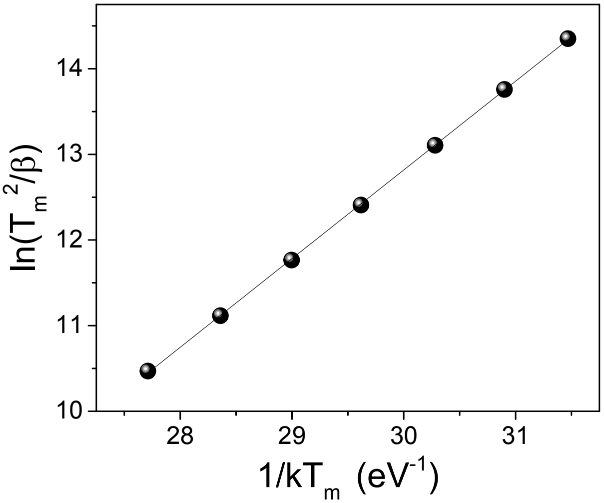

Fig. 2.6. Variable heating rate plot of $LaPO_4$:$0.005Ce^{3+}$,$0.005Er^{3+}$. The used heating rates were 0.08, 0.15, 0.30, 0.63, 1.25, 2.5, and 5 K/s.

Assuming first-order TL-recombination kinetics, the trap depth can be determined from a variable heating rate plot using the relation[28-31]

$$\ln\left(\frac{T_m^2}{\beta}\right)=\frac{E}{kT_m}+\ln\left(\frac{E}{ks}\right) \tag{2.1}$$

where β is the heating rate (K/s), k is the Boltzmann constant (eV/K), and s is the frequency factor (s^{-1}). Fig. 2.6 shows the variable heating rate plot for $LaPO_4$: $0.005Ce^{3+}$,$0.005Er^{3+}$. For the trap depth a value of 1.05 eV is obtained from the slope of the line through the data and for the frequency factor a value of 1.02×10^{12} s^{-1} is obtained from the intercept with the vertical axis. Since all Ln^{3+} codopants locate at the La^{3+} site, we will assume that the frequency factor s remains a constant.[7, 32] The trap depths for the other codopants then Er^{3+} were determined by using T_m from column 2 of Table 2.1 and solving Eq. (2.1) with β=5 K/s. The trap depths are shown in column 3 of Table 2.1.

Fig. 2.7a shows the normalized TL glow curves for $Gd_{1-x}La_xPO_4$:$0.005Ce^{3+}$, $0.005Ho^{3+}$ solid solutions. T_m gradually shifts towards higher temperature with increasing x. The TL glow peak for x=0.25 becomes most broad. From variable heating rate plot fits for x=0, 0.5, 0.75, and 1, as can be found in Fig. S2.2, the trap depths and the frequency factors that are compiled in Table 2.2 were derived.

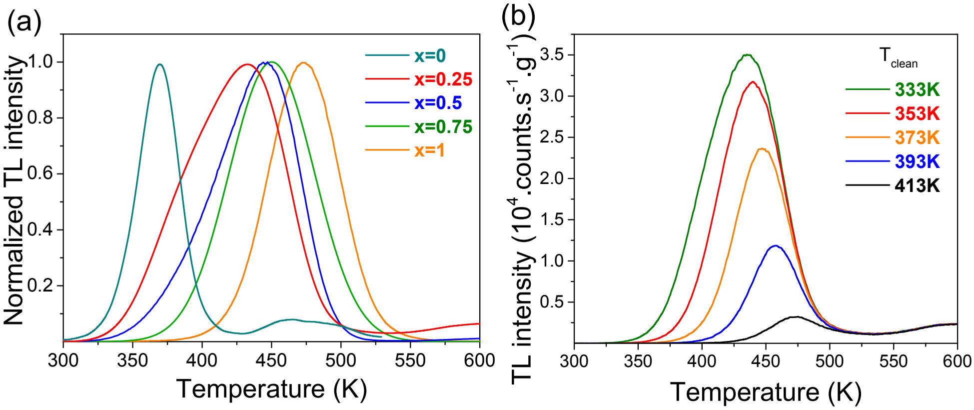

Fig. 2.7. (a) Normalized TL glow curves of $Gd_{1-x}La_xPO_4$:0.005Ce^{3+},0.005Ho^{3+} solid solutions at β=5 K/s. (b) TL glow curves for x=0.25 after a peak cleaning at T_{clean}.

Table 2.2. TL results on $Gd_{1-x}La_xPO_4$:0.005Ce^{3+},0.005Ho^{3+} solid solutions listing the T_m (K), and the trap depth E (eV), and frequency factor s (s^{-1}) as obtained from variable heating rate plots. The data for x=0.25 is from the peak cleaning and the initial rise method.

x	T_m	E	s
0	369	0.84	9.53×10^{10}
0.25	432	0.95-1.20	
0.5	445	1.10	3.58×10^{12}
0.75	451	1.16	2.51×10^{12}
1	474	1.22	2.95×10^{12}

To study the glow peak broadening of the sample with x=0.25 we have applied the peak cleaning technique[33]. After exposure to the β source for 200 s at room temperature, the sample is heated to different peak clean temperature (T_{clean}) and kept at that temperature for 400 s. Subsequently a TL recording at a heating rate of 5 K/s is made. Fig. 2.7b shows that with the increase of T_{clean}, the TL intensity decreases and T_m increases. This shows the presence of a trap depth distribution for the sample with x=0.25, and the increase of T_m is due to the fact that the electrons trapped at shallow traps are liberated at T_{clean} and only the deeper traps remain occupied. The trap depth against T_{clean} can be found by using the initial rise method as explained in the supplementary information in Fig. S2.3. The trap depth varies between 0.9 and 1.2 eV as shown column 3 of Table 2.2. Also for x=0.5 and 0.75 there is peak broadening related to a trap depth distribution and the energies in column 3 of Table 2.2 should be regarded as an average trap depth then.

2.4.3. Engineering hole release in Y-Lu phosphate solid solutions

Fig. 2.8 shows the TL emission (TLEM) plots for YPO_4:0.005Eu^{3+},0.005Tb^{3+}, YPO_4:0.005Sm^{3+},0.005Tb^{3+}, YPO_4:0.005Yb^{3+},0.005Tb^{3+}, and YPO_4:0.005Yb^{3+}. Additional TL emission plots for other $REPO_4$ with other combinations of Ln^{3+} doping can be found in Fig. S2.4.

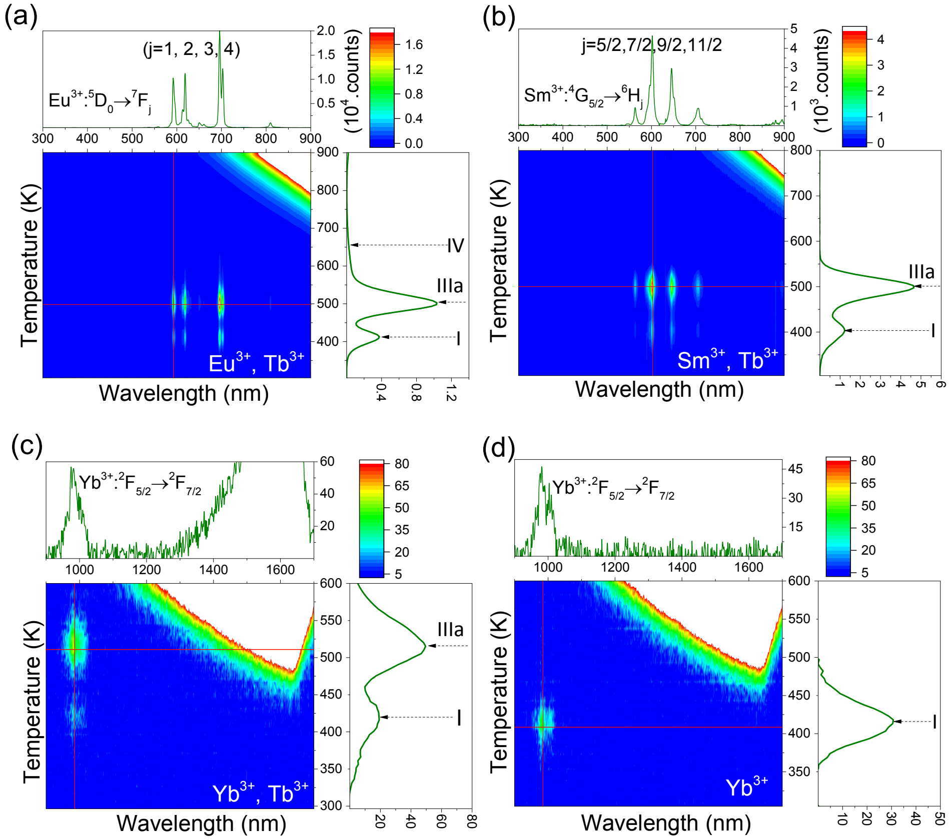

Fig. 2.8. Thermoluminescence emission (TLEM) spectra of (a) YPO_4:0.005Eu^{3+},0.005Tb^{3+}, (b) YPO_4:0.005Sm^{3+},0.005Tb^{3+}, (c) YPO_4:0.005Yb^{3+},0.005Tb^{3+}, and (d) YPO_4:0.005Yb^{3+} at the heating rate of 1 K/s.

The glow peak at ~507 K for YPO_4:0.005Eu^{3+},0.005Tb^{3+}, which will be referred to as peak IIIa, is also observed for YPO_4:0.005Sm^{3+},0.005Tb^{3+} in Fig. 2.8b and YPO_4:0.005Yb^{3+},0.005Tb^{3+} in Fig. 2.8c. From the studies by Bos *et al.* [35] on YPO_4:0.005Sm^{3+},0.005Tb^{3+} and YPO_4:0.005Tm^{3+},0.005Tb^{3+} this glow peak was attributed to hole release from Tb^{4+}. Note that characteristic luminescence originating from Tb^{3+} is absent in Fig. 2.8 but characteristic emission from either

Eu^{3+}, Sm^{3+}, or Yb^{3+} is observed. This applies to YPO_4 but equally well to the other $REPO_4$ in Fig. S2.4.

The effect of replacing Tb^{3+} for Pr^{3+} or for Ce^{3+} is shown in the TL glow curves of Fig. 2.9a and 9b. Information on TLEM can be found in Fig. S2.4. Pr^{3+} gives a glow peak, hereafter referred to as peak IIIb, that is at 10 K lower temperature than peak IIIa for Tb^{3+}. The glow peak is absent when Ce^{3+} is the co-dopant or in case of absence of co-dopants. The VRBE diagram of Fig. 2.1 predicts that Tb^{3+} and Pr^{3+} provide about the same hole trapping depth and therefore peak IIIb is attributed to hole release from Pr^{4+}. From the variable heating rate plot of YPO_4:Eu^{3+},Tb^{3+} we derived a frequency factor of 1.45×10^{13} s^{-1} for hole release from Tb^{4+}. We assumed that the same value applies for hole release from Pr^{4+}, and then by using the observed T_m in Fig. 2.9 and Eq. (2.1) trap depths are derived as shown in Table 2.3.

Glow peak I is despite different sets of lanthanide dopants present in all TL-spectra of Fig. 2.9a and 2.9b. Its origin is not lanthanide related. We attribute it to hole release from unknown defects. The same applies to glow peaks II and IV that are present when Eu^{3+} is used as deep electron trap.

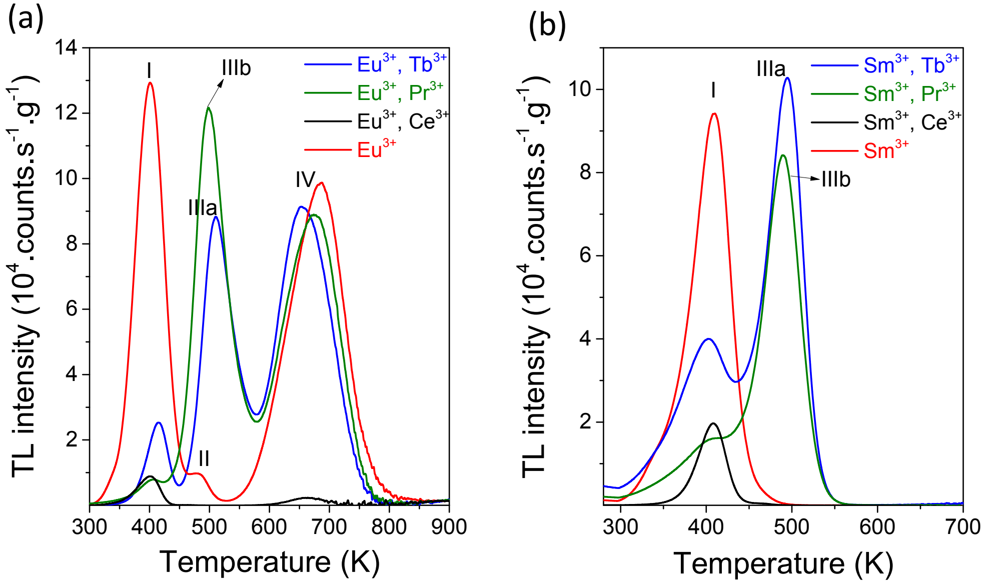

Fig. 2.9. TL glow curves of (a) YPO_4:0.005Eu^{3+},0.005Ln^{3+} and (b) YPO_4:0.005Sm^{3+}, 0.005Ln^{3+} recorded after 2000 s β source radiation monitoring the emission from Eu^{3+} or from Sm^{3+} at the heating rate of 1 K/s.

Table 2.3. TL results for $REPO_4$:0.005Ln^{3+},Tb^{3+} or Pr^{3+} providing the trap depths E (eV) for the glow peaks IIIa and IIIb, and the frequency factor s (s^{-1}).

Compound	s	Ln^{3+}	Tb E(IIIa)	Pr E(IIIb)
YPO_4	1.45×10^{13}	Eu^{3+}	1.45	1.41
YPO_4	1.45×10^{13}	Sm^{3+}	1.42	1.40
YPO_4	1.45×10^{13}	Yb^{3+}	1.46	1.46
$Y_{0.75}Lu_{0.25}PO_4$	4.45×10^{13}	Eu^{3+}	1.52	1.50
$Y_{0.5}Lu_{0.5}PO_4$	2.53×10^{14}	Eu^{3+}	1.65	1.63
$Y_{0.5}Lu_{0.5}PO_4$	2.53×10^{14}	Yb^{3+}	1.62	1.61
$Y_{0.25}Lu_{0.75}PO_4$	1.29×10^{15}	Eu^{3+}	1.78	1.75
$LuPO_4$	1.03×10^{15}	Eu^{3+}	1.84	1.80
$LuPO_4$	1.03×10^{15}	Yb^{3+}	1.79	1.78
$LaPO_4$	2.14×10^{12}	Eu^{3+}	0.63	0.55

Fig. 2.10 shows the TL glow curves for $Y_{1-x}Lu_xPO_4$:0.005Eu^{3+},0.005Tb^{3+} solid solutions. With increasing x, peak IIIa shifts from 507 towards 572 K. The trapping parameters were derived using the variable heating rate plots[13] in Fig. S2.6, and results are compiled in Table 2.3. TL glow curves for $Y_{1-x}Lu_xPO_4$:0.005Eu^{3+}, 0.005Pr^{3+} solid solutions can be found in Fig. S2.7. Like peak IIIa for Tb^{3+}, peak IIIb for Pr^{3+} shifts from 494 towards 560 K with increasing x. The derived trapping parameters are shown in Table 2.3.

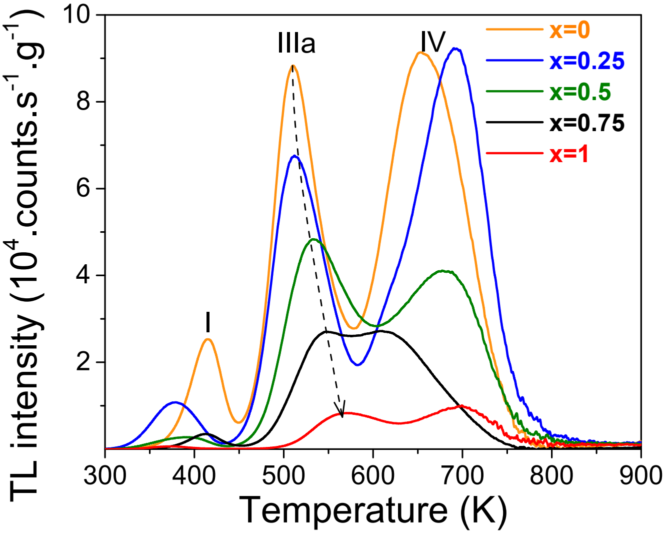

Fig. 2.10. TL glow curves for $Y_{1-x}Lu_xPO_4$:0.005Eu^{3+},0.005Tb^{3+} solid solutions monitoring the red emission from Eu^{3+} at the heating rate of 1 K/s.

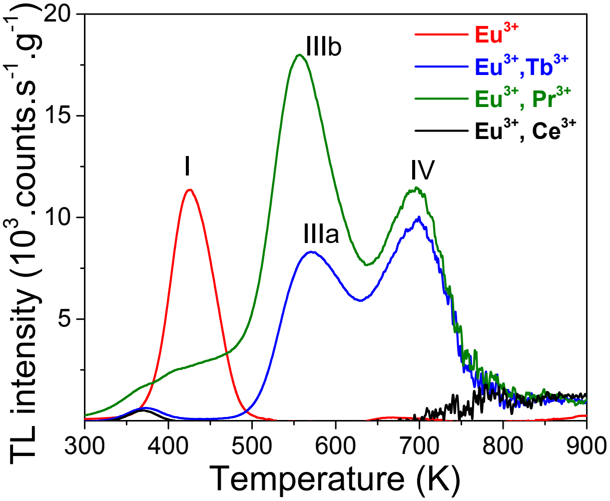

Fig. 2.11. TL glow curves for LuPO4:0.005Eu^{3+},0.005Ln^{3+} (Ln=Tb, Pr, and Ce) samples monitoring the red emission from Eu^{3+} at the heating rate of 1 K/s.

Fig. 2.11 compares the TL glow curves of LuPO4:0.005Eu^{3+},0.005Ln^{3+}. Similar as in Fig. 2.9, the glow peak IIIb for hole release from Pr^{4+} appears at about 10 K lower temperature than that from Tb^{4+}, and also glow peaks I and IV seem to be present. The TL glow curves of the single Eu^{3+} and the Eu^{3+},Ce^{3+}-codoped samples are shown to demonstrate the absence of peaks IIIa and IIIb.

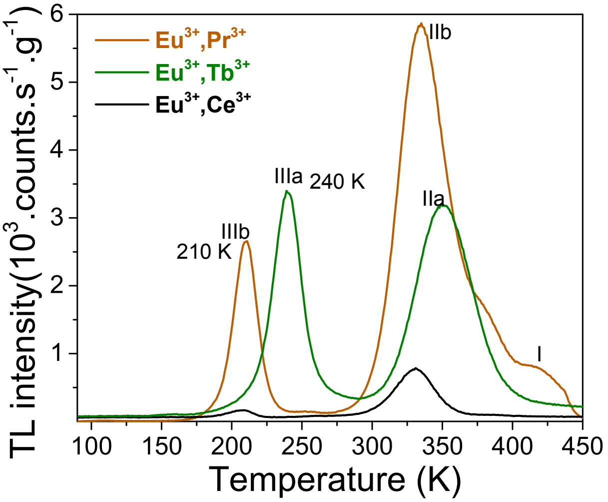

Fig. 2.12. TL glow curves for LaPO4:0.005Eu^{3+},0.005Ln^{3+} (Ln=Tb, Pr, or Ce) samples monitoring the Eu^{3+} emission in the temperature range of 90-450 K at the heating rate of 1 K/s.

Fig. 2.12 shows the low temperature TL (LTTL) glow curves of $LaPO_4$: $0.005Eu^{3+}$,$0.005Ln^{3+}$. Similar as in Fig. 2.9 and 2.11, Pr gives rise to an additional glow peak below RT denoted as IIIb and Tb^{3+} to a glow peak IIIa at about 30 K higher temperature. The TL glow curve of the $LaPO_4$:Eu^{3+},Ce^{3+} is shown to demonstrate the absence of peaks IIIa and IIIb. The glow peaks appearing above room temperature were further also studied with the Riso reader as shown in Fig. S2.8. The variable heating rate plot for glow peak IIa of $LaPO_4$:$0.005Eu^{3+}$, $0.005Tb^{3+}$ as shown in Fig. S2.8b provides the trapping parameters. By assuming a similar frequency factor for glow peaks IIIa and IIIb the activation energies compiled in Table 2.3 were estimated.

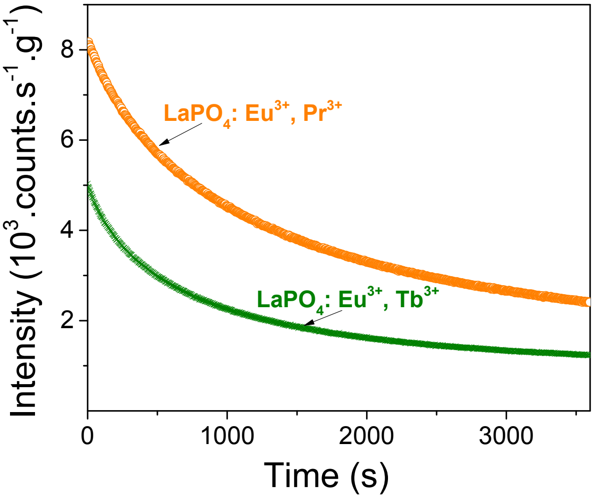

Fig. 2.13. Room temperature isothermal decay curves of $LaPO_4$:$0.005Eu^{3+}$,$0.005Tb^{3+}$ and $LaPO_4$:$0.005Eu^{3+}$,$0.005Pr^{3+}$. A 600 nm bandpass filter (600FS40-50) was used to monitor the red emission of Eu^{3+}.

Because of the intense glow peaks near room temperature in the $LaPO_4$ samples we measured the room temperature isothermal decay curves as shown in Fig. 2.13. $LaPO_4$:$0.005Eu^{3+}$,$0.005Pr^{3+}$ with the most intense glow peak also shows the most intense afterglow.

For $LaPO_4$:$0.005Eu^{3+}$,$0.005Tb^{3+}$ and $LaPO_4$:$0.005Eu^{3+}$,$0.005Pr^{3+}$ we have red afterglow from Eu^{3+}. Fig. 2.14 shows the TL emission (TLEM) spectrum of $LaPO_4$: $0.005Yb^{3+}$,$0.005Pr^{3+}$ where the emission is from Yb^{3+} at 1000 nm in the short wavelength infrared (SWIR) 900-1700 nm range. Additional TL emission plots for other $REPO_4$ with combinations of Yb^{3+} and Tb^{3+} or Pr^{3+} can be found in Fig. S2.4i-S2.4l and in each case IR Yb^{3+} TL-glow is observed. Infrared persistent luminescence from Yb^{3+} appears in $LaPO_4$:$0.005Yb^{3+}$,$0.005Pr^{3+}$ and $LaPO_4$: $0.005Yb^{3+}$,$0.005Tb^{3+}$ at room temperature.

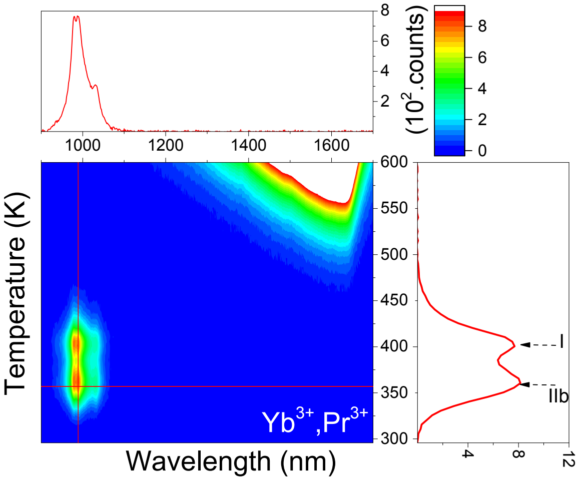

Fig. 2.14. TL emission (TLEM) spectrum for $LaPO_4$:0.005Yb^{3+},0.005Pr^{3+}.

The room temperature afterglow of $LaPO_4$:0.005Eu^{3+},0.005Tb^{3+} and $LaPO_4$: 0.005Eu^{3+},0.005Pr^{3+} is related to the lowest temperature glow peak. To study the origin of this glow peak Fig. 2.15 shows the TL excitation (TLE) spectrum of the low temperature glow peak at 300-380 K of $LaPO_4$:0.005Eu^{3+},0.005Tb^{3+}. A broad TLE band ranging from 200 to 300 nm and peaking at 260 nm is observed. The width and position is similar as that of the photoluminescence excitation (PLE) spectrum of Eu^{3+} single doped $LaPO_4$ also shown in Fig. 2.15. This demonstrates that after Eu^{3+} CT-band excitation, the holes that are generated in the valence band are trapped by the defects responsible for the low temperature glow peak.

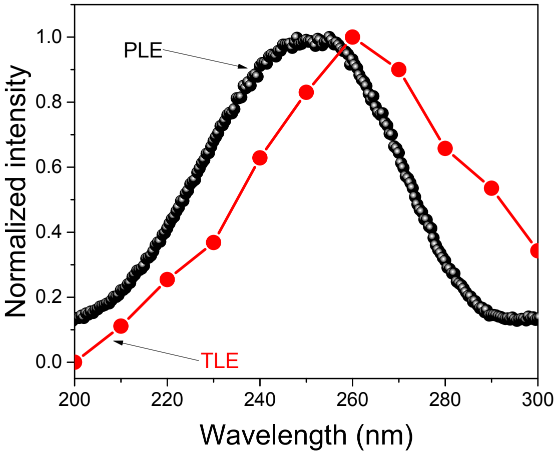

Fig. 2.15. Thermoluminescence excitation (TLE) spectrum of $LaPO_4$:0.005Eu^{3+},0.005Tb^{3+} and photoluminescence excitation (PLE) spectrum (λ_{em}=590 nm) of $LaPO_4$:0.005Eu^{3+} performed at room temperature.

2.5. Discussion

The vacuum referred binding energy (VRBE) diagrams shown in Fig. 2.1 are first discussed, and then we will show how they can be used for tailoring the trapping and release process of electrons and holes in $REPO_4$. The energy of an electron at rest in vacuum is defined as the reference energy, i.e., energy zero[18]. VRBE is defined as the energy needed to extract an electron from a system and bring it to the vaccum[16, 17]. This electron can be from a host band or from an impurity ground or excited state.

Table 2.4. Parameters used to establish the VRBE diagrams for $REPO_4$ (RE=La, Gd, Y, and Lu) in eV and the results from these diagrams.

$REPO_4$	U	E_{Eu}^{2+}	$E_{Eu}^{3+,CT}$	E_V	E^{ex}	E_C	E_{Tb}^{3+}	E_{Pr}^{3+}
La	7.18	-4.16	4.84	-9.00	8.00	-0.49	-7.77	-7.95
Gd	7.15	-4.15	5.14	-9.28	8.05	-0.71	-7.73	-7.91
Y	7.09	-4.12	5.65	-9.77	8.55	-0.63	-7.64	-7.82
Lu	7.08	-4.11	5.74	-9.85	8.60	-0.66	-7.62	-7.80

To construct VRBE diagrams, one first needs the values for the U-parameter that are listed in column 2 of Table 2.4. The U-parameters were derived already for $REPO_4$ (RE=La, Y, and Lu) in Ref. [22] and for $GdPO_4$ it is estimated. From these values the VRBE in the Eu^{2+} ground state is calculated with the chemical shift model and results are shown in column 3 of Table 2.4. The VRBE at the valence band top shown in column 5 can be obtained employing the VB→Eu^{3+} CT-energy as measured in Fig. 2.4 and given in column 4. The VRBE E_C at the conduction band bottom shown in column 7 of Table 2.4 is obtained from the host exciton creation energy E^{ex} in column 6 by adding the exciton binding energy estimated as $0.008(E^{ex})^2$ in Ref. [19]. We will use the most recent parameter sets from Ref. [19] to construct the double zigzag curves which then provide the VRBE in divalent lanthanide ground states and trivalent ground states as listed for Tb and Pr in columns 8 and 9.

2.5.1. Electron trap depth tailoring via conduction band engineering

Fig. 2.5 showed that T_m strongly depends on the type of the lanthanide in $LaPO_4{:}0.005Ce^{3+},0.005Ln^{3+}$. A similar dependence was reported for $GdAlO_3{:}0.01Ce^{3+},0.01Ln^{3+}$[7], $Y_3Al_5O_{12}{:}0.003Ce^{3+}/Pr^{3+}/Tb^{3+},0.003Ln^{3+}$[34], and YPO_4: $0.005Ce^{3+},0.005Ln^{3+}$[35]. Using the derived electron trap depths as listed in column 3 of Table 2.1 we have placed the Ln^{2+} ground state levels below the conduction band in the VRBE diagram of Fig. 2.16a. Apart from a deviation of 0.1-0.4 eV the data from TL glow peak analysis follow the divalent lanthanide zigzag curve in the VRBE diagram.

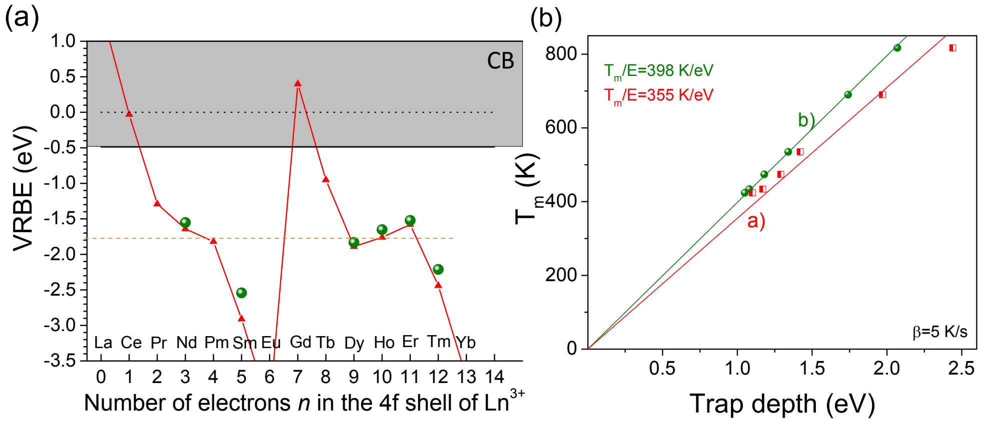

Fig. 2.16. (a) VRBE-diagram for the divalent lanthanides in $LaPO_4$ (▲) together with VRBE data from TL-studies on $LaPO_4$:0.005Ce^{3+},0.005Ln^{3+} (●). (b) T_m against the trap depth as line a) determined from the VRBE diagram and line b) from TL studies on $LaPO_4$:0.005Ce^{3+}, 0.005Ln^{3+}.

Fig. 2.16b shows T_m from Fig. 2.5 for $LaPO_4$:0.005Ce^{3+},0.005Ln^{3+} against the trap depths read from the VRBE diagram and against the trap depths derived by TL glow peak analysis. Proportional relationships are observed with the slope T_m/E=355 K/eV and 398 K/eV, respectively. Assuming first order TL-recombination kinetics Eq. (2.1) can also be written as

$$\frac{T_m}{E} = \frac{11600}{\ln\left(\frac{T_m}{E}\right) + \ln(\frac{s}{\beta}) + \ln\left(T_m\right) - 9.36} \quad \text{K/eV} \qquad (2.2)$$

The frequency factor s in inorganic compounds is typically 10^{13} s^{-1} and $\ln(\frac{s}{\beta})$ is then 28.3 for β=5 K/s. $\ln\left(\frac{T_m}{E}\right)$ and $\ln\left(T_m\right)$ are both near 6 which then implies that the value for the enumerator in Eq. (2.2) is about 31 and almost entirely determined by $\ln(\frac{s}{\beta})$. It also implies that $\frac{T_m}{E}$ will be to good approximation a constant with values of 300-400 K/eV depending on $\ln(\frac{s}{\beta})$ as observed. Proportional relations were also reported for lanthanides in YPO_4[35], $CaSO_4$[36], and $Sr_3Al_xSi_{1-x}O_5$[37] with T_m/E=284 K/eV at β=0.1 K/s, T_m/E=313 K/eV at β=0.42 K/s, and T_m/E=322 K/eV at β=0.1 K/s, respectively. Particularly, for YPO_4 T_m/E=300 K/eV was obtained at β=1 K/s. Fig. 2.11b also shows that the two fitted lines a) and b) deviate. Clearly, taking into account the error by VRBE and considering that there is an uncertainty in the slope of the line based on the thermoluminescence measurements as well, the trend is in accordance.

Fig. 2.2, that was made with the data from Table 2.4, shows the stacked vacuum referred binding energy (VRBE) diagram of $REPO_4$ with the VRBE in the $4f^n$ ground states of Pr^{3+}, Tb^{3+}, and Eu^{2+}. The VRBE diagrams with all lanthanide impurity level locations can be found in Fig. S2.9. The conduction band bottom moves 0.22 eV downward with the substitution of La^{3+} by Gd^{3+} in $Gd_{1-x}La_xPO_4$ solid solutions (column 7 of Table 2.4) and then the Ln^{3+} electron trap depths will decrease. This is consistent with the 105 K TL peak shift in Fig. 2.7a. The same sequence of TL glow peaks of the same Ln^{3+} dopant as in Fig. 2.5 was observed for YPO_4:Ce^{3+},Ln^{3+} at the same heating rate of 5 K/s in Ref. [35]. All glow peaks in YPO_4 are shifted 90-100 K towards lower T_m, as shown in Fig. S2.10. Assuming T_m/E~350 K/eV this corresponds with 0.26 eV more shallow trap depth in YPO_4 whereas Fig. 2.2 and Table 2.4 predict 0.18 eV more shallow trap depth.

From the almost 100 K broad TL glow peak observed for x=0.25 in Fig. 2.7a, a 0.95-1.2 eV wide electron trap depth distribution was found (see Table 2.2). Apparently the VRBE at the conduction band bottom shows site-to-site fluctuations depending on the statistics in replacing La by Gd in the $Gd_{1-x}La_xPO_4$ solid solution at x=0.25. A similar phenomenon was reported for Eu^{3+}-doped SnO_2 nanoparticles[38] and $Y_3Al_{5-x}Ga_xO_{12}$:Ce^{3+},Cr^{3+} solid solutions when changing the ratio of Ga^{3+} to Al^{3+}[13].

2.5.2. Controlling the hole trap depth

The vacuum referred binding energy (VRBE) diagrams of $REPO_4$ in Fig. 2.1 and Fig. S2.9 predict that the holes trapped by Tb^{4+} and Pr^{4+} will be liberated earlier, i.e., at lower temperature than the electrons trapped at the Eu^{2+}, Yb^{2+}, and Sm^{2+} to generate the characteristic 4f-4f emission of Eu^{3+}, Yb^{3+}, and Sm^{3+}.

The room temperature TL excitation spectrum for $LaPO_4$:0.005Eu^{3+},0.005Tb^{3+} in Fig. 2.15 strongly resembles with the VB→Eu^{3+} CT band in Fig. 2.4, i.e., the width is the same but it appears 10 nm redshifted corresponding with 0.2 eV. During CT-band excitation holes are generated in the valence band[2, 7] and this is usually followed by the back transfer of the electron from Eu^{2+} generating Eu^{3+} emission. Struck *et al.* reported on the phenomenon of hole separation from the

Eu^{3+} CT-state in RE_2O_2S (RE=Y^{3+} and La^{3+}) during Eu^{3+}-CT excitation[39]. Dobrov *et al.* reported that a p-type photoconductivity signal was found in La_2O_2S:Eu during the VB→Eu^{3+} CT excitation[40]. Therefore, during CT-band excitation holes can be liberated from the CT-state and subsequently migrate to hole trapping centers that can be host intrinsic defects or intentional defects such as Tb^{3+} and Pr^{3+}. Fig. 2.15 suggests that this occurs in $LaPO_4$:0.005Eu^{3+},0.005Tb^{3+} and that the close to room temperature glow peak in Fig. 2.12 must be attributed to the release of holes from either Tb^{4+} or an intrinsic defect. The 0.2 eV redshift in band location may indicate that the hole trap is close to Eu^{3+} and thus facilitating the hole release.

Fig. 2.8a-2.8c showed TL emission (TLEM) spectra for YPO_4 each with the same Tb^{3+} hole trapping center but with different deep electron trapping centers of Eu^{3+}, Sm^{3+}, and Yb^{3+}. All samples share TL glow peaks I and IIIa with emission from either Eu^{3+}, Sm^{3+} or Yb^{3+}. Peak IIIa was assigned to hole release from Tb^{4+}. Peak I is also observed when the Tb^{3+} hole trap is replaced by the Pr^{3+} or Ce^{3+} hole trap in the samples of Fig. 2.9 and S2.4. We therefore attribute peak I to hole release from an unidentified host associated hole trap. Glow peak IV in Fig. 2.9a, is only observed in Eu^{3+}-doped samples and it seems to be a further unidentified hole trap somehow related to Eu presence.

Using data in columns 4 and 5 of Table 2.3 the average trap depths for Pr^{3+} and Tb^{3+} in YPO_4 are 1.42 and 1.44 eV, which are ~0.6 eV smaller than the predicted ones from the VRBE diagram (1.95 for Pr^{3+} and 2.13 eV for Tb^{3+}). A similar deviation was observed in $GdAlO_3$[7]. When holes are produced in the valence band they trend to form a V_k center by bonding two neighbouring oxygen anions[41, 42]. In a VRBE diagram such V_k center level is then located above the valence band top[7, 43]. We therefore attribute the 0.6 eV energy difference to the binding energy of the V_k center. Under thermal excitation, such V_k center moves towards the electron trapped at Yb^{2+}, Sm^{2+}, or Eu^{2+} producing 4f-4f emission of Yb^{3+}, Sm^{3+}, or Eu^{3+} in YPO_4.

2.5.3. Hole trap depth tailoring via valence band engineering

Since the VRBE in the Tb^{3+} and Pr^{3+} ground states in our phosphate compounds are about the same, the hole trap depths of Tb^{3+} and Pr^{3+} will depend on the VRBE at the valence band top (E_V). Therefore one can tailor the T_m of glow peaks IIIa and IIIb by engineering the VRBE at the valence band top. The stacked diagram in Fig. 2.2 and column 5 in Table 2.4 show that E_V lowers by 0.85 eV in discrete steps in going from La- to Gd- to Y- to Lu-phosphate, and the hole trapping depths and T_m of peaks IIIa and IIIb should increase accordingly.

The results on the $Y_{1-x}Lu_xPO_4$ solid solutions in Fig. 2.10 and S2.7 demonstrate this tailoring. For both Tb and Pr glow peaks IIIa and IIIb shift upward about 65 K when replacing Y^{3+} by Lu^{3+}. Using a T_m/E relationship of typical 350 K/eV this would imply 0.2 eV deeper hole trap depth. From the variable heating rate plots for $Y_{1-x}Lu_xPO_4$:$0.005Eu^{3+}$,$0.005Tb^{3+}$ in Fig. S2.6 about 0.4 eV deeper hole trapping depth is found. The VRBE results in Table 2.4 suggest only 0.1 eV larger trapping depth. This all demonstrates the limitations in accuracy of trapping depths derived from TL glow curve analysis and VRBE diagram. The VRBE diagram that is based on wide CT-band transitions and other experimental input parameters can easily contain errors of several 0.1 eV size, and this same applies for results from TL data. For example, for $LaPO_4$:$0.005Ce^{3+}$,$0.005Ho^{3+}$ electron trap of 1.18 eV is found, but in column 3 of Table 2.2 for the same sample a value of 1.22 eV is obtained. These differences are directly related to different values for the frequency factors. In this work we analyzed the TL-glow peaks assuming first order recombination kinetics and with zero distribution in trapping depths. Such situation is not realistic and reported trapping depth energies and frequency factors should then be treated as indicative.

The VRBE-diagram of $LaPO_4$ in Fig. 2.2 and Table 2.4 predicts that Eu^{3+} can act as a 3.67 eV deep electron trapping center, while Ce^{3+}, Tb^{3+}, and Pr^{3+} as 2.90, 1.23, and 1.05 eV shallow hole trapping centers. Considering that the $LaPO_4$ and YPO_4 compounds are quite similar, we assume that the binding energy of the V_k center in $LaPO_4$ is 0.6 eV like in YPO_4. We then arrive at effective hole trapping depths of 2.30, 0.63, and 0.45 eV for Ce^{3+}, Tb^{3+}, and Pr^{3+}, respectively. One can estimate according to Eq. (2.1) with a heating rate of 1 K/s and the above predicted trapping depths that hole release from Ce^{4+}, Tb^{4+}, and Pr^{4+} in $LaPO_4$ will give glow peaks at T_m ~840, 240, and 170 K, respectively. Clearly, the Ce^{4+} trap is far too deep to release a hole in the measurement range. In contrast, the predicted T_m values for Tb^{4+} and Pr^{4+} hole release are in the range of the appearance of glow peaks IIIa (0.63 eV) and IIIb (0.55 eV) in Fig. 2.12. We therefore tentatively attribute glow peaks IIIa and IIIb to hole release from Tb^{4+} and Pr^{4+}. The intense glow peak just above RT is then assigned to intrinsic hole traps.

The VRBE-diagram for La- and $GdPO_4$ in Fig. 2.2 and the data in Table 2.4 suggests that the Tb^{3+} and Pr^{3+} hole trap depth will increase by about 0.3 eV corresponding with about 100 K shift of T_m. The glow peak maxima are then expected between 300-400 K in $GdPO_4$. TL glow curves for $GdPO_4$:$0.005Eu^{3+}$, $0.005Ln^{3+}$ (Ln=Tb, Pr, and Ce) samples indeed shows glow peaks between 300-400 K in Fig. S2.11. However, since they are also present with Ce^{3+} co-doping and for single Eu^{3+} samples they cannot be assigned to either Tb or Pr. This also applies to $GdPO_4$:$0.005Sm^{3+}$,$0.005Ln^{3+}$.

The data in Table 2.4 from the VRBE diagram places the ground state level of Tb^{3+} ~0.18 eV higher than that of Pr^{3+} and release of holes from Tb^{4+} should then occur at 60-70 K higher temperature than from Pr^{4+}. However, Fig. 2.9, 2.11, and 2.12 show that the Pr^{4+} TL glow peak appears at 10-30 K lower temperature than that of Tb^{4+} in Y-, Lu, and $LaPO_4$. For $GdAlO_3$ it was found in Ref. [7] that the Pr^{4+} glow peak is at 10-30 K higher temperature than that of the Tb^{4+}. Based on these observations it seems that the ground states of Tb^{3+} and Pr^{3+} have in those compounds about the same VRBE value. It provides a hint that the parameter values behind the trivalent lanthanide zigzag curve in the VRBE diagrams needs adjustment or otherwise might be slightly compound dependent.

There is an increasing need for afterglow phosphors that exhibit emission in the short-wave infrared (SWIR) spectral region of ~900-1700 nm, owing to many advanced applications in the field of military, anti-counterfeiting, and bio-imaging[44]. For instance, for military utilizations, the SWIR light is more mysterious than near-infrared light, which cannot be easily probed by conventional techniques such as night-vision spectacles. For bio-imaging, SWIR light is located in the second biological window (~1000-1400 nm) allowing ultra-sensitive and deep-tissue bio-imaging[10]. However, rarely SWIR phosphors are developed since it remains unclear how to design such type of materials[45].

SWIR afterglow can be realized by replacing Eu^{3+} for Yb^{3+} and combining that with Tb^{3+} or Pr^{3+} in La-, Y-, Gd-, and Lu- phosphates or in solid solutions thereof. The VRBE at the VB-top and therewith the Tb^{3+} and Pr^{3+} hole trap depths can then be engineered. The results on the Yb^{3+},Tb^{3+}-codoped YPO_4 in Fig. 2.8c, $Y_{1-x}Lu_xPO_4$ solid solution in Fig. S2.4i, and $LuPO_4$ in Fig. S2.4j demonstrates such engineering.

2.6. Conclusions

The chemical shift model, photoluminescence spectroscopy and thermoluminescence have been combined to study the trapping and release process of electrons and holes in double lanthanide doped rare earth ortho phosphates. In $LaPO_4$:$0.005Ce^{3+}$,$0.005Ln^{3+}$, the Ln^{3+} codopants act as the electron trapping centers, while Ce^{3+} acts as the luminescence center. The electrons liberated from Ln^{2+} recombine with Ce^{4+} yielding Ce^{3+} 5d-4f emission. The electron trap depth generated by lanthanide codopants can be tuned by the choice of Ln^{3+} lanthanide, and for fixed set of lanthanide dopants like in $Gd_{1-x}La_xPO_4$:$0.005Ce^{3+}$,$0.005Ho^{3+}$ solid solutions by tuning x leading to conduction band engineering. For YPO_4:$0.005Ln^{3+}$,$0.005M^{3+}$ (Ln=Sm, Eu, and Yb; M=Pr and Tb), Ln^{3+} acts as electron trapping center and recombination center, while M^{3+} as hole trapping center. Compared with electrons trapped at Ln^{2+}, holes trapped by M^{4+} liberate at lower temperature and recombine with Ln^{2+} to produce Ln^{3+} 4f-4f emission during TL readout. Vacuum referred binding energy (VRBE) at the valence band top can be engineered though the substitution of Y^{3+} by Lu^{3+} or La^{3+} and this enables the tailoring of hole trap depths of Tb^{3+} and Pr^{3+}, and the emitting wavelength can be tailored from red to SWIR by changing the electron traps from Eu^{3+} or Sm^{3+} to Yb^{3+}. Particularly, new SWIR afterglow phosphors with Yb^{3+} infrared emission in ~900-1700 nm have been discovered by tuning the hole trap depth in the ortho phosphates. With the deep understanding of trap level locations and on the transport and trapping processes of charge carriers, such conduction and valence band engineering could be a promising route to deliberate design the electron and hole traps based novel optical storage and persistent phosphors.

2.7. Acknowledgements

T. Lyu acknowledges the China Scholarship Council for his PhD scholarship (Tianshuai Lyu: No. 201608320151). We thank Dr Adrie J.J. Bos and Dr Hongde Luo from Delft University of Technology, for fruitful discussions on afterglow phosphors and luminescence mechanisms.

2.8. Reference

1. Y. Li, M. Gecevicius and J. Qiu, *Chemical Society Reviews*, 2016, **45**, 2090-2136.
2. H. Luo, A. J. J. Bos and P. Dorenbos, *The Journal of Physical Chemistry C*, 2017, **121**, 8760-8769.
3. T. Wang, W. Bian, D. Zhou, J. Qiu, X. Yu and X. Xu, *The Journal of Physical Chemistry C*, 2015, **119**, 14047-14055.
4. Y. Zhuang, Y. Katayama, J. Ueda and S. Tanabe, *Optical Materials*, 2014, **36**, 1907-1912.
5. P. Leblans, D. Vandenbroucke and P. Willems, *Materials*, 2011, **4**, 1034.
6. Y. Wang, Y. Gong, X. Xu and Y. Li, *Journal of Luminescence*, 2013, **133**, 25-29.
7. H. Luo, A. J. J. Bos and P. Dorenbos, *The Journal of Physical Chemistry C*, 2016, **120**, 5916-5925.
8. A. Jain, A. Kumar, S. J. Dhoble and D. R. Peshwe, *Renewable and Sustainable Energy Reviews*, 2016, **65**, 135-153.
9. H. Guo, Y. Wang, G. Li, J. Liu, P. Feng and D. Liu, *Journal of Materials Chemistry C*, 2017.
10. J. Xu, S. Tanabe, A. D. Sontakke and J. Ueda, *Applied Physics Letters*, 2015, **107**, 081903.
11. Z. Pan, Y.-Y. Lu and F. Liu, *Nat Mater*, 2012, **11**, 58-63.
12. J. Ueda, M. Katayama, K. Asami, J. Xu, Y. Inada and S. Tanabe, *Opt. Mater. Express*, 2017, **7**, 2471-2476.

13. J. Ueda, P. Dorenbos, A. J. J. Bos, K. Kuroishi and S. Tanabe, *Journal of Materials Chemistry C*, 2015, **3**, 5642-5651.
14. K. Korthout, K. Van den Eeckhout, J. Botterman, S. Nikitenko, D. Poelman and P. F. Smet, *Physical Review B*, 2011, **84**.
15. K. Chakrabarti, V. K. Mathur, J. F. Rhodes and R. J. Abbundi, *Journal of Applied Physics*, 1988, **64**, 1363-1366.
16. P. Dorenbos, *Physical Review B*, 2012, **85**, 165107.
17. P. Dorenbos, *Journal of Materials Chemistry*, 2012, **22**, 22344-22349.
18. P. Dorenbos, *ECS Journal of Solid State Science and Technology*, 2013, **2**, R3001-R3011.
19. P. Dorenbos, *Optical Materials*, 2017, **69**, 8-22.
20. P. Dorenbos and E. G. Rogers, *ECS Journal of Solid State Science and Technology*, 2014, **3**, R150-R158.
21. P. Dorenbos, *Journal of Luminescence*, 2014, **151**, 224-228.
22. P. Dorenbos, *J. Phys.-Condes. Matter*, 2013, **25**.
23. P. Dorenbos, *Journal of Luminescence*, 2013, **136**, 122-129.
24. A. J. J. Bos, R. M. van Duijvenvoorde, E. van der Kolk, W. Drozdowski and P. Dorenbos, *Journal of Luminescence*, 2011, **131**, 1465-1471.
25. V. S. Levushkina, D. A. Spassky, E. M. Aleksanyan, M. G. Brik, M. S. Tretyakova, B. I. Zadneprovski and A. N. Belsky, *Journal of Luminescence*, 2016, **171**, 33-39.
26. P. Dorenbos, *Journal of Luminescence*, 2005, **111**, 89-104.
27. E. Nakazawa and F. Shiga, *Journal of Luminescence*, 1977, **15**, 255-259.
28. R. Chen and S. A. A. Winer, *Journal of Applied Physics*, 1970, **41**, 5227-&.
29. W. Hoogenstraaten, *Philips Res. Rep*, 1958, **13**, 515–693.
30. R. R. Haering and E. N. Adams, *Physical Review*, 1960, **117**, 451-454.
31. A. J. J. Bos, *Radiation Measurements*, 2006, **41**, S45-S56.
32. A. J. J. Bos, P. Dorenbos, A. Bessière and B. Viana, *Radiation Measurements*, 2008, **43**, 222-226.
33. K. Van den Eeckhout, A. J. J. Bos, D. Poelman and P. F. Smet, *Physical Review B*, 2013, **87**, 045126.
34. F. You, A. J. J. Bos, Q. Shi, S. Huang and P. Dorenbos, *Physical Review B*, 2012, **85**, 115101.
35. A. J. J. Bos, P. Dorenbos, A. Bessière, A. Lecointre, M. Bedu, M. Bettinelli and F. Piccinelli, *Radiation Measurements*, 2011, **46**, 1410-1416.
36. K. S. V. Nambi, V. N. Bapat and A. K. Ganguly, *Journal of Physics C-Solid State Physics*, 1974, **7**, 4403-4415.
37. H. Luo, A. J. J. Bos, A. Dobrowolska and P. Dorenbos, *Physical Chemistry Chemical Physics*, 2015, **17**, 15419-15427.
38. J. Kong, W. Zheng, Y. Liu, R. Li, E. Ma, H. Zhu and X. Chen, *Nanoscale*, 2015, **7**, 11048-11054.

39. C. W. Struck and W. H. Fonger, *Physical Review B*, 1971, **4**, 22-34.
40. W. I. Dobrov and R. A. Buchanan, *Applied Physics Letters*, 1972, **21**, 201-&.
41. P. W. Tasker and A. M. Stoneham, *Journal of Physics and Chemistry of Solids*, 1977, **38**, 1185-1189.
42. R. B. Murray and F. J. Keller, *Physical Review*, 1965, **137**, A942-A948.
43. N. F. Mott and A. M. Stoneham, *Journal of Physics C: Solid State Physics*, 1977, **10**, 3391.
44. F. Liu, Y. Liang, Y. Chen and Z. Pan, *Advanced Optical Materials*, 2016, **4**, 562-566.
45. Y. Liang, F. Liu, Y. Chen, X. Wang, K. Sun and Z. Pan, *Journal of Materials Chemistry C*, 2017, **5**, 6488-6492.

2.9. Supporting information

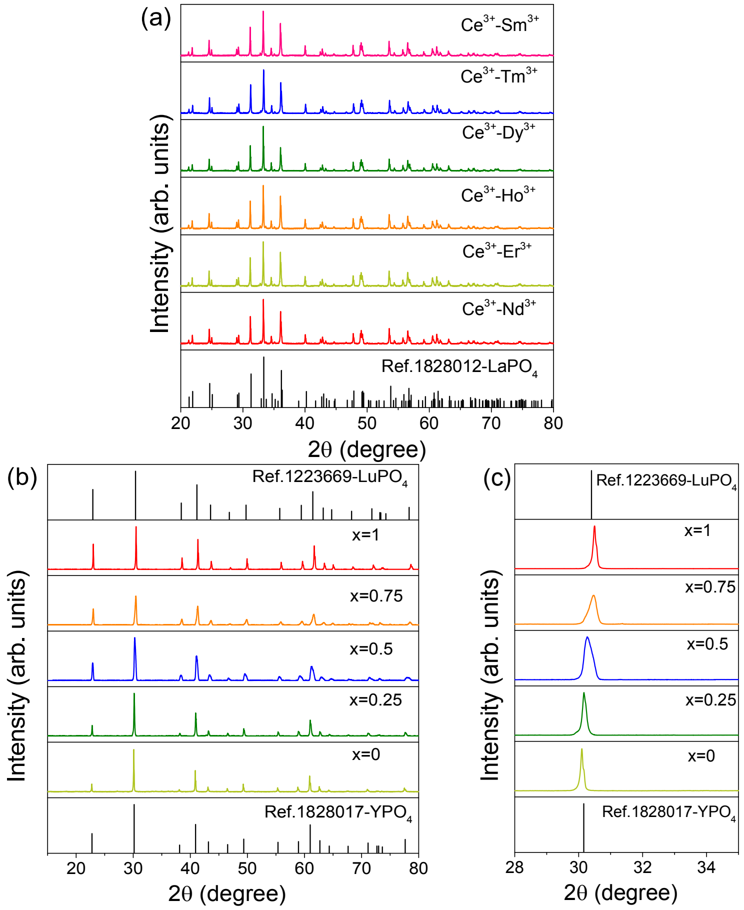

Fig. S2.1. XRD patterns of (a) $LaPO_4$:0.005Ce^{3+},0.005Ln^{3+}. (b) XRD patterns and (c) detailed patterns in the range from 28 to 35° for $Y_{1-x}Lu_xPO_4$:0.005Eu^{3+},0.005Tb^{3+} solid solutions.

Fig. S2.1a shows the XRD patterns of $LaPO_4$:0.005Ce^{3+},0.005Ln^{3+}. All samples are of single phase and match well with the $LaPO_4$ reference (No. 1828012).

Fig. S2.1b shows the XRD patterns of $Y_{1-x}Lu_xPO_4$:0.005Eu^{3+},0.005Tb^{3+}. The XRD peaks show a slight shift towards larger 2θ angles compared to YPO_4 because lutetium ions enter into the larger yttrium sites and decrease the cell volume. With increasing x, solid solution appears since both YPO_4 and $LuPO_4$ have the same crystal structure (space group: $I4_1/amd\ O_2$).

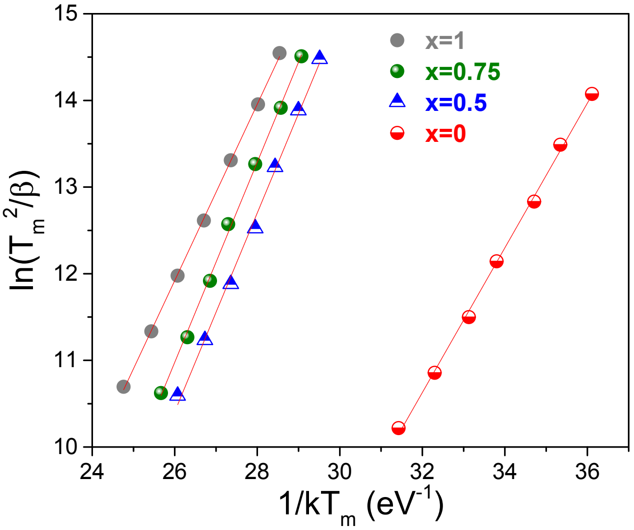

Fig. S2.2. Variable heating rate plots of $Gd_{1-x}La_xPO_4$:0.005Ce^{3+},0.005Ho^{3+} (x=0, 0.5, 0.75, and 1) solid solutions. The used heating rates were 0.08, 0.15, 0.30, 0.63, 1.25, 2.5, and 5 K/s.

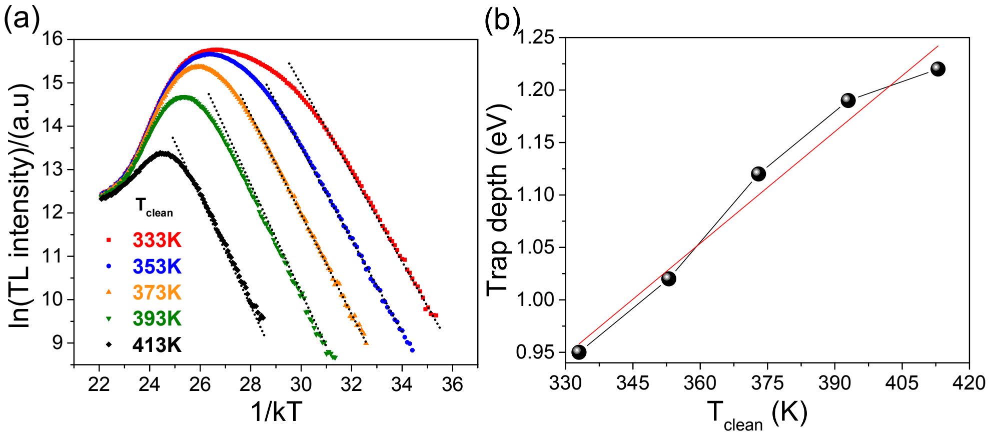

Fig. S2.3. (a) Initial rise analysis on all TL glow curves as a function of T_{clean} for x=0.25. (b) calculated trap depth. The red solid line is a linear fit through the data points.

The initial rise method was used to determine the trap depth at T_{clean}. The rising part of TL intensity (I(T)) can be approximated using[1-6]

$$I(T) = C \times \exp\left(\frac{-E}{kT}\right) \tag{S2.1}$$

where C is a constant. Fig. S2.3a shows the initial rise plots of TL glow curves for x=0.25 after different peak temperature T_{clean}. Straight line sections appear in the low temperature part. With increasing the T_{clean}, the trap depth derived from the slope increases from 0.95 to 1.2 eV as shown in Fig. S2.3b.

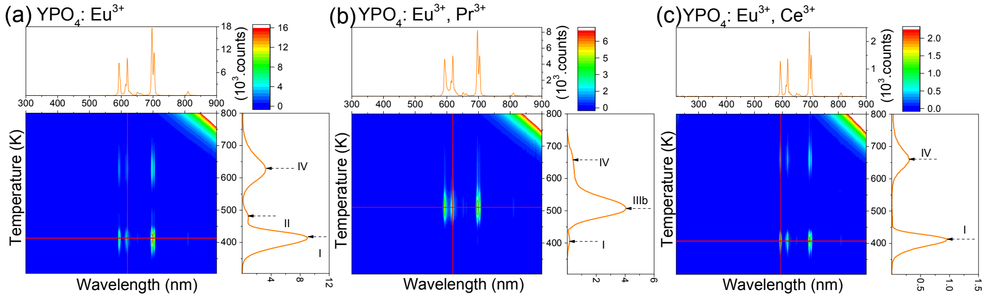

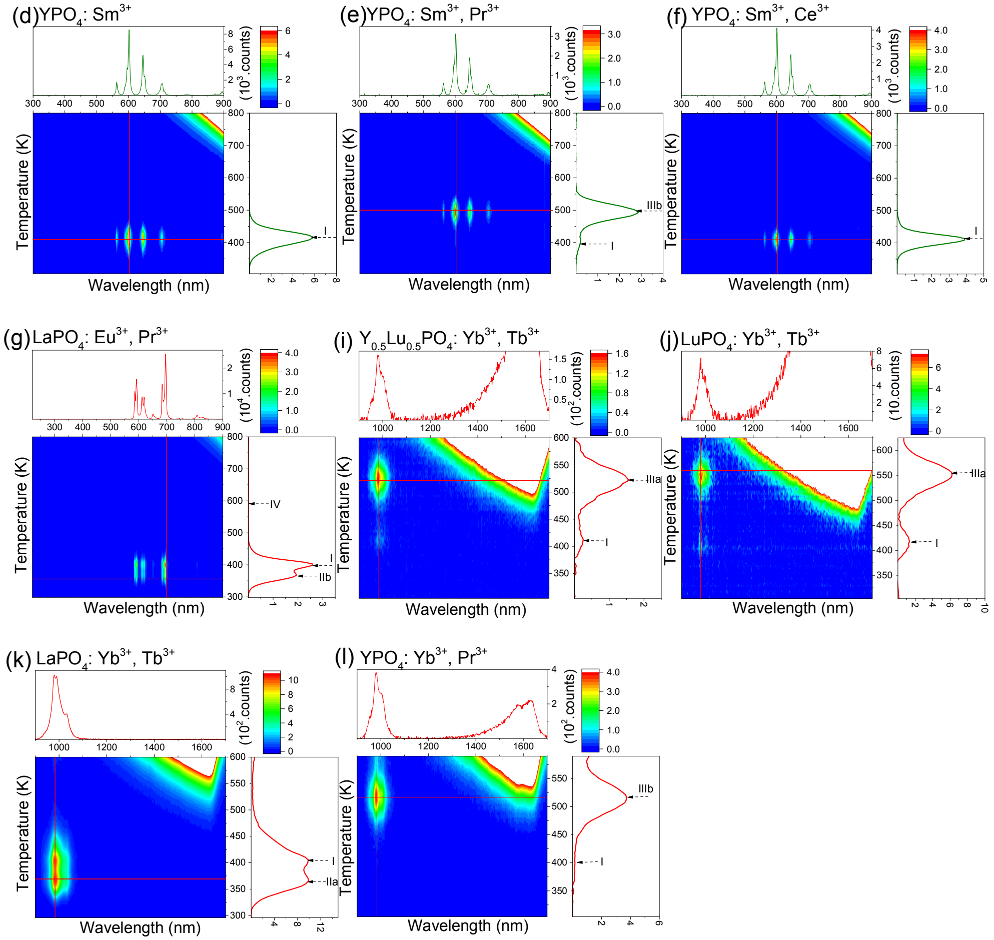

Fig. S2.4. Thermoluminescence emission (TLEM) plots of REPO4:0.005Ln^{3+} (RE=La, Y, and Lu) samples recorded at the heating rate of 1 K/s.

Compared to YPO$_4$:0.005Yb^{3+},0.005Tb^{3+} (Fig. 2.8c), it is also noticed in Fig. S2.4i-j that the glow peak IIIa from the Tb^{3+} hole tapping center shifts about 45 K (0.33 eV) towards higher temperature in the Y$_{1-x}$Lu$_x$PO$_4$:0.005Yb^{3+},0.005Tb^{3+} solid solutions with increasing x leading to the decreasing of the VRBE at the valence band top and the increased hole trap depth of Tb^{3+}. This observation is similar to that of glow peaks IIIa and IIIb shifting in Y$_{1-x}$Lu$_x$PO$_4$:0.005Eu^{3+},0.005Tb^{3+} (Fig. 2.10) and Y$_{1-x}$Lu$_x$PO$_4$:0.005Eu^{3+},0.005Pr^{3+} solid solutions (Fig. S2.7).

Note that the glow at around 1200-1700 nm appears in Fig. S2.4i-l, which is due to blackbody radiation.

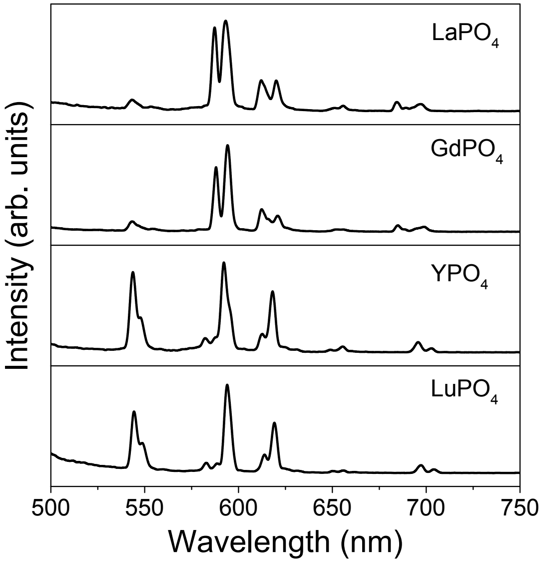

Fig. S2.5. Photoluminescence spectra of REPO$_4$:0.005Eu^{3+},0.005Tb^{3+} (RE=La, Gd, Y, and Lu) at 10 K. Samples were excited at the Eu^{3+}-CT peak maxima.

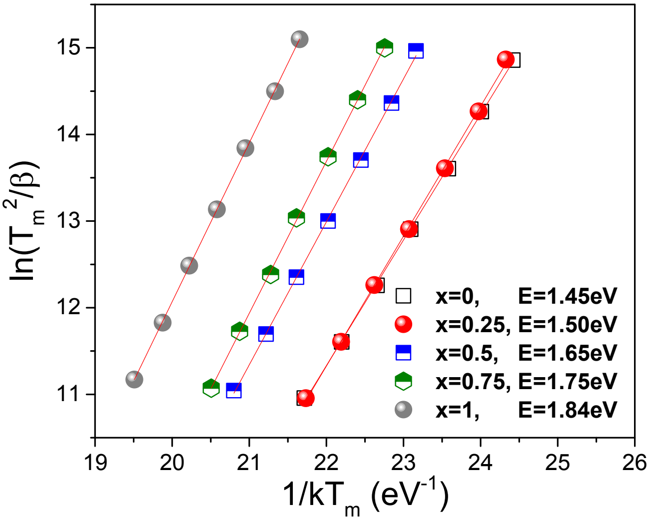

Fig. S2.6. Variable heating rate plots of Y$_{1-x}$Lu$_x$PO$_4$:0.005Eu^{3+},0.005Tb^{3+} solid solutions. The used heating rates were 0.08, 0.15, 0.30, 0.63, 1.25, 2.5, and 5 K/s.

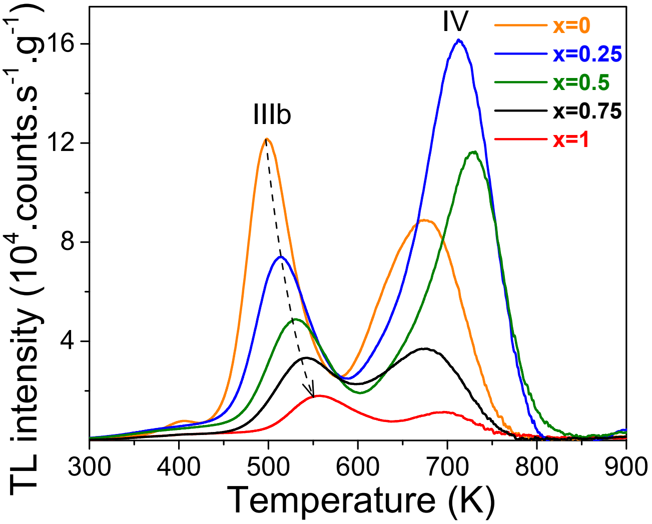

Fig. S2.7. TL glow curves for $Y_{1-x}Lu_xPO_4$:0.005Eu^{3+},0.005Pr^{3+} solid solutions monitoring the emission from Eu^{3+} at the heating rate of 1 K/s.

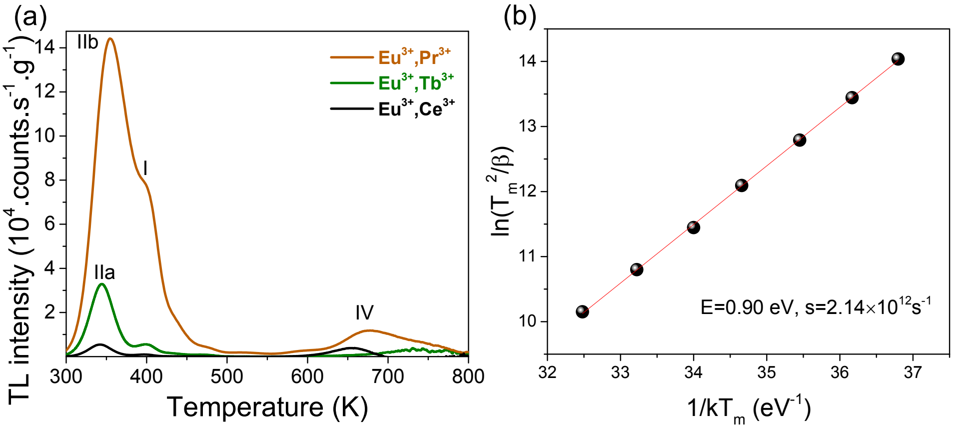

Fig. S2.8. (a) TL glow curves for $LaPO_4$:0.005Eu^{3+},0.005Ln^{3+} (Ln=Tb, Pr, and Ce) monitoring the Eu^{3+} emission at 300-800 K at the heating rate of 1 K/s. (b) variable heating rate plot of $LaPO_4$:0.005Eu^{3+},0.005Tb^{3+} sample. The used heating rates are 0.08, 0.15, 0.30, 0.63, 1.25, 2.5, and 5 K/s.

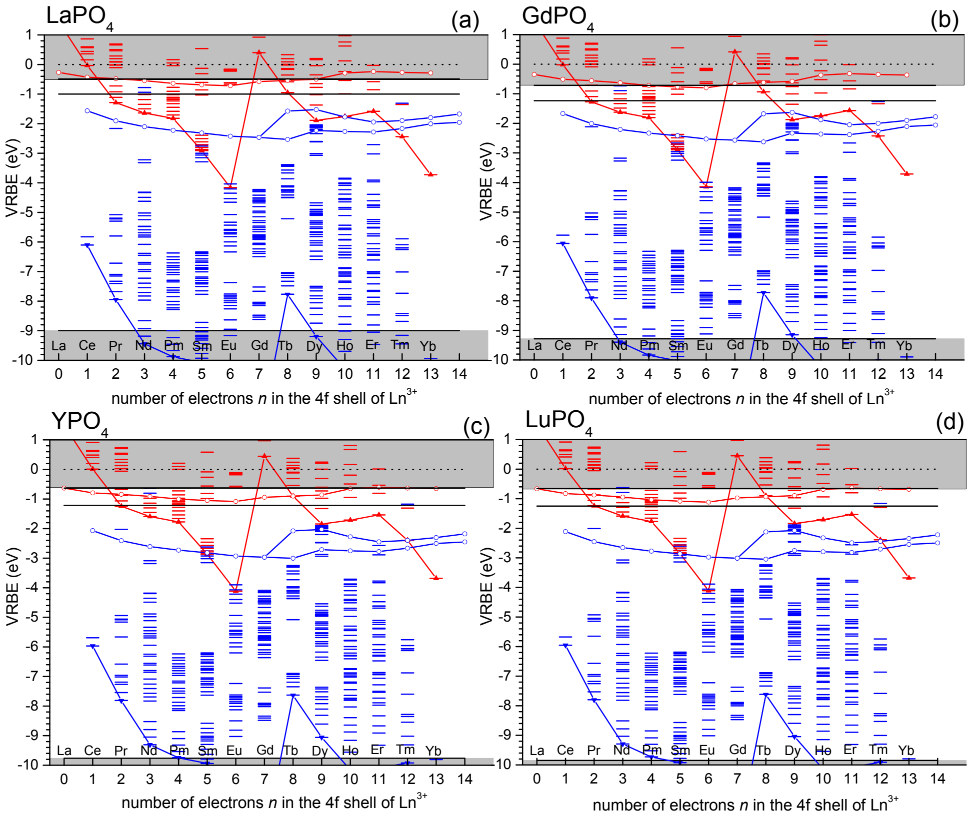

Fig. S2.9. Vacuum referred binding energy (VRBE) diagrams of all lanthanide levels in (a) $LaPO_4$, (b) $GdPO_4$, (c) YPO_4, and (d) $LuPO_4$.

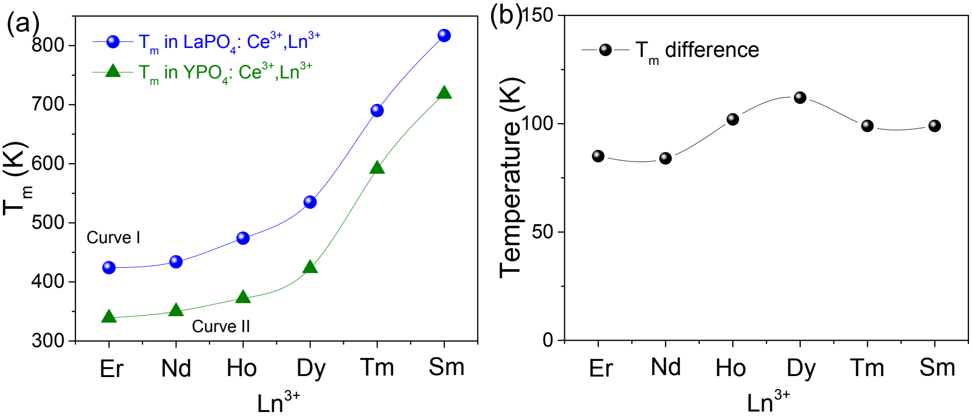

Fig. S2.10. (a) Peaks T_m for the TL glow curves of $REPO_4$:$0.005Ce^{3+}$,$0.005Ln^{3+}$ (RE=La and Y) and (b) T_m difference between curve I and curve II.

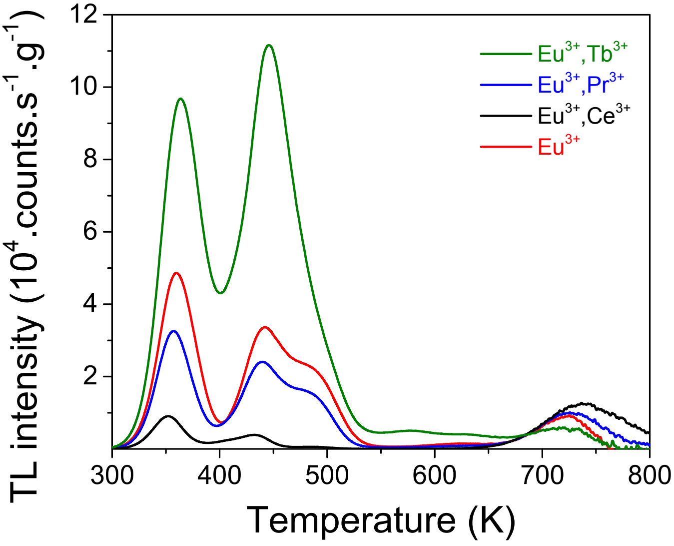

Fig. S2.11. TL glow curves for $GdPO_4$:$0.005Eu^{3+}$,$0.005Ln^{3+}$ (Ln=Tb, Pr, and Ce) samples monitoring the Eu^{3+} emission at the heating rate of 1 K/s.

Reference

1. K. Van den Eeckhout, A. J. J. Bos, D. Poelman and P. F. Smet, *Physical Review B*, 2013, **87**, 045126.
2. J. Nahum and A. Halperin, *Journal of Physics and Chemistry of Solids*, 1963, **24**, 823-834.
3. K. H. Nicholas and J. Woods, *British Journal of Applied Physics*, 1964, **15**, 783.
4. G. F. J. Garlick and A. F. Gibson, *Proceedings of the Physical Society*, 1948, **60**, 574.
5. J. Ueda, P. Dorenbos, A. J. J. Bos, K. Kuroishi and S. Tanabe, *Journal of Materials Chemistry C*, 2015, **3**, 5642-5651.
6. Z. Wang, W. Wang, H. Zhou, J. Zhang, S. Peng, Z. Zhao and Y. Wang, *Inorganic Chemistry*, 2016, **55**, 12822-12831.

3

Bi^{3+} acting both as electron and as hole trap in La-, Y-, and $LuPO_4$

Graphical abstract

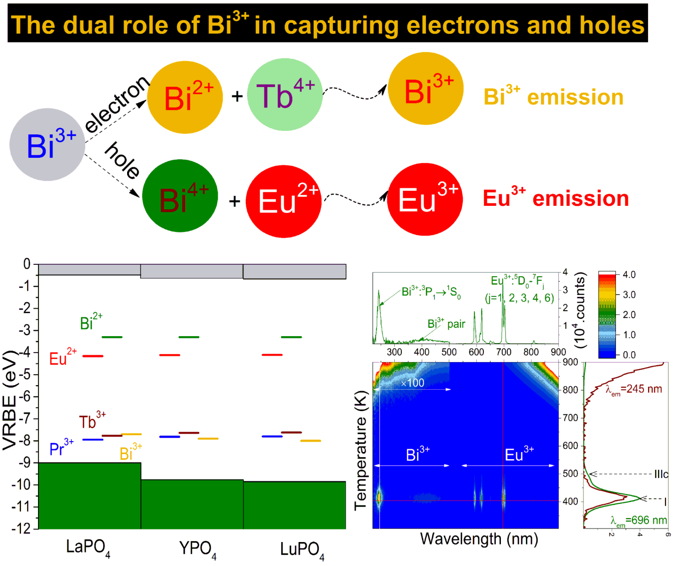

This chapter is based on the publication: **T. Lyu*** and P. Dorenbos, ***Journal of Materials Chemistry C***, 2018, 6, 6240-6249.

3.1. Abstract

Vacuum referred binding energy (VRBE)-guided design of Bi^{3+}-based storage and afterglow materials together with charge carrier trapping processes are explored with a study on bismuth and lanthanide doped rare earth ortho-phosphates. By combining Bi^{3+} with the shallow hole trap of Tb^{3+} or Pr^{3+}, Bi^{3+} appears to act as deep electron trap and as hole recombination center in YPO_4. By combining Bi^{3+} with the deep electron trap of Tm^{3+}, Sm^{3+}, Yb^{3+}, or Eu^{3+}, Bi^{3+} appears to act as shallow hole trap in YPO_4. Here recombination is also realized by means of hole release instead of more commonly reported electron release. Holes are released from Bi^{4+} and then recombine through the valence band with the electrons trapped at Ln^{2+} to produce Ln^{3+} 4f-4f emission. Lu^{3+} was introduced in YPO_4 to engineer the valence band (VB) energy and to tailor the hole trap depth of Bi^{3+} in $Y_{1-x}Lu_xPO_4$ solid solutions. The results show that with increasing x the VRBE at the valence band top moves downward and the hole trap depth of Bi^{3+} increases. With a deep understanding of Bi^{2+} and Bi^{3+} trap level locations and on the charge carrier trapping process, this work broadens the avenue to explore new persistent luminescence and storage materials by using Bi^{3+} both as electron and as hole trap.

3.2. Introduction

The research on trapping and transport of holes and electrons is of interest from a theoretical point of view[1-4] and because of potential applications in a variety of fields such as in night vision[5, 6], in-vivo bioimaging[7-9], information storage[10, 11], and alternating current light emitting diodes (AC-LEDs)[12]. To date few good persistent luminescence and storage phosphors were discovered, such as $SrAl_2O_4:Eu^{2+},Dy^{3+}$[5], $Zn_3Ga_2Ge_2O_{10}:Cr^{3+}$[8], and $BaFBr:Eu^{2+}$[13]. A trial and error method is often used to explore new materials, and there is a strong wish to have a tool that can guide us to deliberate design of storage and afterglow materials based on model prediction[2, 14].

The trapping and release process of holes is scarcely reported so far. Few of the examples are $MgS:Ce^{3+},Sm^{3+}$ by Chakrabarti *et al.* [15] in the 1980s and on YPO_4 by Lyu *et al.* [2] recently. The rare reporting on hole trapping and release processes is due to a lack of knowledge on how to identify a hole release process as compared to an electron release process. To address this issue we need the information on where the holes and electrons are located within the band gap. A model was published in 2012 to construct a vacuum referred binding energy (VRBE) diagram that shows the electron binding energies in the lanthanide levels when doped in inorganic compounds with respect to the vacuum level. It enables one to compare the VRBE at a defect level or a host band in different hosts with respect to the same reference energy[16-18]. Such model can be used to better identify the nature of trapping centers.

Like the Tl^+ and Pb^{2+} ions, the Bi^{3+} ion has a $6s^2$ electron configuration with $^1S_0$ ground state, while its excited states are singlet state $^1P_1$ and triplet states of $^3P_0$, $^3P_1$ and $^3P_2$ originating from the $6s^16p^1$ configuration. The excitation bands from the $^1S_0$ ground state to the $^3P_1$, $^3P_2$ and $^1P_1$ excited states are commonly referred to as A-, B-, and C-band[19]. Moreover, usually a broad excitation band appears, known as the D-band, which is due to the charge transfer from Bi^{3+} to the conduction band[20, 21].

Bi^{2+} as an activator has been reported in a few compounds. In 1994, Blasse *et al.* observed unusual orange luminescence in $SrB_4O_7{:}Bi^{2+}$[22]. Later, Bi^{2+} emission was observed in phosphates, sulphates, borates, and alkaline-earth fluorides for white light emitting diodes[23-26]. Recently Awater *et al.* reported the X-ray excited emission of Bi^{2+} in $Li_2BaP_2O_7$[27] and YPO_4[28]. Bi^{2+} has (Xe) $4f^{14}5d^{10}6s^26p^1$ configuration with ^2P ground state that can split into $^2P_{1/2}$ ground state and excited states of $^2P_{3/2}$ (1) and $^2P_{3/2}$ (2) through spin orbit and crystal field splitting[27]. Characteristic red emission of Bi^{2+} is attributed to the $^2P_{3/2}(1)\rightarrow{}^2P_{1/2}$ transition[26, 29].

Bismuth-based materials have attracted research interest for their various applications such as in electrocatalyst[30] and as high temperature superconductor[31]. Particularly, Bi^{3+} is an excellent activator and sensitizer for luminescent materials that has been studied during the past decades[27, 32-35]. There are rare reports regarding the persistent luminescence from bismuth, and only a few Bi^{3+}-doped afterglow phosphors have been discovered to date[36]. The literatures on Bi^{3+} acting as hole or as electron trap in afterglow and storage phosphors are summarized in Table 3.1. Rare reports are published to discuss the charge carrier trapping and release processes in Bi^{3+}-doped phosphors and the mechanism always remains unidentified. The electron or hole release processes listed in Table 3.1 should be treated as indicative.

Katayama *et al.* [37] reported that Bi^{3+} related defects may act as electron trapping centers in the green persistent $Y_3Al_{5-x}Ga_xO_{12}{:}0.005Ce^{3+},0.005Bi^{3+}$ phosphors. Here Ce^{3+} is the deep hole trapping center and electron donor. After exposure to 460 nm blue light, conduction band (CB) electrons generated through the photoionization process can be captured by Bi^{3+} to form Bi^{2+}. Under thermal excitation at RT, the electrons release gradually from Bi^{2+} to the conduction band and then recombine with Ce^{4+} to ultimately yield Ce^{3+} 5d-4f emission peaked at 505 nm. The electron trap depth produced by Bi^{3+} can be tuned by adjusting x from 0 to 4. The CB-bottom decreases and this demonstrates conduction band engineering.

Recently Zou *et al.* [38] suggest that Bi^{3+} may act as hole trapping and recombination center in the persistent phosphor of $NaLuGeO_4{:}0.05Bi^{3+},0.005Cr^{3+}$.

Bi^{3+} is electron donor, and electrons generated through the photoionization process migrate through the conduction band to be trapped by 1.3 eV deep Cr^{3+} electron trap(s) to form Cr^{2+}. Under 980 nm laser excitation, the electrons release from Cr^{2+} to the conduction band and then recombine with Bi^{4+} to generate Bi^{3+} $^3P_1$-$^1S_0$ emission at 400 nm. Convincing evidence was not provided and not everything is fully clear in the charge carrier trapping and release process in Bi^{3+}-doped afterglow phosphors.

Table 3.1. Bi^{3+} acting as electron (e^-) or as hole (h^+) trap in afterglow and storage phosphors. The symbol $\leftarrow e^-$ means that electrons release at lower temperature than holes, while the symbol $h^+ \rightarrow$ means holes release earlier than electrons.

Compound	h^+	transport	e^-	reference
$Y_3Al_{5-x}Ga_xO_{12}$	Ce^{3+}	$\leftarrow e^-$	Bi^{3+}	[37]
$MgGeO_3$	Mn^{2+}	$\leftarrow e^-$	Bi^{3+}	[39]
$KGaGeO_4$	host defects	$h^+ \rightarrow$	Bi^{3+}	[36]
CaS	host defects	$h^+ \rightarrow$	Bi^{3+}	[40]
$CaWO_4$	Bi^{3+}	$\leftarrow e^-$	$Bi_{Ca}^{\bullet}$	[41]
$NaLuGeO_4$	Bi^{3+}	$\leftarrow e^-$	Cr^{3+}	[38]
$NaLuGeO_4$	Bi^{3+}	$\leftarrow e^-$	Eu^{3+}	[42]
$SrGa_2O_4$	Bi^{3+}	$\leftarrow e^-$	host defects	[43]
$CaGa_2O_4$	Bi^{3+}	$\leftarrow e^-$	host defects	[44]
$CdSiO_3$	Bi^{3+}	$\leftarrow e^-$	host defects	[45]

The objective of the study is to systematically reveal the charge carrier trapping process and to explore deliberate design of bismuth-doped storage and afterglow phosphors based on VRBE diagram predictions and band gap engineering. $REPO_4$ (RE=La, Y, and Lu) are used as model compounds because there is only one crystallographic RE^{3+} site that can be easily substituted by Bi^{3+} and trivalent lanthanides. Fig. 3.1 shows the ground state energies of both Bi^{2+} and Bi^{3+} in the vacuum referred binding energy diagram of YPO_4 as presented by Awater *et al.* in Ref. [28]. Such a VRBE scheme provides a powerful predictive tool. For instance, it predicts that Bi^{3+} can act as a 1.80 eV deep hole trap to generate Bi^{4+} but also as a 2.70 eV deep electron trap to form Bi^{2+}. When combining Bi^{3+} with more than 1.80 eV deep electron trapping centers like Eu^{3+}, Sm^{3+}, Yb^{3+}, or Tm^{3+}, the holes will release from Bi^{4+} earlier, i.e., at lower temperature, than the electrons from Eu^{2+}, Sm^{2+}, Yb^{2+}, or Tm^{2+} to generate Ln^{3+} 4f-4f emission. In this work we will test those type of predictions and provide therewith also an independent confirmation of the results by Awater *et al.* in Ref. [28].

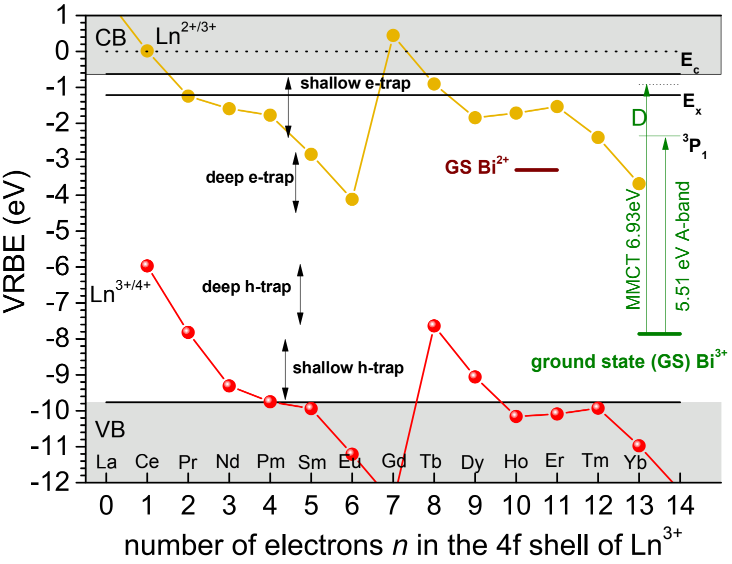

Fig. 3.1. VRBE scheme for YPO_4 including lanthanide, Bi^{3+}, and Bi^{2+} energy level locations. E_c is the binding energy at the conduction band bottom and E_x is the binding energy in the host exciton. The Bi^{3+}→CB metal-to-metal charge transfer (MMCT) band D and the $^3P_1$ excited state of Bi^{3+} are also shown.

3.3. Experimental

All starting chemicals were purchased from Sigma-Aldrich and utilized without further treatments. Samples were synthesized by a conventional high temperature solid state reaction. Appropriate stoichiometric mixtures of Bi_2O_3 (99.999%), $NH_4H_2PO_4$ (99.99%) and rare earth oxides (99.999%) were mixed well with the help of acetone. Subsequently, it was put into a corundum crucible and fired at 400 °C for 5 h and then at 1400 °C for 10 h under ambient atmosphere. After that, the obtained samples were cooled to room temperature (RT) and milled homogeneously before further measurements.

The crystal structure determination of all samples was performed on a PANalytical XPert PRO X-ray diffraction system with a cobalt (Co) Kα (λ=0.178901 nm) X-ray tube (45 KV, 30 mA). The photoluminescence emission (PL) and PL excitation (PLE) spectra were collected on equipment with a VUV/UV branch utilizing a deuterium lamp and an ARC VM502 vacuum monochromator. The emission was detected using a photomultiplier of PerkinElmer Photon Counting Module (MP-1913). The sample temperature was controlled utilizing a closed cycle helium cryostat (HC-4) and a Lake Shore 331 temperature controller. All PLE spectra were corrected for the incident photon flux intensity.

TL recordings above room temperature were recorded with a RISØ TL/OSL reader (Model DA-15) and a DA-20 controller. Samples were first heated to 900 K to empty all relevant traps, and then cooled to room temperature followed by β irradiation using a ^{90}Sr/^{90}Y source at a dose rate of ~0.7 mGy/s in complete darkness. All TL recordings were collected under a flow of nitrogen (N_2) gas and the heating rate is always 1 K/s. A 600 nm bandpass filter (600FS40-50) was placed between the PM tube and the sample to select red emission from Eu^{3+} or Sm^{3+}. In order to select the ultraviolet emission from Bi^{3+} or blue emission from Tm^{3+}, 239 nm bandpass (239FS10-50) and 450 nm bandpass (450FS20-50) filters were used, respectively.

Prior to the recording of the low-temperature TL (LTTL) glow curves (90-450 K), the samples were first heated to 450 K for 3 min to empty all relevant traps and then cooled to 90 K followed by 600 s β irradiation using a ^{90}Sr/^{90}Y beta source at a dose rate of ~0.4 mGy s^{-1}. Liquid nitrogen was utilized as the cooling medium. Each powder sample was pressed into a pill with 0.4 cm diameter, mass <10 mg, and area ~0.2 cm^2. The pill was attached to the cold finger with heating element using silver paint. LTTL measurements were carried out at a heating rate of 1 K/s under vacuum (10^{-7} mbar). The Eu^{3+} emission was monitored by using a 600 nm bandpass filter (600FS40-50) and a PerkinElmer channel PM tube (MP-1393).

For the TL emission (TLEM) spectra, the samples were first heated to 800 K 3 times to empty all relevant traps and then exposed to gamma ray irradiation from a ^{60}Co source to an absorbed dose of ~1 kGy. TL emission was recorded at a heating rate of 1 K/s utilizing a UV to VIS spectrometer (Ocean Optics, QE65000) and a NIR spectrometer (Ocean Optics, NIRQ512) with a HR composite grating (300 lines/mm) and an entrance aperture of 100 μm leading to a wavelength resolution of 3.3 nm (fwhm). The spectral range is 200-900 nm for QE65000 and for NIRQ512 it is 900-1700 nm.

TL excitation (TLE) spectra were recorded by first charging the samples during 600 s with a laser beam produced by a tuneable diode pumped laser system (NT230-100-SH/DUV-SCU). A fiber FBPI600660710/2M purchased from Polymicro Technologies was utilized to transport the laser beam to the RISØ TL/OSL reader. A program was used to record TL glow curves between 300-750 K at a heating rate of 5 K/s when the excitation wavelengths change between 210 and 260 nm. A plot of the integrated intensity of a TL glow peak against illumination wavelength is defined as the TL excitation spectrum of that glow peak[46, 47]. The TLE spectra were finally corrected for the intensity of the laser and the typical transmittance of the fiber and used polarizer. A 600 nm bandpass filter 600FS40-50 was used to select Eu^{3+} emission.

3.4. Results

3.4.1. X-ray diffraction and photoluminescence spectroscopy

The synthesized samples of $Y_{1-x}Lu_xPO_4:0.005Eu^{3+},0.005Bi^{3+}$ form nice solid solutions without any indications for an impurity phase as is evidenced with the XRD patterns in Fig. S3.1.

Fig. 3.2 shows the PL and PLE spectra of La-, Y-, and $LuPO_4$ phosphates recorded at 10 K. Under 166 nm host exciton excitation $LuPO_4:0.005Bi^{3+}$ shows a strong emission band at ~248 nm and weak emission at ~326 nm. A similar spectrum appears under Bi^{3+} A-band excitation at 225 nm, see Fig. S3.2d. Like YPO_4 in Ref. [48], and considering that Y- and $LuPO_4$ have the same crystal structure, we assign the 248 and 326 nm bands to Bi^{3+} $^3P_1 \rightarrow {}^1S_0$ A-band and Bi-pair emission, respectively. Monitoring 248 nm and 326 nm emission, an excitation band at 225 nm appears in Fig. 3.2b. Like in the study from Srivastava *et al.* [48], this band is assigned to the Bi^{3+} A-band. In addition to that work we also performed VUV measurements that reveal the $^1S_0 \rightarrow {}^1P_1$ C-band at 166 nm in Fig. 3.2b. The broad band around 179 nm is like for YPO_4 in Refs. [28, 49] attributed to the Bi^{3+}→CB charge transfer band or D-band.

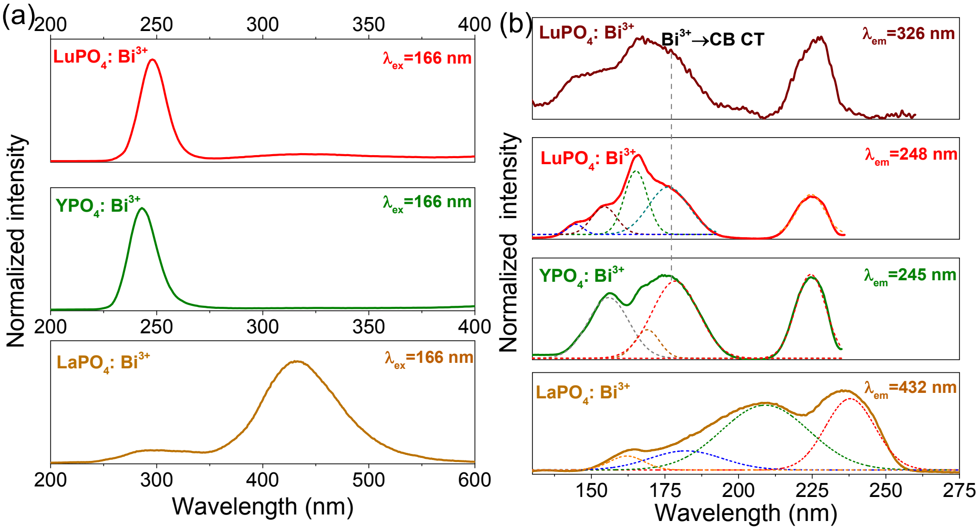

Fig. 3.2. (a) Photoluminescence (PL) and (b) PL excitation (PLE) spectra of $REPO_4:0.005Bi^{3+}$ (RE=Lu and Y) and $LaPO_4:0.002Bi^{3+}$ under 166 nm excitation at 10 K.

The PLE spectrum of LaPO$_4$:0.002Bi^{3+} monitoring at 432 nm in Fig. 3.2b is less well-structured than that of YPO$_4$ and LuPO$_4$. The band at 238 nm is tentatively attributed to the Bi^{3+} $^1S_0\rightarrow{}^3P_1$ transition. Bands C and D cannot be distinguished and instead a broad unstructured band extends from below 175 nm to above 225 nm. LaPO$_4$:0.002Bi^{3+} shows a broad emission near 432 nm, which is attributed to CB→Bi^{3+} charge transfer emission. The host exciton creation band in LaPO$_4$ is known to be located near 155 nm[50-52]. It does, like in Moncorge *et al.* [53], not appear in the Bi^{3+} excitation spectrum indicating inefficient energy transfer.

3.4.2. Bi^{3+} as deep electron trap in Y-Lu phosphate solid solutions

It was shown in Ref. [2] that the trap depths of Tb^{3+} and Pr^{3+} hole trapping centers are shallower than those deep electron trapping centers of Ln^{3+} (Ln=Yb, Sm, and Eu) in YPO$_4$. When co-doping Ln^{3+} with Tb^{3+} or Pr^{3+}, the holes trapped by Tb^{4+} or Pr^{4+} will release at lower temperature to recombine with electrons trapped at Ln^{2+}, generating two characteristic TL glow peaks named IIIa (Tb) and IIIb (Pr) with emission from Ln^{3+}. These all were tested in Ref. [2]. For illustrating these hole release processes the results are reproduced for the Yb^{3+}, Pr^{3+} combination in Fig. 3.3b. The holes trapped by Pr^{4+} are released to recombine with electrons at Yb^{2+}, which yields a typical IIIb (Pr) glow peak with Yb^{3+} $^2F_{5/2}\rightarrow{}^2F_{7/2}$ emission. Let us now turn to the Bi^{3+}-doped YPO$_4$ compounds. Like Yb^{3+}, Bi^{3+} also can act as a deep electron trapping center in YPO$_4$, which will be discussed later. When combining Bi^{3+} with Pr^{3+}, then the holes trapped by Pr^{4+} will release earlier to recombine with electrons at Bi^{2+} producing Bi^{3+} A-band emission in YPO$_4$: 0.005Bi^{3+},0.005Pr^{3+} as shown in Fig. 3.3a. The same now applies to solid solutions Y$_{1-x}$Lu$_x$PO$_4$:0.005Bi^{3+} codoped with 0.005Tb^{3+} or Pr^{3+} as in Fig. S3.3d) and e). Like for Yb^{3+}, Sm^{3+}, and Eu^{3+} ions, it appears that Bi^{3+} also acts as an electron trap in Y$_{1-x}$Lu$_x$PO$_4$ compounds with trap depth that is deeper than the hole trap of Pr^{3+} and Tb^{3+}.

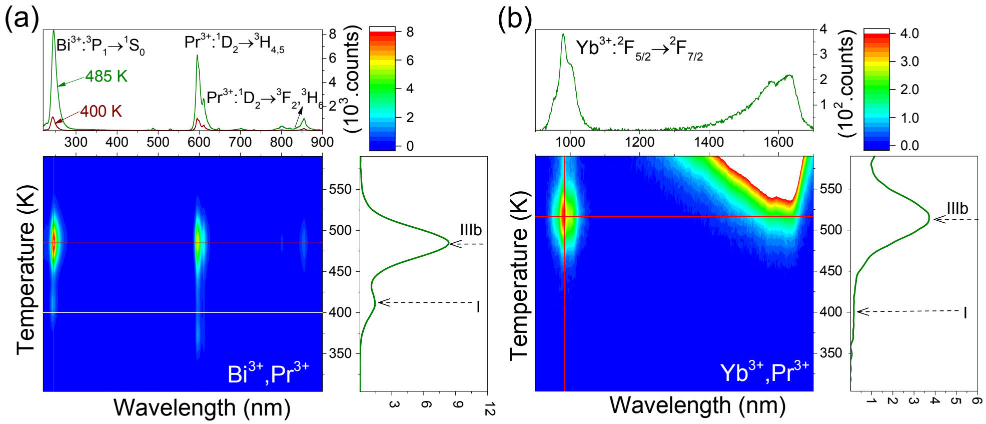

Fig. 3.3. Thermoluminescence emission (TLEM) plots of (a) YPO_4:0.005Bi^{3+},0.005Pr^{3+} and (b) YPO_4:0.005Yb^{3+},0.005Pr^{3+} recorded at a heating rate of 1 K/s. The data on Yb^{3+}-Pr^{3+}-codoped YPO_4 were obtained from Lyu *et al*. [2].

Fig. 3.4a) or b) shows the TL glow curves for solid solutions $Y_{1-x}Lu_xPO_4$: 0.005Bi^{3+} codoped with 0.005Tb^{3+} or Pr^{3+}. When x increases, peaks IIIa and IIIb shift 40 K towards higher temperature. Similar peaks IIIa and IIIb shifting was reported by Lyu *et al*. [2] on $Y_{1-x}Lu_xPO_4$:0.005Ln^{3+},0.005Tb^{3+} or Pr^{3+} (Ln=Yb, Sm, or Eu), where the shifting of peaks IIIa and IIIb was attributed to increased activation energy for hole release from Tb^{4+} and Pr^{4+} due to valence band lowering with increasing x. Upon replacing Ln^{3+} (Ln=Yb, Sm, or Eu) for Bi^{3+} in $Y_{1-x}Lu_xPO_4$:0.005Bi^{3+}, a hole release process from Tb^{4+} or Pr^{4+} still occurs, and the only difference is that TL emission is now from Bi^{3+} instead of from Yb^{3+}, Sm^{3+}, or Eu^{3+}. Note that peak I at ~410 K, that was attributed to hole release from an intrinsic defect in Ref. [2], remains at constant temperature when x changes.

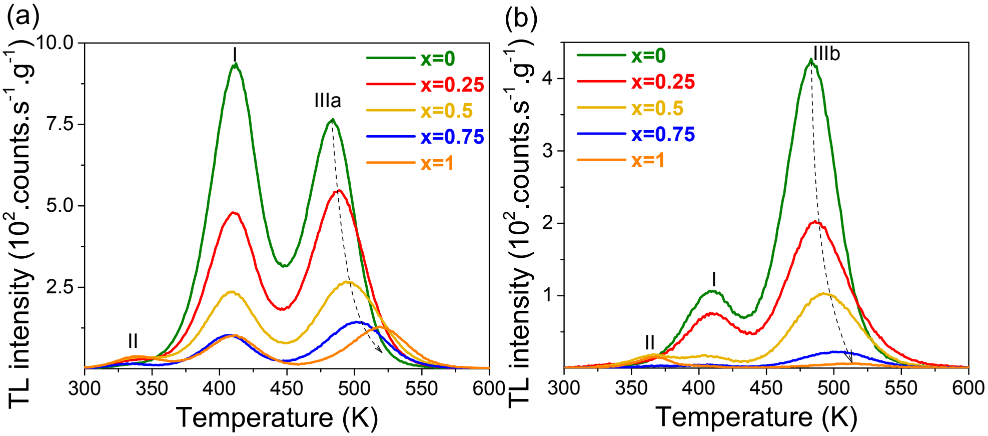

Fig. 3.4. TL glow curves of (a) $Y_{1-x}Lu_xPO_4$:0.005Bi^{3+},0.005Tb^{3+} and (b) $Y_{1-x}Lu_xPO_4$: 0.005Bi^{3+},0.005Pr^{3+} (x=0-1) monitoring Bi^{3+} emission recorded at a heating rate of 1 K/s.

3.4.3. Engineering Bi^{4+} hole release in Y-Lu phosphate solid solutions

Based on the vacuum referred binding energy diagram of YPO_4 as shown in Fig. 3.1, we combined Bi^{3+} with the deep electron trap Eu^{3+} to verify the role of Bi^{3+} as hole trapping and hole release center. Fig. 3.5 shows a characteristic TL emission plot for YPO_4:0.005Eu^{3+},0.005Bi^{3+}. Weak Bi^{3+} emission is observed and 100 times stronger Eu^{3+} 4f-4f emission appears. This shows that Eu^{3+} is the dominant recombination and luminescence center and we deal with hole release during recombination. TL emission plots for three $LaPO_4$ samples with combinations of Bi^{3+} and Ln^{3+} can be found in Fig. S3.7.

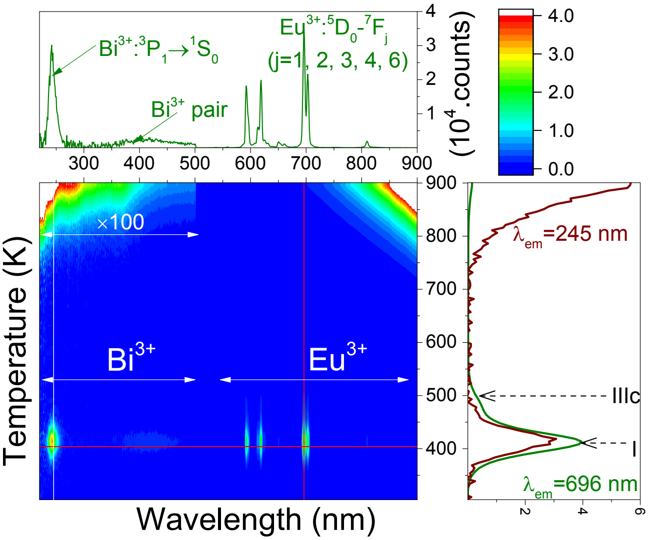

Fig. 3.5. Thermoluminescence emission (TLEM) plot of YPO$_4$:0.005Eu^{3+},0.005Bi^{3+} recorded at a heating rate of 1 K/s.

Like Eu^{3+}, the VRBE scheme of YPO$_4$ in Fig. 3.1 also predicts that Sm^{3+}, Tm^{3+}, and Yb^{3+} act as deep electron traps. Samples of them combined with Bi^{3+} will help to study the hole release process from Bi^{4+}. Fig. 3.6 shows the TL glow curves of YPO$_4$:0.005Bi^{3+} and YPO$_4$:0.005Ln^{3+},0.005Bi^{3+} (Ln=Sm, Eu, or Tm) samples. For YPO$_4$:0.005Yb^{3+},0.005Bi^{3+} a TL emission plot is shown in Fig. S3.3j. The glow peak at ~490 K for YPO$_4$:0.005Bi^{3+}, which will be referred to as peak IIIc, is also observed for YPO$_4$:0.005Sm^{3+},0.005Bi^{3+}, YPO$_4$:0.005Eu^{3+},0.005Bi^{3+}, YPO$_4$:0.005 Tm^{3+},0.005Bi^{3+}, and YPO$_4$:0.005Yb^{3+},0.005Bi^{3+}. Peak IIIc is absent in the Sm^{3+} and Eu^{3+} single doped samples. Note that all Bi^{3+}-doped samples share peak I at ~417 K, which shifts ~5-15 K towards higher temperature as compared to Sm^{3+} or Eu^{3+} single doped samples. This may be attributed to unidentified modification of trap(s) for peak I with Bi^{3+} co-doping. Peak IV seems to be present only in Eu^{3+} doped samples. This all suggests that peaks IIIc is related to hole release and to the presence of Bi^{3+}.

Assuming first-order TL-recombination kinetics, the trap depths in the YPO$_4$:0.005Ln^{3+},0.005Bi^{3+} sample were estimated by employing the peak maximum (T$_m$) of the TL glow curve and solving[54-57]

$$\frac{\beta E}{k{T_m}^2} = s \times \exp\left(-\frac{E}{kT_m}\right) \tag{3.1}$$

where β=1 K s^{-1} is the heating rate, E (eV) is the trap depth, k denotes the Boltzmann constant, and s (s^{-1}) is the frequency factor. Since the concentration of Bi^{3+} is low, we assume that the obtained frequency factors for $Y_{1-x}Lu_xPO_4$: $0.005Eu^{3+}$,$0.005Tb^{3+}$ found in Ref. [2] by variable heating rate plots also apply to $Y_{1-x}Lu_xPO_4 0.005Ln^{3+}$,$0.005Bi^{3+}$. The frequency factors s, and derived trap depths are listed in column 2, and 4 of Table 3.2.

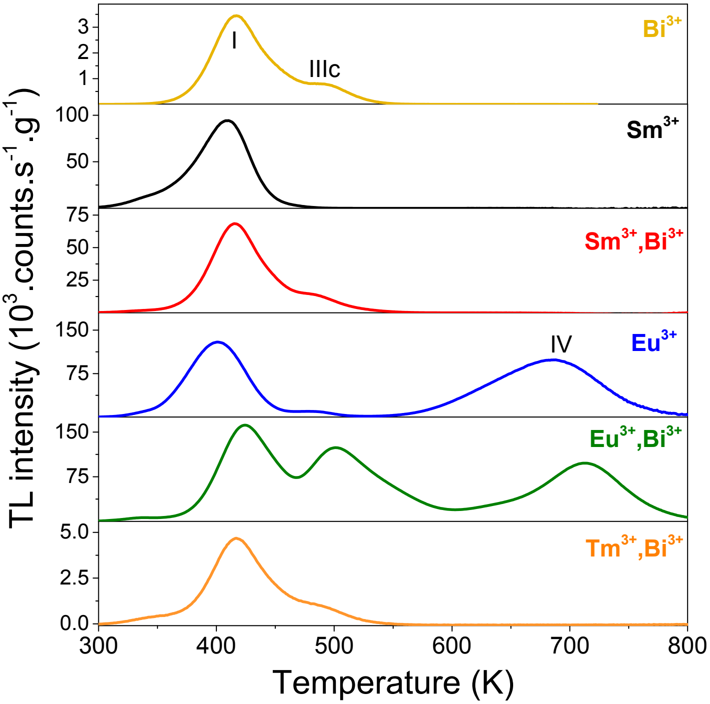

Fig. 3.6. TL glow curves of YPO_4:$0.005Ln^{3+}$,$0.005Bi^{3+}$ (Ln=Sm, Eu, or Tm) recorded after 2000 s β irradiation monitoring the emission from Sm^{3+}, or from Eu^{3+} and Tm^{3+} at a heating rate of 1 K/s. For YPO_4:$0.005Bi^{3+}$ a 239 nm bandpass filter was used to select Bi^{3+} emission.

Compared with YPO_4, the valence band bottom is at ~0.1 eV lower energy in $LuPO_4$. If the Bi^{3+} ground state remains stationary on the VRBE scale, the hole release from Bi^{4+} is predicted to occur at about 30-40 K higher temperature in $LuPO_4$. Fig. 3.7a shows the TL glow curves of $Y_{1-x}Lu_xPO_4$:$0.005Bi^{3+}$,$0.005Eu^{3+}$ solid solutions. With increasing x peak IIIc shifts 56 K towards higher temperature but peak I remains constant. A similar peak shifting of about 66 K was identified in $Y_{1-x}Lu_xPO_4$:$0.005Eu^{3+}$,$0.005Pr^{3+}$ in the study by Lyu *et al.* [2]. Peak IIIb in Fig. 3.7b was attributed to hole release from Pr^{4+}, and the hole trapping depth increases with x. The trapping parameters were derived using T_m as observed in Fig. 3.7a and solving Eq. (3.1) at β=1 K/s. The results are compiled in column 4 of Table 3.2.

Table 3.2. TL results for $REPO_4$:0.005Ln^{3+},0.005Bi^{3+} (RE=Y, Lu, or La) samples providing the frequency factor s (s^{-1}), and the trap depths E (eV) for TL glow peak IIIc.

Compound	s	Ln^{3+}	Bi E(IIIc)
YPO_4	1.45×10^{13}	Sm^{3+}	1.39
YPO_4	1.45×10^{13}	Tm^{3+}	1.39
YPO_4	1.45×10^{13}	Eu^{3+}	1.42
YPO_4	1.45×10^{13}	Yb^{3+}	1.37
$Y_{0.75}Lu_{0.25}PO_4$	4.45×10^{13}	Eu^{3+}	1.53
$Y_{0.5}Lu_{0.5}PO_4$	2.53×10^{14}	Eu^{3+}	1.66
$Y_{0.25}Lu_{0.75}PO_4$	1.29×10^{15}	Eu^{3+}	1.78
$LuPO_4$	1.03×10^{15}	Eu^{3+}	1.79
$LaPO_4$	2.14×10^{12}	Eu^{3+}	0.54

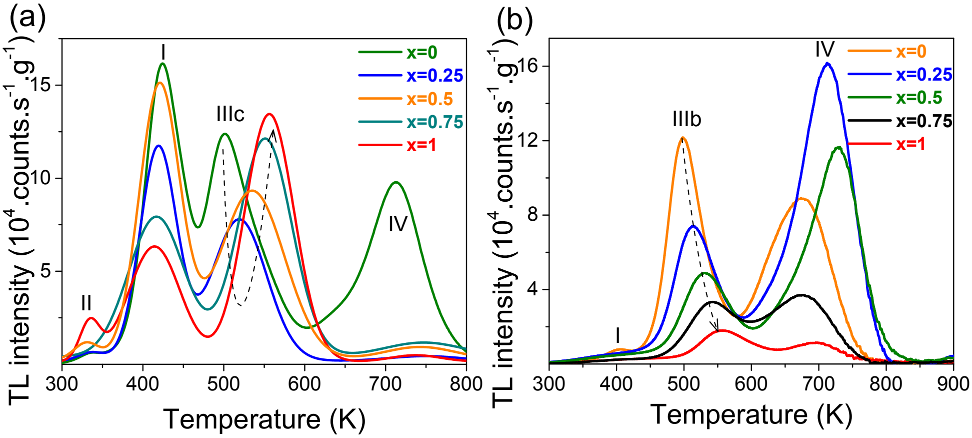

Fig. 3.7. TL glow curves for (a) $Y_{1-x}Lu_xPO_4$:0.005Eu^{3+},0.005Bi^{3+} and (b) $Y_{1-x}Lu_xPO_4$: 0.005Eu^{3+},0.005Pr^{3+} solid solutions monitoring the emission from Eu^{3+} recorded at a heating rate of 1 K/s. The data on Eu^{3+}-Pr^{3+}-codoped samples were obtained from Lyu *et al.* [2].

For $LaPO_4$ it is known that the valence band top is at 0.77 eV higher energy than in YPO_4 [2]. Again assuming that the VRBE in the Bi^{3+} ground state is more or less invariant, hole release from Bi^{4+} is expected to occur at about 320 K lower temperature which would be near 200 K. Therefore a low temperature TL-study was performed. Fig. 3.8 shows the low temperature TL (LTTL) glow curves of $LaPO_4$:0.005Eu^{3+},0.005Bi^{3+} and $LaPO_4$:0.005Eu^{3+},0.005Ln^{3+} (Ln=Tb or Ce).

Similar as peak IIIa attributed to hole release from Tb^{4+} in $LaPO_4$ [2], Bi^{3+} gives rise to a glow peak at the predicted temperature near 206 K that is referred to as IIIc. The LTTL glow curve of $LaPO_4$:0.005Eu^{3+},0.005Ce^{3+} is shown to demonstrate the absence of peaks IIIa and IIIc. Considering that the content of Bi^{3+} is low, we assume that the determined frequency factor for $LaPO_4$:0.005Eu^{3+},0.005Tb^{3+} found in Ref. [2] using variable heating rate plots also applies to $LaPO_4$:0.005Eu^{3+}, 0.005Bi^{3+}. The activation energy compiled in column 4 of Table 3.2 for glow peak IIIc was determined utilizing Eq. (3.1) and T_m as observed in Fig. 3.8 at β=1 K/s.

The glow peaks appearing above room temperature were also further investigated and are shown in Fig. S3.8, and S3.9. $LaPO_4$:0.005Eu^{3+},0.005Bi^{3+} with the most intense glow peak IIc close to RT also shows the most intense Eu^{3+} afterglow luminescence in Fig. S3.10a, which can still be detected after 12 h. In addition Fig. S3.11 shows a TL excitation (TLE) spectrum of the TL glow peak between 300-500 K of $LaPO_4$:0.005Eu^{3+},0.005Bi^{3+} in order to reveal the origin of glow peaks I and IIc.

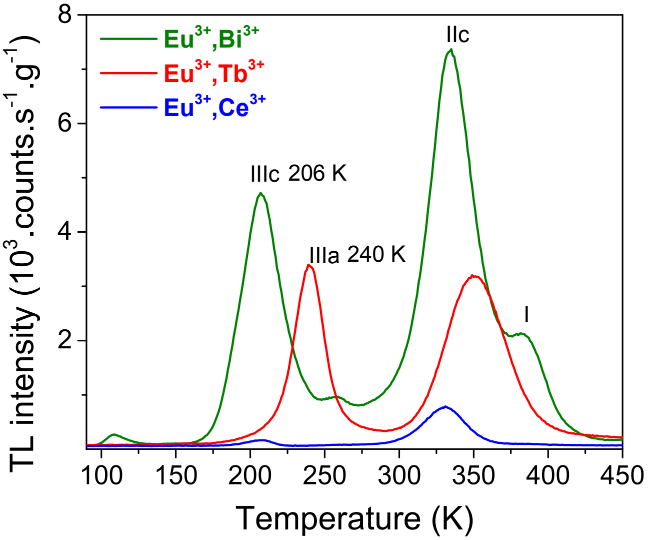

Fig. 3.8. Low-temperature TL (LTTL) glow curves of $LaPO_4$:0.005Eu^{3+},0.005Bi^{3+} and $LaPO_4$:0.005Eu^{3+},0.005Ln^{3+} (Ln=Tb or Ce) monitoring the Eu^{3+} emission at a heating rate of 1 K/s. The data on $LaPO_4$:0.005Eu^{3+},0.005Ln^{3+} were obtained from Lyu *et al.* [2].

To study the origin of glow peak IIIc for the Bi^{3+}, Eu^{3+} combination in Fig. 3.5 and 3.6, the thermoluminescence excitation (TLE) spectrum of the TL glow peak between 470-600 K of YPO_4:0.005Eu^{3+},0.005Bi^{3+} was recorded and shown in Fig. 3.9. A broad TL excitation band extending from 210 to 260 nm is observed. The position resembles the onset of Eu^{3+} CT-band of Eu^{3+} single doped YPO_4 at 210-

260 nm also shown in Fig. 3.9. This shows that after Eu^{3+} CT-band excitation, the holes created in the valence band are captured by Bi^{3+} that is responsible for the TL glow peak IIIc.

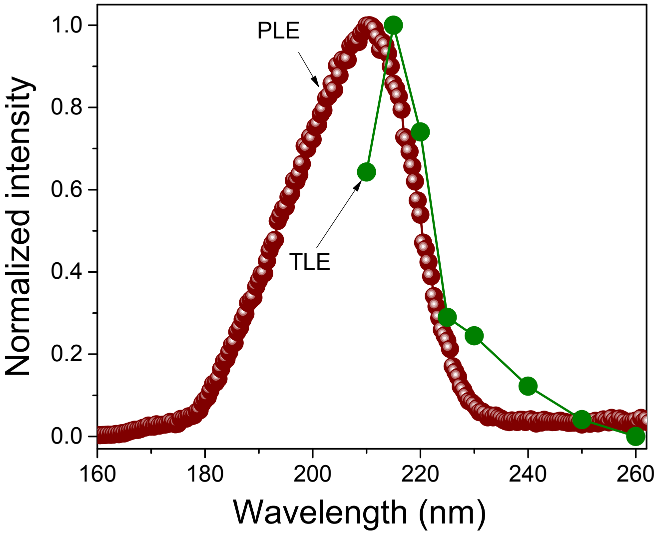

Fig. 3.9. Thermoluminescence excitation (TLE) spectrum of YPO_4:$0.005Eu^{3+}$,$0.005Bi^{3+}$ and photoluminescence excitation (PLE) spectrum of YPO_4:$0.005Eu^{3+}$ monitoring the Eu^{3+} 592 nm emission recorded at room temperature.

3.5. Discussion

The vacuum referred binding energy (VRBE) diagram containing lanthanide, Bi^{3+} and Bi^{2+} energy levels will first be interpreted, and then we will show how it can be utilized to control the hole trapping and detrapping processes in bismuth and lanthanide co-doped rare earth ortho-phosphates.

Fig. 3.10 shows the stacked VRBE diagram of lanthanide doped La-, Y-, and $LuPO_4$ from our previous study in Ref. [2], together with the Bi^{3+} and Bi^{2+} ground state locations based on this work. To determine the VRBE in the $6s^2$ ground state of Bi^{3+}, the metal-to-metal charge transfer (MMCT) energy of an electron from Bi^{3+} to the conduction band, as measured in Fig. 3.2b are used. The $Bi^{3+}\rightarrow$CB CT-bands in $REPO_4$ (RE=Y or Lu) are at 179 nm, and 176 nm, respectively. This energy, see arrow D in Fig. 3.1, is defined as the energy difference between the Bi^{3+} ground state and the energy in between the conduction band bottom and E_x. One then obtains -7.9, and -8 eV for the VRBE in the Bi^{3+} ground states of $REPO_4$:$0.005Bi^{3+}$ (RE=Y or Lu), respectively. The study from Awater *et al.* [19] showed that the VRBE in the Bi^{3+} $^1S_0$ ground state in oxide compounds is found between -5 and -10 eV and for phosphates it is always near -8 eV. Also considering that $REPO_4$ (RE=La, Y, and Lu) are quite similar, we expect that the VRBE in the Bi^{3+} $^1S_0$ ground state in $LaPO_4$ will be located between -7 and -9 eV and at the $Bi^{3+}\rightarrow$CB CT-band between 150 and 200 nm. This is consistent with the fitted Gaussian band at around 180 nm in Fig. 3.2b that is then assumed to be the $Bi^{3+}\rightarrow$CB CT-band. The Bi^{3+} ground state is then determined at -7.7±0.3 eV for $LaPO_4$. It should be noticed that the Bi^{3+} MMCT-band for $LaPO_4$ obtained in this work should be treated as indicative. From the Bi^{2+} radioluminescence in YPO_4 in Ref. [28], the VRBE in the $^2P_{1/2}$ ground state of Bi^{2+} in YPO_4 is estimated at -3.3 eV. Considering that La-, Y-, and $LuPO_4$ are quite similar and the VRBE in the Bi^{2+} ground states in oxide compounds are estimated near -3.5 eV in Ref. [58], like Bi^{2+} in YPO_4, we then expect the Bi^{2+} ground states at -3.3±0.5 eV for other $REPO_4$ (RE=La or Lu). Details about how to construct the VRBE diagram from spectroscopic data can be found in Refs. [16, 18].

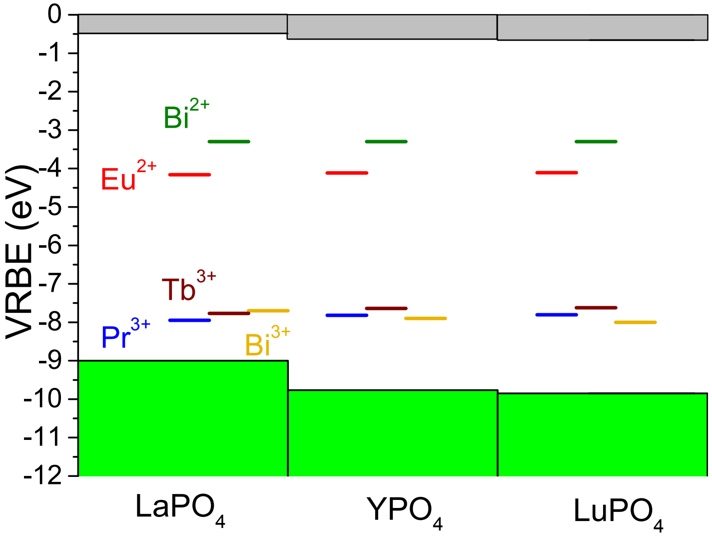

Fig. 3.10. Stacked VRBE diagram of $REPO_4$ (RE=La, Y, or Lu) with the vacuum referred binding energy in the ground states of Eu^{2+}, Pr^{3+}, Tb^{3+}, Bi^{2+}, and Bi^{3+}.

3.5.1. Bi^{3+} as deep electron trap combined with shallow hole trapping centers

The stacked vacuum referred binding energy (VRBE) scheme of YPO_4 in Fig. 3.10 predicts that the holes captured by Pr^{4+} and Tb^{4+} will be released earlier, i.e., at lower temperature than the electrons captured at Bi^{2+} to produce the characteristic emission of Bi^{3+}.

Fig. 3.3a and S3.3b-c shows the TL emission plots for YPO_4 each with the same Bi^{3+} electron trapping center but with different hole trapping centers Pr^{3+}, Ce^{3+}, and Tb^{3+}. Contrary to YPO_4:0.005Bi^{3+},0.005Ce^{3+} with the 3.80 eV deep hole trap on Ce^{3+}, YPO_4:0.005Bi^{3+},0.005Tb^{3+} or Pr^{3+} show glow peaks IIIa and IIIb due to hole release from Tb^{4+} and Pr^{4+} with trap depths of about 1.4 eV. Apparently the electron trap of Bi^{3+} is much deeper which is consistent with the Bi^{2+} location in the VRBE diagram. The holes released from Pr^{4+} or Tb^{4+} recombine with electrons at Bi^{2+} yielding Bi^{3+} A-band emission. The presence of Pr^{3+} and Tb^{3+} emission lines is explained because part of the energy of Bi^{3+} can be transferred to Pr^{3+} or Tb^{3+}, generating the 4f-4f emission[59-61]. The ET processes are further supported by the decreased decay lifetimes of the Bi^{3+} A-band emission in YPO_4:0.005Bi^{3+}, 0.005Pr^{3+} or Tb^{3+} as shown in Fig. S3.12.

Bi^{3+} acting as electron or as hole trap in this work is summarized in Table 3.3. In YPO_4:0.005Bi^{3+},0.005Ln^{3+} (Ln=Tb or Pr) Bi^{3+} acts as deep electron trap and stable recombination center. This is different from the garnets studied by Katayama *et al.* [37] where the CB-bottom is at lower VRBE leading to electron release from Bi^{2+}, see Table 3.1. The hole trapping depths of Tb^{3+} and Pr^{3+} can be engineered via changing x, leading to valence band lowering in $Y_{1-x}Lu_xPO_4$:0.005Bi^{3+},0.005Tb^{3+} or Pr^{3+} in Fig. 3.4.

Table 3.3. Bi^{3+} acting as electron (e^-) or as hole (h^+) trap in $REPO_4$:0.005Ln^{3+},0.005Bi^{3+} (RE=Y, Lu, or La) afterglow phosphors in the present work. The symbol h^+ means that holes release earlier from Tb^{4+}, Pr^{4+}, or Bi^{4+} than electrons from Bi^{2+}, Sm^{2+}, Tm^{2+}, Yb^{3+}, and Eu^{2+}.

Compound	h^+	transport	e^-
YPO_4	Tb^{3+} or Pr^{3+}	$h^+\rightarrow$	Bi^{3+}
$LuPO_4$	Tb^{3+} or Pr^{3+}	$h^+\rightarrow$	Bi^{3+}
$Y_{1-x}Lu_xPO_4$	Tb^{3+} or Pr^{3+}	$h^+\rightarrow$	Bi^{3+}
YPO_4	Bi^{3+}	$h^+\rightarrow$	Bi^{3+}
YPO_4	Bi^{3+}	$h^+\rightarrow$	Sm^{3+}
YPO_4	Bi^{3+}	$h^+\rightarrow$	Tm^{3+}
YPO_4	Bi^{3+}	$h^+\rightarrow$	Yb^{3+}
YPO_4	Bi^{3+}	$h^+\rightarrow$	Eu^{3+}
$Y_{1-x}Lu_xPO_4$	Bi^{3+}	$h^+\rightarrow$	Eu^{3+}
$LaPO_4$	Bi^{3+}	$h^+\rightarrow$	Eu^{3+}

In the TL glow curve of YPO_4:0.005Bi^{3+} in Fig. 3.6 and S3.3a, a glow peak I appears at ~416 K which shows Bi^{3+} $^3P_1\rightarrow{}^1S_0$ emission at 245 nm. In Ref. [28] hole liberation from Bi^{4+} and recombination on Bi^{2+} was assigned to peak I in YPO_4, but in Ref. [2] we attributed the same TL-peak to hole release from an intrinsic defect.

Below we will further motivate this latter assignment and motivate that peak IIIc is due to hole release from Bi^{4+}.

Glow peak I always appears strong in the presence of deep electron traps like Bi^{3+} (Fig. S3.3a), Eu^{3+} (Fig. 3.5), Sm^{3+} (Fig. S3.4 in [2]), and Yb^{3+} (Fig. S3.3i) and emission is then from the electron trapping centre. This already suggest that peak I is due to hole release. When another competing hole trap is present, peak I appears weaker as in YPO_4:Eu^{3+},Pr^{3+} or with Sm^{3+},Pr^{3+} in Fig. S3.4 in [2] which further indicates the hole trap nature of peak I.

3.5.2. Bi^{3+} as shallow hole trap and engineering its depth by valence band changing

The electron release from Sm^{2+}, or Tm^{2+} to the conduction band is known to take place at 718 K, or 591 K at a heating rate of 5 K/s in Ce^{3+} co-doped YPO_4 in Ref. [62]. In Fig. 3.6 we do not observe a TL-glow above 550 K when Sm^{3+} or Tm^{3+} is present in YPO_4. Apparently the electrons trapped on Sm^{2+} and Tm^{2+} have already disappeared due to recombination with holes released at lower temperature. Peak I we already attributed to hole release from an unknown defect, and therefore the remaining peak IIIc is attributed to hole release from Bi^{4+} that recombines with Bi^{2+}, Sm^{2+}, Tm^{2+}, or Eu^{2+} yielding Bi^{3+} $^3P_1 \rightarrow {}^1S_0$, and Ln^{3+} 4f-4f emissions. Moreover, the emission of Bi^{3+} and Ln^{3+} can be further used to design new optical materials. For example, designing possible energy transfer processes from Bi^{3+} and Eu^{3+} to Nd^{3+} provides a new route to deliberate design of infrared bio-imaging probe, which will be published elsewhere.

The onset of the room temperature thermoluminescence excitation (TLE) spectrum of YPO_4:0.005Eu^{3+},0.005Bi^{3+} at 210-260 nm in Fig. 3.9 resembles the onset of the VB→Eu^{3+} charge transfer band of YPO_4:0.005Eu^{3+}. The lower TLE intensity at 210 nm is most likely due to an over estimated illumination intensity on the sample. During CT band excitation, electrons are excited from the valence band to the $4f^7$ ($^8S_{7/2}$) ground state of Eu^{2+} and holes are generated in the valence band which can then be trapped by Bi^{3+} to form Bi^{4+}. During TL readout, the holes release from Bi^{4+} and then recombine with Eu^{2+} and Bi^{2+} to yield Eu^{3+} 4f-4f emission and Bi^{3+} A-band emission.

The VRBE scheme of $REPO_4$ (RE=Y or Lu) in Fig. 3.10 predicts that the VRBEs in the ground states of Bi^{3+} and Pr^{3+} are almost the same, and the temperature of the glow peak due to the hole release from Bi^{4+} and Pr^{4+} and recombination on Eu^{2+} would be almost the same too. The ~66 K shifting of peaks IIIb in $Y_{1-x}Lu_xPO_4$:0.005Eu^{3+},0.005Pr^{3+} was attributed to increased activation energy for the hole release from Pr^{4+} in Ref. [2] as shown in Fig. 3.7b. With increasing x, a glow peak IIIc shift ~56 K also presents in $Y_{1-x}Lu_xPO_4$:0.005Eu^{3+}, 0.005Bi^{3+}, which is consistent with the above VRBE prediction. Like Pr^{3+}, we attribute the shift to the increased activation energy for hole release from Bi^{4+} and recombination on Eu^{2+}. The T_m of glow peak I, that was also attributed to hole release, is almost stationary with changing x. Apparently the VRBE in the responsible hole trap changes along with the changing VRBE at the VB-top which may suggest that the hole trap is somehow related to the anions in the host.

The stacked VRBE scheme of $LaPO_4$ in Fig. 3.10 predicts that Eu^{3+} is a 3.67 eV deep electron trap, while Bi^{3+} and Tb^{3+} act as 1.36, and 1.23 eV shallow hole trapping centers. It means that the temperature of the TL glow peak maximum due to hole release from Bi^{4+} or Tb^{4+} would be almost the same. Fig. 3.8 shows that, like Tb^{3+} for TL glow peak IIIa, Bi^{3+} also gives rise to a glow peak IIIc at 206 K. Glow peak IIIa at 240 K for $LaPO_4$:0.005Eu^{3+},0.005Tb^{3+} in Fig. 3.8 was attributed to hole release from Tb^{4+} in Lyu *et al.* [2]. We therefore tentatively assign glow peak IIIc at 206 K for $LaPO_4$:0.005Eu^{3+},0.005Bi^{3+} in Fig. 3.8 to hole release from Bi^{4+}. It corresponds with a trap depth of 0.54 eV as shown in column 4 of Table 3.2 which is ~0.8 eV smaller than the 1.36 eV predicted from VRBE scheme. A similar deviation with the VRBE prediction was observed for YPO_4:0.005Eu^{3+},0.005Pr^{3+} or Tb^{3+} [2] and for Eu^{3+},Pr^{3+}-, or Eu^{3+},Tb^{3+}-codoped $GdAlO_3$[14] it deviated ~0.3 eV. During the recombination phase the holes do not migrate at the top of the valence band but as trapped hole centers or V_k centers, and the lower activation energy is then attributed to the binding energy of the V_k center. The strong glow peak IIc just above room temperature in Fig. 3.8 for $LaPO_4$:0.005Eu^{3+},0.005Bi^{3+} is attributed to hole release from intrinsic hole trap(s) in $LaPO_4$.

3.6. Conclusions

Photoluminescence spectroscopy, the VRBE scheme, and thermally stimulated luminescence spectra were combined to study electron and hole capture in Bi^{3+} doped phosphors. We showed that Bi^{3+} can act both as electron and as hole trap in lanthanide co-doped rare earth ortho phosphates. In YPO_4:0.005Bi^{3+},0.005Ln^{3+} (Ln=Pr or Tb), the Ln^{3+} co-dopants are the shallow hole trapping centers, while Bi^{3+} acts as the deep electron trapping and the recombination center. The holes release from Ln^{4+} at lower temperature and recombine through the valence band with Bi^{2+} to yield Bi^{3+} $^3P_1 \rightarrow {}^1S_0$ emission. For YPO_4:0.005Ln^{3+},0.005Bi^{3+} (Ln=Tm, Sm, Eu, or Yb), the Ln^{3+} co-dopants act as the deep electron trapping and recombination centers, while Bi^{3+} is the shallow hole trapping center. The holes release from Bi^{4+} at lower temperature than electrons from Ln^{2+} and recombine through valence band with Ln^{2+} to produce Ln^{3+} 4f-4f emission during TL-readout. The vacuum referred binding energy at the valence band top in $Y_{1-x}Lu_xPO_4$: 0.005Eu^{3+},0.005Bi^{3+} can be lowered through changing x, and this leads to the increasing of the Bi^{3+} hole trap depth. By using Bi^{3+} as the shallow hole trap the recombination emission can be adjusted from the ultraviolet to the blue, or the red, or the infrared by varying the deep electron trap from Bi^{3+} to Tm^{3+} or to Sm^{3+} or Eu^{3+}, or Yb^{3+}. With deep understanding of Bi^{2+}, Bi^{3+} and lanthanide trap level locations, one may engineer the charge carrier trapping and release processes involving Bi. Combined with a lanthanide this provides a novel route to deliberate design of optical storage and afterglow materials, such as infrared bio-imaging probes.

3.7. Acknowledgements

T. Lyu acknowledges the China Scholarship Council for his PhD scholarship (Tianshuai Lyu: No. 201608320151). We would like to acknowledge fruitful discussions on afterglow phosphors and luminescence mechanisms with Dr Adrie J.J. Bos from Delft University of Technology.

3.8. Reference

1. K. Van den Eeckhout, D. Poelman and P. F. Smet, *Materials*, 2013, **6**, 2789-2818.
2. T. Lyu and P. Dorenbos, *Journal of Materials Chemistry C*, 2018, **6**, 369-379.
3. Y. Li, M. Gecevicius and J. Qiu, *Chemical Society Reviews*, 2016, **45**, 2090-2136.
4. H. Luo, A. J. J. Bos and P. Dorenbos, *The Journal of Physical Chemistry C*, 2017, **121**, 8760-8769.
5. T. Matsuzawa, Y. Aoki, N. Takeuchi and Y. Murayama, *Journal of the Electrochemical Society*, 1996, **143**, 2670-2673.
6. R. Kabe and C. Adachi, *Nature*, 2017, **550**, 384-387.
7. W. Fan, N. Lu, C. Xu, Y. Liu, J. Lin, S. Wang, Z. Shen, Z. Yang, J. Qu, T. Wang, S. Chen, P. Huang and X. Chen, *ACS Nano*, 2017, **11**, 5864-5872.
8. Z. Pan, Y.-Y. Lu and F. Liu, *Nat Mater*, 2012, **11**, 58-63.
9. Z. Li, Y. Zhang, X. Wu, L. Huang, D. Li, W. Fan and G. Han, *Journal of the American Chemical Society*, 2015, **137**, 5304-5307.
10. L. D. Hu, Y. Fan, L. Liu, X. M. Li, B. Z. Zhao, R. Wang, P. Y. Wang, A. M. El-Toni and F. Zhang, *Advanced Optical Materials*, 2017, **5**, 1700680.
11. F. Liu, W. Yan, Y.-J. Chuang, Z. Zhen, J. Xie and Z. Pan, *Scientific Reports*, 2013, **3**, 1554.
12. Y.-F. Liu, P. Liu, L. Wang, C.-E. Cui, H.-C. Jiang and J. Jiang, *Chemical Communications*, 2017, **53**, 10636-10639.
13. M. Thoms, H. von Seggern and A. Winnacker, *Physical Review B*, 1991, **44**, 9240-9247.
14. H. Luo, A. J. J. Bos and P. Dorenbos, *The Journal of Physical Chemistry C*,

2016, **120**, 5916-5925.
15. K. Chakrabarti, V. K. Mathur, J. F. Rhodes and R. J. Abbundi, *Journal of Applied Physics*, 1988, **64**, 1363-1366.
16. P. Dorenbos, *Physical Review B*, 2012, **85**, 165107.
17. P. Dorenbos, *Journal of Materials Chemistry*, 2012, **22**, 22344-22349.
18. P. Dorenbos, *ECS Journal of Solid State Science and Technology*, 2013, **2**, R3001-R3011.
19. R. H. P. Awater and P. Dorenbos, *Journal of Luminescence*, 2017, **184**, 221-231.
20. P. Boutinaud, *Inorganic Chemistry*, 2013, **52**, 6028-6038.
21. P. Boutinaud and E. Cavalli, *Chemical Physics Letters*, 2011, **503**, 239-243.
22. G. Blasse, A. Meijerink, M. Nomes and J. Zuidema, *Journal of Physics and Chemistry of Solids*, 1994, **55**, 171-174.
23. L. Li, M. Peng, B. Viana, J. Wang, B. Lei, Y. Liu, Q. Zhang and J. Qiu, *Inorganic Chemistry*, 2015, **54**, 6028-6034.
24. M. A. Hamstra, H. F. Folkerts and G. Blasse, *Journal of Materials Chemistry*, 1994, **4**, 1349-1350.
25. A. M. Srivastava, *Journal of Luminescence*, 1998, **78**, 239-243.
26. M. Peng and L. Wondraczek, *Opt. Lett.*, 2009, **34**, 2885-2887.
27. R. H. P. Awater and P. Dorenbos, *The Journal of Physical Chemistry C*, 2016, **120**, 15114-15118.
28. R. H. P. Awater, L. C. Niemeijer-Berghuijs and P. Dorenbos, *Optical Materials*, 2017, **66**, 351-355.
29. H.-T. Sun, J. Zhou and J. Qiu, *Progress in Materials Science*, 2014, **64**, 1-72.
30. J. L. DiMeglio and J. Rosenthal, *Journal of the American Chemical Society*, 2013, **135**, 8798-8801.
31. J. L. Tallon, R. G. Buckley, P. W. Gilberd, M. R. Presland, I. W. M. Brown, M. E. Bowden, L. A. Christian and R. Goguel, *Nature*, 1988, **333**, 153.
32. F. Kang, M. Peng, D. Y. Lei and Q. Zhang, *Chemistry of Materials*, 2016, **28**, 7807-7815.
33. G. Blasse and A. Bril, *Journal of Chemical Physics*, 1968, **48**, 217-222.
34. H. S. Kiliaan and G. Blasse, *Materials Chemistry and Physics*, 1987, **18**, 155-170.
35. A. M. Srivastava, *Materials Research Bulletin*, 2002, **37**, 745-751.
36. W. Sun, R. Pang, H. Li, D. Li, L. Jiang, S. Zhang, J. Fu and C. Li, *Journal of Materials Chemistry C*, 2017, **5**, 1346-1355.
37. Y. Katayama, A. Hashimoto, J. Xu, J. Ueda and S. Tanabe, *Journal of Luminescence*, 2017, **183**, 355-359.
38. Z. Zou, X. Tang, C. Wu, D. Wang, J. Zhang, Z. Ci, S. Du and Y. Wang, *Materials Research Bulletin*, 2018, **97**, 251-259.
39. Y. Katayama, J. Ueda and S. Tanabe, *Opt. Mater. Express*, 2014, **4**, 613-623.

40. D. D. Jia, J. Zhu and B. Q. Wu, *Journal of the Electrochemical Society*, 2000, **147**, 386-389.
41. Y. Jin, Y. Hu, L. Chen, X. Wang, G. Ju and Z. Mu, *Radiation Measurements*, 2013, **51-52**, 18-24.
42. W. Wang, Z. Sun, X. He, Y. Wei, Z. Zou, J. Zhang, Z. Wang, Z. Zhang and Y. Wang, *Journal of Materials Chemistry C*, 2017, **5**, 4310-4318.
43. T. Wang, X. Xu, D. Zhou, Y. Yang, J. Qiu and X. Yu, *Inorganic Chemistry*, 2016, **55**, 894-901.
44. S. Wang, W. Chen, D. Zhou, J. Qiu, X. Xu and X. Yu, *Journal of the American Ceramic Society*, 2017, **100**, 3514-3521.
45. S. Lai, Z. Yang, J. Liao, J. Qiu, Z. Song, Y. Yang and D. Zhou, *Materials Research Bulletin*, 2014, **60**, 714-718.
46. A. J. J. Bos, R. M. van Duijvenvoorde, E. van der Kolk, W. Drozdowski and P. Dorenbos, *Journal of Luminescence*, 2011, **131**, 1465-1471.
47. J. Ueda, P. Dorenbos, A. J. J. Bos, A. Meijerink and S. Tanabe, *The Journal of Physical Chemistry C*, 2015, **119**, 25003-25008.
48. A. M. Srivastava and S. J. Camardello, *Optical Materials*, 2015, **39**, 130-133.
49. E. Cavalli, F. Angiuli, F. Mezzadri, M. Trevisani, M. Bettinelli, P. Boutinaud and M. G. Brik, *J. Phys.-Condes. Matter*, 2014, **26**, 385503.
50. U. Sasum, M. Kloss, A. Rohmann, L. Schwarz and D. Haberland, *Journal of Luminescence*, 1997, **72-74**, 255-256.
51. E. Nakazawa and F. Shiga, *Journal of Luminescence*, 1977, **15**, 255-259.
52. D. Wang and Y. Wang, *Materials Research Bulletin*, 2007, **42**, 2163-2169.
53. R. Moncorge, G. Boulon and J. P. Denis, *Journal of Physics C-Solid State Physics*, 1979, **12**, 1165-1171.
54. S. W. S. McKeever, *Thermoluminescence of Solids*, Cambridge University Press, Cambridge, 1985.
55. R. Chen and S. A. A. Winer, *Journal of Applied Physics*, 1970, **41**, 5227-5232.
56. W. Hoogenstraaten, *Philips Res. Rep*, 1958, **13**, 515–693.
57. J. Ueda, P. Dorenbos, A. J. J. Bos, K. Kuroishi and S. Tanabe, *Journal of Materials Chemistry C*, 2015, **3**, 5642-5651.
58. R. H. P. Awater and P. Dorenbos, *Journal of Luminescence*, 2017, **188**, 487-489.
59. T. Jüstel, P. Huppertz, W. Mayr and D. U. Wiechert, *Journal of Luminescence*, 2004, **106**, 225-233.
60. F. Angiuli, E. Cavalli and A. Belletti, *Journal of Solid State Chemistry*, 2012, **192**, 289-295.
61. G. Blasse and A. Bril, *The Journal of Chemical Physics*, 1967, **47**, 1920-1926.
62. A. J. J. Bos, P. Dorenbos, A. Bessière and B. Viana, *Radiation Measurements*, 2008, **43**, 222-226.

3.9. Supporting information

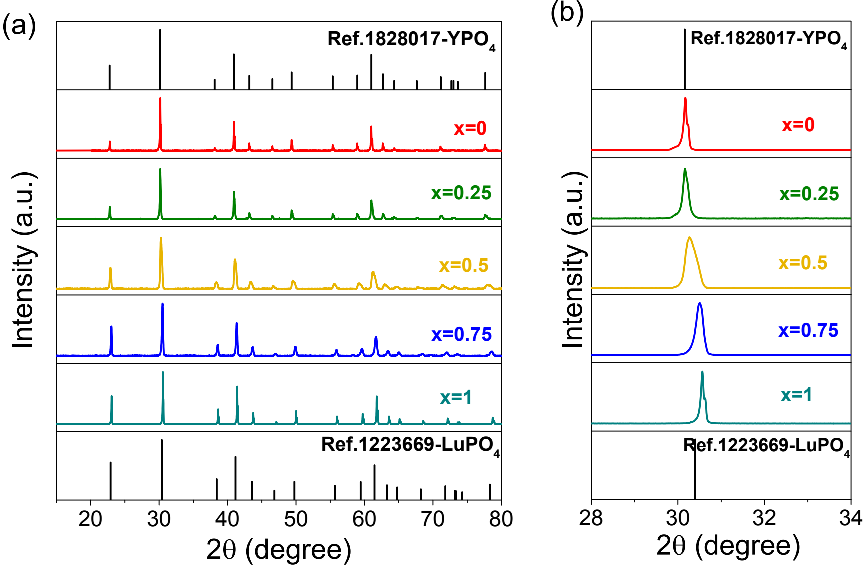

Fig. S3.1. (a) XRD patterns of $Y_{1-x}Lu_xPO_4$:0.005Eu^{3+},0.005Bi^{3+} solid solutions (x=0-1). (b) detailed XRD patterns in the range from 28 to 34°.

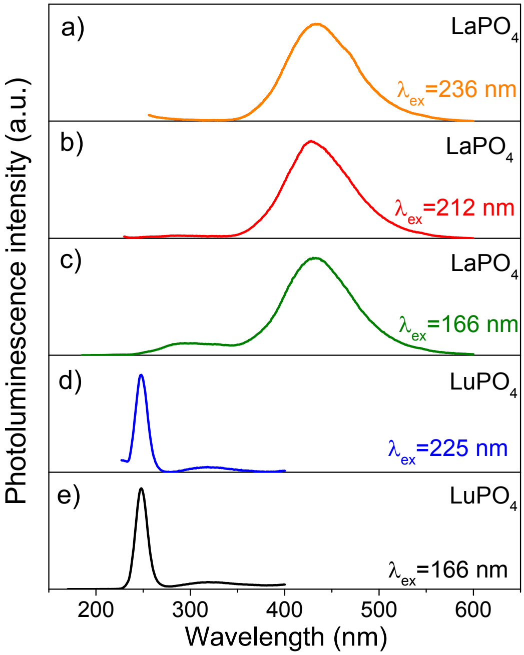

Fig. S3.2. Photoluminescence spectra of $LaPO_4$:0.002Bi^{3+} and $LuPO_4$:0.005Bi^{3+} excited at different excitation wavelength recorded at 10 K.

Fig. S3.2a-c shows the photoluminescence spectra of LaPO4:0.002Bi^{3+} at different excitation wavelength. All spectra share a same band at 432 nm, and the weaker band at 288 nm only appears when excited at 166 nm and 212 nm. From the study by Boutinaud *et al.* [1], the band at 432 nm is tentatively attributed to CB→Bi^{3+} charge transfer emission.

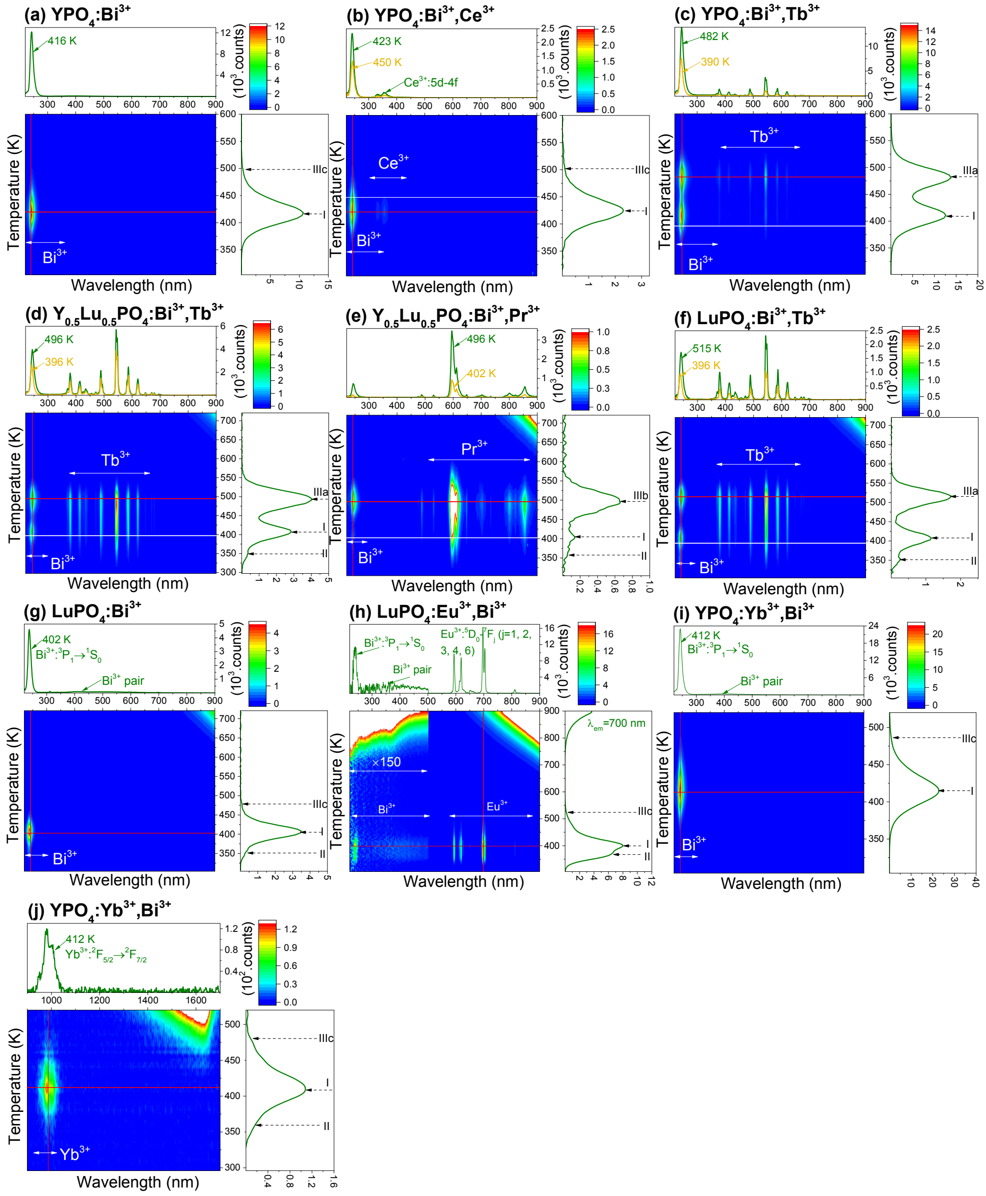

Fig. S3.3. Thermoluminescence emission (TLEM) plots of Bi^{3+} single or Bi^{3+}-Ln^{3+}-codoped $REPO_4$ (RE=Y or Lu; Ln=Tb, Pr, Ce, Eu, or Yb) recorded at a heating rate of 1 K/s. The concentration of each dopant is fixed at 0.5 mol%.

The VRBE diagram in Fig. 3.1 predicts that Ce^{3+} acts as a 3.80 eV deep hole trapping center in YPO_4:$0.005Bi^{3+}$,$0.005Ce^{3+}$ which is deeper than the 2.7 eV Bi^{3+} electron trapping center. The electron will be released earlier from Bi^{2+} than the hole from Ce^{4+}. One then can estimate according to Eq. (3.1) at the heating rate of 1 K/s that electron release from Bi^{2+} to the conduction band bottom in YPO_4 will give rise to a glow peak T_m at ~930 K.

With the VRBE at Bi^{2+} ground state between that of Sm^{2+} and Yb^{2+} we expect that the TL glow appears at between 679 and 965 K as observed for YPO_4:Ce^{3+},Ln^{3+} (Ln=Sm or Yb) in Ref. [2]. Clearly, the Bi^{3+} electron trap is too deep to release an electron in the measurement range, which explains why no additional TL band(s) with Ce^{3+} emission appears in Fig. S3.3b.

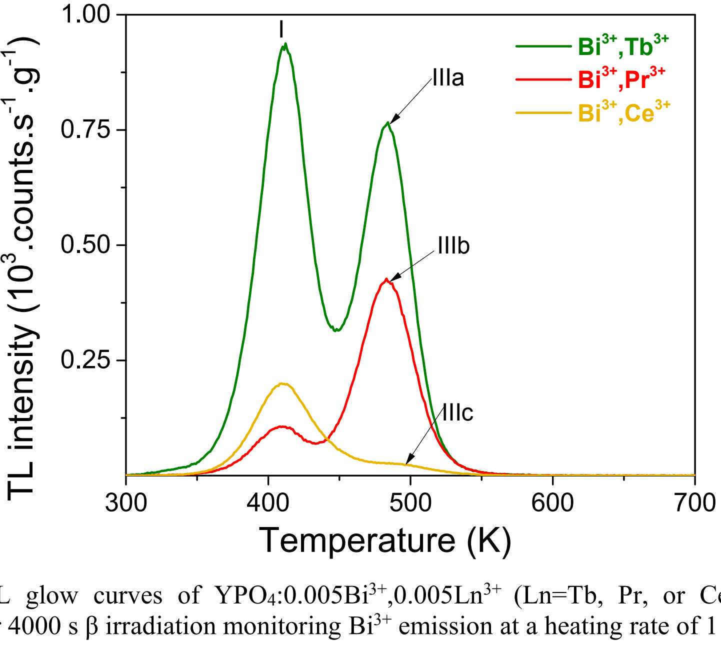

Fig. S3.4. TL glow curves of YPO_4:$0.005Bi^{3+}$,$0.005Ln^{3+}$ (Ln=Tb, Pr, or Ce) samples recorded after 4000 s β irradiation monitoring Bi^{3+} emission at a heating rate of 1 K/s.

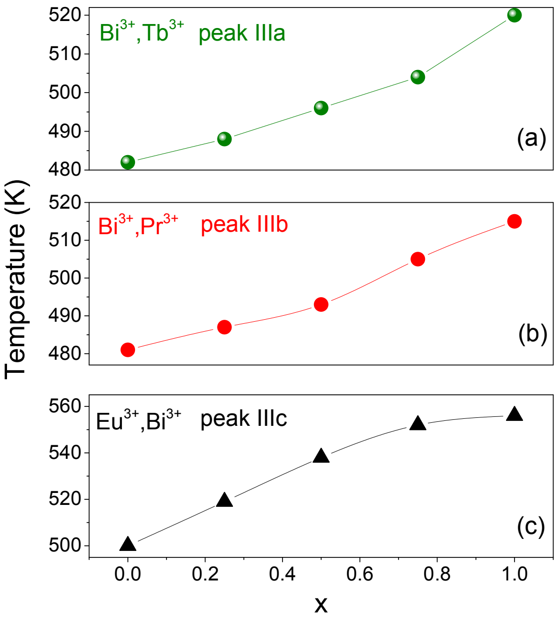

Fig. S3.5. Comparison of TL glow peaks IIIa, IIIb, and IIIc for $Y_{1-x}Lu_xPO_4$:$0.005Bi^{3+}$, $0.005Ln^{3+}$ (Ln=Tb or Pr) and $Y_{1-x}Lu_xPO_4$:$0.005Eu^{3+}$,$0.005Bi^{3+}$ solid solutions (x=0-1).

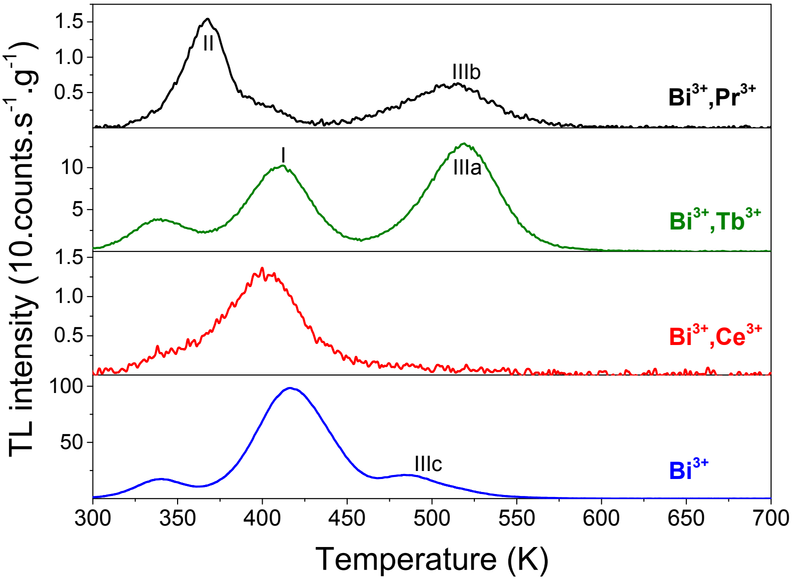

Fig. S3.6. TL glow curves of $LuPO_4$:$0.005Bi^{3+}$,$0.005Ln^{3+}$ (Ln=Pr, Tb, or Ce) recorded after exposure to β source for 4000 s monitoring Bi^{3+} emission at a heating rate of 1 K/s.

Fig. S3.6 shows the TL glow curves for $LuPO_4$:0.005Bi^{3+},0.005Ln^{3+} (Ln=Pr, Tb, or Ce) samples. Similar as in Fig. 3.3a and S3.4 for YPO_4, Tb and Pr also give rise to two peaks IIIa and IIIb in $LuPO_4$:0.005Bi^{3+},0.005Tb^{3+} and $LuPO_4$:0.005Bi^{3+}, 0.005Pr^{3+}. The TL glow curves of the single Bi^{3+} and the Bi^{3+}-Ce^{3+}-codoped samples are shown to illustrate the absence of peaks IIIa and IIIb. These results further support that the glow peaks IIIa and IIIb are due to hole release from Tb^{4+} and Pr^{4+} and recombination on Bi^{2+}.

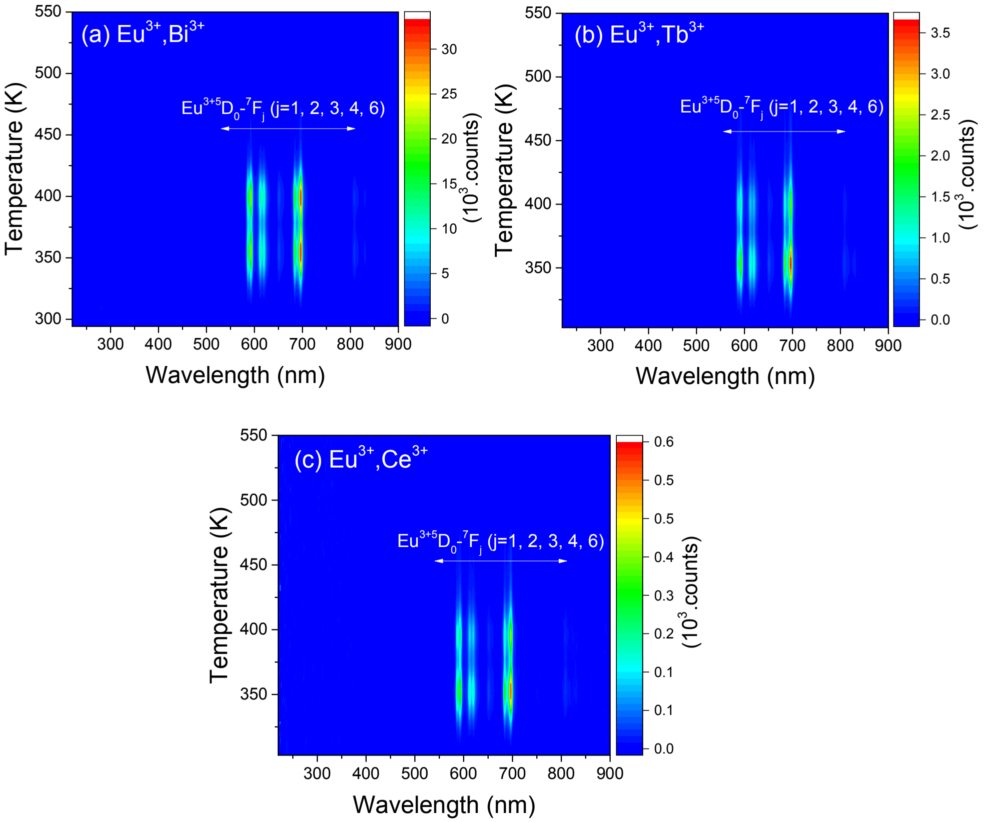

Fig. S3.7. Thermoluminescence emission (TLEM) plots of (a) $LaPO_4$:0.005Eu^{3+},0.005Bi^{3+}, (b) $LaPO_4$:0.005Eu^{3+},0.005Tb^{3+}, and (c) $LaPO_4$:0.005Eu^{3+},0.005Ce^{3+} at a heating rate of 1 K/s.

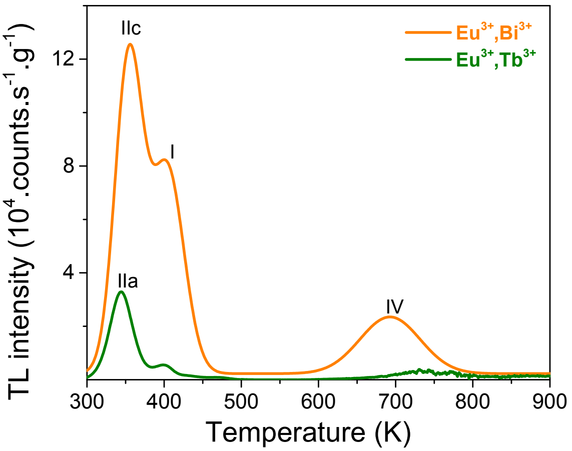

Fig. S3.8. (a) TL glow curves of LaPO$_4$:0.005Eu^{3+},0.005Bi^{3+} and LaPO$_4$:0.005Eu^{3+}, 0.005Tb^{3+} monitoring the red emission from Eu^{3+} recorded at a heating rate of 1 K/s. The data on LaPO$_4$:0.005Eu^{3+},0.005Tb^{3+} were obtained from Lyu *et al*. [3].

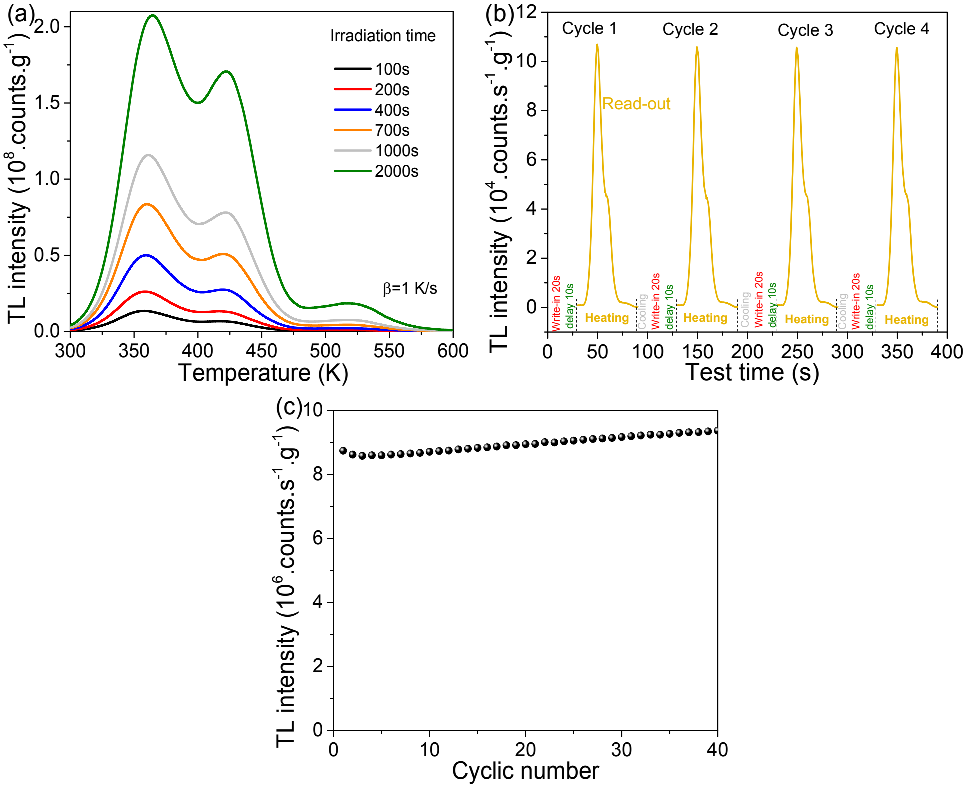

Fig. S3.9. (a) TL glow curves charged by β irradiation at different dose, (b) repeatability test of TL glow curves after 20 s β irradiation, and (c) integrated TL glow intensity as a function of cyclic number for $LaPO_4$:0.005Eu^{3+},0.005Bi^{3+}.

Fig. S3.9a shows the TL glow curves for $LaPO_4$:0.005Eu^{3+},0.005Bi^{3+} charged by a β dose of 70 to 1400 mGy. All TL glow curves show their maxima at the same temperature T_m (± 6 K), suggesting that the first-order TL recombination approximation is justified[4].

Note that a proportional increase of the TL intensity appears when irradiation time increases. This shows that this phosphor has potential application as energy storing materials or as a dosimeter for detection of ionizing radiation. Fig. S3.9b shows a repeatability test of TL glow curves of $LaPO_4$:0.005Eu^{3+},0.005Bi^{3+}. The integrated TL intensities in Fig. S3.9c suggest that this phosphor is relatively stable during the 40 cycle test.

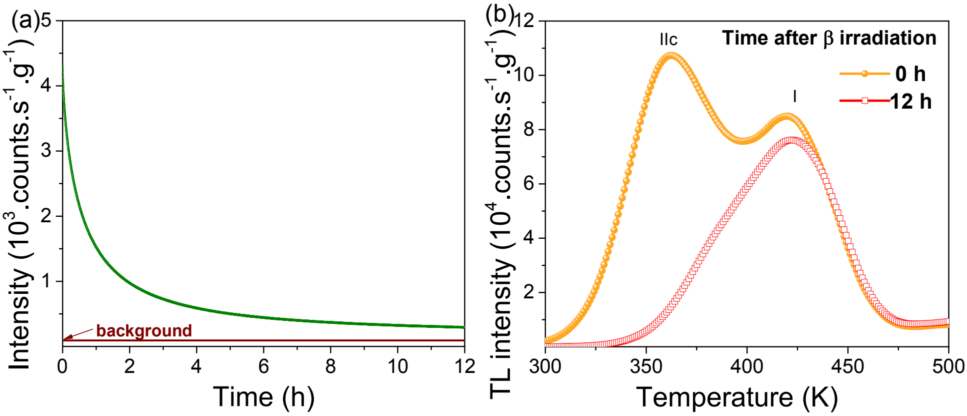

Fig. S3.10. (a). Isothermal decay curve monitoring the Eu^{3+} emission recorded at room temperature and (b) TL glow curves with different waiting time after 2000 s β irradiation for $LaPO_4$:0.005Eu^{3+},0.005Bi^{3+}.

Fig. S3.10a shows that the persistent luminescence from Eu^{3+} can still be detected after 12 h at RT. In order to identify the origin of the afterglow, Fig. S3.10b shows the TL glow curve of $LaPO_4$:0.005Eu^{3+},0.005Bi^{3+} without and with 12 h waiting time after β irradiation. It shows that glow peak IIc disappears almost entirely after 12 h. This suggests that the hole release from a shallow host related hole trap at RT and recombination on Eu^{2+} may be responsible for the Eu^{3+} afterglow.

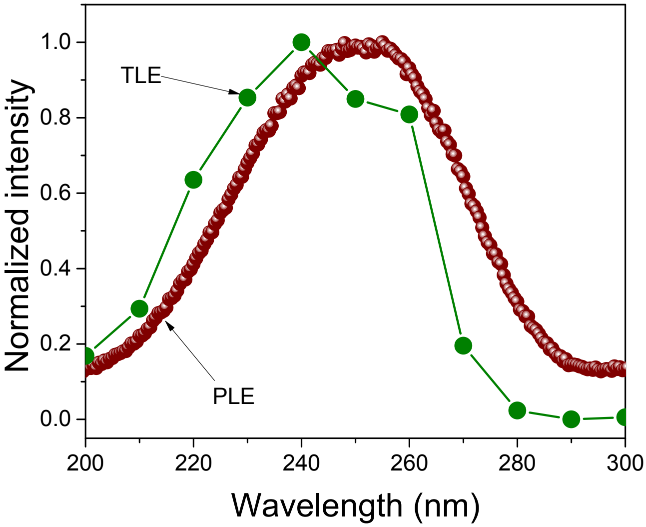

Fig. S3.11. Thermoluminescence excitation (TLE) spectrum of $LaPO_4$:0.005Eu^{3+},0.005Bi^{3+} and photoluminescence excitation (PLE) spectrum of $LaPO_4$:0.005Eu^{3+} monitoring the Eu^{3+} 590 nm emission recorded at room temperature.

TL excitation (TLE) spectra for $LaPO_4$:0.005Eu^{3+},0.005Bi^{3+} were recorded by first illuminating the samples during 4000 s with a monochromatic photon beam generated using a 150 W xenon arc lamp (Hamamatsu L2273) filtered by a monochromator (Oriel Cornerstone 130). This system has a wavelength resolution of 0.8 nm against 0.1 mm slit width. The slit width was set to 1 mm and the wavelength step as 10 nm. A LabVIEW program was used to record TL glow curves in 300-700 K at a heating rate of 5 K/s when the excitation wavelengths change between 200 and 300 nm.

To investigate the origin of glow peaks I and IIc, Fig. S3.11 shows the thermoluminescence excitation (TLE) spectrum of the TL glow peak between 300-500 K for $LaPO_4$:0.005Eu^{3+},0.005Bi^{3+}. A broad TL excitation band extending from 200 to 300 nm and peaking at 240 nm is detected. The position and width resembles with the VB→Eu^{3+} charge transfer band of $LaPO_4$:0.005Eu^{3+}, where the band width is identical but it appears 10 nm blue shifted corresponding with 0.2 eV. During CT band excitation, electrons are excited from the valence band to $4f^7$ ($^8S_{7/2}$) of Eu^{2+} and holes are generated in the valence band which can then be trapped by host intrinsic hole trapping center. During TL readout, the holes release from hole trapping centers and then recombine with Eu^{2+} to yield Eu^{3+} 4f-4f emission. The 0.2 eV blue shift in band location may imply that the hole trap is far from Eu^{3+}, which is not conducive to hole release.

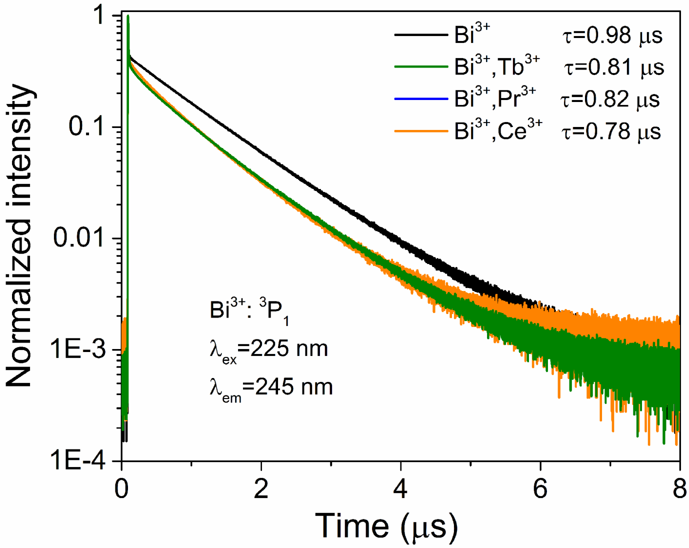

Fig. S3.12. Fluorescence lifetimes of YPO_4:0.005Bi^{3+},0.005Ln^{3+} (Ln=Pr, Tb, or Ce) samples monitoring Bi^{3+} emission at 245 nm.

From the study in Refs. [5, 6] there are spectral overlaps between the Bi^{3+} A-band emission and the excitation bands of Ce^{3+}, Pr^{3+}, and Tb^{3+}, which suggests that there is a probability for the energy transfer from Bi^{3+} to Ce^{3+}, Pr^{3+}, or Tb^{3+}[7-9]. To further show the energy transfer processes, Fig. S3.12 shows photoluminescence decay curves of the Bi^{3+} A-band emission in YPO_4:0.005Bi^{3+},0.005Ln^{3+}. For YPO_4:0.005Bi^{3+}, the decay curve can be well fitted by a single exponential function which can be written as

$$I(t) = I_0 \times \exp(-\frac{t}{\tau}) \qquad \text{(S3.1)}$$

where I_0 and I_t are emission intensities of a sensitizer Bi^{3+} in the absence and presence of an activator Ce^{3+}, Tb^{3+}, or Pr^{3+}, respectively. The lifetime of the Bi^{3+} A-band emission in YPO_4:0.005Bi^{3+} is derived to be 0.98 μs using Eq. (S3.1). With the co-doping of Ce^{3+}, Tb^{3+}, or Pr^{3+}, decay curves deviate from single exponential function and the Bi^{3+} lifetime decreases. This indicates that the co-doping Ln^{3+} modifies the luminescence dynamic of Bi^{3+} because of the energy transfer from Bi^{3+} to Ln^{3+}.

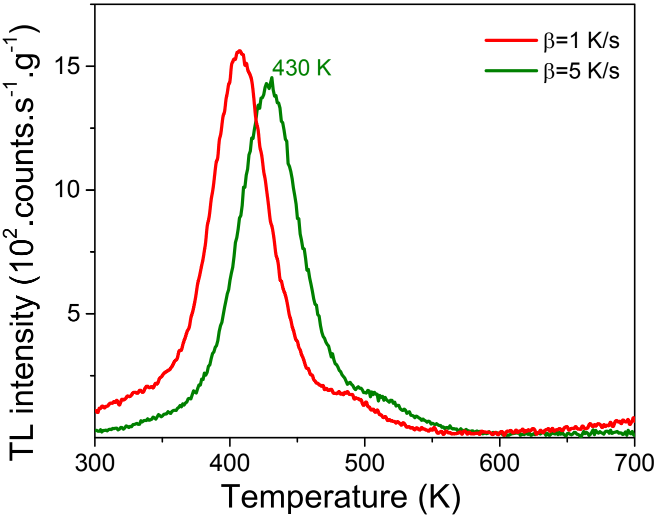

Fig. S3.13. TL glow curves of YPO$_4$:0.005Bi^{3+},0.005Ce^{3+} recorded at different heating rates of 1 and 5 K/s after 400 s β source irradiation. A Hoya C5-58 filter was utilized to select Ce^{3+} emission.

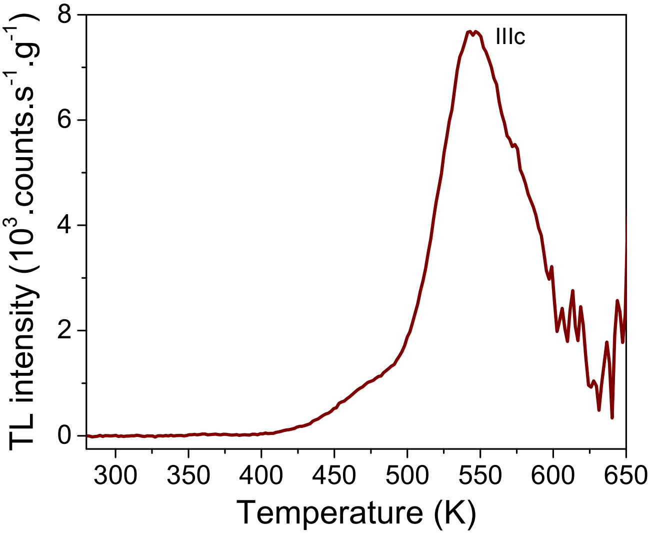

Fig. S3.14. TL glow curve of YPO$_4$:0.005Eu^{3+},0.005Bi^{3+} charged by a laser beam at 212 nm for 600 s recorded at a heating rate of 5 K/s. The Eu^{3+} red emission was monitored.

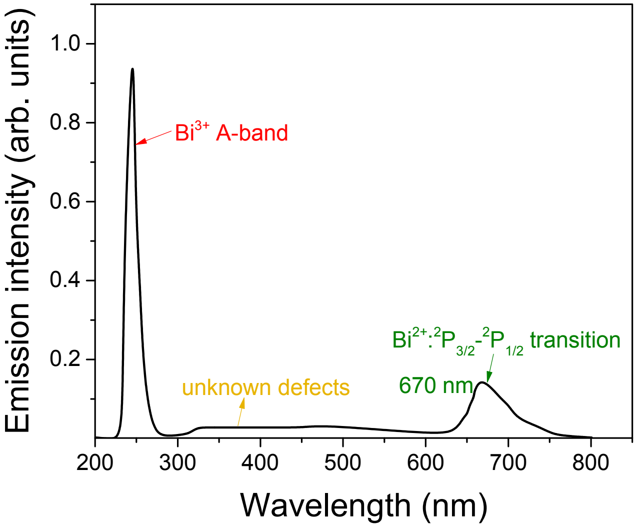

Fig. S3.15. X-ray excited emission spectrum for YPO_4:0.05mol%Bi sample recorded at room temperature. The data were obtained from Awater *et al.* [10].

The emission band peaked at 670 nm has been ascribed in Ref. [10] to Bi^{2+} $^2P_{3/2}\rightarrow^2P_{1/2}$ transition, which is induced via the capturing of an electron from the conduction band by Bi^{3+} to form the excited state of Bi^{2+}.

Reference

1. P. Boutinaud, *Inorganic Chemistry*, 2013, **52**, 6028-6038.
2. A. J. J. Bos, P. Dorenbos, A. Bessière, A. Lecointre, M. Bedu, M. Bettinelli and F. Piccinelli, *Radiation Measurements*, 2011, **46**, 1410-1416.
3. T. Lyu and P. Dorenbos, *Journal of Materials Chemistry C*, 2018, **6**, 369-379.
4. A. J. J. Bos, *Radiation Measurements*, 2006, **41**, S45-S56.
5. T. Jüstel, P. Huppertz, W. Mayr and D. U. Wiechert, *Journal of Luminescence*, 2004, **106**, 225-233.
6. W. Di, X. Wang, B. Chen, H. Lai and X. Zhao, *Optical Materials*, 2005, **27**, 1386-1390.
7. M. Jiao, Y. Jia, W. Lu, W. Lv, Q. Zhao, B. Shao and H. You, *Journal of Materials Chemistry C*, 2014, **2**, 90-97.
8. D. L. Dexter and J. H. Schulman, *The Journal of Chemical Physics*, 1954, **22**, 1063-1070.
9. G. Blasse, *Physics Letters A*, 1968, **28**, 444-445.
10. R. H. P. Awater, L. C. Niemeijer-Berghuijs and P. Dorenbos, *Optical Materials*, 2017, **66**, 351-355.

4

Designing thermally stimulated 1.06 μm Nd^{3+} emission for the second bio-imaging window demonstrated by energy transfer from Bi^{3+} in La-, Gd-, Y-, and $LuPO_4$

Graphical abstract

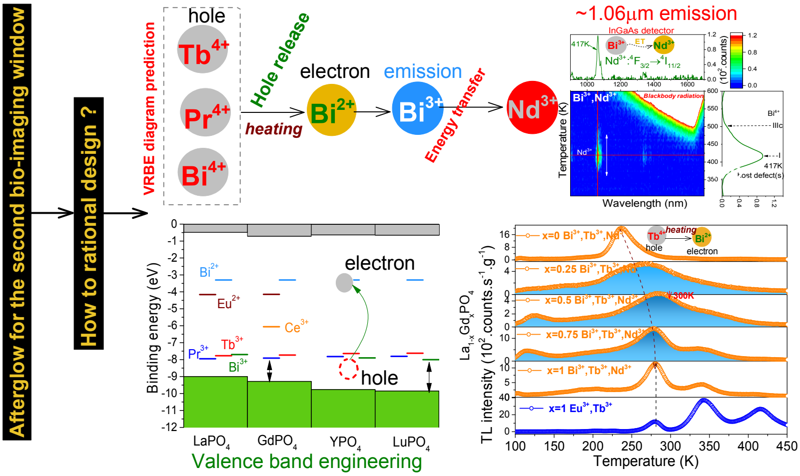

This chapter is based on the publication: **T. Lyu*** and P. Dorenbos, ***Chemical Engineering Journal***, 2019, 372, 978-991.

4.1. Abstract

We report a general methodology to the rational design of thermally stimulated short-wave infrared (SWIR) luminescence between ~900 and 1700 nm by a new combination of using efficient energy transfer from Bi^{3+} to Nd^{3+} and an adjustable hole trap depth via valence band engineering. Predictions from a vacuum referred binding energy (VRBE) diagram are combined with the data from optical spectroscopy and thermoluminescence to show the design concept by using bismuth and lanthanide doped rare earth ortho-phosphates as model examples. Nd^{3+} with its characteristic $^4F_{3/2}\rightarrow{}^4I_j$ (j=9/2, 11/2, 13/2) emission in the SWIR range is first selected as the emitting centre. The energy transfer (ET) processes from Bi^{3+} or Tb^{3+} recombination centres to Nd^{3+} are then discussed. Photoluminescence results show that the energy transfer efficiency of $Bi^{3+}\rightarrow Nd^{3+}$ appears to be much higher than of $Tb^{3+}\rightarrow Nd^{3+}$. To exploit this ET, thermally stimulated Bi^{3+} A-band emission can then be designed by using Bi^{3+} as a ~2.7 eV deep electron trap in YPO_4. By combining Bi^{3+} with Tb^{3+}, Pr^{3+}, or Bi^{3+} itself, the holes trapped at Tb^{4+}, Pr^{4+}, or Bi^{4+} will release earlier than the electrons captured at Bi^{2+}. On recombination with Bi^{2+}, Bi^{3+} in its excited state is formed generating Bi^{3+} A-band emission. Due to the ET of $Bi^{3+}\rightarrow Nd^{3+}$ 1.06 μm Nd^{3+} emission appears in YPO_4. Herein, the thermally stimulated Nd^{3+} SWIR emission is achieved by hole release rather than the more commonly reported electron release. The temperature when thermally stimulated Nd^{3+} SWIR emission appears can further be engineered by changing the Tb^{3+} or Pr^{3+} hole trap depth in $Y_{1-x}Lu_xPO_4$ by adjusting x. Such valence band engineering approach can also be applied to other compounds like $La_{1-x}Gd_xPO_4$ and $Gd_{1-x}La_xAlO_3$ solid solutions. Our work opens the avenue to motivate scientists to explore novel SWIR afterglow phosphors in a design way instead of by trial and error approach.

Keywords: Bismuth; valence band engineering; hole release; energy transfer; afterglow

4.2. Introduction

Afterglow is known as a self-sustained luminescence phenomenon[1-3], where a material is capable of first storing excitation energy[4], and then emitting photons for a particular time after removing the excitation source[5, 6]. This phenomenon has promising applications in various fields[7], including but not limited to information storage[8], traffic signage[9], and alternating current driven LED (AC-LED)[10]. Particularly, nanoscale infrared afterglow probes, with the advanced application in vivo bio-imaging, have attracted ever-increasing attention[11]. One of the famous examples is the $ZnGa_2O_4:Cr^{3+}$ afterglow nano-probe[12], which shows infrared emission from 650 to 750 nm.

Short-wave infrared (SWIR) light with the emission wavelength between ~900-1700 nm exhibits unique spectral properties such as reduced Rayleigh scattering, which lead to many promising applications like in anti-counterfeiting, military night-vision surveillance, and medical imaging[7, 13-16]. For instance, as compared with the near-infrared light with emission wavelength between ~700 and 900 nm, the SWIR light has higher penetration ability in a challenging atmosphere condition like dust, smog, fog, or rain. The SWIR range is in the second bio-imaging window, which shows promising application to arrive at super-sensitive and deep penetration medical bio-imaging. Hong *et al.* [17] reported a type of in vivo fluorescence imaging using Ag_2S quantum dots with adjustable photoluminescence in the ~1100-1400 nm second near-infrared bio-imaging window. With this quantum dots based technique, however, in situ continuous 808 nm laser excitation is required during the optical imaging process, which not only causes tissue auto-fluorescence but also inevitably induces damage to the healthy tissues[18].

Currently, short-wave infrared (SWIR) afterglow luminescence between ~900-1700 nm has attracted research interest. The "self-sustained" SWIR afterglow emission without real-time external excitation not only shows higher penetration in biological tissue compared with the infrared spectral range between ~700-900 nm, but also allows the imaging to be operated in an auto-fluorescence neglectable way[19]. This broadens the avenue to arrive at better medical bio-imaging with high signal-to-noise ratio and super imaging sensitivity[20].

Compared with the many studies on afterglow phosphors with an emission wavelength between 450 nm and 750 nm[9], there are much less studies that focus on the thermally stimulated SWIR luminescence. Properties of several typical infrared afterglow phosphors are summarized in Table 4.1. Only a few reports show the infrared afterglow decay in absolute radiance unit[19] like $mW.sr^{-1}.m^{-2}$ and the charge carrier trapping processes are often unclear. The proposed electron release processes and duration time as provided in Table 4.1 then should be regarded as indicative. It turns out that a trial and error approach appears to be often applied to discover a new SWIR afterglow phosphor, and the real nature of carrier trapping processes is usually not carefully identified such as in Table 4.1. There is a strong wish in the rational design of SWIR afterglow between ~900-1700 nm[7].

Methods to derive the locations of divalent and trivalent lanthanides energy levels within the band gap of inorganic crystals have now been constructed [21, 22]. Using spectroscopic data, one can construct a so-called vacuum referred binding energy (VRBE) diagram[23]. Knowledge regarding the VRBE in defect levels, such as lanthanides, conduction band (CB), or valence band (VB), then provides a powerful tool to predict luminescence and to engineer carrier transport properties[24]. Note that the VRBE-guided method is mainly used to explore visible persistent phosphors[7] and systemic exploration of SWIR afterglow phosphors based on VRBE-guided conduction band or valence band engineering is still lacking. Particularly, to the best of our knowledge, there is no report on the design of SWIR afterglow based on hole release and tailored hole trapping depth via valence band engineering.

Table 4.1. Carrier trapping processes, emission, and afterglow durations for typical infrared afterglow phosphors. The symbol $\leftarrow e^-$ denotes that electrons liberate at a lower temperature than holes.

Compound	h^+	transport	e^-	peak (nm)	duration (h)	ref
$Zn_3Ga_2Ge_2O_{10}$	Cr^{3+}	$\leftarrow e^-$	host defect	696	360	[25]
$ZnGa_2O_4$	Cr^{3+}	$\leftarrow e^-$	host defect	687	5	[9]
$LiGa_5O_8$	Cr^{3+}	$\leftarrow e^-$	host defect	716	1000	[26]
$Zn_3Ga_2SnO_8$	Cr^{3+}	$\leftarrow e^-$	host defect	713	300	[27]
$MgGeO_3$	Yb^{3+}	$\leftarrow e^-$	host defect	1019	100	[28]
$Zn_3Ga_2Ge_2O_{10}$	Ni^{2+}	$\leftarrow e^-$	host defect	1290	12	[20]
$SrAl_2O_4$	Eu^{2+}	$\leftarrow e^-$	Dy^{3+}	1530 (Er^{3+})	0.2	[29]
$Y_3Al_2Ga_3O_{12}$	Ce^{3+}	$\leftarrow e^-$	Cr^{3+}	1532 (Er^{3+})	10	[30]
Ca_2SnO_4	Yb^{3+}	$\leftarrow e^-$	host defect	1000	10	[31]
$MgGeO_3$	Pr^{3+}	$\leftarrow e^-$	host defect	1085	120	[32]
$CdSiO_3$	Pr^{3+}	$\leftarrow e^-$	host defect	1085	120	[32]
$LaAlO_3$	Cr^{3+}	$\leftarrow e^-$	Sm^{3+}	986 (Er^{3+})	1	[19]
$Y_3Al_2Ga_3O_{12}$	Ce^{3+}	$\leftarrow e^-$	Cr^{3+}	1064	10	[33]

In this work, guided by a vacuum referred binding energy (VRBE) diagram, we will demonstrate how to design thermally stimulated Nd^{3+} infrared luminescence between ~900-1700 nm by a new combination of efficient energy transfer from Bi^{3+} to Nd^{3+} and adjustable hole trap depth via valence band engineering in the model La-, Gd-, Y-, and $LuPO_4$ compounds. Here, the thermally stimulated Nd^{3+} SWIR emission is obtained by means of hole release rather than the more commonly reported electron release.

Fig. 4.1 shows the VRBE diagram for YPO_4 with energy level locations of Bi^{2+}, Bi^{3+}, and lanthanides. Here, Tb^{3+}, Pr^{3+}, and Bi^{3+} act as ~1.45 eV, ~1.41 eV, and ~1.42 eV deep hole traps and Nd^{3+} as a ~0.96 eV deep electron trap as evidenced in previous experimental work[34, 35]. The Bi^{3+} is predicted to act as a ~2.7 eV deep electron trap based on the VRBE diagram prediction.

Upon charging by β- or γ-ray irradiation, free charge carriers are created that can migrate via the valence band or conduction band. The electrons can be captured in a Bi^{3+}, or Nd^{3+} electron trap centre forming Bi^{2+}, or Nd^{2+} (arrows 1), and the holes can be captured by Bi^{3+}, Tb^{3+}, or Pr^{3+} generating Bi^{4+}, Tb^{4+}, or Pr^{4+} in their ground states (arrows 2) in YPO_4. Because the trap depth of the 2.7 eV deep Bi^{3+} electron trapping centre is ~1.25 eV deeper than that of the ~1.45 eV deep hole trapping centres of Bi^{3+}, Tb^{3+}, or Pr^{3+}, the hole capturing centres will liberate holes (arrow 3) to combine with electrons at Bi^{2+} yielding Bi^{3+} A-band emission. If there is an efficient energy transfer process from Bi^{3+} to Nd^{3+}, then thermally stimulated Nd^{3+} SWIR luminescence near 1.06 μm can appear. The engineering of the hole trap depth of Tb^{3+} or Pr^{3+} hole trapping centres was demonstrated in $Y_{1-x}Lu_xPO_4$ solid solutions. By increasing x, the valence band (VB) energy can be tailored. The temperature when thermally stimulated Nd^{3+} ~1.06 μm luminescence appears can then be engineered by adjusting the Tb^{3+} or Pr^{3+} hole trap depth in $Y_{1-x}Lu_xPO_4$. We will verify all the above type of expectations, and provide a general VRBE-guided route to the rational design of thermally stimulated SWIR phosphors that can be applied to other inorganic compounds like $La_{1-x}Gd_xPO_4$ and $Gd_{1-x}La_xAlO_3$ solid solutions.

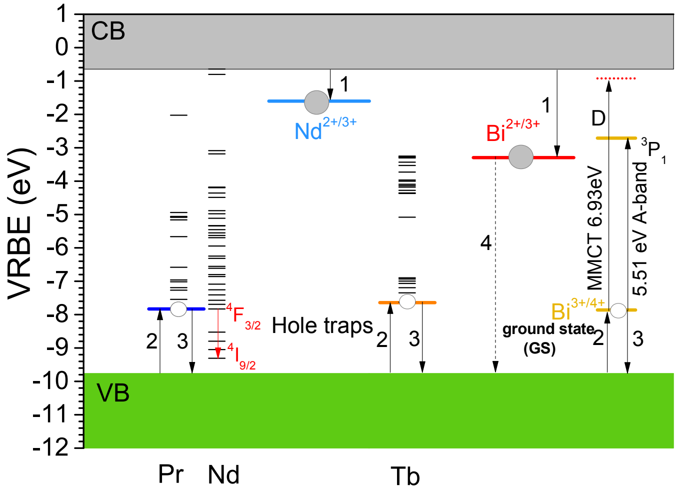

Fig. 4.1. Vacuum referred binding energy (VRBE) diagram of YPO_4 including the energy level locations for the ground states of Nd^{2+}, Pr^{3+}, Tb^{3+}, Bi^{2+}, and Bi^{3+}. The open circles represent holes and the filled circles are electrons. The charge carrier trapping processes indicated using numbered arrows are discussed in the text.

4.3. Experimental

All starting reagents were bought from Sigma-Aldrich and employed without further treatments. Chemical reagents Bi_2O_3 (99.999%), $NH_4H_2PO_4$ (99.99%), and rare earth oxides (99.999%) were utilized as starting raw materials. Samples were synthesized by high-temperature solid-state reactions. Stoichiometric mixtures were thoroughly mixed in acetone. The mixtures were fired at 400 °C for 5 h and then at 1400 °C for 10 h in a covered corundum crucible in ambient atmosphere. The heating rate for the furnace is 3 °C per minute. After cooling, the as-synthesized compounds were ground well before further measurements. Solid solutions $Y_{1-x}Lu_xPO_4$:$0.005Bi^{3+}$,$0.005Ln^{3+}$,$0.005Nd^{3+}$ (Ln^{3+}=Tb or Pr) were prepared for x ranging from 0 to 1. The phase purities of all the samples were checked using a PANalytical XPert PRO x-ray diffraction system equipped with a cobalt Kα (λ=0.178901 nm) X-ray tube.

The photoluminescence (PL) emission and excitation spectra were recorded at room temperature (RT) using a setup that consists of a UV/VIS spectrometer (Ocean Optics, QE65000), a near-infrared (NIR) spectrometer (Ocean Optics, NIRQ512), and a diode-pumped YAG:Nd laser system (NT230-100-SH/DUV-SCU). With an optical parametric oscillator (OPO), the output laser wavelength of a NT230-100-SH/DUV-SCU laser system can be tuned from 192 to 2600 nm. We used a Si-based detector QE65000 with a spectral range of 200-975 nm and an InGaAs based detector NIRQ512 with a spectral range of 900-1700 nm. The fluorescence lifetime curves were measured with a setup that includes a PerkinElmer MP-1913 photomultiplier (PMT), a UV/vis branch, a digitizer module, and an NT230-100-SH/DUV-SCU laser system. For these spectral measurements, all powder samples with different chemical composition were pressed into pills with 0.4 cm diameter and mass <20 mg.

Thermoluminescence (TL) glow curves above room temperature (300-720 K) were recorded with a setup that consists of a RISØ TL/OSL reader (model DA-15), a controller (DA-20), and an EMI9635QA photomultiplier[36]. Prior to the TL measurements, all the samples were heated to 720 K 3 times to empty all relevant traps in complete darkness under a flow of N_2 gas and then cooled to room temperature followed by a β irradiation charging treatment using a $^{90}Sr/^{90}Y$ β source at a dose rate of 0.7 mGy/s. For the TL recording on samples where Bi^{3+} was the recombination centre, a 239 nm bandpass (239FS10-50, Andover Corporation) filter was placed between the PMT tube and the sample during the measurements.

Low-temperature thermoluminescence (LTTL) glow curves (90-450 K) were performed using a setup that consists of a $^{90}Sr/^{90}Y$ β irradiation source, a PerkinElmer channel photomultiplier tube (MP-1393), and a sample chamber that can be cooled to 90 K using liquid nitrogen under vacuum. Prior to the LTTL measurements, all the samples were heated to 450 K to empty all relevant traps and then charged at 90 K using β irradiation for 10 min at a dose rate of ~0.4 mGy/s.

For $LaPO_4$:0.002Bi^{3+},0.005Pr^{3+},0.005Nd^{3+} a 600 nm bandpass (600FS40-50) filter was used to select Pr^{3+} emission, and for $LaPO_4$:0.002Bi^{3+},0.005Tb^{3+}, 0.005Nd^{3+}, a 545 nm bandpass (545FS40-50) filter was used to monitor Tb^{3+} emission.

Thermoluminescence emission spectra (TLEM) were recorded at a heating rate of 1 K/s by using the RISØ TL/OSL reader equipped with a UV/vis QE65000 spectrometer and a near infrared NIR512 spectrometer. All samples were first heated to 720 K to empty relevant traps and then charged at room temperature using γ-ray irradiation from a ^{60} Co source. The TLEM measured by QE65000 was corrected by the wavelength dependent quantum efficiency of the QE65000 spectrometer. A correction for the TLEM recorded by the infrared NIR512 spectrometer was not made.

4.4. Results

4.4.1. Photoluminescence spectroscopy

Fig. 4.2a)-c) shows the excitation-emission wavelength contour plots for YPO_4:0.005Nd^{3+}, YPO_4:0.005Tb^{3+},0.005Nd^{3+}, and YPO_4:0.005Bi^{3+},0.005Nd^{3+}. Characteristic Nd^{3+} 4f-4f excitation bands between 325-600 nm appear in YPO_4:0.005Nd^{3+} in Fig. 4.2a) while monitoring the 870 nm Nd^{3+} $^4F_{3/2}\rightarrow{}^4I_{9/2}$ emission. A weak additional excitation band near 225 nm appears in YPO_4: 0.005Tb^{3+},0.005Nd^{3+} in Fig. 4.2b), which is assigned to the first Tb^{3+} 4f→5d spin allowed transition. The same band is observed for Tb^{3+} singly doped YPO_4 when monitoring the Tb^{3+} emission at 545 nm as shown in Fig. S4.1. Much stronger and broader additional excitation band near 225 nm appears in YPO_4:0.005Bi^{3+}, 0.005Nd^{3+} in Fig. 4.2c) and YPO_4:0.005Bi^{3+},0.02Nd^{3+} in Fig. 4.2d), which is assigned to the Bi^{3+} $^1S_0\rightarrow{}^3P_1$ excitation band. The same band appears in YPO_4:0.005Bi^{3+} in Fig. S4.3.

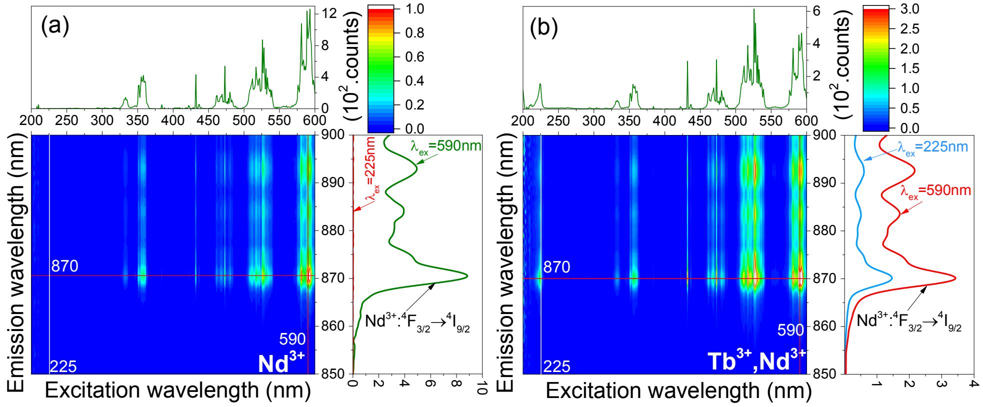

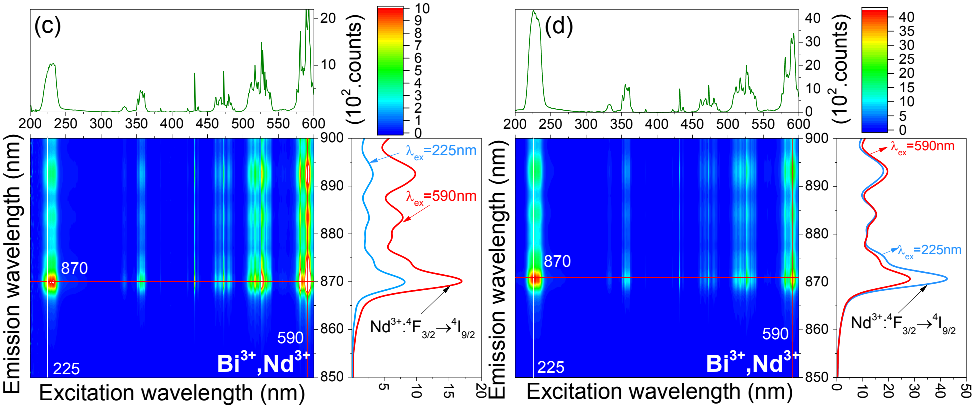

Fig. 4.2. Excitation-emission wavelength contour plots for (a) YPO$_4$:0.005Nd^{3+}, (b) YPO$_4$: 0.005Tb^{3+},0.005Nd^{3+}, (c) YPO$_4$:0.005Bi^{3+},0.005Nd^{3+}, and (d) YPO$_4$:0.005Bi^{3+},0.02Nd^{3+}. The photoluminescence spectra under OPO laser excitation were recorded using a Si-based detector QE65000. A filter 10CGA-610 was used to select the Nd^{3+} emission above 610 nm. All the PL spectra were corrected by both the changes of laser intensity and the wavelength dependent quantum efficiency of the QE65000 detector.

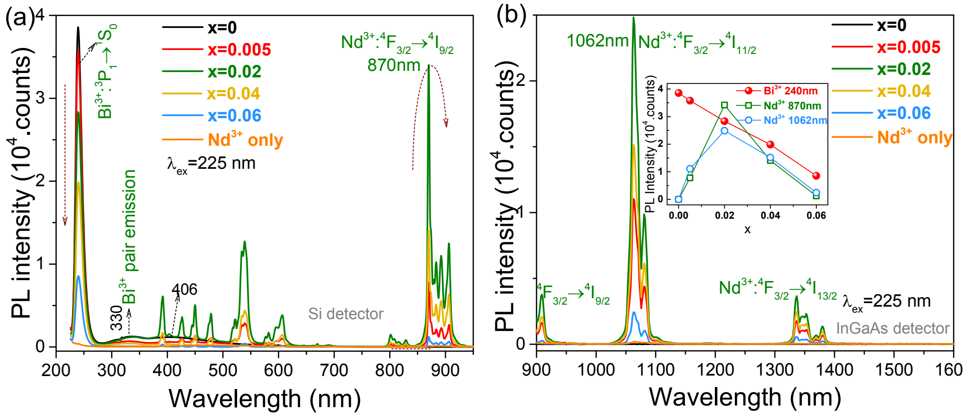

Fig. 4.3. 225 nm OPO laser excited photoluminescence (PL) spectra of YPO$_4$:0.005Bi^{3+}, xNd^{3+} (x=0-0.06) and YPO$_4$:0.005Nd^{3+} crystals, a) between 225-975 nm recorded by a Si-based QE65000 detector, and b) between 900-1600 nm recorded using a InGaAs infrared detector NIRQ512. The inset in b) shows the variation of PL intensities of Bi^{3+} at 240 nm, Nd^{3+} at 870 and 1062 nm with increasing x.

Fig. 4.3 shows the photoluminescence (PL) spectra of YPO$_4$:0.005Bi^{3+},xNd^{3+} (x=0-0.06) and YPO$_4$:0.005Nd^{3+} between 225-1600 nm recorded by Si and InGaAs detectors upon 225 nm excitation corresponding with the Bi^{3+} A-band wavelength. Like in YPO$_4$:Bi^{3+} in [37], the emission band near 240 nm is assigned to the Bi^{3+} $^3P_1$→$^1S_0$ A-band. The broad 368-600 nm emission band peaked near 406 nm is of unknown origin. The emission band centred near 330 nm is assigned to Bi^{4+}-Bi^{2+} pair emission[38]. With increasing x in YPO_4:0.005Bi^{3+},xNd^{3+}, the photoluminescence intensity of the Bi^{3+} A-band at 240 nm continually decreases as shown in the inset of Fig. 4.3b), while both the PL intensities of Nd^{3+} at 870 nm and at 1062 nm first increase from x=0 to x=0.02, and then decrease with further increasing x due to the concentration quenching effect of Nd^{3+} emission[39].

Fig. 4.3 demonstrates efficient energy transfer from Bi^{3+} to Nd^{3+} and to further identify this energy transfer process, fluorescence decay measurements of Bi^{3+} $^3P_1 \rightarrow {}^1S_0$ emission at 245 nm were carried out for the YPO_4:0.005Bi^{3+},xNd^{3+} (x=0-0.06) samples as shown in Fig. 4.4a). All decay curves can be well fitted using the following single exponential formula plus a constant background intensity[40]:

$$I(t) = I_{b.g.} + I_0 \times \exp(-\frac{t}{\tau}) \tag{4.1}$$

Where $I_{b.g.}$ is the background intensity, I_0 and I(t) stand for the Bi^{3+} $^3P_1 \rightarrow {}^1S_0$ emission intensities at time 0 and t, respectively. With Eq. (4.1) the lifetimes of the Bi^{3+} $^3P_1 \rightarrow {}^1S_0$ are determined and shown in Fig. 4.4b). The Bi^{3+} lifetime appears to decrease continually from 1.13 μs for x=0 to 0.52 μs for x=0.06 with increasing x, indicating an extra decay pathway because of a non-radiative energy transfer from the Bi^{3+} $^3P_1$ level to Nd^{3+}.

The lifetime τ or decay rate Γ for the excited $^3P_1$ state is related to the radiative decay rate, hereafter referred to as Γ_v ($=\tau_v^{-1}$), and the non-radiative decay rate named as Γ_{nr} which consists of the non-radiative rates by multi-phonon relaxation (Γ_{phon}) to lower energy states and by an energy transfer process (Γ_{ET}) to Nd^{3+}. The following relation applies[19]

$$\Gamma_{tot} = \Gamma_v + \Gamma_{phon} + \Gamma_{ET} = \tau_{Bi,Nd}^{-1} \tag{4.2}$$

$$\eta_{ET} = \frac{\Gamma_{ET}}{\Gamma_v + \Gamma_{phon} + \Gamma_{ET}} = 1 - \frac{\tau_{Bi,Nd}}{\tau_{Bi}} \tag{4.3}$$

where Γ_{tot} represents the total decay rate, and τ_{Bi} and $\tau_{Bi,Nd}$ stand for the fluorescence lifetimes for the Bi^{3+} $^3P_1$ level in the Bi^{3+} singly and Bi^{3+}-Nd^{3+}-doped YPO_4. Using Eq. (4.3) the ET efficiencies η_{ET} from the Bi^{3+} $^3P_1$ level to Nd^{3+} are estimated and shown in Fig. 4.4b). The η_{ET} appears to increase with increasing x and arrives at 53.98% when x=0.06.

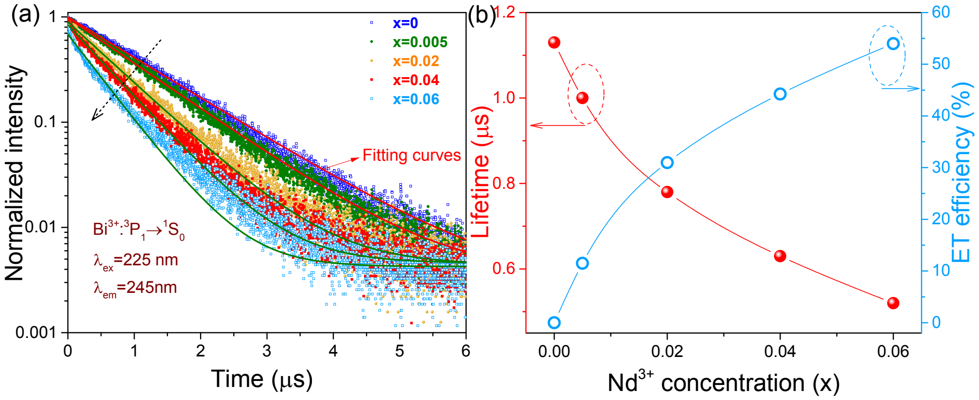

Fig. 4.4. (a) Fluorescence decay curves and (b) lifetime of Bi^{3+} A-band emission ($^3P_1 \rightarrow {}^1S_0$) at 245 nm upon 225 nm excitation as a function of Nd^{3+} concentration (x) in YPO_4:$0.005Bi^{3+}$,xNd^{3+} (x=0-0.06) recorded at room temperature. The Nd^{3+} concentration dependence of the energy transfer efficiency of $Bi^{3+} \rightarrow Nd^{3+}$ in YPO_4:$0.005Bi^{3+}$,xNd^{3+} is shown.

4.4.2. Thermally stimulated luminescence

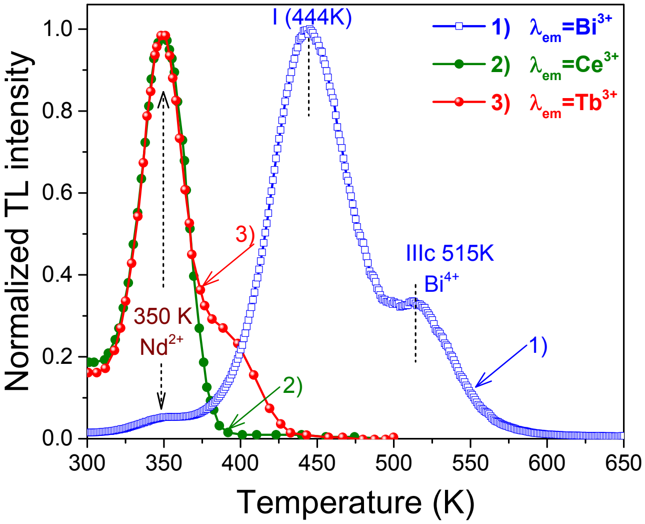

Fig. 4.5. Normalized TL glow curves for 1) YPO_4:$0.005Bi^{3+}$,$0.005Nd^{3+}$, 2) YPO_4:$0.005Ce^{3+}$, $0.005Nd^{3+}$, and 3) YPO_4:$0.005Tb^{3+}$,$0.005Nd^{3+}$ recorded at a heating rate of 5 K/s monitoring characteristic emission either from Bi^{3+}, Ce^{3+}, or Tb^{3+}. The data on YPO_4:$0.005Ln^{3+}$,Nd^{3+} (Ln=Ce^{3+} or Tb^{3+}) crystals were derived from Bos *et al.* [41].

Fig. 4.5 presents the thermoluminescence glow curves of YPO_4:0.005Bi^{3+}, 0.005Nd^{3+}, and YPO_4:0.005Ln^{3+},0.005Nd^{3+} (Ln=Ce^{3+} or Tb^{3+}) after charging with β irradiation. A TL glow peak near 350 K appears in all samples where the recombination emission is either from Bi^{3+} $^3P_1 \rightarrow {}^1S_0$, Ce^{3+} 5d→4f, or Tb^{3+} 4f→4f transitions. From the work by Bos *et al.* [41] on YPO_4:0.005Ce^{3+},0.005Nd^{3+} and YPO_4:0.005Tb^{3+},0.005Nd^{3+}, this 350 K glow peak was assigned to electron release from Nd^{2+} and recombination with the hole on Ce^{4+} or Tb^{4+}. Depending on analysis methods[2, 42-45] a trapping depth E (eV) between 0.89 and 0.98 eV from this 350 K glow peak in YPO_4 was obtained[46] that agrees with the VRBE diagram. Compared with the experimental ~1.42 eV Bi^{3+} hole trap depth found in Ref. [35], the electrons trapped at Nd^{2+} liberate at a lower temperature than the holes trapped at Bi^{4+}. They will recombine with the holes on Bi^{4+} to give the TL glow near 350 K with typical Bi^{3+} A-band emission in YPO_4:0.005Bi^{3+},0.005Nd^{3+}.

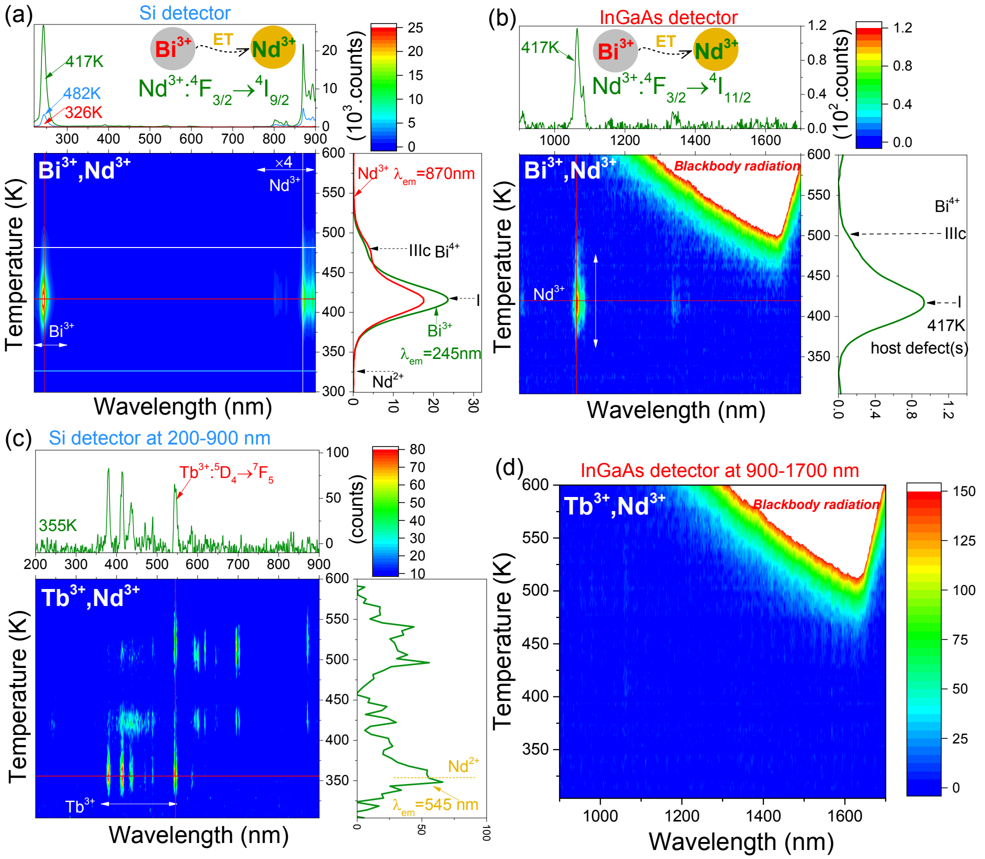

Fig. 4.6. Thermoluminescence emission (TLEM) plots for (a),(b) YPO_4:0.005Bi^{3+}, 0.005Nd^{3+} and (c),(d) YPO_4:0.005Tb^{3+},0.005Nd^{3+} recorded at a heating rate of 1 K/s after γ-ray irradiation from a ^{60}Co source. The emission signal from each sample has been

measured using a Si detector QE65000 at 200-900 nm and an InGaAs detector at 900-1700 nm.

Thermoluminescence emission (TLEM) spectra were recorded for YPO_4:0.005Nd^{3+}, YPO_4:0.005Bi^{3+},0.005Nd^{3+}, and YPO_4:0.005Tb^{3+},0.005Nd^{3+} in order to clarify the role of Nd^{3+} as a 1.06 μm emitting centre during the TL readout. No TL glow peaks with typical Nd^{3+} luminescence between 200-1700 nm were observed for YPO_4:0.005Nd^{3+}. Fig. 4.6a) shows the TL emission spectrum for YPO_4:0.005Bi^{3+},0.005Nd^{3+} recorded by a Si spectrometer. Not only characteristic Bi^{3+} A-band but also Nd^{3+} $^4F_{3/2}\rightarrow{}^4I_{9/2}$ emission near 870 nm appears when co-doping Bi^{3+} in YPO_4:0.005Nd^{3+}. From the study in Ref. [35] for YPO_4:0.005Bi^{3+}, the TL glow peaks IIIc and I that are also present in Fig. 4.5 were attributed to hole release from Bi^{4+} and from a host-related hole trapping centre respectively. The holes recombine with the electrons captured at Bi^{2+} to generate Bi^{3+} A-band emission. Fig. 4.6b) shows the TLEM spectrum of YPO_4:0.005Bi^{3+},0.005Nd^{3+} recorded by an InGaAs detector in the wavelength range from 900 to 1700 nm. Thermally stimulated Nd^{3+} $^4F_{3/2}\rightarrow{}^4I_{11/2}$ emission near 1.06 μm emerges. The TL glow peaks I and IIIc when monitoring the Bi^{3+} A-band emission or when monitoring the Nd^{3+} 4f-4f emission near 870 nm and 1.06 μm appear to have the same shape. The cut-off of black body radiation above 1650 nm in Fig. 4.6b) is an artefact because intensity was not corrected for the wavelength dependent quantum efficiency of the InGaAs NIR512 detector.

Fig. 4.6c) and d) show the TL emission spectra for YPO_4:0.005Tb^{3+},0.005Nd^{3+} in the wavelength region from 200 to 1700 nm. Characteristic Tb^{3+} $^5D_4\rightarrow{}^7F_5$ emission at 545 nm with associated TL glow band near 350 K appears in Fig. 4.6c), which is 300 times weaker than Bi^{3+} A-band emission in YPO_4:0.005Bi^{3+}, 0.005Nd^{3+} in Fig. 4.6a). Note that the characteristic Nd^{3+} 4f-4f emission near 870 nm and 1.06 μm does not appear in YPO_4:0.005Tb^{3+},0.005Nd^{3+}.

Fig. 4.6a) shows that the Bi^{3+} A-band emission of the Bi^{4+} hole release glow peak IIIc is about 7 times weaker than that of the intrinsic defect hole release glow peak I in YPO_4:0.005Bi^{3+},0.005Nd^{3+}. The VRBE diagram of YPO_4 in Fig. 4.1 shows that Bi^{3+}, Tb^{3+}, and Pr^{3+} have almost the same ~1.42 eV hole trap depth. Their hole trapping capacity, however, may be different. We, therefore, combined Tb^{3+} or Pr^{3+} as a shallow hole trapping centre with Bi^{3+} and Nd^{3+} into YPO_4 to explore thermally stimulated luminescence of Nd^{3+} near 1.06 μm for the second bio-imaging window. Fig. 4.7a) shows the TLEM spectrum for YPO_4:0.005Bi^{3+}, 0.005Tb^{3+},0.005Nd^{3+} after γ-ray irradiation and recorded by a Si detector in the wavelength region from 200 to 925 nm. Characteristic Bi^{3+} A-band, Tb^{3+} 4f-4f, and Nd^{3+} $^4F_{3/2}\rightarrow{}^4I_{9/2}$ emission near 870 nm all appear. From previous study on YPO_4:0.005Bi^{3+},0.005Tb^{3+} (Fig. S4.3c) in Ref. [35], the TL glow peak IIIa monitoring the Bi^{3+} A-band emission was attributed to hole liberation from Tb^{4+} and recombination with an electron captured at Bi^{2+}. The simultaneous appearance of Tb^{3+} 4f-4f emission was attributed to the energy transfer from Bi^{3+} to Tb^{3+}[37]. Fig. 4.7b) is the TLEM plot for YPO_4:0.005Bi^{3+},0.005Tb^{3+},0.005Nd^{3+} recorded by an InGaAs spectrometer between 900-1700 nm. Thermally stimulated Nd^{3+} emission near 1.06 μm appears, and the TL glow peak IIIa near 484 K when monitoring the Bi^{3+} A-band emission at 245 nm, or when monitoring Nd^{3+} emission at 1.06 μm or at 870 nm shares the same shape.

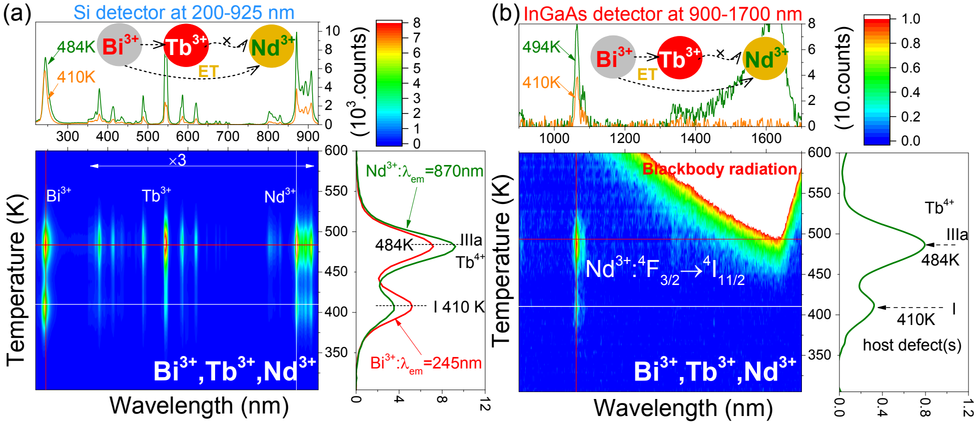

Fig. 4.7. TL emission (TLEM) spectra for a YPO_4:0.005Bi^{3+},0.005Tb^{3+},0.005Nd^{3+} sample recorded using (a) a Si detector at 200-925 nm and (b) an InGaAs detector at 900-1700 nm at a heating rate of 1 K/s after γ-ray irradiation.

4.5. Discussion

We will first deal with the energy transfer (ET) process from Bi^{3+} to Nd^{3+} in YPO_4. Then, a new combination of that efficient energy transfer from Bi^{3+} to Nd^{3+} and using adjustable hole trap depth by valence band engineering guided by vacuum referred binding energy diagram is presented to the rational design of thermally stimulated Nd^{3+} infrared emission near ~1.06 μm.

4.5.1. 1.06 μm Nd^{3+} emission via energy transfer from Bi^{3+} or Tb^{3+}

Fig. 4.8 shows the energy level diagram for Bi^{3+}, Nd^{3+}, and Tb^{3+} in YPO_4. The excited $^3P_1$ state of Bi^{3+} is energetically close to the Nd^{3+} $^2F2_{7/2}$ and $^2F2_{5/2}$ levels, indicating that an energy transfer process from Bi^{3+} to Nd^{3+} is energetically possible. The excited Nd^{3+} $^2F2_{7/2}$ and $^2F2_{5/2}$ levels can relax to $^4F_{3/2}$ level through non-radiative relaxation to yield Nd^{3+} $^4F_{3/2}\rightarrow^4I_j$ (j=9/2, 11/2, and 13/2) infrared emission near 870 nm, 1062 nm, and 1337 nm respectively. This is observed in Fig. 4.2c) where the characteristic Bi^{3+} A-band ($^1S_0\rightarrow^3P_1$) in the photoluminescence excitation spectrum of Bi^{3+}-Nd^{3+}-codoped YPO_4 appears when monitoring Nd^{3+} emission. This Bi^{3+} A-band increases 3 times with increasing Nd^{3+} concentration in Fig. 4.2d), revealing that a more efficient energy transfer process from Bi^{3+} to Nd^{3+} occurs in YPO_4:$0.005Bi^{3+}$,$0.02Nd^{3+}$. The same energy transfer is demonstrated in Fig. 4.3 and quantified further in Fig. 4.4.

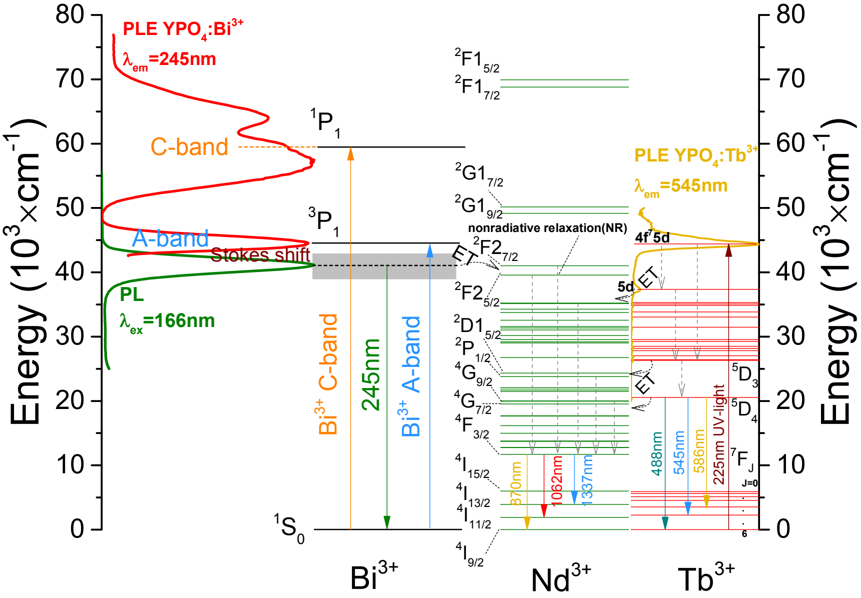

Fig. 4.8. Energy level diagrams of Bi^{3+}, Nd^{3+}, and Tb^{3+} in YPO_4. The possible energy transfer routes of Bi^{3+}→Nd^{3+} and Tb^{3+}→Nd^{3+} are indicated. The experimental energy levels for Nd^{3+} were derived from Ref. [47], and for Tb^{3+} 5d and Bi^{3+}, the levels were derived from the experimental spectroscopy in this work.

Fig. 4.8 also shows that the first spin allowed Tb^{3+} $4f^75d$ excited state is not resonant with Nd^{3+} excited states. The Tb^{3+} ions in that 5d state can relax very rapidly via non-radiative relaxation to the $^5D_3$, $^5D_4$ levels or high spin [HS] $4f^75d$ near 37300 cm^{-1} [48] which are energetically close to Nd^{3+} levels, suggesting the possibility of energy transfer from Tb^{3+} $^5D_3$, $^5D_4$ or spin-forbidden $4f^75d$ levels to Nd^{3+} levels like $^4G_{7/2}$. If energy transfer from Tb^{3+} to Nd^{3+} is present, then a Tb^{3+} 4f-5d excitation band is expected in the PL excitation spectrum of Tb^{3+}-Nd^{3+}-codoped YPO_4 when monitoring Nd^{3+} emission. Fig. 4.2b) shows that a weak Tb^{3+} 4f-5d excitation band near 225 nm indeed appears in YPO_4:$0.005Tb^{3+}$,$0.005Nd^{3+}$ while monitoring the Nd^{3+} 870 nm emission. Considering that the additional excitation band near 225 nm induced by Tb^{3+} co-doping is much smaller than the one by Bi^{3+} co-doping in YPO_4:$0.005Nd^{3+}$, the energy transfer efficiency of

Bi^{3+}→Nd^{3+} in YPO_4:0.005Bi^{3+},0.005Nd^{3+} appears to be much higher than that of Tb^{3+}→Nd^{3+} in YPO_4:0.005Tb^{3+}, 0.005Nd^{3+}.

4.5.2. Tuneable thermally stimulated luminescence of Nd^{3+} near 1.06 μm by engineering hole trap depths of Tb^{3+} and Pr^{3+} in $Y_{1-x}Lu_xPO_4$ and $La_{1-x}Gd_xPO_4$

Fig. 4.9a) shows that the vacuum referred binding energy (VRBE) in the $^2P_{1/2}$ ground state of Bi^{2+} is near -3.3 eV and the VRBE in the Bi^{3+} $^1S_0$, Tb^{3+} and Pr^{3+} $4f^n$ ground states are near -7.8 eV in the La-, Y-, and $LuPO_4$ compounds. Bi^{3+} will act as an about 2.7 eV deep electron trapping centre, while Bi^{3+}, Tb^{3+}, and Pr^{3+} will act as hole trapping centres which hole trap depths depend on the VRBE at the valence band top. That valence band top rises by 0.85 eV in discrete steps from Lu-, to Y-, Gd-, and to $LaPO_4$. The hole trap depths and the temperature T_m for TL glow peaks due to hole release from Tb^{4+}, Pr^{4+}, or Bi^{4+} should decrease accordingly. We will focus on using Tb^{3+} and Pr^{3+} as tuneable hole traps to demonstrate the concept of deliberate design of persistent Nd^{3+} SWIR luminescence via valence band engineering.

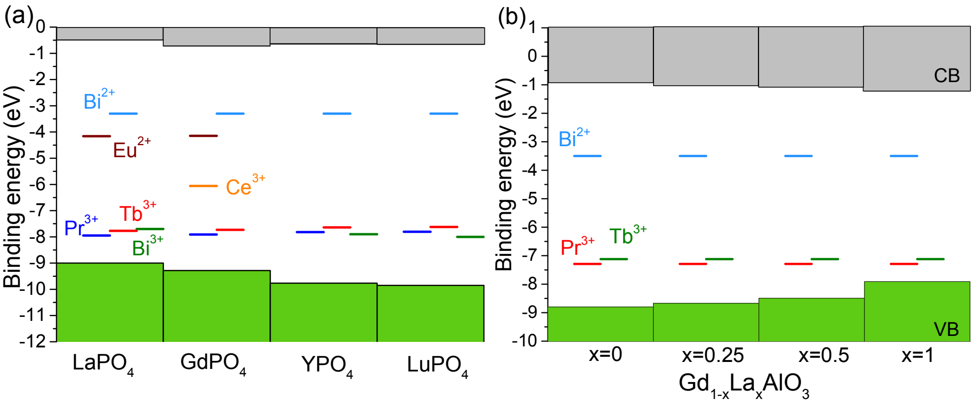

Fig. 4.9. Stacked VRBE diagrams for (a) $REPO_4$ and (b) $Gd_{1-x}La_xAlO_3$ solid solutions including the vacuum referred binding energy in the ground states of Pr^{3+}, Tb^{3+}, Ce^{3+}, Eu^{2+}, Bi^{3+}, and Bi^{2+}. The data on constructing the diagram (a) were obtained from Refs. [34, 35]. For diagram (b) the Tb^{3+} and Pr^{3+} levels were obtained from Ref. [49] and the Bi^{2+} level near -3.5 eV for oxide compounds from Ref. [50] was used.

First, we testified the adjustable thermally stimulated Nd^{3+} SWIR emission in $Y_{1-x}Lu_xPO_4$ solid solutions as shown in Fig. S4.4-6. Although we demonstrated that the temperature of hole release can be tuned, the T_m of the TL glow peaks from Tb^{4+} and Pr^{4+} are at a too high temperature of 500 K and shift the wrong direction.

They need to be shifted close to 300 K in order to realize Nd^{3+} SWIR afterglow for applications.

Fig. 4.9a) shows that the VRBE at the valence band top of $LaPO_4$ is about 0.85 eV higher than that in $LuPO_4$ which implies that the TL glow peaks from Tb^{4+} and Pr^{4+} should move towards RT. Bi^{3+} and lanthanide-doped $LaPO_4$ phosphors were thus synthesized to explore Nd^{3+} SWIR afterglow at room temperature. Fig. S4.7a) shows a TL emission plot for $LaPO_4$:0.002Bi^{3+},0.005Pr^{3+},0.005Nd^{3+} after γ-ray irradiation. The TL glow peaks I and IIb when monitoring the Pr^{3+} 4f-4f emission or when monitoring the Nd^{3+} emission near 900 nm and 1.07 μm appear to share the same shape. Because glow peak IIb is near RT, Nd^{3+} SWIR afterglow appears in $LaPO_4$:0.002Bi^{3+},0.005Pr^{3+},0.005Nd^{3+} in Fig. S4.7b).

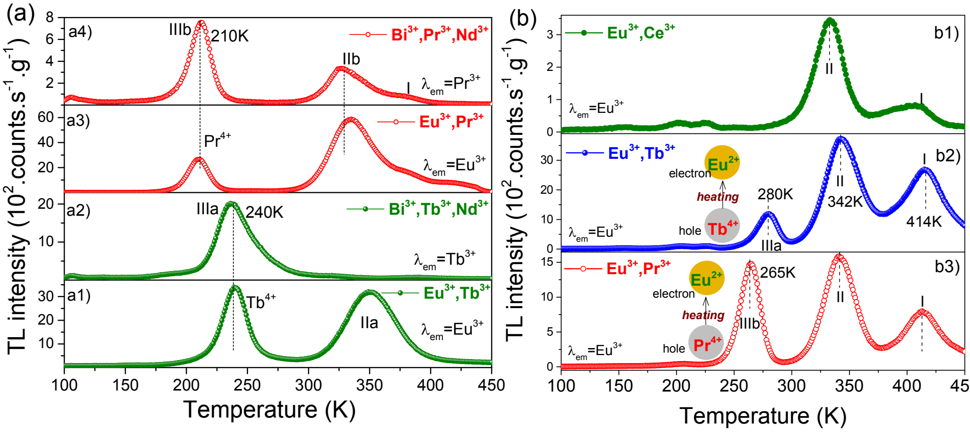

Fig. 4.10. Low-temperature TL glow curves for (a) Bi^{3+} and Ln^{3+} doped $LaPO_4$ and (b) $GdPO_4$:0.005Eu^{3+},0.005Ln^{3+} (Ln=Ce, Tb, or Pr) recorded at a heating rate of 1 K/s after 600s β irradiation in the temperature range between 100-450 K. Eu^{3+} emission was monitored in a1)-a3) and b1-b3). The green Tb^{3+} and red Pr^{3+} emissions were respectively selected in a2) and a4). The TL intensities were corrected by sample mass and irradiation time.

To identify the charge carrier trapping processes, Fig. 4.10a) shows the low-temperature TL glow curves for Bi^{3+} and lanthanides doped $LaPO_4$ by monitoring emission from Eu^{3+}, Pr^{3+}, or Tb^{3+}. Herein, Bi^{3+} and Eu^{3+} are predicted to act as ~2.81 and ~3.67 eV deep electron traps based on the VRBE diagram in Fig. 4.9a), while Tb^{3+} and Pr^{3+} act as 0.63 and 0.55 eV shallow hole trapping centres in $LaPO_4$ based on the previous experimental work in Ref. [34]. By combining the deep electron trap Eu^{3+} with the shallow hole trap Tb^{3+} or Pr^{3+}, the holes trapped at Tb^{4+} or Pr^{4+} are liberated to recombine with the electrons at Eu^{2+} producing Eu^{3+} red emission[34] with TL peaks IIIa (Tb) near 240 K in Fig. 4.10a1) and IIIb (Pr) near 210 K in Fig. 4.10a3). The same glow peaks IIIa in Fig. 4.10a2) and IIIb in Fig.

4.10a4) indeed appear when Eu^{3+} is replaced by the 2.81 eV deep electron trap Bi^{3+}. Hole release from Tb^{4+} or Pr^{4+} like in Fig. 4.10a1) or 10a3) is also present in $LaPO_4$:0.002Bi^{3+},0.005Tb^{3+},0.005Nd^{3+} and $LaPO_4$:0.002Bi^{3+},0.005Pr^{3+},0.005Nd^{3+} in Fig. 4.10a2) and 10a4) where instead of at Eu the recombination is at Bi.

This again demonstrates that the temperature of hole release and related SWIR emission can be engineered. However, in $LaPO_4$ the glow peaks IIIa and IIIb are shifted too far and appear below room temperature. The TL glow peaks I and IIb with red Pr^{3+} emission in Fig. 4.10a4) cannot be attributed to electron release from host-related electron traps with recombination on Pr^{4+} because the holes trapped at Pr^{4+} have already disappeared as a result of recombination with the electrons at Bi^{2+} near 210 K. Therefore, they are attributed to hole release from unidentified defect centres in $LaPO_4$. The appearance of Pr^{3+}, Nd^{3+}, or Tb^{3+} emission in Fig. 4.10a4) and also Fig. S4.7a)-8 is assigned to energy transfer from Bi^{3+}, which is similar as that in YPO_4 in Fig. 4.7 and other solid solutions $Y_{1-x}Lu_xPO_4$ in Fig. S4.5. Supporting evidence is the appearance of the same TL glow peaks I and IIb when monitoring the emission either from Pr^{3+} or Nd^{3+} in Fig. S4.7a) or from Tb^{3+} in Fig. S4.8. This is also supported by the spectral overlap of $LaPO_4$:0.002Bi^{3+} at 325-600 nm emission (Fig. S4.10) with the 4f-4f excitation bands of Tb^{3+}[51], Pr^{3+}[52], and Nd^{3+} like in Fig. 4.2a), which indicates the possibility of ET from Bi^{3+} to Tb^{3+}, Pr^{3+}, or Nd^{3+} in $LaPO_4$.

The method using $Bi^{3+} \rightarrow Nd^{3+}$ ET and engineering the hole trapping depths of Tb^{3+}, Pr^{3+}, or intrinsic hole trapping centres by valence band changing in the phosphate compounds can also be applied to solid solutions like $La_{1-x}Gd_xPO_4$ and $Gd_{1-x}La_xAlO_3$. Fig. 4.9a) demonstrates that the VRBE at the valence band top of $GdPO_4$ is about 0.3 eV lower than in $LaPO_4$ which indicates that the TL glow peaks IIIa near 240 K and IIIb near 210 K in Fig. 4.10a2) and a4) should move towards room temperature in $La_{1-x}Gd_xPO_4$ by increasing x.

To further demonstrate the design methodology of SWR afterglow phosphors in $La_{1-x}Gd_xPO_4$ solid solutions, the hole detrapping processes of Tb^{3+} and Pr^{3+} hole capturing centres are first studied in $GdPO_4$. Fig. 4.10b) shows the low-temperature TL glow curves for $GdPO_4$:0.005Eu^{3+},0.005Ln^{3+}. Compared with Ce^{3+} codoping in $GdPO_4$ in Fig. 4.10b1), Tb^{3+} gave rise to a new TL glow peak near 280 K named as IIIa in Fig. 4.10b2) and Pr^{3+} to a TL peak denoted as IIIb at about 15 K lower temperature in Fig. 4.10b3). The TL glow peak I for $GdPO_4$:0.005Eu^{3+},0.005Tb^{3+} was further studied by a variable heating rate plot using RISØ TL/OSL reader in Fig. S4.12b). This provides a frequency factor of 1.07×10^{12} s^{-1}, which is assumed to apply to TL glow peaks IIIa and IIIb. Their trapping depths E (eV) are then determined by employing the temperature T_m at the maximum of the glow curve and solving the following first-order TL-recombination kinetics formula[44, 45]:

$$\frac{\beta E}{k{T_m}^2} = s \times \exp\left(-\frac{E}{kT_m}\right) \tag{4.4}$$

where β=1 K/s represents the heating rate, k denotes the Boltzmann constant (8.62×10^{-5} eV/K), and s is the frequency factor (1.07×10^{12} s^{-1}). With Eq. (4.4), the trap depths for IIIa and IIIb are respectively derived to be 0.72, and 0.68 eV.

The vacuum referred binding energy (VRBE) scheme for $GdPO_4$ in Fig. 4.9a) predicts that Eu^{3+} and Bi^{3+} act as ~3.43, and 2.78 eV deep electron traps, while Tb^{3+}, Pr^{3+}, and Ce^{3+} act as 1.56, 1.38, and 3.23 eV deep hole traps. When holes are produced in the valence band, they tend to be shared between two neighbouring oxygen anions to form a thermally activated V_k centre[53, 54] located above the valence band top in a VRBE scheme[34, 55]. Since La-, Gd-, YPO_4 are quite similar, the binding energy for a V_k centre in $GdPO_4$ is assumed to be about 0.6 eV, like in La- and YPO_4[34]. The effective hole trap depths of Tb^{3+}, Pr^{3+}, and Ce^{3+} are then determined to be 0.96, 0.78, and 2.63 eV, respectively. Using Eq. (4.4) with β=1 K/s and the above predicted hole trap depths, one can estimate that the hole liberation from Tb^{4+}, Pr^{4+}, or Ce^{4+} in $GdPO_4$ gives TL glow peaks T_m near 369, 302, and 980 K, respectively. Obviously, the Ce^{4+} hole trap is far too deep to liberate a hole between 100-450 K. The estimated TL peaks T_m for hole liberation from Tb^{4+} and Pr^{4+} traps are in the measurement range, and we assign the TL glow peaks IIIa (0.72 eV) and IIIb (0.68 eV) to the hole liberation from Tb^{4+} in Fig. 4.10b2) and Pr^{4+} in Fig. 4.10b3). Considering that glow peaks I and II appear in all three samples, they are attributed hole liberation from intrinsic host defect(s) and recombination with the electrons trapped at Eu^{2+}.

Like $LaPO_4$ in Fig. 4.10a), Bi^{3+} and/or Ln^{3+} doped $La_{1-x}Gd_xPO_4$ solid solutions were further synthesized to explore the rational design of Nd^{3+} SWIR afterglow by using adjustable hole trap depth of Tb^{3+} and Pr^{3+}.

Fig. 4.11 shows the low-temperature TL glow curves for Bi^{3+} and/or Ln^{3+} doped $La_{1-x}Gd_xPO_4$ with x range from 0 to 1. For the samples each with the same Pr^{3+} hole trap but with different electron trap of Eu^{3+} in Fig. 4.11a1)-a3) and of Bi^{3+} in Fig. 4.11a4)-a6), the glow peak IIIb shares almost the same shape. It shifts from 210 K to 265 K with increasing x in $La_{1-x}Gd_xPO_4$ (also see Fig. S4.15), which is attributed to the increased activation energy for the hole release from the Pr^{3+} hole capturing centre as a result of valence band lowering by increasing x. Similar to Pr^{3+}, Tb^{3+} as a shallow hole capturing centre also gives a systemic shifting of TL glow peak IIIa in $La_{1-x}Gd_xPO_4$:$0.002Bi^{3+}$,$0.005Tb^{3+}$,$0.005Nd^{3+}$ in Fig. 4.11a7)-a11). Note that the glow peaks IIIa and IIIb become broader in the solid solutions compared with that of $LaPO_4$ and $GdPO_4$, suggesting a broader trap distribution. This indicates that the

VRBE at the valence band top exhibits site-to-site fluctuations based on the statistics in $La_{1-x}Gd_xPO_4$ when La is replaced by Gd. Particularly, for x from 0.25 to 0.75 in Fig. 4.11a8)-a10), the broad IIIa glow peak covers the room temperature (295 K) range, which results in the Nd^{3+} SWIR afterglow as shown in Fig. 4.12. Upon thermal stimulation at RT, the shallow Tb^{4+} hole trap spontaneously liberates holes to recombine with electrons at Bi^{2+}, producing Bi^{3+} in its excited state followed by Nd^{3+} SWIR persistent luminescence as a result of energy transfer from Bi^{3+}.

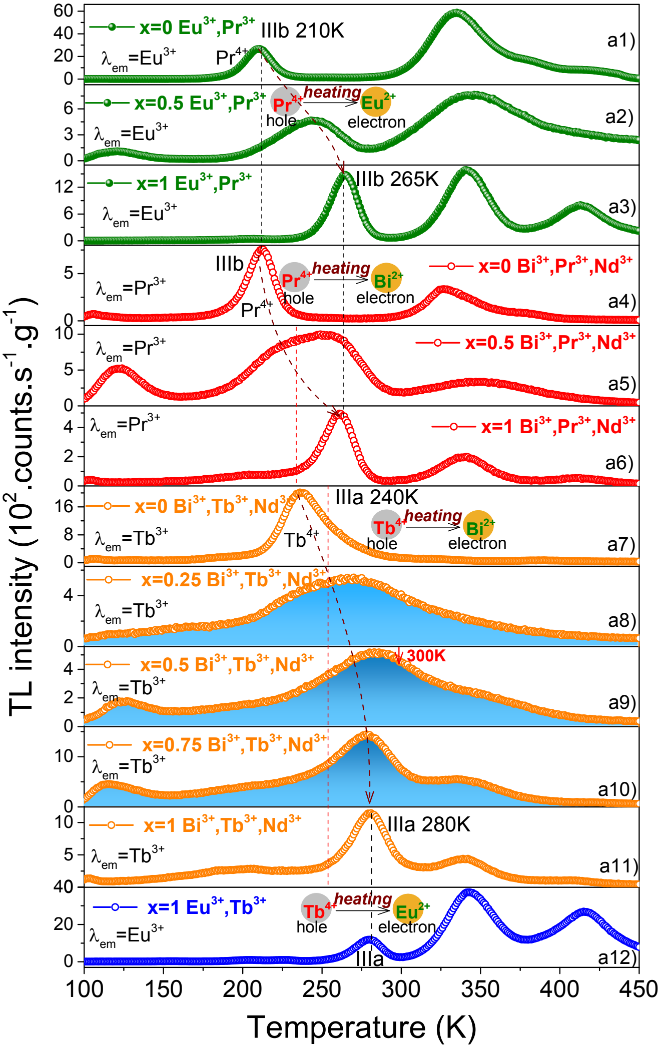

Fig. 4.11. Low-temperature TL glow curves for Bi^{3+} and/or Ln^{3+} doped $La_{1-x}Gd_xPO_4$ (x=0-1) recorded at a heating of 1 K/s after 600s β irradiation. A 600 nm bandpass filter 600FS40-

50 was used to select Eu^{3+} emission in a1)-a3) and a12), and to monitor Pr^{3+} red emission in a4)-a6). A 550 nm bandpass 550FS40-50 was used to monitor Tb^{3+} green emission in a7)-a11).

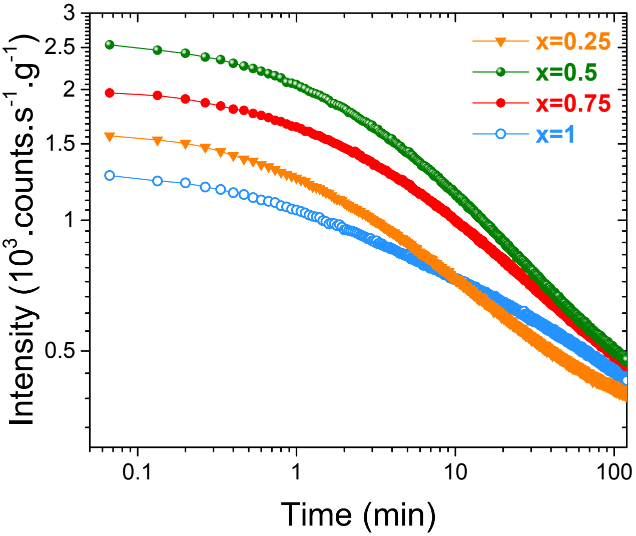

Fig. 4.12. Room temperature (295 K) isothermal decay curves after β irradiation while monitoring the emission from 400-900 nm for $La_{1-x}Gd_xPO_4$:0.002Bi^{3+},0.005Tb^{3+},0.005Nd^{3+}.

Fig. 4.9b), as another illustrating example, shows the stacked VRBE diagram for $Gd_{1-x}La_xAlO_3$ solid solutions where one can also engineer the hole trap depths of Tb^{3+} and Pr^{3+} by increasing x[49]. By combining Bi^{3+} with Tb^{3+} or Pr^{3+}, the holes trapped at Tb^{4+} or Pr^{4+} are predicted to release at a lower temperature than the electrons trapped at Bi^{2+}. On recombination with Bi^{2+}, Bi^{3+} in its excited state is formed giving Bi^{3+} emission and also Nd^{3+} SWIR luminescence by energy transfer from Bi^{3+} to Nd^{3+}. Tuneable thermally stimulated Nd^{3+} SWIR emission is proposed through valence band engineering and using the possible energy transfer from Bi^{3+} to Nd^{3+} because the broad Bi^{3+} emission band at 300-680 in $GdAlO_3$[56] and $LaAlO_3$[21, 57] overlaps with the Nd^{3+} 4f-4f excitation bands like in Fig. 4.2a). Note that Bi^{3+} can act both as electron and as hole capturing centre like in La-, Y-, and $LuPO_4$[35], one may also engineer the hole release from Bi^{4+} and the recombination with the electrons at Bi^{2+} followed by Nd^{3+} SWIR emission via ET of $Bi^{3+}\rightarrow Nd^{3+}$ in Bi^{3+}-Nd^{3+}-codoped compounds.

4.6. Conclusions

Data from thermoluminescence, fluorescence decay curves, photoluminescence spectroscopy, and ideas from constructed VRBE schemes have been combined to demonstrate the concept of rational design of thermally stimulated Nd^{3+}

luminescence between ~900-1700 nm. A new combination of using efficient energy transfer from Bi^{3+} to Nd^{3+} and using an adjustable hole trap depth via valence band engineering is presented in bismuth and lanthanides doped rare earth ortho-phosphate model compounds. We demonstrated that 1.06 µm Nd^{3+} photoluminescence can be realized by efficient energy transfer (ET) from Bi^{3+} to Nd^{3+} rather than by ET from Tb^{3+} to Nd^{3+} in YPO_4. The temperature of thermally stimulated Bi^{3+} emission needs then to be designed to further exploit the above energy transfer process from Bi^{3+} to Nd^{3+}. By combing ~2.7 eV deep Bi^{3+} electron trap with ~1.42 eV deep hole traps of Tb^{3+}, Pr^{3+}, or Bi^{3+} in ortho phosphate compounds the holes captured at Tb^{4+}, Pr^{4+}, or Bi^{4+} liberate at a lower temperature than that of electrons captured at Bi^{2+}. On recombination with Bi^{3+}, Bi^{3+} in its excited state is formed producing Bi^{3+} A-band emission and also owing to energy transfer from Bi^{3+} to Nd^{3+} the SWIR Nd^{3+} ${}^4F_{3/2}\rightarrow{}^4I_j$ (j=9/2, 11/2, 13/2) emissions appear in YPO_4:0.005Bi^{3+},0.005Nd^{3+} and YPO_4:0.005Bi^{3+},0.005Ln^{3+},0.005Nd^{3+} (Ln=Tb and Pr). Here, the thermally stimulated Nd^{3+} SWIR emission is obtained by means of hole release rather than the more commonly reported electron release. We demonstrated that the temperature when thermally stimulated Nd^{3+} 1.06 µm emission appears can be tailored by valence band engineering in $Y_{1-x}Lu_xPO_4$ and $La_{1-x}Gd_xPO_4$, resulting in Tb^{3+} and Pr^{3+} hole trap depth changing. The tailoring was demonstrated for $Y_{1-x}Lu_xPO_4$ and $La_{1-x}Gd_xPO_4$ but can equally well be applied to other compounds like the solid solutions $Gd_{1-x}La_xAlO_3$. Our work shows a new general technique to deep understand afterglow mechanisms and to the rational design of SWIR afterglow phosphors by a new combination of efficient energy transfer from Bi^{3+} to Nd^{3+} and using adjustable hole release processes by valence band engineering. This work also opens the avenue to motivate scientists to explore novel SWIR afterglow phosphors in a design way instead of by trial and error approach.

4.7. Acknowledgements

T. Lyu thanks the financial support from the China Scholarship Council for his PhD research (Tianshuai Lyu: 201608320151). We acknowledge Evert. P. J. Merkx from the Delft University of Technology for supporting the recording of the photoluminescence excitation spectra of Nd^{3+}-doped YPO_4 crystals using the OPO laser beam.

4.8. Reference

[1] S.W.S. McKeever, Thermoluminescence of Solids, Cambridge University Press, Cambridge, 1985.
[2] R. Chen, S.W. McKeever, Theory of thermoluminescence and related phenomena, World Scientific1997.

[3] A.J.J. Bos, Thermoluminescence as a Research Tool to Investigate Luminescence Mechanisms, Materials 10 (2017) 1357.

[4] Y. Zhang, R. Huang, H. Li, D. Hou, Z. Lin, J. Song, Y. Guo, H. Lin, C. Song, Z. Lin, J. Robertson, Germanium substitution endowing Cr^{3+}-doped zinc aluminate phosphors with bright and super-long near-infrared persistent luminescence, Acta Materialia 155 (2018) 214-221.

[5] T. Matsuzawa, Y. Aoki, N. Takeuchi, Y. Murayama, New long phosphorescent phosphor with high brightness, $SrAl_2O_4:Eu^{2+},Dy^{3+}$, Journal of the Electrochemical Society 143 (1996) 2670-2673.

[6] A.J.J. Bos, Theory of thermoluminescence, Radiation Measurements 41 (2006) S45-S56.

[7] J. Xu, S. Tanabe, Persistent luminescence instead of phosphorescence: History, mechanism, and perspective, Journal of Luminescence 205 (2019) 581-620.

[8] Y. Zhuang, Y. Lv, L. Wang, W. Chen, T.-L. Zhou, T. Takeda, N. Hirosaki, R.-J. Xie, Trap Depth Engineering of $SrSi_2O_2N_2:Ln^{2+},Ln^{3+}$ (Ln^{2+} = Yb, Eu; Ln^{3+} = Dy, Ho, Er) Persistent Luminescence Materials for Information Storage Applications, ACS Applied Materials & Interfaces 10 (2018) 1854-1864.

[9] Y. Li, M. Gecevicius, J. Qiu, Long persistent phosphors-from fundamentals to applications, Chemical Society Reviews 45 (2016) 2090-2136.

[10] H. Lin, B. Wang, Q. Huang, F. Huang, J. Xu, H. Chen, Z. Lin, J. Wang, T. Hu, Y. Wang, $Lu_2CaMg_2(Si_{1-x}Ge_x)_3O_{12}:Ce^{3+}$ solid-solution phosphors: bandgap engineering for blue-light activated afterglow applicable to AC-LED, Journal of Materials Chemistry C 4 (2016) 10329-10338.

[11] J. Wang, Q. Ma, Y. Wang, H. Shen, Q. Yuan, Recent progress in biomedical applications of persistent luminescence nanoparticles, Nanoscale 9 (2017) 6204-6218.

[12] T. Maldiney, A. Bessière, J. Seguin, E. Teston, S.K. Sharma, B. Viana, A.J.J. Bos, P. Dorenbos, M. Bessodes, D. Gourier, D. Scherman, C. Richard, The in vivo activation of persistent nanophosphors for optical imaging of vascularization, tumours and grafted cells, Nat Mater 13 (2014) 418-426.

[13] A.M. Smith, M.C. Mancini, S. Nie, Second window for in vivo imaging, Nature Nanotechnology 4 (2009) 710.

[14] D. Chen, J. Huang, T.J. Jackson, Vegetation water content estimation for corn and soybeans using spectral indices derived from MODIS near- and short-wave infrared bands, Remote Sensing of Environment 98 (2005) 225-236.

[15] A. Zhang, Z. Sun, M. Jia, G. Liu, F. Lin, Z. Fu, Simultaneous luminescence in Ⅰ, Ⅱ and III biological windows realized by using the energy transfer of $Yb^{3+} \rightarrow Er^{3+}/Ho^{3+} \rightarrow Cr^{3+}$, Chemical Engineering Journal 365 (2019) 400-404.

[16] S. Zhou, N. Jiang, B. Zhu, H. Yang, S. Ye, G. Lakshminarayana, J. Hao, J. Qiu, Multifunctional Bismuth-Doped Nanoporous Silica Glass: From Blue-Green,

Orange, Red, and White Light Sources to Ultra-Broadband Infrared Amplifiers, Advanced Functional Materials 18 (2008) 1407-1413.

[17] G. Hong, J.T. Robinson, Y. Zhang, S. Diao, A.L. Antaris, Q. Wang, H. Dai, In Vivo Fluorescence Imaging with Ag_2S Quantum Dots in the Second Near‐Infrared Region, Angewandte Chemie 124 (2012) 9956-9959.

[18] W. Fan, N. Lu, C. Xu, Y. Liu, J. Lin, S. Wang, Z. Shen, Z. Yang, J. Qu, T. Wang, S. Chen, P. Huang, X. Chen, Enhanced Afterglow Performance of Persistent Luminescence Implants for Efficient Repeatable Photodynamic Therapy, ACS Nano 11 (2017) 5864-5872.

[19] J. Xu, D. Murata, Y. Katayama, J. Ueda, S. Tanabe, Cr^{3+}/Er^{3+} co-doped $LaAlO_3$ perovskite phosphor: a near-infrared persistent luminescence probe covering the first and third biological windows, Journal of Materials Chemistry B 5 (2017) 6385-6393.

[20] F. Liu, Y. Liang, Y. Chen, Z. Pan, Divalent Nickel-Activated Gallate-Based Persistent Phosphors in the Short-Wave Infrared, Advanced Optical Materials 4 (2016) 562-566.

[21] R.H.P. Awater, P. Dorenbos, The Bi^{3+} 6s and 6p electron binding energies in relation to the chemical environment of inorganic compounds, Journal of Luminescence 184 (2017) 221-231.

[22] P. Dorenbos, A Review on How Lanthanide Impurity Levels Change with Chemistry and Structure of Inorganic Compounds, ECS Journal of Solid State Science and Technology 2 (2013) R3001-R3011.

[23] P. Dorenbos, Modeling the chemical shift of lanthanide 4f electron binding energies, Physical Review B 85 (2012) 165107.

[24] J. Ueda, S. Miyano, S. Tanabe, Formation of Deep Electron Traps by Yb^{3+} Codoping Leads to Super-Long Persistent Luminescence in Ce^{3+}-Doped Yttrium Aluminum Gallium Garnet Phosphors, ACS Applied Materials & Interfaces 10 (2018) 20652-20660.

[25] Z. Pan, Y.-Y. Lu, F. Liu, Sunlight-activated long-persistent luminescence in the near-infrared from Cr^{3+}-doped zinc gallogermanates, Nat Mater 11 (2012) 58-63.

[26] F. Liu, W. Yan, Y.-J. Chuang, Z. Zhen, J. Xie, Z. Pan, Photostimulated near-infrared persistent luminescence as a new optical read-out from Cr^{3+}-doped $LiGa_5O_8$, Scientific Reports 3 (2013) 1554.

[27] Y. Li, S. Zhou, Y. Li, K. Sharafudeen, Z. Ma, G. Dong, M. Peng, J. Qiu, Long persistent and photo-stimulated luminescence in Cr^{3+}-doped Zn-Ga-Sn-O phosphors for deep and reproducible tissue imaging, Journal of Materials Chemistry C 2 (2014) 2657-2663.

[28] Y.-J. Liang, F. Liu, Y.-F. Chen, X.-J. Wang, K.-N. Sun, Z. Pan, New function of the Yb^{3+} ion as an efficient emitter of persistent luminescence in the short-wave infrared, Light Sci Appl. 5 (2016) e16124.

[29] N. Yu, F. Liu, X. Li, Z. Pan, Near infrared long-persistent phosphorescence in $SrAl_2O_4:Eu^{2+},Dy^{3+},Er^{3+}$ phosphors based on persistent energy transfer, Applied Physics Letters 95 (2009) 231110.

[30] J. Xu, D. Murata, J. Ueda, S. Tanabe, Near-infrared long persistent luminescence of Er^{3+} in garnet for the third bio-imaging window, Journal of Materials Chemistry C 4 (2016) 11096-11103.

[31] Y. Liang, F. Liu, Y. Chen, X. Wang, K. Sun, Z. Pan, Extending the applications for lanthanide ions: efficient emitters in short-wave infrared persistent luminescence, Journal of Materials Chemistry C 5 (2017) 6488-6492.

[32] Y. Liang, F. Liu, Y. Chen, X. Wang, K. Sun, Z. Pan, Red/near-infrared/short-wave infrared multi-band persistent luminescence in Pr^{3+}-doped persistent phosphors, Dalton Transactions 46 (2017) 11149-11153.

[33] J. Xu, S. Tanabe, A.D. Sontakke, J. Ueda, Near-infrared multi-wavelengths long persistent luminescence of Nd^{3+} ion through persistent energy transfer in Ce^{3+}, Cr^{3+} co-doped $Y_3Al_2Ga_3O_{12}$ for the first and second bio-imaging windows, Applied Physics Letters 107 (2015) 081903.

[34] T. Lyu, P. Dorenbos, Charge carrier trapping processes in lanthanide doped $LaPO_4$, $GdPO_4$, YPO_4, and $LuPO_4$, Journal of Materials Chemistry C 6 (2018) 369-379.

[35] T. Lyu, P. Dorenbos, Bi^{3+} acting both as an electron and as a hole trap in La-, Y-, and $LuPO_4$, Journal of Materials Chemistry C 6 (2018) 6240-6249.

[36] F. You, A.J.J. Bos, Q. Shi, S. Huang, P. Dorenbos, Thermoluminescence investigation of donor (Ce^{3+}, Pr^{3+}, Tb^{3+}) acceptor (Eu^{3+}, Yb^{3+}) pairs in $Y_3Al_5O_{12}$, Physical Review B 85 (2012) 115101.

[37] R.H.P. Awater, L.C. Niemeijer-Berghuijs, P. Dorenbos, Luminescence and charge carrier trapping in YPO_4:Bi, Optical Materials 66 (2017) 351-355.

[38] P. Dorenbos, Charge transfer bands in optical materials and related defect level location, Optical Materials 69 (2017) 8-22.

[39] D.L. Dexter, J.H. Schulman, Theory of Concentration Quenching in Inorganic Phosphors, The Journal of Chemical Physics 22 (1954) 1063-1070.

[40] M. Jiao, Y. Jia, W. Lu, W. Lv, Q. Zhao, B. Shao, H. You, $Sr_3GdNa(PO_4)_3F:Eu^{2+},Mn^{2+}$: a potential color tunable phosphor for white LEDs, Journal of Materials Chemistry C 2 (2014) 90-97.

[41] A.J.J. Bos, P. Dorenbos, A. Bessière, A. Lecointre, M. Bedu, M. Bettinelli, F. Piccinelli, Study of TL glow curves of YPO_4 double doped with lanthanide ions, Radiation Measurements 46 (2011) 1410-1416.

[42] M. Puchalska, P. Bilski, GlowFit—a new tool for thermoluminescence glow-curve deconvolution, Radiation Measurements 41 (2006) 659-664.

[43] J. Azorín, Determination of thermoluminescence parameters from glow curves—I. A review, International Journal of Radiation Applications and

Instrumentation. Part D. Nuclear Tracks and Radiation Measurements 11 (1986) 159-166.

[44] W. Hoogenstraaten, Electron traps in zinc–sulphide phosphors, Philips Res. Rep 13 (1958) 515–693.

[45] R. Chen, S.A.A. Winer, Effects of Various Heating Rates on Glow Curves, Journal of Applied Physics 41 (1970) 5227-5232.

[46] A.J.J. Bos, P. Dorenbos, A. Bessière, B. Viana, Lanthanide energy levels in YPO_4, Radiation Measurements 43 (2008) 222-226.

[47] W. Jean-François, M. Ali, T.-B. Wan-Ü Lydia, C. Norbert, L. Omar, S. Nissan, S. Jack, Analysis of the free ion Nd^{3+} spectrum (Nd IV), Journal of Physics B: Atomic, Molecular and Optical Physics 40 (2007) 3957-3972.

[48] T. Hoshina, S. Kuboniwa, 4f-5d Transition of Tb^{3+} and Ce^{3+} in MPO_4 (M=Sc, Y and Lu), Journal of the Physical Society of Japan 31 (1971) 828-840.

[49] H. Luo, A.J.J. Bos, P. Dorenbos, Controlled Electron–Hole Trapping and Detrapping Process in $GdAlO_3$ by Valence Band Engineering, The Journal of Physical Chemistry C 120 (2016) 5916-5925.

[50] R.H.P. Awater, P. Dorenbos, Towards a general concentration quenching model of Bi^{3+} luminescence, Journal of Luminescence 188 (2017) 487-489.

[51] A. Mraouefel, L. Guerbous, A. Boukerika, M. Diaf, A. Mendoud, M. Seraiche, M. Taibeche, M.S.E. Hamroun, N. Baadji, Effect of the vanadium concentration on structural and photoluminescence of $YP_{1-x}V_xO_4$: 1 at. % Tb^{3+} nanophosphors, Optical Materials 65 (2017) 129-136.

[52] A. Lecointre, A. Bessière, A.J.J. Bos, P. Dorenbos, B. Viana, S. Jacquart, Designing a Red Persistent Luminescence Phosphor: The Example of YPO_4:Pr^{3+},Ln^{3+} (Ln = Nd, Er, Ho, Dy), The Journal of Physical Chemistry C 115 (2011) 4217-4227.

[53] P.W. Tasker, A.M. Stoneham, An appraisal of the molecular model for the V_k centre, Journal of Physics and Chemistry of Solids 38 (1977) 1185-1189.

[54] R. Gazzinelli, G.M. Ribeiro, M.L. de Siqueira, ESR and endor studies of the VK center in SrF_2, Solid State Communications 13 (1973) 1131-1134.

[55] N.F. Mott, A.M. Stoneham, The lifetime of electrons, holes and excitons before self-trapping, Journal of Physics C: Solid State Physics 10 (1977) 3391.

[56] A.M. Srivastava, H.A. Comanzo, The ultraviolet and visible luminescence of Bi^{3+} in the orthorhombic perovskite, $GdAlO_3$, Optical Materials 63 (2017) 118-121.

[57] L.I. van Steensel, S.G. Bokhove, A.M. van de Craats, J. de Blank, G. Blasse, The luminescence of Bi^{3+} in $LalnO_3$ and some other perovskites, Materials Research Bulletin 30 (1995) 1359-1362.

4.9. Supporting information

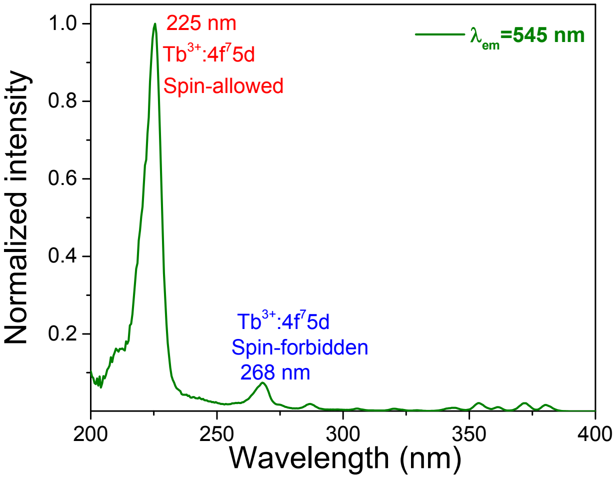

Fig. S4.1 Normalized photoluminescence excitation spectrum monitoring at Tb^{3+} 545 nm for YPO_4:$0.005Tb^{3+}$ recorded at room temperature.

The excitation band near 225 nm is attributed to the first Tb^{3+} $4f^8 \rightarrow 4f^75d$ spin allowed transition[1, 2] in YPO_4. The excitation band near 268 nm is assigned to Tb^{3+} 4f-5d spin-forbidden transition[3].

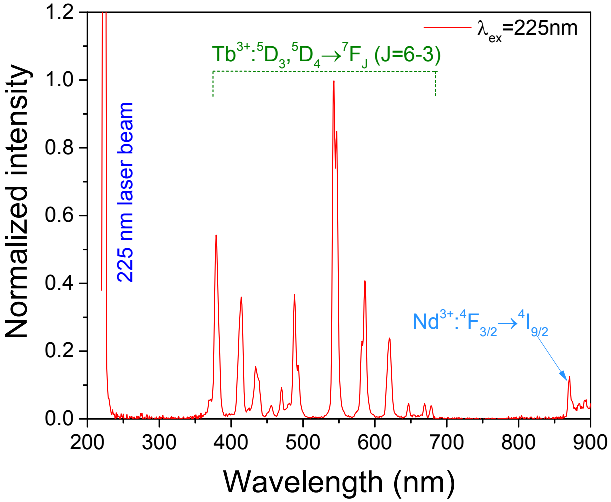

Fig. S4.2. Corrected photoluminescence spectrum of YPO_4:$0.005Tb^{3+}$,$0.005Nd^{3+}$ under Tb^{3+} 4f-5d excitation at 225 nm recorded at room temperature. An OPO laser beam was used as the excitation source and the emission signal was detected using a Si detector (QE65000) that has a spectral response between 200-975 nm.

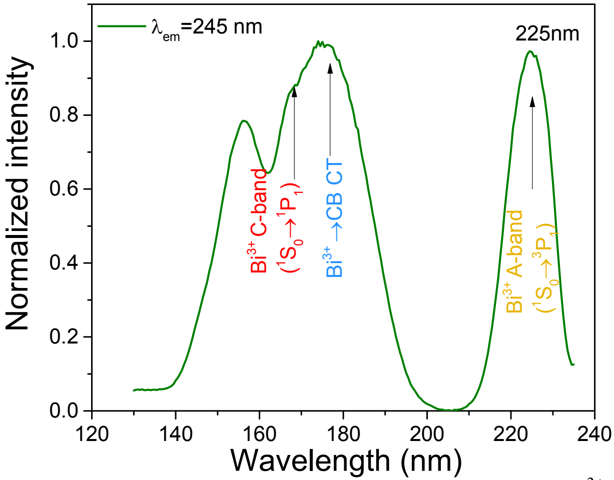

Fig. S4.3. Photoluminescence excitation spectrum monitoring the Bi^{3+} A-band emission at 245 nm for YPO_4:0.005Bi^{3+} recorded at 10 K. The data were obtained from Ref. [4].

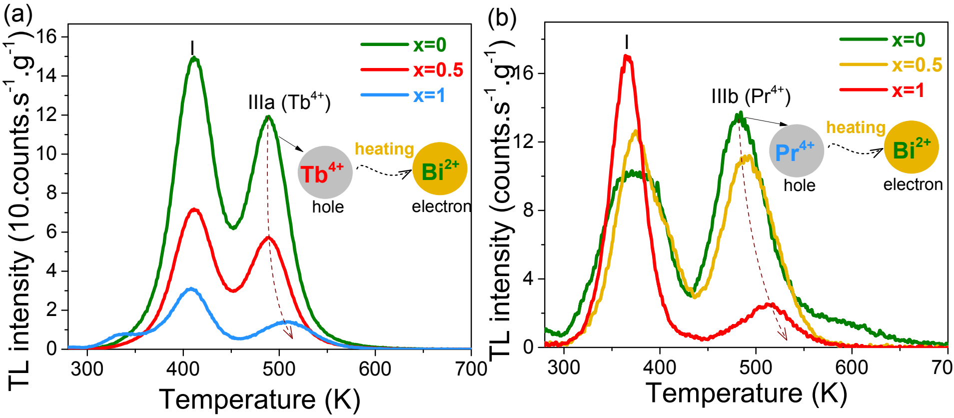

Fig. S4.4. Thermoluminescence glow curves of (a) $Y_{1-x}Lu_xPO_4$:0.005Bi^{3+},0.005Tb^{3+}, 0.005Nd^{3+}, and (b) $Y_{1-x}Lu_xPO_4$:0.005Bi^{3+},0.005Pr^{3+},0.005Nd^{3+} recorded at a heating rate of 1 K/s after β irradiation. The Bi^{3+} A-band emission was monitored, and the TL intensity was corrected by sample mass and irradiation time.

Fig. S4.4a) shows the TL glow curves for $Y_{1-x}Lu_xPO_4$:0.005Bi^{3+},0.005Tb^{3+}, 0.005Nd^{3+} (x=0-1) monitoring the Bi^{3+} A-band emission after β irradiation. The TL glow peak IIIa in Fig. S4.4a) appears to shift about 30 K towards higher temperature with increasing x. This is assigned to the increased activation energy for the hole liberation from the Tb^{3+} hole trapping centre as a result of valence band lowering by rising x[4]. Like Tb^{3+}, Pr^{3+} as a shallow hole trap also gives rise to a systematic shifting of glow peak IIIb in $Y_{1-x}Lu_xPO_4$:0.005Bi^{3+},0.005Pr^{3+},0.005Nd^{3+} in Fig. S4.4b).

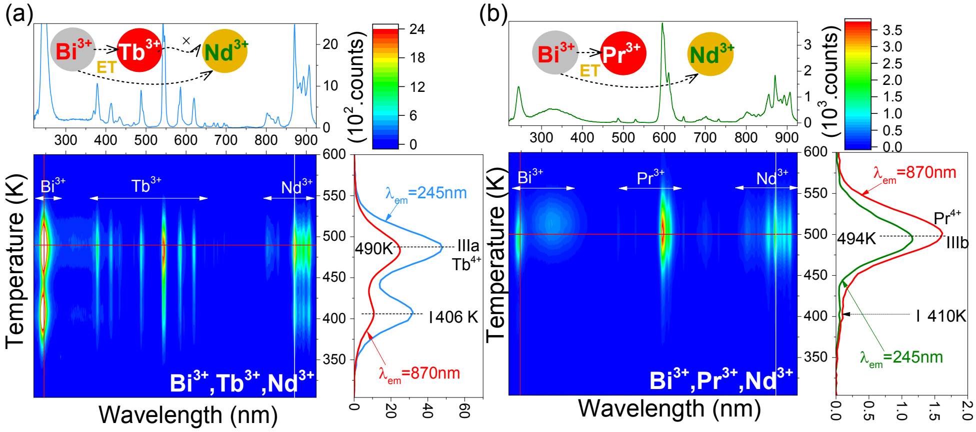

Fig. S4.5. TLEM plots for (a) $Y_{1-x}Lu_xPO_4$:0.005Bi^{3+}, 0.005Tb^{3+},0.005Nd^{3+} (x=0.5) and (b) $Y_{1-x}Lu_xPO_4$:0.005Bi^{3+},0.005Pr^{3+},0.005Nd^{3+} (x=0.5) solid solutions recorded at a heating rate of 1 K/s after γ-ray irradiation.

Fig. S4.5a) or b) show the TL emission spectra for solid solutions $Y_{1-x}Lu_xPO_4$: 0.005Bi^{3+},0.005Nd^{3+} (x=0.5) co-activated with 0.005Tb^{3+} or Pr^{3+} after γ-ray irradiation. The glow peaks IIIa or IIIb when monitoring the Bi^{3+} A-band emission at 245 nm, or when monitoring the Nd^{3+} emission at 870 nm share the same shape. The same applies to YPO_4 in Fig. 4.7 and other 0.005Tb^{3+} or Pr^{3+} codoped $Y_{1-x}Lu_xPO_4$:0.005Bi^{3+},0.005Nd^{3+} with x ranging from 0 to 1 in Fig. S4.6. During TL-readout, the holes at Tb^{4+} or Pr^{4+} liberate at a lower temperature than the electrons trapped at Bi^{2+}. On recombination with Bi^{2+}, Bi^{3+} in the excited state is formed yielding A-band emission and due to efficient energy transfer, also Nd^{3+} infrared emissions near 870 nm and 1.06 µm appear in $Y_{1-x}Lu_xPO_4$.

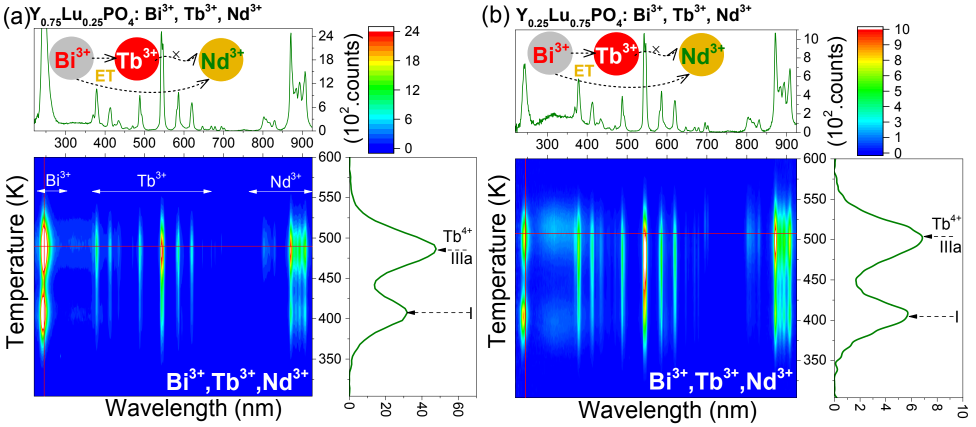

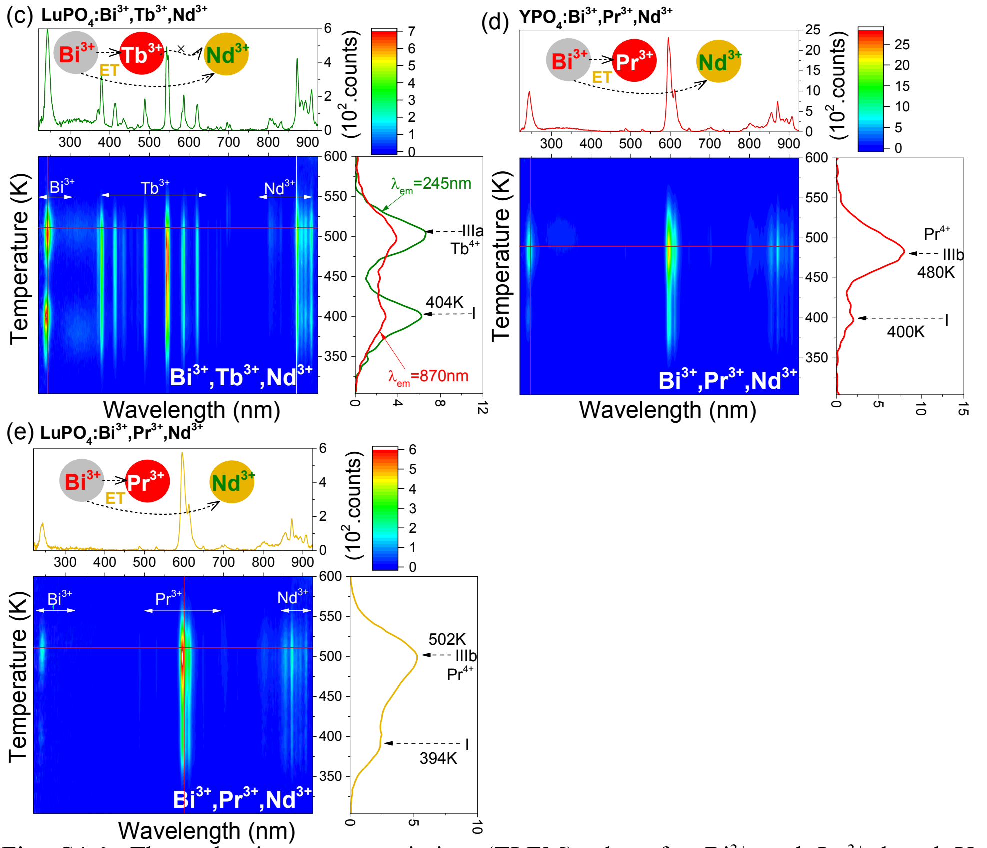

Fig. S4.6. Thermoluminescence emission (TLEM) plots for Bi^{3+} and Ln^{3+}-doped Y$_{1-x}$Lu$_x$PO$_4$ crystals at a heating rate of 1 K/s after γ-ray irradiation. The doping concentration of Bi^{3+} and Ln^{3+} is fixed to 0.5mol%.

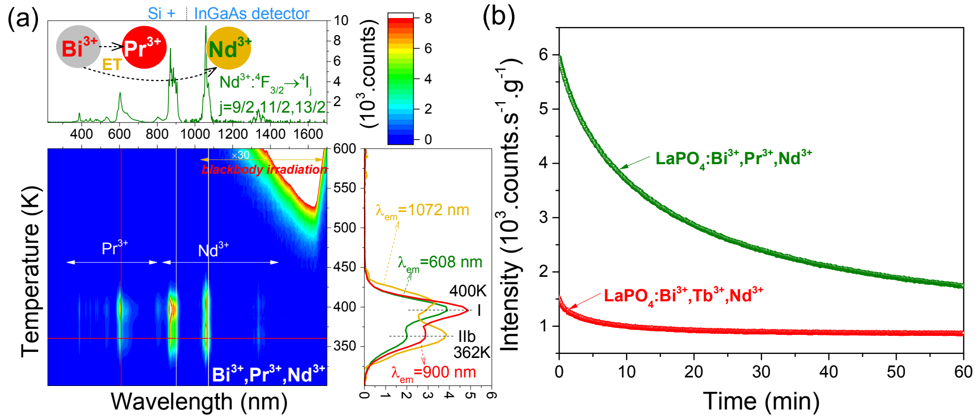

Fig. S4.7. (a) TLEM plot for $LaPO_4:0.002Bi^{3+},0.005Pr^{3+},0.005Nd^{3+}$ at β=1 K/s after γ-ray irradiation and (b) room temperature isothermal decay curves for Bi^{3+} and Ln^{3+} doped $LaPO_4$ after β irradiation while monitoring the emission from 400-900 nm.

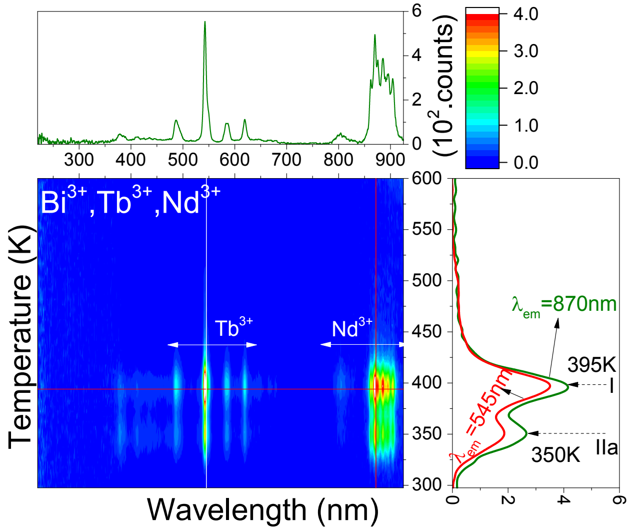

Fig. S4.8. TLEM plot for $LaPO_4:0.002Bi^{3+},0.005Tb^{3+},0.005Nd^{3+}$ recorded at a heating rate of 1 K/s after γ-ray irradiation.

Fig. S4.8 shows that the TL glow curves IIa and I monitoring Tb^{3+} 4f-4f emission at 545 nm or Nd^{3+} emission near 870 nm share the same shape in $LaPO_4:0.002Bi^{3+},0.005Tb^{3+},0.005Nd^{3+}$.

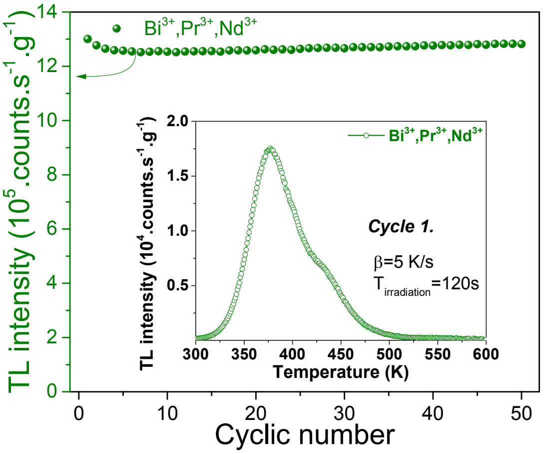

Fig. S4.9. Repeatability test by integrating TL glow area against cyclic number for $LaPO_4: 0.002Bi^{3+},0.005Pr^{3+},0.005Nd^{3+}$ monitoring red emission from Pr^{3+}. The inset shows a TL glow curve for cycle 1.

The integrated thermoluminescence area of LaPO4:0.002Bi^{3+},0.005Pr^{3+}, 0.005Nd^{3+} in Fig. S4.9 demonstrates that this phosphor is thermally stable within the 50 cycle test.

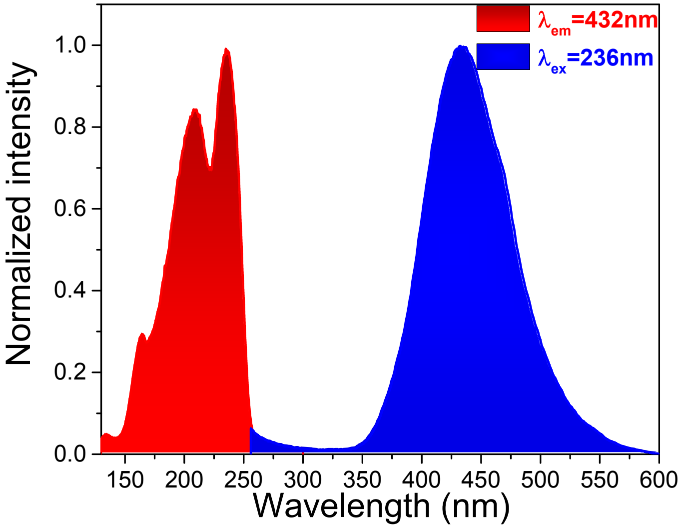

Fig. S4.10. Photoluminescence excitation and emission spectra of LaPO4:0.002Bi^{3+} recorded at 10 K.

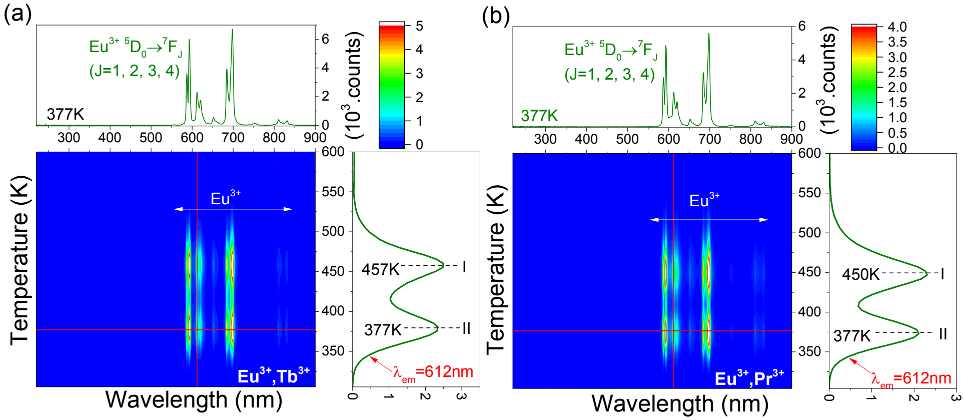

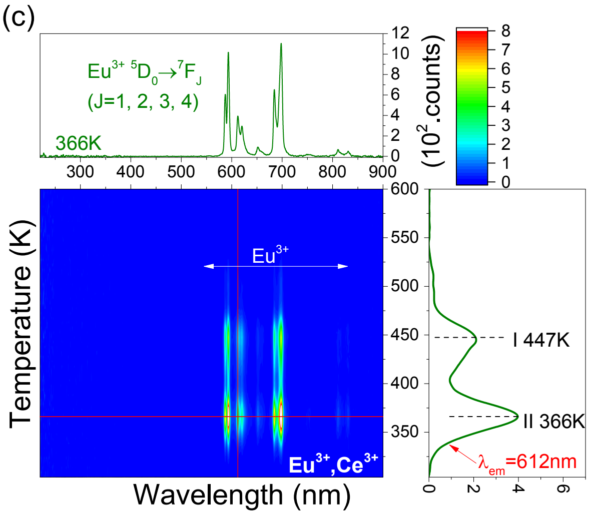

Fig. S4.11. TL emission (TLEM) plots for (a) GdPO$_4$:0.005Eu^{3+},0.005Tb^{3+}, (b) GdPO$_4$: 0.005Eu^{3+},0.005Pr^{3+}, and (c) GdPO$_4$:0.005Eu^{3+},0.005Ce^{3+} at β=1 K/s after γ-ray irradiation.

Fig. S4.11 shows the TL emission spectra of GdPO$_4$ each with the same Eu^{3+} electron trap but with different hole trap either from Tb^{3+}, Pr^{3+}, or Ce^{3+}. Only Eu^{3+} 4f-4f emission appears in the three samples, which share the same TL peaks I near 450 K and II near 377 K.

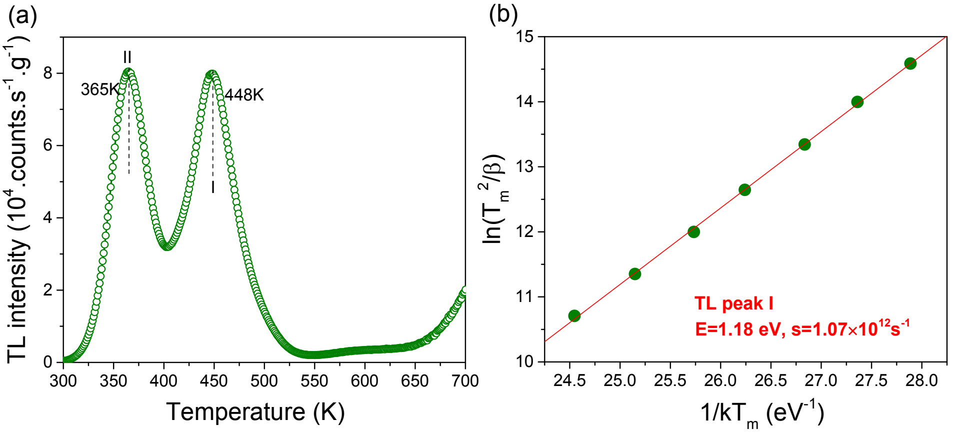

Fig. S4.12. (a) Thermoluminescence glow curves for GdPO$_4$:0.005Eu^{3+},0.005Tb^{3+} recorded at a heating of 1 K/s after 400s β irradiation while monitoring red Eu^{3+} emission by using a 600 nm bandpass filter 600FS40-50. (b) variable heating rate plot for TL glow peak I in a). The applied heating rates in b) are 0.08, 0.15, 0.3, 0.63, 1.25, 2.5, and 5 K/s.

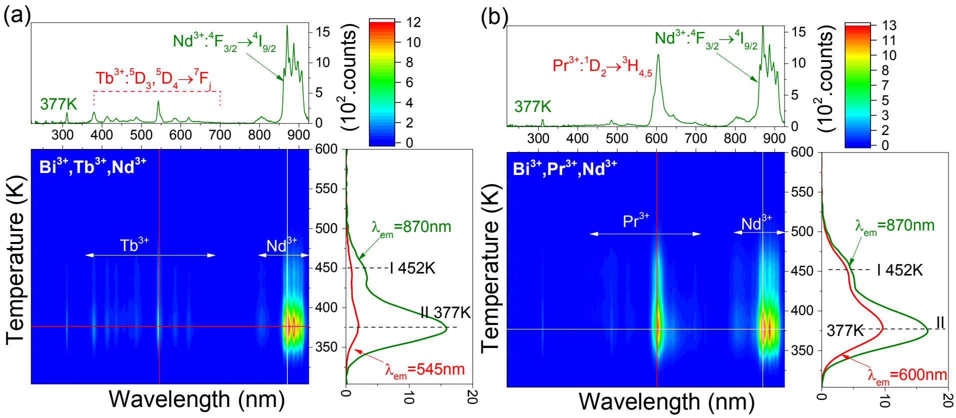

Fig. S4.13. TL emission (TLEM) spectra for (a) Ln=Tb^{3+} and (b) Ln=Pr^{3+} codoped $La_{1-x}Gd_xPO_4$:0.002Bi^{3+},0.005Ln^{3+},0.005Nd^{3+} (x=0.75) at β=1 K/s after γ-ray irradiation.

Fig. S4.13a) or b) show the TL emission plot for solid solutions $La_{1-x}Gd_xPO_4$:0.002Bi^{3+},0.005Nd^{3+} (x=0.75) co-doped with 0.005Tb^{3+} or Pr^{3+} after γ-ray charging treatment. The TL glow peaks I or II when monitoring the characteristic emission either from Tb^{3+}, Nd^{3+}, or Pr^{3+} have the same shape. This same applies to other 0.005Tb^{3+} or Pr^{3+} co-activated $La_{1-x}Gd_xPO_4$ with x range from 0 to 1 in Fig. S4.14. The appearance of Tb^{3+}, Pr^{3+}, and Nd^{3+} emission in $La_{1-x}Gd_xPO_4$ is attributed to energy transfer from Bi^{3+}, like in $Y_{1-x}Lu_xPO_4$ in Fig. S4.5.

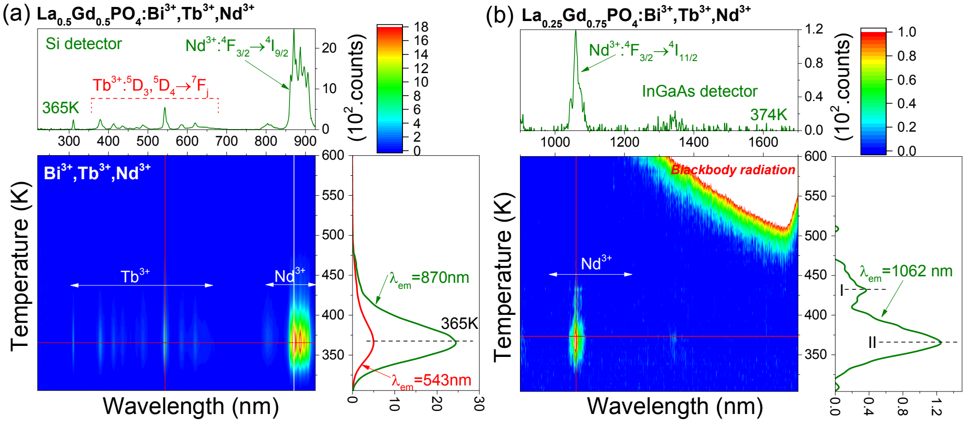

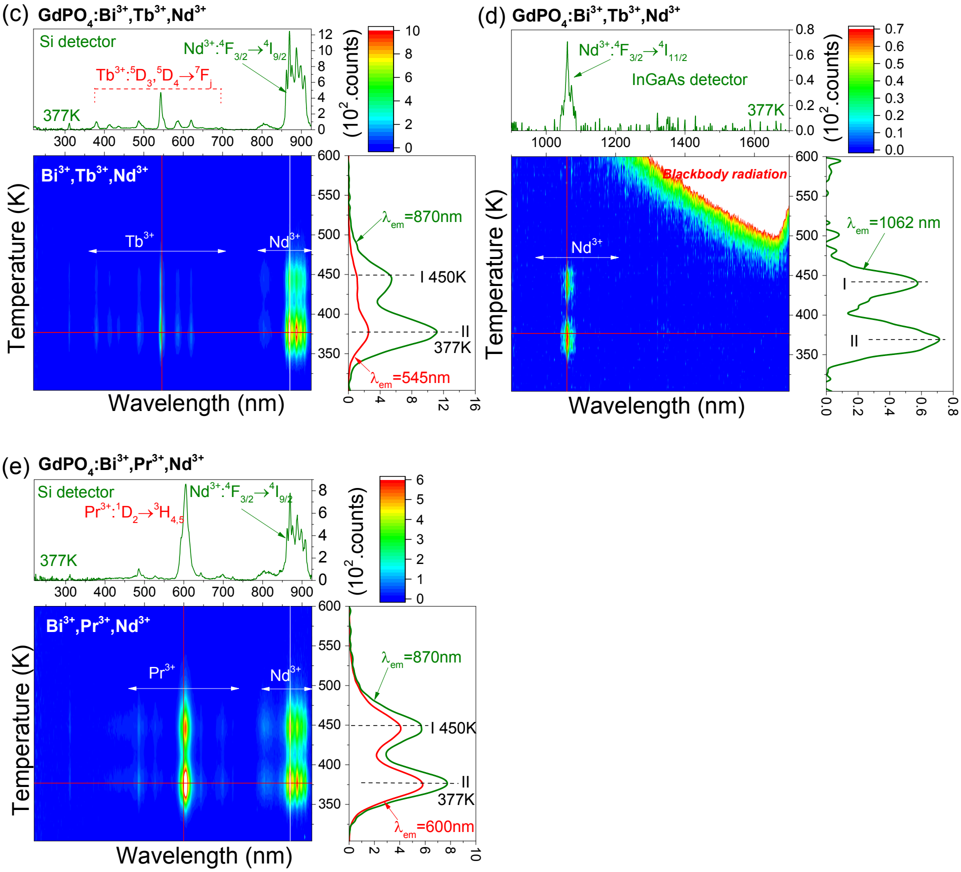

Fig. S4.14. TL emission (TLEM) plots for Bi^{3+} and Ln^{3+} doped La$_{1-x}$Gd$_x$PO$_4$ samples recorded at a heating rate of 1 K/s after γ-ray irradiation charging treatment. The doping contents of Bi^{3+} and Ln^{3+} are respectively fixed to 0.2% and 0.5%.

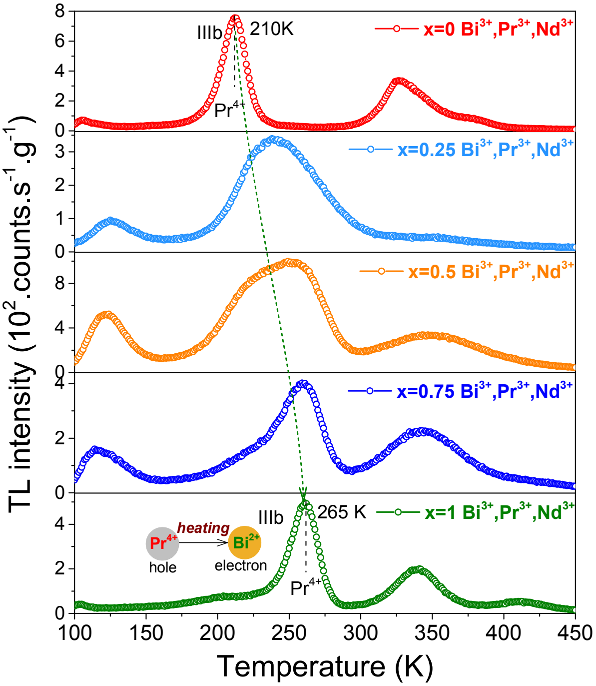

Fig. S4.15. Low-temperature TL glow curves for $La_{1-x}Gd_xPO_4$:0.002Bi^{3+},0.005Pr^{3+}, 0.005Nd^{3+} (x=0-1) samples recorded at a heating rate of 1 K/s after 600s β irradiation in the temperature range between 100-450 K. A 600 nm bandpass filter 600FS40-50 was used to monitor Pr^{3+} emission and the TL intensities were corrected by sample mass and irradiation time.

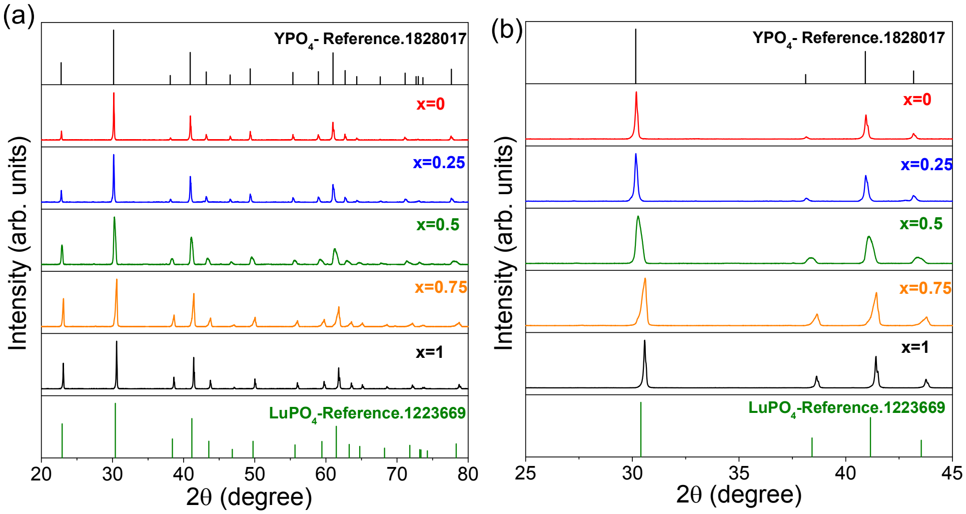

Fig. S4.16. (a) XRD patterns of $Y_{1-x}Lu_xPO_4$:0.005Bi^{3+},0.005Tb^{3+},0.005Nd^{3+} (x=0, 0.25, 0.5, 0.75, and 1.0) samples. (b) detailed XRD patterns in the range from 25 to 45°.

Fig. S4.16 gives the X-ray diffraction (XRD) patterns for $Y_{1-x}Lu_xPO_4$: 0.005Bi^{3+},0.005Tb^{3+},0.005Nd^{3+} (x=0-1). With increasing x, slight shift of XRD peaks towards higher 2θ angle appears in the $Y_{1-x}Lu_xPO_4$ solid solutions. This is due to the decrease of the cell volume when Y^{3+} is replaced by the smaller Lu^{3+} ion.

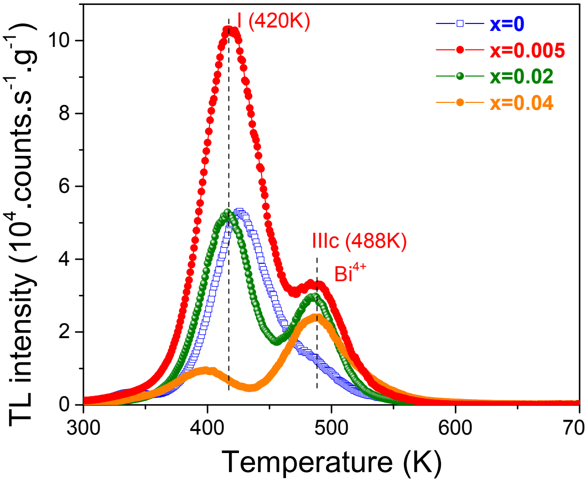

Fig. S4.17. TL glow curves for YPO_4:0.005Bi^{3+},xNd^{3+} (x=0-0.04) recorded at a heating rate of 1 K/s after 1200s β irradiation while monitoring the emission from Bi^{3+}. The TL intensities were corrected by sample mass and irradiation time.

Fig. S4.17 shows that, as compared with x=0.005, both TL peaks I and IIIc gradually decrease with increasing x. This may be due to the higher energy transfer efficiency from Bi^{3+} to Nd^{3+} when x increases.

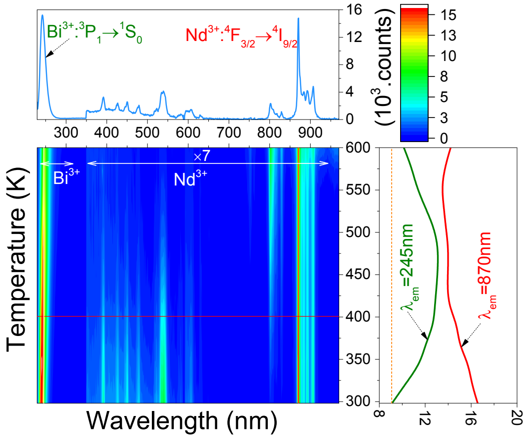

Fig. S4.18. 2D contour plot of temperature dependent photoluminescence for $YPO_4:0.005Bi^{3+},0.005Nd^{3+}$ under Bi^{3+} A-band excitation using 228 nm OPO laser.

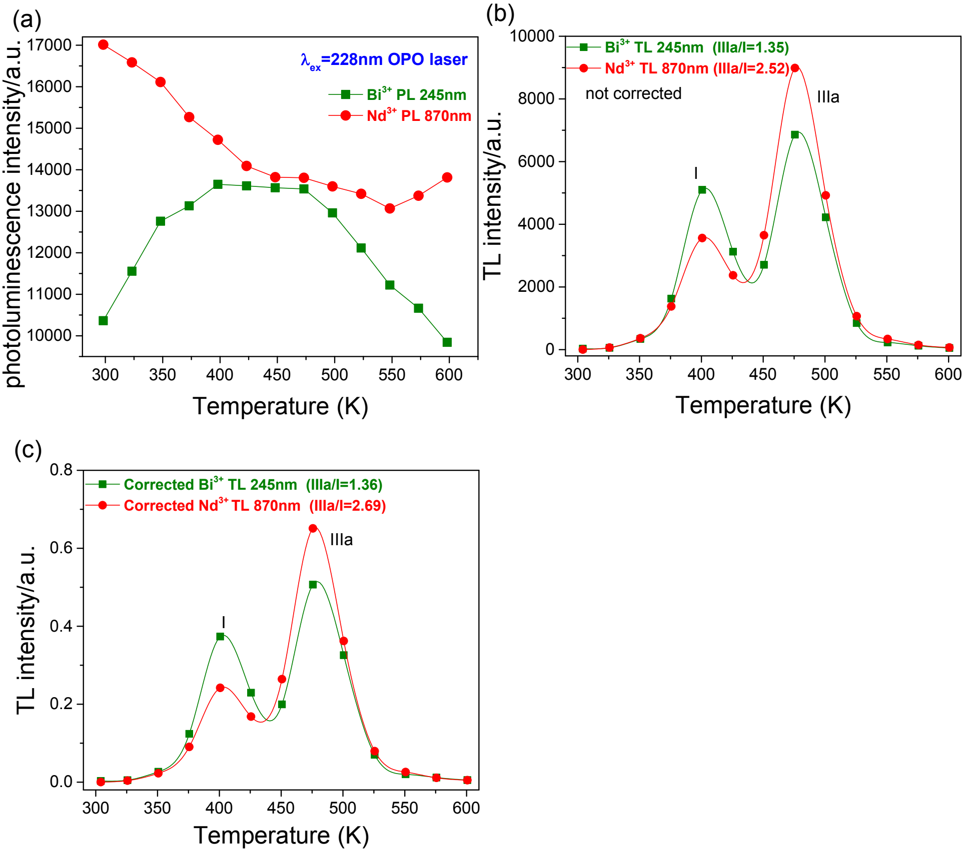

Fig. S4.19. (a) Temperature dependence of Bi^{3+} 245 nm and Nd^{3+} 870 nm emission upon 228 nm excitation in $YPO_4:0.005Bi^{3+},0.005Nd^{3+}$. (b), (c) TL glow curves for YPO_4: $0.005Bi^{3+},0.005Tb^{3+},0.005Nd^{3+}$ monitoring Bi^{3+} or Nd^{3+} emission at β=1 K/s after γ-irradiation. The TL curves in (c) were corrected by the temperature dependence of Bi^{3+} or Nd^{3+} emission in (a).

Fig. S4.19b)-c) shows that the TL intensity ratios of peaks IIIa to I slightly increase to 1.36 for Bi^{3+} 245 nm emission and to 2.69 for Nd^{3+} 870 nm emission after the TL glow curves were corrected by the temperature dependence of Bi^{3+} or Nd^{3+} emission in Fig. S4.19a).

Fig. S4.19a) shows the Bi^{3+} A-band emission quenches at a lower temperature than the Nd^{3+} 4f-4f emission. Bi^{3+} emission can be quenched by non-radiative transitions but also by increased transfer efficiency to Nd^{3+}. The quenching of Bi^{3+}

A-band emission starts above 500 K and that cannot explain the data in Fig. 4.7a) and S4.19c). With higher temperature the Bi^{3+} A-band emission will broaden (Fig. S4.18) which may enhance energy transfer efficiency from Bi^{3+} to Nd^{3+} resulting in decreased Bi^{3+} emission and increased Nd^{3+} emission. This may explain higher TL ratio of peak IIIc to I when Nd^{3+} 870 nm is monitored.

Reference

1. K. S. Sohn, Y. Y. Choi, H. D. Park and Y. G. Choi, *Journal of The Electrochemical Society*, 2000, **147**, 2375-2379.
2. W. Di, X. Wang, B. Chen, H. Lai and X. Zhao, *Optical Materials*, 2005, **27**, 1386-1390.
3. T. Hoshina and S. Kuboniwa, *Journal of the Physical Society of Japan*, 1971, **31**, 828-840.
4. T. Lyu and P. Dorenbos, *Journal of Materials Chemistry C*, 2018, **6**, 6240-6249.

5

Vacuum referred binding energies of bismuth and lanthanide levels in ARE(Si,Ge)O$_4$ (A=Li, Na; RE=Y, Lu); towards designing charge carrier trapping processes for energy storage

Graphical abstract

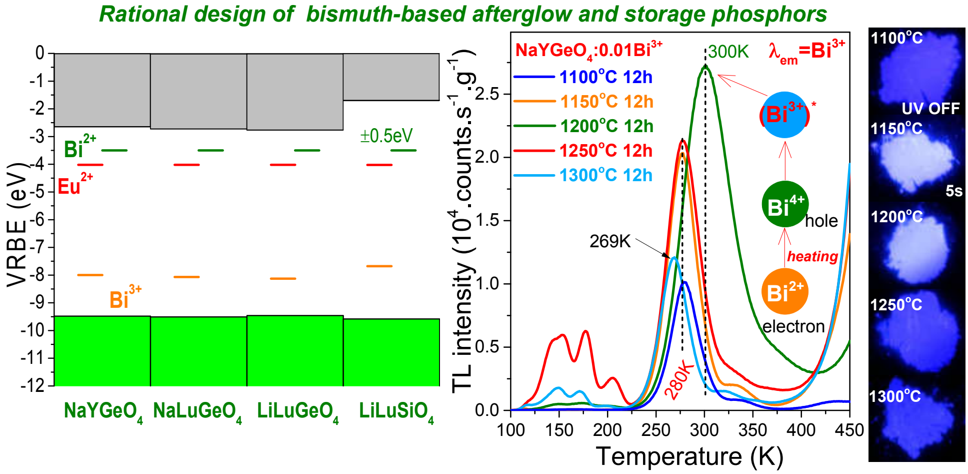

This chapter is based on the publication: **T. Lyu*** and P. Dorenbos, ***Chemistry of Materials***, 2020, 32, 1192-1209.

5.1. Abstract

Developing a feasible design principle for solid-state materials for persistent luminescence and storage phosphors with high charge carrier storage capacity remains one of the crucial challenges. Here we report a methodology for such rational design via vacuum referred binding energy (VRBE) diagram aided band structure engineering and crystal synthesis optimization. The ARE(Si,Ge)O_4 (A=Li, Na; RE=Y, Lu) crystal system was selected as a model example. Low-temperature (10 K) photoluminescence excitation and emission spectra of bismuth and lanthanide-doped ARE(Si,Ge)O_4 system were first systematically studied, and the corresponding VRBE schemes were then established. Guided by these VRBE schemes, Bi^{3+} afterglow and storage phosphor properties were explored in $NaLu_{1-x}Y_xGeO_4$. By combining Bi^{3+} with Bi^{3+} itself or Eu^{3+}, Bi^{3+} appears to act as a deep hole trapping centre, while Bi^{3+} and Eu^{3+} act as less deep electron traps. Trap depth tunable afterglow and storage were realized in $NaLu_{1-x}Y_xGeO_4:0.01Bi^{3+}$ and $NaLu_{1-x}Y_xGeO_4:0.01Bi^{3+},0.001Eu^{3+}$ by adjusting x leading to conduction band engineering. More than 28h of Bi^{3+} persistent luminescence was measurable in $NaYGeO_4:0.01Bi^{3+}$ due to electron release from Bi^{2+} and recombination with a hole at Bi^{4+}. The charge carrier storage capacity in $NaYGeO_4:0.01Bi^{3+}$ was discovered to increase ~7 times via optimizing synthesis condition at 1200 °C during 24h. The thermoluminescence (TL) intensity of the optimized $NaYGeO_4:0.001Bi^{3+}$ and $NaYGeO_4:0.01Bi^{3+},0.001Eu^{3+}$ is ~3, and ~7 times higher than the TL of the state-of-the-art X-ray storage phosphor BaFBr(I):Eu. Proof-of-concept colour tuning for anti-counterfeiting application was demonstrated by combining the discovered and optimized $NaYGeO_4:0.01Bi^{3+}$ afterglow phosphor with perovskite $CsPbBr_3$, and CdSe quantum dots. Information storage application was demonstrated by UV-light or X-ray charged $NaYGeO_4:0.01Bi^{3+},0.001Eu^{3+}$ phosphor dispersed in a silicone gel imaging film. This work not only reports excellent storage phosphors but more importantly provides a design principle that can initiate more exploration of afterglow and storage phosphors in a designed way through combining VRBE scheme guided band structure engineering and crystal synthesis optimization.

5.2. Introduction

Storage phosphors are information storage materials which capture electrons and holes in host defect traps after exposure to ionizing radiation[1-5]. It has widespread applications like in dosimetry of X-rays, electrons or γ-rays[6-9], digital dental radiograph imaging system[10], and computed radiography (CR) using X-ray charged storage phosphor film[11, 12]. Like a storage phosphor, an afterglow phosphor is another type of energy storage material which can first capture charge carriers in defect trap(s) upon absorbing excitation energy, but then can gradually emit photons when excitation radiation is removed[13, 14]. Afterglow phosphors are proposed to be used in anti-counterfeiting application because the afterglow colour and/or intensity may change as a function of time in the dark[15-18]. To date, few really good afterglow and storage phosphors were discovered. One of the important reasons is that a majority of research work is based on an approach by trial and error, and the charge carrier trapping processes are often not deeply and systematically studied. This does not provide enough insights and guidance for further research. Developing an effective design principle in solid-state materials for persistent luminescence and storage phosphors with high charge carrier storage capacity is a challenge.

A persistent luminescence or storage phosphor is constituted of the compound lattice, the recombination centre, and the electron and hole capturing centres that are often lattice impurities or intrinsic defect(s)[19]. The properties of the recombination centres and the host lattices determine the emission decay time and the emitting wavelength that can change from deep ultraviolet to even infrared. The trap depths of the electron and hole trapping centres and their distribution within the compound lattice decide how long the electrons and holes are trapped. For a persistent luminescence phosphor, shallow traps (<~0.7 eV) are required to produce thermally stimulated afterglow at room temperature (RT)[19, 20]. For a storage phosphor, deep traps (>~1 eV) are required to avoid energy loss via thermal fading at RT[5, 11]. Rational design of afterglow and storage phosphors is possible if one can tailor the trap depths of the electron and hole capturing centres. If the charge carrier storage capacity can further be optimized by synthesis conditions, then a good storage phosphor may appear.

In X-ray computed radiography, the image information of patients is first stored in a storage phosphor imaging film and then read out by scanning the film point by point with a stimulation photon source like a solid-state laser beam with wavelength ranging from 375 to 1800 nm[21, 22]. The photo-stimulated light is rapidly recorded with a photomultiplier tube that has a high quantum efficiency from 300 nm to 450 nm. In current flying-spot computed radiography digitizers, the read-out time for each pixel is less than 2 μs[11]. The light emission from the phosphor at the previous pixel should have decayed to at least 1/e of its initial emission intensity when the phosphor at the present pixel is stimulated. Therefore, for use in flying-spot scanners the decay time of a recombination centre in a storage phosphor should be <~2 μs. Other requirements for a good storage phosphor for computed radiography, as proposed in Refs. [11, 22], are high X-ray absorption and conversion efficiency to trapped electrons and holes, slow fading, good chemical stability, and optical erasure ability of stored information. Today BaFBr(I):Eu is the state-of-the-art X-ray storage phosphor[12, 23-25]. Unfortunately, its durability is limited because it is hygroscopic. The exploration of better storage phosphors is going on[26-28]. Recently, Dobrowolska *et al.* [5] reported an excellent storage phosphor $LiLuSiO_4$:Ce,Tm with high charge carrier storage capacity using a typical trial-and-error approach. However, the nature of the trap(s) in $LiLuSiO_4$:Ce,Tm still remains unknown and design principles for storage phosphors were not proposed.

For afterglow phosphors, most of the research work is focused on Eu^{2+}, Ce^{3+}, or Cr^{3+} doped compounds[29-31]. Bismuth-based materials are of current research interest because of their promising applications in various fields like in semiconductor[32], quantum dots[33], or topological insulator[34]. Particularly, Bi^{3+} as an emission centre has been widely used in photoluminescence phosphors[35-37]. However, Bi^{3+}-based afterglow or storage phosphor development is rarely reported[38-40]. Recently Wang *et al.* [41] reported the Bi^{3+} persistent luminescence in Bi^{3+} and Eu^{3+} doped $NaLuGeO_4$. The charge carrier trapping processes are not fully clear because Bi^{3+} may act as a hole trap but also as an electron trap. Deep understanding of the electron and hole trapping processes in bismuth-doped compounds will be helpful to accelerate the exploration of better afterglow and storage phosphors.

Methods were proposed to determine the locations of the divalent and trivalent lanthanides, Bi^{3+} or Bi^{2+} energy levels within the band gap of inorganic compounds[42-45]. With spectroscopic data, one may construct a vacuum referred binding energy (VRBE) scheme[46]. Knowledge on the VRBE in defect levels like lanthanides, valence band (VB), conduction band (VB), or bismuth then offers an effective way to predict, understand and even tailor electron and hole capturing processes. Up to now, the VRBE-guided method has mainly been applied to explore afterglow phosphors in lanthanide and/or Cr^{3+}-doped garnet compounds[29], and only a few good afterglow phosphors were developed. Particularly, to the best of our knowledge, there is rare reporting on the design of Bi^{3+} afterglow or storage phosphor by a combination of VRBE-aided band structure engineering and optimizing crystal synthesis conditions.

The objective of this work is to show how to design Bi^{3+} afterglow and storage phosphors using VRBE-aided band structure engineering and crystal synthesis optimization. Because of the good storage properties of $LiLuSiO_4$, the ARE(Si,Ge)O_4 (A=Li, Na; RE=Y, Lu) family of materials was selected for further research. Low-temperature (10 K) photoluminescence excitation and emission spectra of the bismuth and lanthanide-doped ARE(Si,Ge)O_4 system were first systematically investigated and the corresponding VRBE schemes were then established like in Fig. 5.1 which act as a basis for our research. d. 5.1a) predicts how the electron or hole trapping depth can be tailored by changing the conduction band or valence band energies with crystal composition modulation. Fig. 5.1b) helps to select potential combinations of hole and electron capturing centres. To demonstrate the design principle, in this work, we will mainly focus on $NaLu_{1-x}Y_xGeO_4$ crystals and study the charge trapping processes regarding bismuth and europium in detail. The effects of crystal synthesis optimization on charge carrier storage capacity were studied in $NaYGeO_4$:$0.01Bi^{3+}$. Proof-of-concept colour tuning for anti-counterfeiting application was demonstrated by combining the discovered $NaYGeO_4$:$0.01Bi^{3+}$ afterglow phosphor with perovskite $CsPbBr_3$, and CdSe quantum dots. Information storage application was demonstrated by an UV-light and X-ray charged $NaYGeO_4$:$0.01Bi^{3+}$,$0.001Eu^{3+}$ phosphor dispersed in a silicone gel imaging film.

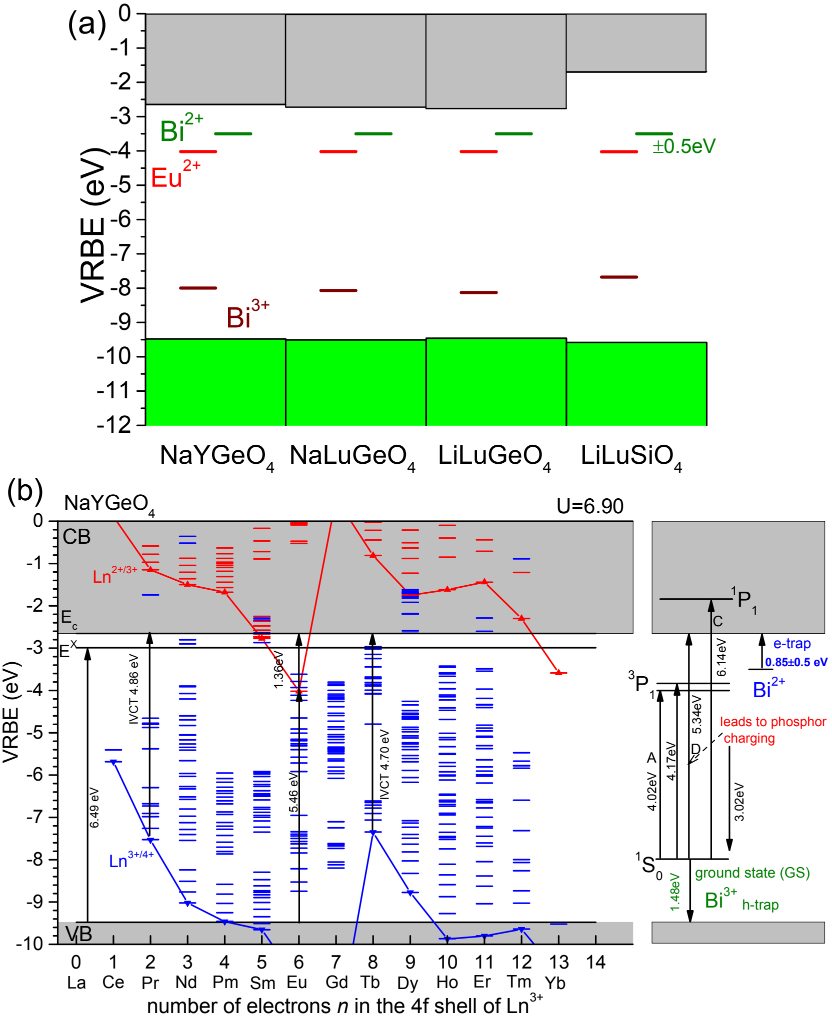

Fig. 5.1. Vacuum referred binding energy (VRBE) diagrams of (a) $NaYGeO_4$ related family of compounds, and (b) $NaYGeO_4$ including the VRBE in the ground states of lanthanides, Bi^{2+}, and Bi^{3+}. Arrows indicate experimentally observed transitions.

5.3. Experimental

SiO_2 (99.99%) crystals with 0.2-0.7 mm dimension were purchased from Umicore and ground into fine particles. Other starting chemicals were purchased from Sigma-Aldrich and utilized without further treatment. A series of Bi^{3+} and/or lanthanide activated $NaLu_{1-x}Y_xGeO_4$, $Na_{1-x}Li_xLuGeO_4$, $LiLuSi_{1-x}Ge_xO_4$, $LiLu_{0.25}Y_{0.75}Si_{1-x}Ge_xO_4$, and $LiLu_{1-x}Y_xSiO_4$ were synthesized via typical high-temperature solid-state reactions. For the compounds containing Li, an excess of 10% Li^+ above the normal stoichiometry was added to compensate for the loss of Li^+ at high temperature. The appropriate mixtures of SiO_2 (99.99%), GeO_2 (99.99%), Li_2CO_3 (99.99%), Na_2CO_3 (99.99%), and other rare earth oxides with high purity of 4 N (99.99%) were mixed well and then fired in corundum crucibles under ambient atmosphere at 800 °C for 8h and then 1150 °C for 12h. Finally, the obtained crystals were naturally cooled to room temperature (RT) and then ground into homogeneous powder before further measurements. The applied heating rate of the furnace is 3 °C/min. Particularly, to optimize the Bi^{3+} persistent luminescence in $NaYGeO_4$:$0.01Bi^{3+}$, its synthesis conditions were explored by changing the temperature from 1100 °C to 1300 °C and duration time from 3h to 24h.

All crystals were identified using a PANalytical XPert PRO X-ray diffraction setup equipped with a Co Kα (λ=0.178901 nm) X-ray tube operated at 45 kV and 40 mA. The recorded X-ray diffraction (XRD) patterns were compared with the standard reference from Pearson's Crystal Database. The photoluminescence (PL) emission and excitation (PLE) spectra were measured by utilizing a system that includes a VUV/UV branch using a water-cooled deuterium (D_2) lamp with an ARC VM505 vacuum monochromator and a UV/VIS branch utilizing a 500 W Hamamatsu CW Xe lamp with a Gemini 180 monochromator. A PerkinElmer MP-1913 photomultiplier was employed as the signal detector. The crystals can be cooled to 10 K utilizing a closed helium cryostat (HC-4) with a Lake Shore 331 temperature controller in vacuum. All shown PLE spectra have been corrected by the incident photon flux. For the fluorescence decay curve, it was recorded using the above PL setup that further combines a wavelength tuneable YAG:Nd laser system (NT230-100-SH/DUV-SCU) with a digitizer module.

High-temperature thermoluminescence (TL) glow curves (300-823 K) were measured with a setup that contains an EMI 9635QA photomultiplier tube, a RISØ TL/OSL reader (model DA-15) and a DA-20 controller. All crystals were first heated to 823 K for 3 times to empty all traps and then cooled to RT followed by beta irradiation utilizing a $^{90}Sr/^{90}Y$ source with a dose rate of ~0.7 mGy/s under nitrogen gas in darkness. Low-temperature TL glow curves (LTTL) between 90-450 K were measured using a facility which contains a PerkinElmer channel photomultiplier tube (MP-1393) and a $^{90}Sr/^{90}Y$ beta irradiation source with a dose rate of ~0.4 mGy/s. Prior to the LTTL measurements at a heating rate of 1 K/s, powder samples were pressed into pills with area ~0.2 cm^2 and mass <~5 mg. The pills were attached to a metal unit with heating elements by silver paint. The pills were first heated to 450 K for 3 mins in darkness and then cooled to 90 K using liquid nitrogen followed by 600s beta irradiation in a vacuum (10^{-7} mbar). A 400 nm bandpass filter (400FS40-50, Andover Corporation) was placed between the PM tube and the pills to select the characteristic Bi^{3+} emission in $NaLu_{1-x}Y_xGeO_4:0.01Bi^{3+}$. All measured TL glow curves have been corrected by the sample mass and β irradiation time, and glow intensity is expressed in counts/g/s where counts are an instrumental unit.

Thermoluminescence emission (TLEM) spectra were measured with a facility that combines a UV/vis QE65000 spectrometer with a RISØ TL/OSL reader. The powder samples were heated to 823 K to empty all traps and then cooled to RT followed by gamma irradiation from a ^{60}Co source to an absorbed dose of ~2.5 kGy. The TLEM spectra recorded by QE65000 have been corrected by its wavelength-dependent quantum efficiency.

Thermoluminescence excitation (TLE) spectra were performed by first charging the crystals during 300s with monochromatic photons produced by a 150 W xenon arc lamp (Hamamatsu L2273) which was filtered with a monochromator (Oriel Cornerstone 130). The TLE facility has a wavelength resolution of 8 nm against 1 mm slit width. Here, the slit width was fixed to 1 mm and the wavelength step was set as 10 nm for all TLE measurements in this work. The TLE facility was programmed by LabVIEW to measure all TL glow from RT to 723 K at a heating rate of 5 K/s at illumination wavelengths from 200 to 400 nm. A so-called TLE plot like in Fig. 5.9c was constructed by integrating the intensity of a TL glow peak and displaying it versus the charging wavelength[19, 47]. A 400 nm bandpass filter (400FS40-50) was used to monitor Bi^{3+} emission. All recorded TLE curves have been corrected for the charging time, sample mass, and wavelength-dependent excitation intensity of the xenon arc lamp.

The photographs of Bi^{3+} related emission were taken with an iPhone 8Plus. A Hg lamp with the main emission near 254 nm was utilized to charge $NaYGeO_4:0.01Bi^{3+}$. For the phosphor dispersed in a silicone gel, appropriate mixtures of phosphor and silicone were mixed homogeneously to produce a uniform film on a glass substrate. The film was then put in vacuum for 10 min to remove air bubbles and placed in the air at room temperature for 12h or at 60 °C for 2h. Scanning electron microscope (SEM) images and energy-dispersive X-ray spectroscopy (EDX) mapping for $NaYGeO_4$:0.01Bi^{3+} were recorded with JEOL JSM-IT100.

5.4. Results

5.4.1. X-ray diffraction and photoluminescence spectroscopy

Fig. 5.2a) shows the X-ray diffraction patterns (XRD) for the $NaYGeO_4$: 0.01Bi^{3+} synthesized at 1200 °C during 3-24h. All samples match well with the standard $NaYGeO_4$ reference (No. 2060220), indicating that high purity samples were synthesized.

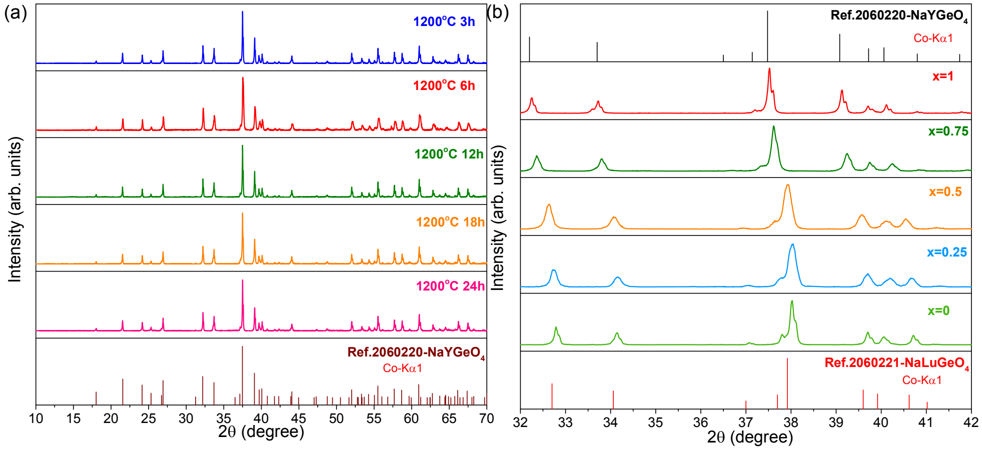

Fig. 5.2. XRD patterns for (a) $NaYGeO_4$:0.01Bi^{3+} synthesized at 1200 °C during 3h to 24h and (b) $NaLu_{1-x}Y_xGeO_4$:0.01Bi^{3+},0.001Eu^{3+} (x=0-1) solid solutions.

Fig. 5.2b) shows part of the XRD patterns for $NaLu_{1-x}Y_xGeO_4$:0.01Bi^{3+}, 0.001Eu^{3+} with different content of Y^{3+}. Compared with the $NaLuGeO_4$ reference (No. 2060221), the XRD peaks slightly shift towards smaller 2θ angles. This demonstrates that the yttrium cations enter into the smaller lutetium site and increase the cell volume. With increasing x, nice solid solutions appear in the synthesized crystals of $NaLu_{1-x}Y_xGeO_4$:0.01Bi^{3+},0.001Eu^{3+}, $Na_{1-x}Li_xLuGeO_4$: 0.01Bi^{3+}, or $LiLuSi_{1-x}Ge_xO_4$ (x=0-1) where impurity phases are absent as is evidenced with the X-ray diffraction patterns in Fig. S5.2.

Fig. 5.3a) shows the excitation spectra for $LiLuSi_{1-x}Ge_xO_4$:0.01Eu^{3+}. A broad band near 225 nm is observed, which slightly shifts to ~228 nm with increasing x. Like in the study of Sidorenko *et al.* [48], this band is attributed to the charge transfer (CT) band where an electron is excited from the valence band to Eu^{3+} forming Eu^{2+} in its ground state.

Fig. 5.3b)-3c) shows the excitation and emission spectra of undoped $LiLuSi_{1-x}Ge_xO_4$ at 10 K. Several excitation peaks near 179, 202, 238, and 316 nm appear. With increasing x, the excitation peaks do not exhibit a gradual shift, while the emission peaks near 320 and 422 nm shift towards lower energy.

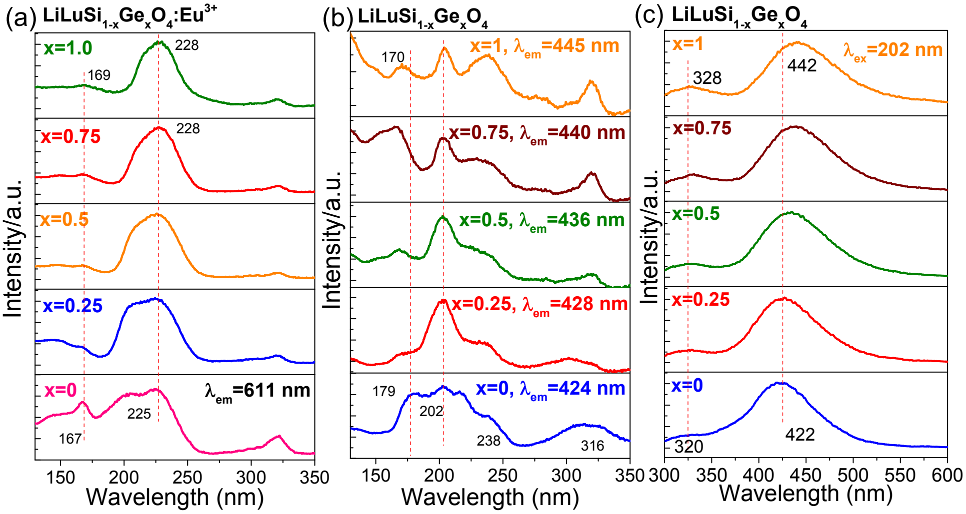

Fig. 5.3. Photoluminescence excitation (PLE) and emission (PL) spectra for (a) $LiLuSi_{1-x}Ge_xO_4:0.01Eu^{3+}$ monitoring Eu^{3+} 611 nm and (b)-(c) undoped $LiLuSi_{1-x}Ge_xO_4$ at 10 K.

Fig. 5.4a)-b) show the photoluminescence excitation and emission for undoped, Bi^{3+} or Eu^{3+} single activated $NaLuGeO_4$ crystals at 10 K. $NaLuGeO_4:0.01Eu^{3+}$ shows 4f-4f emission upon 227 nm excitation and its excitation spectrum monitoring at 612 nm gives rise to two excitation bands peaked at 227 and 196.5 nm. Like in the study of Blasse *et al.* [49], the 227 nm band is known as a charge transfer (CT) band. When the host is excited at 198 nm, a broad emission band appears between 330-600 nm. Its excitation spectrum monitoring at 450 nm shows a strong excitation band near 196.5 nm that is the same as the one observed when monitored Eu^{3+} emission in $NaLuGeO_4:0.01Eu^{3+}$. This band near 196.5 nm will be assigned to host exciton creation.

When $NaLuGeO_4:0.01Bi^{3+}$ is excited at 232 or 296 nm, a broad Bi^{3+} A-band emission with a maximum wavelength near 418 nm appears. Its excitation spectrum is composed of five bands near 166, 202, 232, 296, and 308 nm. Considering the Jahn-Teller splitting for the $^3P_1$ excited state for the s^2-type ions like Bi^{3+} and Tl^{+}[37, 50, 51], the low-energy excitation bands located at 296 and 308 nm are like in Ref. [41] attributed to the Jahn-Teller split $^1S_0 \rightarrow {}^3P_1$ transition. The assignment of the excitation band near 232 nm to $Bi^{3+} \rightarrow$CB charge transfer (CT) band, also known as the Bi^{3+} D-band, and the assignment of the 202 nm band to the C-band, will be discussed in the discussion part. Similar PLE and PL spectra for isostructural $NaYGeO_4$:0.01Bi^{3+} or Eu^{3+} can be found in Fig. S5.3.

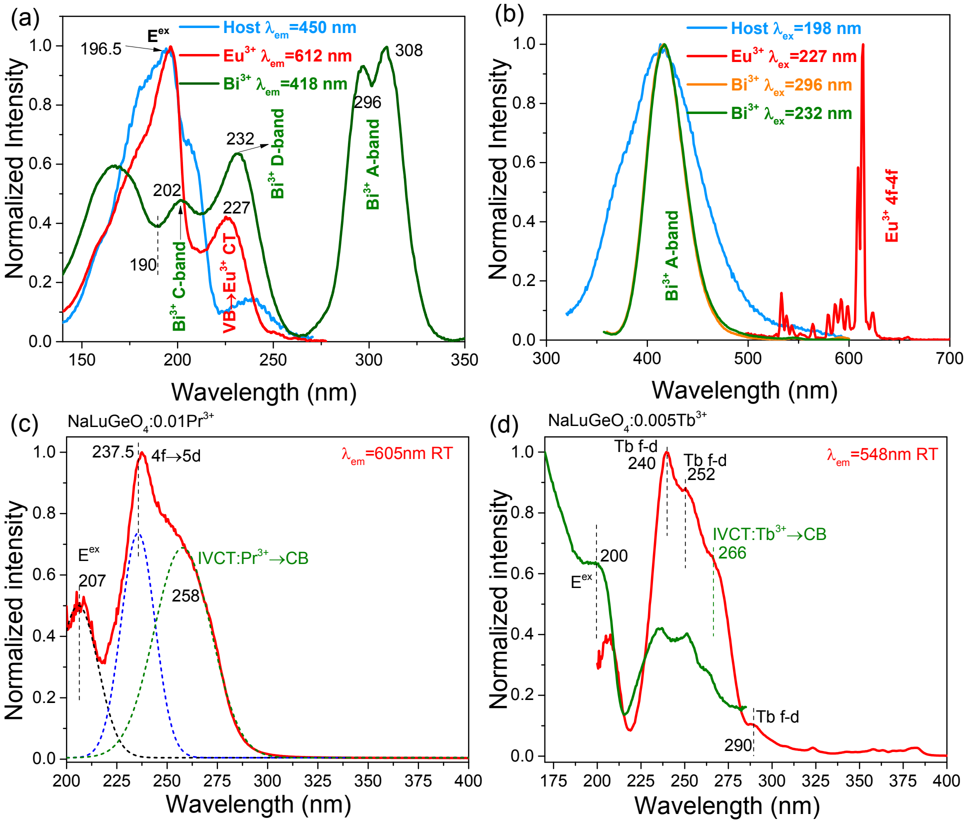

Fig. 5.4. Photoluminescence excitation (PLE) and emission spectra for (a)-(b) $NaLuGeO_4$ host, $NaLuGeO_4$:0.01Bi^{3+}, and $NaLuGeO_4$:0.01Eu^{3+} at 10 K, and PLE spectra for (c) $NaLuGeO_4$:0.01Pr^{3+} and (d) $NaLuGeO_4$:0.005Tb^{3+} at RT.

Fig. 5.4c)-4d) shows the photoluminescence excitation spectra for Tb^{3+} or Pr^{3+} single activated $NaLuGeO_4$ while monitoring the typical Tb^{3+} 548 nm or Pr^{3+} 605 nm emission shown in Fig. S5.5. A broad shoulder band near 258 nm appears for $NaLuGeO_4$:0.01Pr^{3+} in Fig. 5.4c), 266 nm for $NaLuGeO_4$:0.005Tb^{3+} in Fig. 5.4d), 260 nm for $LiLuGeO_4$:0.01Pr^{3+} in Fig. S5.5a), and 270 nm for $LiLuGeO_4$:0.01Tb^{3+} in Fig. S5.5b). The wavelength difference between that for Pr^{3+} and Tb^{3+} is ~10 nm in both compounds. Similar PLE spectra for $NaYGeO_4$ can be found in Fig. S5.5g)-h). In the discussion section these peaks are assigned to Intervalence Charge Transfer Bands (IVCT)[43] caused by electron transfer from the Tb^{3+} or Pr^{3+} 4f ground state to the conduction band.

To further reveal the nature of Bi^{3+} emission, Fig. 5.5a)-b) show the excitation and emission spectra of $Na_{1-x}Li_xLuGeO_4$:0.01Bi^{3+} solid solutions at 10 K. With increasing x, all excitation bands remain stationary, while the Bi^{3+} emission peak wavelength decreases gradually from 418 nm for x=0 to 360 nm for x=1 upon Bi^{3+} D-band excitation. The same applies to the emission bands when excited by the Bi^{3+} A-band at 308 nm, as shown in Fig. S5.4.

Fig. 5.5c)-d) shows the excitation and emission spectra for $LiLuSi_{1-x}Ge_xO_4$:0.01Bi^{3+} solid solutions at 10 K. The excitation peak near 160 nm remains stationary with increasing x, while a gradual red-shift appears in the Bi^{3+} A-, C-, and D- excitation bands and Bi^{3+} A-emission band. The same applies to the double solid solutions $LiLu_{0.25}Y_{0.75}Si_{1-x}Ge_xO_4$:0.01$Bi^{3+}$ in Fig. S5.6.

Fig. 5.5e)-5f) shows the PLE and PL spectra for $LiLu_{1-x}Y_xSiO_4$:0.01Bi^{3+} at 10K. The excitation peak near 160 nm, Bi^{3+} C-band near 190 nm, D-band near 207 nm, A-bands near 278 and 290 nm remain stationary. A red-shift of about 7 nm appears in the Bi^{3+} A-band emission with increasing x. Note that the 160 nm excitation band is an artefact due to the deuterium lamp spectrum correction.

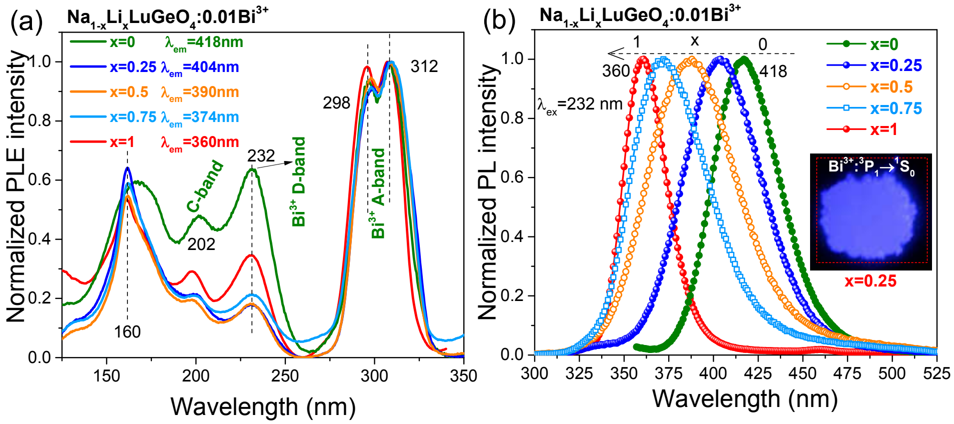

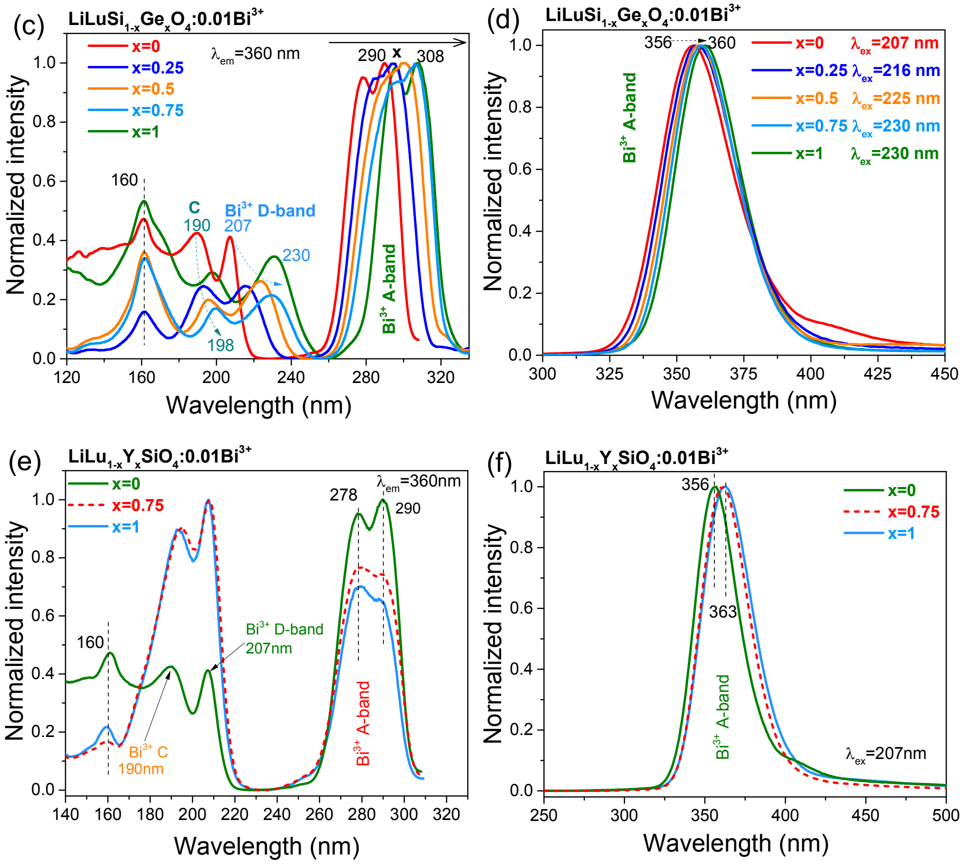

Fig. 5.5. Photoluminescence excitation and emission spectra for (a)-(b) $Na_{1-x}Li_xLuGeO_4$: $0.01Bi^{3+}$, (c)-(d) $LiLuSi_{1-x}Ge_xO_4$:$0.01Bi^{3+}$, and (e)-(f) $LiLu_{1-x}Y_xSiO_4$:$0.01Bi^{3+}$ recorded at 10 K. An afterglow photograph of $Na_{1-x}Li_xLuGeO_4$:$0.01Bi^{3+}$ (x=0.25) after Hg lamp irradiation for 5s is shown in b). The shoulder emission band near 414 nm in d) and f) for $LiLuSiO_4$:$0.01Bi^{3+}$ is attributed to the 2nd order transmission of excitation light at 207 nm. This band is absent in other samples when a 305 nm longer wavelength pass filter is used.

5.4.2. Engineering the electron trap depth of Bi^{3+} and Eu^{3+} and crystal synthesis optimization

TL emission (TLEM) studies were performed to identify the recombination centre in Bi^{3+} or Bi^{3+},Eu^{3+}-codoped $NaYGeO_4$ crystals as shown in Fig. 5.6. Additional TLEM plots for other $NaLu_{1-x}Y_xGeO_4$ with different Eu^{3+} concentration or Y^{3+} content can be found in Fig. S5.9. For $NaYGeO_4$:$0.01Bi^{3+}$, TL peaks near 373, 446, 515, and 614 K with broad Bi^{3+} A-band emission peaked at ~400 nm appear. After co-doping Eu^{3+} in $NaYGeO_4$:0.01Bi^{3+},0.001Eu^{3+} in Fig. 5.6b), an about 10 times stronger Bi^{3+} TL peak near 390 K emerges. Not only typical Bi^{3+} A-band emission but also weak Eu^{3+} 4f-4f emission is observed. This is attributed to Bi^{3+}→Eu^{3+} energy transfer because the TL peaks when monitoring the Eu^{3+} 4f-4f emission or when monitoring the Bi^{3+} A-band emission appear to share the same shape. This applies to $NaYGeO_4$:0.01Bi^{3+},0.001Eu^{3+} in Fig. 5.6c), $NaYGeO_4$: 0.01Bi^{3+},0.006Eu^{3+} in Fig. 5.6d), and also to other $NaLu_{1-x}Y_xGeO_4$:0.01Bi^{3+},xEu^{3+} in Fig. S5.9. Note that the ratio of Eu^{3+} 4f-4f emission to Bi^{3+} A-band emission increases from 0.02 to 0.12 with increasing x in Fig. 5.6b)-d).

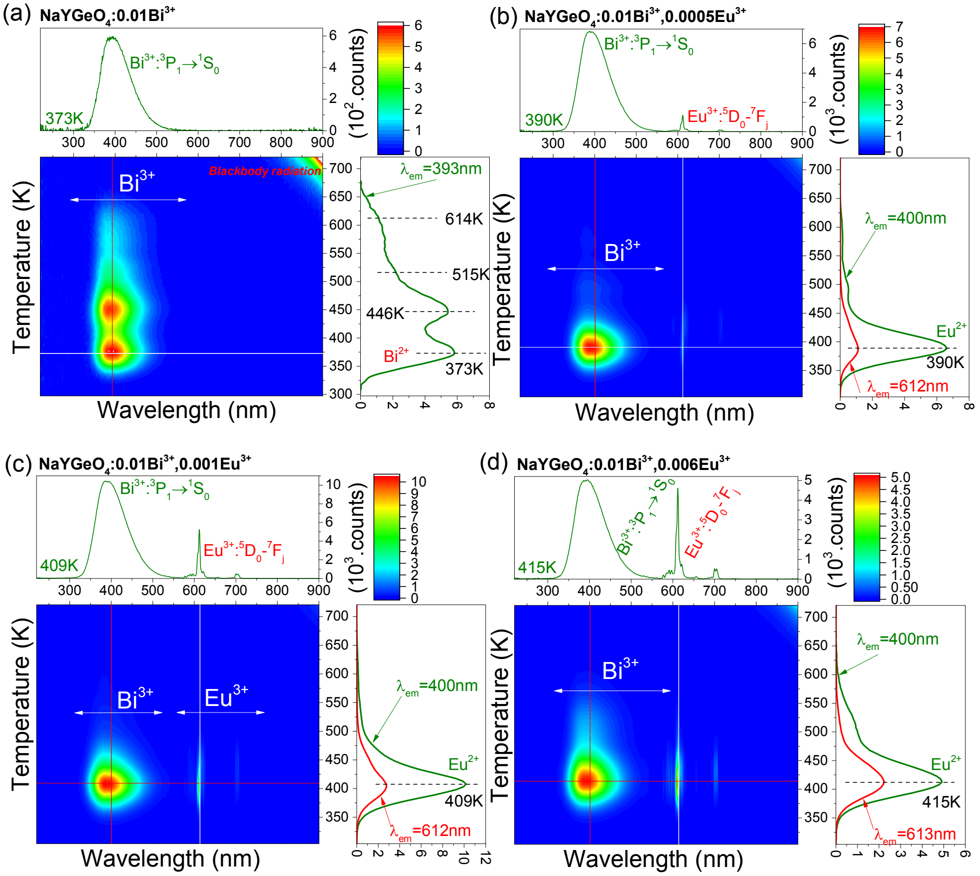

Fig. 5.6. Thermoluminescence emission (TLEM) spectra for (a) $NaYGeO_4$:0.01Bi^{3+} synthesized at 1200 °C during 24h, (b) $NaYGeO_4$:0.01Bi^{3+},0.0005Eu^{3+}, (c) $NaYGeO_4$: 0.01Bi^{3+},0.001Eu^{3+}, and (d) $NaYGeO_4$:0.01Bi^{3+},0.006Eu^{3+} at β=1 K/s after γ-ray irradiation.

Fig. 5.1a) shows that the VRBE in the ground state of Eu^{2+} and Bi^{2+} appears near -4.0 and -3.5±0.5 eV, respectively. It suggests that Bi^{3+} acts as a 0.5±0.5 eV shallower electron trap than Eu^{3+} in $NaYGeO_4$. Bi^{3+} single doped $NaLu_{1-x}Y_xGeO_4$ samples were synthesized to study the charge carrier trapping process. Fig. 5.7a) shows the low-temperature TL glow curves for $NaLu_{1-x}Y_xGeO_4$:0.01Bi^{3+} solid solutions. With increasing x, the TL glow near 226 K, that will be attributed to electron liberation from Bi^{2+}, shifts ~69 K towards higher temperature.

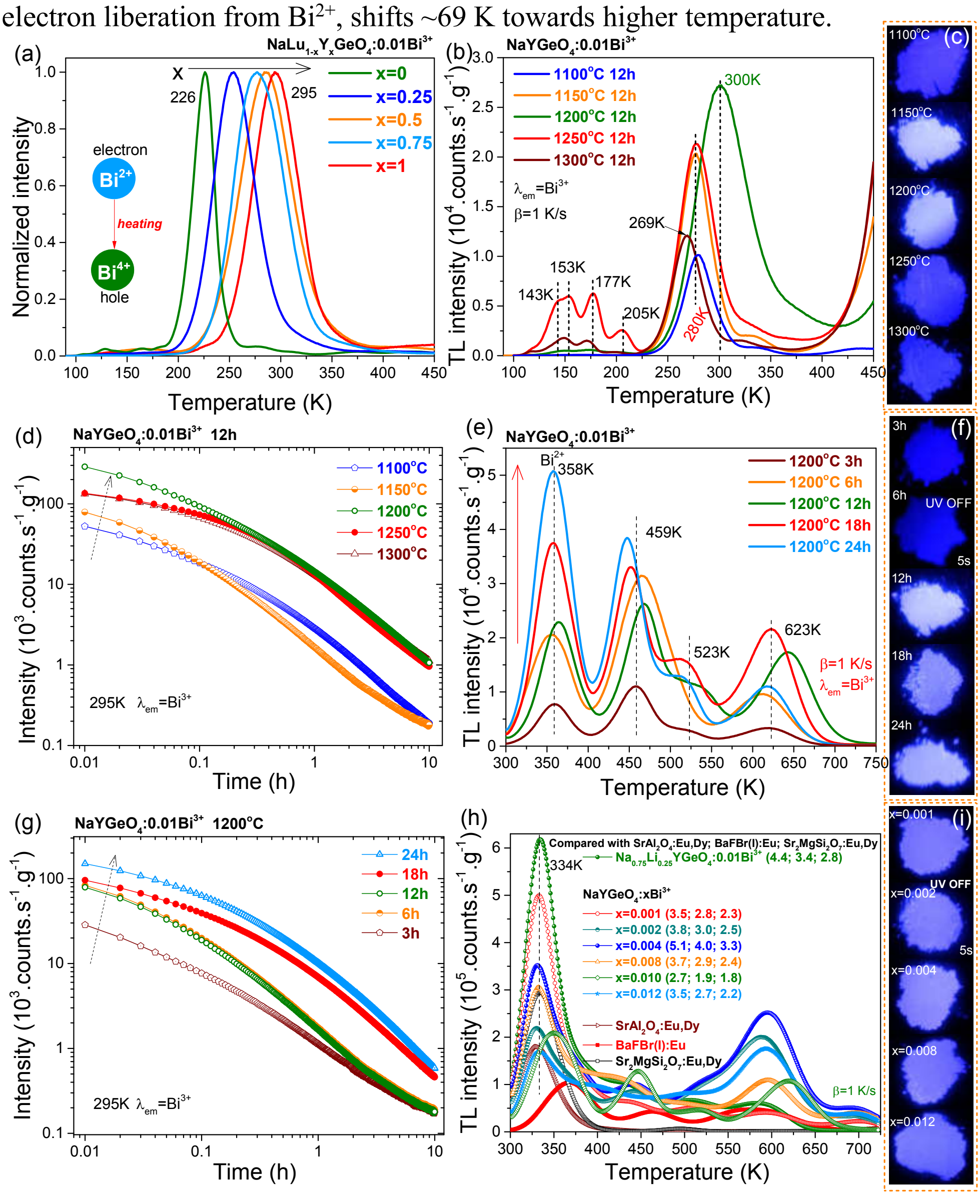

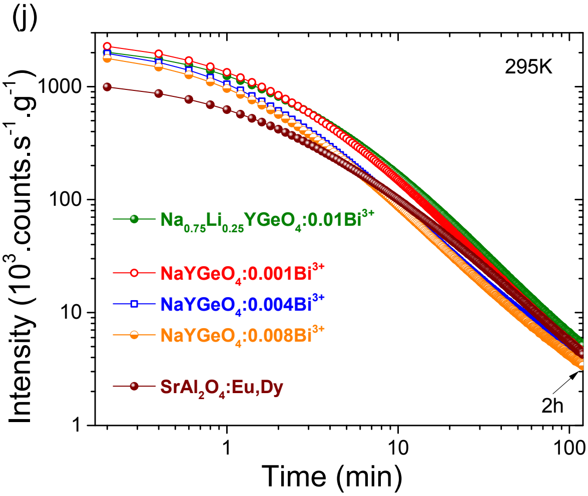

Fig. 5.7. (a) Low-temperature TL glow curves at β=1 K/s monitoring Bi^{3+} emission for $NaLu_{1-x}Y_xGeO_4$:0.01Bi^{3+} after β irradiation. TL glow curves, photographs after Hg lamp irradiation for 5s, and RT isothermal decay curves for $NaYGeO_4$:0.01Bi^{3+} synthesized at b)-d) different temperature, e)-g) at 1200 °C with different duration time, and h)-j) $NaYGeO_4$:xBi^{3+} and $Na_{0.75}Li_{0.25}YGeO_4$:0.01Bi^{3+} synthesized at 1200 °C during 24h.

Since the TL peak for $NaYGeO_4$:0.01Bi^{3+} is near 300 K in Fig. 5.7a), Bi^{3+} persistent luminescence is expected at RT. To optimize the charge carrier storage capacity for obtaining stronger Bi^{3+} afterglow, synthesis optimization is explored. Fig. 5.7b) shows that the TL peak maximum changes between 269 and 300 K depending on the synthesis temperature at 1100-1300 °C. Note that a ~4.8 times stronger TL peak near 300 K appears when the synthesis temperature is increased from 1100 °C to 1200 °C. The stronger Bi^{3+} afterglow is evidenced by the photographs in Fig. 5.7c) and the RT isothermal decay curves in Fig. 5.7d). Fig. 5.7e)-f) shows the TL glow curves, and photographs for $NaYGeO_4$:0.01Bi^{3+} synthesized at 1200 °C with different duration time. An about 7 times stronger Bi^{2+} TL peak near 358 K appears with increasing the duration time from 3h to 24h, which results in stronger Bi^{3+} afterglow as shown in Fig. 5.7g). For the $NaYGeO_4$:0.01Bi^{3+} sample synthesized at 1200 °C during 12h, the Bi^{2+} peak near 358 K in Fig. 5.7e) is ~58 K higher than the Bi^{2+} peak near 300 K in Fig. 5.7b). In the above RT TL experiment, a large part of the TL glow has already faded at the start of the recording. The 58 K shift is therefore attributed to a peak cleaning effect at RT as is further demonstrated in Fig. S5.10.

Fig. 5.7h)-7i) shows the TL glow curves, and photographs for $NaYGeO_4$:xBi^{3+} and $Na_{0.75}Li_{0.25}YGeO_4$:0.01Bi^{3+} samples synthesized at 1200 °C during 24h. The TL glow near 300-400 K appears to increase ~2.5 times when x changes from 0.01

to 0.001 or when 25% Na^+ is replaced by Li^+, which results in strong Bi^{3+} afterglow in Fig. 5.7j). The ratios of integrated TL between 300-723 K of $NaYGeO_4{:}xBi^{3+}$ and $Na_{0.75}Li_{0.25}YGeO_4{:}0.01Bi^{3+}$ to that of commercial phosphors $SrAl_2O_4$:Eu,Dy (G-300M, LumiNova), BaFBr(I):Eu (Agfa-Gevaert), and $Sr_2MgSi_2O_7$:Eu,Dy are provided in the legend of Fig. 5.7h).

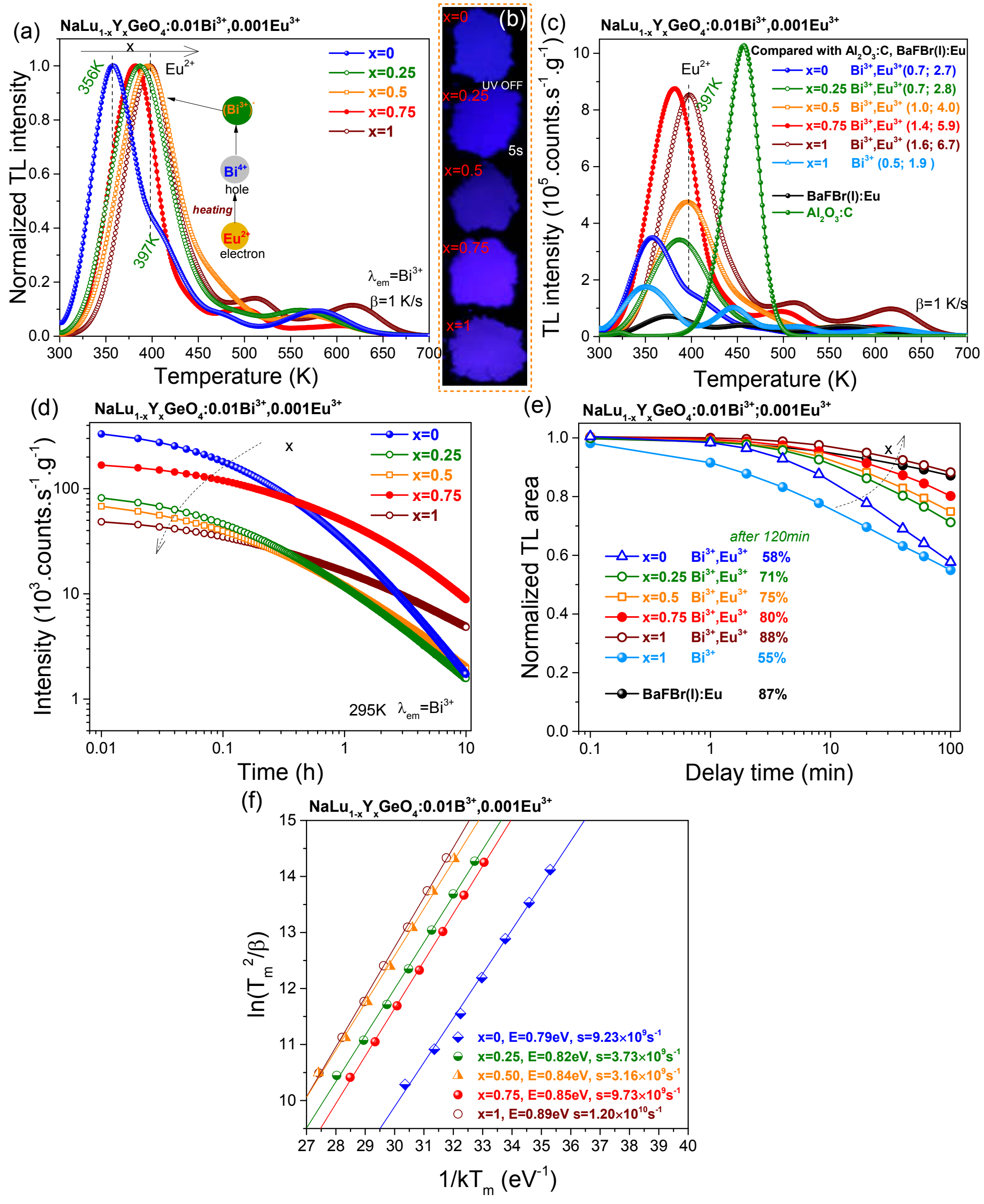

Fig. 5.8. (a), (c) TL glow curves at β=1 K/s monitoring Bi^{3+} emission, (b) photographs after Hg lamp irradiation for 5s, (d) RT isothermal decay curves, (e) TL fading characteristics, and (f) variable heating rate plots for $NaLu_{1-x}Y_xGeO_4$:$0.01Bi^{3+}$,$0.001Eu^{3+}$. The applied heating rates were 0.08, 0.15, 0.3, 0.63, 1.25, 2.5, and 5 K/s.

Fig. 5.1a) suggests that Eu^{3+} may act as a ~0.5±0.5 eV deeper electron trap than Bi^{3+}. The storage phosphor properties of Bi^{3+},Eu^{3+}-codoped $NaLu_{1-x}Y_xGeO_4$ solid solutions were therefore explored. Fig. 5.8a) and 8c) show the normalized and unnormalized TL glow curves for $NaLu_{1-x}Y_xGeO_4$:$0.01Bi^{3+}$,$0.001Eu^{3+}$ after β irradiation. The ratios of integrated TL between 300-700 K of $NaLu_{1-x}Y_xGeO_4$:$0.01Bi^{3+}$,$0.001Eu^{3+}$ to that of commercial storage phosphor BaFBr(I):Eu or a Al_2O_3:C single crystal (Landauer Inc.) are shown in the legend of Fig. 5.8c). The maximal ratios of 6.7 and 1.6 appear when x=1. With increasing x, the TL glow peak attributed to electron release from Eu^{2+} near 356 K shifts ~41 K towards higher temperature in Fig. 5.8c), which gives rise to decreased initial Bi^{3+} afterglow in Fig. 5.8d) and less TL fading in Fig. 5.8e). For the x=1 phosphor after 2h waiting time, the integrated TL intensity remains 88%, which is almost the same as that of BaFBr(I):Eu (87%). Note that the Eu^{2+} TL peak temperature of 397 K in Fig. 5.8c) for the x=1 phosphor is about 12 K lower than that of the Eu^{2+} TL peak in Fig. 5.6c). In the TLEM experiments in Fig. 5.6, there is about 0.5 h delay time between γ-ray charging and TL recording, and a small part of the Eu^{2+} TL glow has already faded at RT before the start of TL recording.

The trapping depths for $NaLu_{1-x}Y_xGeO_4$:$0.01Bi^{3+}$,$0.001Eu^{3+}$ were determined by utilizing a variable heating rate plot and equation[19, 52-54]:

$$\ln\left(\frac{T_m^{\,2}}{\beta}\right)=\frac{E}{kT_m}+\ln\left(\frac{E}{ks}\right) \tag{5.1}$$

where β is the heating rate that can change from 0.08 to 5 K/s, k represents the Boltzmann constant (8.62×10^{-5} eV/K), and s stands for the frequency factor (s^{-1}). Fig. 5.8f) shows the variable heating rate plots for $NaLu_{1-x}Y_xGeO_4$:$0.01Bi^{3+}$, $0.001Eu^{3+}$ that provide the trap depths as shown in column 4 and the frequency factors in column 2 of Table 5.1.

Because the Eu^{3+} content is very low, we assumed that the above-derived s values also apply to $NaLu_{1-x}Y_xGeO_4$:$0.01Bi^{3+}$. Assuming a first-order TL-recombination kinetic, the corresponding trapping depths E (eV) for the Bi^{2+} TL peaks in $NaLu_{1-x}Y_xGeO_4$:$0.01Bi^{3+}$ in Fig. 5.7a) can then be derived by using the temperature T_m at the maximum of the TL glow curve and solving Eq. (5.1) with β=1 K/s and s values in column 2. The obtained results are provided in column 6 of

Table 5.1. Actually, first-order kinetics does not apply and one should regard the obtained values as indicative.

Table 5.1. TL results for solid solutions $NaLu_{1-x}Y_xGeO_4$:0.01Bi^{3+} and $NaLu_{1-x}Y_xGeO_4$: 0.01Bi^{3+},0.001Eu^{3+} giving the frequency factor s (s^{-1}) and trapping depths E (eV) for the Eu^{2+} and Bi^{2+} glow peaks (T_m).

x	s	T_m Eu^{2+} (K)	Eu E (eV)	T_m Bi^{2+} (K)	Bi E (eV)
0	9.23×10^9	356	0.79	226	0.49
0.25	3.73×10^9	386	0.82	254	0.53
0.50	3.16×10^9	394	0.84	285	0.59
0.75	9.73×10^9	382	0.85	277	0.61
1	1.20×10^{10}	397	0.89	295	0.65

To further unravel the charge carrier trapping processes regarding Bi^{3+}, Fig. 5.9a) and 9b) show the TL excitation (TLE) plots for Bi^{3+} and Bi^{3+},Eu^{3+}-codoped $NaYGeO_4$. Additional TLE plots under other synthesis conditions or Eu^{3+} concentration for $NaLu_{1-x}Y_xGeO_4$ are given in Fig. S5.15. All traps corresponding with the TL peaks near 383 K (from Bi^{2+}), 492, 562, or 666 K in Fig. 5.9a) or the Eu^{2+} TL peak near 422 K in Fig. 5.9b) can be charged by photons near 230 nm. A comparison of TLE plots with photoluminescence spectra is shown in Fig. 5.9c). For all samples, a broad thermoluminescence excitation band peaked at about 230 nm and ranging between 200-270 nm appears in Fig. 5.9c3)-c11). Its width and peak position overlaps with that of the Bi^{3+} D-band in Fig. 5.9c1) or VB→Eu^{3+} CT band in Fig. 5.9c2).

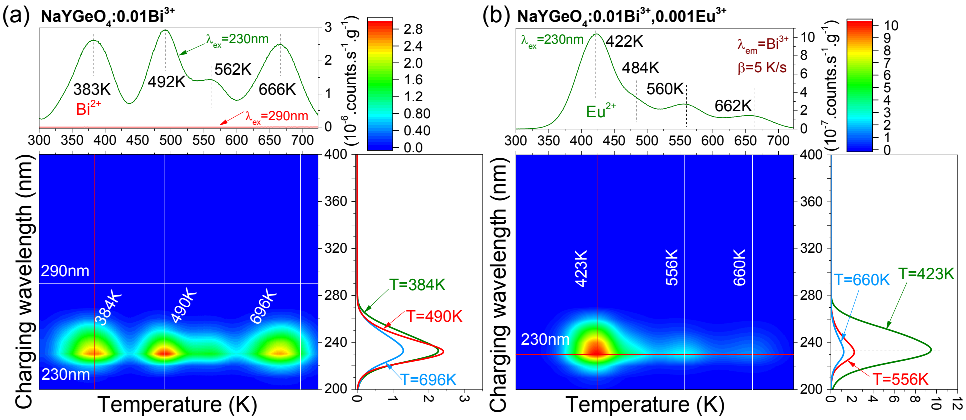

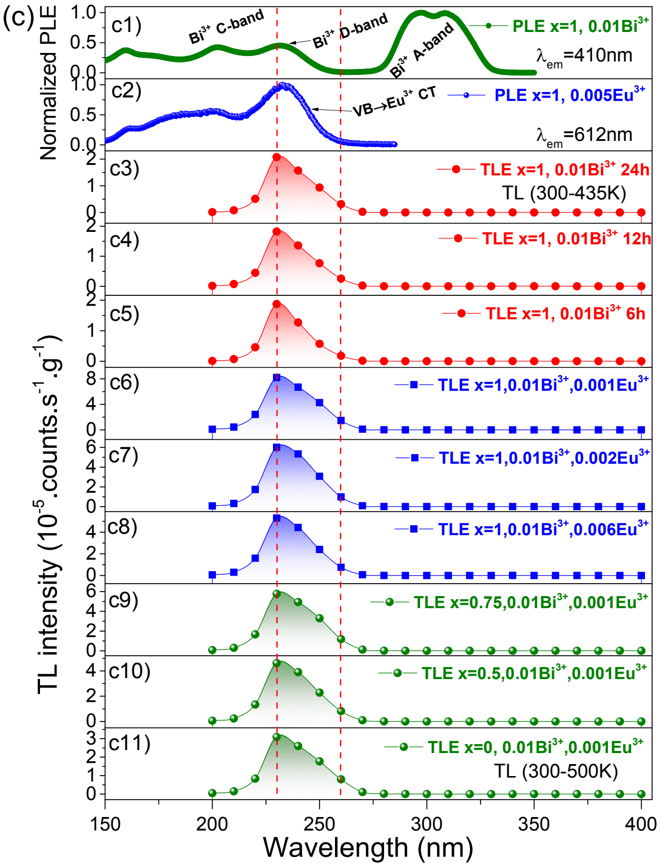

Fig. 5.9. TL excitation (TLE) plots at β=5 K/s while monitoring the Bi^{3+} emission for (a) $NaYGeO_4:0.01Bi^{3+}$ synthesized at 1200 ºC during 24h, (b) $NaYGeO_4:0.01Bi^{3+},0.001Eu^{3+}$, and (c) $NaLu_{1-x}Y_xGeO_4:0.01Bi^{3+},0.001Eu^{3+}$. The TL glow peak between 300-435 K in a) was integrated to establish the TLE plots in c3)-c5) and for c6)-c11) it is between 300-500 K in b). c1) and c2) shows the photoluminescence excitation spectra for $NaYGeO_4:0.01Bi^{3+}$ at 10 K and $NaYGeO_4:0.005Eu^{3+}$ at RT, respectively.

5.4.3. Evaluating the potential applications for information storage

Fig. 5.10 shows the TL glow curves for $NaYGeO_4:0.01Bi^{3+}$, $NaYGeO_4:0.01Bi^{3+},0.001Eu^{3+}$, and BaFBr(I):Eu. After exposure to water for 0.5h, the TL intensity of BaFBr(I):Eu almost completely disappeared. The integrated TL intensity remains 69% for $NaYGeO_4:0.01Bi^{3+}$, $0.001Eu^{3+}$, 56% for $NaYGeO_4:0.01Bi^{3+}$, 7% for BaFBr(I):Eu, and 81% for $NaLu_{0.25}Y_{0.75}GeO_4:0.01Bi^{3+},0.001Eu^{3+}$ in Fig. S5.16a).

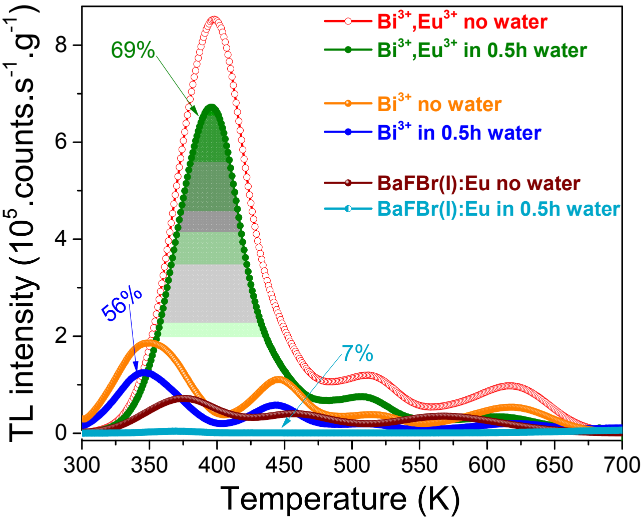

Fig. 5.10. TL glow curves at β=1 K/s for $NaYGeO_4$:0.01Bi^{3+}, $NaYGeO_4$:0.01Bi^{3+},0.001Eu^{3+} and BaFBr(I):Eu after exposure to water after beta irradiation.

The stored information is usually read out using a stimulating photon beam. For comparison with commercial phosphor, Fig. 5.11 shows part of TL glow curves after optical stimulation. Additional plots for other $NaLu_{1-x}Y_xGeO_4$ are shown in Fig. S5.18.

Fig. 5.11 and S5.18 shows that 10s 475 nm LED stimulation liberates ~27, 14, 57, 56, 95, and 41% of the stored charge carriers during β-ray irradiation for $NaYGeO_4$:0.01Bi^{3+}, $NaYGeO_4$:0.01Bi^{3+},0.001Eu^{3+}, $NaYGeO_4$:0.01Bi^{3+},0.002Eu^{3+}, $NaY_{0.75}Lu_{0.25}GeO_4$:0.01Bi^{3+},0.001Eu^{3+}, BaFBr(I):Eu, and Al_2O_3:C, respectively. Note that the relative amount of liberated charge carriers is smaller, but the absolute amount is about 2 and 4 times higher in $NaYGeO_4$:0.01Bi^{3+},0.002Eu^{3+} and $NaY_{0.75}Lu_{0.25}GeO_4$:0.01Bi^{3+},0.001Eu^{3+} than that in BaFBr(I):Eu and Al_2O_3:C, respectively. This means that a lower dose can be used to arrive at the same signal which is beneficial for patients. Fig. S5.18a)-b) shows that charge carriers liberated between 300-425 K are partly transferred to the deeper traps.

Fig. 5.11a)-11b) demonstrates that about 95% of stored information can be erased by increasing the stimulation time to 1200s, indicating potential use as optically stimulated storage phosphors. BaFBr(I):Eu is erased much more efficiently at 475 nm.

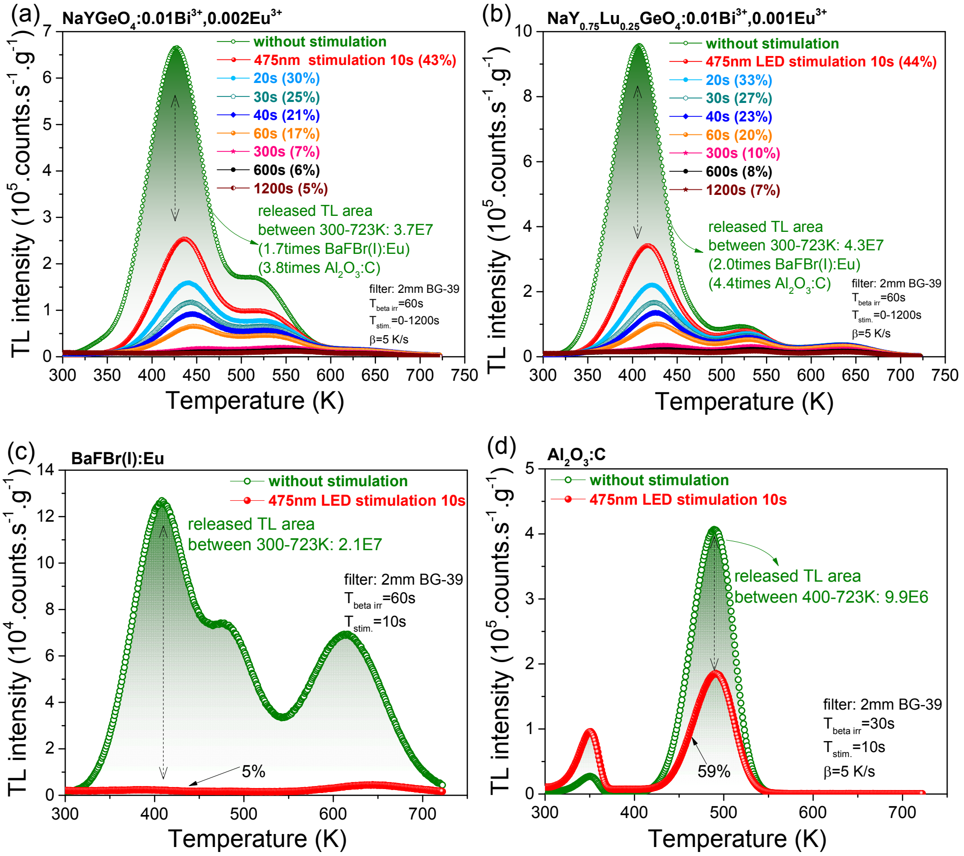

Fig. 5.11. TL glow curves at β=5 K/s for (a) NaYGeO$_4$:0.01Bi^{3+},0.002Eu^{3+}, (b) NaY$_{0.75}$Lu$_{0.25}$GeO$_4$:0.01B^{3+},0.001Eu^{3+}, (c) BaFBr(I):Eu, and (d) Al$_2$O$_3$:C single crystal measured after beta irradiation and after beta irradiation followed by 475 nm LED optical stimulation with different duration.

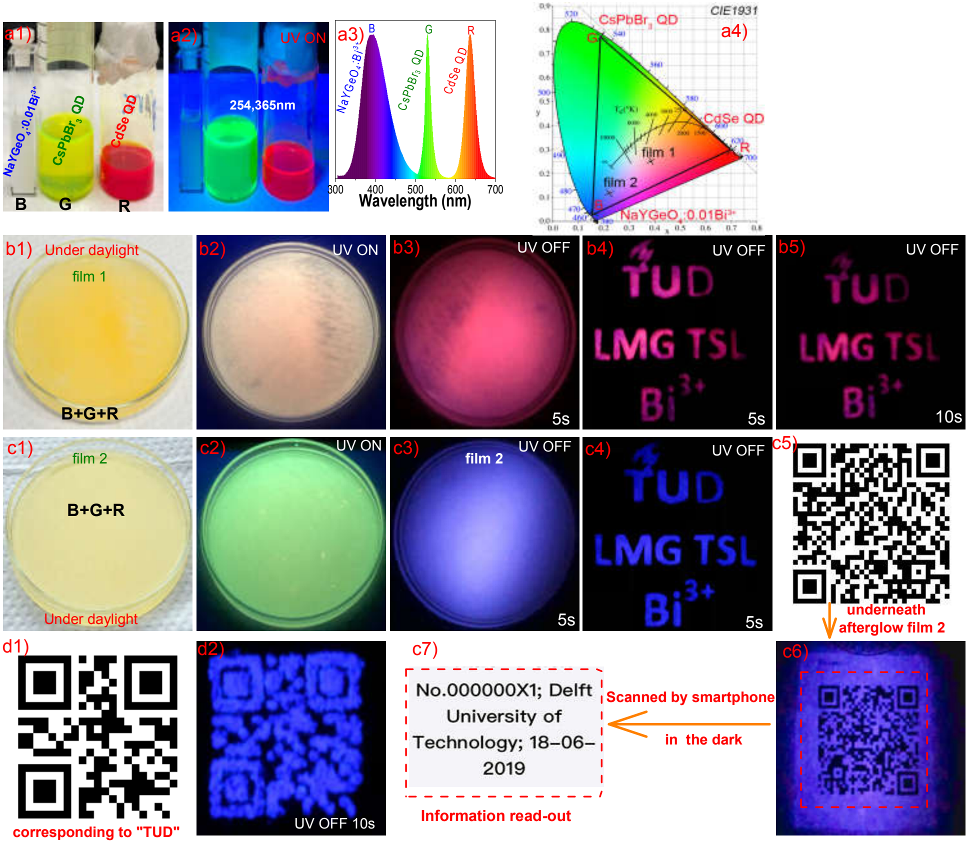

Fig. 5.12. Proof-of-concept colour tuning for anti-counterfeiting application by combining an afterglow film with quantum dot (QD) phosphors. Photographs of NaYGeO$_4$:0.01Bi^{3+}, CsPbBr$_3$ and CdSe QDs under a1) daylight, a2) UV-light, and a3) corresponding PL spectra, and a4) color coordinates. b1)-b5) shows the CdSe QD rich afterglow film 1 and its application to display texts. c1)-c7) shows the CsPbBr$_3$ QD rich film 2 and its application to display texts or a QR code on paper in the dark. d1)-d2) Bi^{3+} afterglow from NaYGeO$_4$:0.01Bi^{3+} to display a QR code in the dark.

To add security features for anti-counterfeiting application, we explored tailoring of the afterglow colour. Fig. 5.12a1)-12a4) shows that CsPbBr$_3$ and CdSe quantum dots (QD) have green or red photoluminescence but no afterglow. Red emission due to an energy transfer from NaYGeO$_4$:0.01Bi^{3+} afterglow to QDs appears in film 1 in Fig. 5.12b3) which is composed of NaYGeO$_4$:0.01Bi^{3+}, CsPbBr$_3$ and CdSe QDs. The afterglow spectrum for film 1 in Fig. S5.22a) shows that the emission from CdSe QD is stronger than that from CsPbBr$_3$ QD and from the Bi^{3+} A-band, resulting in the red colour. Cyan afterglow appears in film 2 in Fig.

5.12c3), where the ratio of CdSe to $CsPbBr_3$ is lower than that in film 1. Fig. 5.12b4)-b5) and c4) shows that texts can be clearly displayed using the red and cyan afterglow.

A QR code was generated by computer software using the text of "No.000000X1; Delft University of Technology; 18-06-2019" and "TUD" as shown in Fig. 5.12c5) and 12d1). One may print the QR code in Fig. 5.12d1) using an afterglow $NaYGeO_4$:0.01Bi^{3+} phosphor. This QR code appears in the dark in Fig. 5.12d2) due to Bi^{3+} afterglow, which has potential anti-counterfeiting application on paper like bank notes.

A paper printed with a QR code using black ink in Fig. 5.12c5) is visible in the dark in Fig. 5.12c6) due to the cyan afterglow from film 2 underneath the paper in Fig. 5.12c3). The QR code can be scanned in the dark with smart phone software to read out the hidden text information of "No.000000X1; Delft University of Technology; 18-06-2019" as shown in Fig. 5.12c7).

$NaYGeO_4$:0.01Bi^{3+},0.001Eu^{3+} phosphor dispersed in a silicone gel film in Fig. 5.13a1) is placed underneath a black mask in Fig. 5.13a2). The text of TUD LMG TSL Bi^{3+} is stored when the 254 nm UV-light goes through the empty area of the mask and charges the film. The text is visible due to Bi^{3+} afterglow in the dark in Fig. 5.13a3). The Bi^{3+} afterglow intensity from $NaYGeO_4$:0.01Bi^{3+},0.001Eu^{3+} decreases rapidly and the text is invisible 60s after switching UV-off. However, after UV-off for 1h, the text appears again in Fig. 5.13a5)-13a6) due to thermally stimulated Bi^{3+} emission upon heating to ~380 K. The similar applies to an X-ray image of a chicken bone stored in the film as shown in Fig. 5.13b1)-13b6). The thermally stimulated Bi^{3+} emission near 380 K in the rectangle area in Fig. 5.13b3)-13b6) is weak because a large part of X-rays has been absorbed by the chicken bone during X-ray exposure.

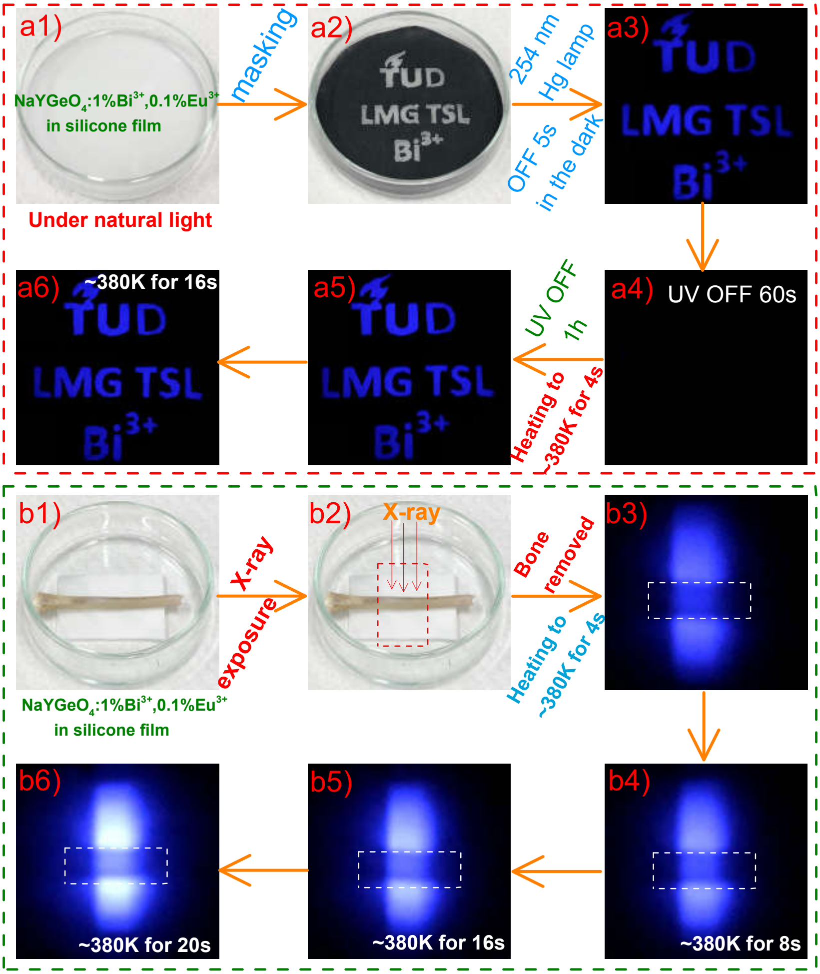

Fig. 5.13. Proof-of-concept information storage using NaYGeO$_4$:0.01Bi^{3+},0.001Eu^{3+} phosphor dispersed in a silicone gel film. Information storage and display of text of TUD LMG TSL Bi^{3+} in a1)-a6) and of an X-ray image of a chicken bone in b1)-b6) is demonstrated. The chicken bone was removed before heating in b3)-b6) and the mask was not removed in a3)-a6). The white rectangle dash line is drawn to guide eyes.

5.5. Discussion

We will first address the photoluminescence spectroscopy regarding the bismuth and lanthanides activated ARE(Si, Ge)O$_4$ (A=Li, Na; RE=Y, Lu). Then, the results are used to establish the so-called vacuum referred binding energy

(VRBE) diagrams. It enables us to compare the binding energy of an electron in impurity defects like Bi^{3+}, Bi^{2+}, or divalent and trivalent lanthanides within the band gap for different compounds with respect to the vacuum energy reference. Finally, we will show how to explore and explain Bi^{3+} persistent luminescence and storage phosphors using the crystal synthesis optimization in $NaLu_{1-x}Y_xGeO_4$ based on the constructed VRBE schemes.

5.5.1. Vacuum referred binding energy diagrams of ARE(Si,Ge)O_4 (A=Li, Na; RE=Y, Lu)

Fig. 5.3a) shows the excitation spectra for $LiLuSi_{1-x}Ge_xO_4$:$0.01Eu^{3+}$ at 10 K. The peaks near 167 nm appear to be the same with increasing x. The same applies to the excitation peak near 160 nm in Fig. 5.5, which is all attributed to an artefact from the deuterium lamp correction. The Eu^{3+} charge transfer (CT) energy is known as the energy to excite an electron from the valence band top to Eu^{3+} generating Eu^{2+} in its $4f^7$ ground state[55]. The VRBE in the Eu^{2+} ground state is always near -4 eV for oxide compounds[56]. It means that the Eu^{3+}-CT band energy provides direct information about the position of the valence band top. Fig. 5.3a) shows that the Eu^{3+}-CT band near 5.56 eV for x=0 slightly shifts to 5.44 eV for x=1. Considering the Eu^{3+}-CT energy lowering in $LiLuSi_{1-x}Ge_xO_4$, the valence band top increases by ~0.12 eV with increasing x from 0 to 1. The Eu^{3+}-CT band is near 5.49 eV for $NaLuGeO_4$ in Fig. 5.4a) and 5.46 eV for $NaYGeO_4$ in Fig. S5.3. It means that the VB top VRBE of $NaLuGeO_4$ or $NaYGeO_4$ is similar to that of $LiLuGeO_4$. Considering that CT-band energies are not more accurate than ±0.1 eV. The VRBE at the VB-top for all compounds studied are almost the same. Slight (<0.1 eV) differences can only be revealed by a changing T_m of glow peaks.

Fig. 5.3b)-3c) shows the PL excitation and emission spectra for undoped $LiLuSi_{1-x}Ge_xO_4$ at 10 K. The excitation and emission features are associated with unknown host intrinsic defect(s) and the host exciton creation energies for $LiLuSiO_4$ and $LiLuGeO_4$ cannot be determined with these excitation spectra. From previous work in Refs. [48, 57], the host exciton creation is known to occur near 7.45 eV (166 nm) for $LiLuSiO_4$. Note that a host exciton creation band is absent in the excitation spectrum of $LiLuSiO_4$ in Fig. 5.3b) implying inefficient energy transfer from the host exciton to the intrinsic defect(s).

Fig. 5.4a) shows the excitation spectra for undoped, Eu^{3+} and Bi^{3+} single doped $NaLuGeO_4$ at 10 K. The excitation peak near 196.5 nm is common to the undoped and Eu^{3+} doped $NaLuGeO_4$ and is attributed to the host exciton creation. For $NaYGeO_4$:$0.01Eu^{3+}$ in Fig. S5.3a), a similar peak near 195 nm appears indicating that the band gap of $NaLuGeO_4$ is ~0.05±0.1 eV smaller than that of $NaYGeO_4$. The band to band excitation not only generates excitons but also yields emission from host intrinsic defects or dopant like Eu^{3+} in Fig. 5.4b) via excitation energy transfer from the host exciton. Note that a dip near 190 nm appears in the excitation spectrum for $NaLuGeO_4$:$0.01Bi^{3+}$ in Fig. 5.4a). It means that energy transfer from the exciton to Bi^{3+} is much less efficient than that from exciton to Eu^{3+}.

The electron transfer from the Tb^{3+} or Pr^{3+} 4f ground state to the conduction band (CB) was also explored. This transition is known as the intervalence charge transfer (IVCT)[43, 58, 59] which is often observed when the lowest 5d level is higher than the CB-bottom like in $LuNbO_4$[60]. IVCT gives information about the position of the conduction band with respect to the Pr and Tb ground states. The germanium-based compounds often have a low-lying conduction band like in $(Sr, Ca)_3(Y, Lu)_2Ge_3O_{12}$ that leads to a low Ce^{3+} emission quenching temperature[56]. For Ce-doped $NaLuGeO_4$, we observed very weak emission only at 10 K (data not presented here). This means that the relaxed Ce^{3+} 5d level is close below the conduction band bottom and emission from Ce^{3+} 5d-4f is quenched above 10 K. Since the 5d-level of Tb^{3+} and Pr^{3+} is at about the same VRBE as that of Ce^{3+}, they are also close to the CB bottom. This also implies that the $Tb^{3+}\rightarrow$CB or $Pr^{3+}\rightarrow$CB IVCT bands may be observed in $NaLuGeO_4$.

Fig. 5.4c)-4d) shows the excitation spectra for Pr^{3+} or Tb^{3+} doped $NaLuGeO_4$. Three peaks near 207, 236, and 258 nm appear for $NaLuGeO_4$:$0.01Pr^{3+}$ in Fig. 5.4c). The excitation band near 207 nm is common for Pr^{3+} or Tb^{3+} doped samples that is likely associated with host exciton creation at RT. Considering the low-lying conduction band for $NaLuGeO_4$, the lowest energy 258 nm shoulder band is attributed to $Pr^{3+}\rightarrow$CB IVCT and the higher energy band near 238 nm to Pr^{3+} 4f→5d. The similar applies to $LiLuGeO_4$:$0.01Pr^{3+}$ in Fig. S5.5a). About 10 nm longer wavelength bands near 266 nm for $NaLuGeO_4$:$0.005Tb^{3+}$ in Fig. 5.4d) and near 270 nm for $LiLuGeO_4$:$0.01Tb^{3+}$ in Fig. S5.5b) appear. In Tb^{3+} or Pr^{3+} doped $LuNbO_4$[43], the band due to $Tb^{3+}\rightarrow$CB IVCT is present at ~10 nm longer wavelength than that of $Pr^{3+}\rightarrow$CB IVCT. Here the bands near 266 and 270 nm are attributed to $Tb^{3+}\rightarrow$CB IVCT.

For the method to establish VRBE schemes like in Fig. 5.1 using spectroscopic data compiled in Table 5.2 we refer to Refs. [42, 44, 46]. For each compound, we used a U-value of 6.90 eV which then determines the VRBE in the Eu^{2+} ground state but also for all other divalent and trivalent lanthanides. The $E_{Eu}^{3+,CT}$ energy then defines E_V and adding E^{ex} plus the exciton binding energy provides E_C. One may equally well add the IVCT-band energies for Pr^{3+} and Tb^{3+} to their ground state energies to obtain E_C. In Table 5.2 we adopted energies for E_C that are consistent with both methods. It also supports the assignment of the excitation band near 195-205 nm in Ge based $NaREGeO_4$ (RE=Y, Lu) compounds in Fig. 5.4a) and S5.3a) to exciton creation. Note that our band gap E^{ex} near 6.3 eV and $E_{Eu}{}^{3+,CT}$ energy 5.49 eV for $NaLuGeO_4$ are quite different from those used by Wang *et al.* [41] (4.4 eV and 3.77 eV).

Table 5.2. Parameters and data utilized to construct the VRBE schemes of the $NaYGeO_4$ related compound family in eV, and level energies determined from these schemes.

Compound	U	$E_{Eu}{}^{2+}$	$E_{Eu}{}^{3+,CT}$	E_V	E^{ex}	E_C	$E_{Bi}{}^{3+,CT}$	$E_{Bi}{}^{3+}$
$NaYGeO_4$	6.90	-4.02	5.46	-9.48	6.49	-2.65	5.35	-8.00
$NaLuGeO_4$	6.90	-4.02	5.49	-9.51	6.45	-2.72	5.34	-8.07
$LiLuGeO_4$	6.90	-4.02	5.44	-9.46	6.37	-2.76	5.37	-8.13
$LiLuSiO_4$	6.90	-4.02	5.56	-9.58	7.45	-1.69	5.99	-7.68
$LiYSiO_4$	6.90	-4.02	5.51	-9.53	7.55	-1.52	5.98	-7.50

Fig. 5.4a) shows the excitation spectrum for $NaLuGeO_4$:$0.01Bi^{3+}$ at 10 K. An empirical equation regarding the relation between the Bi^{3+} A-band (E_A) and the C-band (E_{BiC}) was proposed as Eq. (5.2)[61]:

$$E_{BiC} = 3.236 + 2.290 \times (E_A - 2.972)^{0.856} \tag{5.2}$$

With the Bi^{3+} $^1S_0 \rightarrow {}^3P_1$ A-band near 296 and 308 nm for $NaLuGeO_4$:$0.01Bi^{3+}$, the Bi^{3+} $^1S_0 \rightarrow {}^1P_1$ C-band is then predicted near 208-220 nm. This value is close to the experimentally observed high-energy band near 202 nm which is therefore attributed to the Bi^{3+} C-band. The relatively low-energy band near 232 nm is then assigned to the Bi^{3+} to CB charge transfer or D-band. It means that afterglow or storage phosphors can be charged via Bi^{3+} D-band excitation. This is consistent with the TL excitation spectra in Fig. 5.9.

With the Bi^{3+} A-band near 278 and 290 nm for $LiLuSiO_4$:$0.01Bi^{3+}$ in Fig. 5.5e), the Bi^{3+} C-band is predicted by Eq. (5.2) near 192-203 nm which resembles the experimental band near 190 nm. We therefore attribute the band near 190 nm to the Bi^{3+} C-band and the band near 207 nm to the Bi^{3+} D-band. Subtracting the Bi^{3+} D-band energies in column 8 from E_C, the VRBEs in Bi^{3+} $^1S_0$ ground states are obtained as listed in column 9 of Table 5.2. These values are consistent with Ref. [44] where the VRBE in the $^1S_0$ ground state of Bi^{3+} in a wide range of oxide compounds was found between -5 and -10 eV. A study by Awater *et al.* [45] showed that the VRBE in the Bi^{2+} $^2P_{1/2}$ ground state is near 3.5±0.5 eV in oxide compounds. We assume that this Bi^{2+} value also applies to ARE(Si, Ge)O_4 (A=Li, Na; RE=Y, Lu) in this work. For $NaREGeO_4$ (RE=Y, Lu), the predicted VRBE in the Bi^{2+} ground state will be compared with the TL results in the next section.

Fig. 5.5a)-5b) shows the excitation and emission spectra for $Na_{1-x}Li_xLuGeO_4$:0.01Bi^{3+} solid solutions. With increasing x, the Bi^{3+} A-, C-, or D-excitation bands remain stationary, while the Bi^{3+} A-band emission gradually shifts from 418 to 360 nm. This means that more Li leads to weaker host lattice relaxation resulting in emission of higher energy photons. Similar result emerges in $LiLu_{1-x}Y_xSiO_4$:0.01Bi^{3+} in Fig. 5.5e)-5f), where an about 7 nm larger Stokes shift appears with increasing x. Apparently, replacing Lu by Y contributes to slightly stronger host lattice relaxation. For $LiLuSi_{1-x}Ge_xO_4$:0.01Bi^{3+} in Fig. 5.5c)-d), a ~14 nm smaller Stokes shift appears. Considering the excitation band shifting, it is likely associated with the nephelauxetic effect when Si is replaced by Ge.

5.5.2. Designing Bi^{3+} afterglow and storage phosphor via conduction band engineering and crystal synthesis optimization

The stacked VRBE diagram for $NaREGeO_4$ (RE=Y, Lu) in Fig. 5.1a) illustrates that Bi^{3+} will act as a ~1.5 eV deep hole capturing centre, while Bi^{3+} and Eu^{3+} will act as ~0.8±0.5 and ~1.3 eV deep electron capturing centres in $NaLuGeO_4$. Electrons trapped to form Bi^{2+} or Eu^{2+} are then expected to be liberated at a lower temperature than holes captured at Bi^{4+} to generate Bi^{3+} typical emission. The stacked VRBE diagram in Fig. 5.1a) and column 7 of Table 5.2 further shows that the VRBE at the conduction band bottom (E_C) slightly changes when replacing Lu for Y in $NaREGeO_4$. It means that one may tailor the glow peak temperature due to electron liberation from Eu^{2+} or Bi^{2+} and recombination with holes at Bi^{4+} through engineering the VRBE at the CB-bottom.

The results for $NaLu_{1-x}Y_xGeO_4$ solid solutions in Fig. 5.7a) and 8a) show this tailoring. With increasing x, the TL glow peak related to electron release from Bi^{2+} shifts about 69 K from 226 to ~295 K in $NaLu_{1-x}Y_xGeO_4$:0.01Bi^{3+} and the TL peak related to electron release from Eu^{2+} shifts about 41 K from 356 to 397 K in $NaLu_{1-x}Y_xGeO_4$:0.01Bi^{3+},0.001Eu^{3+}. For the trap depth difference, a value of ~0.1 or ~0.16 eV is respectively derived from the Eu^{2+} or Bi^{2+} TL peaks in Table 5.1. This means that the CB-bottom moves up about 0.1-0.16 eV when Lu is replaced by Y in $NaLu_{1-x}Y_xGeO_4$. This is consistent with the 0.07 eV difference in the VRBE scheme in Fig. 5.1a) when considering the error margins in the VRBE scheme based on broad CT-band transitions and the errors in the derived trap depth by TL measurement[19]. The above TL results also support our assumption that the VRBE in the Bi^{2+} ground state is near -3.5±0.5 eV[45] for $NaREGeO_4$ (RE=Y, Lu). More specifically, with the Bi^{3+} electron trap depth in column 6 of Table 5.1 and E_C in column 7 of Table 5.2, the VRBE in Bi^{2+} $^2P_{1/2}$ ground state is determined to be near -3.2 and -3.3 eV for $NaLuGeO_4$ and $NaYGeO_4$, respectively.

Bi^{3+} afterglow appears when the TL glow peak for electron release from Bi^{2+} nicely shifts to near 295 K with increasing x in $NaLu_{1-x}Y_xGeO_4$ in Fig. 5.7a). The Bi^{2+} TL peak and afterglow intensity are found to be enhanced via optimizing synthesis temperature in Fig. 5.7b)-7d) and synthesis duration time in Fig. 5.7e)-7g). Note that the Bi^{2+} TL peak maximum changes between 269 and 300 K with increasing temperature from 1100 to 1300 ^{o}C, implying that the VRBE at the conduction band and/or the Bi^{2+} ground state slightly (~0.1 eV) depends on the synthesis temperature. Fig. 5.7e) shows that the Bi^{2+} TL peak intensity near 358 K increases about 7 times when the synthesis duration time increases from 3h to 24h at 1200 ^{o}C. Small crystals about 1-5 μm tend to form aggregates at 3h synthesis duration in Fig. S5.13a). With increasing synthesis duration time to 24 h in Fig. S5.13e)-f), aggregates of about 5-20 μm appear, which may either increase the number of Bi^{3+} electron traps or promote the capture of free electrons during β-ray charging. Fig. 5.7h) shows that the Bi^{2+} TL peak intensity was found to further increase about 2.5 times when the doped Bi^{3+} concentration decreases from 1% to 0.1% or when 25% Na^{+} is replaced by Li^{+} to form solid solution $Na_{0.75}Li_{0.25}YGeO_4$: $0.01Bi^{3+}$. The crystal synthesis optimization and composition modulation showed that one may engineer afterglow phosphor performance, and here the optimized TL intensity of both $NaYGeO_4$:$0.001Bi^{3+}$ and $Na_{0.75}Li_{0.25}YGeO_4$:$0.01Bi^{3+}$ is about 4 and 3 times higher than that of the commercial $SrAl_2O_4$:Eu,Dy and BaFBr(I):Eu phosphors after β-irradiation in Fig. 5.7h).

With increasing x in $NaLu_{1-x}Y_xGeO_4$:$0.01Bi^{3+}$,$0.001Eu^{3+}$, the Eu^{2+} glow peak, like that of Bi^{2+} above, shifts towards higher temperature, which leads to the formation of a Bi^{3+} storage phosphor in Fig. 5.8c). This is consistent with the decrease of the initial Bi^{3+} afterglow intensity in Fig. 5.8d) and the weaker TL fading in Fig. 5.8e). Fig. S5.12a) shows the TL glow peaks for $NaYGeO_4$:$0.01Bi^{3+}$,xEu^{3+}. The TL peak intensity first increases, and then decrease gradually when x>0.1%. Appropriate content of 0.1% Eu^{3+} can produce enough Eu^{3+} electron traps but more Eu^{3+} also leads to an enhanced energy transfer from Bi^{3+}→Eu^{3+} leading to increased Eu^{3+} emission in Fig. 5.6b)-6d) to which the used photomultiplier tube is not sensitive. This slow Eu^{3+} 4f-4f transition is not suitable for an optically stimulated storage phosphor. Note that Bi^{3+} emission near 350-500 nm in Fig. S5.3b) with 0.33 μs decay time in Fig. S5.24 appears to match well with the traditional photomultiplier tube.

The band at 230 nm in the RT thermoluminescence excitation (TLE) spectra of $NaLu_{1-x}Y_xGeO_4$:$0.01Bi^{3+}$ or $0.01Bi^{3+}$,$0.001Eu^{3+}$ in Fig. 5.9c3)-c11) coincides with the Bi^{3+} D-band in Fig. 5.9c1) but also the VB→Eu^{3+} CT-band in Fig. 5.9c2). During D-band excitation like in Fig. 5.1b), electrons are excited from the Bi^{3+} $^1S_0$ ground state to the conduction band and are subsequently captured at intentional defects such as Bi^{3+} and Eu^{3+} or other host intrinsic defects like those responsible for the TL peaks near 492, 562, and 666 K in Fig. 5.9a). For VB→Eu^{3+} CT-band excitation, electrons are excited from the valence band to Eu^{2+} 4f^7 ground state and holes are produced in the valence band that can subsequently be trapped by intrinsic host hole traps or a Bi^{3+} hole trap centre to form Bi^{4+}[19, 62]. For both alternatives, Eu^{2+} and Bi^{4+} are created. In the former one additional intrinsic electron traps are charged and in the latter one additional intrinsic hole traps are charged. Fig. 5.7a) shows that the electrons captured at Bi^{2+} in NaYGeO$_4$ have already gone because of recombination with holes at Bi^{4+} near 300 K. Therefore, the Eu^{2+} TL glow peak near 422 K, and other TL peaks near 484, 560, and 662 K in NaYGeO$_4$:0.01Bi^{3+},0.001Eu^{3+} in Fig. 5.9b) cannot be attributed to hole release from Bi^{4+} or other host intrinsic hole traps to recombine with electrons at Bi^{2+} giving Bi^{3+} emission. Note that these TL peaks at ~484, 560, and 662 K can also be observed in NaYGeO$_4$:0.01Bi^{3+} in Fig. 5.9a). The charging route in NaYGeO$_4$:0.01Bi^{3+},0.001Eu^{3+} is then likely realized via the Bi^{3+} D-band instead of the VB→Eu^{3+} CT-band. During TL-readout in Fig. 5.9a)-9b), the electrons first liberate from Bi^{2+}, Eu^{2+}, or host intrinsic defects to recombine with holes at Bi^{4+} to produce Bi^{3+} A-band emission and Eu^{3+} 4f-4f emission via energy transfer from Bi^{3+}. Based on the VRBE scheme for NaYGeO$_4$ in Fig. 5.1b), the Bi^{3+} excited $^3P_1$ state is ~1.2 eV below the CB-bottom. This gap is too large to enable effective thermal ionization of an electron from the $^3P_1$ excited state to the CB-bottom at RT. This explains why Bi^{3+} has an intense A-band excitation but A-band excitation cannot charge the phosphor in Fig. 5.9.

5.5.3. Anti-counterfeiting application and information storage using Bi^{3+} afterglow and storage phosphors

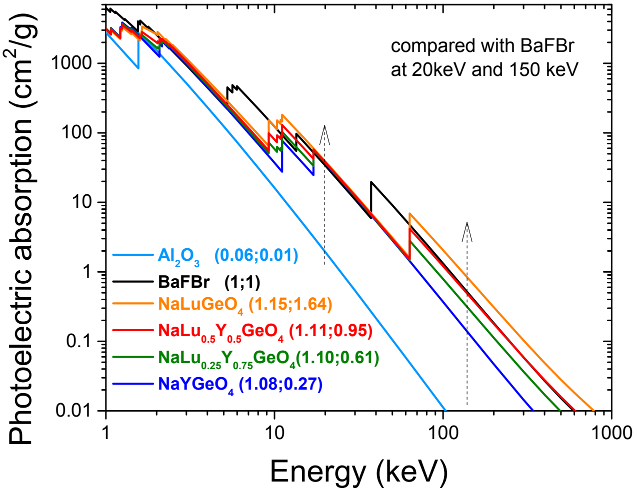

Fig. 5.14. The photoelectric absorption coefficient for $NaLu_{1-x}Y_xSiO_4$, Al_2O_3, and BaFBr. The arrows demonstrate the characteristic energies for mammography at 20 keV and bone radiography at 150 keV.

Fig. 5.14 shows the photoelectric absorption coefficient for $NaLu_{1-x}Y_xSiO_4$ (x=0, 0.5, 0.75, and 1). At 20 keV, $NaLu_{1-x}Y_xSiO_4$ has 10% more absorption than BaFBr. This implies that a $NaLu_{1-x}Y_xSiO_4$ phosphor receives the same dose as BaFBr as a lower X-ray exposure to the patient. At E=150 keV, the photoelectric absorption ratio of $NaLu_{1-x}Y_xSiO_4$ to BaFBr increases from 0.27 for x=1 to 1.64 for x=0 because more lutetium ions lead to more photoelectric absorption of X-rays.

We concluded that only the Bi^{3+} D-band near 230 nm can charge $NaYGeO_4$:$0.01Bi^{3+}$ and $NaYGeO_4$:$0.01Bi^{3+}$,$0.001Eu^{3+}$ phosphors. It means that it is not necessary to keep the storage phosphor $NaYGeO_4$:$0.01Bi^{3+}$,$0.001Eu^{3+}$ in dark during X-ray charging. To develop a Bi^{3+} afterglow phosphor that can be charged by sunlight, one has to use a compound with a relatively low energy Bi^{3+} D-band. $CaMoO_4$[63] with 3.83 eV and $ScVO_4$[64] with 3.49 eV are such compounds. One may also try compounds like $Y_3Ga_5O_{12}$[44] in which the Bi^{3+} $^3P_1$ excited state is close to the CB-bottom.

The red emission in Fig. 5.12b3) is attributed to a reabsorption process of $NaYGeO_4$:$0.01Bi^{3+}$ afterglow by $CsPbBr_3$ and CdSe QDs. One supporting evidence is the spectral overlap between the Bi^{3+} A-band emission near 350-500 nm in Fig. 5.12a3) and the broad 200-475 nm excitation band for $CsPbBr_3$ and CdSe QDs[65, 66] in Fig. S5.23. Another one is that a large decrease of lifetime of the Bi^{3+} $^3P_1 \rightarrow {}^1S_0$ is not observed in films 1 and 2 as compared with $NaYGeO_4$:$0.01Bi^{3+}$ in Fig. S5.24. Note that the emission of $CsPbBr_3$ QD near 520 nm overlaps with the excitation spectrum of CdSe QD in Fig. S5.23. This means that the green emission of $CsPbBr_3$ QD can partly be re-absorbed by CdSe QD. Decreasing the ratio of CdSe to $CsPbBr_3$ QD can generate less red emission from CdSe QD, which leads to the colour change from red in film 1 to cyan in film 2.

5.6. Conclusions

A design principle to discover, develop, and optimize new afterglow and storage phosphors for energy storage was demonstrated by combining vacuum referred binding energy (VRBE) diagrams, band structure engineering, and crystal synthesis optimization. Based on previous research for the $LiLuSiO_4$ compound, the ARE(Si,Ge)O_4 (A=Li, Na; RE=Y, Lu) crystal system was selected after screening the Pearson's crystal data. Low-temperature spectroscopy for lanthanides and bismuth-doped ARE(Si,Ge)O_4 was first studied. This was used to establish the stacked VRBE schemes for ARE(Si,Ge)O_4 with the VRBE in lanthanide and bismuth energy levels, which guide us in the interpretation of spectra and TL results and eventually to design charge carrier trapping processes. As a demonstration, Bi^{3+} afterglow and storage phosphors were explored in $NaLu_{1-x}Y_xGeO_4$. By combining Bi^{3+} with Bi^{3+} itself or Eu^{3+}, Bi^{3+} emerges to act as deep hole capturing centre, while Bi^{3+} and Eu^{3+} act as less deep electron traps. Trap depth tunable Bi^{3+} afterglow and storage phosphors respectively appears in $NaLu_{1-x}Y_xGeO_4$:0.01Bi^{3+} and $NaLu_{1-x}Y_xGeO_4$:0.01Bi^{3+},0.001Eu^{3+} via changing x resulting in conduction band engineering. More than 28h of Bi^{3+} afterglow was measurable in $NaYGeO_4$:0.01Bi^{3+} due to electron release from Bi^{2+} and recombination with a hole at Bi^{4+}. The charge carrier storage capacity in $NaYGeO_4$:0.01Bi^{3+} was found to increase ~7 times through optimizing synthesis conditions at 1200 °C during 24h. The thermoluminescence (TL) intensity of the optimized $NaYGeO_4$:0.001Bi^{3+} and $NaYGeO_4$:0.01Bi^{3+},0.001Eu^{3+} is ~3, and ~7 times higher than the TL of the commercial X-ray storage phosphor BaFBr(I):Eu, respectively. Proof-of-concept colour tuning for anti-counterfeiting application was demonstrated by mixing the discovered and optimized $NaYGeO_4$:0.01Bi^{3+} afterglow phosphor with perovskite $CsPbBr_3$, and CdSe quantum dots. Information storage application was demonstrated by UV-light or X-ray charged $NaYGeO_4$:0.01Bi^{3+},0.001Eu^{3+} phosphor dispersed in a silicone gel imaging film. This work not only reports excellent afterglow and storage phosphors but more importantly provides a general design principle through combining VRBE scheme guided band structure engineering and crystal synthesis optimization. Therefore, it can enable discovery of new afterglow and storage phosphors for energy storage in a designed way instead of by a traditional trial-and-error approach.

5.7. Acknowledgements

T. Lyu acknowledges the financial support from the China Scholarship Council for his PhD research (Tianshuai Lyu: 201608320151). We thank Dr Adrie J.J. Bos and Jaco Geuchies for providing the Al_2O_3:C single crystal, $CsPbBr_3$ and CdSe quantum dots, and Giacomo B. F. Bosco for SEM measurement at the Delft University of Technology.

5.8. Reference

1. Shi, H.; An, Z., Ultraviolet afterglow. *Nature Photonics* **2019,** 13, (2), 74-75.
2. Gao, Y.; Li, R.; Zheng, W.; Shang, X.; Wei, J.; Zhang, M.; Xu, J.; You, W.; Chen, Z.; Chen, X., Broadband NIR photostimulated luminescence nanoprobes based on CaS:Eu^{2+},Sm^{3+} nanocrystals. *Chemical Science* **2019,** 10, (21), 5452-5460.

3. Fan, W.; Tang, W.; Lau, J.; Shen, Z.; Xie, J.; Shi, J.; Chen, X., Breaking the Depth Dependence by Nanotechnology-Enhanced X-Ray-Excited Deep Cancer Theranostics. *Advanced Materials* **2019,** 31, (12), 1806381.
4. Yang, Y.-M.; Li, Z.-Y.; Zhang, J.-Y.; Lu, Y.; Guo, S.-Q.; Zhao, Q.; Wang, X.; Yong, Z.-J.; Li, H.; Ma, J.-P.; Kuroiwa, Y.; Moriyoshi, C.; Hu, L.-L.; Zhang, L.-Y.; Zheng, L.-R.; Sun, H.-T., X-ray-activated long persistent phosphors featuring strong UVC afterglow emissions. *Light: Science & Applications* **2018,** 7, (1), 88.
5. Dobrowolska, A.; Bos, A. J. J.; Dorenbos, P., High Charge Carrier Storage Capacity in Lithium Lutetium Silicate Doped with Cerium and Thulium. *physica status solidi (RRL) – Rapid Research Letters* **2019,** 13, (3), 1800502.
6. Seggern, H. v., Photostimulable x-ray storage phosphors: a review of present understanding. *Brazilian Journal of Physics* **1999,** 29, 254-268.
7. Cameron, J. R.; Zimmerman, D.; Kenney, G.; Buch, R.; Bland, R.; Grant, R., Thermoluminescent Radiation Dosimetry Utilizing LiF. *Health Physics* **1964,** 10, (1), 25-29.
8. Cameron, J. R.; Daniels, F.; Johnson, N.; Kenney, G., Radiation Dosimeter Utilizing the Thermoluminescence of Lithium Fluoride. *Science* **1961,** 134, (3475), 333-334.
9. McKeever, S. W. S.; Moscovitch, M.; Townsend, P. D., *Thermoluminescence dosimetry materials: properties and uses*. Nuclear Technology Publishing: United Kingdom, 1995.
10. Bedard, A.; Davis, T. D.; Angelopoulos, C., Storage phosphor plates: how durable are they as a digital dental radiographic system. *J Contemp Dent Pract* **2004,** 5, (2), 57-69.
11. Leblans, P.; Vandenbroucke, D.; Willems, P., Storage Phosphors for Medical Imaging. *Materials* **2011,** 4, (6), 1034.
12. Thoms, M.; von Seggern, H.; Winnacker, A., Spatial correlation and photostimulability of defect centers in the x-ray-storage phosphor BaFBr:Eu^{2+}. *Physical Review B* **1991,** 44, (17), 9240-9247.
13. Li, Y.; Gecevicius, M.; Qiu, J., Long persistent phosphors-from fundamentals to applications. *Chemical Society Reviews* **2016,** 45, (8), 2090-2136.
14. Lyu, T.; Dorenbos, P., Designing thermally stimulated 1.06 μm Nd^{3+} emission for the second bio-imaging window demonstrated by energy transfer from Bi^{3+} in La-, Gd-, Y-, and $LuPO_4$. *Chemical Engineering Journal* **2019,** 372, 978-991.
15. Ren, W.; Lin, G.; Clarke, C.; Zhou, J.; Jin, D., Optical Nanomaterials and Enabling Technologies for High-Security-Level Anticounterfeiting. *Advanced Materials* **2019,** 0, (0), 1901430.
16. Liu, Z.; Zhao, L.; Chen, W.; Fan, X.; Yang, X.; Tian, S.; Yu, X.; Qiu, J.; Xu, X., Multiple anti-counterfeiting realized in $NaBaScSi_2O_7$ with a single activator of Eu^{2+}. *Journal of Materials Chemistry C* **2018,** 6, (41), 11137-11143.

17. Sun, Z.; Yang, J.; Huai, L.; Wang, W.; Ma, Z.; Sang, J.; Zhang, J.; Li, H.; Ci, Z.; Wang, Y., Spy Must Be Spotted: A Multistimuli-Responsive Luminescent Material for Dynamic Multimodal Anticounterfeiting and Encryption. *ACS Applied Materials & Interfaces* **2018,** 10, (25), 21451-21457.
18. Zhang, J.-C.; Pan, C.; Zhu, Y.-F.; Zhao, L.-Z.; He, H.-W.; Liu, X.; Qiu, J., Achieving Thermo-Mechano-Opto-Responsive Bitemporal Colorful Luminescence via Multiplexing of Dual Lanthanides in Piezoelectric Particles and its Multidimensional Anticounterfeiting. *Advanced Materials* **2018,** 30, (49), 1804644.
19. Lyu, T.; Dorenbos, P., Charge carrier trapping processes in lanthanide doped $LaPO_4$, $GdPO_4$, YPO_4, and $LuPO_4$. *Journal of Materials Chemistry C* **2018,** 6, (2), 369-379.
20. Smet, P. F.; Botterman, J.; Van den Eeckhout, K.; Korthout, K.; Poelman, D., Persistent luminescence in nitride and oxynitride phosphors: A review. *Optical Materials* **2014,** 36, (11), 1913-1919.
21. Lakshmanan, A. R., Radiation induced defects and photostimulated luminescence process in BaFBr: Eu^{2+}. *physica status solidi (a)* **1996,** 153, (1), 3-27.
22. Schweizer, S., Physics and Current Understanding of X-Ray Storage Phosphors. *physica status solidi (a)* **2001,** 187, (2), 335-393.
23. Takahashi, K.; Kohda, K.; Miyahara, J.; Kanemitsu, Y.; Amitani, K.; Shionoya, S., Mechanism of photostimulated luminescence in $BaFX:Eu^{2+}$ (X=Cl,Br) phosphors. *Journal of Luminescence* **1984,** 31-32, 266-268.
24. Rüter, H. H.; Seggern, H. v.; Reininger, R.; Saile, V., Creation of photostimulable centers in $BaFBr:Eu^{2+}$ single crystals by vacuum ultraviolet radiation. *Physical Review Letters* **1990,** 65, (19), 2438-2441.
25. Seggern, H. v.; Voigt, T.; Knüpfer, W.; Lange, G., Physical model of photostimulated luminescence of x-ray irradiated $BaFBr:Eu^{2+}$. *Journal of Applied Physics* **1988,** 64, (3), 1405-1412.
26. Schweizer, S.; Hobbs, L. W.; Secu, M.; Spaeth, J.-M.; Edgar, A.; Williams, G. V. M., Photostimulated luminescence in Eu-doped fluorochlorozirconate glass ceramics. *Applied Physics Letters* **2003,** 83, (3), 449-451.
27. Riesen, H.; Kaczmarek, W. A., Efficient X-ray Generation of Sm^{2+} in Nanocrystalline $BaFCl/Sm^{3+}$: a Photoluminescent X-ray Storage Phosphor. *Inorganic Chemistry* **2007,** 46, (18), 7235-7237.
28. Yanagida, T.; Okada, G.; Kawaguchi, N., Ionizing-radiation-induced storage-luminescence for dosimetric applications. *Journal of Luminescence* **2019,** 207, 14-21.
29. Xu, J.; Tanabe, S., Persistent luminescence instead of phosphorescence: History, mechanism, and perspective. *Journal of Luminescence* **2019,** 205, 581-620.

30. Van den Eeckhout, K.; Smet, P. F.; Poelman, D., Persistent luminescence in Eu^{2+}-doped compounds: a review. *Materials* **2010,** 3, 2536.
31. Pan, Z.; Lu, Y.-Y.; Liu, F., Sunlight-activated long-persistent luminescence in the near-infrared from Cr^{3+}-doped zinc gallogermanates. *Nat Mater* **2012,** 11, (1), 58-63.
32. Yang, M.-M.; Iqbal, A. N.; Peters, J. J. P.; Sanchez, A. M.; Alexe, M., Strain-gradient mediated local conduction in strained bismuth ferrite films. *Nature Communications* **2019,** 10, (1), 2791.
33. Leng, M.; Yang, Y.; Zeng, K.; Chen, Z.; Tan, Z.; Li, S.; Li, J.; Xu, B.; Li, D.; Hautzinger, M. P.; Fu, Y.; Zhai, T.; Xu, L.; Niu, G.; Jin, S.; Tang, J., All-Inorganic Bismuth-Based Perovskite Quantum Dots with Bright Blue Photoluminescence and Excellent Stability. *Advanced Functional Materials* **2018,** 28, (1), 1704446.
34. Noguchi, R.; Takahashi, T.; Kuroda, K.; Ochi, M.; Shirasawa, T.; Sakano, M.; Bareille, C.; Nakayama, M.; Watson, M. D.; Yaji, K.; Harasawa, A.; Iwasawa, H.; Dudin, P.; Kim, T. K.; Hoesch, M.; Kandyba, V.; Giampietri, A.; Barinov, A.; Shin, S.; Arita, R.; Sasagawa, T.; Kondo, T., A weak topological insulator state in quasi-one-dimensional bismuth iodide. *Nature* **2019,** 566, (7745), 518-522.
35. Han, J.; Pan, F.; Molokeev, M. S.; Dai, J.; Peng, M.; Zhou, W.; Wang, J., Redefinition of Crystal Structure and Bi^{3+} Yellow Luminescence with Strong Near-Ultraviolet Excitation in $La_3BWO_9:Bi^{3+}$ Phosphor for White Light-Emitting Diodes. *ACS Applied Materials & Interfaces* **2018,** 10, (16), 13660-13668.
36. Sun, H.-T.; Zhou, J.; Qiu, J., Recent advances in bismuth activated photonic materials. *Progress in Materials Science* **2014,** 64, 1-72.
37. Swart, H. C.; Kroon, R. E., Ultraviolet and visible luminescence from bismuth doped materials. *Optical Materials: X* **2019,** 2, 100025.
38. Lyu, T.; Dorenbos, P., Bi^{3+} acting both as an electron and as a hole trap in La-, Y-, and $LuPO_4$. *Journal of Materials Chemistry C* **2018,** 6, (23), 6240-6249.
39. Wang, X.; Boutinaud, P.; Li, L.; Cao, J.; Xiong, P.; Li, X.; Luo, H.; Peng, M., Novel persistent and tribo-luminescence from bismuth ion pairs doped strontium gallate. *Journal of Materials Chemistry C* **2018,** 6, (38), 10367-10375.
40. Sun, W.; Pang, R.; Li, H.; Li, D.; Jiang, L.; Zhang, S.; Fu, J.; Li, C., Investigation of a novel color tunable long afterglow phosphor $KGaGeO_4:Bi^{3+}$: luminescence properties and mechanism. *Journal of Materials Chemistry C* **2017,** 5, (6), 1346-1355.
41. Wang, W.; Sun, Z.; He, X.; Wei, Y.; Zou, Z.; Zhang, J.; Wang, Z.; Zhang, Z.; Wang, Y., How to design ultraviolet emitting persistent materials for potential

multifunctional applications: a living example of a $NaLuGeO_4:Bi^{3+},Eu^{3+}$ phosphor. *Journal of Materials Chemistry C* **2017,** 5, (17), 4310-4318.

42. Dorenbos, P., A Review on How Lanthanide Impurity Levels Change with Chemistry and Structure of Inorganic Compounds. *ECS Journal of Solid State Science and Technology* **2013,** 2, (2), R3001-R3011.
43. Dorenbos, P., Charge transfer bands in optical materials and related defect level location. *Optical Materials* **2017,** 69, 8-22.
44. Awater, R. H. P.; Dorenbos, P., The Bi^{3+} 6s and 6p electron binding energies in relation to the chemical environment of inorganic compounds. *Journal of Luminescence* **2017,** 184, 221-231.
45. Awater, R. H. P.; Dorenbos, P., Towards a general concentration quenching model of Bi^{3+} luminescence. *Journal of Luminescence* **2017,** 188, 487-489.
46. Dorenbos, P., Modeling the chemical shift of lanthanide 4f electron binding energies. *Physical Review B* **2012,** 85, (16), 165107.
47. Bos, A. J. J.; van Duijvenvoorde, R. M.; van der Kolk, E.; Drozdowski, W.; Dorenbos, P., Thermoluminescence excitation spectroscopy: A versatile technique to study persistent luminescence phosphors. *Journal of Luminescence* **2011,** 131, (7), 1465-1471.
48. Sidorenko, A. V.; Dorenbos, P.; Bos, A. J. J.; van Eijk, C. W. E.; Rodnyi, P. A., Lanthanide level location and charge carrier trapping in $LiLnSiO_4:Ce^{3+}$, Sm^{3+}, Ln = Y or Lu. *J. Phys.-Condes. Matter* **2006,** 18, (19), 4503-4514.
49. Blasse, G.; Bril, A., Structure and Eu^{3+}-fluorescence of lithium and sodium lanthanide silicates and germanates. *Journal of Inorganic and Nuclear Chemistry* **1967,** 29, (9), 2231-2241.
50. Oomen, E. W. J. L.; Smit, W. M. A.; Blasse, G., Jahn-Teller effect in the emission and excitation spectra of the Sb^{3+} ion in LPO_4 (L=Sc,Lu,Y). *Physical Review B* **1988,** 37, (1), 18-26.
51. Fukuda, A., Jahn-Teller Effect on the Structure of the Emission Produced by Excitation in the A Band of KI: Tl-Type Phosphors. Two Kinds of Minima on the $^3T_{1u}$ Adiabatic Potential-Energy Surface. *Physical Review B* **1970,** 1, (10), 4161-4178.
52. Hoogenstraaten, W., Electron traps in zinc–sulphide phosphors. *Philips Res. Rep* **1958,** 13, 515–693.
53. Chen, R.; Winer, S. A. A., Effects of Various Heating Rates on Glow Curves. *Journal of Applied Physics* **1970,** 41, (13), 5227-5232.
54. Azorín, J., Determination of thermoluminescence parameters from glow curves—I. A review. *International Journal of Radiation Applications and Instrumentation. Part D. Nuclear Tracks and Radiation Measurements* **1986,** 11, (3), 159-166.
55. Liu, X.; Li, L.; Noh, H. M.; Moon, B. K.; Choi, B. C.; Jeong, J. H., Chemical bond properties and charge transfer bands of O^{2-}–Eu^{3+}, O^{2-}–Mo^{6+} and O^{2-}–W^{6+}

in Eu^{3+}-doped garnet hosts $Ln_3M_5O_{12}$ and ABO_4 molybdate and tungstate phosphors. *Dalton Transactions* **2014,** 43, (23), 8814-8825.

56. Luo, H.; Ning, L.; Dong, Y.; Bos, A. J. J.; Dorenbos, P., Electronic Structure and Site Occupancy of Lanthanide-Doped $(Sr, Ca)_3(Y, Lu)_2Ge_3O_{12}$ Garnets: A Spectroscopic and First-Principles Study. *The Journal of Physical Chemistry C* **2016,** 120, (50), 28743-28752.
57. Dobrowolska, A.; Bos, A. J. J.; Dorenbos, P., Synthesis optimization and charge carrier transfer mechanism in $LiLuSiO_4$:Ce, Tm storage phosphor. *Radiation Measurements* **2019,** 127, 106147.
58. Dorenbos, P., The Pr^{3+} and Tb^{3+} ground state locations in compounds obtained from thermoluminescence and intervalence charge transfer studies. *Optical Materials* **2019,** 91, 333-337.
59. Boutinaud, P.; Bettinelli, M.; Diaz, F., Intervalence charge transfer in Pr^{3+}- and Tb^{3+}-doped double tungstate crystals $KRE(WO_4)_2$ (RE=Y, Gd, Yb, Lu). *Optical Materials* **2010,** 32, (12), 1659-1663.
60. Liu, C.; Pan, F.; Peng, Q.; Zhou, W.; Shi, R.; Zhou, L.; Zhang, J.; Chen, J.; Liang, H., Excitation Wavelength Dependent Luminescence of $LuNbO_4$:Pr^{3+}—Influences of Intervalence Charge Transfer and Host Sensitization. *The Journal of Physical Chemistry C* **2016,** 120, (45), 26044-26053.
61. Wang, L.; Sun, Q.; Liu, Q.; Shi, J., Investigation and application of quantitative relationship between sp energy levels of Bi^{3+} ion and host lattice. *Journal of Solid State Chemistry* **2012,** 191, 142-146.
62. Luo, H.; Bos, A. J. J.; Dorenbos, P., Charge Carrier Trapping Processes in RE_2O_2S (RE = La, Gd, Y, and Lu). *The Journal of Physical Chemistry C* **2017,** 121, (16), 8760-8769.
63. Boutinaud, P.; Cavalli, E., Predicting metal-to-metal charge transfer in closed-shell transition metal oxides doped with Bi^{3+} or Pb^{2+}. *Chemical Physics Letters* **2011,** 503, (4), 239-243.
64. Kang, F.; Yang, X.; Peng, M.; Wondraczek, L.; Ma, Z.; Zhang, Q.; Qiu, J., Red Photoluminescence from Bi^{3+} and the Influence of the Oxygen-Vacancy Perturbation in $ScVO_4$: A Combined Experimental and Theoretical Study. *The Journal of Physical Chemistry C* **2014,** 118, (14), 7515-7522.
65. Wei, Y.; Cheng, Z.; Lin, J., An overview on enhancing the stability of lead halide perovskite quantum dots and their applications in phosphor-converted LEDs. *Chemical Society Reviews* **2019,** 48, (1), 310-350.
66. Mongin, C.; Moroz, P.; Zamkov, M.; Castellano, F. N., Thermally activated delayed photoluminescence from pyrenyl-functionalized CdSe quantum dots. *Nature Chemistry* **2018,** 10, 225.

5.9. Supporting information

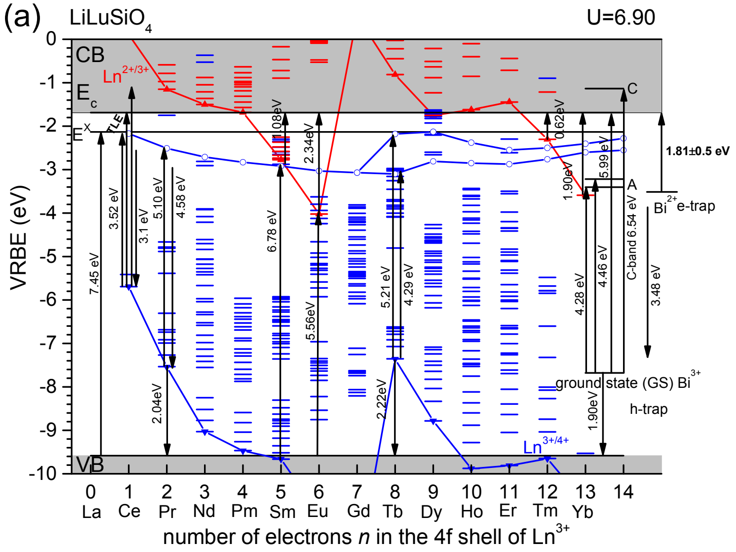

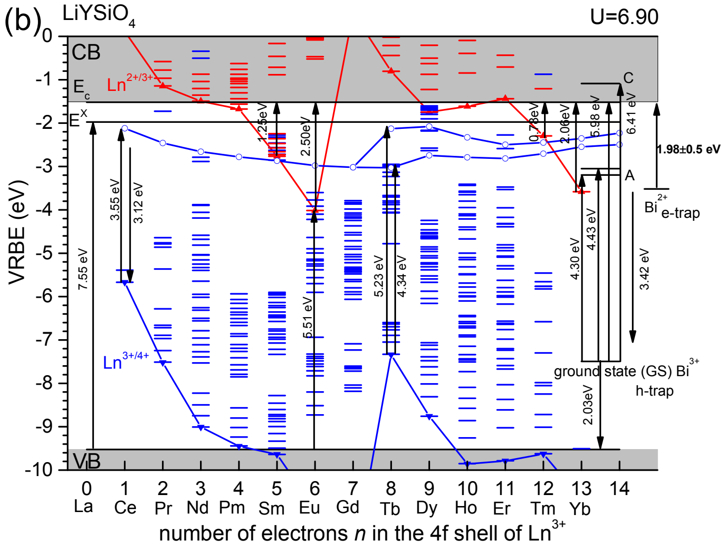

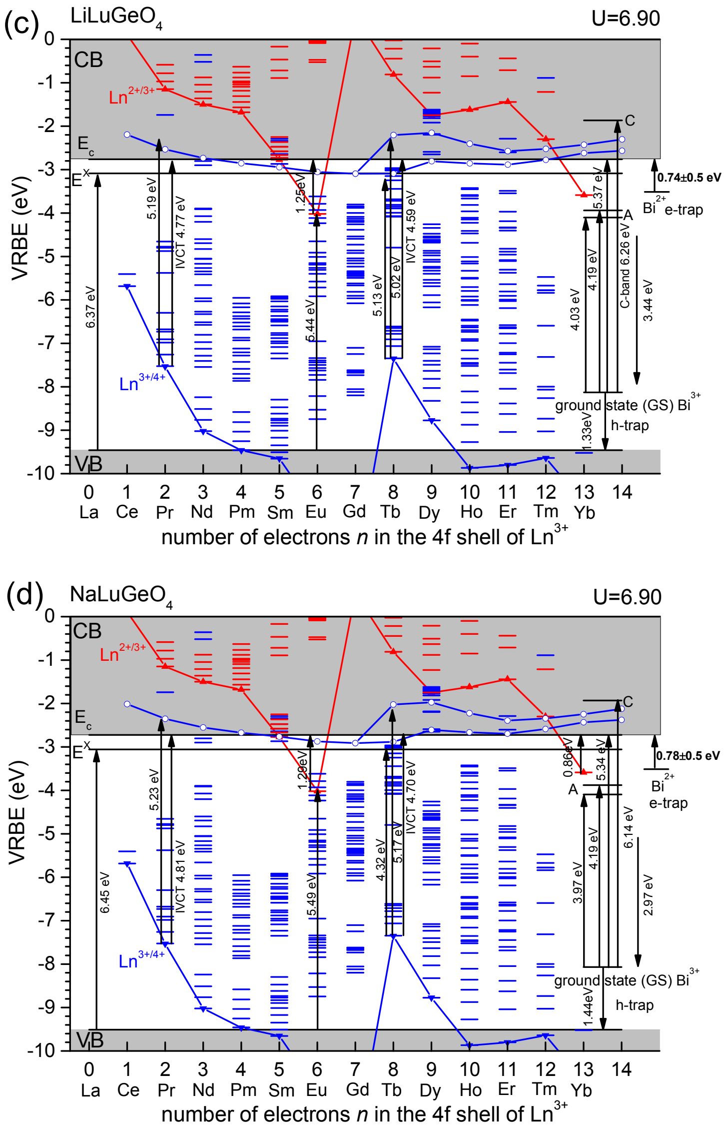

Fig. S5.1. Vacuum referred binding energy (VRBE) schemes of a) $LiLuSiO_4$, b) $LiYSiO_4$, c) $LiLuGeO_4$, and d) $NaLuGeO_4$ providing the VRBE in the ground states of different lanthanides, Bi^{2+}, and Bi^{3+}. Arrows indicate experimentally observed transitions.

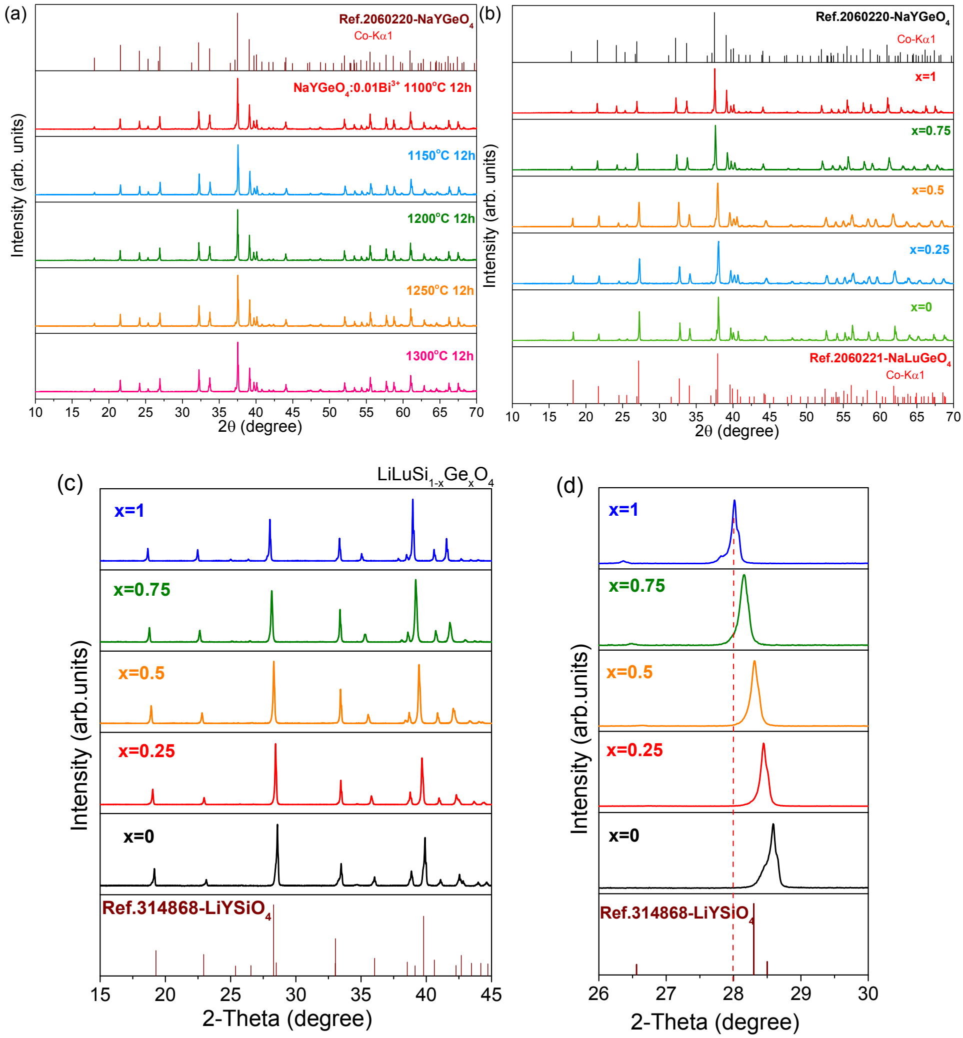
(a)
Ref.2060220-NaYGeO4
Co-Kα1
NaYGeO4:0.01Bi3+ 1100°C 12h
1150°C 12h
1200°C 12h
1250°C 12h
1300°C 12h
Intensity (arb. units)
2θ (degree)
(b)
Ref.2060220-NaYGeO4
Co-Kα1
x=1
x=0.75
x=0.5
x=0.25
x=0
Ref.2060221-NaLuGeO4
Co-Kα1
Intensity (arb. units)
2θ (degree)
(c)
LiLuSi1-xGexO4
x=1
x=0.75
x=0.5
x=0.25
x=0
Ref.314868-LiYSiO4
Intensity (arb.units)
2-Theta (degree)
(d)
x=1
x=0.75
x=0.5
x=0.25
x=0
Ref.314868-LiYSiO4
Intensity (arb.units)
2-Theta (degree)

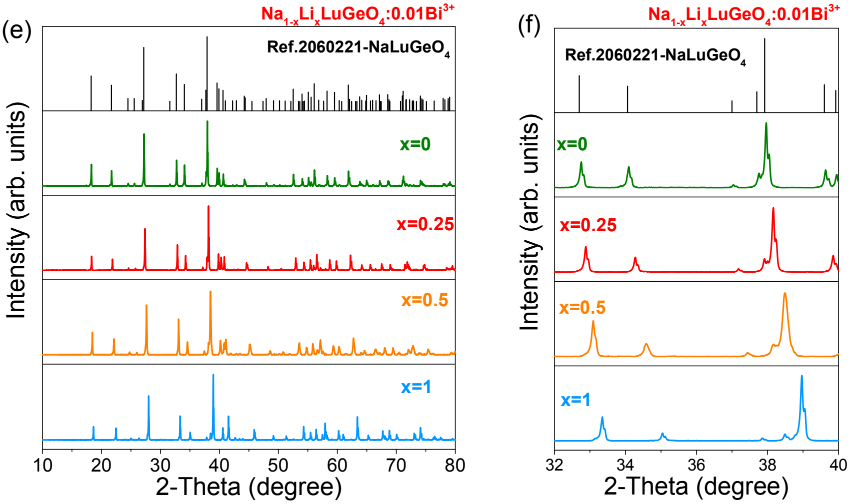

Fig. S5.2. XRD patterns for (a) $NaYGeO_4$:$0.01Bi^{3+}$ synthesized at different temperature, (b) $NaLu_{1-x}Y_xGeO_4$:$0.01Bi^{3+}$,$0.001Eu^{3+}$, (c)-(d) $LiLuSi_{1-x}Ge_xO_4$, and (e)-(f) $Na_{1-x}Li_xLuGeO_4$: $0.01Bi^{3+}$ solid solutions recorded at room temperature.

Fig. S5.2a) shows the XRD patterns for $NaYGeO_4$:$0.01Bi^{3+}$ synthesized at 1100-1300 °C during 12h. All samples match well with the standard $NaYGeO_4$ reference (No.2060220), demonstrating that single phase phosphors were synthesized.

Fig. S5.2c)-2d) shows the XRD patterns for undoped $LiLuSi_{1-x}Ge_xO_4$. Compared with the $LiYSiO_4$ reference (No.314868), the XRD patterns slightly shift towards smaller 2θ angles because the bigger germanium ions enter into the silicon site resulting in the increase of the cell volume. Solid solutions appear in $LiLuSi_{1-x}Ge_xO_4$ with increasing x.

Fig. S5.2e)-2f) shows the XRD patterns of $Na_{1-x}Li_xLuGeO_4$:$0.01Bi^{3+}$. With increasing x, the peaks slightly shift towards larger 2θ angles as compared with the $NaLuGeO_4$ reference (No. 2060221). This verifies that the smaller lithium cations enter the sodium site and decrease the cell volume. Solid solutions appear in $Na_{1-x}Li_xLuGeO_4$:$0.01Bi^{3+}$ with increasing x.

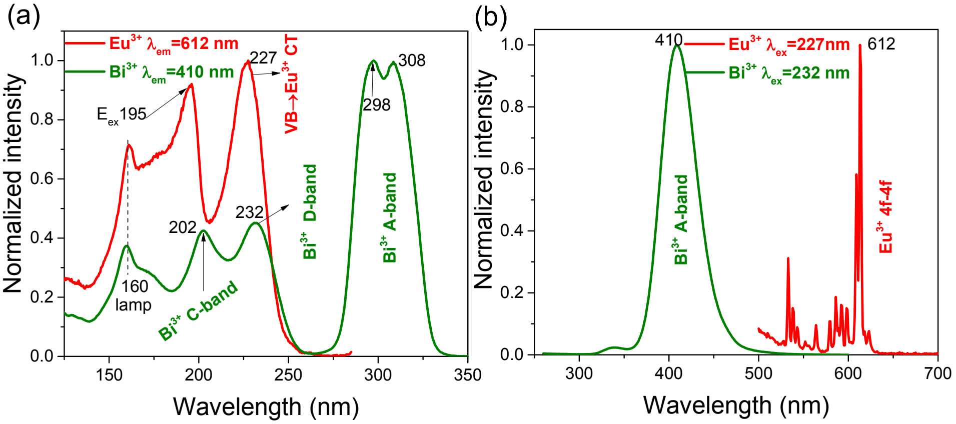

Fig. S5.3. (a) Photoluminescence excitation (PLE) and (b) emission spectra for $NaYGeO_4$: $0.01Bi^{3+}$ and $NaYGeO_4$:$0.01Eu^{3+}$ recorded at 10 K.

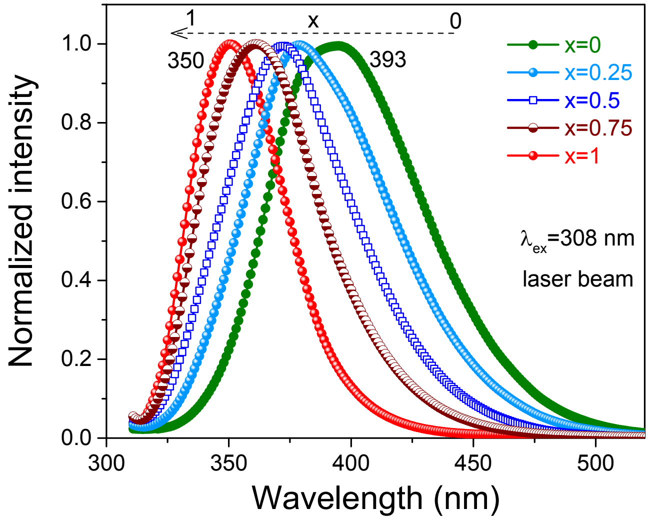

Fig. S5.4. Photoluminescence spectra of solid solutions $Na_{1-x}Li_xLuGeO_4$:$0.01Bi^{3+}$ (x=0-1) upon 308 nm OPO laser excitation recorded by a Si-based QE65Pro detector at room temperature.

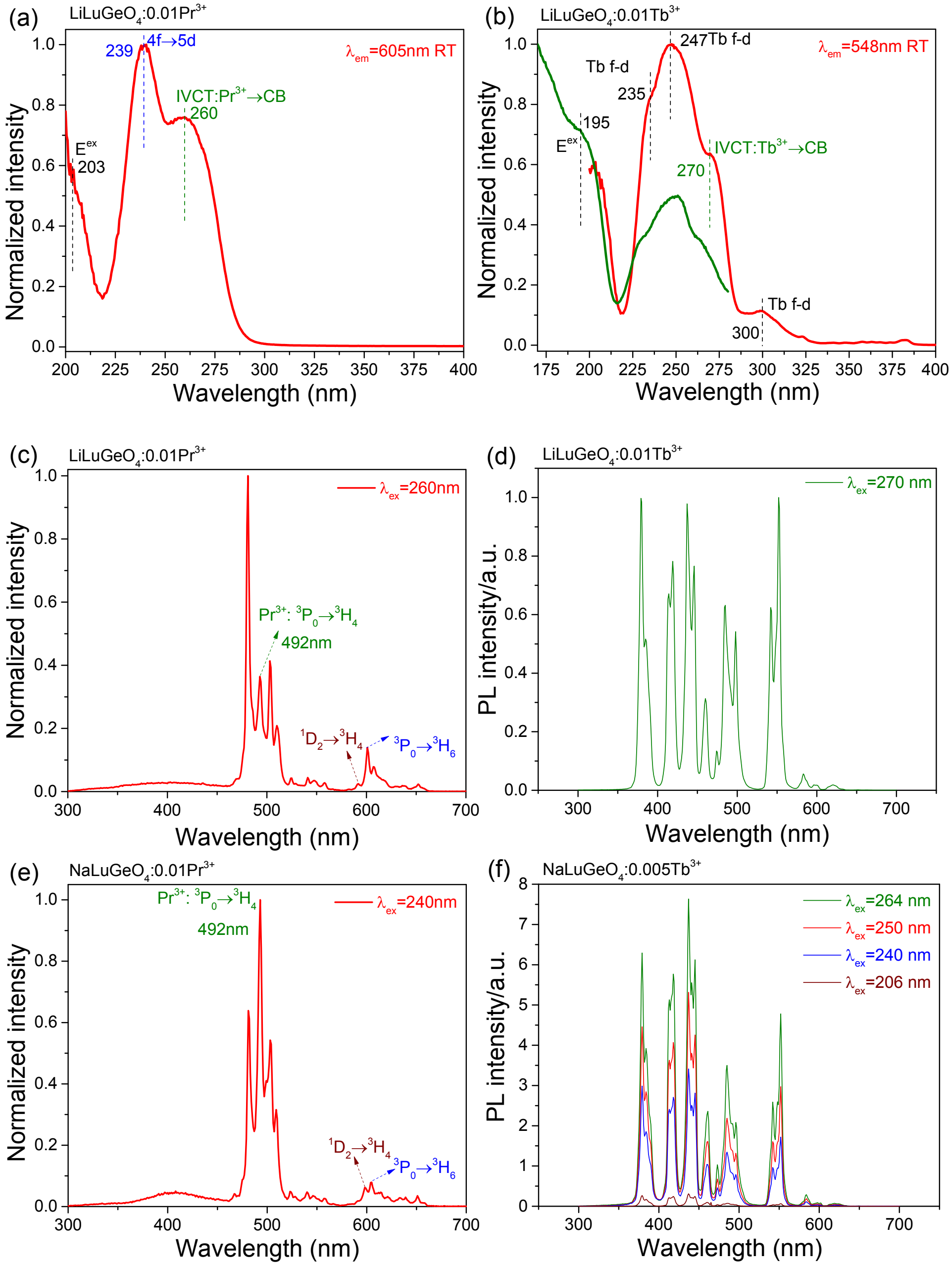
(a)
LiLuGeO4:0.01Pr3+
λem=605nm RT
239
4f→5d
IVCT:Pr3+→CB
260
Eex
203
Normalized intensity
Wavelength (nm)
(b)
LiLuGeO4:0.01Tb3+
λem=548nm RT
247Tb f-d
Tb f-d
235
195
Eex
IVCT:Tb3+→CB
270
Tb f-d
300
Normalized intensity
Wavelength (nm)
(c)
LiLuGeO4:0.01Pr3+
λex=260nm
Pr3+: 3P0→3H4
492nm
1D2→3H4
3P0→3H6
Normalized intensity
Wavelength (nm)
(d)
LiLuGeO4:0.01Tb3+
λex=270 nm
PL intensity/a.u.
Wavelength (nm)
(e)
NaLuGeO4:0.01Pr3+
Pr3+: 3P0→3H4
492nm
λex=240nm
1D2→3H4
3P0→3H6
Normalized intensity
Wavelength (nm)
(f)
NaLuGeO4:0.005Tb3+
λex=264 nm
λex=250 nm
λex=240 nm
λex=206 nm
PL intensity/a.u.
Wavelength (nm)

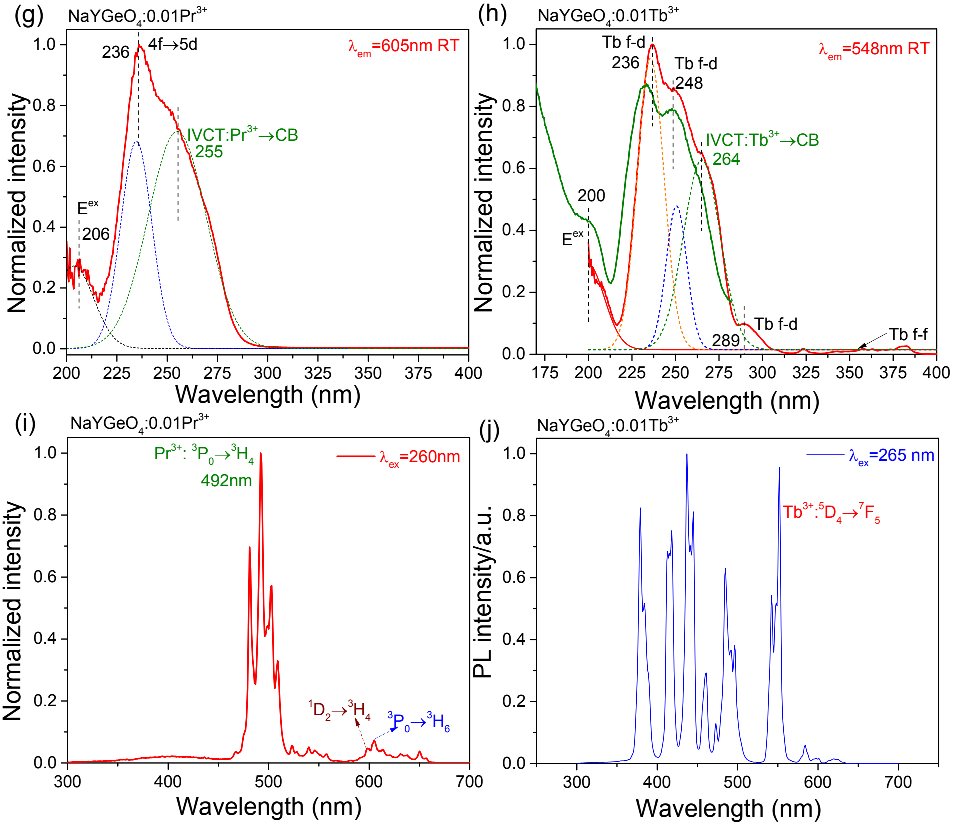

Fig. S5.5. Photoluminescence excitation and emission spectra for Tb^{3+} or Pr^{3+} single doped a)-d) LiLuGeO$_4$, e)-f) NaLuGeO$_4$, and g)-j) NaYGeO$_4$ recorded at room temperature.

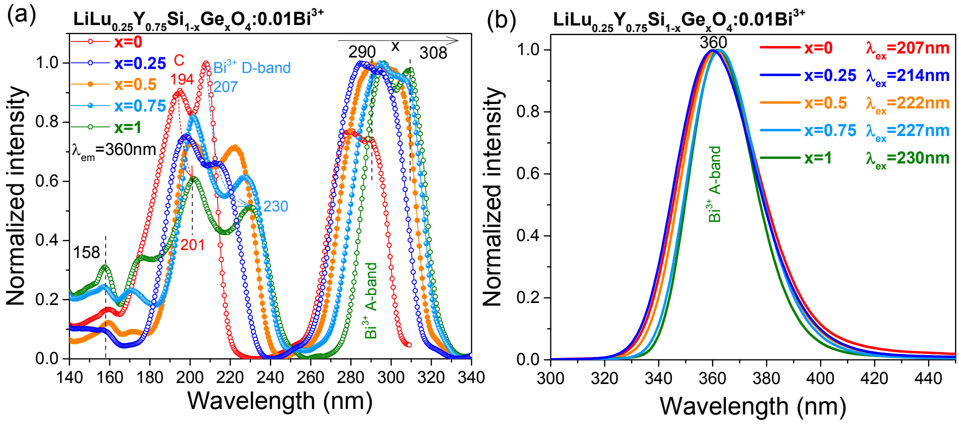

Fig. S5.6. Photoluminescence (a) excitation and (b) emission spectra for $LiLu_{0.25}Y_{0.75}Si_{1-x}Ge_xO_4{:}0.01Bi^{3+}$ solid solutions recorded at 10 K.

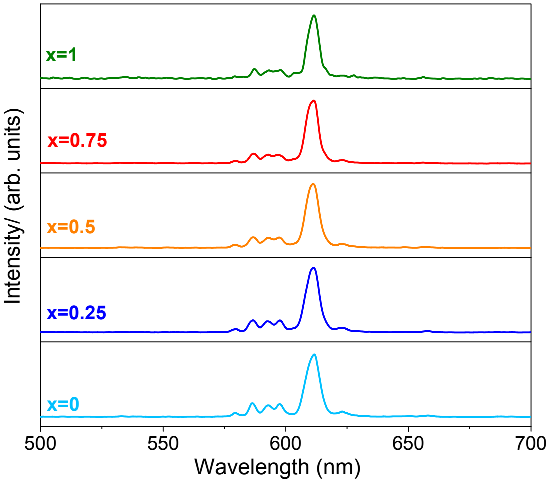

Fig. S5.7. Photoluminescence spectra for $LiLuSi_{1-x}Ge_xO_4{:}0.01Eu^{3+}$ solid solutions under Eu^{3+} CT-band excitation at 220 nm recorded at 10 K.

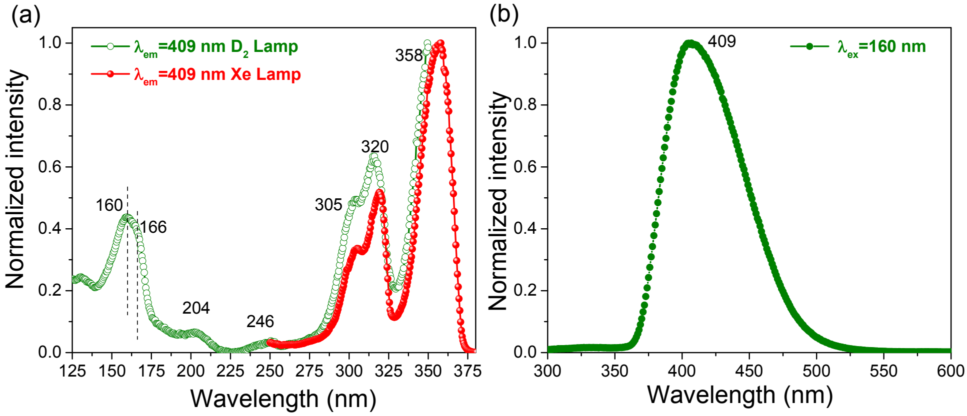

Fig. S5.8. Photoluminescence (a) excitation and (b) emission spectra for $LiLuSiO_4{:}0.01Ce^{3+}$ recorded at 10 K. The excitation spectrum between 125-350 nm in (a) was measured using a deuterium lamp (olive line). The excitation spectrum from 250 to 375 nm was recorded by a xenon lamp (red line).

Fig. S5.8a) shows that the excitation peaks near 358, 320, and 305 nm agree with previous work in Ref. [1] which are attributed to the Ce^{3+} $4f \rightarrow 5d_{1,2,3}$ transitions. The peaks near 246 and 204 nm are likely due to host intrinsic defects. The peak near 160 and a shoulder near 166 nm is assigned to an artefact by the deuterium lamp spectrum correction and host exciton creation, respectively.

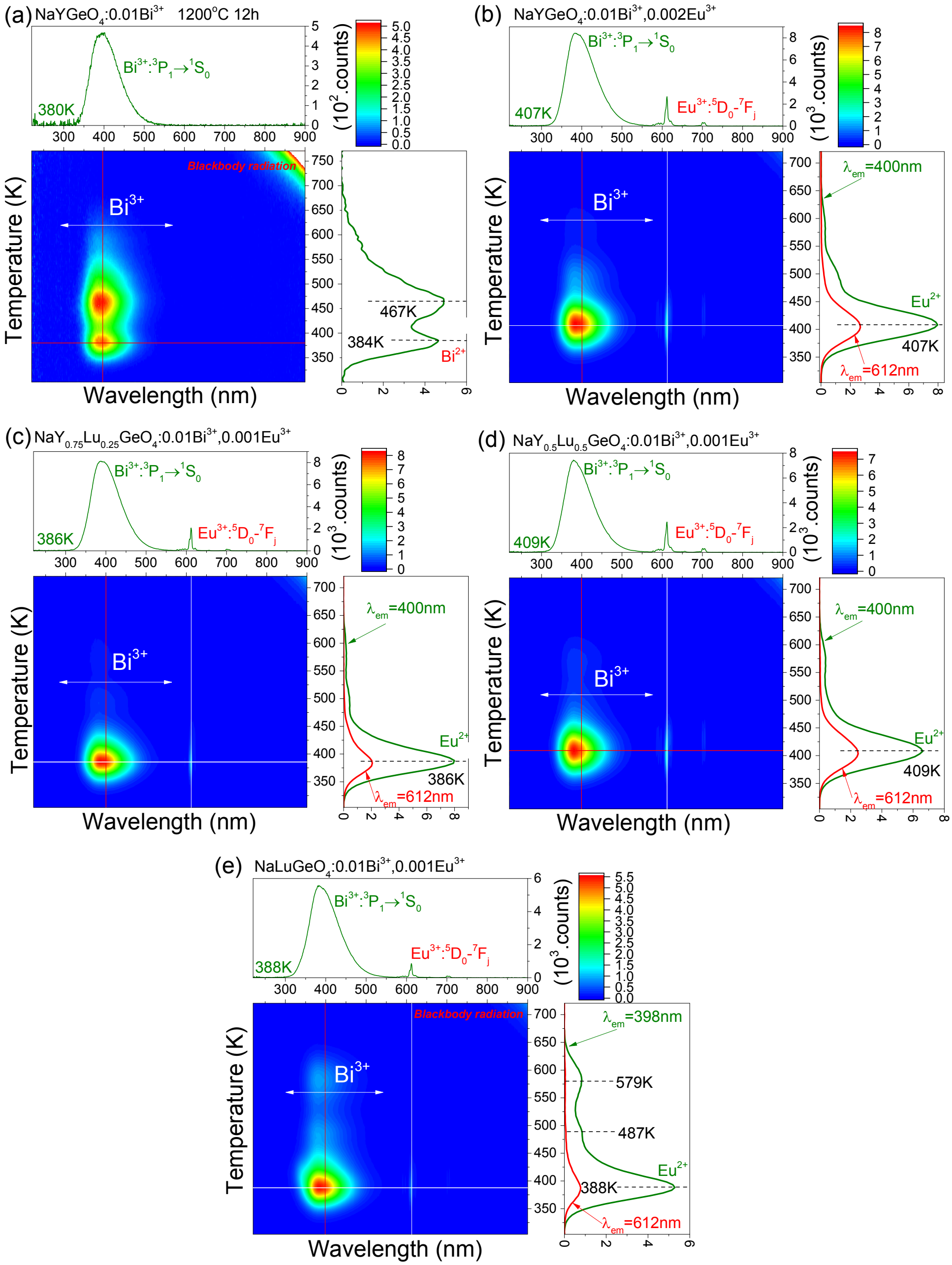

Fig. S5.9. TL emission plots for (a) $NaYGeO_4$:$0.01Bi^{3+}$ synthesized at 1200 ºC during 12h, (b) $NaYGeO_4$:$0.01Bi^{3+}$,$0.002Eu^{3+}$, (c) $NaY_{0.75}Lu_{0.25}GeO_4$:$0.01Bi^{3+}$,$0.001Eu^{3+}$, (d) $NaY_{0.5}$

$Lu_{0.5}GeO_4$:0.01Bi^{3+},0.001Eu^{3+}, and $NaLuGeO_4$:0.01Bi^{3+},0.001Eu^{3+} measured at a heating rate of 1 K/s after γ-ray irradiation.

Fig. S5.9b)-S9e) shows that for the Bi^{3+},Eu^{3+}-codoped samples, the TL glow curve when monitoring the Eu^{3+} red emission or the Bi^{3+} emission shares the same shape. Eu^{3+} emission is attributed to the energy transfer from Bi^{3+} to Eu^{3+2}.

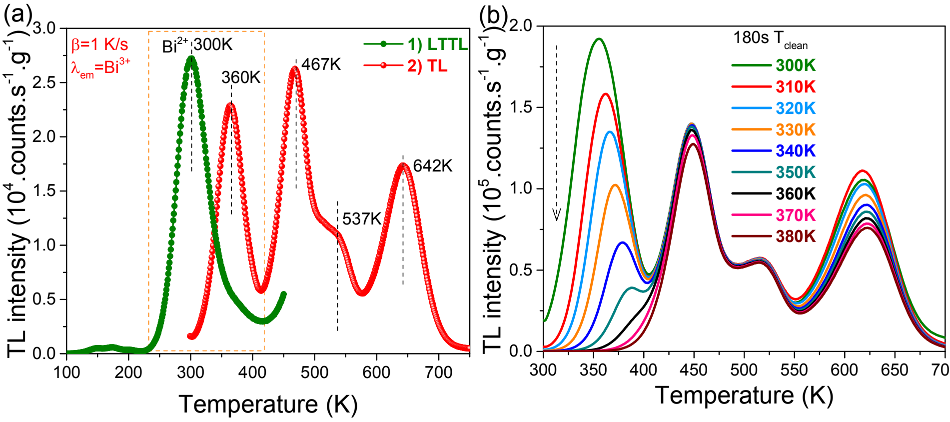

Fig. S5.10. (a) A comparison of a low-temperature (LTTL) and an above RT TL-recording on the same sample of $NaYGeO_4$:0.01Bi^{3+} and (b) TL glow curves after 180s peak cleaning at T_{clean} for $NaYGeO_4$:0.01Bi^{3+} synthesized at 1200 °C during 12h recorded at β=1 K/s after 600s β irradiation. The Bi^{3+} emission was monitored.

Fig. S5.10a) shows that the TL glow peak near RT shifts from 300 to 360 K which is due to TL peak cleaning effect at 300 K. Note that a trap distribution[3] leads to changing TL peak T_m near 300 K for $NaYGeO_4$:0.01Bi^{3+} in Fig. S5.10b).

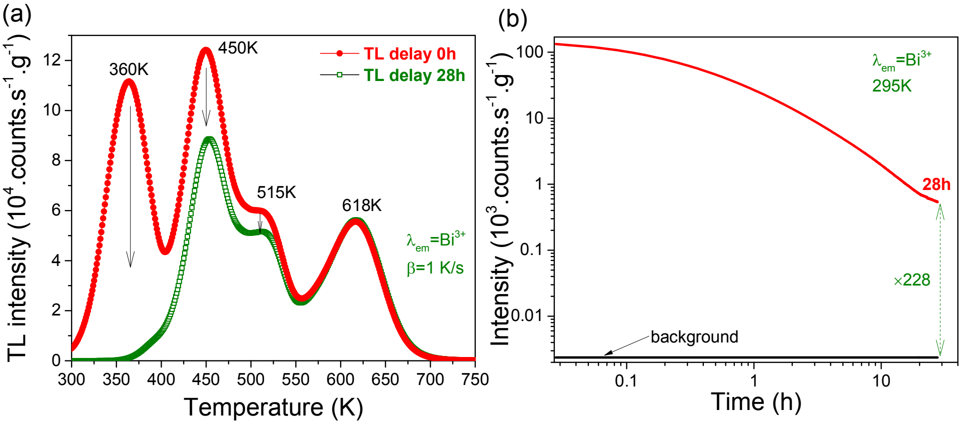

Fig. S5.11. (a) TL glow curves at β=1 K/s while monitoring the Bi^{3+} emission for $NaYGeO_4$:0.01Bi^{3+} synthesized at 1200 °C during 24h after β irradiation and after β irradiation followed by 28h waiting time, (b) corresponding room temperature (295 K) isothermal decay curve.

Fig. S5.11a) demonstrates that TL fading appears for the glow peaks near 360, 450, and 515 K, which gives rise to the 28h Bi^{3+} persistent luminescence in Fig. S5.11b).

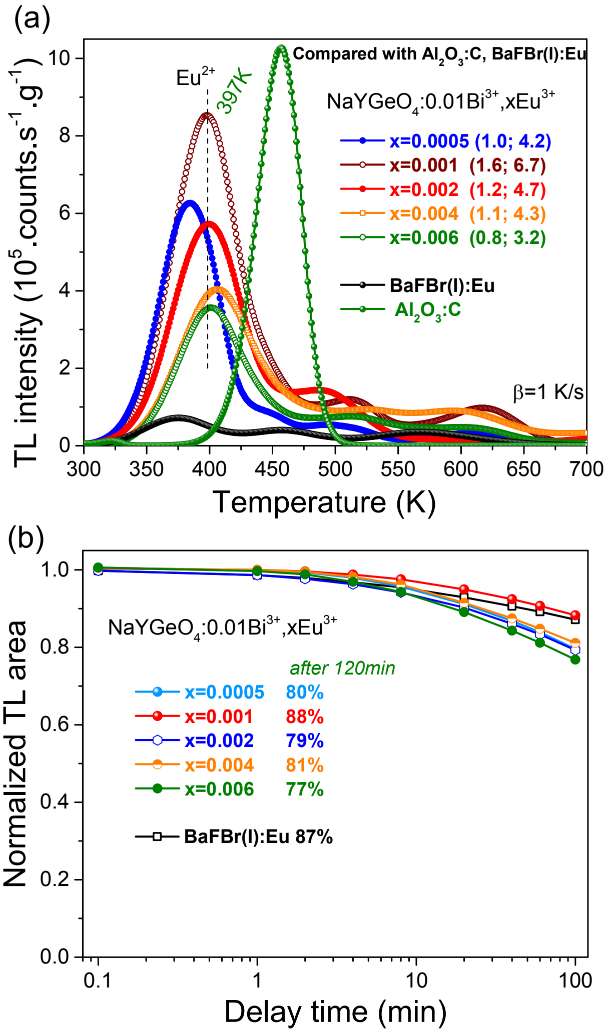

Fig. S5.12. (a) TL glow curves and (b) TL fading characteristics for $NaYGeO_4$:0.01Bi^{3+}, xEu^{3+} (x=0.0005-0.006) while monitoring the Bi^{3+} emission after beta irradiation.

Fig. S5.12a) shows the TL glow curves for $NaYGeO_4$:0.01Bi^{3+},xEu^{3+}. With increasing x, the TL glow peak jumps around 397 K and the TL intensity ratio of

$NaYGeO_4:0.01Bi^{3+},xEu^{3+}$ to BaFBr(I):Eu or $Al_2O_3:C$ first increases when x=0.1% and then decreases.

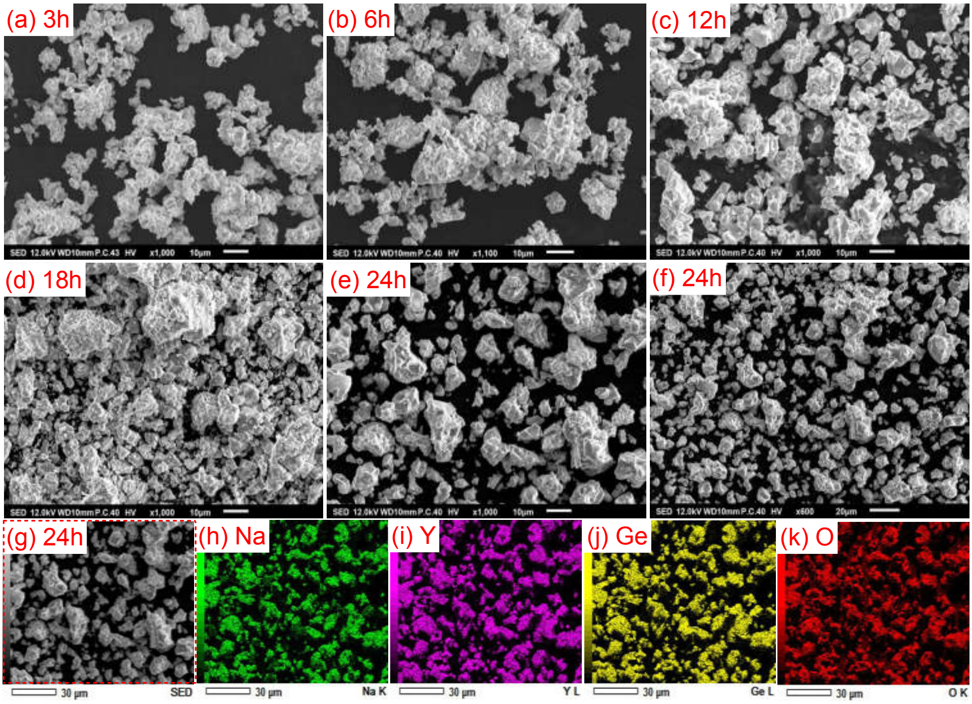

Fig. S5.13. SEM images for $NaYGeO_4:0.01Bi^{3+}$ synthesized at 1200 °C during a) 3h, b) 6h, c) 12h, d) 18h, and e)-g) 24h. Energy dispersive X-ray spectroscopy (EDX) mapping of h) Na, i) Y, j) Ge, and k) O corresponding to the crystals shown in g).

Fig. S5.13a)-13f) shows the SEM images for $NaYGeO_4:0.01Bi^{3+}$ synthesized at 1200 °C during 3-24h. Better storage properties with longer synthesis time can be due to a changing distribution of trapping centres on the atomic scale. It can also be related to the particle morphology. Therefore we made a SEM analysis. The elemental mapping in Fig. S5.13g)-k) demonstrates that the elements Na, Y, Ge, and O are homogeneously distributed in all crystals.

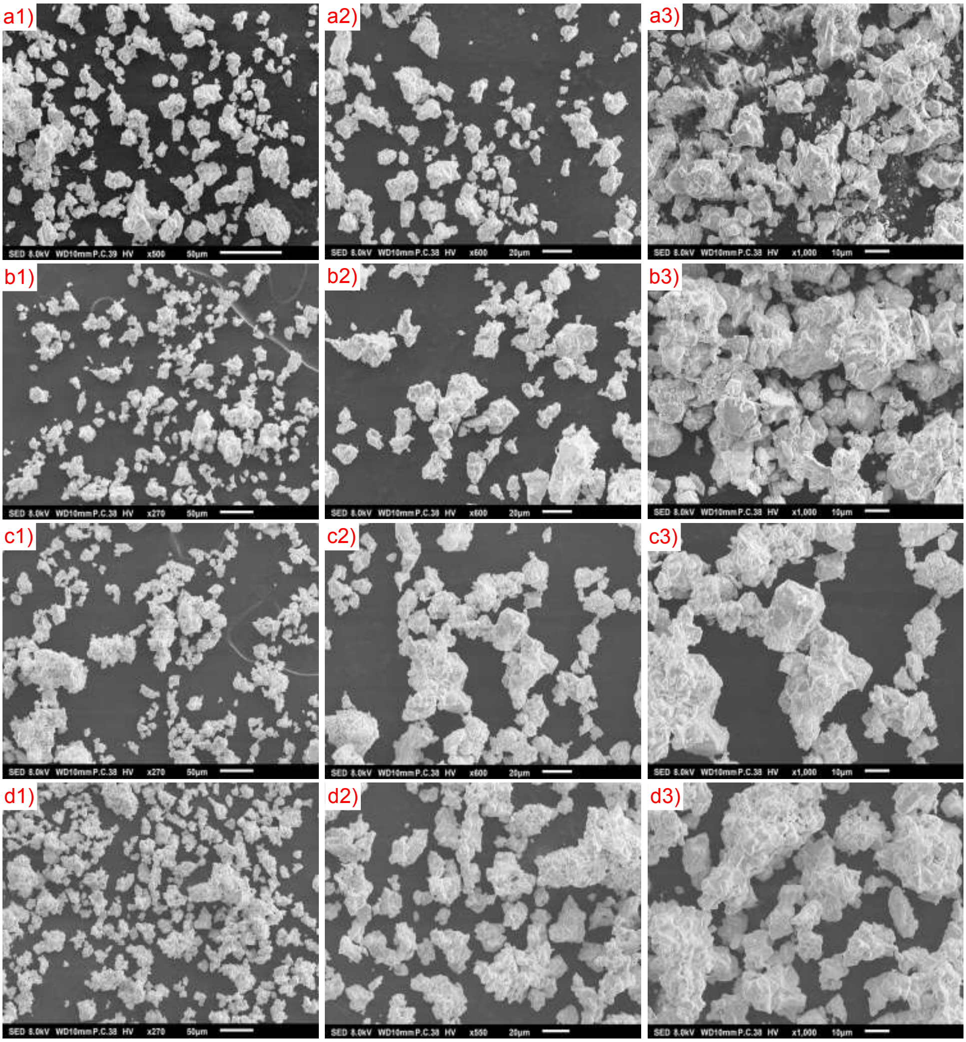

Fig. S5.14. SEM images for a1)-a3) $NaYGeO_4$:0.01Bi^{3+},0.001Eu^{3+}, b1)-b3) $NaYGeO_4$: 0.01Bi^{3+},0.002Eu^{3+}, c1)-c3) $NaYGeO_4$:0.01Bi^{3+},0.006Eu^{3+}, and d1)-d3) $NaY_{0.75}Lu_{0.25}GeO_4$: 0.01Bi^{3+}, 0.001Eu^{3+} synthesized at 1200 °C during 12h.

Fig. S5.14 shows that about 2~10 µm micro crystals form crystal aggregates up to ~5-30 µm.

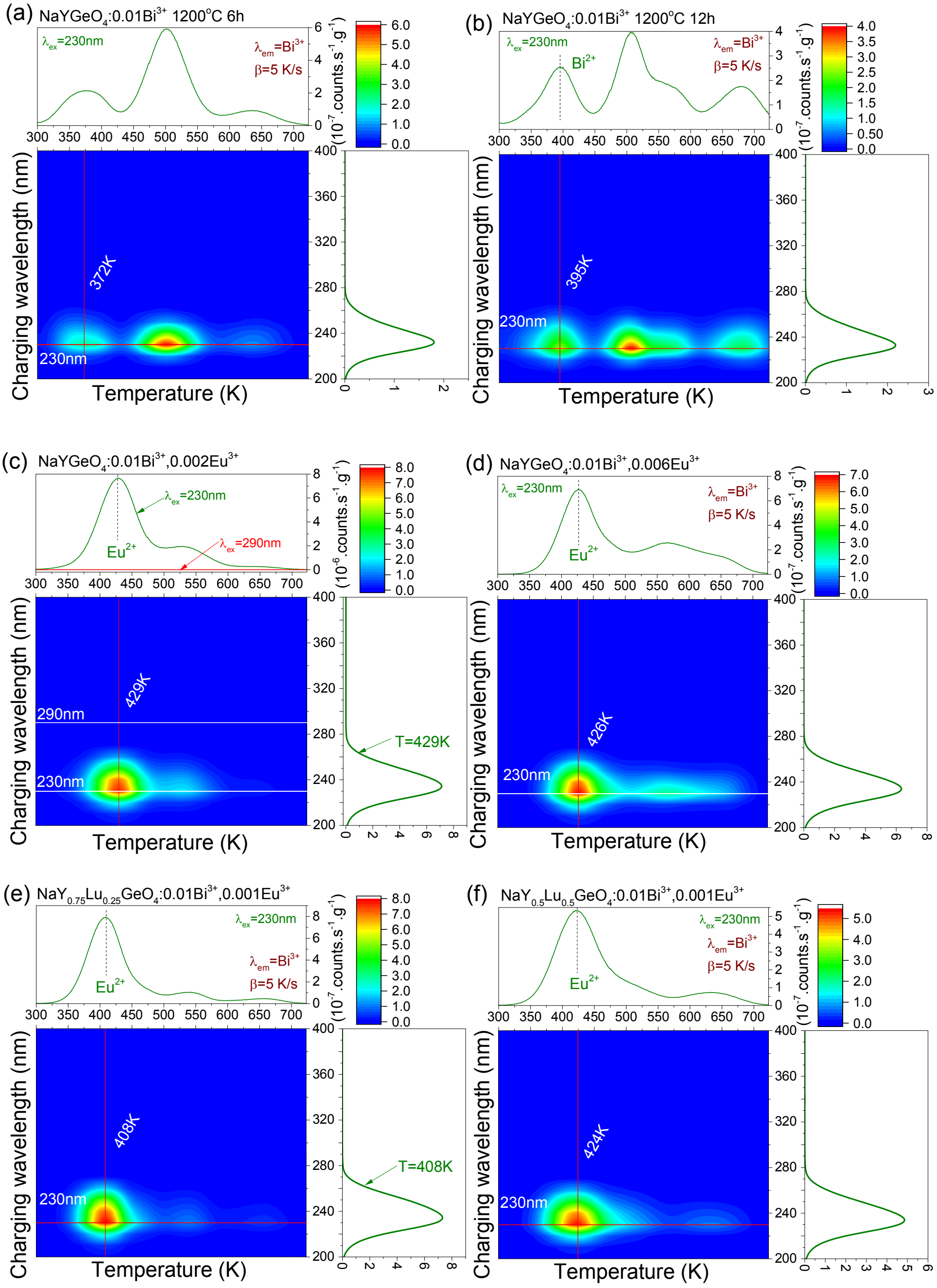
(a) NaYGeO$_4$:0.01Bi^{3+} 1200°C 6h
λ_{ex}=230nm
λ_{em}=Bi^{3+}
β=5 K/s
372K
230nm
(b) NaYGeO$_4$:0.01Bi^{3+} 1200°C 12h
λ_{ex}=230nm
Bi^{2+}
λ_{em}=Bi^{3+}
β=5 K/s
395K
230nm
(c) NaYGeO$_4$:0.01Bi^{3+},0.002Eu^{3+}
λ_{ex}=230nm
Eu^{2+}
λ_{ex}=290nm
429K
290nm
230nm
T=429K
(10^{-6}.counts.s^{-1}.g^{-1})
(d) NaYGeO$_4$:0.01Bi^{3+},0.006Eu^{3+}
λ_{ex}=230nm
Eu^{2+}
λ_{em}=Bi^{3+}
β=5 K/s
426K
230nm
(e) NaY$_{0.75}$Lu$_{0.25}$GeO$_4$:0.01Bi^{3+},0.001Eu^{3+}
λ_{ex}=230nm
Eu^{2+}
λ_{em}=Bi^{3+}
β=5 K/s
408K
230nm
T=408K
(f) NaY$_{0.5}$Lu$_{0.5}$GeO$_4$:0.01Bi^{3+},0.001Eu^{3+}
λ_{ex}=230nm
λ_{em}=Bi^{3+}
β=5 K/s
Eu^{2+}
424K
230nm
Charging wavelength (nm)
Temperature (K)
(10^{-7}.counts.s^{-1}.g^{-1})
300 350 400 450 500 550 600 650 700
200 240 280 320 360 400

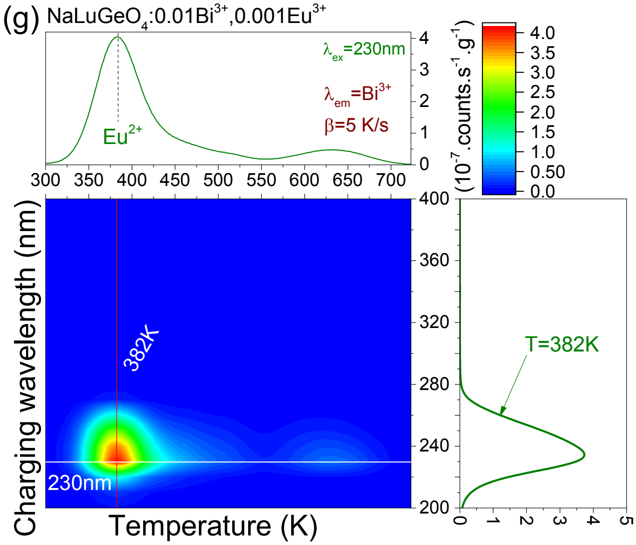

Fig. S5.15. TL excitation (TLE) spectra for NaYGeO$_4$:0.01Bi^{3+} synthesized at 1200 °C during (a) 6h and (b) 12h, (c) NaYGeO$_4$:0.01Bi^{3+},0.002Eu^{3+}, (d) NaYGeO$_4$:0.01Bi^{3+}, 0.006Eu^{3+}, (e) NaY$_{0.75}$Lu$_{0.25}$GeO$_4$:0.01Bi^{3+},0.001Eu^{3+}, and (f) NaY$_{0.5}$Lu$_{0.5}$GeO$_4$:0.01Bi^{3+}, 0.001Eu^{3+}, and (g) NaLuGeO$_4$:0.01Bi^{3+},0.001Eu^{3+}. The TL glow curves were recorded at a heating rate of 5 K/s while monitoring the Bi^{3+} emission.

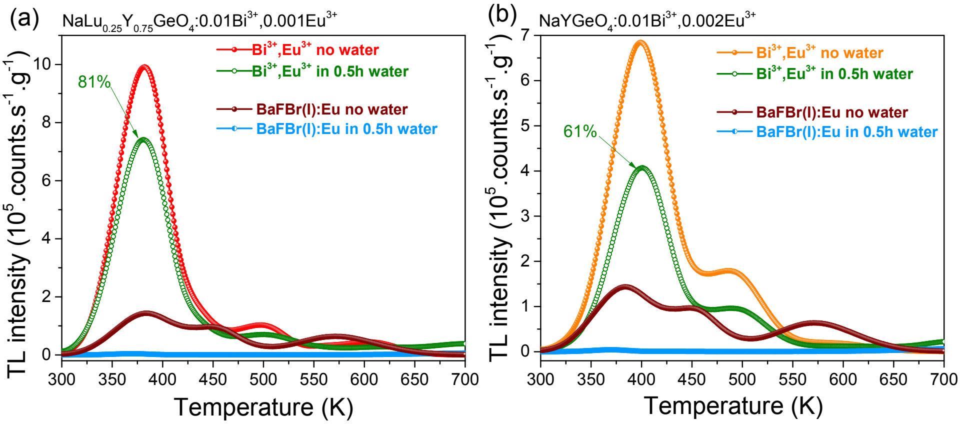

Fig. S5.16. TL glow curves recorded at a heating rate of 1 K/s after β irradiation for (a) NaLu$_{0.25}$Y$_{0.75}$GeO$_4$:0.01Bi^{3+},0.001Eu^{3+} solid solution and (b) NaYGeO$_4$:0.01Bi^{3+},0.002Eu^{3+} without and with exposure to water for 0.5h as compared with the commercial storage phosphor BaFBr(I):Eu. The emission from Bi^{3+} or Eu^{2+} was monitored.

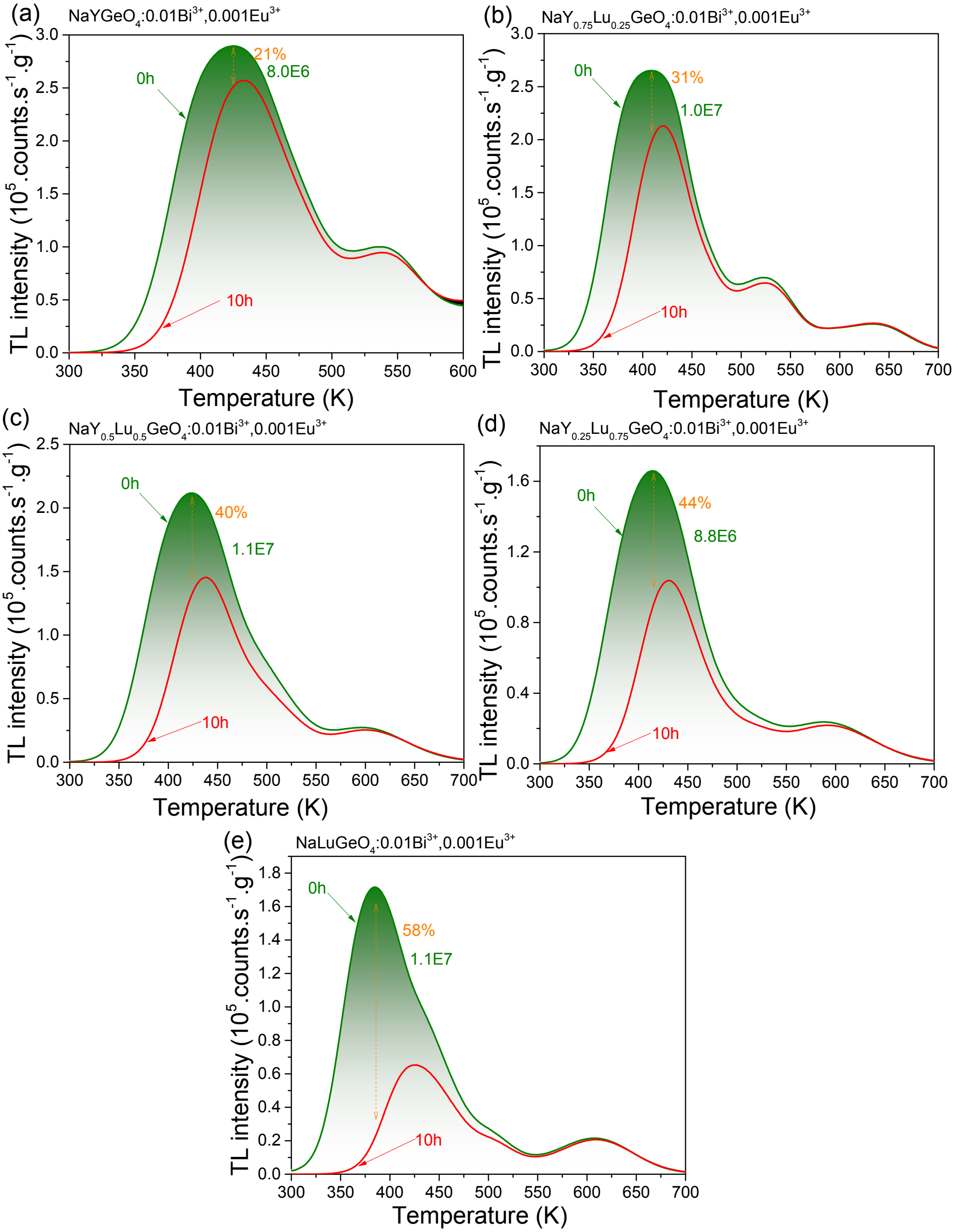

Fig. S5.17. TL glow curves for NaLu$_{1-x}$Y$_x$GeO$_4$:0.01Bi^{3+},0.001Eu^{3+} (x=0-1) crystals measured at a heating rate of 5 K/s while monitoring the Bi^{3+} emission after 600s beta irradiation with 0h and 10h delay time.

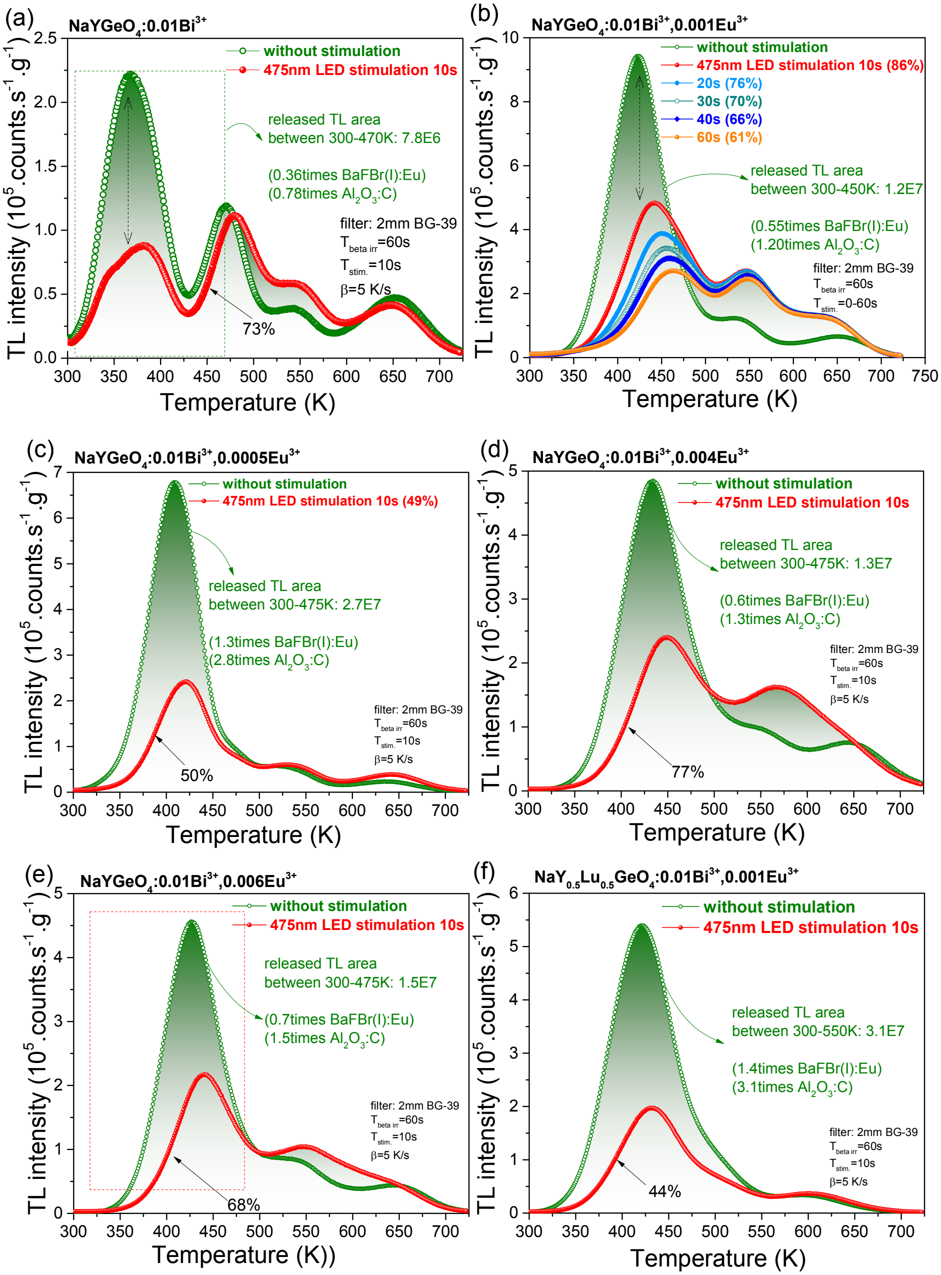
(a)
NaYGeO4:0.01Bi3+
without stimulation
475nm LED stimulation 10s
released TL area
between 300-470K: 7.8E6
(0.36times BaFBr(I):Eu)
(0.78times Al2O3:C)
filter: 2mm BG-39
Tbeta irr=60s
Tstim.=10s
β=5 K/s
73%
TL intensity (10^5.counts.s^-1.g^-1)
Temperature (K)
(b)
NaYGeO4:0.01Bi3+,0.001Eu3+
without stimulation
475nm LED stimulation 10s (86%)
20s (76%)
30s (70%)
40s (66%)
60s (61%)
released TL area
between 300-450K: 1.2E7
(0.55times BaFBr(I):Eu)
(1.20times Al2O3:C)
filter: 2mm BG-39
Tbeta irr=60s
Tstim.=0-60s
TL intensity (10^5.counts.s^-1.g^-1)
Temperature (K)
(c)
NaYGeO4:0.01Bi3+,0.0005Eu3+
without stimulation
475nm LED stimulation 10s (49%)
released TL area
between 300-475K: 2.7E7
(1.3times BaFBr(I):Eu)
(2.8times Al2O3:C)
filter: 2mm BG-39
Tbeta irr=60s
Tstim.=10s
β=5 K/s
50%
TL intensity (10^5.counts.s^-1.g^-1)
Temperature (K)
(d)
NaYGeO4:0.01Bi3+,0.004Eu3+
without stimulation
475nm LED stimulation 10s
released TL area
between 300-475K: 1.3E7
(0.6times BaFBr(I):Eu)
(1.3times Al2O3:C)
filter: 2mm BG-39
Tbeta irr=60s
Tstim.=10s
β=5 K/s
77%
TL intensity (10^5.counts.s^-1.g^-1)
Temperature (K)
(e)
NaYGeO4:0.01Bi3+,0.006Eu3+
without stimulation
475nm LED stimulation 10s
released TL area
between 300-475K: 1.5E7
(0.7times BaFBr(I):Eu)
(1.5times Al2O3:C)
filter: 2mm BG-39
Tbeta irr=60s
Tstim.=10s
β=5 K/s
68%
TL intensity (10^5.counts.s^-1.g^-1)
Temperature (K))
(f)
NaY0.5Lu0.5GeO4:0.01Bi3+,0.001Eu3+
without stimulation
475nm LED stimulation 10s
released TL area
between 300-550K: 3.1E7
(1.4times BaFBr(I):Eu)
(3.1times Al2O3:C)
filter: 2mm BG-39
Tbeta irr=60s
Tstim.=10s
β=5 K/s
44%
TL intensity (10^5.counts.s^-1.g^-1)
Temperature (K)

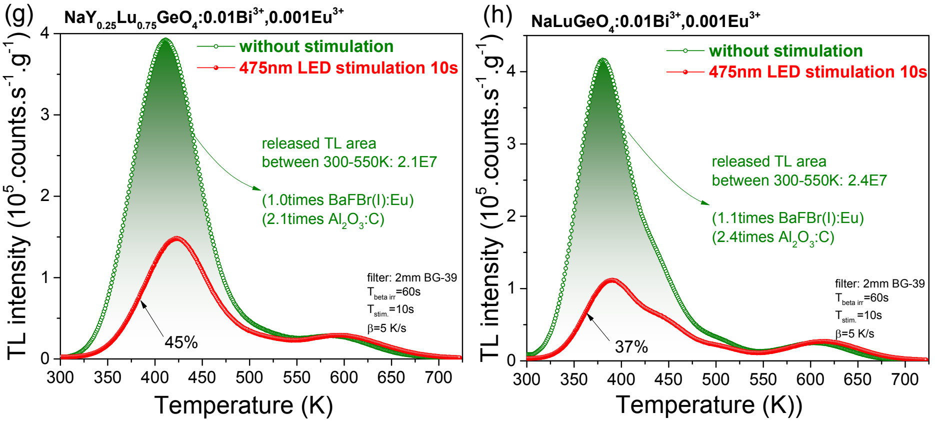

Fig. S5.18. TL glow curves at β=5 K/s while monitoring the Bi^{3+} emission for (a) $NaYGeO_4$:$0.01Bi^{3+}$, (b) $NaYGeO_4$:$0.01Bi^{3+}$,$0.001Eu^{3+}$, (c) $NaYGeO_4$:$0.01Bi^{3+}$,$0.0005Eu^{3+}$, (d) $NaYGeO_4$:$0.01Bi^{3+}$,$0.004Eu^{3+}$, (e) $NaYGeO_4$:$0.01Bi^{3+}$,$0.006Eu^{3+}$, (f) $NaY_{0.5}Lu_{0.5}GeO_4$: $0.01Bi^{3+}$,$0.001Eu^{3+}$, (g) $NaY_{0.25}Lu_{0.75}GeO_4$:$0.01Bi^{3+}$,$0.001Eu^{3+}$, and (h) $NaLuGeO_4$:$0.01Bi^{3+}$, $0.001Eu^{3+}$ after beta irradiation and after beta irradiation followed by 10s 475 nm blue LED optical stimulation.

Table S5.1. Released TL areas for Bi^{3+} and/or Eu^{3+} doped $NaLu_{1-x}Y_xGeO_4$ after β irradiation followed by 10s of 475 nm blue LED stimulation.

Compound	released area
BaFBr(I):Eu	2.1
Al_2O_3:C	1.0
x=0; 1%Bi^{3+},0.1%Eu^{3+}	2.4
x=0.25;1%Bi^{3+},0.1%Eu^{3+}	2.1
x=0.50;1%Bi^{3+},0.1%Eu^{3+}	3.1
x=0.75;1%Bi^{3+},0.1%Eu^{3+}	4.4
x=1; 1%Bi^{3+},0.05%Eu^{3+}	2.7
x=1; 1%Bi^{3+},0.1%Eu^{3+}	1.2
x=1; 1%Bi^{3+},0.2%Eu^{3+}	3.7
x=1; 1%Bi^{3+},0.4%Eu^{3+}	1.3
x=1; 1%Bi^{3+},0.6%Eu^{3+}	1.5
x=1; 1%Bi^{3+}	0.8

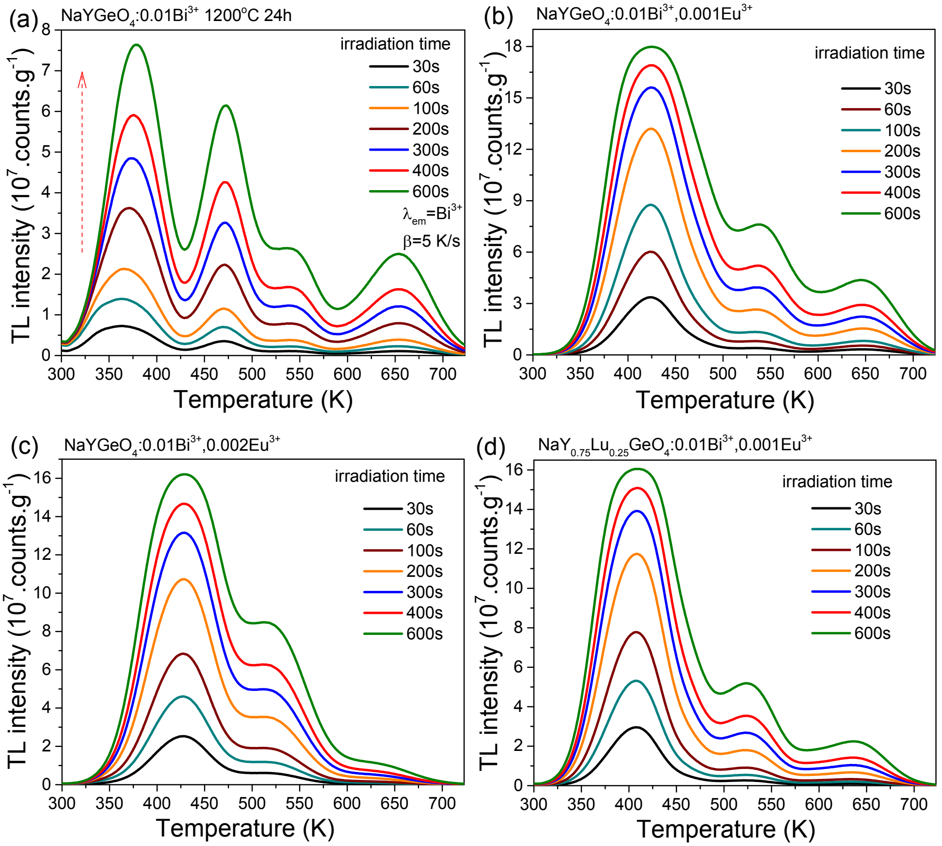

Fig. S5.19. TL glow curves for (a) NaYGeO$_4$:0.01Bi^{3+}, (b) NaYGeO$_4$:0.01Bi^{3+},0.001Eu^{3+}, (c) NaYGeO$_4$:0.01Bi^{3+},0.002Eu^{3+}, and (d) NaY$_{0.75}$Lu$_{0.25}$GeO$_4$:0.01Bi^{3+},0.001Eu^{3+} with different beta irradiation dose recorded at a heating of 5 K/s while monitoring the Bi^{3+} emission.

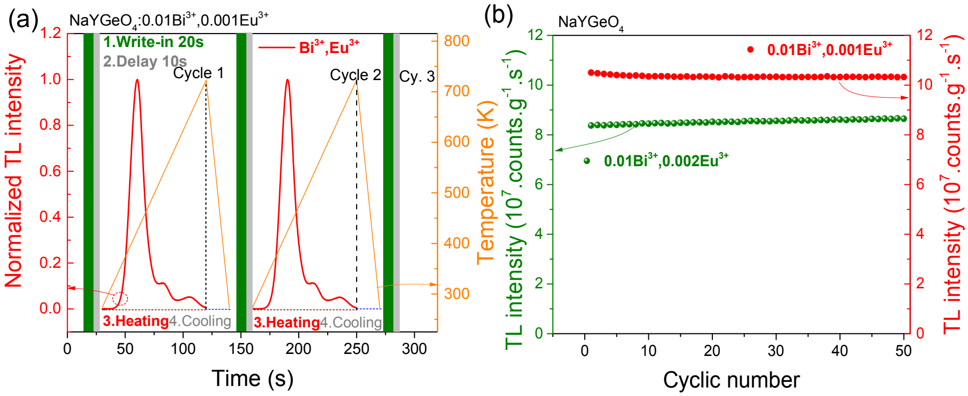

Fig. S5.20. Repeatability test for (a) the TL glow curves and (b) corresponding integrated TL intensities as a function of cyclic number for $NaYGeO_4:0.01Bi^{3+},0.001Eu^{3+}$ and $NaYGeO_4:0.01Bi^{3+},0.002Eu^{3+}$ after 20s beta irradiation recorded at a heating rate of 5 K/s while monitoring the Bi^{3+} emission.

The repeatability test for the TL glow curve as a function of the cyclic number in Fig. 5.S20b) shows that the developed Bi^{3+} storage phosphors are relatively stable after β-ray charging.

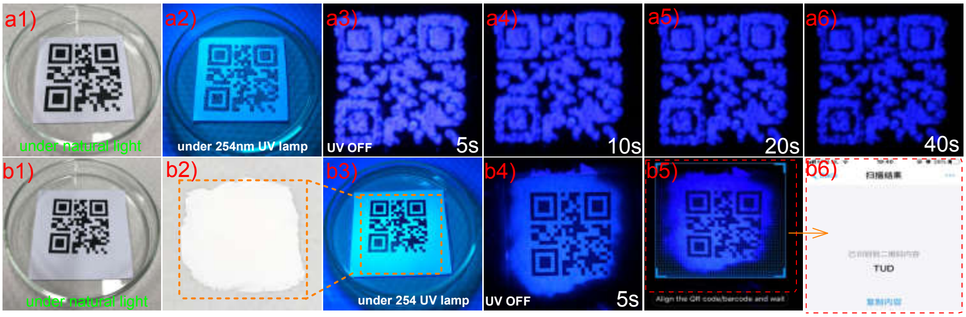

Fig. S5.21. Proof-of-concept information display by using Bi^{3+} persistent luminescence from $NaYGeO_4:0.01Bi^{3+}$.

A QR code generated by computer software using the text of TUD has been printed on a paper as shown in Fig. S5.21a1) and b1). The black area of the QR code covered by an afterglow $NaYGeO_4:0.01Bi^{3+}$ phosphor is exposed to 254 nm UV-light in Fig. S5.21a2).

The afterglow $NaYGeO_4:0.01Bi^{3+}$ phosphor film in Fig. S5.21b2) is first charged by 254 nm UV-light and then is placed underneath a paper printed with a QR code in Fig. S5.21b3).

QR code is visible due to Bi^{3+} afterglow in the dark in Fig. S5.21a3)-a6) and S5.21b4). Particularly, Fig. S5.21b5)-b6) shows that the QR code in the dark can be scanned by mobile phone software to read out the hidden information of TUD.

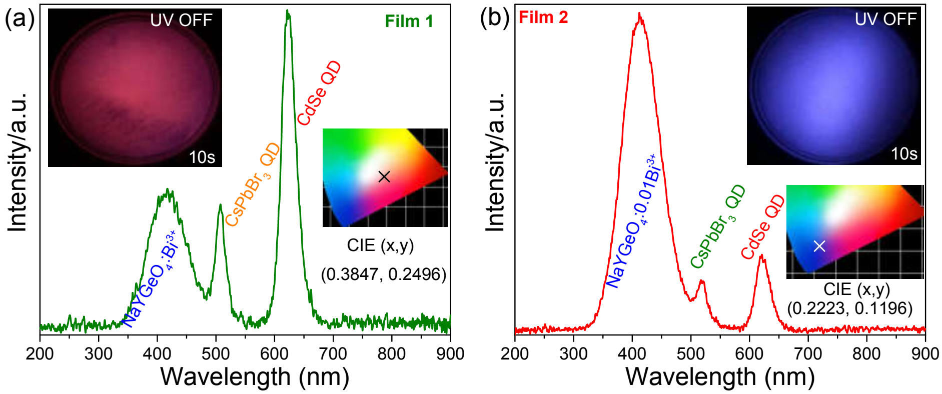

Fig. S5.22. Afterglow spectra for (a) film 1 and (b) film 2 after 5s Hg lamp illumination. The inset shows the corresponding afterglow photograph and colour coordinates.

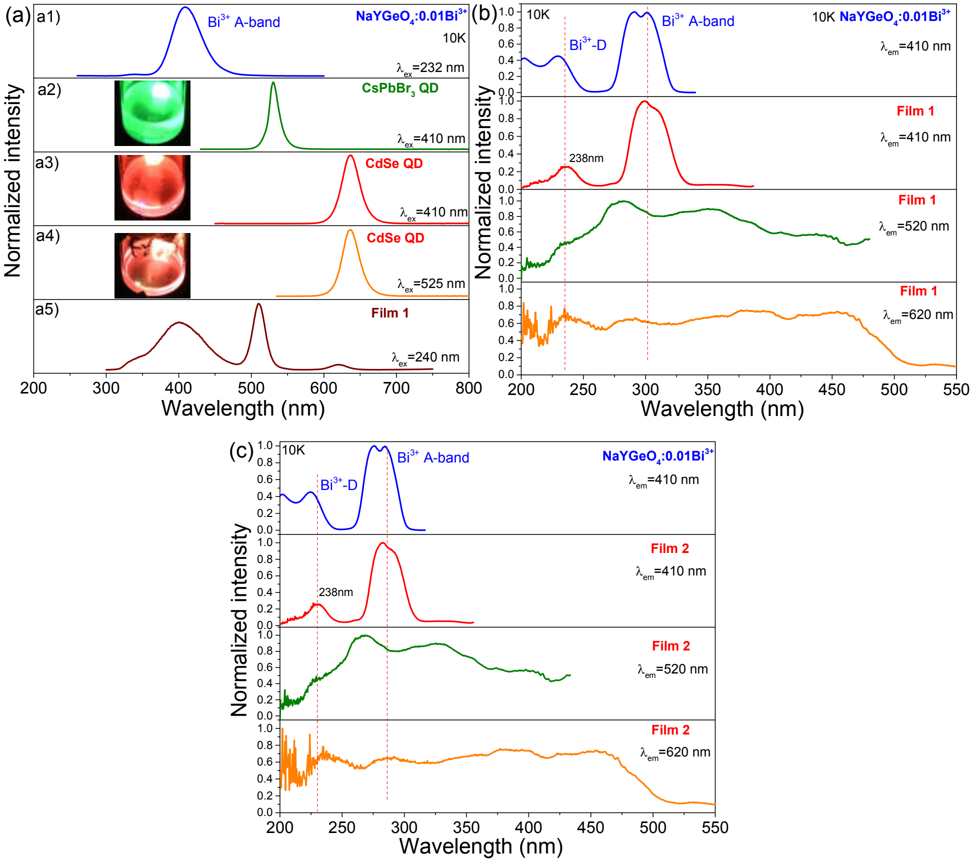

Fig. S5.23. Photoluminescence excitation and emission spectra for $NaYGeO_4$:0.01Bi^{3+} at 10K, $CsPbBr_3$ quantum dots (QD), CdSe QD, film 1, and film 2 recorded at room temperature. The insets in a2)-a4) show the corresponding photographs of $CsPbBr_3$ QD and CdSe QD emission under 410 and 525 nm excitation.

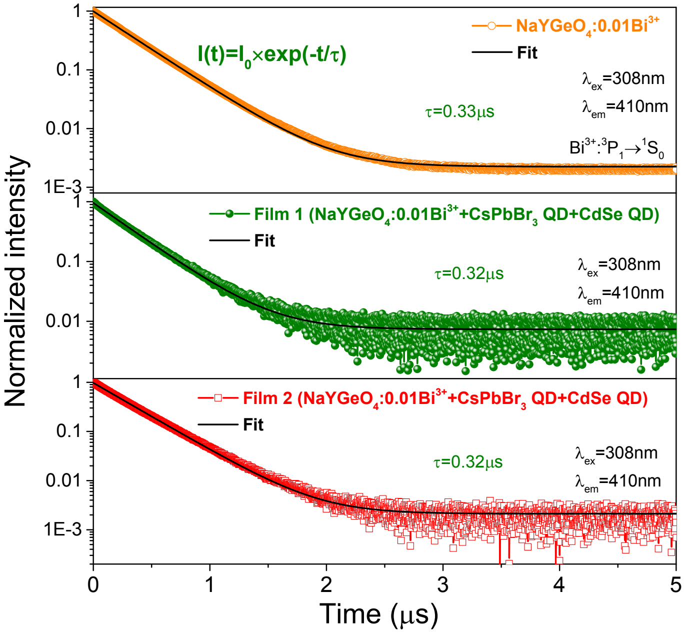

Fig. S5.24. Fluorescence decay curve of Bi^{3+} emission at 410 nm upon 308 nm excitation in $NaYGeO_4$:0.01Bi^{3+}, film 1 and film 2 measured at room temperature.

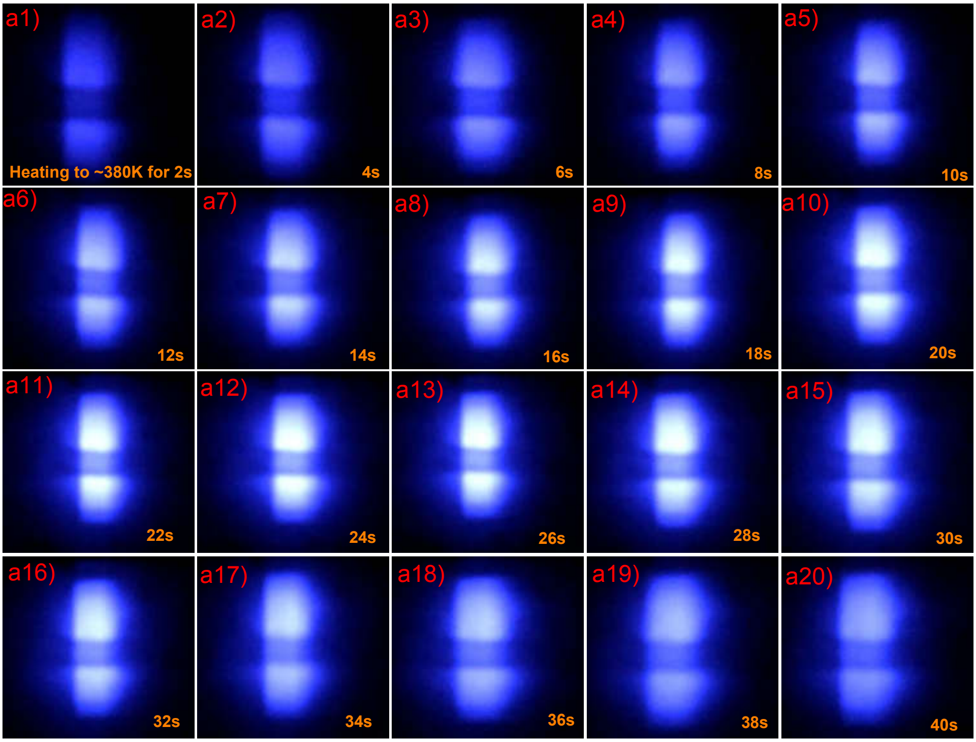

Fig. S5.25. Photographs of X-ray charged $NaYGeO_4$:0.01Bi^{3+},0.001Eu^{3+} phosphor dispersed in a silicone gel film heated to ~380 K with different duration time. The film was covered by a chicken bone during X-ray charging.

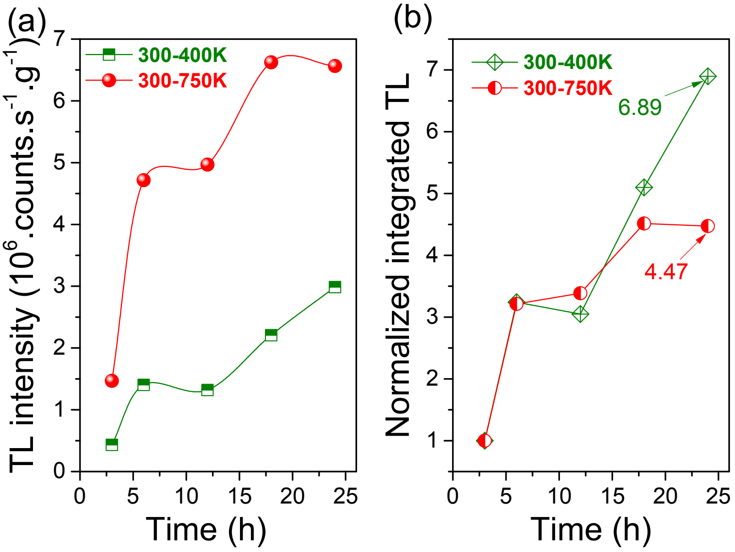

Fig. S5.26. (a) Unnormalized and (b) normalized TL intensities for $NaYGeO_4$:0.01Bi^{3+} synthesized at 1200 ^oC with different duration time.

Reference

1. A. V. Sidorenko, P. Dorenbos, A. J. J. Bos, C. W. E. van Eijk and P. A. Rodnyi, *J. Phys.-Condes. Matter*, 2006, **18**, 4503-4514.
2. T. Lyu and P. Dorenbos, *Chemical Engineering Journal*, 2019, **372**, 978-991.
3. K. Van den Eeckhout, A. J. J. Bos, D. Poelman and P. F. Smet, *Physical Review B*, 2013, **87**, 045126.

6

Towards information storage by designing both electron and hole detrapping processes in bismuth and lanthanide-doped $LiRE(Si,Ge)O_4$ (RE=Y, Lu) with high charge carrier storage capacity

Graphical abstract

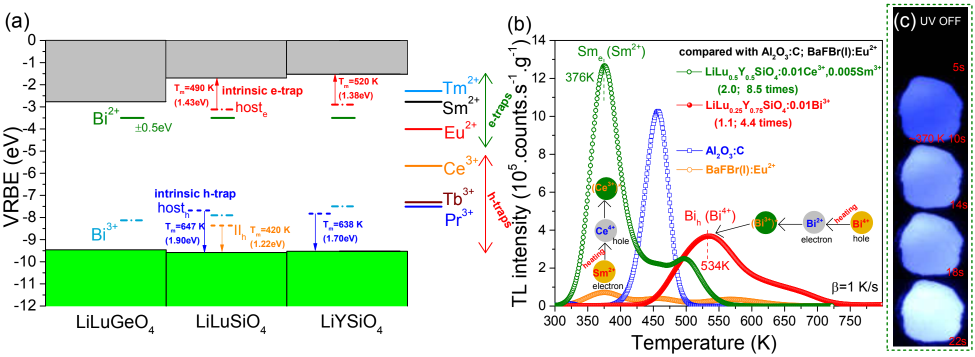

This chapter is based on the publication that has been published in ***Chemical Engineering Journal***: **T. Lyu*** and P. Dorenbos (2020) 124776.

6.1. Abstract

The development of storage phosphors with high charge carrier storage capacity is a current challenge in information storage applications. Here, guided by vacuum referred binding energy (VRBE) diagrams, both the trapping and detrapping processes of electrons and holes are explored in the bismuth and lanthanide-doped LiRE(Si,Ge)O_4 (RE=Y, Lu) family of compounds. By combining Tm^{3+} with the deep hole traps of Ln^{3+} (Ln=Ce, Tb, or Pr) or Bi^{3+} in $LiLuSiO_4$, Tm^{3+} appears to act as a less deep electron capturing centre. The electrons released from Tm^{2+} recombine with holes at Ln^{4+} and Bi^{4+} to produce typical Ln^{3+} 4f-4f or 5d-4f emission and Bi^{3+} A-band emission. The electron trap depth produced by lanthanide ions can be tuned by the choice of Ln^{3+} (Ln=Tm or Sm), and for fixed pair of Ln^{3+} and/or Bi^{3+} dopants like in $LiLu_{1-x}Y_xSiO_4{:}0.01Ce^{3+},0.01Ln^{3+}$ and $LiLu_{1-x}Y_xSiO_4{:}0.01Bi^{3+},0.01Sm^{3+}$ solid solutions, by adjusting x, resulting in the engineering of the VRBE at the conduction band bottom. The thermoluminescence (TL) intensity of the optimized $LiLu_{0.5}Y_{0.5}SiO_4{:}0.01Ce^{3+},0.005Sm^{3+}$ is about 8.5 times higher than that of the commercial X-ray $BaFBr(I){:}Eu^{2+}$ storage phosphor. By combining deep Eu^{3+} or Bi^{3+} electron traps with Ln^{3+} (Ln=Tb or Pr) or Bi^{3+}, Ln^{3+} and Bi^{3+} appear to act as less deep hole capturing centres in $LiLuSiO_4$. Here the recombination is achieved through hole liberation rather than the more commonly reported electron liberation. The holes are released from Ln^{4+} and Bi^{4+} to recombine with electrons at Eu^{2+} or Bi^{2+} to give characteristic Eu^{3+} 4f-4f and Bi^{3+} A-band emissions. The tailoring of Ln^{3+} and Bi^{3+} hole trap depths by crystal composition modulation is discussed in $LiLu_{1-x}Y_xSiO_4$ and $LiLu_{0.25}Y_{0.75}Si_{1-y}Ge_yO_4{:}0.01Bi^{3+}$ solid solutions. The TL intensity of the optimized $LiLu_{0.25}Y_{0.75}SiO_4{:}0.01Bi^{3+}$ is ~4.4 times higher than that of the commercial $BaFBr(I){:}Eu^{2+}$. Proof-of-concept information storage will be demonstrated with X-ray or UV-light charged $LiLu_{0.5}Y_{0.5}SiO_4{:}0.01Ce^{3+},0.01Sm^{3+}$ and $LiLu_{0.25}Y_{0.75}SiO_4{:}0.01Bi^{3+}$ phosphors dispersed in silicone gel imaging plates. This work not only reports excellent Ce^{3+} and Bi^{3+} based storage phosphors but also can inspire future research to develop Ce^{3+} and Bi^{3+} based storage phosphors for energy storage in a rational design approach rather than by a trial-and-error method.

Keywords: Energy conversion, energy storage, bismuth, hole liberation, trap engineering

6.2. Introduction

Charge carrier trapping processes have attracted attention for rational design of afterglow and storage phosphors and from a theoretical point of view[1, 2]. The electron capturing and liberation processes have been widely studied for afterglow phosphors[3-8]. Korthout *et al.* reported the valence change of Eu^{2+} in the commercial afterglow phosphor $SrAl_2O_4{:}Eu^{2+},Dy^{3+}$ utilizing X-ray absorption near-edge spectroscopy (XANES)[9]. A partial oxidation of Eu^{2+} to Eu^{3+} appears after exposing the phosphor to X-rays. A valence state change of Dy^{3+} was not detected although it does play a role in the electron trapping process. Eu^{2+} is proposed to be an electron donor and the electrons liberated by photoionization migrate freely in the conduction band (CB) to be trapped by the electron capturing centre(s). A similar partial oxidation of Ce^{3+} to Ce^{4+} and a reduction of Cr^{3+} to Cr^{2+} appears in $Y_3Al_2Ga_3O_{12}$:Ce^{3+},Cr^{3+} afterglow phosphor by XANES[10]. Here Ce^{3+} is the electron donor and Cr^{3+} acts as the electron acceptor.

Holes can also be released to recombine with an electron capturing centre through the valence band (VB) or by a migrating V_k centre[2, 11]. Hole detrapping processes are rarely reported. In 1988, Chakrabarti *et al.* reported that Sm^{3+} is a recombination centre and Ce^{3+} is a hole capturing centre in MgS:Ce^{3+},Sm^{3+}[12]. The holes are liberated from Ce^{4+} to recombine with electrons trapped at Sm^{2+} to give typical 4f-4f emission of Sm^{3+}. The other three examples are from recent studies on afterglow phosphors by Lyu *et al.* on $REPO_4$[13-15] and Luo *et al.* on $Gd_{1-x}La_xAlO_3$[2] and RE_2O_2S[11] where hole detrapping processes from Bi^{4+}, Tb^{4+}, or Pr^{4+} were identified in $REPO_4$ and $Gd_{1-x}La_xAlO_3$. For RE_2O_2S, a hole detrapping process resulting in Ti^{4+} charge transfer emission is observed. There are rare reports on good storage phosphors discussing the hole-capturing and detrapping processes.

Bi^{3+} is a famous activator for photonic materials which is widely investigated[16]. However, Bi^{3+} doped storage phosphors are rarely reported and only a few Bi^{3+}-activated persistent luminescence phosphors have appeared up to now[14, 17]. The trapping and detrapping processes regarding bismuth are complex and often remain unclear. A recent study on Bi^{3+}-doped $REPO_4$ indicates that Bi^{3+} not only can act as an electron trapping centre but also as a hole capturing centre[14]. More studies are required to unravel the charge carrier detrapping processes regarding bismuth to obtain more insights for rational design of bismuth activated storage phosphors.

Methods have been established to derive the energy level locations of the dopants like Cr^{2+}, Cr^{3+}, Bi^{2+}, Bi^{3+}, and divalent and trivalent lanthanides within the band gap of inorganic compounds[5, 18-21]. Based on experimental spectroscopy, a vacuum referred binding energy (VRBE) diagram with host band and impurity energy level locations could be established to guide the exploration of charge carrier trapping materials[22]. Knowledge on the VRBE in dopant levels provides a tool to predict the trapping depths and determine what dopant may capture an electron and what dopant may capture a hole, which helps to explain and even adjust carrier trapping processes. The VRBE-aided methodology is so far mainly used in lanthanide and/or transition metal activated garnet compounds[3, 23] and other oxide compounds like $Ca_3Si_2O_7$[24] and Sr_3SiO_5[25, 26] to develop persistent luminescence phosphors. To the best of our knowledge, the VRBE-guided exploration of bismuth and/or lanthanide doped storage phosphors is rarely reported up to now.

The research on optical data storage is of interest because of the challenges for storage of fast-growing amount of data[27-34]. Storage phosphors are information storage materials which trap electrons and holes in host related defect traps after absorbing ionizing radiation[35-40]. They have been applied as storage media in information storage applications[41-46], like digital dental radiographic imaging facility[47] and computed radiography (CR) based on an X-ray storage phosphor plate[45]. Today BaFBr(I):Eu^{2+} is the widely utilized commercial X-ray storage phosphor[45, 48]. Nevertheless, it is hygroscopic which limits its long-term durability after exposure in air. Scientists are exploring better storage phosphors in various crystals like $BaCl_2$:Eu^{2+}[49], CsBr:Eu^{2+}[50, 51], and Lu_2O_3[52]. Sidorenko *et al.* [53] reported the storage properties of $LiLnSiO_4$:Ce^{3+},Sm^{3+} (Ln=Y or Lu). After charging, $LiLuSiO_4$, Sm^{2+} liberates electrons already near room temperature (RT) resulting in strong fading of stored information. Situation is better in $LiYSiO_4$ with the Sm^{2+} TL glow peak near 390 K but a low density of the host material makes it less suited for application as X-ray storage phosphor. Recently, Dobrowolska *et al.* [35, 54] reported excellent storage capacity of optimized $LiLuSiO_4$:Ce^{3+},Tm^{3+}. Its thermoluminescence (TL) intensity is about 4 times higher than that of commercial BaFBr(I):Eu^{2+} storage phosphor after β irradiation. However, this phosphor was developed by a trial-and-error approach. The nature of the trap(s) and the role of thulium codoping in $LiLuSiO_4$:Ce,Tm are still unclear. This finding motivated a deeper study into the family of related compounds $LiLuSiO_4$, $LiLuGeO_4$, and solid solutions $NaLu_{1-x}Y_xGeO_4$ in Ref. [55] with using other dopants like Bi^{3+} and Eu^{3+}.

The spectroscopy of Bi^{3+} in $LiYSiO_4$ and $LiLuSiO_4$ and their solid solutions was already discussed in Ref. [55]. Also the spectroscopy of the lanthanides in these compounds is well known and with that information the VRBE schemes with all the relevant levels in the band gap were constructed in the Ref. [55]. In this work, with the knowledge and VRBE diagrams from in Ref. [55], we return to the silicate solid solutions of the family of $LiLuSiO_4$, $LiYSiO_4$, and $LiLuGeO_4$. Here the focus is on 1) the engineering aspects of storage and afterglow phosphors and 2) developing and optimizing phosphors for application. Crystal composition modulation and dopant combinations using Bi^{3+}, Pr^{3+}, Tb^{3+}, Ce^{3+}, Tm^{3+}, or Sm^{3+} are explored with the aim to engineer either the recombination centre, the dominant glow peak temperature, or to optimize the afterglow or storage performance.

The VRBE diagram known for $LiLuSiO_4$ is shown in Fig. 6.1a)[55]. The VRBE of an electron at the ground states of divalent and trivalent lanthanides is linked by two zigzag curves a and b. The VRBE in the ground states of Bi^{3+} and Bi^{2+} is also provided. Fig. 6.1a) illustrates that Tm^{3+}, Sm^{3+}, Bi^{3+}, and Eu^{3+} act as ~0.62, ~1.08,

~1.81±0.5, and ~2.34 eV deep electron capturing centres, while Ce^{3+}, Pr^{3+}, Tb^{3+}, and Bi^{3+} act as ~3.89, ~2.04, ~2.22, and ~1.90 eV deep hole capturing centres.

For afterglow phosphor application at RT, shallow trap depth (<~1 eV) is required. For storage phosphor application at RT, deep trap depth (>~1 eV) is needed. Fig. 6.1a) guides us to choose a proper combination of electron and hole trapping centres to engineer an electron or hole release process for a specific application. It was demonstrated that one may combine a deep hole trap like Ce, Pr, Tb, or Bi with a less deep electron trap like Tm or Sm to arrive at recombination at the hole trap generating either Ce, Tb, Pr, or Bi emission. One may also combine a hole trap like Pr, Tb, or Bi with a deeper electron trap like Eu or Bi to arrive at recombination at the electron trap leading to Eu or Bi emission. For instance, red Eu^{3+} 4f-4f emission may appear for the Eu^{3+}-Bi^{3+} or Eu^{3+}-Tb^{3+} pairs in $LiLuSiO_4$ when a hole is liberated from Bi^{4+} or Tb^{4+} to recombine with electrons at Eu^{2+} because Bi^{3+} and Tb^{3+} may act as less deep hole traps than the electron trap depth on Eu. By making solid solutions like $LiLu_{1-x}Y_xSiO_4$, $LiLuSi_{1-y}Ge_yO_4$, or $LiLu_{1-x}Y_xSi_{1-y}Ge_yO_4$, the VB-top and CB-bottom may be shifted up or down as predicted in the stacked VRBE scheme in Fig. 6.1b), leading to ~100 K shift of the temperature of glow peak maxima. Herewith one may tune the trap depth.

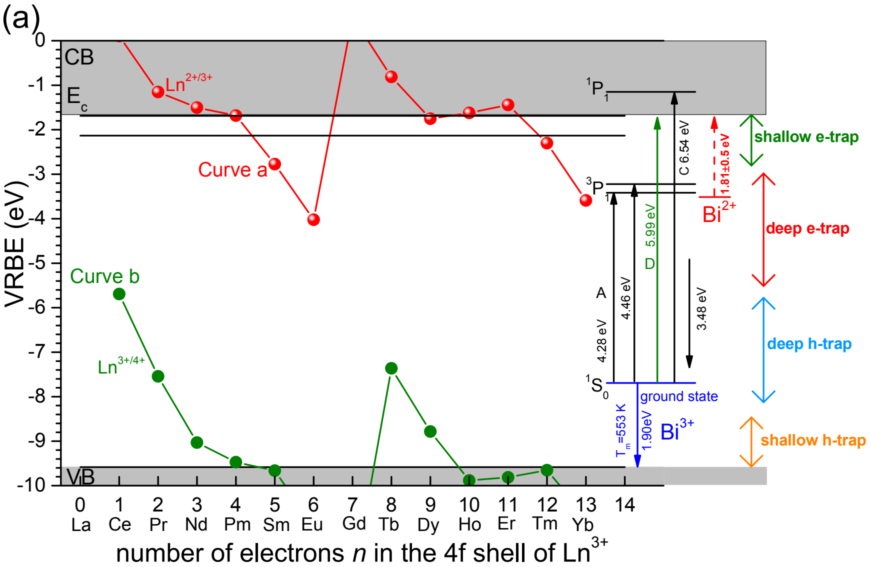

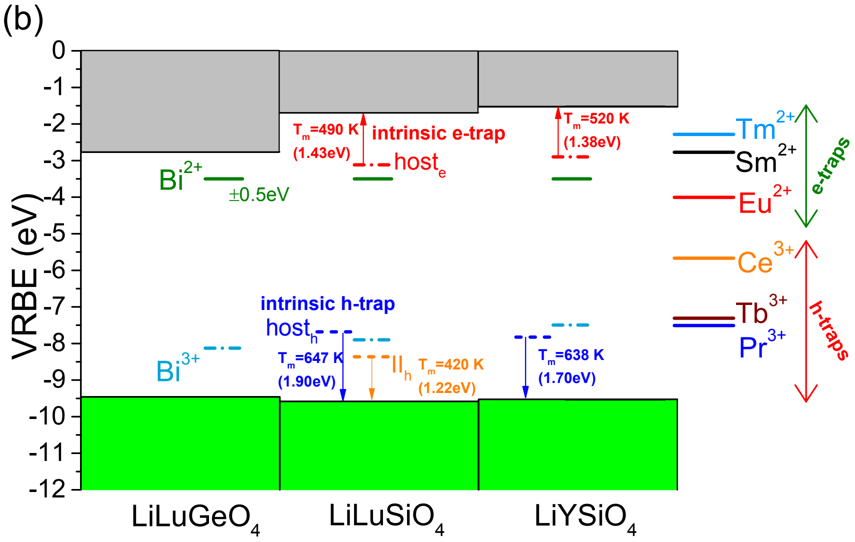

Fig. 6.1. Vacuum referred binding energy (VRBE) diagram for (a) $\mathrm{LiLuSiO_4}$ and (b) stacked VRBE scheme for $\mathrm{LiLuSiO_4}$ related family of compounds showing the VRBE in the ground states of $\mathrm{Bi^{2+}}$, $\mathrm{Bi^{3+}}$, and lanthanides. Experimentally observed transitions are denoted by arrows. The TL glow peaks $\mathrm{II_h}$ in Fig. 6.3a), $\mathrm{host_h}$ in Fig. 6.4c), and $\mathrm{host_e}$ in Fig. 6.5b) are used to determine the energy level locations of the intrinsic e-traps and h-traps in Fig. 6.1b).

6.3. Experimental

Lanthanides and/or bismuth activated $\mathrm{LiLu_{1-x}Y_xSiO_4}$ and $\mathrm{LiLu_{0.25}Y_{0.75}Si_{1-y}Ge_yO_4}$ compounds were synthesized using a high-temperature solid-state reaction method. 0.2-0.7 mm $\mathrm{SiO_2}$ (99.99%) crystals were purchased from Umicore company and then milled to small crystals. The other starting reagents were purchased from Sigma-Aldrich and used without further treatment. To compensate for the volatilization of lithium at high temperature, an excess of 10% $\mathrm{Li^+}$ above the stoichiometry ratio was used. The appropriate chemicals of rare earth oxides with high purity (99.99%), $\mathrm{SiO_2}$ (99.99%), $\mathrm{Li_2CO_3}$ (99.99%), $\mathrm{Bi_2O_3}$ (99.999%), and $\mathrm{GeO_2}$ (99.99%) were mixed well by adding acetone. The obtained mixture (~0.6 g) was placed in a corundum crucible and then fired at 800 °C for 8 h and at 1150 °C for 15 h in ambient atmosphere. For the compounds without bismuth doping, the mixture was further heated at 1170 °C for 5h under an atmosphere of $\mathrm{H_2/N_2}$ ($\mathrm{H_2}$: $\mathrm{N_2}$ 7 %: 93%). To optimize the charge carrier storage capacity for $\mathrm{LiLu_{0.25}Y_{0.75}SiO_4}$: $\mathrm{0.01Bi^{3+}}$ solid solution, the starting mixture was first fired at 800 °C for 8 h and then at 1200 °C for 24h under ambient atmosphere. The optimized $\mathrm{LiLu_{0.5}Y_{0.5}SiO_4}$: $\mathrm{0.01Ce^{3+},0.005Sm^{3+}}$ was synthesized at 800 °C for 2 h and then at 1170 °C for 10 h under an atmosphere of H_2/N_2 (H_2: N_2 7 %: 93%) for 3 times in a tube furnace. The utilized heating rate for the furnace is 3 °C/min. The obtained crystals were naturally cooled down to room temperature (RT) and ground to fine powders before further measurements.

The synthesized crystal structure was checked by an X-ray diffraction facility (PANalytical XPert PRO) using cobalt Kα radiation (λ=0.178901 nm) at 45 kV and 40 mA. For the temperature-dependent XRD patterns for $LiLu_{0.25}Y_{0.75}Si_{1-y}Ge_yO_4$: $0.01Bi^{3+}$ (y=0.25), another facility using copper Kα1 radiation (λ=0.154060 nm) and a temperature-tailorable sample holder were utilized. The photoluminescence emission (PL) and PL excitation (PLE) spectra were recorded using a facility that contains a UV/VIS branch utilizing a Horiba Gemini 180 monochromator and a Newport 66921 Xe lamp and a VUV/UV branch with an ARC VM502 vacuum monochromator and a water-cooled deuterium lamp. The emission from samples was recorded with a PerkinElmer MP-1993 photomultiplier. The excitation spectra were corrected by the wavelength-dependent lamp intensity. The Ce^{3+} and Bi^{3+} fluorescence decay curves were collected by the above facility which further connects with a waveform digitizer module and a pulsed YAG:Nd laser source (NT230-100-SH/DUV-SCU) that contains an optical parametric oscillator (OPO). The laser pulse repetition rate is 100 Hz and the pulse duration is 2-5 ns.

High-temperature thermoluminescence (TL) glow curves ranging from ~300 to 900 K were recorded using a facility which is composed of a RISØ TL/OSL reader (model DA-15), a DA-20 controller, and an EMI 9635QA photomultiplier tube. Prior to the TL measurement, the compounds were heated in the dark at a heating rate of 5 K/s from RT to ~900 K to empty the randomly trapped charge carriers and then cooled to room temperature. This was repeated 2 times more. The compounds were then charged by β-ray irradiation from a $^{90}Sr/^{90}Y$ source at a dose rate of ~0.7 mGy/s in nitrogen gas atmosphere.

Low-temperature TL (LTTL) glow curves were measured with a facility which contains a $^{90}Sr/^{90}Y$ β-ray source with a dose rate of ~0.4 mGy/s and a Perkin-Elmer channel photomultiplier tube (MP-1393) photon detector. Prior to the LTTL measurements, the compounds were pressed into pills with mass <10 mg and then heated to 450 K for 180s to liberate the randomly captured charge carriers under vacuum in the dark. The compounds were cooled to 90 K using liquid nitrogen and then irradiated with β irradiation. A 600 nm bandpass filter of 600FS40-50 (Andover Corporation) was placed between the compounds and the photomultiplier to select the Pr^{3+} or Eu^{3+} red emission. 350, 400, and 550 nm bandpass filters of 350FS40-50, 400FS40-50, and 550FS40-50 were utilized to select the characteristic ultraviolet Bi^{3+}, blue Ce^{3+}, and green Tb^{3+} emissions, respectively. For the TL intensity comparison of the synthesized compounds in this work with the commercial BaFBr(I):Eu^{2+} storage phosphor and an Al_2O_3:C crystal chip, a 300-700 nm bandpass filter of Schott BG-39 was used. The TL intensities were corrected by the sample mass and β irradiation time and then expressed in counts/s/g.

To identify the emission centres during TL readout, thermoluminescence emission (TLEM) spectra were recorded on a setup which combines the RISØ TL/OSL reader and a UV/vis QE65000 (Ocean Optics) spectrometer. Prior to the TLEM measurements, the compounds were heated to ~900 K to empty all traps and then cooled to room temperature followed by γ-ray charging in the dark using a ^{60}Co source. The TLEM plots measured by QE65000 at a heating rate of 1 K/s were corrected by the wavelength-dependent quantum efficiency of QE65000.

Prior to recording thermoluminescence excitation (TLE) spectra, compounds were heated to ~723 K to empty all traps and cooled to RT. The compounds were then illuminated during 800s by monochromatic photons from a setup that is composed of a monochromator (Oriel Cornerstone 130) and a 150 W xenon arc lamp (Hamamatsu L2273). This setup has a wavelength resolution of 0.8 nm against 0.1 mm slit width. In this work, a 1 mm slit width was used. The setup is programmed by LabVIEW to automatically collect the TL glow curves from RT to ~723 K when the illumination wavelength ranged from 200 to 400 nm with steps of 10 nm. A TLE plot like in Fig. 6.7d) was established by integrating TL glow peaks and displaying integrated intensity against the illumination wavelength[11, 56]. The measured TL intensities were corrected by the illumination time, compound mass, and the xenon lamp intensities as a function of wavelength. A filter was placed between the compounds and the photomultiplier tube to select the Ce^{3+} or Bi^{3+} characteristic emission.

To compare the readout speed of stored information in storage phosphors, the TL glow curves after β-ray charging followed by photon stimulation were recorded on the above RISØ TL/OSL reader, which further connects a 475 nm blue LED or a wavelength-tailored laser beam produced from the NT230-100-SH/DUV-SCU facility. The scanning electron microscope (SEM) images and the energy-dispersive X-ray spectroscopy (EDX) mapping for solid solutions $LiLu_{0.5}Y_{0.5}SiO_4$:0.01Ce^{3+},0.01Sm^{3+}, $LiLu_{0.25}Y_{0.75}SiO_4$:0.01Bi^{3+}, and $LiLu_{0.25}Y_{0.75}Si_{0.75}Ge_{0.25}O_4$:0.01$Bi^{3+}$ were measured using JEOL JSM-IT100 facility. A 254 nm Hg lamp and an UV-lamp with the main emission near 365 nm were used to charge the $LiLu_{0.5}Y_{0.5}SiO_4$:0.01Ce^{3+},0.01Sm^{3+} storage phosphor. An iPhone 8Plus was utilized to take the photographs for Ce^{3+} related emission. For the $LiLu_{0.5}Y_{0.5}SiO_4$:0.01Ce^{3+},0.01Sm^{3+} dispersed in silicone film, the silicone gel was mixed well with an appropriate amount of storage phosphor to form a gel film on a glass substrate. The film was placed in a vacuum for 300s to remove air bubbles and then put in air at RT for 10h.

6.4. Results

6.4.1. X-ray diffraction patterns for solid solutions

The X-ray diffraction (XRD) patterns for $LiLu_{1-x}Y_xSiO_4$:0.01Ce^{3+},0.01Sm^{3+} (x=0-1) with different content of yttrium are shown in Fig. 6.2a). With increasing x, the XRD peaks slightly shift towards smaller 2θ angles. This confirms that the yttrium cations enter the lutetium site and increase the cell volume because yttrium has a larger ionic radius than lutetium. The patterns evidence that solid solutions appear in the prepared crystals of $LiLu_{1-x}Y_xSiO_4$:0.01Ce^{3+},0.01Sm^{3+} in Fig. 6.2a), and for $LiLu_{0.25}Y_{0.75}Si_{1-y}Ge_yO_4$:0.01$Bi^{3+}$ the same in Fig. S6.2.

Fig. 6.2b) shows the XRD patterns for the double solid solution $LiLu_{0.25}Y_{0.75}Si_{1-y}Ge_yO_4$:0.01$Bi^{3+}$ (y=0.25). Impurity phases or structural change are absent when the solid solution was heated from 298 to 598 K.

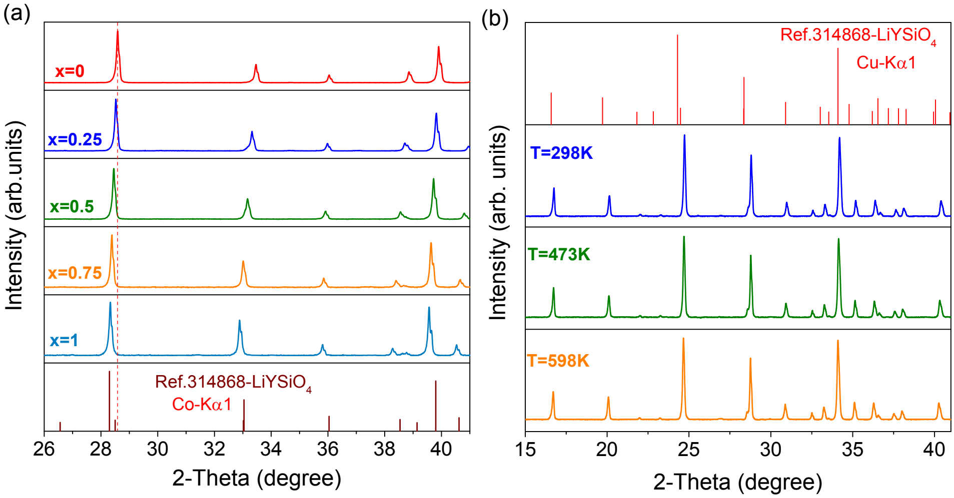

Fig. 6.2. XRD patterns of (a) $LiLu_{1-x}Y_xSiO_4$:0.01Ce^{3+},0.01Sm^{3+} (x=0-1) recorded at RT, and (b) $LiLu_{0.25}Y_{0.75}Si_{1-y}Ge_yO_4$:0.01$Bi^{3+}$ (y=0.25) solid solution recorded at 298, 473, and 598 K.

6.4.2. Engineering hole liberation from Tb^{4+}, Pr^{4+}, and Bi^{4+} in $LiLu_{1-x}Y_xSiO_4$ solid solutions

TL emission (TLEM) studies were carried out to identify the recombination centres in Ln^{3+} and/or Bi^{3+} doped $LiLu_{1-x}Y_xSiO_4$ in Fig. 6.3. Additional TLEM spectra for other $LiLu_{1-x}Y_xSi_{1-y}Ge_yO_4$ phosphors with other combinations of Ln^{3+} doping or different yttrium or germanium content can be found in Fig. S6.3-S6.5 and S6.14.

For $LiLuSiO_4$:0.01Eu^{3+} in Fig. 6.3a), TL peaks near 373, 420, 497, 556, and 752 K with characteristic Eu^{3+} 4f-4f red emission emerge, that will be referred to as peaks I_h, II_h, III_h, IV_h, and V_h, respectively. Upon co-doping Tb^{3+} in $LiLuSiO_4$:0.01Eu^{3+},0.01Tb^{3+} in Fig. 6.3b), a broad and intense TL peak near 572 K named Tb_h (Tb^{4+}), that will be attributed to hole release from Tb^{4+}, appears while monitoring the Eu^{3+} red emission. The similar applies to Pr^{3+} co-doping in $LiLuSiO_4$:0.01Eu^{3+},0.01Pr^{3+} in Fig. 6.3c) where a TL peak near 582 K named Pr_h (Pr^{4+}) emerges.

Replacing Tb^{3+} or Pr^{3+} by the hole trapping centre of Bi^{3+}, again characteristic Eu^{3+} 4f-4f emission appears in $LiLu_{0.5}Y_{0.5}SiO_4$:0.01Eu^{3+},0.01Bi^{3+} with TL glow peaks near 535 and 632 K in Fig. 6.3d). Fig. 6.3e) shows the TLEM plot for $LiLu_{0.5}Y_{0.5}SiO_4$:0.01Bi^{3+},0.01Sm^{3+} where Sm^{3+} acts as a less deep electron trap than Bi^{3+} and Eu^{3+}. Broad Bi^{3+} A-band emission peaking at ~360 nm with a weak TL peak near 367 K named peak Sm_e, that will be assigned to electron liberation from Sm^{2+}, and a broad TL glow peak (Bi_h) ranging from 425 to 700 K and peaking near 532 K emerges. The ~532 K TL peak is also observed in $LiLu_{0.5}Y_{0.5}SiO_4$:0.01Eu^{3+},0.01Bi^{3+} in Fig. 6.3d), which will be attributed to hole liberation from Bi^{4+}. Note that not only characteristic Bi^{3+} A-band emission but also typical Sm^{3+} red 4f-4f emission appears in Fig. 6.3e). It is ascribed to an energy transfer process from Bi^{3+} to Sm^{3+} because the TL glow curves in Fig. 3e) share the same shape when selecting the Bi^{3+} A-band emission or when selecting the Sm^{3+} 4f-4f emission. This applies also for $LiLu_{1-x}Y_xSiO_4$:0.01Bi^{3+},0.01Sm^{3+} with x=0.25 and 0.75 in Fig. S6.14b)-c). The energy transfer from Bi^{3+} to Sm^{3+} is further evidenced by photoluminescence excitation spectra of $LiYSiO_4$: 0.01Bi^{3+},0.01Sm^{3+} in Fig. S6.19c). Like in Fig. 6.3d)-e), a Bi_h (Bi^{4+}) TL peak near 510 K appears in the TL emission plot for the double solid solution $LiLu_{0.25}Y_{0.75}Si_{0.75}Ge_{0.25}O_4$:0.01$Bi^{3+}$ in Fig. 6.3f).

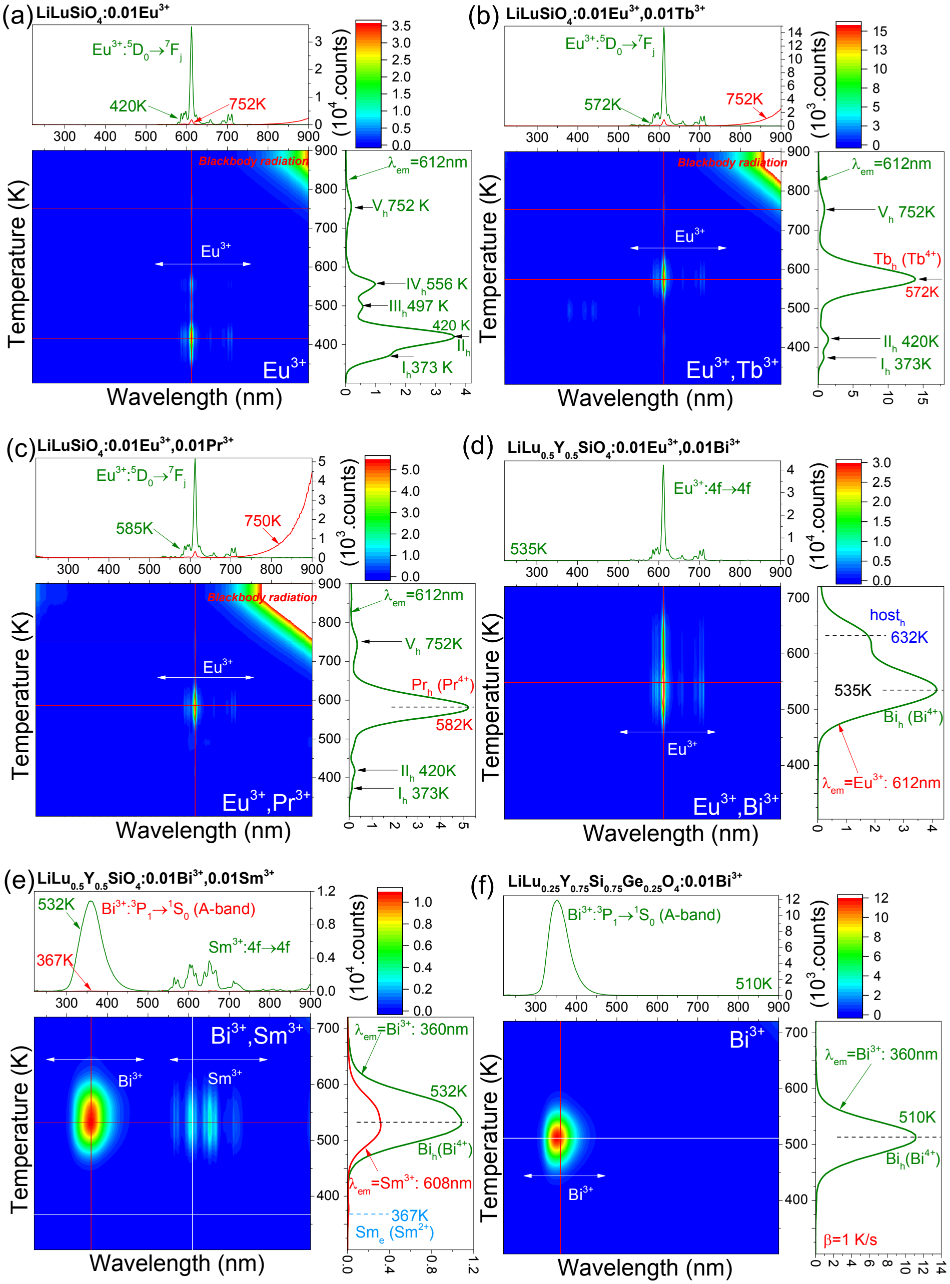

Fig. 6.3. TL emission (TLEM) plots for (a) LiLuSiO$_4$:0.01Eu^{3+}, (b) LiLuSiO$_4$:0.01Eu^{3+}, 0.01Tb^{3+}, (c) LiLuSiO$_4$:0.01Eu^{3+},0.01Pr^{3+}, (d) LiLu$_{0.5}$Y$_{0.5}$SiO$_4$:0.01Eu^{3+},0.01Bi^{3+}, (e)

$LiLu_{0.5}Y_{0.5}SiO_4$:0.01Bi^{3+},0.01Sm^{3+}, and (f) double solid solution $LiLu_{0.25}Y_{0.75}Si_{0.75}Ge_{0.25}O_4$: 0.01$Bi^{3+}$ recorded at a heating rate of 1 K/s after γ-ray irradiation.

Fig. 6.1b) shows that the VRBE in the valence band top of $LiYSiO_4$ is about 0.1 eV higher than that of $LiLuSiO_4$. Because the VRBEs in the ground states of lanthanides are almost invariant, it implies that the temperature of a TL glow peak due to hole liberation from Tb^{4+} or Pr^{4+} should decrease. Ln^{3+} and/or Bi^{3+} doped $LiLu_{1-x}Y_xSiO_4$ crystals were synthesized to further study and explore such hole trapping process.

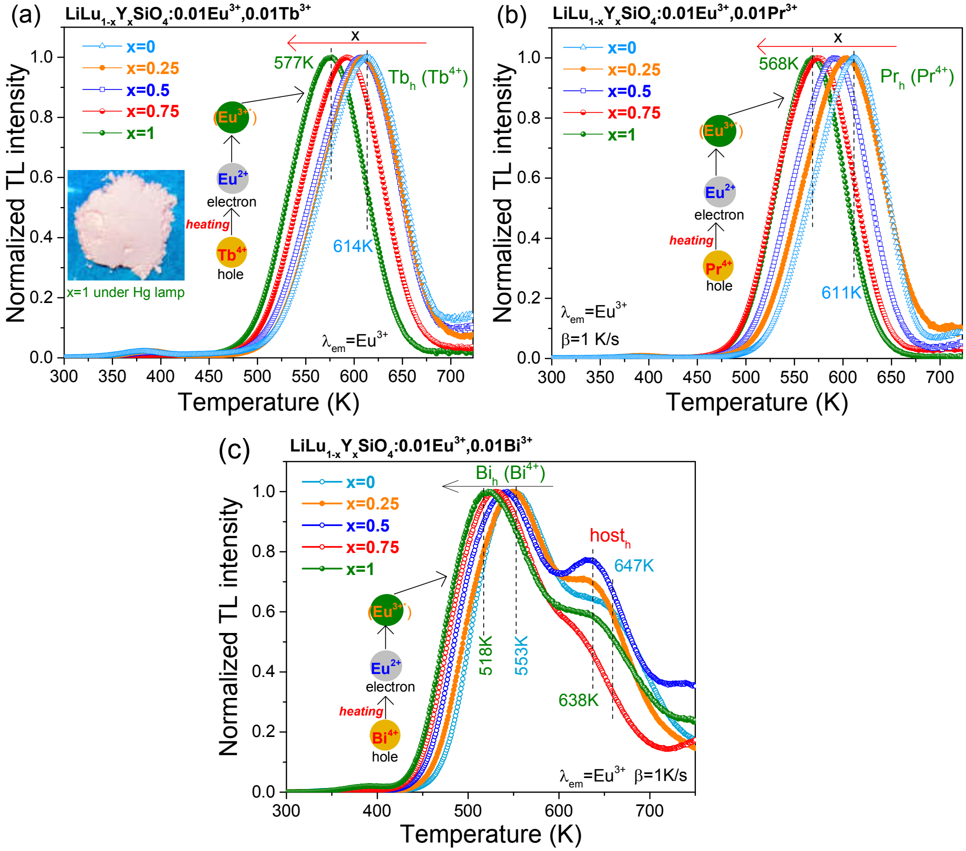

Fig. 6.4. Normalized TL glow curves for (a) $LiLu_{1-x}Y_xSiO_4$:0.01Eu^{3+},0.01Tb^{3+}, (b) $LiLu_{1-x}Y_xSiO_4$:0.01Eu^{3+},0.01Pr^{3+}, and (c) $LiLu_{1-x}Y_xSiO_4$:0.01Eu^{3+},0.01Bi^{3+} solid solutions while monitoring the Eu^{3+} red emission recorded at a heating of 1 K/s after β irradiation. The inset in a) shows a photograph of $LiYSiO_4$:0.01Eu^{3+},0.01Tb^{3+} under Hg lamp illumination.

Fig. 6.4a) shows the normalized TL glow curves for $LiLu_{1-x}Y_xSiO_4$:0.01Eu^{3+}, 0.01Tb^{3+} solid solutions after β irradiation. The as recorded TL glow curves are shown in Fig. S6.8a). With increasing x, the Tb_h (Tb^{4+}) TL glow peak near 614 K shifts about 37 K towards lower temperature, confirming the above prediction. The same applies to $LiLu_{1-x}Y_xSiO_4$:0.01Eu^{3+},0.01Pr^{3+} solid solutions as shown in Fig. 6.4b), where a ~43 K TL peak lowering appears with increasing x. Note that the Tb_h (T_m) and Pr_h (T_m) in $LiLuSiO_4$ in Fig. 6.4a)-b) are about 35 K higher than that in Fig. 6.3b)-c). The compounds in Fig. 6.4 were synthesized ~2 years later with respect to that in Fig. 6.3b)-c), and the synthesis conditions may have been slightly different.

Fig. 6.4c) shows the TL glow curves for $LiLu_{1-x}Y_xSiO_4$:0.01Eu^{3+},0.01Bi^{3+} after β irradiation. The TL glow peak Bi_h near 553 K gradually shifts ~35 K towards lower temperature when x increases. Note that the TL glow peak near 647 K named peak $host_h$, that will be attributed to hole liberation from intrinsic host-related hole trap(s), shifts only about 10 K towards lower temperature with increasing x. The derived energy level locations of the intrinsic defect(s) corresponding with these $host_h$ TL peaks for x=0 and x=1 are shown in Fig. 6.1b). They are determined by adding the derived hole trap depths to the valence band top. Considering that hole liberation and transport may be realized via V_k centre creation, the derived level locations of the intrinsic hole defect(s) may move up in the VRBE diagram in Fig. 6.1b).

6.4.3. Engineering electron liberation from Tm^{2+} and Sm^{2+} in $LiLu_{1-x}Y_xSiO_4$ solid solutions

In Fig. 6.1b) the conduction band bottom moves ~0.17 eV upward with the full substitution of Lu^{3+} by Y^{3+} in $LiLu_{1-x}Y_xSiO_4$ solid solutions, and an increase of the Ln^{3+} electron trapping depths is then expected. Fig. 6.5a) shows the low-temperature TL glow curves for $LiLu_{1-x}Y_xSiO_4$:0.01Ce^{3+},0.01Tm^{3+} solid solutions after β irradiation. Here Ce^{3+} acts as a deep hole trap and Tm^{3+} as a less deep electron trap. With increasing x, the TL glow peak named peak Tm_e (Tm^{2+}) near 144 K shifts ~42 K towards higher temperature.

The Tm_e TL glow peak in $LiLu_{1-x}Y_xSiO_4$ in Fig. 6.5a) is at a too low temperature of 144-186 K for afterglow or storage phosphor applications. It needs to be shifted close to 400 K or even higher in order to avoid TL fading at RT for storage phosphor application. Fig. 6.1a) shows that Sm^{3+} acts as a ~0.47 eV deeper electron trap than Tm^{3+}. The storage phosphor properties of Sm^{3+} co-doped $LiLu_{1-x}Y_xSiO_4$ (x=0-1) crystals were therefore explored.

Fig. 6.5b) and S6.11a) show the normalized and unnormalized TL glow curves for $LiLu_{1-x}Y_xSiO_4$:0.01Ce^{3+},0.01Sm^{3+} solid solutions after β irradiation. With increasing x, the TL glow peak named peak Sm_e (Sm^{2+}), that will be assigned to electron liberation from Sm^{2+}, gradually shifts about 54 K from 348 K towards higher temperature in Fig. 6.5b). The shifting leads to almost 3 orders of magnitude decreased initial Ce^{3+} persistent luminescence in Fig. S6.11b), and less TL fading as shown in Fig. S6.11c). For the x=0.75 phosphor after 100 minutes delay time, the integrated TL intensity between 300-723 K remains ~85%, which is comparable to that of BaFBr(I):Eu^{2+} (87%). The optimal concentration of the Sm^{3+} co-dopant at which Sm_e glow is most intense, is about 1% in $LiLu_{0.5}Y_{0.5}SiO_4$:0.01Ce^{3+},zSm^{3+} (z=0.1%-1.6%) solid solutions as demonstrated in Fig. S6.12a). The legend of Fig. 6.5b) and S6.11a) provides the ratios of integrated TL between 300-723 K of $LiLu_{1-x}Y_xSiO_4$:0.01Ce^{3+},0.01Sm^{3+} to that of the commercial X-ray storage phosphor BaFBr(I):Eu^{2+} (Agfa-Gevaert). The maximal ratio of 5.7 is obtained when x=0.5. Note that the TL peak near 490 K named peak $host_e$ for the x=0 phosphor, that has been attributed to electron liberation from host intrinsic defect(s) in Refs. [53, 54], first shifts ~30 K towards higher temperature from x=0 to x=0.5, but then remains constant near 520 K with further increasing x in $LiLu_{1-x}Y_xSiO_4$:0.01Ce^{3+},0.01Sm^{3+}.

Since Bi^{3+} can also act as a hole capturing centre, $LiLu_{1-x}Y_xSiO_4$:0.01Bi^{3+},0.01Sm^{3+} was explored and its normalized TL glow curves after β irradiation are shown in Fig. 6.5c). The as recorded TL glow curves are shown in Fig. S6.15a). With increasing x, the Sm_e TL glow peak near 343 K shifts ~53 K towards higher temperature in the inset of Fig. 6.5c), which shares the same trend as that in $LiLu_{1-x}Y_xSiO_4$:0.01Ce^{3+},0.01Sm^{3+} in Fig. 6.5b). The Bi_h TL glow peak near 553 K gradually shifts in the opposite direction ~35 K towards lower temperature when x increases. The same appears in $LiLu_{1-x}Y_xSiO_4$:0.01Eu^{3+}, 0.01Bi^{3+} in Fig. 6.4c) above, where the recombination centre is Eu^{3+} instead of Bi^{3+}. The ratios of integrated TL between 300-723 K of $LiLu_{1-x}Y_xSiO_4$:0.01Bi^{3+}, 0.01Sm^{3+} to that of BaFBr(I):Eu^{2+} are provided in the legend of Fig. 6.5c). The maximal ratio of 3 is observed when x=0.75.

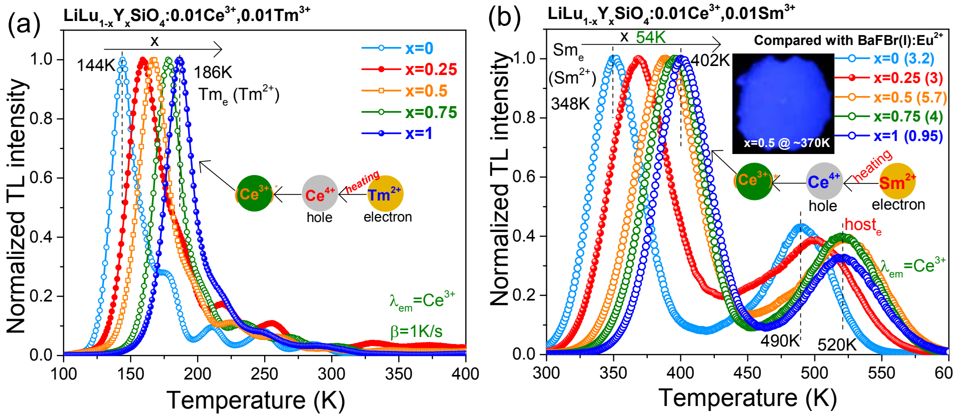

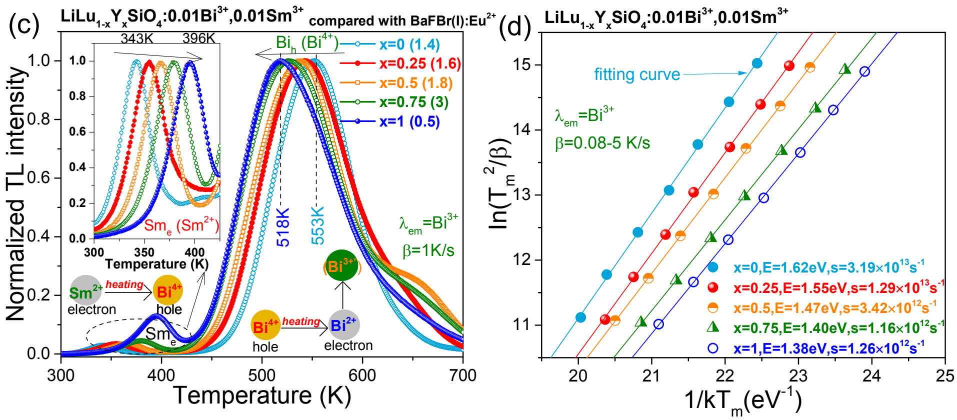

Fig. 6.5. TL glow curves for (a) $LiLu_{1-x}Y_xSiO_4$:$0.01Ce^{3+}$,$0.01Tm^{3+}$, (b) $LiLu_{1-x}Y_xSiO_4$:$0.01Ce^{3+}$,$0.01Sm^{3+}$, and (c) $LiLu_{1-x}Y_xSiO_4$:$0.01Bi^{3+}$,$0.01Sm^{3+}$ recorded at a heating rate of 1 K/s after β irradiation. (d) Variable heating rate plots for Bi_h (Bi^{4+}) TL peaks of $LiLu_{1-x}Y_xSiO_4$:$0.01Bi^{3+}$,$0.01Sm^{3+}$. The Ce^{3+} emission was monitored in a)-b), and the Bi^{3+} emission was selected in c)-d). A photograph for the x=0.5 phosphor heated at ~370 K after Hg lamp charging is shown in b).

The hole trapping depths E (eV) of the Bi_h TL glow in $LiLu_{1-x}Y_xSiO_4$:$0.01Bi^{3+}$, $0.01Sm^{3+}$ were derived using a variable heating rate plot and the first-order TL-recombination kinetics equation[11, 57-59]:

$$\ln\left(\frac{T_m^{\ 2}}{\beta}\right)=\frac{E}{kT_m}+\ln\left(\frac{E}{ks}\right) \tag{6.1}$$

in which k represents the Boltzmann constant (8.62×10^{-5} eV/K), s denotes the frequency factor (s^{-1}), and β is the heating rate of 0.08, 0.15, 0.3, 0.63, 1.25, 2.5, and 5 K/s. Fig. 6.5d) shows the variable heating rate plots for $LiLu_{1-x}Y_xSiO_4$:$0.01Bi^{3+}$,$0.01Sm^{3+}$ that give the frequency factors as listed in column 2, and the trapping depths in column 4 of Table 6.1 for the Bi_h TL glow peak in Fig. 6.5c).

Considering that the doped content of Bi^{3+} is low, we assume that the above determined frequency factors also apply to $LiLu_{1-x}Y_xSiO_4$:$0.01Ce^{3+}$,$0.01Ln^{3+}$ (Ln=Sm or Tm), and $LiLu_{1-x}Y_xSiO_4$:$0.01Eu^{3+}$,$0.01Ln^{3+}$ (Ln=Tb or Pr). Assuming first-order TL-recombination kinetics, the hole trapping depths E (eV) for the Tb_h (Tb^{4+}) and Pr_h (Pr^{4+}) TL glow peaks in $LiLu_{1-x}Y_xSiO_4$:$0.01Eu^{3+}$,$0.01Ln^{3+}$ in Fig. 6.4a)-b), the Tm_e (Tm^{2+}) TL peaks in $LiLu_{1-x}Y_xSiO_4$:$0.01Ce^{3+}$,$0.01Tm^{3+}$ in Fig. 6.5a), and the Sm_e (Sm^{2+}) TL glow peaks in $LiLu_{1-x}Y_xSiO_4$:$0.01Ce^{3+}$,$0.01Ln^{3+}$ in Fig. 6.5b) are determined by solving Eq. (6.1) with a temperature maximum (T_m) of a TL glow peak, β=1 K/s, and the above-obtained s values as listed in column 2 of Table 6.1. The determined results are given in columns 6, 8, 10, and 12 of Table 6.1. Considering that there is a trap depth distribution in the prepared solid solutions, the obtained trap depths in Table 6.1 should be treated as indicative.

Table 6.1. TL results for $LiLu_{1-x}Y_xSiO_4$:0.01Bi^{3+},0.01Sm^{3+}, $LiLu_{1-x}Y_xSiO_4$:0.01Ce^{3+}, 0.01Ln^{3+} (Ln=Sm or Tm), and $LiLu_{1-x}Y_xSiO_4$:0.01Eu^{3+},0.01Ln^{3+} (Ln=Tb or Pr) providing the frequency factors s (s^{-1}) and trap depths E (eV) for the Bi_h (Bi^{4+}), Tb_h (Tb^{4+}), Pr_h (Pr^{4+}), Sm_e (Sm^{2+}), and Tm_e (Tm^{2+}) TL glow peaks (T_m, K).

x	s	T_m Bi_h	E Bi_h	T_m Tb_h	E Tb_h	T_m Pr_h	E Pr_h	T_m Sm_e	E Sm_e	T_m Tm_e	E Tm_e
0	3.19×10^{13}	553	1.62	614	1.80	611	1.79	348	1.00	144	0.40
0.25	1.29×10^{13}	543	1.55	610	1.74	605	1.73	367	1.03	158	0.43
0.5	3.42×10^{12}	538	1.47	607	1.67	592	1.62	387	1.05	167	0.44
0.75	1.16×10^{12}	527	1.40	592	1.57	575	1.52	396	1.04	178	0.46
1	1.26×10^{12}	518	1.38	577	1.53	568	1.51	402	1.06	186	0.48

6.4.4. Engineering Bi^{4+} hole detrapping in $LiLu_{0.25}Y_{0.75}Si_{1-y}Ge_yO_4$ solid solutions

We explored further tailoring of the Bi_h (Bi^{4+}) TL glow peak in Bi^{3+} single doped $LiLu_{0.25}Y_{0.75}Si_{1-y}Ge_yO_4$:0.01$Bi^{3+}$ solid solutions. Fig. 6.1b) illustrates that the main effect of adding germanium is the ~0.6-1.0 eV lowering of the CB-bottom and in addition, the VB-top may change a few 0.1 eV. Fig. 6.6a) and S6.16 show the normalized and unnormalized TL glow curves for $LiLu_{0.25}Y_{0.75}Si_{1-y}Ge_yO_4$: 0.01$Bi^{3+}$ solid solutions after β irradiation. The Bi_h TL glow peak near 538 K gradually shifts ~144 K towards 394 K from y=0 to y=0.75, implying that the VB-top moves up or the Bi^{3+} ground state moves down or both movements are combined. For the y=1 phosphor, TL glow peaks near 327 K (weak), 371, 425, and 520 K emerge. Due to the lowering of the CB-bottom, we arrive at a situation where the Bi_e (Bi^{2+}) electron trap depth of ~0.74±0.5 eV becomes less deep than the Bi^{3+} hole trap depth of ~1.33 eV in $LiLuGeO_4$ in Fig. 6.1b). The same will apply to $LiLu_{0.25}Y_{0.75}GeO_4$. The dominant TL peak near 371 K is therefore tentatively attributed to electron release from Bi^{2+} to recombine with holes trapped at Bi^{4+} to give Bi^{3+} A-band emission as shown in Fig. S6.14h). The 371 K TL glow peak is referred to as the Bi_e (Bi^{2+}) glow peak. The TL peak shifting in Fig. 6.6a) results in more than a factor of 100 increased initial Bi^{3+} afterglow intensity in Fig. 6.6b), and stronger TL fading as demonstrated in Fig. 6.6c). The ratios of integrated TL between 300-723 K of $LiLu_{0.25}Y_{0.75}$ $Si_{1-y}Ge_yO_4$:0.01Bi^{3+} to that of BaFBr(I):Eu^{2+} are shown in the legend of Fig. 6.6a) and S6.16. The maximal ratio of 1.7 is obtained when y=0.75.

The trapping depths E (eV) for the Bi_h (Bi^{4+}) and Bi_e (Bi^{2+}) TL glow peaks in $LiLu_{0.25}Y_{0.75}Si_{1-y}Ge_yO_4$:0.01$Bi^{3+}$ in Fig. 6.6a) were derived from variable heating rate plots using Eq. (6.1) where the heating rate changes between 0.08-5 K/s after β irradiation. Fig. 6.6d) shows the plots for $LiLu_{0.25}Y_{0.75}Si_{1-y}Ge_yO_4$:0.01$Bi^{3+}$ that gives the trapping depths and the frequency factors as listed in the legend of Fig. 6.6d).

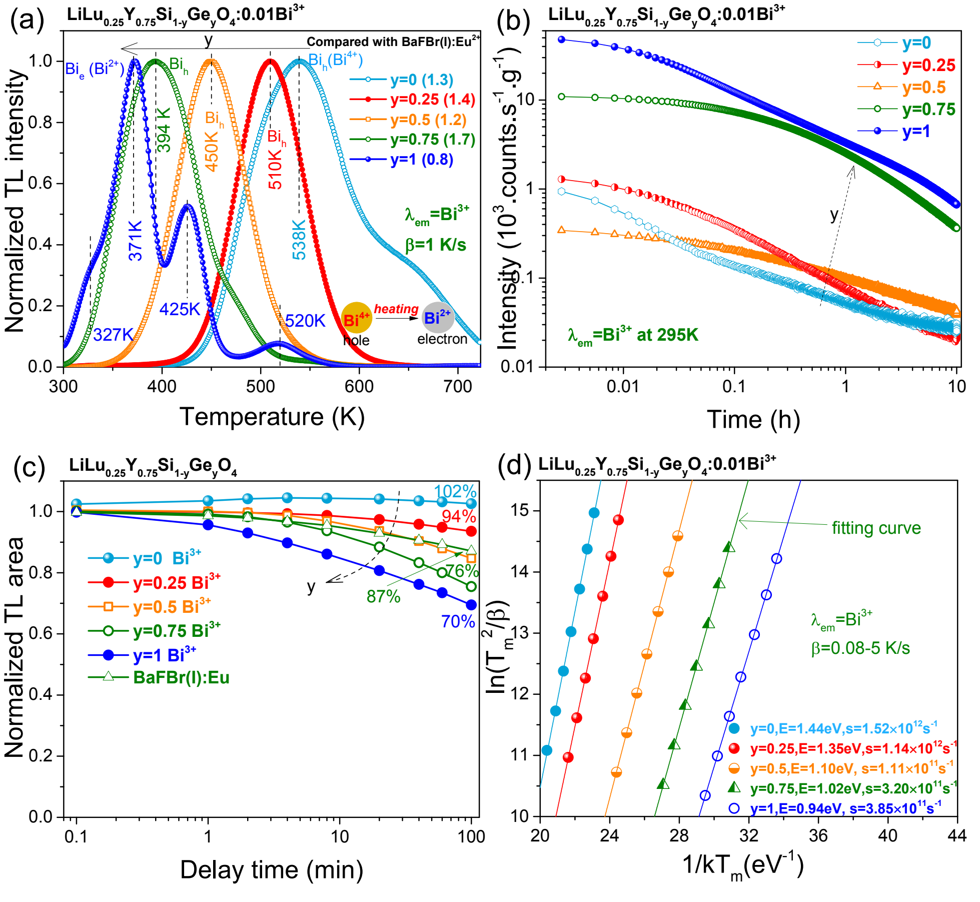

Fig. 6.6. (a) TL glow curves recorded at a heating rate of 1 K/s, (b) RT isothermal decay curves, (c) TL fading characteristics, and (d) variable heating rate plots for $LiLu_{0.25}Y_{0.75}Si_{1-y}Ge_yO_4$:0.01$Bi^{3+}$ solid solutions while monitoring the Bi^{3+} emission after β-ray irradiation.

Fig. 6.7a) and b) show the TL excitation (TLE) spectra for $LiLu_{0.25}Y_{0.75}SiO_4$ with Bi^{3+},Sm^{3+} and with Bi^{3+} only. For the $LiLu_{0.25}Y_{0.75}Si_{0.75}Ge_{0.25}O_4$:0.01$Bi^{3+}$ solid solution, the TLE spectrum is shown in Fig. 6.7c). Additional TLE spectra for other $LiLu_{0.25}Y_{0.75}Si_{1-y}Ge_yO_4$:0.01$Bi^{3+}$ phosphors can be found in Fig. S6.18. The

Sm_e TL glow peak near 410 K in Fig. 6.7a), and the Bi_h TL glow peak near 560 K in Fig. 6.7b) and near 530 K in Fig. 6.7c) can both be filled using photons near 210 nm. Fig. 6.7d) shows the TL excitation (TLE) plots determined by integrating the TL glow peak between 450-723 K in Fig. 6.7b) and 300-723 K in Fig. 6.7c) and S6.18 for $LiLu_{0.25}Y_{0.75}Si_{1-y}Ge_yO_4$:0.01$Bi^{3+}$. Columns 2 and 3 of Table 6.2 compare the TLE peak wavelengths with the photoluminescence excitation (PLE) peak wavelengths of Bi^{3+} D-bands for $LiLu_{0.25}Y_{0.75}Si_{1-y}Ge_yO_4$:0.01$Bi^{3+}$ from Fig. S6.19a). With increasing y, the TLE maximum near 210 nm gradually shifts 20 nm towards longer wavelength, which shares the same trend as that of the Bi^{3+} D- excitation band shifting in $LiLu_{0.25}Y_{0.75}Si_{1-y}Ge_yO_4$:0.01$Bi^{3+}$ phosphors.

Table 6.2. Comparison of the TL excitation (TLE) plots, the Bi_h and Bi_e TL glow peaks, and the Bi^{3+} D- excitation bands from spectroscopy for $LiLu_{0.25}Y_{0.75}Si_{1-y}Ge_yO_4$:0.01$Bi^{3+}$ (y=0-1).

y	TLE peak	Bi^{3+} D-band	Bi_h TL peak at β=5 K/s	Bi_h TL peak at β=1 K/s
0	210 nm	207 nm	566 K	538 K
0.25	220 nm	214 nm	532 K	510 K
0.5	230 nm	223 nm	471 K	450 K
0.75	230 nm	227 nm	408 K	394 K
1	230 nm	230 nm	396 K (Bi_e)	371 K (Bi_e)
source	Fig. 6.7d)	Fig. S6.19a)	Fig. 6.7b)-c) and S6.18	Fig. 6.6a)

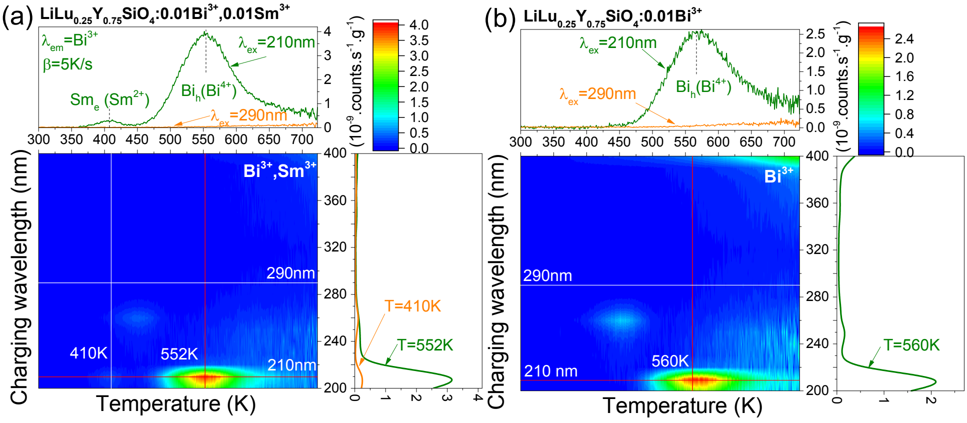

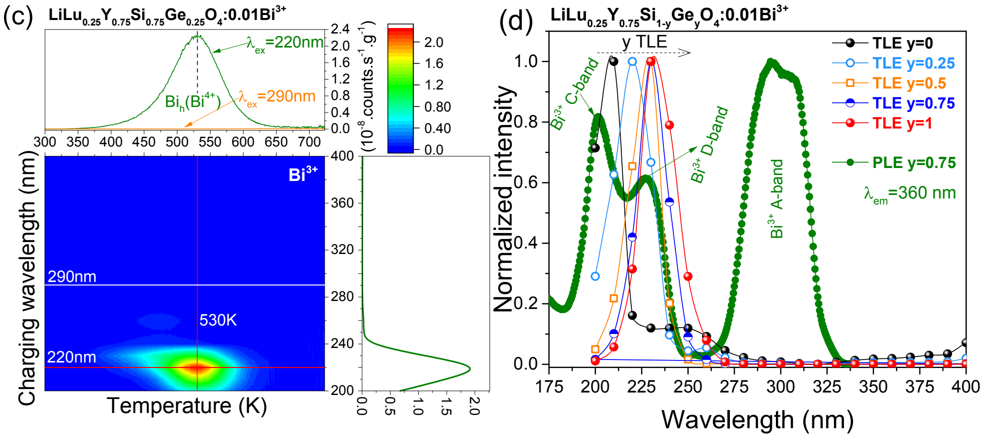

Fig. 6.7. (a)-(d) TL excitation (TLE) spectra recorded at a heating rate of 5 K/s for $LiLu_{0.25}Y_{0.75}SiO_4$:0.01Bi^{3+},0.01Sm^{3+} and $LiLu_{0.25}Y_{0.75}Si_{1-y}Ge_yO_4$:0.01$Bi^{3+}$. The TLE plots in d) are constructed by integrating the TL glow peak between 450-723 K in b) and 300-723 K in c). The photoluminescence excitation spectrum monitoring the Bi^{3+} A-band emission (360 nm) for $LiLu_{0.25}Y_{0.75}Si_{1-y}Ge_yO_4$:0.01$Bi^{3+}$ (y=0.75) at 10 K is shown in d).

6.4.5. Evaluating the potential application for information storage

The crystal synthesis of $LiLu_{0.25}Y_{0.75}SiO_4$:0.01Bi^{3+} and $LiLu_{0.5}Y_{0.5}SiO_4$: 0.01Ce^{3+},0.005Sm^{3+} solid solutions was optimized in order to further increase the charge carrier storage capacity for achieving more efficient information storage. Fig. 6.8a) and 6.8c) show the TL glow curves and TL fading characteristics for the optimized samples. The ratio of integrated TL intensity between 300-800 K of $LiLu_{0.25}Y_{0.75}SiO_4$:0.01Bi^{3+} to that of commercial Al_2O_3:C or BaFBr(I):Eu^{2+} is about 1.1 and 4.4. For $LiLu_{0.25}Y_{0.75}SiO_4$:0.01Bi^{3+} after 10h delay time, the integrated TL intensity remains 96%, which is ~20% higher than that of BaFBr(I):Eu^{2+}. The ratio of integrated TL intensity between 300-723 K of $LiLu_{0.5}Y_{0.5}SiO_4$:0.01Ce^{3+}, 0.005Sm^{3+} to that of BaFBr(I):Eu^{2+} is about 8.5, which is higher than that of ~4 in the optimized $LiLuSiO_4$:Ce^{3+},Tm^{3+} in Ref. [35] and of ~7 in the optimized $NaYGeO_4$:0.01Bi^{3+},0.001Eu^{3+} in Ref. [55].

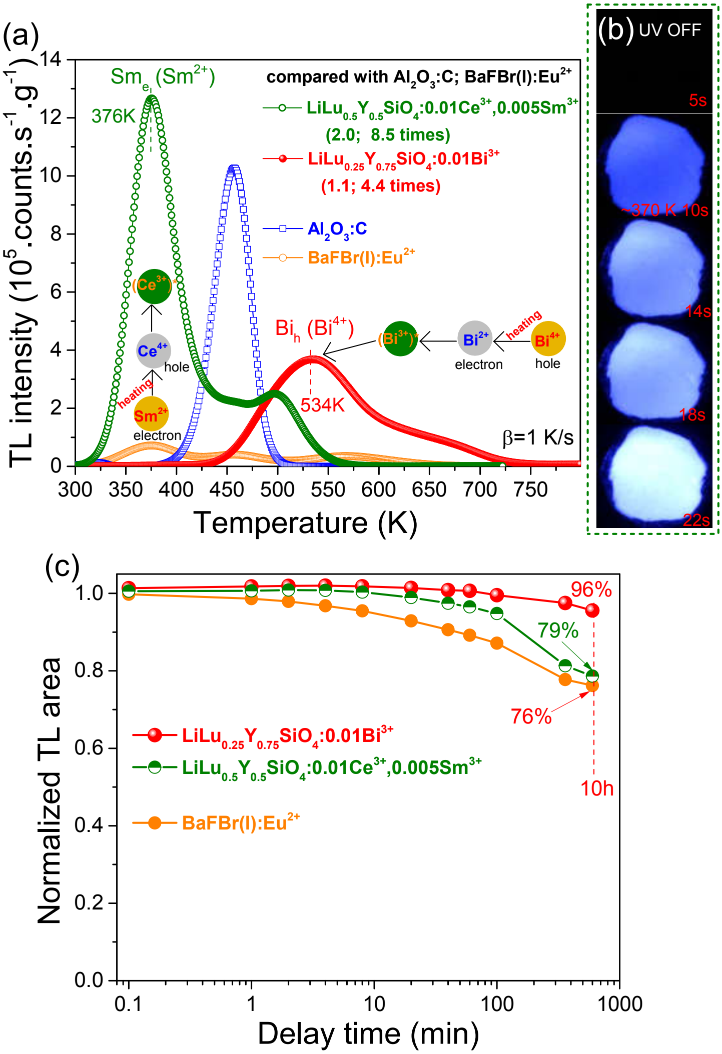

Fig. 6.8. (a) TL glow curves at β=1 K/s, and (c) TL fading characteristics for the optimized $LiLu_{0.25}Y_{0.75}SiO_4$:$0.01Bi^{3+}$ and $LiLu_{0.5}Y_{0.5}SiO_4$:$0.01Ce^{3+}$,$0.005Sm^{3+}$ after β-ray irradiation. (b) Photographs of thermally stimulated emission of $LiLu_{0.5}Y_{0.5}SiO_4$:$0.01Ce^{3+}$,$0.005Sm^{3+}$ at ~370 K with different duration time after Hg lamp charging.

For storage phosphor application, the stored charge carriers during X-ray or other excitation source exposure are often read out by photon stimulation. Fig. 6.9 compares the TL glow curves of the optimized samples in this work after photon stimulation with various duration times. Additional TL curves for other $LiLu_{1-x}Y_xSi_{1-y}Ge_yO_4$ can be found in Fig. S6.24.

Fig. 6.9 and S6.24 demonstrate that 10s of 475 nm photon stimulation releases ~38, 54, 42, 95, and 41% of the charge carriers stored during β irradiation of $LiLu_{0.5}Y_{0.5}SiO_4$:0.01Ce^{3+},0.01Sm^{3+}, $LiLu_{0.25}Y_{0.75}SiO_4$:0.01Ce^{3+},0.01Sm^{3+}, $LiLu_{0.25}Y_{0.75}SiO_4$:0.01Bi^{3+}, BaFBr(I):Eu^{2+}, and Al_2O_3:C, respectively. The relative amount of released charge carriers in $LiLu_{0.5}Y_{0.5}SiO_4$:0.01Ce^{3+},0.01Sm^{3+} in Fig. 6.9a) or $LiLu_{0.25}Y_{0.75}SiO_4$:0.01Bi^{3+} in Fig. 6.9c) is smaller than that in BaFBr(I):Eu^{2+}, but their absolute amount is ~2.4, 5.2 times, and ~1.3, 2.7 times higher than that in BaFBr(I):Eu^{2+} and Al_2O_3:C, respectively.

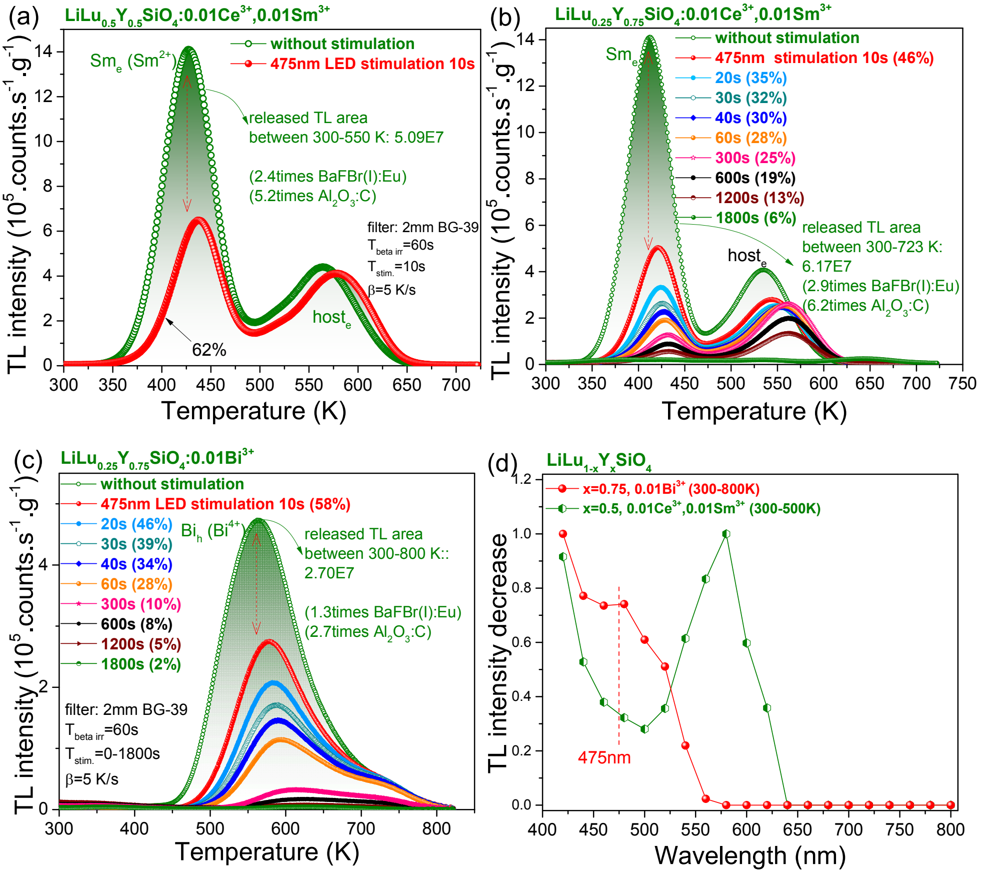

Fig. 6.9. TL glow curves at β=5 K/s for (a) $LiLu_{0.5}Y_{0.5}SiO_4$:0.01Ce^{3+},0.01Sm^{3+}, (b) $LiLu_{0.25}Y_{0.75}SiO_4$:0.01Ce^{3+},0.01Sm^{3+}, and (c) $LiLu_{0.25}Y_{0.75}SiO_4$:0.01Bi^{3+} recorded after β-ray irradiation and after β-ray irradiation followed by 475 nm LED optical stimulation with different duration time. (d) Stimulation spectra where the decrease of integrated TL intensity between 300-500 K for $LiLu_{0.5}Y_{0.5}SiO_4$:0.01Ce^{3+},0.01Sm^{3+} in a) and between 300-800 K for $LiLu_{0.25}Y_{0.75}SiO_4$:0.01Bi^{3+} in c) after different energy photon stimulation.

Fig. 6.9b)-c) shows that ~94% and ~98% of stored charge carriers can be liberated when the stimulation time increases to 1800s. The same applies to other $LiLu_{0.25}Y_{0.75}Si_{1-y}Ge_yO_4$ phosphors as shown in Fig. S6.24g)-h). Fig. 6.9d) shows the stimulation spectra with different stimulation photon wavelength. For the $LiLu_{0.5}Y_{0.5}SiO_4$:0.01Ce^{3+},0.01Sm^{3+} phosphor, a stimulation peak near 580 nm appears. The information stored by the $LiLu_{0.25}Y_{0.75}SiO_4$:0.01Bi^{3+} phosphor is erased more efficiently at 410 nm.

Fig. 6.10 demonstrates proof-of-concept information storage and readout using the developed phosphor. $LiLu_{0.5}Y_{0.5}SiO_4$:0.01Ce^{3+},0.01Sm^{3+} phosphor is first dispersed in a ~2 mm thick silicone gel to form "plate I", which is then placed underneath a chicken bone to be X-ray exposed as demonstrated in Fig. 6.10a2). "Plate I" was heated to ~370 K and after 12 and 32 seconds a photo of the afterglow was made. The X-ray image of the chicken bone shape appears as a weaker thermally stimulated Ce^{3+} emission intensity in Fig. 6.10a3) and a4). This is due to the absorption of X-rays by the chicken bone during X-ray exposure. The resolution of the image in Fig. 6.10a3) and a4) is rather poor, but when an image was made with a ~0.5 mm thick plate II it improves as shown in Fig. 6.10a6). The similar applies to another X-ray image of a chicken bone stored in "plate III" in Fig. S6.31a4)-a6), where the $LiLu_{0.25}Y_{0.75}SiO_4$:0.01Bi^{3+},0.01Sm^{3+} storage phosphor was used. Here the X-ray image is obtained because of afterglow from hole liberation from Bi^{4+} and recombination with Bi^{2+} followed by energy transfer from Bi^{3+} to Sm^{3+}, as illustrated in Fig. S6.31a7). Note that the used optical sensor of the smartphone is not sensitive to the main thermally stimulated Bi^{3+} emission near 360 nm in $LiLu_{0.25}Y_{0.75}SiO_4$:0.01Bi^{3+},0.01Sm^{3+}.

"Plate I" in Fig. 6.10b1) is placed underneath a black mask as shown in Fig. 6.10b2). $LiLu_{1-x}Y_xSiO_4$:0.01Ce^{3+},0.01Sm^{3+} can be charged by 260 nm light as shown in Fig. S6.13. When the UV-light near 260 nm passes through the open area of the black mask it charges "plate I". The information of text of "LMG TUD TSL Ce^{3+}" is then stored in the "plate I" in Fig. 6.10b3). The text is not visible in the dark when the UV-light is switched off in Fig. 6.10b4). The text emerges again in Fig. 6.10b5) when the "plate I" is heated to ~370 K with duration time of ~15s because of thermally stimulated Ce^{3+} emission. The mechanism is demonstrated in Fig. 6.10b6).

A QR code printed on a sheet of white paper in Fig. 6.10c1) was generated by the text of "This is a nice storage phosphor for information storage from TUD!" with computer software. The QR code is visible in the dark in Fig. 6.10c2) because of the ~370 K thermally stimulated Ce^{3+} emission from "plate I" underneath the paper as a backlight display source shining through the sheet in Fig. 6.10c2). The

QR code was scanned using a mobile phone software in the dark to read out the hidden text above as demonstrated in Fig. 6.10c3).

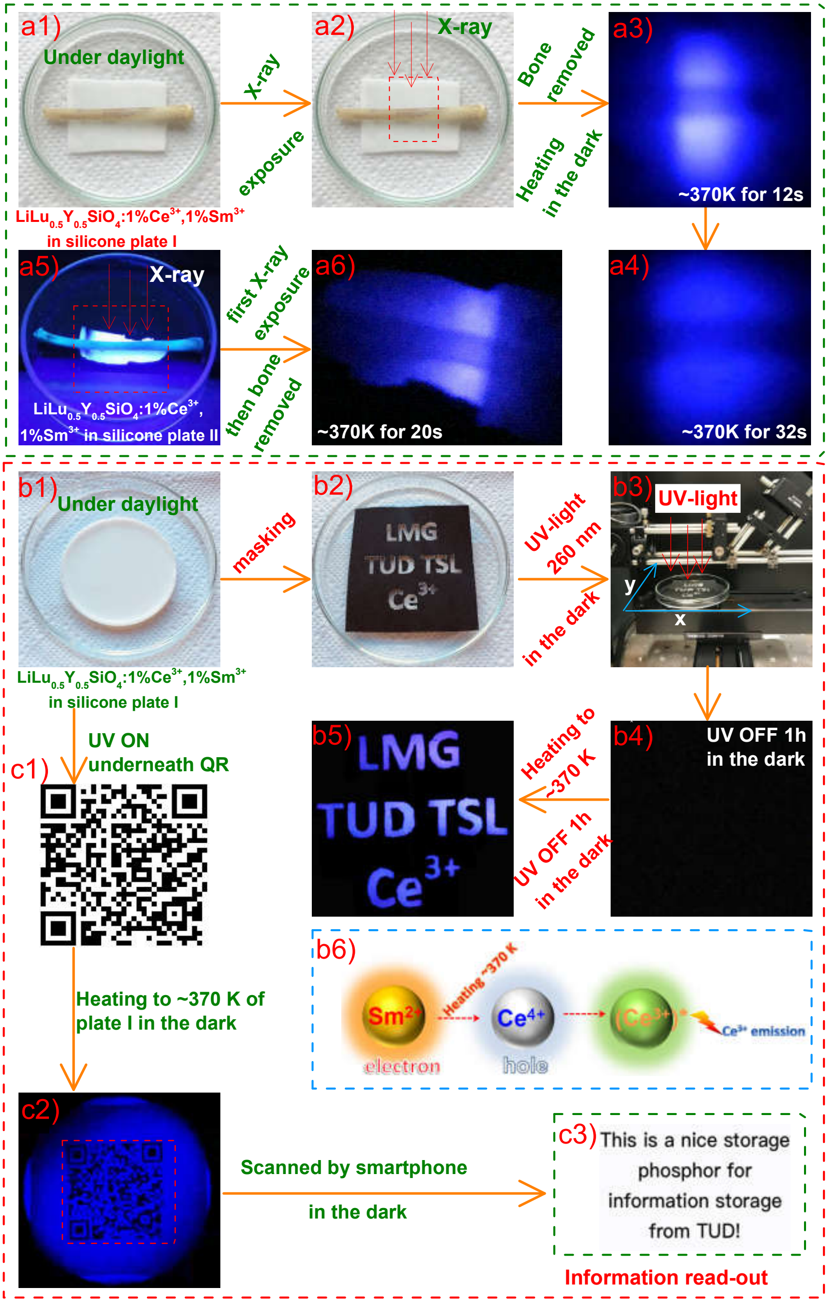

Fig. 6.10. Proof-of-concept information storage application by using $LiLu_{0.5}Y_{0.5}SiO_4$: $0.01Ce^{3+}$,$0.01Sm^{3+}$ dispersed in the silicone gel plates I and II. Information storage and display of an X-ray photograph of a chicken bone in a1)-a6), of text of LMG TUD TSL Ce^{3+} in b1)-b5), and of a QR code on a paper in the dark in c1)-c3). b6) illustrates the thermally stimulated luminescence process for b5). The chicken bone was removed before heating in a3)-a4), and a6), and the mask was not removed during heating in b5). The thickness is ~2 mm for plate I in a2) and ~0.5 mm for plate II in a5). Both the plates in a2) and a5) were heated to ~370 K for 3 minutes to empty all traps in the dark before X-ray exposure.

6.5. Discussion

Based on low-temperature (10 K) photoluminescence spectroscopy in Ref. [55], the constructed vacuum referred binding energy (VRBE) diagrams including bismuth and lanthanide levels for $LiLuSiO_4$ related family of compounds are shown in Fig. 6.1 and S6.1. We will show how these VRBE schemes can be verified and made more accurate by thermoluminescence study, and how they guide the design of both the electron and hole trapping processes in the lanthanide and/or bismuth doped $LiRE(Si,Ge)O_4$ (RE=Y or Lu) towards storage phosphors with high charge carrier storage capacity for information storage. Here let us call this approach the '*engineering game'*.

The essence of the game is to combine a hole trapping defect with an electron trapping defect in a controlled fashion. In sequence of decreasing hole trap depths in Fig. 6.1a) and 1b) one may select Ce^{3+}, Pr^{3+}~Tb^{3+}, and Bi^{3+} where Ce^{3+} is the deepest h-trap and Bi^{3+} is the shallowest h-trap. In sequence of decreasing electron trap depths one may select Eu^{3+}, Bi^{3+}, Yb^{3+}, Sm^{3+}, and Tm^{3+}. We will call these trapping centres '*the players*". In addition to these controlled trapping centres one has to deal with the intrinsic e-traps and h-traps, and in this work we will show how one may discriminate one type from another.

Fig. 6.1b) illustrates that our '*playing field'* are the solid solutions $LiLu_{1-x}Y_xSi_{1-y}Ge_yO_4$ where we have focused on the silicates (y=0). A small excursion was made for x=0.75 where y was changed from 0 to 1.

The *'rules of the game'* are actually the physical mechanism of carrier trapping and recombination. 1) If the hole trap is deeper than the electron trap, then the electron is released at a lower temperature than the hole. Recombination takes place at the hole centre leading to hole-trap luminescence. 2) if the e-trap is deeper than the h-trap, the hole will be released at a lower temperature to recombine with the electrons at the e-trap leading to e-trap emission. 3) by changing the VRBE at the VB-top via changing x or y in solid solutions the hole trapping depths will change likewise. 4) changing the VRBE at the CB-bottom by changing x or y in solid solutions affects the e-trapping depths.

The *'strategy of the game'* is to find combinations of e-trap and h-trap for a specific purpose and then engineer x and y towards either optimal storage phosphor or optimal afterglow phosphor performance.

6.5.1. Playing with the colour of recombination emission

Guided by the VRBE diagram in Fig. 6.1a), the combination of a deep h-trap formed by Ln^{3+} (Ln=Ce, Tb, or Pr) or Bi^{3+} with a less deep e-trap formed by Tm^{3+} or Sm^{3+} was explored with the aim to engineer the recombination emission in $LiLu_{1-x}Y_xSiO_4$. Compared with the Ce^{3+} or Bi^{3+} single doped $LiLuSiO_4$ in Fig. S6.7a), an additional TL glow peak near 144 K emerges in Tm^{3+}-codoped $LiLuSiO_4$ in Fig. 6.5a) and S6.7a). The corresponding 0.40 eV electron trap depth in Table 6.1 is smaller than the predicted hole trap depths of Ce^{3+}, Tb^{3+}, Pr^{3+}, and Bi^{3+}. Considering the largely systematic error margins of few 0.1 eV in VRBE diagrams based on broad charge transfer band transitions[13, 60], the 0.40 eV is still regarded as consistent with the ~0.62 eV electron trap depth of Tm^{3+} in the VRBE diagram in Fig. 6.1a). The 144 K Tm_e TL glow peak is therefore attributed to electron liberation from Tm^{2+} to recombine with holes at Ce^{4+}, Pr^{4+}, Tb^{4+}, and Bi^{4+} to give characteristic 5d-4f or 4f-4f emission of Ce^{3+}, Pr^{3+}, and Tb^{3+}, and Bi^{3+} A-band emission in Fig. S6.7a). This is further supported in Fig. S6.7b) where a same Tm_e TL peak near 186 K appears in all four Tm^{3+}-codoped $LiYSiO_4$:$0.01Ln^{3+}$, $0.01Tm^{3+}$ (Ln=Ce, Pr, or Tb) and $LiYSiO_4$:$0.01Bi^{3+}$,$0.01Tm^{3+}$ samples. These results imply that one may engineer the recombination emission by the choice of deep hole trapping centres of Ce^{3+}, Pr^{3+}, Tb^{3+}, or Bi^{3+} when combined with the less deep Tm^{3+} electron trapping centre.

Fig. 6.1a) illustrates that one may also engineer the recombination colour by combining the deep e-traps of Eu^{3+} and Bi^{3+} with less deep h-traps of Tb^{3+}, Pr^{3+}, and Bi^{3+} in $LiLuSiO_4$. Indeed hole liberation from Tb^{4+}, Pr^{4+}, and Bi^{4+} that recombines with electrons at Eu^{2+} to give characteristic Eu^{3+} 4f-4f emission was identified, which is evidenced by the TL emission spectra and the corresponding TL glow peaks Tb_h, Pr_h, and Bi_h in Fig. 6.3b)-d). If the e-trap of Eu^{3+} is not present as in Fig. 6.3e) and 6.3f), the Bi_h TL glow peaks near 532 K and near 510 K with Bi^{3+} A-band emission appear because of the hole liberation from Bi^{4+} to recombine with electrons captured at Bi^{2+}. Here it demonstrates that one can tailor the recombination emission from Eu^{3+} 4f-4f emission to Bi^{3+} A-band emission by replacing the e-trap of Eu^{3+} by that of Bi^{3+} and using the hole liberation from Bi^{4+}.

6.5.2. Playing with the electron trapping depth

Fig. 6.1a) and 6.1b) predict that Sm^{3+} acts as a ~0.46 eV deeper electron trap than Tm^{3+} which would correspond to a higher T_m for the corresponding TL glow peak. Fig. S6.7c) shows that indeed an additional TL peak near 345 K emerges in all the three Sm^{3+}-codoped $LiLuSiO_4$:0.01Ln^{3+},0.01Sm^{3+} (Ln=Pr, Tb, or Ce) compared with the Ln^{3+} single doped samples. The ~345 K TL peak also appears in $LiLuSiO_4$:0.01Bi^{3+},0.01Sm^{3+} in Fig. 6.5c). The experimentally derived 1.0 eV electron trap depth for the 345 K TL peak in Table 6.1 is consistent with the predicted ~1.08 eV electron trap depth of Sm^{3+} and is less deep than the predicted hole trap depths of Pr^{3+}, Tb^{3+}, Ce^{3+}, and Bi^{3+} based on the VRBE scheme in Fig. 6.1a). We therefore attribute the TL peak near 345 K to the electron release from Sm^{2+} to recombine with holes at Pr^{4+}, Tb^{4+}, Ce^{4+}, and Bi^{4+} generating characteristic Pr^{3+}, Tb^{3+}, Ce^{3+}, and Bi^{3+} emission, respectively. The above result implies that one may engineer the electron trap depth by the choice of lanthanides like Tm^{3+} and Sm^{3+}. Since the TL peak shifts about 200 K close to room temperature by replacing the e-trap of Tm^{3+} by that of Sm^{3+} in the $LiLuSiO_4$:0.01Ce^{3+},0.01Ln^{3+} in Fig. 6.5a)-b), Ce^{3+} afterglow emerges in $LiLuSiO_4$:0.01Ce^{3+},0.01Sm^{3+} in Fig. S6.11b). One may again engineer the afterglow colour by replacing the hole trapping centre of Ce^{3+} by Tb^{3+} or Pr^{3+}, producing typical Tb^{3+} and Pr^{3+} afterglow as demonstrated in Fig. S6.10.

Above the players were Tm and Sm but one may also enlarge the playing field by studying solid solutions. The results for Ln^{3+} and/or Bi^{3+} doped $LiLu_{1-x}Y_xSiO_4$ solid solutions in Fig. 6.5a)-c) demonstrate the electron trap depth tailoring of Tm^{3+} and Sm^{3+} by conduction band engineering. Here Ce^{3+} and Bi^{3+} act as deep hole capturing centres and Tm^{3+} and Sm^{3+} are less deep electron trapping centres. An about 0.1 eV trap depth increase is determined from both the Sm_e and Tm_e TL glow peaks in columns 10 and 12 of Table 6.1 when x increases from 0 to 1. It indicates that the conduction band bottom moves up by ~0.1 eV in $LiLu_{1-x}Y_xSiO_4$ with increasing x, which is to be compared with the predicted 0.17 eV increase in the stacked VRBE scheme as shown in Fig. 6.1b). We therefore attribute the about 50 K shifting of Tm_e and Sm_e TL peaks towards higher temperature to the increased activation energy for electron liberation from Tm^{2+} and Sm^{2+} as a result of conduction band rising with increasing x in $LiLu_{1-x}Y_xSiO_4$. The above result also demonstrates that thermoluminescence is a sensitive technique to determine a small (~0.1 eV) energy difference in a VRBE scheme.

The above results imply that one may design a storage phosphor via tailoring the electron trap depth by a combination of conduction band engineering and a choice of Ln^{3+} like the above Tm^{3+} and Sm^{3+} co-dopants. By further synthesis optimization, a good storage phosphor may appear like $LiLu_{0.5}Y_{0.5}SiO_4$:0.01Ce^{3+},

$0.005Sm^{3+}$ in Fig. 6.8a)-b) where after β irradiation its integrated TL intensity between 300-723 K is about 2 and 8.5 times higher than that of commercial Al_2O_3:C and BaFBr(I):Eu^{2+} storage phosphors.

Intrinsic host-related electron traps can also be very important for a high charge carrier storage capacity[35]. Using Eq. (6.1) with the frequency factor in column 2 of Table 6.1 and β=1 K/s, the trapping depths for the host$_e$ TL peaks in $LiLu_{1-x}Y_xSiO_4$: $0.01Ce^{3+}$,$0.01Sm^{3+}$ in Fig. 6.5b) are determined between ~1.43 and ~1.38 eV. They are ~3 eV less deep than the predicted Ce^{3+} hole trap depth in Fig. 6.1a). We therefore attribute these TL peaks to host-related intrinsic electron traps. The VRBE at the intrinsic defect(s) corresponding with these TL peaks is indicated in Fig. 6.1b). It is derived by subtracting the experimentally determined electron trap depth from the conduction band bottom. The VRBE in $LiYSiO_4$ is different from that in $LiLuSiO_4$ indicating that the VRBE at the intrinsic defect(s) is more dependent on the compound composition than that of Sm^{2+} in $LiLu_{1-x}Y_xSiO_4$: $0.01Ce^{3+}$,$0.01Sm^{3+}$.

6.5.3. Playing with the hole trapping depth

The vacuum referred binding energy (VRBE) scheme for $LiLuSiO_4$ in Fig. 6.1a) illustrates that Ce^{3+}, Pr^{3+}, Tb^{3+}, and Bi^{3+} will act as ~3.89, ~2.04, ~2.22, and ~1.90 eV deep hole trapping centres, while Eu^{3+}, Yb^{3+}, and Bi^{3+} will act as ~2.34, ~1.90, and ~1.81±0.5 eV deep electron trapping centres in $LiLuSiO_4$. Holes captured to form Pr^{4+}, Tb^{4+}, and Bi^{4+} are then predicted to be released earlier, i.e., at a lower temperature, than the electrons at Eu^{2+} to upon recombination produce characteristic red 4f-4f emission of Eu^{3+}.

Using Eq. (6.1) with the frequency factor in column 2 of Table 6.1 and β=1 K/s, the trapping depths for TL peaks denoted I_h to V_h in $LiLuSiO_4$ in Fig. 6.3a) are determined to be ~1.08, 1.22, 1.45, 1.63, and 2.21 eV, which are less deep than the predicted Eu^{3+} electron trap depth of ~2.34 eV in Fig. 6.1a). These I_h-V_h TL peaks are therefore attributed to host-related intrinsic hole traps. We have drawn the derived level location for the II_h hole trap in Fig. 6.1b). The trapping depths for TL peaks Tb_h near 572 K and Pr_h near 582 K in Fig. 6.3b)-c) are derived to be ~1.67, and ~1.70 eV, respectively. During TL-readout, the activation energies required to liberate holes from Tb^{4+} (1.67 eV) and from Pr^{4+} (1.70 eV) are about 0.7 eV smaller than that to liberate electrons from Eu^{2+} (~2.34 eV). Therefore, the holes liberate from Tb^{4+} and Pr^{4+} to recombine with the electrons captured at Eu^{2+} to generate the TL glow peaks Tb_h and Pr_h with characteristic red 4f-4f emission of Eu^{3+}.

Columns 6 and 8 of Table 6.1 show that the experimentally determined average hole trap depth for both Tb^{3+} and Pr^{3+} is ~1.80 eV in $LiLuSiO_4$, and ~1.52 eV in $LiYSiO_4$, respectively. It is about 0.33, and 0.61 eV smaller compared with the ones estimated from the VRBE scheme (2.22 eV for Tb^{3+} and 2.04 eV for Pr^{3+}) in Fig. 6.1a). Similar deviation about 0.6 eV appeared in YPO_4[13], and about 0.3 eV emerged in $GdAlO_3$[2]. It may suggest there are errors and uncertainties in VRBE scheme construction. However, holes generated in the valence band tend to create a V_k centre by bonding with two neighbouring oxygen anions[61-63]. Bonding means that the hole state moves up in a VRBE diagram[2, 13, 64]. The ~0.33, and ~0.61 eV energy differences in $LiLuSiO_4$ and $LiYSiO_4$ could also be largely attributed to the binding energies of the V_k centres. Upon thermal stimulation during TL-readout, holes are liberated from Tb^{4+} or Pr^{4+} to form a V_k centre, which then migrates to recombine with electrons trapped at Eu^{2+} to generate characteristic 4f-4f emission of Eu^{3+} in $LiLuSiO_4$ or $LiYSiO_4$.

The VRBE scheme in Fig. 6.1a) was constructed with the method outlined in Ref. [60] where the ground state of Pr^{3+} is 0.18 eV below that of Tb^{3+}. One then expects that the Pr_h TL glow peak appears at about 60-70 K lower temperature than the Tb_h TL glow peak. In Refs. [65, 66] experimental evidence was presented that the ground state of Pr^{3+} and Tb^{3+} should be at similar energy and also slightly compound dependent. This is now further confirmed in this work. The Pr^{4+} TL glow peak appears at only about 10 K lower temperature than that of Tb^{4+} in $LiLu_{1-x}Y_xSiO_4$:$0.01Eu^{3+}$,$0.01Ln^{3+}$ (Ln=Tb or Pr) in Fig. 6.4a)-b) and YPO_4:$0.01Eu^{3+}$, $0.01Ln^{3+}$ in Ref. [13]. Columns 6 and 8 of Table 6.1 show that the experimentally derived hole trap depth of Tb^{3+} is almost the same as that of Pr^{3+} in $LiLu_{1-x}Y_xSiO_4$.

Fig. 6.1a) illustrates that Bi^{3+} acts as a ~1.90 eV deep hole trap, while Eu^{3+} and Bi^{3+} act as ~2.34 and ~1.81±0.5 eV deep electron traps in $LiLuSiO_4$. The TLEM plots in Fig. 6.3d)-e) for $LiLu_{0.5}Y_{0.5}SiO_4$:$0.01Eu^{3+}$,$0.01Bi^{3+}$ and $LiLu_{0.5}Y_{0.5}SiO_4$: $0.01Bi^{3+}$,$0.01Sm^{3+}$ share the same Bi_h TL peak near 532-535 K. A slightly higher Bi_h TL peak near 553 K emerges in $LiLuSiO_4$ in Fig. 6.4c). Bi_h hole trap depth in $LiLuSiO_4$ is determined to be 1.62 eV in Table 6.1, which is ~0.3 eV smaller than that predicted by the Bi^{3+} $^1S_0$ ground state level based on Bi^{3+} D-band in the VRBE diagram in Fig. 6.1a). Like the Tb^{4+} and Pr^{4+} hole detrapping processes discussed above, the ~0.3 eV energy difference may be due to the errors and uncertainties in VRBE diagram construction, but also could be largely attributed to the binding energy of the V_k centre. Note that the Bi^{3+} hole trap depth (1.90 eV) is less deep than the predicted electron trap depth of Eu^{3+} (~2.34 eV) in Fig. 6.1a). During TL-readout, a hole is therefore released from Bi^{4+} earlier to generate a V_k centre, which then migrates to recombine with electrons at Eu^{2+} to produce the Bi_h TL peak near 535 K with Eu^{3+} 4f-4f emission in $LiLu_{0.5}Y_{0.5}SiO_4$ in Fig. 6.3d). Considering that the same Bi_h TL peak appears in Fig. 6.3e) where Bi^{3+} is the recombination centre instead of Eu^{3+}, hole liberation from Bi^{4+} to recombine with electrons at Bi^{2+} to produce Bi^{3+} A-band emission is supported. The above result also supports the assumption that the VRBE at the Bi^{2+} ground state in $LiRESiO_4$ is near about -3.5±0.5 eV, and that Bi^{3+} acts as a deeper electron trap than hole trap. The Sm^{3+} 4f-4f emission in Fig. 6.3e) is then attributed to energy transfer of $Bi^{3+} \rightarrow Sm^{3+}$.

The TL results for Ln^{3+} and/or Bi^{3+} doped $LiLu_{1-x}Y_xSiO_4$ in Fig. 6.4 and 6.5c), and $LiLu_{0.25}Y_{0.75}Si_{1-y}Ge_yO_4$:0.01$Bi^{3+}$ solid solutions in Fig. 6.6a) demonstrate the hole trap depth tailoring of Tb_h, Pr_h, and Bi_h TL peaks. An about 0.25 eV trap depth decrease is derived from the Bi_h, Tb_h, and Pr_h TL peaks in columns 4, 6, and 8 of Table 6.1 with increasing x in $LiLu_{1-x}Y_xSiO_4$. It is to be compared with the ~0.1 eV raising of the VB-top in the stacked VRBE diagram in Fig. 6.1b). We therefore attribute the about 40 K shifting of Tb_h, Pr_h, and Bi_h TL peaks towards lower temperature in Fig. 6.4a)-c) to the decreased activation energy for hole release from Tb^{4+}, Pr^{4+}, and Bi^{4+} because of valence band rising with increasing x in $LiLu_{1-x}Y_xSiO_4$. This again demonstrates that a small (~0.1 eV) energy difference in a VRBE diagram can be probed using the sensitive thermoluminescence technique.

Fig. 6.6a) and column 5 of Table 6.2 show that the Bi_h (Bi^{4+}) TL peak can be lowered from ~538 K to ~394 K by increasing y from 0 to 0.75 in $LiLu_{0.25}Y_{0.75}Si_{1-y}Ge_yO_4$:0.01$Bi^{3+}$. It corresponds with ~0.42 eV decrease of the Bi^{3+} hole trap depths as determined from the variable heating rate plots in Fig. 6.6d). This is to be compared with the predicted ~0.57 eV decrease of the Bi^{3+} hole trap depth when Si^{4+} is totally replaced for Ge^{4+} in $LiLuSi_{1-y}Ge_yO_4$ in the stacked VRBE diagram in Fig. 6.1b). We therefore attribute the ~144 K shifting of the Bi_h TL peak towards lower temperature to the decreased activation energy for hole liberation from Bi^{4+} with increasing y in $LiLu_{0.25}Y_{0.75}Si_{1-y}Ge_yO_4$:0.01$Bi^{3+}$. The results in columns 2 and 3 of Table 6.2 demonstrate that the TLE maximum coincides with the $Bi^{3+} \rightarrow$CB D-band. The Bi^{3+} D-band energies were used to place the ground state levels of Bi^{3+} below the CB bottom in Fig. 6.1a) and b). During Bi^{3+} D-band excitation, electrons from the $^1S_0$ ground state of Bi^{3+} are excited to the conduction band, which then can be captured by electron traps like the Bi^{3+} and Sm^{3+} in Fig. 6.7a)-c) or other host-related electron traps like those responsible for the TL glow peak at about 354, 452, and 559 K in Fig. S6.18c), and Bi^{4+} remains.

The result in Fig. 6.6a) also implies that one can design Bi^{3+} based storage phosphors in $LiLu_{0.25}Y_{0.75}Si_{1-y}Ge_yO_4$:0.01$Bi^{3+}$ by engineering the Bi^{3+} hole trap depth through changing the ratio of silicon to germanium. With increasing silicon content, the TL peak shifts from 371 K to 538 K, which is consistent with the decrease of the Bi^{3+} persistent luminescence in Fig. 6.6b) and the less TL fading in Fig. 6.6c). With further crystal synthesis optimization, a good storage phosphor may appear like $LiLu_{0.25}Y_{0.75}SiO_4$:0.01Bi^{3+} in Fig. 6.8a) in which the integrated TL intensity between 300-800 K is about 4.4 times higher than that of commercial BaFBr(I):Eu^{2+} phosphor after β irradiation.

6.5.4. Information storage application using Ce^{3+} and Bi^{3+} storage phosphors

The TL excitation spectra in Fig. S6.13c) show that the Ce^{3+} 4f-5d_1 excitation band near 350 nm can charge the $LiLuSiO_4$:0.01Ce^{3+},0.01Sm^{3+}. It implies that $LiLu_{1-x}Y_xSiO_4$:0.01Ce^{3+},0.01Sm^{3+} when applied as a storage phosphor needs to be kept in the dark during X-ray exposure. For the Bi^{3+}-doped $LiLu_{1-x}Y_xSiO_4$ in Fig. 6.5c) and $LiLu_{0.25}Y_{0.75}Si_{1-y}Ge_yO_4$ in Fig. 6.6a), only the Bi^{3+} D-band near 210-230 nm can fill the traps. This means that such Bi^{3+}-based storage phosphor can be kept in daylight during X-ray exposure.

The TL emission spectra in Fig. S6.3) show that the thermally stimulated Ce^{3+} 5d-4f emission which has ~39 ns fluorescence decay time in Fig. S6.25 appears in the visible region, while the Bi^{3+} A-band emission peaking near 360 nm in Fig. 6.3e) with ~0.5 μs fluorescence decay time in Fig. S6.26-S6.27 emerges largely in the ultraviolet region. Both thermally stimulated Ce^{3+} and Bi^{3+} emissions in $LiLu_{1-x}Y_xSiO_4$ phosphors match well with a traditional photomultiplier tube and are quite intense compared with the commercial BaFBr(I):Eu^{2+} storage phosphor in Fig. 6.8a). This combined with better TL fading characteristics in Fig. 6.8c) and the photon stimulation ability of the charge carriers stored during β-ray exposure in Fig. 6.9 indicates that the developed phosphors have potential application as optically stimulated storage phosphors for information storage as demonstrated in Fig. 6.10 and S6.29-S6.31.

6.6. Conclusions

The methodology to rational design of storage phosphors with high charge carrier storage capacity for information storage has been explored by studying both the trapping and detrapping processes of electrons and holes in the bismuth and lanthanide-doped LiRE(Si,Ge)O_4 (RE=Y, Lu) family of compounds. For $LiLuSiO_4$: 0.01Ln^{3+},0.01Tm^{3+} (Ln=Ce, Pr, or Tb) and $LiLuSiO_4$:0.01Bi^{3+},0.01Tm^{3+}, the Tm^{3+} acts as an electron trap, while the Ln^{3+} and Bi^{3+} codopants are the hole traps and recombination centres. The electrons are released from Tm^{2+} to recombine with holes captured at Ln^{4+} and Bi^{4+} to generate characteristic Ln^{3+} 4f-4f or 5d-4f emission and Bi^{3+} A-band emission. The electron trap depth can be controlled by the choice of Tm^{3+} or Sm^{3+} codopant, and for fixed pair of Bi^{3+} and/or Ln^{3+} dopants like in $LiLu_{1-x}Y_xSiO_4$:0.01Ce^{3+},0.01Ln^{3+} (Ln=Tm or Sm) and $LiLu_{1-x}Y_xSiO_4$: 0.01Bi^{3+},0.01Sm^{3+} solid solutions, by changing x, resulting in conduction band engineering. The integrated TL intensity of the optimized $LiLu_{0.5}Y_{0.5}SiO_4$:

$0.01Ce^{3+}$,$0.005Sm^{3+}$ is about 8.5 times higher than that of the commercial BaFBr(I):Eu^{2+} storage phosphor after β irradiation. In $LiLuSiO_4$:$0.01Eu^{3+}$,$0.01Ln^{3+}$ (Ln=Tb or Pr), $LiLuSiO_4$:$0.01Eu^{3+}$,$0.01Bi^{3+}$, and $LiLuSiO_4$:$0.01Bi^{3+}$, the Eu^{3+} and Bi^{3+} act as the deep electron traps and recombination centres, while Tb^{3+}, Pr^{3+}, and Bi^{3+} act as the less deep hole traps. The holes are liberated from Tb^{4+}, Pr^{4+}, and Bi^{4+} to recombine with electrons at Eu^{2+} and Bi^{2+} to produce typical Eu^{3+} 4f-4f and Bi^{3+} A-band emissions. The hole trap depth can be controlled by the choice of Tb^{3+}, Pr^{3+}, and Bi^{3+}, and for the fixed pair of Ln^{3+} and/or Bi^{3+} like in $LiLu_{1-x}Y_xSiO_4$: $0.01Eu^{3+}$,$0.01Ln^{3+}$ (Ln=Tb or Pr), $LiLu_{1-x}Y_xSiO_4$:$0.01Eu^{3+}$,$0.01Bi^{3+}$, and $LiLu_{1-x}Y_xSiO_4$:$0.01Bi^{3+}$, by tailoring x, resulting in valence band engineering. The VRBE at the CB-bottom and VB-top can be engineered by replacing Si^{4+} for Ge^{4+} in $LiLu_{0.25}Y_{0.75}Si_{1-y}Ge_yO_4$:$0.01Bi^{3+}$, leading to the tailoring of Bi^{3+} hole trap depth. The TL intensity of the optimized $LiLu_{0.25}Y_{0.75}SiO_4$:$0.01Bi^{3+}$ is ~4.4 times higher than that of the commercial BaFBr(I):Eu^{2+}. Proof-of-concept information storage was demonstrated with X-ray or UV-light charged $LiLu_{0.5}Y_{0.5}SiO_4$:$0.01Ce^{3+}$, $0.01Sm^{3+}$ and $LiLu_{0.25}Y_{0.75}SiO_4$:$0.01Bi^{3+}$ phosphors dispersed in silicone gel imaging plates. This paper not only reports excellent Ce^{3+} and Bi^{3+} based storage phosphors but more importantly demonstrates a feasible strategy to discover Ce^{3+} and Bi^{3+} based storage phosphors based on tailoring trapping, detrapping, and recombination processes of both electrons and holes. This work can also inspire future research to develop Ce^{3+} and Bi^{3+} based storage phosphors for energy storage in a rational design approach rather than using a trial-and-error method.

6.7. Acknowledgements

T. Lyu acknowledges the China Scholarship Council for his PhD scholarship (Tianshuai Lyu: No. 201608320151).

6.8. Reference

1. Y. Li, M. Gecevicius and J. Qiu, *Chemical Society Reviews*, 2016, **45**, 2090-2136.
2. H. Luo, A. J. J. Bos and P. Dorenbos, *The Journal of Physical Chemistry C*, 2016, **120**, 5916-5925.
3. J. Xu and S. Tanabe, *Journal of Luminescence*, 2019, **205**, 581-620.
4. J. Ueda, J. L. Leaño, C. Richard, K. Asami, S. Tanabe and R.-S. Liu, *Journal of Materials Chemistry C*, 2019, **7**, 1705-1712.
5. J. Ueda, P. Dorenbos, A. J. J. Bos, K. Kuroishi and S. Tanabe, *Journal of Materials Chemistry C*, 2015, **3**, 5642-5651.
6. Y. Zhuang, Y. Lv, Y. Li, T. Zhou, J. Xu, J. Ueda, S. Tanabe and R.-J. Xie, *Inorganic Chemistry*, 2016, **55**, 11890-11897.
7. T. Wang, W. Bian, D. Zhou, J. Qiu, X. Yu and X. Xu, *The Journal of Physical*

Chemistry C, 2015, **119**, 14047-14055.

8. S. Wang, X. Liu, B. Qu, Z. Song, Z. Wang, S. Zhang, F. Wang, W.-T. Geng and Q. Liu, *Journal of Materials Chemistry C*, 2019, **7**, 12544-12551.
9. K. Korthout, K. Van den Eeckhout, J. Botterman, S. Nikitenko, D. Poelman and P. F. Smet, *Physical Review B*, 2011, **84**, 085140.
10. J. Ueda, M. Katayama, K. Asami, J. Xu, Y. Inada and S. Tanabe, *Opt. Mater. Express*, 2017, **7**, 2471-2476.
11. H. Luo, A. J. J. Bos and P. Dorenbos, *The Journal of Physical Chemistry C*, 2017, **121**, 8760-8769.
12. K. Chakrabarti, V. K. Mathur, J. F. Rhodes and R. J. Abbundi, *Journal of Applied Physics*, 1988, **64**, 1363-1366.
13. T. Lyu and P. Dorenbos, *Journal of Materials Chemistry C*, 2018, **6**, 369-379.
14. T. Lyu and P. Dorenbos, *Journal of Materials Chemistry C*, 2018, **6**, 6240-6249.
15. T. Lyu and P. Dorenbos, *Chemical Engineering Journal*, 2019, **372**, 978-991.
16. H.-T. Sun, J. Zhou and J. Qiu, *Progress in Materials Science*, 2014, **64**, 1-72.
17. X. Wang, P. Boutinaud, L. Li, J. Cao, P. Xiong, X. Li, H. Luo and M. Peng, *Journal of Materials Chemistry C*, 2018, **6**, 10367-10375.
18. H. Luo and P. Dorenbos, *Journal of Materials Chemistry C*, 2018, **6**, 4977-4984.
19. R. H. P. Awater and P. Dorenbos, *Journal of Luminescence*, 2017, **184**, 221-231.
20. R. H. P. Awater, L. C. Niemeijer-Berghuijs and P. Dorenbos, *Optical Materials*, 2017, **66**, 351-355.
21. P. Dorenbos, *ECS Journal of Solid State Science and Technology*, 2013, **2**, R3001-R3011.
22. P. Dorenbos, *Physical Review B*, 2012, **85**, 165107.
23. J. Ueda and S. Tanabe, *Optical Materials: X*, 2019, **1**, 100018.
24. J. Ueda, R. Maki and S. Tanabe, *Inorganic Chemistry*, 2017, **56**, 10353-10360.
25. H. Luo, A. J. J. Bos, A. Dobrowolska and P. Dorenbos, *Physical Chemistry Chemical Physics*, 2015, **17**, 15419-15427.
26. Z. Wang, Z. Song, L. Ning and Q. Liu, *Journal of Materials Chemistry C*, 2020, **8**, 1143-1150.
27. M. Gu, Q. Zhang and S. Lamon, *Nature Reviews Materials*, 2016, **1**, 16070.
28. X. Huang, Q. Guo, D. Yang, X. Xiao, X. Liu, Z. Xia, F. Fan, J. Qiu and G. Dong, *Nature Photonics*, 2020, **14**, 82-88.
29. Y. Zhuang, L. Wang, Y. Lv, T.-L. Zhou and R.-J. Xie, *Advanced Functional Materials*, 2018, **28**, 1705769.
30. M. Gu, X. Li and Y. Cao, *Light: Science & Applications*, 2014, **3**, e177-e177.
31. D. Genovese, A. Aliprandi, E. A. Prasetyanto, M. Mauro, M. Hirtz, H. Fuchs, Y. Fujita, H. Uji-I, S. Lebedkin, M. Kappes and L. De Cola, *Advanced Functional Materials*, 2016, **26**, 5271-5278.

32. H. Sun, S. Liu, W. Lin, K. Y. Zhang, W. Lv, X. Huang, F. Huo, H. Yang, G. Jenkins, Q. Zhao and W. Huang, *Nature Communications*, 2014, **5**, 3601.
33. S. Hirata, K.-S. Lee and T. Watanabe, *Advanced Functional Materials*, 2008, **18**, 2869-2879.
34. B. H. Cumpston, S. P. Ananthavel, S. Barlow, D. L. Dyer, J. E. Ehrlich, L. L. Erskine, A. A. Heikal, S. M. Kuebler, I. Y. S. Lee, D. McCord-Maughon, J. Qin, H. Röckel, M. Rumi, X.-L. Wu, S. R. Marder and J. W. Perry, *Nature*, 1999, **398**, 51-54.
35. A. Dobrowolska, A. J. J. Bos and P. Dorenbos, *physica status solidi (RRL) – Rapid Research Letters*, 2019, **13**, 1800502.
36. M. Thoms, H. von Seggern and A. Winnacker, *Physical Review B*, 1991, **44**, 9240-9247.
37. Y. Gao, R. Li, W. Zheng, X. Shang, J. Wei, M. Zhang, J. Xu, W. You, Z. Chen and X. Chen, *Chemical Science*, 2019, **10**, 5452-5460.
38. H. Shi and Z. An, *Nature Photonics*, 2019, **13**, 74-75.
39. Y.-M. Yang, Z.-Y. Li, J.-Y. Zhang, Y. Lu, S.-Q. Guo, Q. Zhao, X. Wang, Z.-J. Yong, H. Li, J.-P. Ma, Y. Kuroiwa, C. Moriyoshi, L.-L. Hu, L.-Y. Zhang, L.-R. Zheng and H.-T. Sun, *Light: Science & Applications*, 2018, **7**, 88.
40. S. Lin, H. Lin, C. Ma, Y. Cheng, S. Ye, F. Lin, R. Li, J. Xu and Y. Wang, *Light: Science & Applications*, 2020, **9**, 22.
41. S. Lin, H. Lin, Q. Huang, Y. Cheng, J. Xu, J. Wang, X. Xiang, C. Wang, L. Zhang and Y. Wang, *Laser & Photonics Reviews*, 2019, **0**, 1900006.
42. W. Li, Y. Zhuang, P. Zheng, T.-L. Zhou, J. Xu, J. Ueda, S. Tanabe, L. Wang and R.-J. Xie, *ACS Applied Materials & Interfaces*, 2018, **10**, 27150-27159.
43. C. Wang, Y. Jin, Y. Lv, G. Ju, D. Liu, L. Chen, Z. Li and Y. Hu, *Journal of Materials Chemistry C*, 2018, **6**, 6058-6067.
44. Z. Liu, L. Zhao, W. Chen, X. Fan, X. Yang, S. Tian, X. Yu, J. Qiu and X. Xu, *Journal of Materials Chemistry C*, 2018, **6**, 11137-11143.
45. P. Leblans, D. Vandenbroucke and P. Willems, *Materials*, 2011, **4**, 1034.
46. C. Chen, Y. Zhuang, D. Tu, X. Wang, C. Pan and R.-J. Xie, *Nano Energy*, 2020, **68**, 104329.
47. A. Bedard, T. D. Davis and C. Angelopoulos, *J Contemp Dent Pract*, 2004, **5**, 57-69.
48. K. Takahashi, K. Kohda, J. Miyahara, Y. Kanemitsu, K. Amitani and S. Shionoya, *Journal of Luminescence*, 1984, **31-32**, 266-268.
49. S. Schweizer, L. W. Hobbs, M. Secu, J.-M. Spaeth, A. Edgar and G. V. M. Williams, *Applied Physics Letters*, 2003, **83**, 449-451.
50. G. A. Appleby, J. Zimmermann, S. Hesse, O. Karg and H. v. Seggern, *Journal of Applied Physics*, 2009, **105**, 073511.
51. H. Vrielinck, F. Loncke, J. P. Tahon, P. Leblans, P. Matthys and F. Callens, *Physical Review B*, 2011, **83**, 054102.

52. D. Kulesza, P. Bolek, A. J. J. Bos and E. Zych, *Coordination Chemistry Reviews*, 2016, **325**, 29-40.
53. A. V. Sidorenko, P. Dorenbos, A. J. J. Bos, C. W. E. van Eijk and P. A. Rodnyi, *J. Phys.-Condes. Matter*, 2006, **18**, 4503-4514.
54. A. Dobrowolska, A. J. J. Bos and P. Dorenbos, *Radiation Measurements*, 2019, **127**, 106147.
55. T. Lyu and P. Dorenbos, *Chemistry of Materials*, 2020, **32**, 1192-1209.
56. A. J. J. Bos, R. M. van Duijvenvoorde, E. van der Kolk, W. Drozdowski and P. Dorenbos, *Journal of Luminescence*, 2011, **131**, 1465-1471.
57. W. Hoogenstraaten, *Philips Res. Rep*, 1958, **13**, 515–693.
58. R. Chen and S. A. A. Winer, *Journal of Applied Physics*, 1970, **41**, 5227-5232.
59. J. Azorín, *International Journal of Radiation Applications and Instrumentation. Part D. Nuclear Tracks and Radiation Measurements*, 1986, **11**, 159-166.
60. P. Dorenbos, *Optical Materials*, 2017, **69**, 8-22.
61. P. W. Tasker and A. M. Stoneham, *Journal of Physics and Chemistry of Solids*, 1977, **38**, 1185-1189.
62. R. B. Murray and F. J. Keller, *Physical Review*, 1965, **137**, A942-A948.
63. R. Gazzinelli, G. M. Ribeiro and M. L. de Siqueira, *Solid State Communications*, 1973, **13**, 1131-1134.
64. N. F. Mott and A. M. Stoneham, *Journal of Physics C: Solid State Physics*, 1977, **10**, 3391.
65. P. Dorenbos, *Optical Materials*, 2019, **91**, 333-337.
66. P. Dorenbos, *Journal of Luminescence*, 2019, **214**, 116536.

6.9. Supporting Information

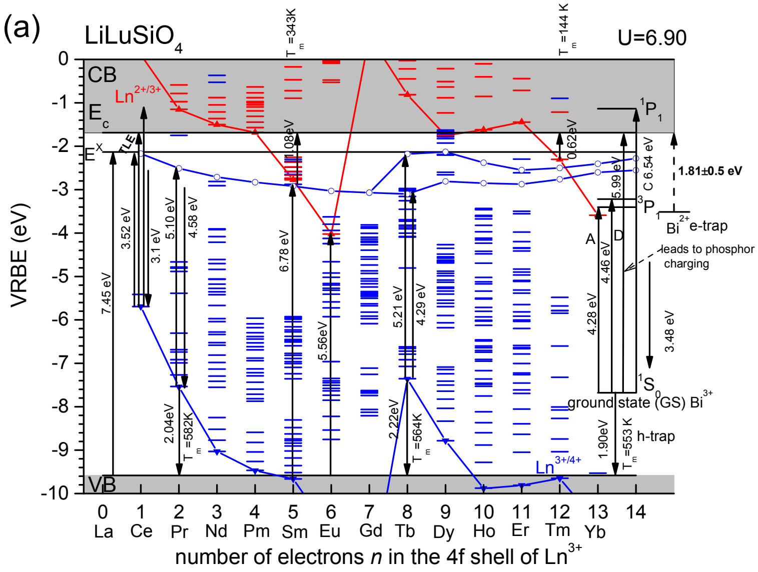

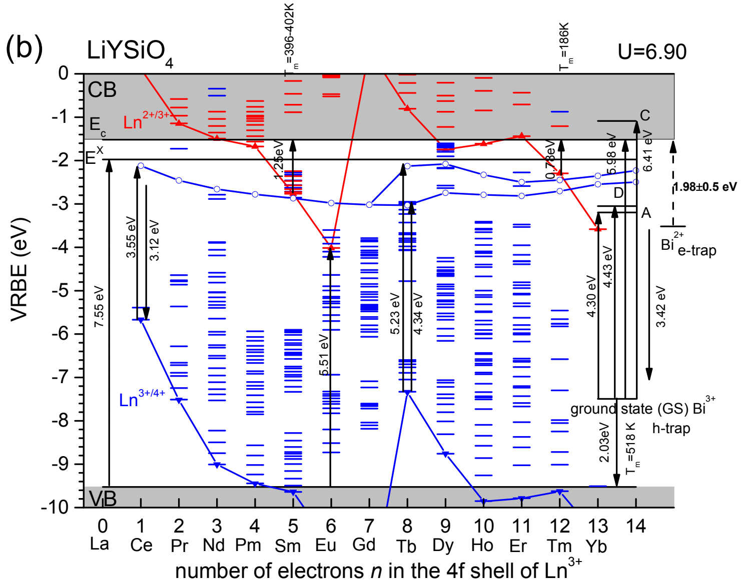

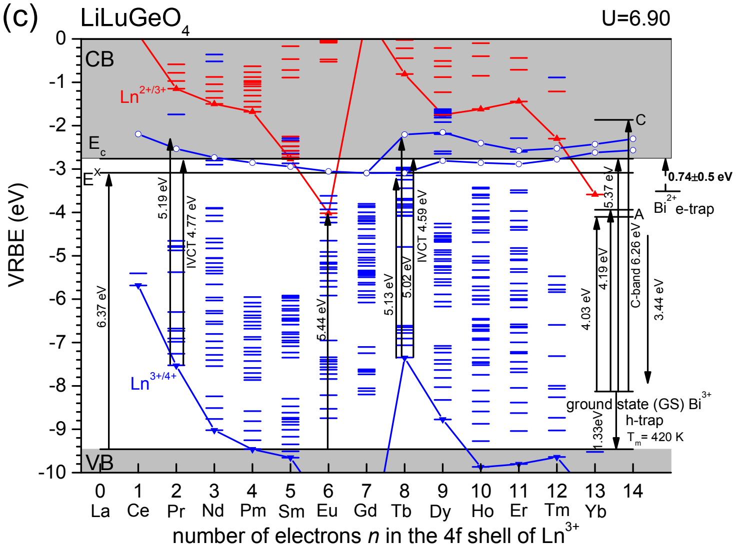

Fig. S6.1. Vacuum referred binding energy (VRBE) schemes derived from spectroscopic data of a) $LiLuSiO_4$, b) $LiYSiO_4$, and c) $LiLuGeO_4$ providing the VRBE in the ground states of Bi^{3+}, Bi^{2+}, and different lanthanides. Arrows indicate experimentally observed transitions.

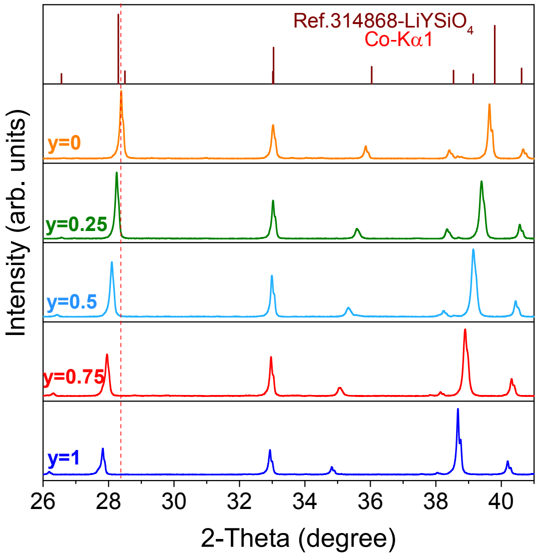

Fig. S6.2. XRD patterns for $LiLu_{0.25}Y_{0.75}Si_{1-y}Ge_yO_4$:$0.01Bi^{3+}$ solid solutions recorded at room temperature.

Fig. S6.2 shows the XRD patterns for $LiLu_{0.25}Y_{0.75}Si_{1-y}Ge_yO_4$:0.01$Bi^{3+}$. Double solid solutions appear in $LiLu_{0.25}Y_{0.75}Si_{1-y}Ge_yO_4$:0.01$Bi^{3+}$ when 0<y<1. With increasing y, the XRD peaks shift slightly to smaller angles because the cell volume increases when silicon ions are replaced by larger germanium ions.

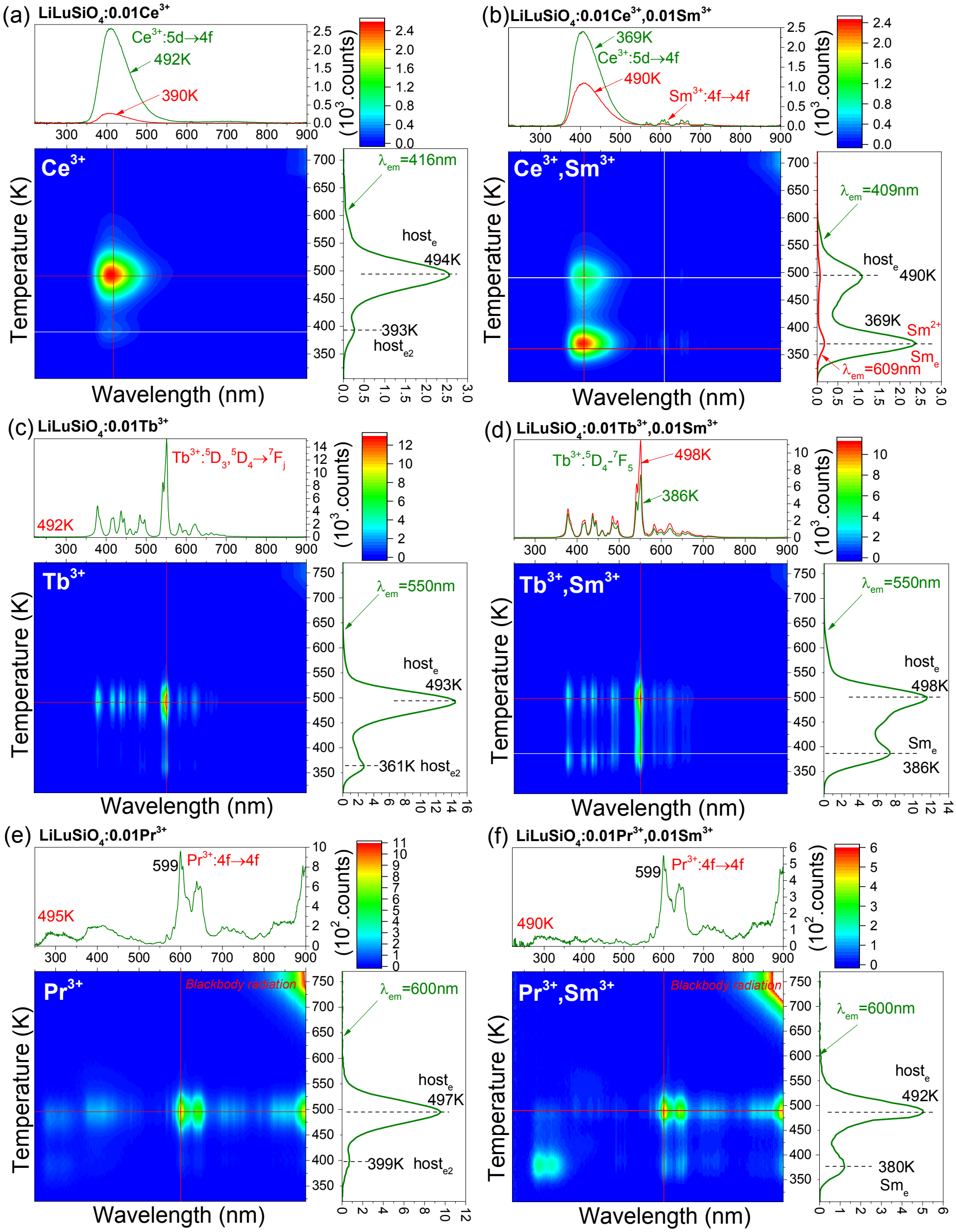

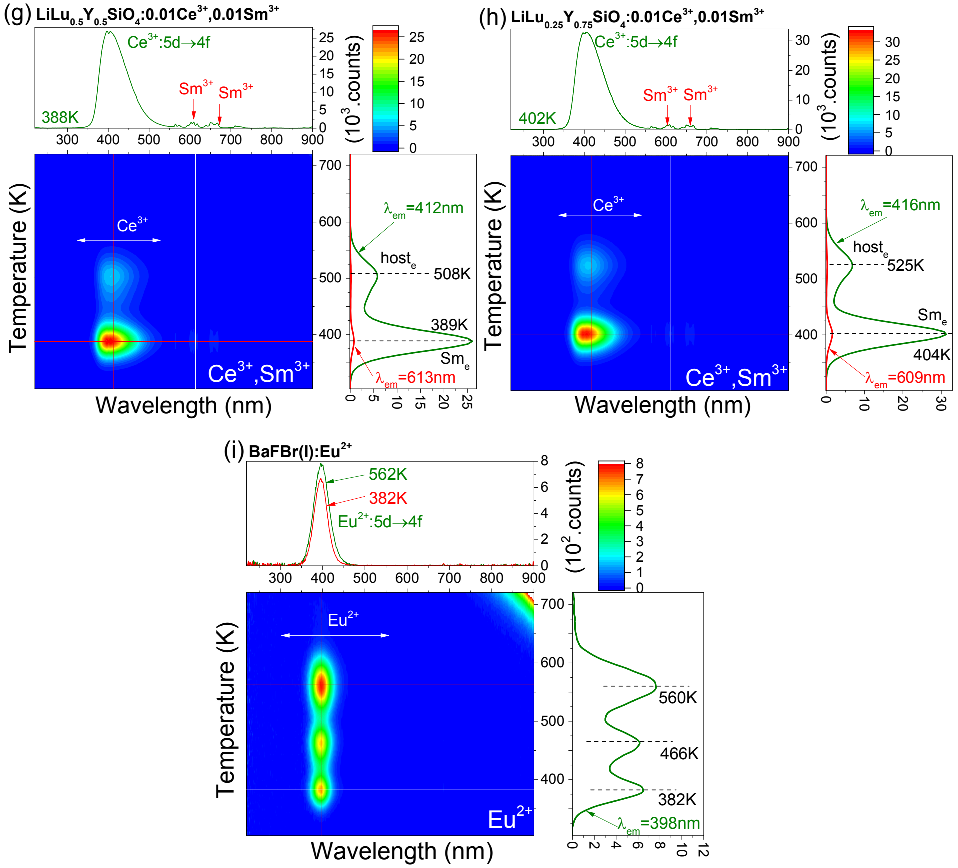

Fig. S6.3. TL emission plots for Ln^{3+}-doped LiLu$_{1-x}$Y$_x$SiO$_4$ and commercial storage BaFBr(I):Eu^{2+} phosphor recorded at a heating rate of 1 K/s after γ-ray irradiation.

Fig. S6.3b) shows the TL emission (TLEM) plot for LiLuSiO$_4$:0.01Ce^{3+}, 0.01Sm^{3+}. The TL glow peak when monitoring the Ce^{3+} emission or Sm^{3+} 4f-4f emission near 609 nm appears to share the same shape because of energy transfer from Ce^{3+} to Sm^{3+}[1]. At the Sm$_e$ TL peak near 369 K, the Sm^{3+} emission intensity is weak and the ratio of emission intensity of Sm^{3+} to that of Ce^{3+} is ~0.06. Similar results appear in LiLu$_{1-x}$Y$_x$SiO$_4$:0.01Ce^{3+},0.01Sm^{3+} (x=0.5 and 0.75) solid solutions as shown in Fig. S6.3g)-h).

Fig. S6.3i) shows the TL emission plot for the commercial BaFBr(I):Eu^{2+} storage phosphor. Broad Eu^{2+} 5d-4f emission band ranged from 325 to 475 nm appears, which is at similar wavelength as the Ce^{3+} 5d-4f emission band in the LiLu$_{1-x}$Y$_x$SiO$_4$:0.01Ce^{3+},0.01Sm^{3+} solid solutions in Fig. S6.3g)-h).

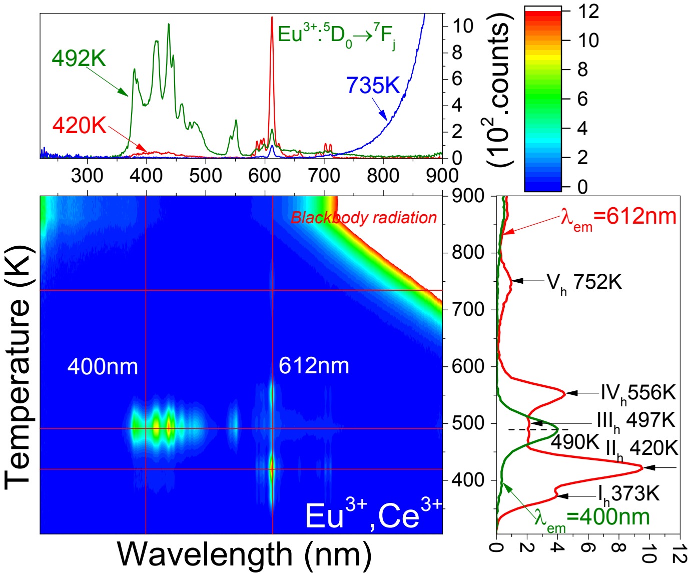

Fig. S6.4. TL emission (TLEM) plots for LiLuSiO$_4$:0.01Eu^{3+},0.01Ce^{3+} measured at a heating rate of 1 K/s after γ-ray irradiation.

Fig. S6.4 shows that the Tb$_h$ and Pr$_h$ TL peaks are absent in LiLuSiO$_4$:0.01Eu^{3+}, 0.01Ce^{3+}, but it shares the same I$_h$-V$_h$ TL peaks as in LiLuSiO$_4$:0.01Eu^{3+} in Fig. 6.3a) when the Eu^{3+} emission is monitored. Note that TL peaks near 400 and 490 K with Ce^{3+} emission appear in LiLuSiO$_4$:0.01Eu^{3+},0.01Ce^{3+}.

The hole capturing depth of Ce^{3+} in LiLuSiO$_4$ predicted from the VRBE scheme in Fig. S6.1a) is ~3.89 eV. Using Eq. (6.1) with β=1 K/s and the predicted Ce^{3+} trap depth, the temperature of hole release from Ce^{4+} is well above 1000 K. Clearly, the Ce^{4+} hole trap is too deep to release a hole between 300-900 K. The electrons trapped at less deep electron trap centres like the host defects corresponding with TL peaks near 400 K and 490 K in Fig. S6.4 will liberate earlier to recombine with holes at Ce^{4+} to generate Ce^{3+} typical 5d-4f emission.

For Eu^{2+} we predict a TL peak near 790 K due to electron release from Eu^{2+}. Its recombination with holes at Ce^{4+} was not observed. This may be attributed to the thermal quenching of Ce^{3+} emission at 790 K, or the electrons at Eu^{2+} have already gone because of recombination with holes liberated from host-related I$_h$-V$_h$ hole traps at a lower temperature in Fig. S6.4.

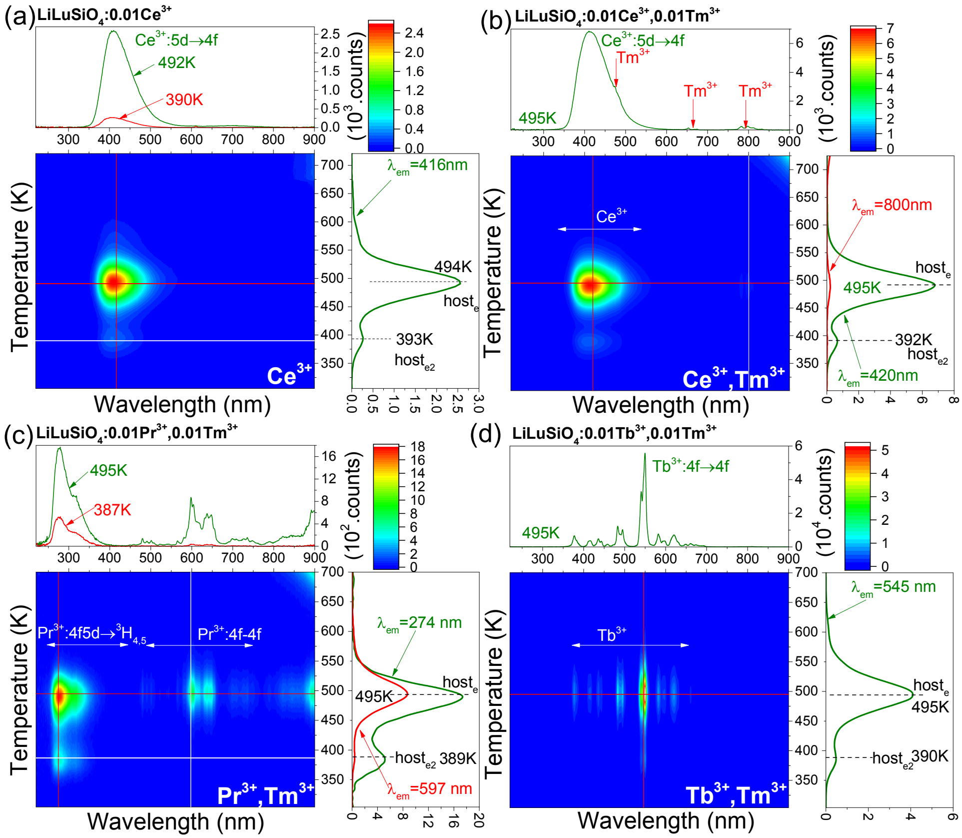

Fig. S6.5. TL emission (TLEM) plots for (a) $LiLuSiO_4:0.01Ce^{3+}$, (b) $LiLuSiO_4:0.01Ce^{3+}$, $0.01Tm^{3+}$, (c) $LiLuSiO_4:0.01Pr^{3+},0.01Tm^{3+}$, and (d) $LiLuSiO_4:0.01Tb^{3+},0.01Tm^{3+}$ recorded at a heating rate of 1 K/s after γ-ray irradiation.

TL emission plots were recorded to identify the recombination centres in $LiLuSiO_4:0.01Ce^{3+}$, and $LiLuSiO_4:0.01Ln^{3+},0.01Tm^{3+}$ (Ln=Ce, Pr, or Tb) in Fig. S6.5. Characteristic Ce^{3+} 5d-4f emission with two TL glow peaks near 393, and 494 K named $host_{e2}$ and $host_e$ for $LiLuSiO_4:0.01Ce^{3+}$ in Fig. S6.5a), is also observed for $LiLuSiO_4:0.01Eu^{3+},0.01Ce^{3+}$ in Fig. S6.4, and for $LiLuSiO_4:0.01Ce^{3+}$, $0.01Tm^{3+}$ in Fig. S6.5b).

The effect of replacing Ce^{3+} by Pr^{3+} or Tb^{3+} is shown in the TLEM plots in Fig. S6.5c)-5d). The $host_e$ and $host_{e2}$ TL glow peaks in Fig. S6.5a)-5b) also appear in $LiLuSiO_4:0.01Ln^{3+},0.01Tm^{3+}$ (Ln=Pr or Tb) in Fig. S6.5c)-5d), where the recombination centres are Pr^{3+} and Tb^{3+} instead of Ce^{3+}. Apparently, the Tm^{3+} co-doping does not create additional TL peak(s) in the above RT TL glow curves in Fig. S6.5. Note that both Pr^{3+} 5d-4f and 4f-4f emissions appear in

$LiLuSiO_4$:0.01Pr^{3+},0.01Tm^{3+} in Fig. S6.5c). The TL glow peaks when monitoring the Pr^{3+} 5d-4f or Pr^{3+} 4f-4f emission in Fig. S6.5c), or when monitoring the Ce^{3+} or Tm^{3+} emission in Fig. S6.5b) appear to share the same shape.

Using Eq. (6.1) with β=1/s, the trap depths for $host_e$ and $host_{e2}$ TL peaks are determined to be ~1.14, and ~1.44 eV, which are less deep than that of the hole traps formed by Ce^{3+}, Pr^{3+}, and Tb^{3+} as predicted in Fig. S6.1a). The $host_{e2}$ and $host_e$ TL peaks near 393, and 494 K are therefore attributed to electron release from host-related intrinsic electron traps to recombine with holes at Ce^{4+}, Pr^{4+}, and Tb^{4+}, producing typical Ce^{3+} emission in Fig. S6.5a)-b), Pr^{3+} emission in Fig. S6.5c), and Tb^{3+} emission in Fig. S6.5d).

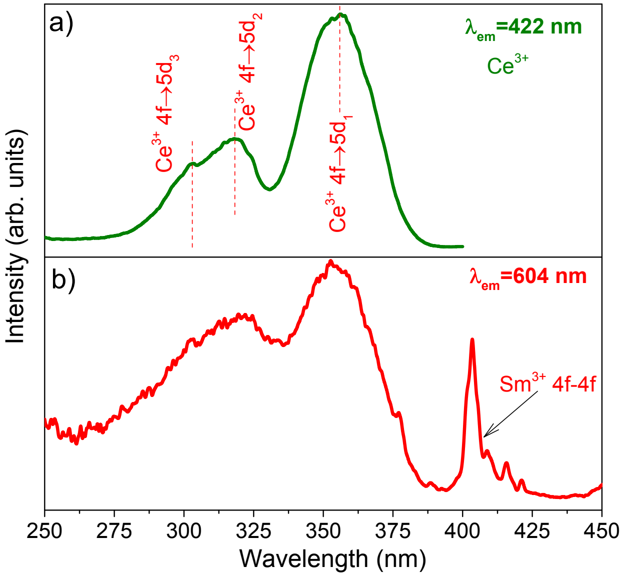

Fig. S6.6. Photoluminescence excitation spectra of $LiLuSiO_4$:0.01Ce^{3+},0.01Sm^{3+} monitoring the Ce^{3+} emission at 422 nm, and the Sm^{3+} red emission at 604 nm recorded at room temperature.

Not only Sm^{3+} 4f-4f sharp excitation bands but also Ce^{3+} 4f→$5d_{1,2,3}$ excitation bands appear in the excitation spectrum of $LiLuSiO_4$:0.01Ce^{3+},0.01Sm^{3+} in Fig. S6.6b) when the Sm^{3+} 604 nm emission is monitored. It evidences that energy transfer from Ce^{3+} $5d_{1,2,3}$ to Sm^{3+} occurs in $LiLuSiO_4$:0.01Ce^{3+},0.01Sm^{3+}.

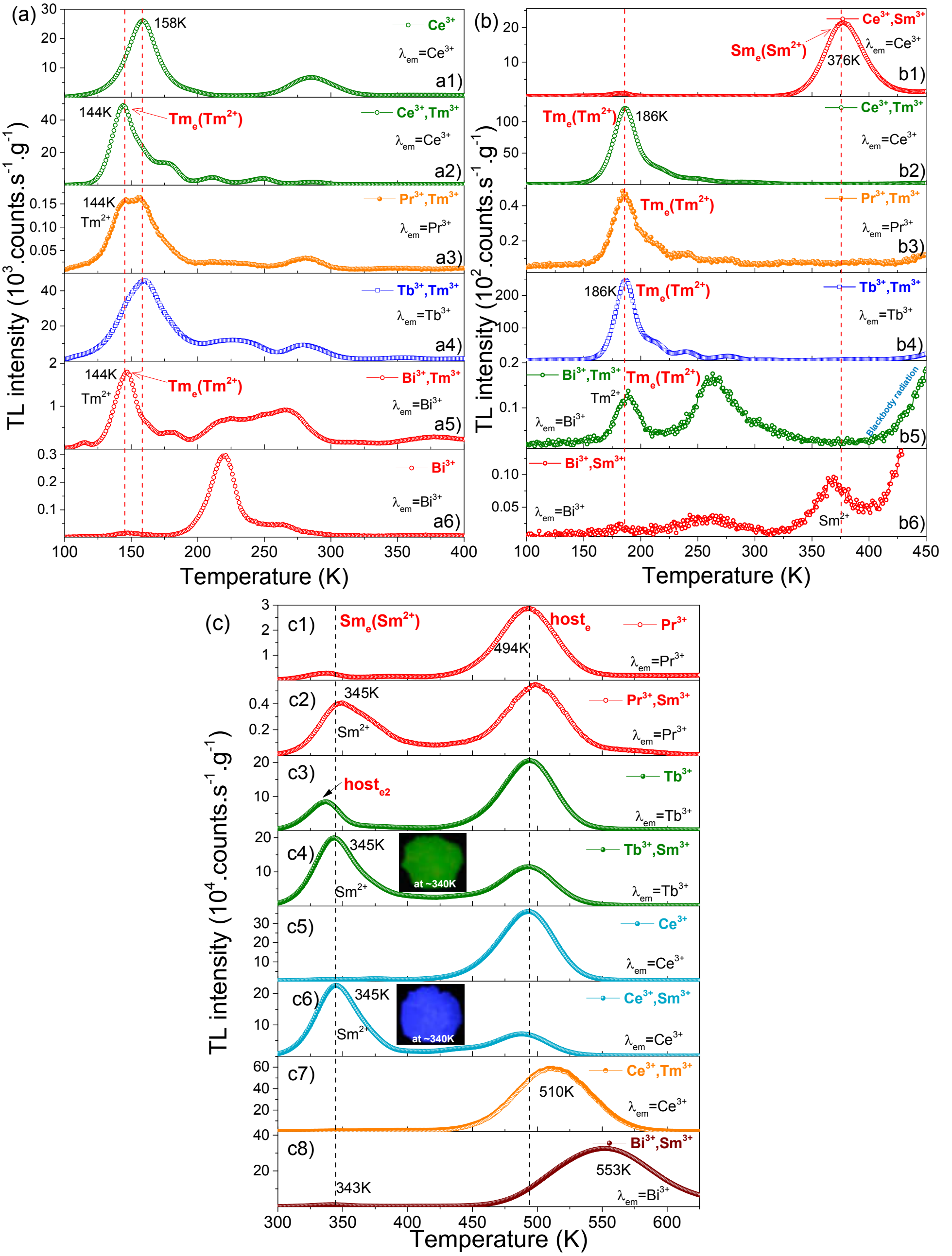

Fig. S6.7. TL glow curves for Ln^{3+} and/or Bi^{3+} doped (a), (c) LiLuSiO$_4$, and (b) LiYSiO$_4$ at β=1 K/s after β irradiation. The monitored emissions are indicated in the legend. The doped content of Ln^{3+} or Bi^{3+} is fixed at 1%. Two photos for Tb^{3+},Sm^{3+} or Ce^{3+},Sm^{3+}-codoped $LiLuSiO_4$ heated at ~340 K after Hg lamp charging are shown in the inset of Fig. S6.7c).

Fig. S6.1a) predicts that Tm^{3+} acts as a ~0.62 eV deep electron trap. Fig. S6.7a) shows the low-temperature TL glow curves for Ln^{3+} and/or Bi^{3+} doped $LiLuSiO_4$. Compared with $LiLuSiO_4$:0.01Ce^{3+} in Fig. S6.7a1), the Tm^{3+} co-dopant induces a Tm_e TL glow peak near 144 K in $LiLuSiO_4$:0.01Ce^{3+},0.01Tm^{3+} in Fig. S6.7a2), which is attributed to electron liberation from Tm^{2+}. The same applies to $LiLuSiO_4$:0.01Ln^{3+},0.01Tm^{3+} (Ln=Pr or Tb) in Fig. S6.7a3)-a4), and $LiLuSiO_4$:0.01Bi^{3+},0.01Tm^{3+} in Fig. S6.7a5) where each compound has the same Tm^{3+} electron trapping centre but with different hole capturing centres of Pr^{3+}, Tb^{3+}, and Bi^{3+}. Note that this 144 K Tm_e TL peak is absent in Bi^{3+} single doped $LiLuSiO_4$ in Fig. S6.7a6).

To further unravel the electron release process from Tm^{2+}, Fig. S6.7b) shows the low-temperature TL glow curves for Ln^{3+} and/or Bi^{3+} doped $LiYSiO_4$ phosphors after β irradiation. Like $LiLuSiO_4$ in Fig. S6.7a), a common Tm_e TL glow peak now near 186 K was observed in all the prepared crystals of $LiYSiO_4$:0.01Ln^{3+},0.01Tm^{3+} (Ln=Ce, Pr, or Tb) in Fig. S6.7b2)-b4), and $LiYSiO_4$:0.01Bi^{3+},0.01Tm^{3+} in Fig. S6.7b5), where the recombination emissions of blue Ce^{3+} 5d-4f, red Pr^{3+} 4f-4f, green Tb^{3+} 4f-4f, and ultraviolet Bi^{3+} A-band transitions are monitored. Note that this 186 K Tm_e TL glow peak is absent in both $LiYSiO_4$:0.01Ce^{3+}, 0.01Sm^{3+} in Fig. S6.7b1), and $LiYSiO_4$:0.01Bi^{3+},0.01Sm^{3+} in Fig. S6.7b6) where Sm^{3+} acts as the electron trap instead of Tm^{3+}.

Fig. S6.7c) shows the above RT TL glow curves for Ln^{3+} doped $LiLuSiO_4$ after β irradiation. Compared with $LiLuSiO_4$:0.01Pr^{3+} in Fig. S6.7c1), the Sm^{3+} co-dopant induces a Sm_e TL glow peak near 345 K, which is attributed to electron liberation from Sm^{2+} in $LiLuSiO_4$:0.01Pr^{3+},0.01Sm^{3+} in Fig. S6.7c2). The same applies to $LiLuSiO_4$:0.01Ln^{3+},0.01Sm^{3+} (Ln=Tb or Ce) in Fig. S6.7c4) and S6.7c6) where each crystal has the same Sm^{3+} electron trap but with different hole capturing centres of Tb^{3+}, and Ce^{3+}. The Sm_e TL peak is close to 300 K, and RT afterglow of Ce^{3+}, Pr^{3+}, and Tb^{3+} appears in $LiLuSiO_4$:0.01Ln^{3+},0.01Sm^{3+} (Ln=Ce, Pr, or Tb) in Fig. S6.9-S6.10. The synthesized compounds in Fig. S6.7c1)-c6) all share a common $host_e$ TL peak near 494 K. Note that this TL peak shifts ~15K towards higher temperature in Fig. S6.7c7) when Tm^{3+} is the co-dopant.

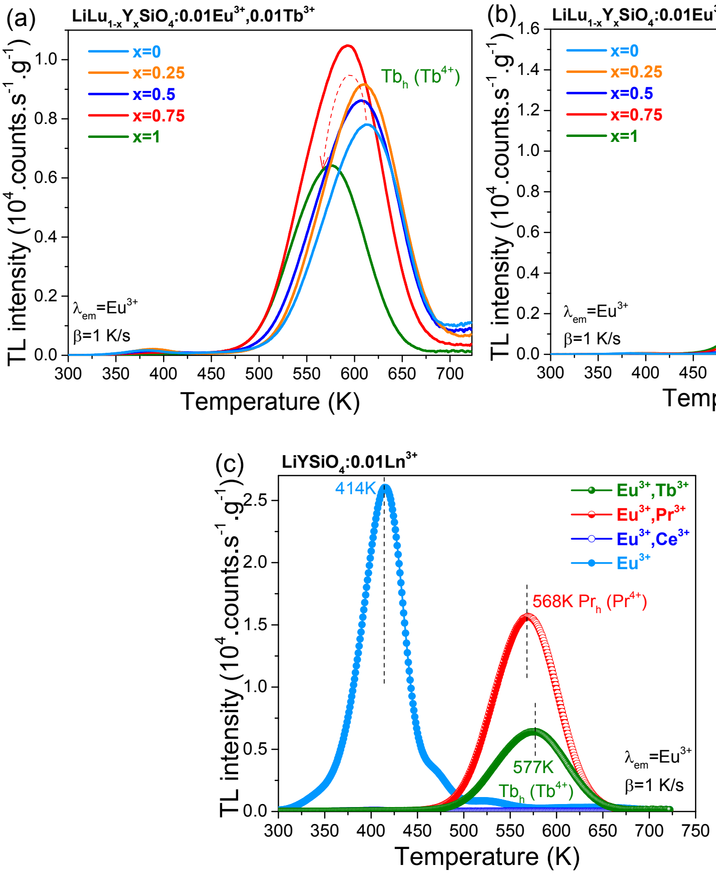

Fig. S6.8. TL glow curves for (a) $LiLu_{1-x}Y_xSiO_4$:0.01Eu^{3+},0.001Tb^{3+}, (b) $LiLu_{1-x}Y_xSiO_4$: 0.01Eu^{3+},0.01Pr^{3+} solid solutions, and (c) $LiYSiO_4$:0.01Eu^{3+},0.01Ln^{3+} (Ln=Tb, Pr, or Ce) while monitoring the Eu^{3+} red emission at a heating of 1 K/s after β irradiation.

Fig. S6.8c) shows the TL glow curves of $LiYSiO_4$:0.01Eu^{3+}, and $LiYSiO_4$:0.01Eu^{3+},0.01Ln^{3+} (Ln=Tb, Pr, or Ce) after β irradiation. The co-dopant of Tb^{3+} or Pr^{3+} in $LiYSiO_4$:0.01Eu^{3+} induces additional TL peaks Tb_h (Tb^{4+}) near 577 K, and Pr_h (Pr^{4+}) near 568 K, respectively. The new TL peaks Tb_h and Pr_h are absent in $LiYSiO_4$:0.01Eu^{3+}, and $LiYSiO_4$: 0.01Eu^{3+},0.01Ce^{3+}.

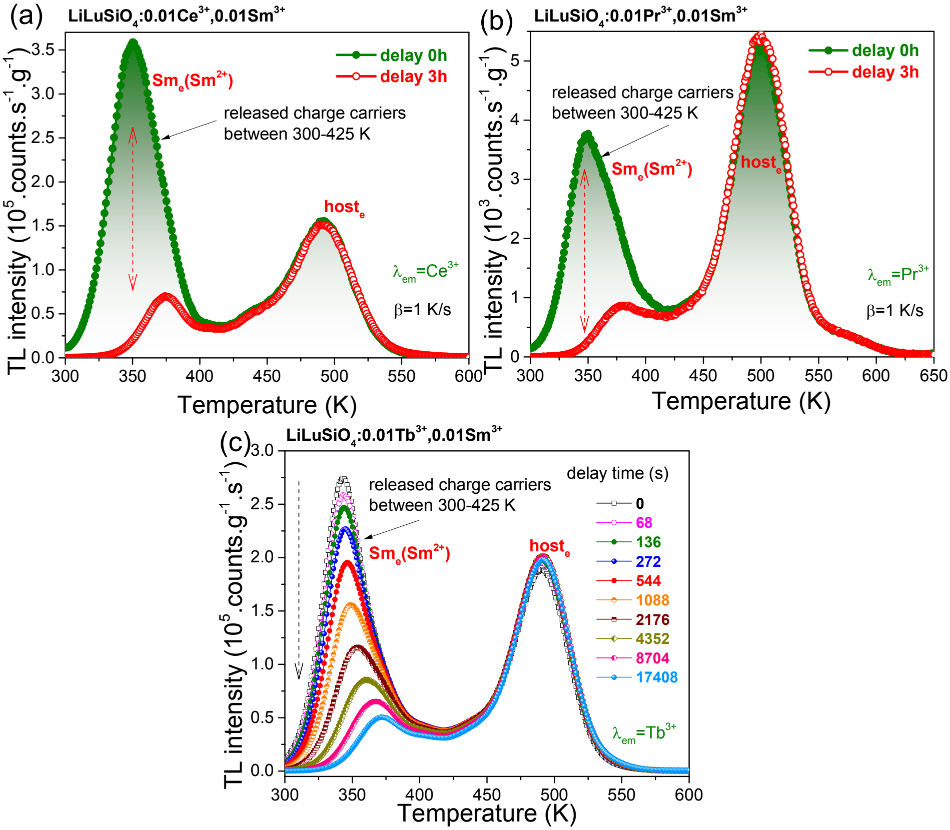

Fig. S6.9. TL glow curves at β=1 K/s for LiLuSiO4:0.01Ln^{3+},0.01Sm^{3+} (Ln=Ce, Pr, or Tb) with different delay time after β irradiation. The Ce^{3+}, Pr^{3+}, and Tb^{3+} emissions were monitored in a), b), and c), respectively.

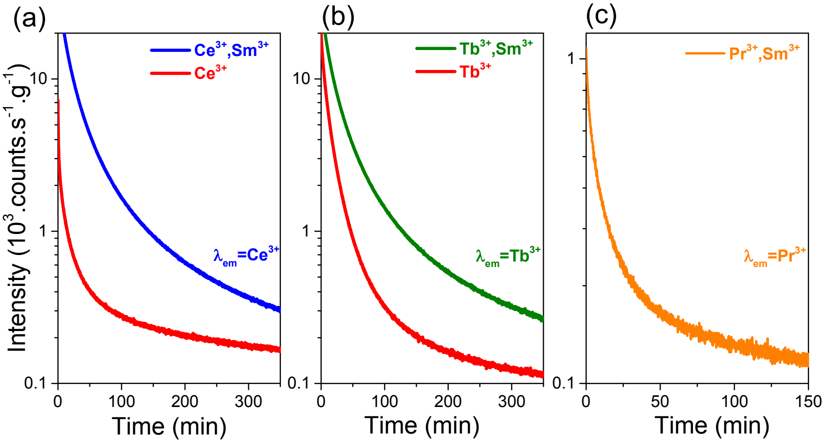

Fig. S6.10. Room temperature (295 K) isothermal decay curves of $LiLuSiO_4$:$0.01Ln^{3+}$, $0.01Sm^{3+}$ (Ln=Ce, Tb, or Pr) after β irradiation. The Ce^{3+}, Tb^{3+}, and Pr^{3+} emissions were monitored in a), b), and c), respectively.

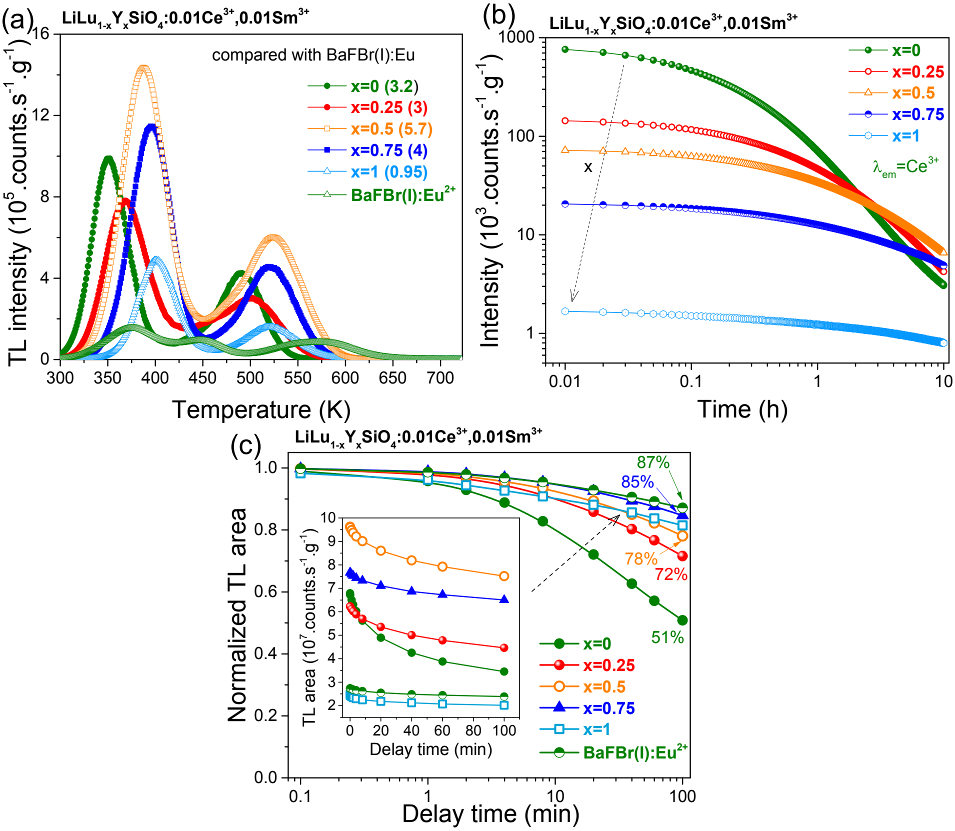

Fig. S6.11. (a) TL glow curves at β=1 K/s , (b) RT (295 K) isothermal decay curves, and (c) TL fading characteristics for $LiLu_{1-x}Y_xSiO_4$:$0.01Ce^{3+}$,$0.01Sm^{3+}$ while monitoring the Ce^{3+} emission after β irradiation.

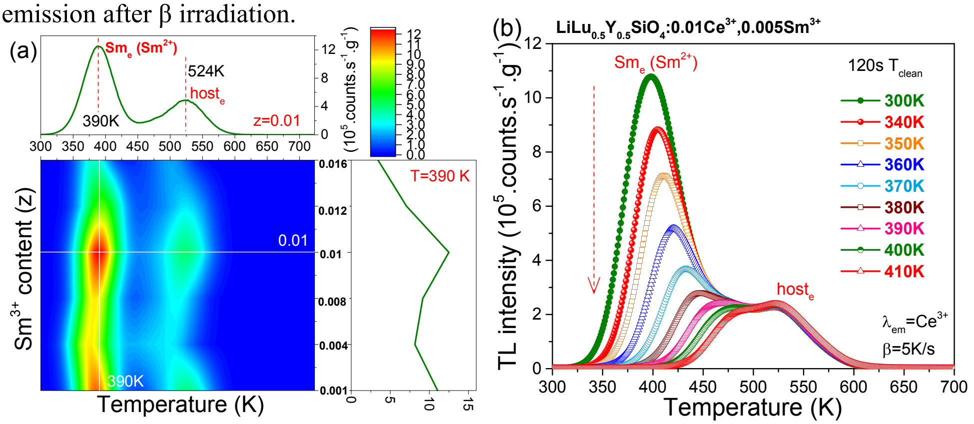

Fig. S6.12. (a) 2D mapping plot of TL glow curves at β=1 K/s for $LiLu_{0.5}Y_{0.5}SiO_4$:$0.01Ce^{3+}$, zSm^{3+} (z=0.1%-1.6%) solid solutions, and (b) TL glow curves after 120s peak cleaning at T_{clean} at β=5 K/s for the optimized $LiLu_{0.5}Y_{0.5}SiO_4$:$0.01Ce^{3+}$,$0.005Sm^{3+}$ after β irradiation while selecting the Ce^{3+} emission.

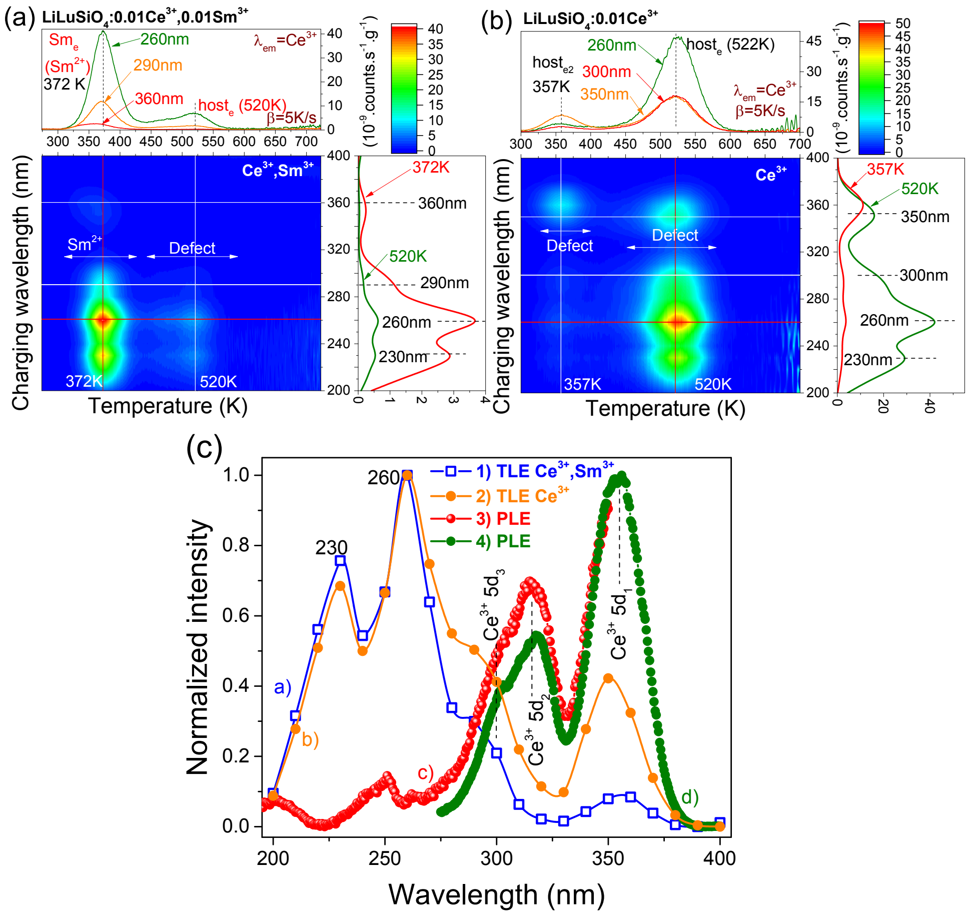

Fig. S6.13. (a)-(c) TL excitation (TLE) plots at β=5 K/s for $LiLuSiO_4$:$0.01Ce^{3+}$,$0.01Sm^{3+}$, and $LiLuSiO_4$:$0.01Ce^{3+}$. The TLE plots in c) are constructed by integrating the Sm_e TL peak between 300-450 K in a), and the $host_e$ TL peak between 450-600 K in b). The photoluminescence excitation spectrum measured by deuterium lamp in 3) and Xenon lamp in 4) while monitoring the Ce^{3+} emission for $LiLuSiO_4$:$0.01Ce^{3+}$ at 10 K is shown in c).

TL excitation spectra for Ce^{3+} and Ce^{3+},Sm^{3+}-doped $LiLuSiO_4$ are shown in Fig. S6.13a)-b). All traps corresponding with the Sm_e TL glow peak near 372 K, and the $host_e$ TL peak near 520 K in Fig. S6.13a), or the $host_{e2}$ TL peak near 357 K in Fig. S6.13b) can be charged using photons near 360, 290, 260, and 230 nm.

Fig. S6.13c) compares the photoluminescence excitation (PLE) spectrum of LiLuSiO$_4$:0.01Ce^{3+} with the TLE plots derived by integrating the Sm$_e$ TL glow peak between 300-450 K in Fig. S6.13a), and the host$_e$ TL peak between 450-600 K in Fig. S6.13b). The PLE bands of Ce^{3+} 4f→5d$_{1,\ 3}$ overlap with both the TLE plots 1) and 2) near 275-400 nm in Fig. S6.13c). Note that two additional TL excitation bands near 260 and 230 nm appear.

The band at 350 nm in the RT TL excitation plots of LiLuSiO$_4$:0.01Ce^{3+}, and LiLuSiO$_4$:0.01Ce^{3+},0.01Sm^{3+} in Fig. S6.13c) overlaps with the Ce^{3+} 4f-5d$_1$ excitation band of LiLuSiO$_4$:0.01Ce^{3+}. During 350 nm (~3.5 eV) optical stimulation, electrons are excited from the Ce^{3+} 4f ground state to 5d$_1$. Fig. S6.1a) shows that the excited 5d$_1$ state of Ce^{3+} is ~0.5 eV below the conduction band bottom in the VRBE scheme for LiLuSiO$_4$. Considering the errors and uncertainties in VRBE scheme construction, the electrons might be transported from the 5d$_1$ level to conduction band, which then charge Sm^{3+} electron trap and defect(s) responsible for the Sm$_e$ TL peak near 372 K in Fig. S6.13a), and host-related host$_{e2}$ and host$_e$ TL peaks near 357 and 522 K in Fig. S6.13b).

Fig. S6.1a) shows that the Ce^{3+} 5d$_3$ level is close to the CB-bottom. During Ce^{3+} 5d$_3$ band excitation, electrons are excited from Ce^{3+} 4f ground state to the conduction band[2], which then are trapped at intentional defect Sm^{3+} or other host-related intrinsic defects responsible for the host$_{e2}$ and host$_e$ TL peaks near 357 and 522 K in Fig. S6.13b). During higher energy photon excitation at 230 and 260 nm, electrons are excited from Ce^{3+} 4f ground state or from host-related impurity states to the conduction band, which subsequently charge all the electron traps in LiLuSiO$_4$ in Fig. S6.13a)-b).

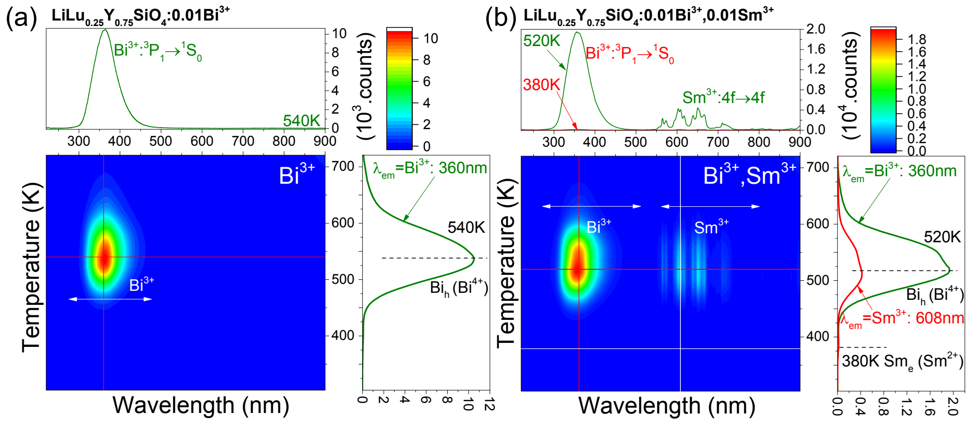

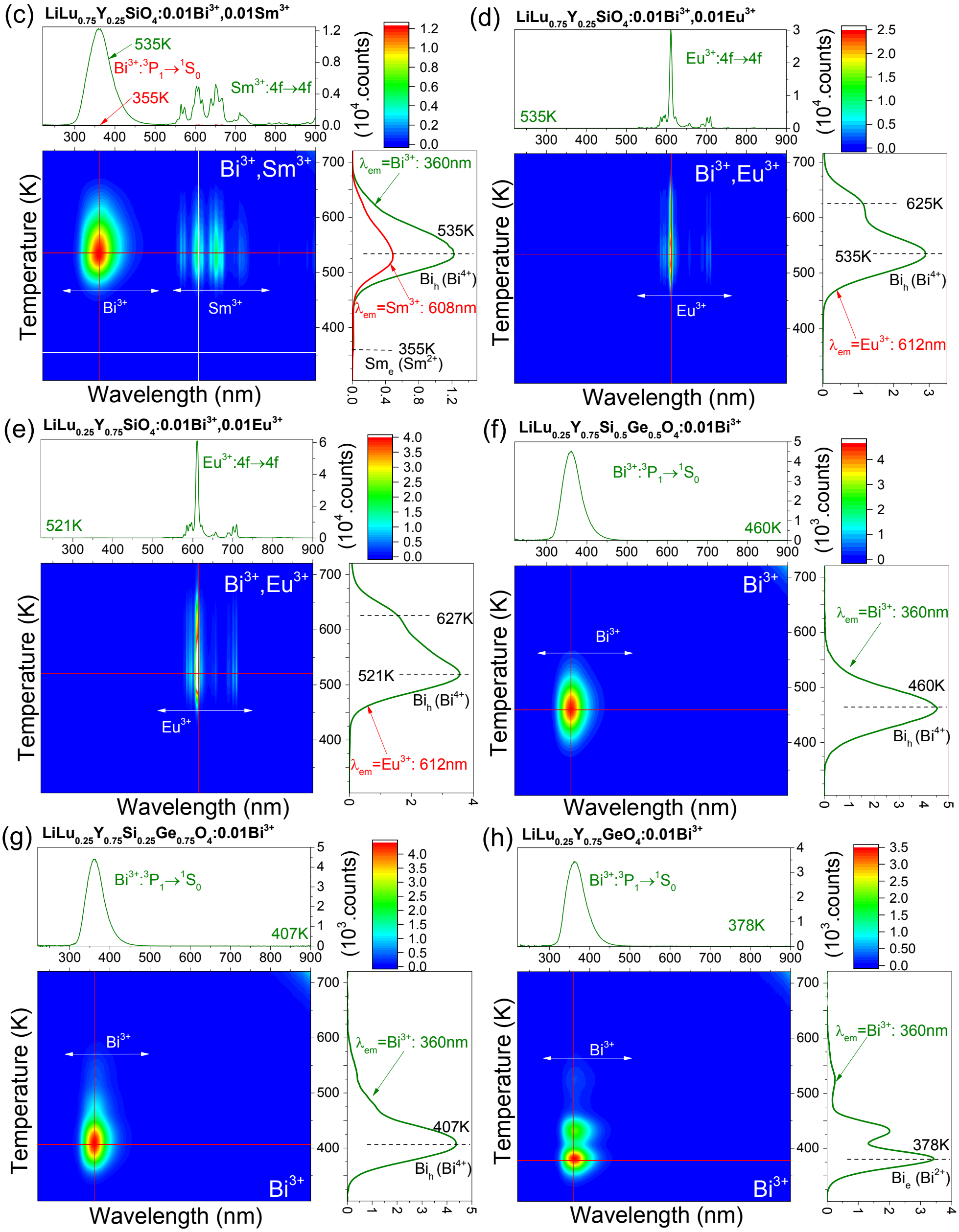

Fig. S6.14. TL emission (TLEM) plots for lanthanide and/or Bi^{3+} doped $LiLu_{1-x}Y_xSi_{1-y}Ge_yO_4$ solid solutions recorded at a heating rate of 1 K/s after γ-ray irradiation. The doped content of lanthanide or Bi^{3+} is 1 mol%.

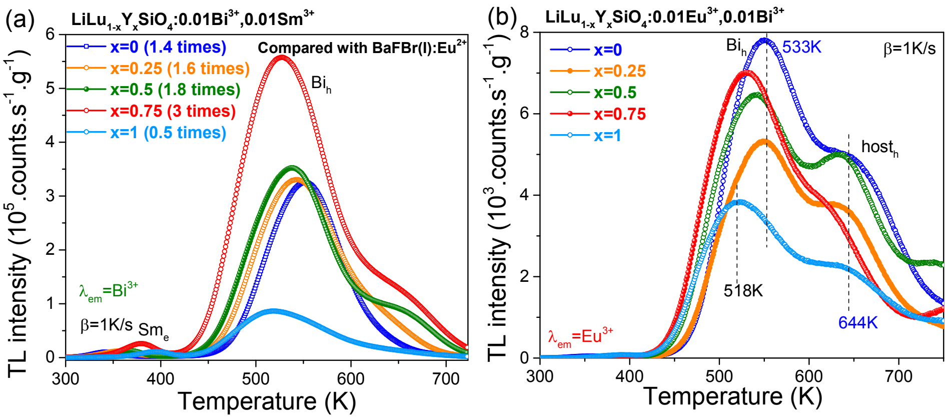

Fig. S6.15. TL glow curves of (a) $LiLu_{1-x}Y_xSiO_4$:0.01Bi^{3+},0.01Sm^{3+}, and (b) $LiLu_{1-x}Y_xSiO_4$: 0.01Eu^{3+},0.01Bi^{3+} recorded at β=1 K/s after β irradiation. The Bi^{3+}, and Eu^{3+} emissions were monitored in a), and b), respectively.

The ratios of the integrated TL intensity between 300-723 K of $LiLu_{1-x}Y_xSiO_4$: 0.01Bi^{3+},0.01Sm^{3+} (x=0-1) to that of the commercial BaFBr(I):Eu^{2+} storage phosphor are listed in the legend of Fig. S6.15a). The maximum ratio of 3 appears when x=0.75.

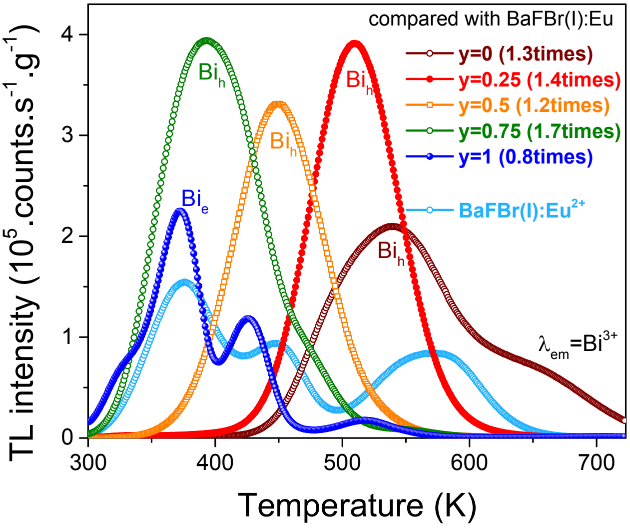

Fig. S6.16. TL glow curves of $LiLu_{0.25}Y_{0.75}Si_{1-y}Ge_yO_4$:0.01$Bi^{3+}$ (y=0-1), and the commercial X-ray storage BaFBr(I):Eu^{2+} phosphor recorded at a heating rate of 1 K/s after β irradiation while monitoring the Bi^{3+} or Eu^{2+} emission. The ratios of the integrated TL intensity between 300-723 K of $LiLu_{0.25}Y_{0.75}Si_{1-y}Ge_yO_4$:0.01$Bi^{3+}$ to that of BaFBr(I):Eu^{2+} are shown in the legend.

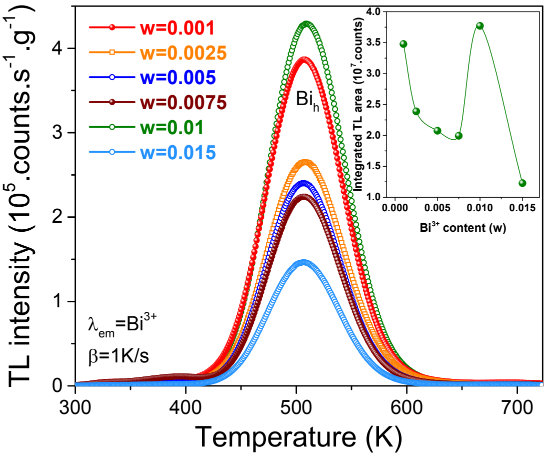

Fig. S6.17. TL glow curves of $LiLu_{0.25}Y_{0.75}Si_{0.75}Ge_{0.25}O_4$:wBi^{3+} (w=0.001-0.015) solid solutions recorded at a heating rate of 1 K/s after β irradiation while monitoring the Bi^{3+} emission.

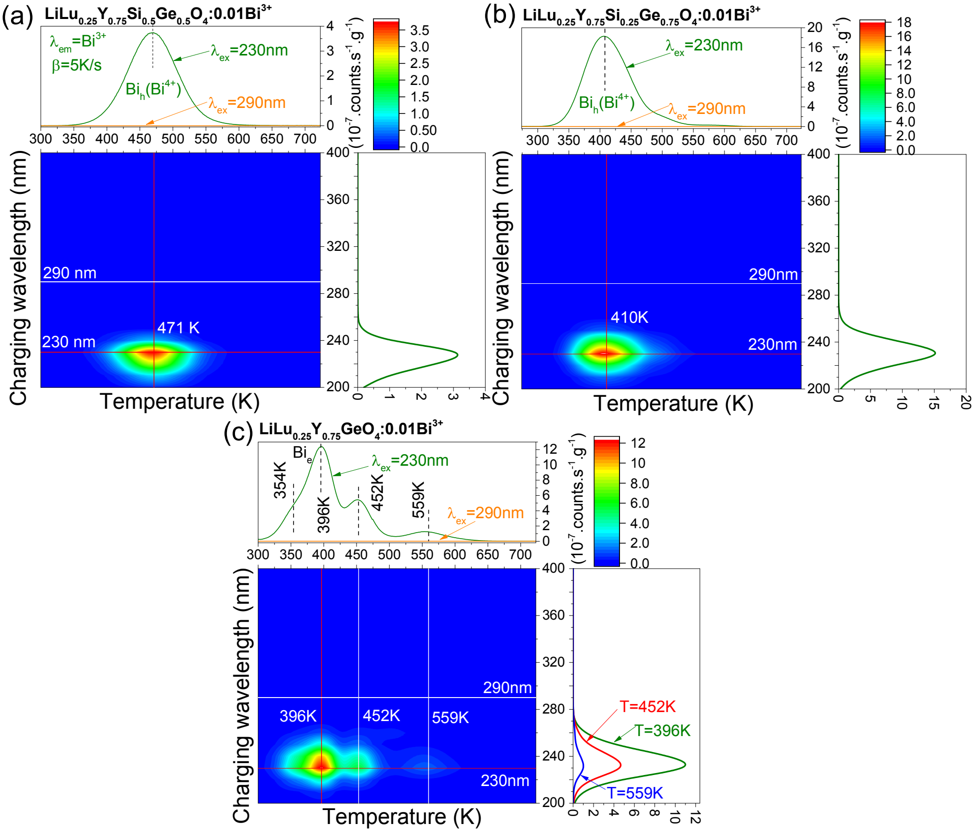

Fig. S6.18. TL excitation (TLE) spectra recorded at a heating rate of 5 K/s while monitoring the Bi^{3+} emission for $LiLu_{0.25}Y_{0.75}Si_{1-y}Ge_yO_4$:$0.01Bi^{3+}$ (y=0.5, 0.75, and 1) solid solutions.

Fig. 6.1a) and S6.1c) show that the excited $^3P_1$ level of Bi^{3+} is near ~1.5 eV and ~1.2 eV below the conduction band bottom in $LiLuSiO_4$ and $LiLuGeO_4$. Clearly, this gap is too large and efficient RT thermal ionization of electrons from the $^3P_1$ level to the conduction band is not expected, which implies that the strong Bi^{3+} A-band excitation cannot charge the $LiLu_{0.25}Y_{0.75}Si_{1-y}Ge_yO_4$:$0.01Bi^{3+}$ phosphors in Fig. 6.7d) and S6.18.

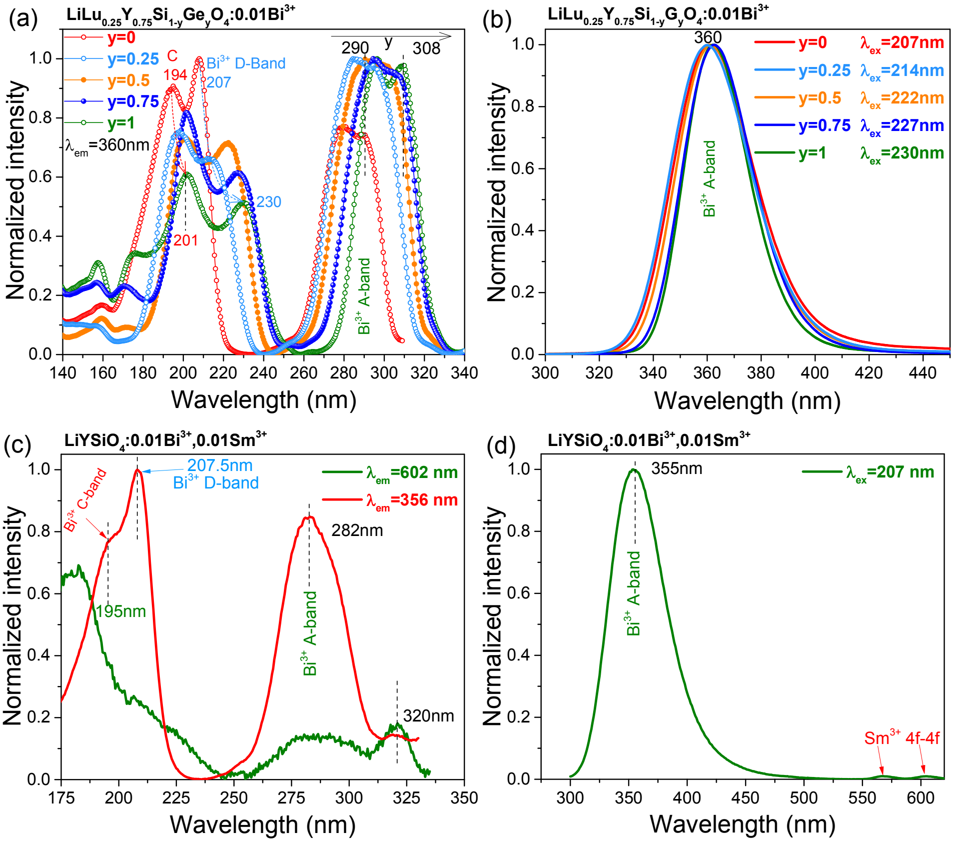

Fig. S6.19. Photoluminescence excitation and emission spectra for (a)-(b) $LiLu_{0.25}Y_{0.75}Si_{1-y}Ge_yO_4$:$0.01Bi^{3+}$ (y=0-1) solid solutions at 10 K, and (c)-(d) $LiYSiO_4$:$0.01Bi^{3+}$,$0.01Sm^{3+}$ recorded at room temperature. The data for a)-b) were obtained from Ref. [3].

Fig. S6.19c) shows that the Bi^{3+} excitation A-band near 282 nm appears when the Sm^{3+} red emission is monitored. This is due to an energy transfer process from Bi^{3+} to Sm^{3+} in $\mathrm{LiYSiO4{:}0.01Bi^{3+},0.01Sm^{3+}}$.

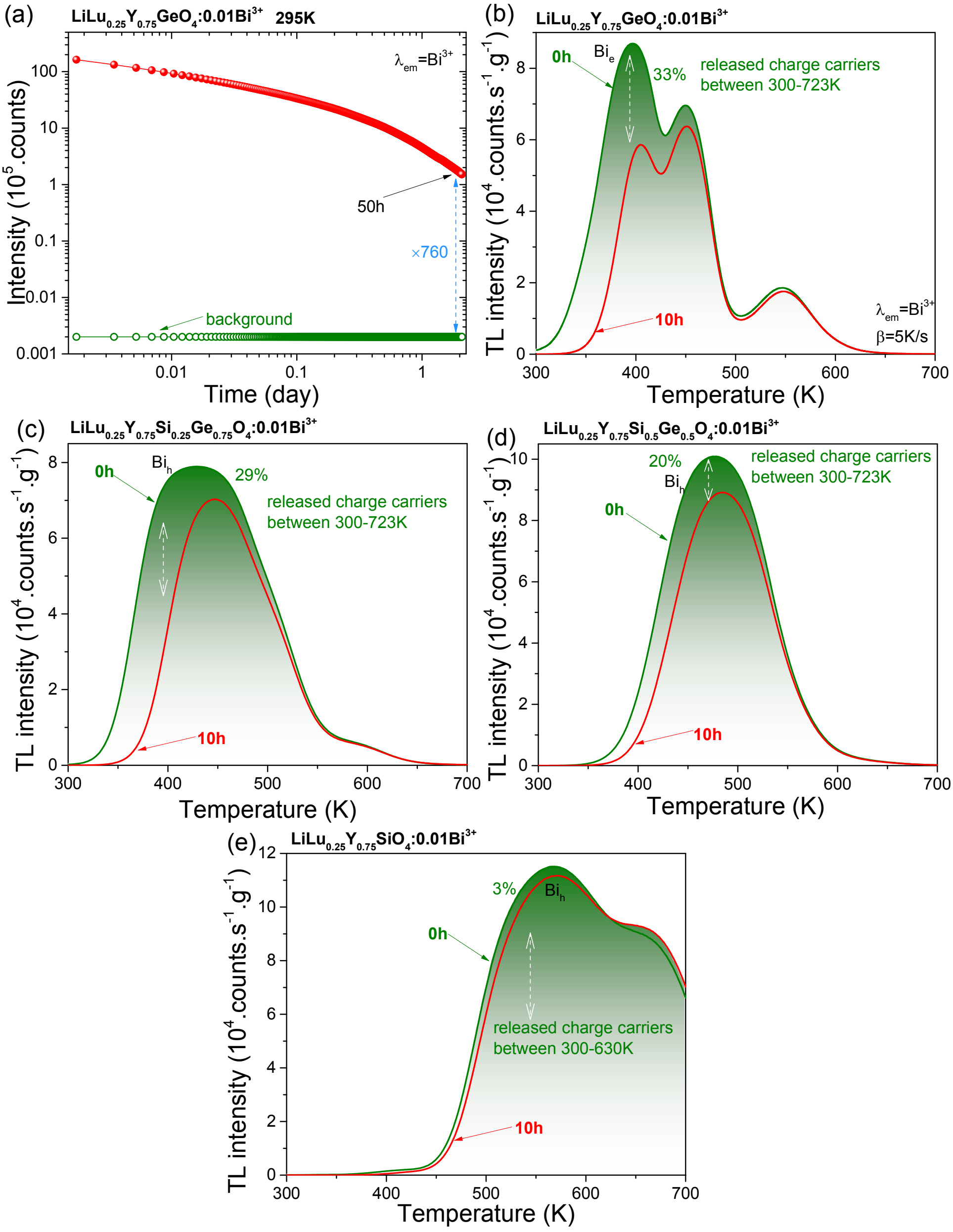

Fig. S6.20. (a) Room temperature (295 K) isothermal decay curves for $LiLu_{0.25}Y_{0.75}GeO_4$: $0.01Bi^{3+}$, and (b)-(e) TL glow curves for $LiLu_{0.25}Y_{0.75}Si_{1-y}Ge_yO_4$:$0.01Bi^{3+}$ (y=0-1) solid solutions without and with 10h delay time after β irradiation while monitoring the Bi^{3+} emission at β=5 K/s.

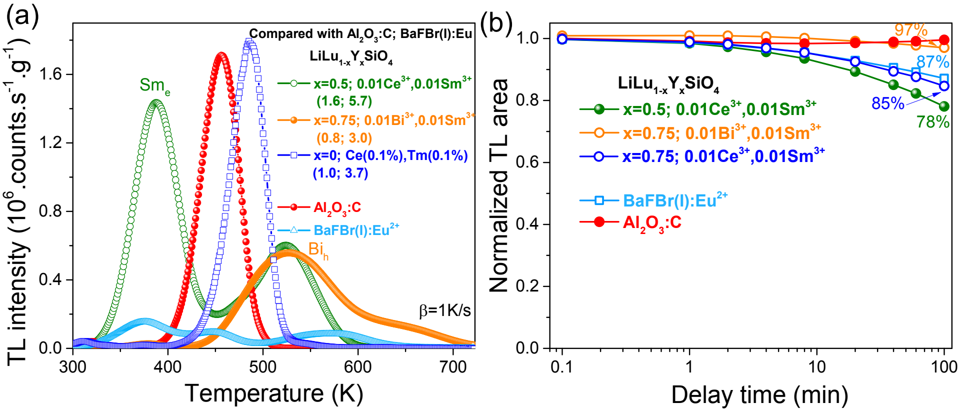

Fig. S6.21. (a) TL glow curves at β=1 K/s, and (b) TL fading characteristics for optimized samples in this work, commercial Al_2O_3:C single crystal, and BaFBr(I):Eu^{2+} storage phosphor after β-ray irradiation.

Fig. S6.21a) compares the TL glow curves of optimized Bi^{3+} and/or Ln^{3+} doped $LiLu_{1-x}Y_xSiO_4$ in this work, $LiLuSiO_4$:0.1%Ce^{3+},0.1%Tm^{3+} from Ref. [4], and the commercial storage phosphors of BaFBr(I):Eu^{2+}, and Al_2O_3:C single crystal chip after β irradiation. The ratios of integrated TL between 300-723 K of optimized samples to that of Al_2O_3:C, and BaFBr(I):Eu^{2+} are provided in the legend of Fig. S6.21a).

Fig. S6.21b) compares the TL fading characteristics for the optimized samples in this work, BaFBr(I):Eu^{2+}, and Al_2O_3:C after β irradiation. For the Bi^{3+},Sm^{3+}-codoped x=0.75 phosphor after 1.7h delay time, the integrated TL intensity between 300-723 K remains ~97%, which is ~10% higher than that of BaFBr(I):Eu^{2+} (87%).

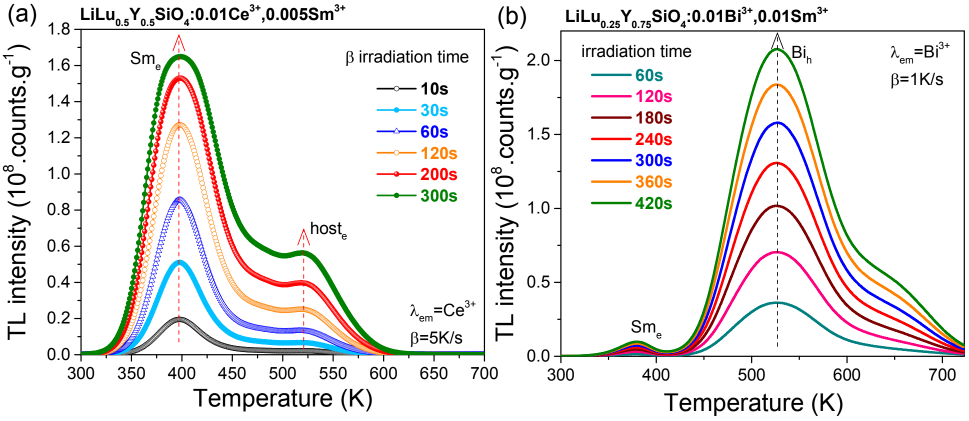

Fig. S6.22. TL glow curves for (a) $LiLu_{0.5}Y_{0.5}SiO_4:0.01Ce^{3+},0.005Sm^{3+}$ and (b) $LiLu_{0.25}Y_{0.75}SiO_4:0.01Bi^{3+},0.01Sm^{3+}$ solid solutions with different β irradiation time. The Ce^{3+} and Bi^{3+} emissions were monitored in a), and b), respectively.

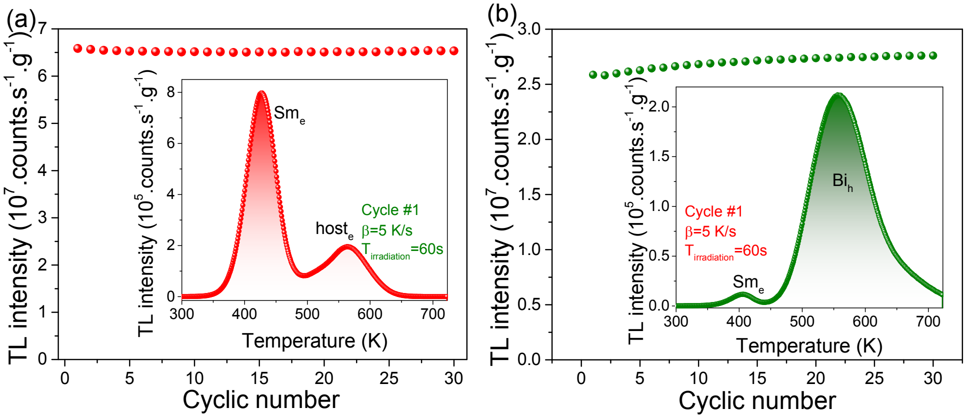

Fig. S6.23. TL glow curves for (a) $LiLu_{0.5}Y_{0.5}SiO_4:0.01Ce^{3+},0.01Sm^{3+}$ monitoring the Ce^{3+} emission, and (b) $LiLu_{0.25}Y_{0.75}SiO_4:0.01Bi^{3+},0.01Sm^{3+}$ solid solution monitoring the Bi^{3+} emission at β=5 K/s as a function of cyclic number.

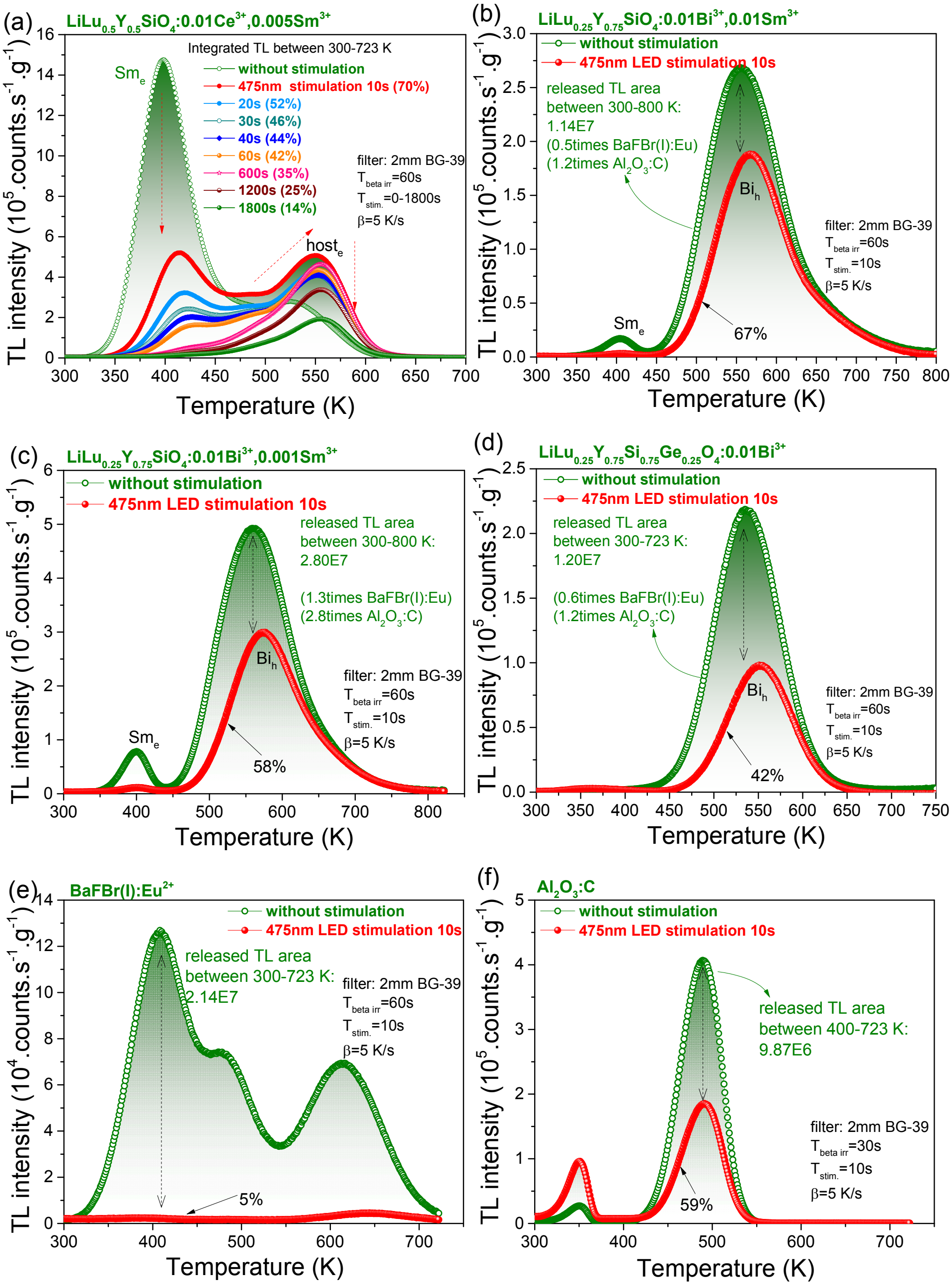
(a)
LiLu$_{0.5}$Y$_{0.5}$SiO$_4$:0.01Ce^{3+},0.005Sm^{3+}
Integrated TL between 300-723 K
without stimulation
475nm stimulation 10s (70%)
20s (52%)
30s (46%)
40s (44%)
60s (42%)
600s (35%)
1200s (25%)
1800s (14%)
Sm$_e$
host$_e$
filter: 2mm BG-39
T$_{beta\ irr}$=60s
T$_{stim.}$=0-1800s
β=5 K/s
TL intensity (10^5.counts.s^{-1}.g^{-1})
Temperature (K)
(b)
LiLu$_{0.25}$Y$_{0.75}$SiO$_4$:0.01Bi^{3+},0.01Sm^{3+}
without stimulation
475nm LED stimulation 10s
released TL area
between 300-800 K:
1.14E7
(0.5times BaFBr(I):Eu)
(1.2times Al$_2$O$_3$:C)
Bi$_h$
Sm$_e$
67%
filter: 2mm BG-39
T$_{beta\ irr}$=60s
T$_{stim.}$=10s
β=5 K/s
TL intensity (10^5.counts.s^{-1}.g^{-1})
Temperature (K)
(c)
LiLu$_{0.25}$Y$_{0.75}$SiO$_4$:0.01Bi^{3+},0.001Sm^{3+}
without stimulation
475nm LED stimulation 10s
released TL area
between 300-800 K:
2.80E7
(1.3times BaFBr(I):Eu)
(2.8times Al$_2$O$_3$:C)
Bi$_h$
Sm$_e$
58%
filter: 2mm BG-39
T$_{beta\ irr}$=60s
T$_{stim.}$=10s
β=5 K/s
TL intensity (10^5.counts.s^{-1}.g^{-1})
Temperature (K)
(d)
LiLu$_{0.25}$Y$_{0.75}$Si$_{0.75}$Ge$_{0.25}$O$_4$:0.01Bi^{3+}
without stimulation
475nm LED stimulation 10s
released TL area
between 300-723 K:
1.20E7
(0.6times BaFBr(I):Eu)
(1.2times Al$_2$O$_3$:C)
Bi$_h$
42%
filter: 2mm BG-39
T$_{beta\ irr}$=60s
T$_{stim.}$=10s
β=5 K/s
TL intensity (10^5.counts.s^{-1}.g^{-1})
Temperature (K)
(e)
BaFBr(I):Eu^{2+}
without stimulation
475nm LED stimulation 10s
released TL area
between 300-723 K:
2.14E7
5%
filter: 2mm BG-39
T$_{beta\ irr}$=60s
T$_{stim.}$=10s
β=5 K/s
TL intensity (10^4.counts.s^{-1}.g^{-1})
Temperature (K)
(f)
Al$_2$O$_3$:C
without stimulation
475nm LED stimulation 10s
released TL area
between 400-723 K:
9.87E6
59%
filter: 2mm BG-39
T$_{beta\ irr}$=30s
T$_{stim.}$=10s
β=5 K/s
TL intensity (10^5.counts.s^{-1}.g^{-1})
Temperature (K)

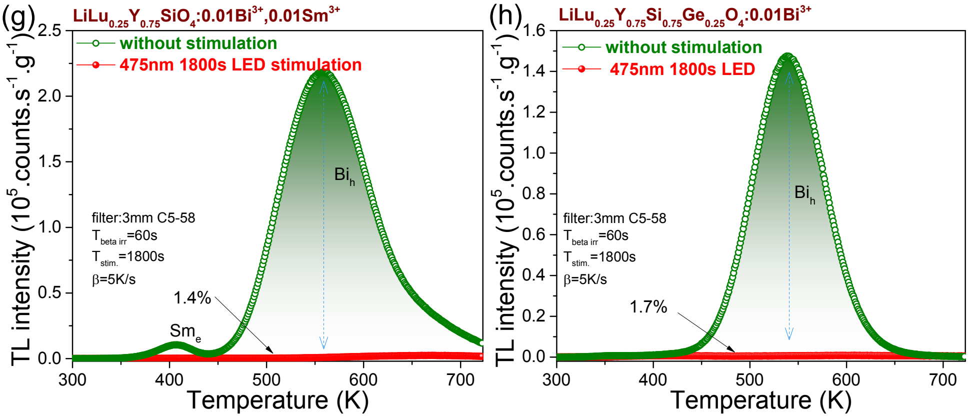

Fig. S6.24. (a)-(h) TL glow curves for Bi^{3+} and/or Ln^{3+} doped $LiLu_{1-x}Y_xSi_{1-y}Ge_yO_4$ compounds in this work, commercial BaFBr(I):Eu^{2+} and Al_2O_3:C phosphors recorded at a heating rate of 5 K/s after β irradiation and after β irradiation followed by 475 nm LED optical stimulation with different duration time.

Fig. S6.24 demonstrates that 10s of 475 nm light stimulation releases ~30, 33, 42, 58, 95, 41% of the charge carriers stored during β-ray exposure for $LiLu_{0.5}Y_{0.5}SiO_4$:0.01Ce^{3+},0.005Sm^{3+}, $LiLu_{0.25}Y_{0.75}SiO_4$:0.01Bi^{3+},0.01Sm^{3+}, $LiLu_{0.25}Y_{0.75}SiO_4$:0.01Bi^{3+},0.001Sm^{3+}, $LiLu_{0.25}Y_{0.75}Si_{0.75}Ge_{0.25}O_4$:0.01$Bi^{3+}$, commercial BaFBr(I):$Eu^{2+}$, and Al_2O_3:C, respectively.

Fig. S6.24g)-h) shows that 98% of the charge carriers stored during β-ray exposure can be liberated by 1800s of blue LED stimulation.

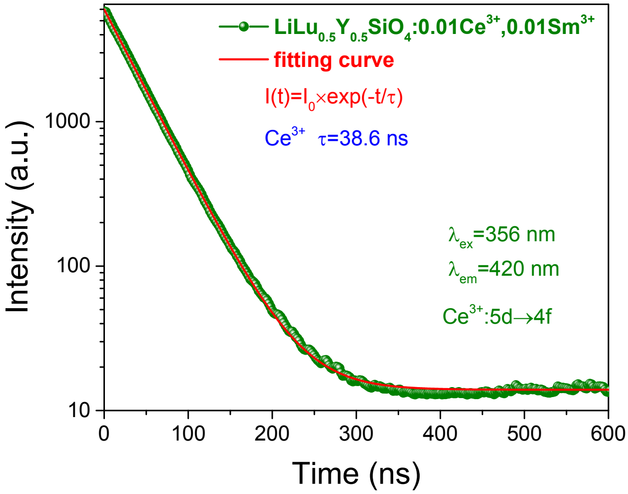

Fig. S6.25. Fluorescence decay curve of Ce^{3+} 5d→4f emission at 420 nm under 356 nm excitation in $LiLu_{0.5}Y_{0.5}SiO_4$:0.01Ce^{3+},0.01Sm^{3+} measured at room temperature.

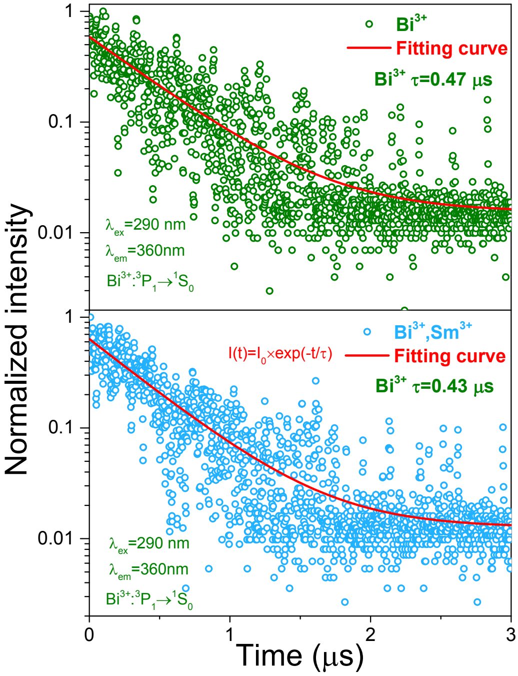

Fig. S6.26. Fluorescence decay curves of Bi^{3+} emission at 360 nm under 290 nm excitation in $LiYSiO_4$:$0.01Bi^{3+}$, and $LiYSiO_4$:$0.01Bi^{3+}$,$0.01Sm^{3+}$ measured at room temperature.

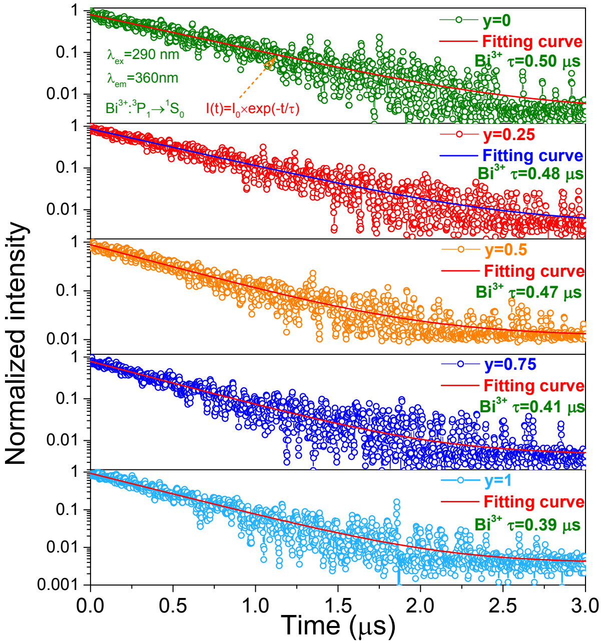

Fig. S6.27. Fluorescence decay curves of Bi^{3+} emission at 360 nm under 290 nm excitation in $LiLu_{0.25}Y_{0.75}Si_{1-y}Ge_yO_4$:0.01$Bi^{3+}$ (y=0-1) solid solutions measured at room temperature.

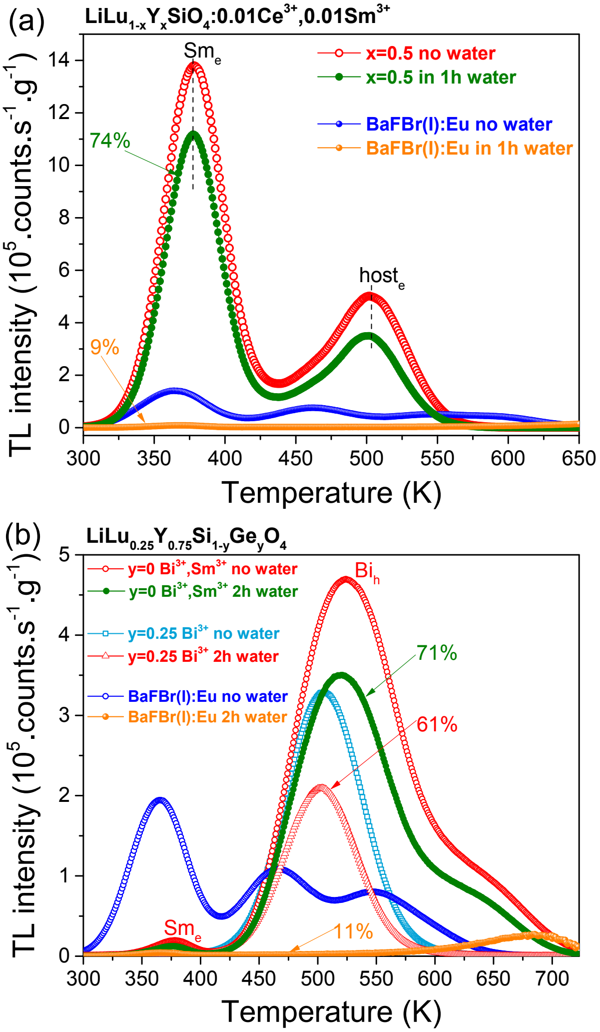

Fig. S6.28. TL glow curves at β=1 K/s after β irradiation for (a) BaFBr(I):Eu^{2+}, $LiLu_{1-x}Y_xSiO_4$:0.01Ce^{3+},0.01Sm^{3+} (x=0.5), and (b) $LiLu_{0.25}Y_{0.75}Si_{1-y}Ge_yO_4$:0.01$Bi^{3+}$ or codoped with 0.01Sm^{3+} after exposure to water. The Ce^{3+}, Bi^{3+} or Eu^{2+} emissions were monitored.

Fig. S6.28 shows the TL glow curves for $LiLu_{0.5}Y_{0.5}SiO_4$:0.01Ce^{3+},0.01Sm^{3+}, $LiLu_{0.25}Y_{0.75}SiO_4$:0.01Bi^{3+},0.01Sm^{3+}, $LiLu_{0.25}Y_{0.75}Si_{1-y}Ge_yO_4$:0.01$Bi^{3+}$ (y=0.25), and BaFBr(I):Eu^{2+} after β irradiation. The integrated TL intensity between 300-723 K remains 74% for $LiLu_{0.5}Y_{0.5}SiO_4$:0.01Ce^{3+},0.01Sm^{3+}, 71% for $LiLu_{0.25}Y_{0.75}SiO_4$:

$0.01Bi^{3+}$,$0.01Sm^{3+}$, 61% for $LiLu_{0.25}Y_{0.75}Si_{1-y}Ge_yO_4$:$0.01Bi^{3+}$ (y=0.25), and ~9% for BaFBr(I):Eu^{2+}.

Fig. S6.29. Proof-of-concept information storage application by using $LiLu_{0.5}Y_{0.5}SiO_4$: $0.01Ce^{3+}$,$0.01Sm^{3+}$ phosphor dispersed in a silicone gel plate. Information storage and display of an X-ray photograph of a chip in a1)-a3), and of different logos in b1)-e3).

Fig. S6.29a3) shows that the emission from the rectangle area of the film is relatively intense. This is because a large part of X-ray photons has not been absorbed by the chip during X-ray exposure.

Fig. S6.29b1) shows that a Chinese word is written using the $LiLu_{0.5}Y_{0.5}SiO_4$:0.01Ce^{3+},0.01Sm^{3+} phosphor dispersed in a silicone gel film. The information of the word is stored in the film when the film is charged by the UV-light. The similar applies to other logos as shown in Fig. S6.29c1)-e1).

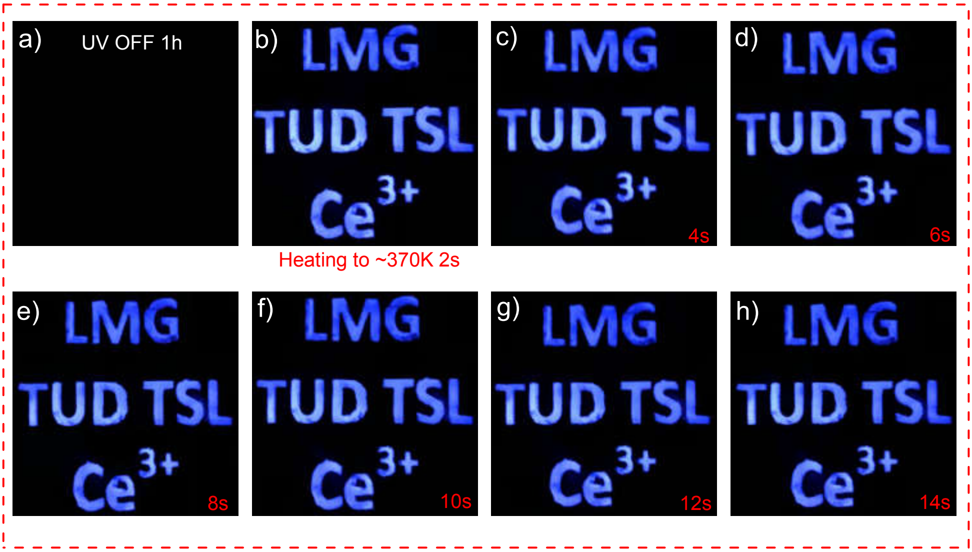

Fig. S6.30. Storage of text of "LMG TUD TSL Ce^{3+}" and its readout by heating to ~370 K with different duration time in the dark using the optimized $LiLu_{0.5}Y_{0.5}SiO_4$:0.01Ce^{3+}, 0.005Sm^{3+} storage phosphor. The $LiLu_{0.5}Y_{0.5}SiO_4$:0.01Ce^{3+},0.005Sm^{3+} phosphor was placed underneath a mask, and was charged with a Hg lamp for 30s.

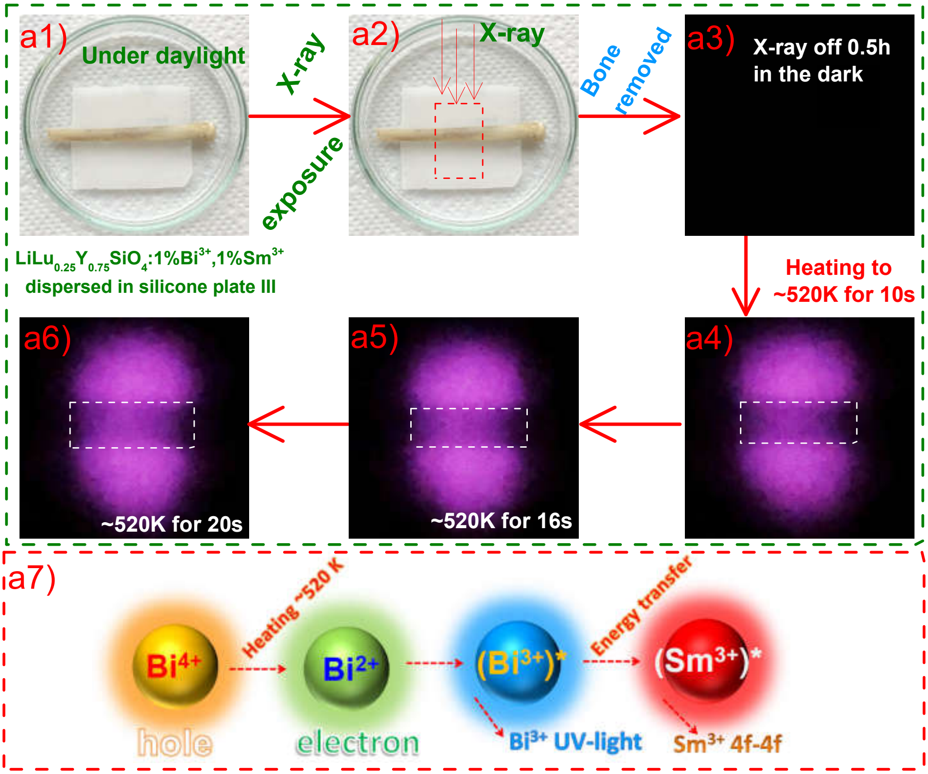

Fig. S6.31. Proof-of-concept information storage application by using $LiLu_{0.25}Y_{0.75}SiO_4$: $0.01Bi^{3+}$,$0.01Sm^{3+}$ dispersed in a 2 mm thick silicone gel plate III. Information storage and display of an X-ray image of a chicken bone in a1)-a6), and a7) corresponding thermally stimulated luminescence processes. The chicken bone was removed before heating in a4)-a6).

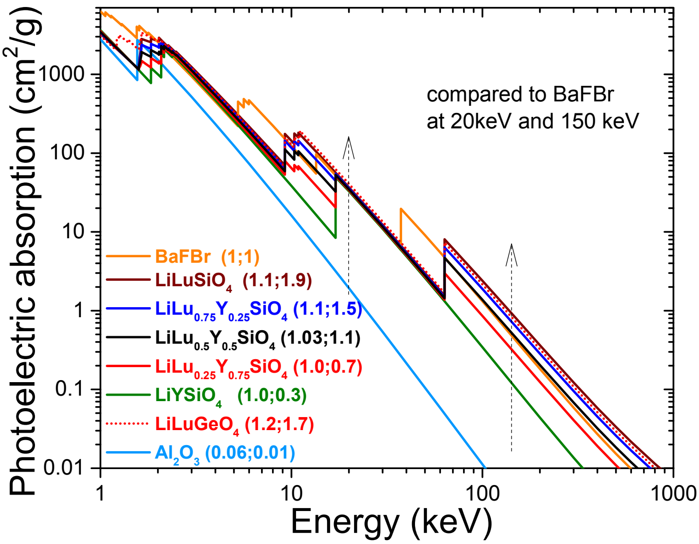

Fig. S6.32. Photoelectric absorption coefficient for the compounds studied in this work. The arrows show typical energies for mammography at 20 keV and bone radiography at 150 keV.

The photoelectric absorption coefficient for $LiLuGeO_4$ and $LiLu_{1-x}Y_xSiO_4$ (x=0-1) is shown in Fig. S6.32. $LiLu_{1-x}Y_xSiO_4$ (x<0.5) has about 10% more absorption compared with BaFBr at 20 keV. $LiLuGeO_4$ has about 20%, and 70% more absorption than BaFBr at 20 and 150 keV. This means that the $LiLu_{1-x}Y_xSiO_4$ (x<0.5) and $LiLuGeO_4$ phosphors obtain a higher dose than BaFBr with a same X-ray exposure to the patient. Note that the photoelectric absorption ratio of $LiLu_{1-x}Y_xSiO_4$ to BaFBr at E=150 keV increases from 0.3 for x=1 to 1.9 for x=0. This is because more Lu^{3+} can result in more photoelectric absorption of X-ray compared with Y^{3+}.

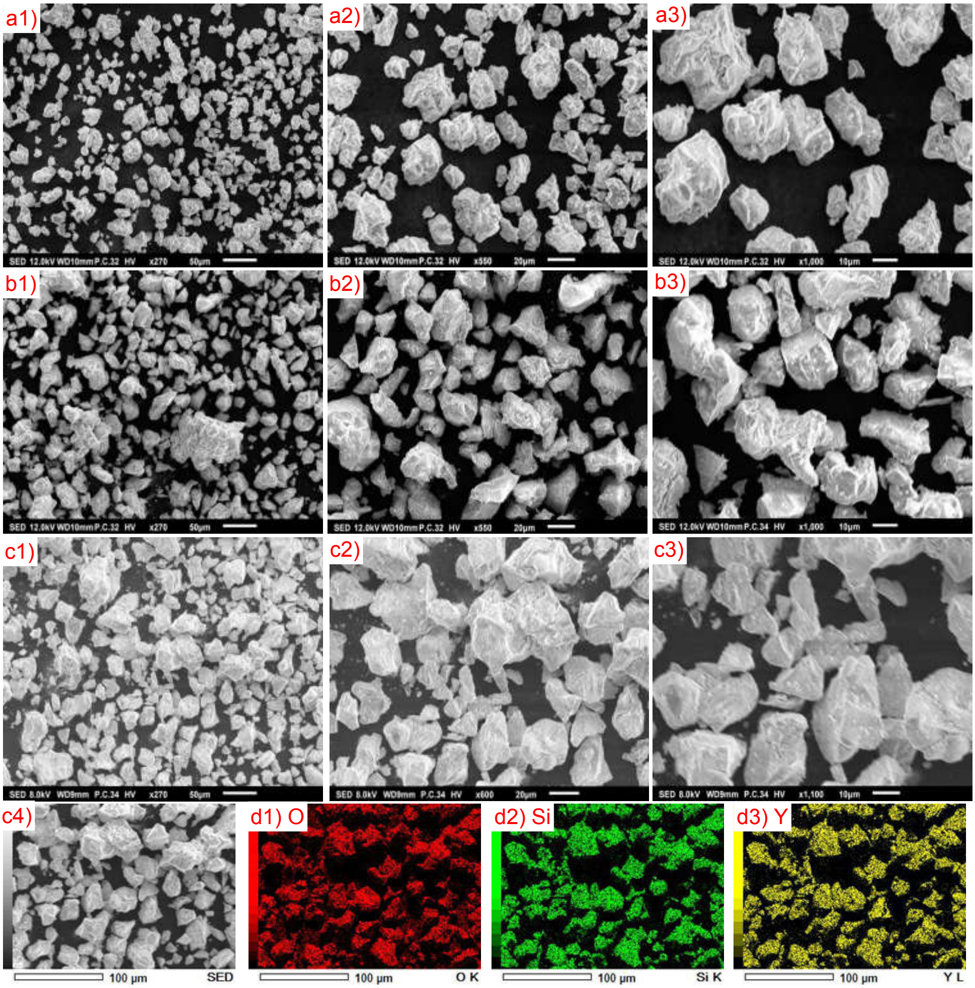

Fig. S6.33. SEM images for a1)-a3) $LiLu_{0.5}Y_{0.5}SiO_4$:0.01Ce^{3+},0.01Sm^{3+}, b1)-b3) $LiLu_{0.25}Y_{0.75}Si_{0.75}Ge_{0.25}O_4$:0.01$Bi^{3+}$, and c1)-c4) $LiLu_{0.25}Y_{0.75}SiO_4$:0.01Bi^{3+} solid solution. Energy dispersive X-ray spectroscopy (EDX) mapping of d1) O, d2) Si, and d3) Y for crystals in c4).

Fig. S6.33a1)-c3) shows that crystal aggregates about 10-40 µm based on about 5-20 µm microcrystals appear. The elemental mapping in Fig. S6.33d1)-d3) shows that the elements of O, Si, and Y are uniformly distributed in the synthesized $LiLu_{0.25}Y_{0.75}SiO_4$:0.01Bi^{3+} solid solution.

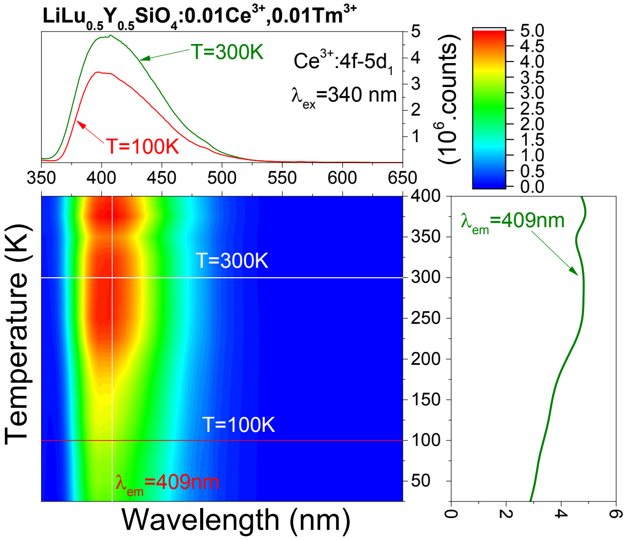

Fig. S6.34. 2D contour plot for temperature dependent photoluminescence (PL) spectra of $LiLu_{0.5}Y_{0.5}SiO_4$:0.01Ce^{3+},0.01Tm^{3+} solid solution upon Ce^{3+} 4f→5d$_1$ excitation at 340 nm.

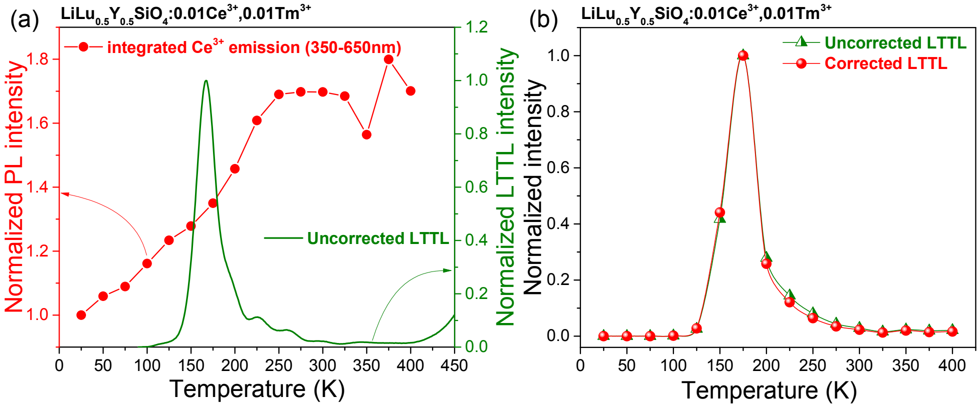

Fig. S6.35. (a) Thermal quenching curve of Ce^{3+} emission and uncorrected low-temperature TL glow curve (LTTL) of $LiLu_{0.5}Y_{0.5}SiO_4$:0.01Ce^{3+},0.01Tm^{3+}. (b) A comparison of uncorrected and corrected LTTL curves of $LiLu_{0.5}Y_{0.5}SiO_4$:0.01Ce^{3+},0.01Tm^{3+}.

The integrated Ce^{3+} emission between 350 and 650 nm as a function of temperature in Fig. S6.34 is used to determine the Ce^{3+} thermal quenching curve as shown in Fig. S6.35a). The corrected LTTL curve in Fig. S6.35b) is obtained from the uncorrected LTTL curve by correcting the thermal quenching curve of Ce^{3+} emission in Fig. S6.35a).

The result in Fig. S6.35b) shows that the shape of LTTL curve of $LiLu_{0.5}Y_{0.5}SiO_4$:0.01Ce^{3+},0.01Tm^{3+} solid solution does not alter significantly after correcting the thermal quenching curve of Ce^{3+} emission.

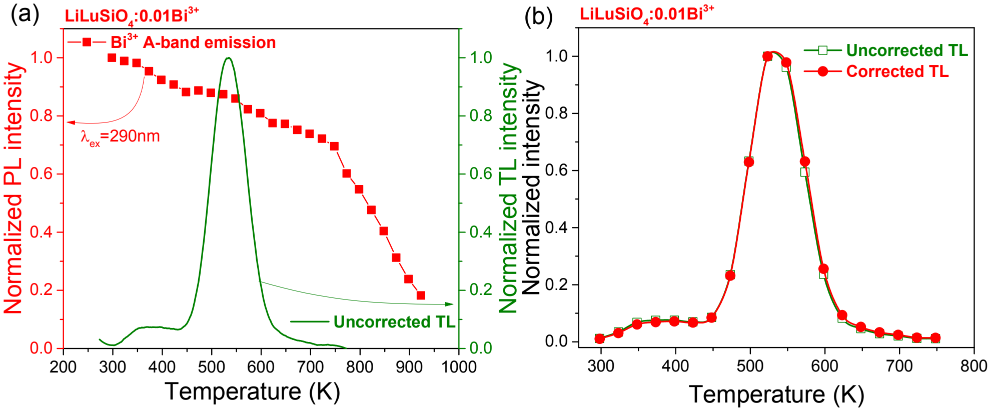

Fig. S6.36. (a) Thermal quenching curve of Bi^{3+} A-band emission and uncorrected TL glow curve of $LiLuSiO_4$:0.01Bi^{3+}. (b) A comparison of uncorrected and corrected TL glow curves of $LiLuSiO_4$:0.01Bi^{3+}.

The integrated Bi^{3+} A-band emission upon 290 nm excitation as a function of temperature is used to determine the Bi^{3+} thermal quenching curve in Fig. S6.36a). The corrected TL glow curve as shown in Fig. S6.36b) is obtained from the uncorrected TL glow curve by correcting the thermal quenching curve of Bi^{3+} A-band emission in Fig. S6.36a).

Fig. S6.36b) shows that the shape of the TL glow curve of $LiLuSiO_4$:0.01Bi^{3+} does not change significantly after correcting the thermal quenching curve of Bi^{3+} A-band emission.

Reference

1. T. Lyu and P. Dorenbos, *Chemical Engineering Journal*, 2019, **372**, 978-991.
2. A. Dobrowolska, A. J. J. Bos and P. Dorenbos, *Radiation Measurements*, 2019, **127**, 106147.
3. T. Lyu and P. Dorenbos, *Chemistry of Materials*, 2020, **32**, 1192-1209.
4. A. Dobrowolska, A. J. J. Bos and P. Dorenbos, *physica status solidi (RRL) – Rapid Research Letters*, 2019, **13**, 1800502.

7

Summary

In this thesis, we have studied two types of charge carrier capturing and detrapping processes: (a) electron capturing and electron liberation; (b) hole capturing and hole liberation. Both the (a) and (b) processes can be utilized for the rational design of afterglow and storage phosphors in different compounds.

The "electron capturing and electron liberation" model has been discussed in detail in the first part of Chapter 2, Chapter 5, and a part of Chapter 6. In Chapters 2 and 6, Ce^{3+} appears to act as deep hole capturing and recombination centre, while the other lanthanide co-dopants Ln^{3+} (Ln=Er, Nd, Ho, Dy, Tm, or Sm) are less deep electron capturing centres. In Chapter 5, Bi^{3+} acts as deep hole capturing and recombination centre while the Bi^{3+} and Eu^{3+} co-dopants are less deep electron capturing centres. Different electron trap depth can be realized by a choice of lanthanide codopants or Bi^{3+} co-doping.

In this thesis, the VRBE at the conduction band bottom is important for designing afterglow and storage phosphors. For a fixed set of lanthanide and/or bismuth dopants like in $Gd_{1-x}La_xPO_4$:Ce^{3+},Ho^{3+} (Chapter 2), $NaLu_{1-x}Y_xGeO_4$:Bi^{3+} (Chapter 5), and $LiLu_{1-x}Y_xSiO_4$:Ce^{3+},Sm^{3+} solid solutions (Chapter 6), tailorable electron trap depth of Ho^{3+}, Bi^{3+}, or Sm^{3+} can be obtained by adjusting x leading to conduction band engineering. It means that one can engineer the TL glow peak temperature for afterglow or storage phosphor applications.

The "hole capturing and hole liberation" model has been discussed in detail in the second part of Chapter 2, Chapter 3, Chapter 4, and a part of Chapter 6. In these chapters, Tb^{3+}, Pr^{3+}, and Bi^{3+} appear to act as hole capturing centres with trapping depths less deep than the electron trapping on Eu^{3+} and Bi^{3+}. Eu^{3+} and Bi^{3+} act then as recombination centres. Compared with the common "electron capturing and electron liberation" model, the "hole capturing and hole liberation" model gives us a new method to develop afterglow and storage phosphors. In this hole liberation model, the VRBE at the valence band top is crucial for designing a hole trap. For a fixed set of lanthanide and/or bismuth dopants like in $Y_{1-x}Lu_xPO_4$:Eu^{3+},Tb^{3+} in Chapter 2, $Y_{1-x}Lu_xPO_4$:Eu^{3+},Bi^{3+} in Chapter 3, $La_{1-x}Gd_xPO_4$:Bi^{3+},Tb^{3+},Nd^{3+} in Chapter 4, $LiLu_{1-x}Y_xSiO_4$:Eu^{3+},Tb^{3+}, and $LiLu_{0.25}Y_{0.75}Si_{1-y}Ge_yO_4$:$Bi^{3+}$ solid solutions in Chapter 6, adjustable hole trap depth of Tb^{3+}, Pr^{3+}, or Bi^{3+} can be realized by changing x or y leading to valence band engineering.

Chapter 2 reveals that: (1) Ln^{3+} (Ln=Sm, Eu, or Yb) ions in YPO_4 act as deep electron trapping and recombination centres while Tb^{3+} and Pr^{3+} are less deep hole capturing centres; (2) the holes are liberated from Tb^{4+} or Pr^{4+} at a lower temperature than electrons to recombine with the electrons trapped at Ln^{2+} to produce the characteristic 4f-4f emission of Ln^{3+} during TL-readout; (3) the hole traps in $LaPO_4$:Eu^{3+},Tb^{3+} can be filled by the Eu^{3+} charge transfer excitation.

Chapter 3 reveals that: (1) Bi^{3+} can act in YPO_4 as a deep electron capturing centre while Tb^{3+} and Pr^{3+} act as less deep hole capturing centres; (2) During the TL-readout, the holes are liberated from Tb^{4+} or Pr^{4+} at a lower temperature than the electrons to recombine with the electrons at Bi^{2+} to give characteristic Bi^{3+} A-band emission; (3) Bi^{3+} can act as a less deep hole capturing centre while the Ln^{3+} (Ln=Tm, Sm, Eu, or Yb) ions are the deep electron capturing centres in YPO_4; (4) During the TL-readout, the holes are liberated from Bi^{4+} at a lower temperature than the electrons to recombine with the electrons trapped at Ln^{2+} to give typical Ln^{3+} 4f-4f emission; (5) the hole traps in $YPO_4:Eu^{3+},Bi^{3+}$ can be filled using Eu^{3+} charge transfer excitation energy.

On the basis of the results in Chapters 2 and 3, Chapter 4 reveals that one can rationally design a Nd^{3+} SWIR afterglow phosphor for the second bio-imaging window. It was achieved by combining efficient energy transfer from Bi^{3+} to Nd^{3+} with a tailorable hole trap depth by valence band engineering in $La_{1-x}Gd_xPO_4:Bi^{3+},Tb^{3+},Nd^{3+}$ by adjusting x. This was the first time that the hole liberation model has been used to develop SWIR afterglow phosphor.

Chapter 6 reveals that: (1) Tb^{3+}, Pr^{3+}, and Bi^{3+} in $LiLuSiO_4$ capture holes less deep than that Eu^{3+} and Bi^{3+} trap electrons; (2) During TL-readout, the holes are liberated earlier from Tb^{4+}, Pr^{4+}, or Bi^{4+} than the electrons to recombine with electrons captured at Eu^{2+} or Bi^{2+} to generate the typical Eu^{3+} 4f-4f emission or Bi^{3+} A-band emission; (3) the hole trap depths of Tb^{3+}, Pr^{3+}, or Bi^{3+} can be tailored by adjusting x in $LiLu_{1-x}Y_xSiO_4$ resulting in valence band engineering; (4) the Bi^{3+} hole trap in $LiLu_{1-x}Y_xSiO_4:Bi^{3+}$ or $LiLu_{0.25}Y_{0.75}Si_{1-y}Ge_yO_4:Bi^{3+}$ can be charged by Bi^{3+} D-band excitation; (5) we for the first time demonstrate that a good Bi^{3+} storage phosphor can be developed with $LiLu_{1-x}Y_xSiO_4:Bi^{3+}$ by the “hole capturing and hole liberation” model.

In this thesis, the effect of crystal synthesis conditions on the charge carrier storage capacity in different compounds was studied. The charge carrier storage capacity of $NaYGeO_4:Bi^{3+}$ and $NaYGeO_4:Bi^{3+},Eu^{3+}$ in Chapter 5 and of $LiLu_{0.5}Y_{0.5}SiO_4:Ce^{3+},Sm^{3+}$ and $LiLu_{0.25}Y_{0.75}SiO_4:Bi^{3+}$ in Chapter 6 can be improved significantly via changing crystal synthesis conditions. From the results in Chapters 2-6, we conclude that one can rationally design good afterglow and storage phosphors by combining vacuum referred binding energy (VRBE) diagram based “electron capturing and electron liberation” and “hole capturing and hole liberation” models with band structure engineering and crystal synthesis optimization.

Samenvating

In dit proefschrift hebben we twee typen ladingvangst- en ladingvrijlatingsprocessen onderzocht: (a) elektronenvangst en elektronvrijlating; (b) gatenvangst en gatenvrijlating. Beide processen (a) en (b) kunnen worden toegepast voor rationeel ontwerp van nagloei- en opslagfosforen in verschillende materialen.

Het 'elektronenvangst en elektronenvrijlatings'-model wordt gedetailleerd besproken in het eerste deel van Hoofdstuk 2, Hoofdstuk 5, en ten dele in Hoofdstuk 6. In Hoofdstuk 2 en 6 blijkt dat Ce^{3+} zich gedraagt als diepe gatenvanger en recombinatiecentrum, terwijl de andere lanthanide co-dopanten Ln^{3+} (Ln=Er, Nd, Ho, Dy, Tm, of Sm) minder diepe elektronenvangst centra zijn. In Hoofdstuk 5, gedraagt Bi^{3+} zich als een diepe gatenvanger en recombinatiecentrum terwijl de Bi^{3+} en Eu^{3+} co-dopanten minder diepe elektronenvangst centra zijn. Verschillende elektronenval dieptes kunnen worden gerealiseerd door de juiste keuze van de lanthanide co-dopanten of door Bi^{3+} co-dopering.

In dit proefschrift is de VRBE bij de bodem van de geleidingsband belangrijke voor het ontwerpen van nagloei- en opslagfosforen. Voor een vaste set van lanthanide en/of bismuth dopanten zoals in $Gd_{1-x}La_xPO_4$:Ce^{3+},Ho^{3+} (Hoofdstuk 2), $NaLu_{1-x}Y_xGeO_4$:Bi^{3+} (Hoofdstuk 5), en $LiLu_{1-x}Y_xSiO_4$:Ce^{3+},Sm^{3+} vaste stof oplossingen (Hoofdstuk 6), kunnen passende elektronenval dieptes van Ho^{3+}, Bi^{3+}, of Sm^{3+} worden verkregen door geleidingsband modificaties door aanpassing van x. Dit betekent dat men de TL gloeipiek temperatuur kan aanpassen voor nagloei- en opslagfosfor toepassingen.

Het 'gatenvangst en gatenvrijlatings'-model wordt in detail beschreven in het tweede deel van Hoofdstuk 2, Hoofdstuk 3, Hoofdstuk 4, en deels in Hoofdstuk 6. In deze hoofdstukken blijken Tb^{3+}, Pr^{3+}, en Bi^{3+} zich te gedragen als gatenvangers met valdiepte minder diep dan de elektronval op Eu^{3+} en Bi^{3+}. Eu^{3+} en Bi^{3+} fungeren dan als recombinatie centra. In vergelijking met het gebruikelijke 'elektronenvangst en elektronenvrijlatings'-model geeft het 'gatenvangst en gatenvrijlatings'-model ons een nieuwe methode om nagloei- en opslagfosforen te ontwikkelen. In dit gatenvrijlatingsmodel is de VRBE aan de top van de valentieband cruciaal voor het ontwerpen van een gatenval. Voor een vaste set lanthanide and/of bismuth dopanten zoals, in $Y_{1-x}Lu_xPO_4$:Eu^{3+},Tb^{3+} in Hoofdstuk 2, $Y_{1-x}Lu_xPO_4$:Eu^{3+},Bi^{3+} in Hoofdstuk 3, $La_{1-x}Gd_xPO_4$:Bi^{3+},Tb^{3+},Nd^{3+} in Hoofdstuk 4, $LiLu_{1-x}Y_xSiO_4$:Eu^{3+},Tb^{3+} en $LiLu_{0.25}Y_{0.75}Si_{1-y}Ge_yO_4$:$Bi^{3+}$ vaste stof oplossingen in

Hoofdstuk 6, kunnen aanpasbare gatenval dieptes van Tb^{3+}, Pr^{3+}, of Bi^{3+} gerealiseerd worden door valentieband modificatie door verandering van x of y .

Hoofdstuk 2 onthult dat: (1) Ln^{3+} (Ln=Sm, Eu, of Yb) ionen in YPO_4 zich gedragen als diepe elektronenval en recombinatie centra, terwijl Tb^{3+} en Pr^{3+} minder diepe gatenvangst centra zijn; (2) de gaten worden vrijgelaten van Tb^{4+} of Pr^{4+} bij een lagere temperatuur dan de elektronen om vervolgens te recombineren met elektronen gevangen op Ln^{2+} om karakteristieke 4f-4f emissie van Ln^{3+} te genereren gedurende de TL-uitlezing; (3) de gatenvallen in $LaPO_4$:Eu^{3+},Tb^{3+} kunnen gevuld worden door de Eu^{3+} ladingsoverdracht excitatie.

Hoofdstuk 3 onthult dat: (1) Bi^{3+} zich in YPO_4 kan gedragen als diepe elektronenvangst centrum terwijl Tb^{3+} en Pr^{3+} als minder diepe gatenvangst centra fungeren; (2) tijdens de TL-uitlezing, worden de gaten op Tb^{4+} of Pr^{4+} bij lagere temperatuur vrijgelaten dan de elektronen, om vervolgens te recombineren met de elektronen bij Bi^{2+} om hiermee karakteristieke Bi^{3+} A-band emissie te geven; (3) Bi^{3+} kan in YPO_4 als minder diepe gatenvangst centrum dienen terwijl de Ln^{3+} (Ln=Tm, Sm, Eu, of Yb) ionen de diepe elektronenvangst centra zijn; (4) Tijdens de TL-uitlezing worden de gaten bij lagere temperatuur vrijgelaten van Bi^{4+} dan de elektronen om dan te recombineren met elektronen gevangen in Ln^{2+} en karakteristieke Ln^{3+} 4f-4f emissie te geven; (5) de gatenvallen in YPO_4:Eu^{3+},Bi^{3+} kunnen gevuld worden door de Eu^{3+} ladingsoverdracht excitatie.

Op basis van de resultaten in Hoofdstuk 2 en 3, onthult Hoofdstuk 4 dat men rationeel een Nd^{3+} SWIR nagloeifosfor kan ontwerpen voor het tweede bio-imaging venster. Dit wordt bereikt door efficiënte energie overdracht van Bi^{3+} naar Nd^{3+} te combineren met een passende gatenval diepte verkregen door valentieband verschuiving in $La_{1-x}Gd_xPO_4$:Bi^{3+},Tb^{3+},Nd^{3+} door variatie van x. Dit is voor het eerst dat het gatenvrijlatingsmodel is gebruikt om een SWIR nagloeifosfor te ontwikkelen.

Hoofdstuk 6 onthult dat: (1) Tb^{3+}, Pr^{3+}, en Bi^{3+} in $LiLuSiO_4$ gaten minder diep vangen dan dat Eu^{3+} en Bi^{3+} elektronen vangen; (2) Tijdens TL-uitlezing worden de gaten eerder vrijgelaten van Tb^{4+}, Pr^{4+}, of Bi^{4+} dan de elektronen om te recombineren met de elektronen gevangen in Eu^{2+} of Bi^{2+} om karakteristieke Eu^{3+} 4f-4f emissie of Bi^{3+} A-band emissie te genereren; (3) de diepte van de gatenvallen van Tb^{3+}, Pr^{3+}, of Bi^{3+} in $LiLu_{1-x}Y_xSiO_4$ kunnen aangepast worden door valentieband verschuiving door x te variëren; (4) de Bi^{3+} gatenval in $LiLu_{1-x}Y_xSiO_4$:Bi^{3+} of $LiLu_{0.25}Y_{0.75}Si_{1-y}Ge_yO_4$:$Bi^{3+}$ kan gevuld worden door Bi^{3+} D-band excitatie; (5) wij hebben voor het eerst gedemonstreerd dat een goede Bi^{3+} opslagfosfor vervaardigd kan worden met $LiLu_{1-x}Y_xSiO_4$:Bi^{3+} door het ‘gatenvangst en gatenvrijlatings’-model.

In dit proefschrift is het effect van kristal synthese condities op de ladingsdrager opslagcapaciteit bestudeerd voor verschillende materialen. De ladingsdrager opslagcapaciteit van $NaYGeO_4:Bi^{3+}$ en $NaYGeO_4:Bi^{3+},Eu^{3+}$ in Hoofdstuk 5 en van $LiLu_{0.5}Y_{0.5}SiO_4:Ce^{3+},Sm^{3+}$ en $LiLu_{0.25}Y_{0.75}SiO_4:Bi^{3+}$ in Hoofdstuk 6 kunnen significant verbeterd worden door de kristal synthese condities aan te passen. Met de resultaten in Hoofdstukken 2-6 concluderen we dat men rationeel goede nagloei- en opslagfosforen kan ontwerpen door op Vacuum Referred Binding Energy (VRBE) diagram gebaseerde ‘elektronenvangst en elektronenvrijlating’ en ‘gatenvangst en gatenvrijlatings’-modellen te combineren met geleidings- en valentieband manipulatie en optimalisering van de kristalsynthese.

Acknowledgments

The PhD research at TU Delft is really a nice training for becoming a good scientist in material science. I learned a lot of knowledge not only on material science but more importantly about the methodology how to do a good scientific research. This research experience definitely has an important impact on my research career. This thesis was not possible without helps from all the people I met during my PhD journey at Delft.

First and foremost, special thanks go to my supervisor and promotor Prof. Dr. Pieter Dorenbos. Pieter, thank you for giving me this opportunity to study at your group and for financially supporting my PhD research project. I deeply appreciate everything you taught me during the past four years. With your guidance, I become a more and more independent researcher.

I would like to thank Dr. Anna Dobrowolska who developed the good storage phosphor $LiLuSiO_4:Ce^{3+},Tm^{3+}$ in the luminescence research group. I learned from your samples, experimental notebooks, and the published journal articles.

I am grateful to Dr. Hongde Luo who showed me how to use the experimental facilities in the luminescence research group at the beginning few months of my project. Thank you, Dr. Hongde Luo, for the nice discussion on photoluminescence and thermoluminescence properties of inorganic solid materials. You also inspire me on how to select a good research topic.

Special thanks go to Dr. Adrie Bos who taught me how to use thermoluminescence setup. I greatly appreciate that you provided me with the commercial storage phosphors that were used in this thesis.

I am thankful for the technical assistance provided by John Vlieland, Aday Josef, and Johan de Haas in the Luminescence Materials section. Without their support, I would not have been able to carry out all the nice measurements during the limited time at the Reactor Institute Delft.

I extend my thanks to all the colleagues in our group: Dr. Bert Hintzen, Dr. E. van der Kolk, Roy Awater, Weronika Wolszczak, Maarten Plokker, Giacomo Bizinoto Ferreira Bosco, Evert Merkx, Jumpei Ueda, Trudy Beentjes, etc. Thank you for creating a good research atmosphere. I also thank other people like Beien Wang, Ziyao Wang, and Mubiao Xie who helped me in some way to complete my thesis on time.

I would like to thank the support from the China Scholarship Council for my PhD scholarship.

Finally, I would like to deeply thank all the supports from my wife and her parents.

Tianshuai Lyu (吕天帅)
September 2020
Delft, the Netherlands

List of Publications

Publications related to this thesis

[1] **T. Lyu***, P. Dorenbos, Towards information storage by designing both electron and hole detrapping processes in bismuth and lanthanide-doped LiRE(Si,Ge)O_4 (RE=Y, Lu) with high charge carrier storage capacity, ***Chemical Engineering Journal*** (2020), 124776, DOI: https://doi.org/10.1016/j.cej.2020.124776.

[2] **T. Lyu***, P. Dorenbos, Vacuum referred binding energies of bismuth and lanthanide levels in ARE(Si,Ge)O_4 (A=Li, Na; RE=Y, Lu); towards designing charge carrier trapping processes for energy storage, ***Chemistry of Materials*** 32 (2020) 1192-1209.

[3] **T. Lyu***, P. Dorenbos, Designing thermally stimulated 1.06 μm Nd^{3+} emission for the second bio-imaging window demonstrated by energy transfer from Bi^{3+} in La-, Gd-, Y-, and $LuPO_4$, ***Chemical Engineering Journal*** 372 (2019) 978-991.

[4] **T. Lyu***, P. Dorenbos, Bi^{3+} acting both as an electron and as a hole trap in La-, Y-, and $LuPO_4$, ***Journal of Materials Chemistry C*** 6 (2018) 6240-6249.

[5] **T. Lyu***, P. Dorenbos, Charge carrier trapping processes in lanthanide doped $LaPO_4$, $GdPO_4$, YPO_4, and $LuPO_4$, ***Journal of Materials Chemistry C*** 6 (2018) 369-379.

Other Publications

[6] **T. Lyu**, P. Dorenbos, The dual role of Bi^{3+} in capturing electrons and holes in ARE(Si,Ge)O_4 (A=Li, Na; RE=Y, Lu) towards designing Bi^{3+} afterglow and storage phosphors, (2020) ***Manuscript in preparation***.

[7] **T. Lyu**, P. Dorenbos, Modelling zero-thermal-quenching phosphors by exploring both electron and hole trapping processes, (2020) ***Manuscript in preparation***.

[8] **T. Lyu**, P. Dorenbos, Charge carrier trapping processes in UCr_4C_4-type narrow band emission compounds, (2020) ***Manuscript in preparation***.

[9] **T.-S. Lv**, X.-H. Xu, X. Yu, J.-B. Qiu, Evolution in the Oxidation Valences and Sensitization Effect of Copper Through Modifying Glass Structure and Sn^{2+}/Si Codoping, ***Journal of the American Ceramic Society*** 98 (2015) 2078-2085.

[10] **T. Lv**, X. Xu, D. Zhou, J. Qiu, Influence of Cu^+ cations on photoluminescence properties of Tb^{3+} in Cu^+–Na^+ ion-exchanged sodium-borosilicate glasses, ***Journal of Non-Crystalline Solids*** 409 (2015) 14-19.

[11] **T. Lv**, X. Xu, X. Yu, D. Zhou, J. Qiu, Multi-wavelength-driven solar spectral conversion in P_2O_5-ZnO-Li_2O glasses for improving greenhouse photosynthetic activity, ***Ceramics International*** 41 (2015) 645-650.

[12] **T.-S. Lv**, X.-H. Xu, D.-C. Zhou, H.-L. Yu, J.-B. Qiu, Efficient multi-wavelength-driven spectral conversion from ultraviolet to visible in transparent borosilicate glasses, ***Ceramics International*** 40 (2014) 12367-12373.

[13] **T. Lv**, X. Xu, X. Yu, H. Yu, D. Zhou, J. Qiu, Tunable Mission and Trichromatic White-Emitting in Oxyfluoride Glasses by Utilization of Cu^+ Ions as Multiple Energy-Transfer Creators, ***Journal of the American Ceramic Society*** 97 (2014) 2897-2902.

[14] **T.-S. Lv**, X.-H. Xu, D.-J. Wang, L. Sun, J.-B. Qiu, Fabrication, structure and photoluminescence properties of Eu^{3+}-activated red-emitting $Ba_2Gd_2Si_4O_{13}$ phosphors for solid-state lighting, ***Optoelectronics Letters*** 10 (2014) 106-110.

[15] **T.-S. Lv**, X.-H. Xu, X. Yu, H.-L. Yu, D.-J. Wang, D.-C. Zhou, J.-B. Qiu, Tunable full-color emitting borosilicate glasses via utilization of Ce^{3+} ions as multiple energy transfer contributors, ***Journal of Non-Crystalline Solids*** 385 (2014) 163-168.

[16] **T.S. Lv**, X.H. Xu, D.C. Zhou, J.B. Qiu, Deep-UV-Driven Emission-Tailorable Borosilicate Glasses by Utilization of Sn^{2+} Cations as Versatile Energy-Transfer Establishers, ***ECS Journal of Solid State Science and Technology*** 3 (2014) R89-R94.

Curriculum vitae

Tianshuai Lyu (Lv)

Tianshuai Lyu (Lv) was born in Guizhou province of China in July 1989. He graduated from the Anshun second high school in 2008. He obtained his bachelor degree in Materials Science and Chemistry in 2012 from the Faculty of Materials Science and Engineering at the Tianjin University of Technology in China. The topic of his bachelor thesis is on the photoluminescence and thermoluminescence properties of $SrAl_2O_4:Eu^{2+},Dy^{3+}$ based glass ceramics. In June 2015, he received his master degree in Materials Science from the Faculty of Materials Science and Engineering at the Kunming University of Science and Technology in China. His master research was supervised by Prof. Xuhui Xu and Prof. Jianbei Qiu. The topic of his master thesis is about photoluminescence properties of Ce^{3+}, Sn^{2+}, and Cu^{+} based oxide glasses for white-emitting LED-based lighting. He came to the Netherlands in October of 2016 and joined the Luminescence Materials Group at the Faculty of Applied Sciences at Delft University of Technology. His PhD project entitled “Engineering afterglow and storage phosphors” was carried out under the supervision of Prof. Pieter Dorenbos. His current research interest is the discovery of new optical materials for energy storage applications.